Spring 2021

Photonic Signal Processing Using Nonlocal Brillouin Interactions

Shai Gertler
Yale University Graduate School of Arts and Sciences, shaigertler@gmail.com

Abstract

Photonic Signal Processing Using Nonlocal Brillouin Interactions

Shai Gertler

2021

In this dissertation, we explore the possibilities offered by the unique properties of Brillouin scattering to implement signal-processing operations in photonic devices. Brillouin scattering —the coupling of light and sound waves— enables access to long-lived acoustic modes directly from the optical domain and results in processes very different compared with other optical systems. Furthermore, when utilized to process microwave signals, Brillouin-active photonic systems are compelling for their ability to bridge the vastly different frequency scales of microwave and optical signals.

We analyze the dynamics of forward Brillouin scattering, showing how they can give rise to a nonlocal effect, in stark contrast with other optical nonlinear interactions. We describe how these unusual properties can be exploited to engineer new types of devices, where highly delocalized acoustic modes mediate scattering processes between spatially separated light waves. Examining the potential of utilizing this scheme to perform filtering operations, we identify a path towards low-noise and low-distortion performance for these Brillouin-based technologies. Furthermore, we show how these photonic-phononic devices can be implemented in a standard silicon platform.

Using these devices, we present tunable narrowband microwave-photonic filters, performing both bandpass and notch filtering operations demonstrating sharp frequency roll-off and excellent out-of-band rejection, previously unattainable in silicon photonics. Looking forward, we explore the potential of utilizing multiple optical spatial modes in such devices, showing their unique properties, and study new waveguide designs that could enable silicon Brillouin-active devices to handle higher optical power. In addition to bringing greatly enhanced functionality to silicon photonics, we demonstrate the reliability and robustness of the devices, key features for high-impact optomechanical applications. The photonic circuits demonstrated here could be another step towards integrated signal processing systems.

Photonic Signal Processing Using Nonlocal Brillouin Interactions

A Dissertation
Presented to the Faculty of the Graduate School
of
Yale University
in Candidacy for the Degree of
Doctor of Philosophy

by
Shai Gertler

Dissertation Director: Peter T. Rakich

June 2021

Contents

Acknowledgements

This dissertation is the culmination of work done over the past few years, which would have not happened without the help of many people.

First of all, I thank my advisor, Prof. Peter Rakich. Although my resume might be quite different than that of many other students, I am grateful for the trust you had to take me into the group. Your positive attitude is truly inspiring, and your kindness, encouragement, and guidance, have made the last few years a memorable experience. You always remember that we are all people before we are students or scientists, and I have learned from you much more than only physics.

I would also like to thank Prof. Hui Cao, Prof. Owen Miller, and Prof. Avi Zadok for taking the time to be on my dissertation committee, and for their teaching and mentorship over the years.

Work in the Rakich lab has always been a team effort, and I thank all group members I had worked with, past and present: Ryan, Will, Prash, Eric, Nils, Yishu, Royce, Freek, David, Taekwan, Naijun, Maggie, Haotian, and Yanni.

I especially want to thank Prash, Eric, and Nils who have become some of my closest friends. I was lucky enough not only to have learned from them immensely, but we also share great memories of nights out in New Haven, and adventures in Tel Aviv and Kathmandu.

Despite its somewhat gloomy outer appearance, Becton Center has been a welcoming and supportive environment over the past few years, thanks to the wonderful people occupying it. The Applied Physics administrative staff — Maria Rao, Terri Evangeliste, Nuch Graves, Giselle Maillet, and Alex Bozzi for their help and support, and for fostering the Applied Physics family. Our conversations at coffee breaks were the highlight of many days, and always gave a morale boost which was much more important than the caffeine.

The fabrication experts, Dr. Michael Rooks at YINQE and the Becton Cleanroom team, Dr. Yong Sun, Sean Rinehart, Kelly Woods, as well as Michael Powers, Chris Tillinghast, and Jim Agresta for sharing their expertise.

I have had the privilege of befriending many of the people in our department, and I especially want to thank Hasan, Wen, and Stefan, from my time working at the Hui Cao lab.

I also want to thank Dr. Larry Wilen with whom I had the pleasure of working as a teaching fellow. The hours we spent constructing strange new musical instruments were a lot of fun and a refreshing contrast from my usual work.

I thank my friends from New Haven and around the world — Abhi, Rimpi, Chen, Naor, Zachi, Tabea, Dan, Laura, Bill, Beth, Jay, Dev, Josh, Alex, Ziming, Michael, Scott, Noam, Tanya, Olga, Sam, Eyal, Rotem, and many others who were part of my life over this period.

My wonderful neighbors, Keith, Emilia, Kenny, and Uri, the 20 Eld St. family, for making our house a real home, which was particularly important in this last socially-distant year.

Finally, my supporting family, especially my parents who have encouraged me in everything I have ever done, cultivated my curiosity, and always remind me not to forget to make time for music.

And Sandra — we're on this journey together.

Musical snippets: Robert Schumann. *Op.15*, 1838.

List of Figures

List of Tables

Chapter 1

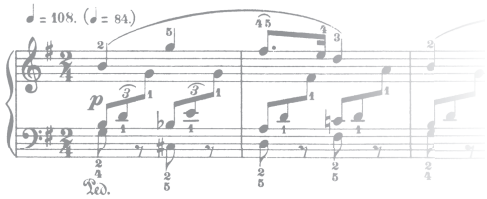

Introduction

1.1 A brief history of Brillouin scattering

Inelastic light scattering was first discussed by Lord Rayleigh, Larmor, and Raman in the early twentieth century [1–3], and has since opened the door to an entire field of research, deepening our understanding into light-matter interaction, and leading to numerous technological applications. One of these scattering phenomena is Brillouin scattering, in which light interacts with sound waves resulting in a nonlinear optical effect. Here, we summarize some of the important landmarks in the discovery and research of Brillouin scattering over the past century.

When inelastic scattering occurs, light exchanges energy with the medium, resulting in a change of the optical wavelength. The change in energy can be the result of the motion of particles in the medium due to thermal fluctuations, Doppler-shifting the frequencies of the optical fields. When considering vibrations of molecules, this results in what we now refer to as *Raman* scattering, first demonstrated in 1922 [4]. The first theoretical predictions of light scattering from traveling acoustic waves were reported by Brillouin in 1922 [5] and Mandelstam is said to have made similar predictions as early as 1918, although his results were not published until 1926 [6]. This effect —light interacting with acoustic waves— now referred to as *Brillouin* scattering, was first measured in liquids using a mercury lamp

in 1930 by Gross [7], and further experimental demonstrations were soon to follow [8–10]. Interestingly, in 1932 Debye studied light scattering from acoustic waves generated in liquid using a quartz crystal and a radio-frequency generator [11], showing multiple scattering orders, as is obtained by a grating. Such scattering phenomena were subsequently used as a technique for the measurement of material properties [12–14], however, all of these measurements relied on thermally-induced motion in a material, where the acoustic fields are not affected much by the propagation of light —commonly referred to as *Brillouin light scattering* (BLS).

Only after the introduction of the laser in 1960 [15], providing a bright, coherent light source, *stimulated Brillouin scattering* (SBS) could be demonstrated experimentally in quartz and sapphire by Chiao, Townes, and Stoicheff in 1964 [16]. In the same year, Bloembergen presented a theoretical framework describing stimulated Brillouin and stimulated Raman scattering processes, where the coupling between light and sound waves is derived both classically and quantum mechanically [17]. In a stimulated process, light does not only scatter off the acoustic waves present in the material but also drives the acoustic waves through optical forces. Subsequently, stimulated Brillouin scattering was also measured in liquids [18, 19] and gases [20].

With the development of optical fiber, extremely long optical interaction lengths were possible with the novel platform, opening a new era of nonlinear optical experiments. Thereafter, Brillouin scattering was demonstrated in fiber in 1972 [21]. In the context of optical communication, Brillouin scattering sets a limit to the power handling capability of a system, as it depletes the optical signal and results in unwanted back reflections [22, 23]. The mitigation of these effects in fiber-based systems is an active area of research [24–26].

Brillouin interactions were studied up to this point in a backward geometry, where the incident and scattered light counter-propagate to fulfill the necessary conditions for efficient scattering. However, optical fibers enabled the demonstration of Brillouin scattering in a forward geometry, where the optical fields co-propagate, which was experimentally demonstrated in 1985 [27]. This can be achieved in systems that confine sound waves in the transverse direction, as is the case with an optical fiber. Forward Brillouin scattering

was later shown to be possible between distinct optical modes, first demonstrated in 1990 in dual-mode fiber [28].

The development of photonic-crystal fibers enabled the design of structures confining light and sound waves to small spatial regions compared with typical optical fibers, resulting in even stronger interactions [29, 30]. Furthermore, hollow-core fibers enable the measurement of Brillouin scattering with gases trapped within the fiber [31, 32], and by using liquid-core fibers unprecedented forward Brillouin gain in liquids has been demonstrated [33].

An insightful perspective of the history of Brillouin scattering can be found in Ref. [34].

1.1.1 Integrated Brillouin photonics

The advances in integrated photonic circuits over the last decade have opened the door to a new class of tailorable acousto-optic interactions. Through the use of micro- and nano-fabrication techniques, the confinement of fields to small spatial regions, with a high degree of control over the device geometry, has produced many new Brillouin-active systems [35]. These include micro-resonators [36–38] and micro-spheres [39, 40] utilizing high quality-factor whispering-gallery modes. In the context of integrated waveguides, backward Brillouin scattering was first demonstrated in a As_2S_3 chalcogenide rib waveguide [41], showing extremely high gain thanks to its property of guiding both light and sound in the waveguide core. Weaker Brillouin scattering has been reported in silicon nitride (Si_3N_4) [42], however, silicon nitride waveguides have shown Brillouin lasing utilizing the acoustic waves in an adjacent silica (SiO_2) layer [43]. Achieving Brillouin scattering in a standard silicon-on-insulator (SOI) —perhaps the most well-developed photonic integrated circuit platform— has been challenging, requiring the separation of wave-guiding structures from the buried oxide layer to prevent strong acoustic dissipation [44].

1.1.2 Brillouin scattering in silicon

Silicon has numerous advantages as a photonic platform due to its high refractive index, the ability to integrate electrical components in the same material layer, and vast fabrication

knowledge and infrastructure thanks to the CMOS industry [45–48]. Furthermore, the development of optical components within the silicon platform, including detectors [49, 50] modulators, filters [51,52] [53], amplifiers [54], and lasers [55,56] could enable fully integrated silicon-photonic circuits for future technologies [57–59].

In the context of nonlinear optics, the tight confinement of light within a small waveguide results in strong optical nonlinearities such as Kerr [54,60] and Raman [55,61], which can be utilized for silicon-photonic technologies [62]. However, the buried oxide under the silicon guiding layer has a lower sound velocity compared with silicon, such that the acoustic fields taking part in Brillouin interactions dissipate into the device substrate.

Only once device geometries separating the waveguides from the silica under-cladding were designed, Brillouin scattering was measured in silicon for the first time [44], showing gain orders-of-magnitude larger than possible in optical fiber. These devices utilized a silicon waveguide embedded in a tensile silicon nitride membrane which was used for guiding acoustic modes. Interestingly, the photo-elastic properties of silicon show the strongest Brillouin interaction in a forward geometry, such that all optical fields are co-propagating.

Subsequent device designs have utilized a standard silicon-on-insulator platform, demonstrating net Brillouin gain [63, 64]. Additionally, by using multi-mode waveguides, forward inter-modal scattering has been demonstrated in silicon between two distinct spatial modes [65]. The vastly different properties of inter-modal scattering has enabled the demonstration of high-gain amplifiers [66], lasers [56] and nonreciprocal optical transmission [65].

1.2 Brillouin-based technologies

Brillouin scattering has several unique properties that make it an attractive scientific research tool, as well as having high-impact technological applications. The acoustic waves taking part in Brillouin interactions are typically in the microwave range, making it an ideal candidate for many microwave-photonic systems [67]. The slow speed of sound, typically five orders of magnitude slower than that of light, enables long delay times that can be useful for information storage and filtering [68]. Furthermore, the acoustic properties can

be tailored by tuning the optical wavelength, or through the device geometry [69]. Interestingly, the dependence of these properties on the strain, temperature, and the environment can be utilized to design high-resolution distributed sensors [70]. Additionally, by utilizing traveling acoustic waves, nonreciprocal light propagation can be engineered [71]. In this section, we present a summary of applications utilizing Brillouin scattering. Further review of the subject can be found in Refs. [35, 72].

The unique dynamics of Brillouin scattering, with its inherent nonlinear nature, have been used to demonstrate optical pulse shaping [73], pulse compression [74–76], optical limiting [77], beam combining [78,79], and mode filtering [80–82]. Recently, Brillouin scattering was also used to study exceptional points in an optical fiber [83].

Another interesting property of Brillouin scattering is that the backward scattered light produced through the Brillouin process is a phase conjugated version of the incident light [84,85]. Such phase conjugation can be of practical use, for example, to reverse aberrations and distortions in the wavefront of an optical beam, improving beam quality and power scaling [86].

The acoustic properties of a material are highly dependent on temperature and strain, which in turn translate into a measurable optical response [87–89]. This has been used to develop Brillouin-based fiber sensors, enabling distributed measurements of strain and temperature over large ranges (∼100 km) and high resolution (∼10 mm) [90–93]. More recently, forward Brillouin scattering has been used in fiber sensors, where the unique properties of forward Brillouin interactions enable the sensing of material properties and the environment outside the fiber [94–97].

Brillouin-enhanced four-wave-mixing, also referred to as a Brillouin dynamic grating, is a scheme in which two 'pump' laser beams are used to produce periodic refractive index variations in an optical fiber through electrostrictive optical forces. This perturbation acts as a narrowband Bragg grating, reflecting a separate 'probe' beam [98, 99]. Such schemes have been used to produce filters [100–102], distributed fiber sensors [103, 104], as well as phase conjugation [105, 106], and other signal processing operations [107, 108]. This process has also been demonstrated in a chip-integrated platform [109].

Brillouin scattering can be used for amplification, where power is transferred from a strong 'pump' laser source to a weak input signal through the scattering process. This effect was first used to demonstrate amplification of short pulses using gas cells [110, 111]. In fiber optics, the fiber itself can be utilized as the gain medium. For example, Brillouin amplification has been used to offset propagation losses in optical fiber over large distances [112–117].

The first demonstration of Brillouin lasing used a segment of optical fiber to provide gain within a free-space optical resonator [118]. Subsequently, using optical fiber couplers, all-fiber Brillouin lasers were demonstrated to have low threshold power [119] and high coherence [120, 121]. More recently, Brillouin lasers have also been demonstrated on-chip within several material platforms [43, 56, 122, 123]. An intriguing application of Brillouin lasers is to design optical gyroscopes, utilizing the Sagnac effect to detect the phase shift between two counter-propagating laser modes. Such schemes have been demonstrated in Brillouin fiber lasers [124, 125], and more recently in chip-scale resonators [126, 127].

The Brillouin process does not only amplify a probe signal but also induces a frequency-dependent phase shift, which changes the effective velocity of light propagating in the medium. The controlled phase shift can be used to generate 'slow' and 'fast' light, which can be tuned using an optical pump tone [128]. Such schemes can have applications in the processing of data in communication systems and as well as enhancing nonlinear interactions [129], and this effect has been demonstrated in multiple types of optical fibers [130–132], as well as in integrated platforms [133]. Furthermore, this strategy could be used for the storage of optical pulses which can be retrieved at a later time [68, 134, 135].

Another active area of research where Brillouin scattering can have a potential technological impact is the design of chip-integrated optical isolators. The traveling-wave nature of the acoustic field can be utilized to produce nonreciprocal optical transmission [136], as was first demonstrated in photonic crystal fiber [71, 137], and more recently in a chip-integrated platform [138, 139].

In the field of microwave-photonic systems —where the optical domain is utilized to perform RF signal processing operations— Brillouin-based devices have shown great promise

as a strategy to develop new technology. Brillouin scattering provides a natural interface between the optical and microwave domains, combining wide-band operation possible in photonic systems, and high spectral resolution enabled by the acoustic field properties. An important example is microwave-photonic filters, where Brillouin scattering enables filtering with a spectral resolution that is challenging to achieve in all-optical systems thanks to the long lifetime of the acoustic waves taking part in the interaction. This is similar to the role played by acoustic waves in microwave systems [140], which are accessible directly from the optical domain using Brillouin interactions. The possible tunability of such schemes — challenging to achieve with typical microwave components— has been demonstrated both in optical fibers [69, 141], as well as chip-integrated systems [142–144].

The frequency shift imparted on optical tones by the Brillouin scattering process enables the generation of microwave signals through optical mixing. For example, by combining unshifted light with Brillouin-scattered light, microwave signals can be synthesized [145], and methods utilizing Brillouin scattering for amplification of specific sidebands of a modulated signal have also been demonstrated [146, 147]. Additionally, utilizing Brillouin scattering within an optoelectronic oscillator can result in higher coherence of the microwave signals [148]. Another intriguing method to generate low-noise microwave signals is by using cascaded Brillouin lasing, in which a frequency comb is generated [149]. Using ultra-high quality factor cavities, many lasing tones can be produced through multiple Brillouin interactions [150, 151], and by combining different comb lines on a photodiode, highly coherent microwave signals can be produced [38].

Our final example of Brillouin-based microwave-photonic signal processing is implementing an RF phase shifter. Brillouin scattering can be used to induce a phase shift to a modulation sideband of an optical carrier encoding RF information, resulting in a phase shift of the RF signal after its conversion back to the microwave domain, enabling wideband operation and large phase shifts [152, 153].

1.3 Summary of dissertation

In this dissertation, we will explore how the unique properties of forward Brillouin interactions can be utilized for novel device designs, with applications in microwave and optical signal processing. We report recent results, both theoretical analyses as well as experimental demonstrations, and explore possible future directions for optical and microwave technologies utilizing traveling-wave acousto-optic interactions. The dissertation is structured as follows:

Chapter 2

We start by introducing Brillouin scattering theory in the context of nonlinear optical phenomena. Focusing on guided-mode systems, we analyze three types of Brillouin interactions, namely backward scattering, forward inter-modal scattering, and forward intra-modal scattering. Using a Hamiltonian formalism, we will analyze the dynamics of the optical and acoustic fields taking part in each process.

Chapter 3

Next, we study the unique nonlocal nature of forward Brillouin interactions, namely how optical fields in two spatially separated waveguides take part in the same nonlinear process. Using a Hamiltonian framework, we theoretically analyze possible devices utilizing such interactions and show how these nonlocal interactions can utilize acoustic multi-mode interference to produce a multi-pole frequency response, very different from typical acoustic resonances. This chapter is based on work published in Ref. [154]:

S. Gertler, P. Kharel, E. A. Kittlaus, N. T. Otterstrom, and P. T. Rakich. "Shaping nonlinear optical response using nonlocal forward Brillouin interactions," *New Journal of Physics*, 22(4):043017, 2020.

Chapter 4

Here, we will introduce the concept of a microwave-photonic link, where microwave signals are encoded onto an optical carrier for transmission and processing before demodulating

them back to the microwave domain. We will analyze in detail an example of a microwave-photonic link, defining the parameters and figures of merit useful for design and analysis, as well as possible noise sources. Additionally, we will explore the opportunities that Brillouin-based devices enable for microwave-photonic technologies.

Chapter 5

In this chapter we focus on a novel *photonic-phononic emit-receive* (PPER) scheme, utilizing nonlocal Brillouin interactions for microwave-photonic filtering. Using the framework developed in Chapters 3 and 4, we will analyze a PPER-based microwave-photonic bandpass filter, exploring the microwave link properties, noise sources, and nonlinearities. We will identify paths towards high-performance systems based on these schemes, and analyze in detail the opportunities of operating at low temperatures, where Brillouin noise and acoustic dissipation are vastly reduced. This chapter is based on work published in Ref. [155]:

S. Gertler, E. A. Kittlaus, N. T. Otterstrom, P. Kharel, and P. T. Rakich. "Microwave filtering using forward Brillouin scattering in photonic-phononic emit-receive devices," *Journal of Lightwave Technology*, 38(19):5248–5261, 2020.

Chapter 6

We will describe practical design considerations when implementing a multi-pole PPER device in a standard silicon-on-insulator platform. We will show how acoustic mode engineering enables the controlled coupling of acoustic modes required for multi-pole frequency response, and demonstrate how it can be tailored through the device geometry. Additionally, we will show that these silicon devices are a feasible strategy for real-world applications, demonstrating high yield and robust performance using standard CMOS fabrication methods. This chapter is based on work published in Ref. [156]:

S. Gertler, E. A. Kittlaus, N. T. Otterstrom, and P. T. Rakich. "Tunable microwave photonic filtering with high out-of-band rejection in silicon," *APL Photonics*, 5(9):096103, 2020.

Chapter 7

Using the devices discussed in the previous chapter, we present new microwave-photonic multi-pole filters with ∼100× higher spectral resolution than previously possible in silicon photonics. Additionally, we will demonstrate how such filters can be tuned over a large spectral range without degrading their narrowband lineshape. This chapter is based on work published in Ref. [156]:

S. Gertler, E. A. Kittlaus, N. T. Otterstrom, and P. T. Rakich. "Tunable microwave photonic filtering with high out-of-band rejection in silicon," *APL Photonics*, 5(9):096103, 2020.

Chapter 8

In this chapter, we will show how a narrowband microwave-photonic notch filter —suppressing a narrow spectral band— can be obtained by utilizing a PPER device within an interferometer. Through coherent signal interference, we will demonstrate filters with ∼MHz resolution, and up to 60 dB of signal suppression. Furthermore, we will show how acoustic band engineering can be utilized to suppress possible distortions in the filter pass-band, and how both single- as well as multi-pole filters can be obtained. Additionally, we show that the notch-frequency can be tuned, enabling selective suppression of interfering signals with record-high spectral resolution in an integrated silicon-photonic chip.

Chapter 9

Here, we will explore the possibilities of using inter-modal Brillouin scattering within a PPER scheme, which has vastly different properties compared to the intra-modal process we have considered so far. We will analyze the fields propagating in such a device, and show how nonreciprocal transmission can arise. Such devices could be used to produce integrated optical isolators, and we will explore strategies to enhance their potential performance. Finally, we will present inter-modal PPER devices utilizing acoustic-mode interference to produce a narrow two-pole frequency response, which could be used for novel optical and microwave signal processing schemes. Parts of this chapter are based on work published in

Ref. [139]:

E. A. Kittlaus, N. T. Otterstrom, P. Kharel, S. Gertler, and P. T. Rakich. "Nonreciprocal interband Brillouin modulation," *Nature Photonics*, 12(10):613–619, 2018.

Chapter 10

Finally, we will address one of the fundamental limitations in silicon photonics, namely its limited power handling due to nonlinear loss. As nonlinear loss depends on the effective area of the optical modes, we study possible Brillouin-active waveguide designs where optical power is distributed between multiple guiding regions. Additionally, we will explore a different strategy of power distribution, where a signal is processed in multiple Brillouin-active regions in parallel. We will show how such a scheme can be implemented using a balanced Mach-Zehnder interferometer, which has the added benefit of separating a strong pump tone from a weak signal at the device output port.

Chapter 2

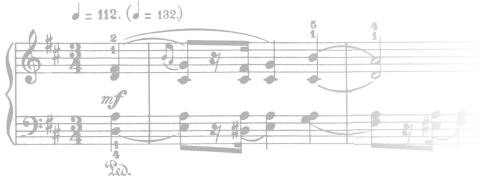

Brillouin scattering

2.1 Nonlinear optics and optical forces

We start our analysis of this optical phenomenon, as might be expected, by introducing Maxwell's equations [157, 158]

$$\begin{aligned} \nabla \times \mathbf{E} &= -\frac{\partial}{\partial t}\mathbf{B}, & \nabla \cdot \mathbf{D} &= \rho, \\ \nabla \times \mathbf{H} &= \frac{\partial}{\partial t}\mathbf{D} + \mathbf{J}, & \nabla \cdot \mathbf{B} &= 0, \end{aligned} \tag{2.1}$$

where $\mathbf{E}$ and $\mathbf{H}$ are the electric and magnetic field vectors, and $\mathbf{D}$ and $\mathbf{B}$ are the electric and magnetic displacement fields, respectively. The constitutive relations between the polarization of the medium and the displacement fields are defined by

$$\mathbf{D} = \epsilon_0 \mathbf{E} + \mathbf{P}, \qquad \mathbf{B} = \mu_0 \mathbf{H} + \mu_0 \mathbf{M}, \tag{2.2}$$

where ϵ_0 and μ_0 are the vacuum permittivity and vacuum permeability, respectively, related by $\epsilon_0 \mu_0 = c^{-2}$, where c is the speed of light in vacuum.

Throughout this work, we will be interested in charge-neutral dielectric systems where there are no free charges ($\rho = 0$) and no free currents ($\mathbf{J} = 0$), and assume that the medium

is nonmagnetic ($\mathbf{M} = 0$), which enables us use Eqs. (2.1) and (2.2) to arrive at

$$\nabla \times \nabla \times \mathbf{E} + \frac{1}{c^2}\frac{\partial^2}{\partial t^2}\mathbf{E} = -\frac{1}{\epsilon_0 c^2}\frac{\partial^2}{\partial t^2}\mathbf{P}. \tag{2.3}$$

The polarization density ($\mathbf{P}$) represents the response of a material to an electric field ($\mathbf{E}$), and we can expect them to have some functional relationship, which we can express as a power series

$$\mathbf{P} = \epsilon_0\chi^{(1)}\mathbf{E} + \underbrace{\epsilon_0\chi^{(2)}\mathbf{E}\mathbf{E} + \epsilon_0\chi^{(3)}\mathbf{E}\mathbf{E}\mathbf{E} + \dots}_{\mathbf{P}^{\mathrm{NL}}} \tag{2.4}$$

Here, we have factored out ϵ_0 and expressed the series coefficients as the susceptibilities $\chi^{(n)}$. For simplicity, in the equation above and for the rest of this section we assume scalar fields[1] and instantaneous material response[2]. The first term of the series is the linear response of the material, and we denote the rest of the series —describing the *nonlinear* response— as $\mathbf{P}^{\mathrm{NL}}$. Plugging Eq.(2.4) into Eq. (2.3) yields the nonlinear wave equation

$$\nabla \times \nabla \times \mathbf{E} + \frac{\epsilon_r}{c^2}\frac{\partial^2}{\partial t^2}\mathbf{E} = -\frac{1}{\epsilon_0 c^2}\frac{\partial^2}{\partial t^2}\mathbf{P}^{\mathrm{NL}}, \tag{2.5}$$

where $\epsilon_r = 1 + \chi^{(1)}$ is the dielectric constant of the medium. This is the general form of the electric field wave equation commonly used in nonlinear optics [157], where we see that the polarization acts as a source term driving the electric fields.

We can see from Eq. (2.4) that the driving term includes products of the electric field, leading to frequency mixing, such that the spectral contents of the polarization can include sum and difference combinations of the electric field frequency components. For example, in a second-order ($\chi^{(2)}$) process, a field with two frequency components $E(t) = E_1\cos(\omega_1 t) + E_2\cos(\omega_2 t)$ will result in polarization $P(t) \propto E^2(t) = P_0 + P_1\cos(2\omega_1 t) + P_1\cos(2\omega_2 t) + P_{12}\cos((\omega_1 - \omega_2)t) + P_{21}\cos((\omega_2 - \omega_1)t)$, leading to nonlinear phenomena such as second-harmonic generation, sum-frequency generation and difference-frequency

1. More generally, the susceptibilities are tensors relating the different components of the fields $P_i = \epsilon_0\sum_j \chi^{(1)}_{ij}E_j + \epsilon_0\sum_{jk}\chi^{(2)}_{ijk}E_jE_k + \epsilon_0\sum_{jk\ell}\chi^{(3)}_{ijk\ell}E_jE_kE_\ell \dots$.

2. This is equivalent to assuming a lossless, dispersionless material. In the general case, we will have $P(t) = \epsilon_0\int_0^\infty dt'\chi^{(1)}(t-t')E(t') + \epsilon_0\int_0^\infty dt'dt''\chi^{(2)}(t',t'')E(t-t')E(t-t'') + \dots$.

generation. A common example of a third-order ($\chi^{(3)}$) nonlinearity is the *Kerr* effect, where the refractive index of a medium depends on the intensity of the electric field through electronic degrees of freedom. Another third-order effect is *Raman* scattering, arising from vibrational degrees of freedom in the material lattice structure, also referred to as optical phonons. In this work, we will focus on *Brillouin* scattering, in which the interaction of the electric fields with acoustic waves in the materials —also referred to as *acoustic phonons*— results in a third-order optical nonlinearity, as we shall describe in the next sections.

The effects of acoustic waves on an optical medium can be separated into two terms: *photoelasticity* and the effects of a *moving boundary*.[3] The time-depended perturbation of the optical properties results in light scattering from an optical field, with an induced wavelength shift.

Photoelasticity refers to the change in the electric susceptibility (or equivalently, refractive index) under mechanical strain. This is commonly described using a photoelastic tensor $p_{ijk\ell}$, relating the optical susceptibility tensor element χ_{ij}^{PE} to the strain tensor element $S_{k\ell}$ [160]

$$\chi_{ij}^{\mathrm{PE}} = \epsilon_r^2 \sum_{k\ell} p_{ijk\ell} S_{k\ell} = \epsilon_r^2 \sum_{k\ell} p_{ijk\ell} \partial_k u_\ell, \tag{2.6}$$

where in the last step we have used the symmetry of the photoelestic tensor to express this in terms of the mechanical displacement component u_ℓ [159].

The moving boundary term is the displacement of material boundaries by the acoustic waves, which deforms the optical fields at material interfaces, as a consequence of the continuity conditions for the electric fields across dielectric boundaries. Since this occurs only at material boundaries, it is not present in bulk geometries. This effect grows as the cross-section of waveguides is reduced, and in sub-wavelength scale waveguides, it can be the dominant interaction [161].

These processes describe the effects of acoustic fields present in the material, on the optical fields propagating in the medium, without considering the back-action of the light waves on the acoustic fields. This is the case of *spontaneous* Brillouin scattering, where phonons

3. In some cases there may be a third term corresponding to the effects of dynamic magnetic coupling, however, it is very weak and can be ignored in most cases [159].

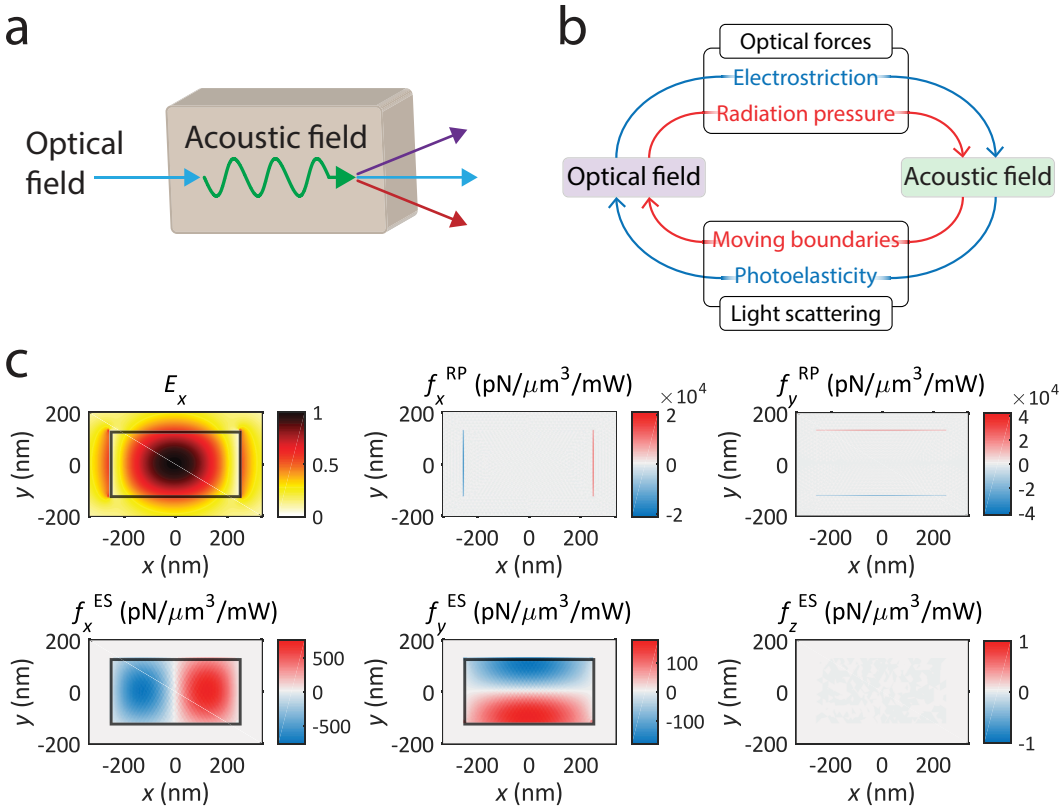

Figure 2.1: **(a)** In a Brillouin scattering process, light interacts with acoustic waves in a medium. The scattering is inelastic, resulting in frequency shifts of the optical field. **(b)** Electric fields in a material can drive acoustic fields through optical forces, namely radiation pressure and electrostriction. The acoustic fields can result in light scattering, yielding a self-reinforcing feedback loop. **(c)** Simulating optical forces as a result of a TE-like mode guided in a 250 × 500 nm silicon waveguide. E_x: x-component of the electric field at a wavelength $\lambda = 1550$ nm, f_i^{RP}: radiation pressure forces ($i = \{x, y\}$), f_i^{ES}: electrostrictive pressure ($i = \{x, y, z\}$). The forces are normalized by the optical power.

are present in the material as a result of the thermal occupation of the acoustic mode (with a scattering rate that is proportional to the temperature). This can also be the case in acousto-optic modulators, which use electromechanical transduction to generate strong acoustic waves in the medium regardless of the presence of the optical fields. In contrast, in *stimulated* Brillouin scattering, the optical fields themselves generate forces, driving the same acoustic waves that scatter light. This feedback loop, between optical forces and light scattering, is illustrated schematically in Fig. 2.1(b). For each of the light-scattering mechanisms we have described, photoelasticity and moving boundaries, there is a corresponding driving mechanism, namely *electrostriction* and *radiation pressure*, respectively [159].

Electrostriction is the strain induced in a dielectric material as a result of electromagnetic fields. This can be expressed in terms of the electrostrictively-induced stress [162]

$$\langle \sigma_{ij}^{\mathrm{PE}} \rangle = -\frac{1}{2}\epsilon_0 \epsilon_r^2 \sum_{k\ell} p_{ijk\ell} \langle E_k E_\ell \rangle, \tag{2.7}$$

which can be related to an electrostricive force[4], $f^{\mathrm{ES}} = -\nabla \cdot \sigma^{\mathrm{PE}}$.

Radiation pressure can be interpreted as the result of the reflections of light off waveguide boundaries, which is the mechanism used to guide optical fields. The momentum transferred between the optical fields and the waveguide surface due to this reflection results in a force that can be derived directly from the Maxwell stress tensor [163], or from the continuity conditions derived from Maxwell's equations [159]. The force resulting from radiation pressure imparted by the optical field on waveguide boundaries is given by $f^{\mathrm{RP}} = -\nabla \cdot \sigma^{\mathrm{RP}}$, where

$$\sigma_{ij}^{\mathrm{RP}} = -T_{ij} = -\epsilon_0 \epsilon_r \left(E_i E_j - \frac{1}{2}\delta_{ij} |E|^2 \right) - \mu_0 \mu_r \left(H_i H_j - \frac{1}{2}\delta_{ij} |H|^2 \right), \tag{2.8}$$

and T_{ij} is the commonly used Maxwell stress tensor element[5] [162]. Fig. 2.1(c) shows the simulation of a TE-like optical mode in a silicon waveguide and the calculated optical forces it generates. We can see that radiation pressure only impacts the boundaries of the waveguide, while electrostriction is present in the volume of the waveguide. Furthermore, the simulation shows us that the x-polarized electric field generates the strongest electrostrictive forces along the x axis. This is due to the fact that in silicon, the largest photoelastic tensor element is p_{11}, coupling the electric field with a parallel strain component.

Both electrostrictive and radiation pressure forces scale with the light field intensity $f \propto \mathbf{E}^2$ (see Eqs. (2.7) and (2.8)) and contribute to a $\chi^{(3)}$ nonlinearity through Brillouin

4. Electrostrictive forces include both a body force inside the material, as well as an electrostrictive pressure at interfaces where discontinuous stresses are present [163].

5. This is the form of the Maxwell stress tensor to be used in dielectrics, such that its divergence gives us the forces on material boundaries, and does not represent body stress (the diagonal elements do not represent pressure). For further discussion see Refs. [164, 165].

interactions. We can see this by analyzing the elastic displacement[6] driven by the optical forces, which can be written as a wave equation

$$\frac{\partial^2}{\partial t^2}u + \Gamma\partial_t u - v_{\mathrm{ac}}^2\nabla^2 u = \frac{1}{\rho}\langle f\rangle, \tag{2.9}$$

where Γ is the acoustic damping rate, v_{ac} the acoustic velocity and ρ the material density. We see that the displacement is proportional to the force, such that $u \propto \mathbf{E}^2$ and since the acoustic displacement linearly affects the optical susceptibility $\chi^{\mathrm{NL}} \propto u$ (see Eq. (2.6) for example), overall we have $\chi^{\mathrm{NL}} \propto \mathbf{E}^2$. In terms of nonlinear polarization [157], this is a third-order optical nonlinearity $\mathbf{P}^{\mathrm{NL}} = \epsilon_0\chi^{\mathrm{NL}}\mathbf{E} \propto \mathbf{E}^3$.

Summarizing this analysis, we have shown that Brillouin scattering is an acousto-optic process in which optical fields generate optical forces, driving acoustic waves in the medium, which in turn scatter light, as illustrated in Fig. 2.1(b). The interaction of the optical fields with the acoustic waves in the material result in an optical nonlinearity consistent with a $\chi^{(3)}$ process. Interestingly, the optical forces and light-scattering mechanisms are linked through thermodynamics and energy conservation considerations [159, 166, 167]. In fact, they can be described as conjugate processes and will be represented by a single coupling rate when we derive Brillouin scattering dynamics in Section 2.3.

The strength of Brillouin interactions is commonly quantified through a *Brillouin gain* coefficient G_{B}. As we will show in detail in the next section, the Brillouin gain describes the energy transfer between two optical fields coupled through a Brillouin interaction [157]

$$\frac{\partial}{\partial z}I_{\mathrm{p}} = -G_{\mathrm{B}}I_{\mathrm{p}}I_{\mathrm{s}}, \qquad \frac{\partial}{\partial z}I_{\mathrm{s}} = -G_{\mathrm{B}}I_{\mathrm{p}}I_{\mathrm{s}}, \tag{2.10}$$

where I_{p}, I_{s} are optical intensities of a 'pump' and a red-shifted 'Stokes' wave[7]. The Brillouin gain can be directly calculated from the optical forces and acoustic modes present

6. The displacement field is defined here as the motion of nuclei from their equilibrium position.

7. In this example, we are assuming a backward Brillouin process, where the pump and Stokes waves are counter-propagating.

in the system [161, 163]

$$G_{\mathrm{B}}(\Omega) = \sum_m \left(\frac{2\omega}{\Omega_m \Gamma_m v^2}\right) \left|\langle \mathbf{f}, \mathbf{u}_m \rangle\right|^2 \left(\frac{(\Gamma_m/2)^2}{(\Omega_m - \Omega)^2 + (\Gamma_m/2)^2}\right), \tag{2.11}$$

where ω and v are the optical frequency and group velocity, respectively, and $\mathbf{u}_m$ denotes the m^{th} acoustic mode, with resonant frequency Ω_m and dissipation rate Γ_m. The electric and acoustic fields in this calculation are normalized such that $\langle \mathbf{E}, \epsilon_0 \epsilon_r \mathbf{E} \rangle = \langle \mathbf{u}_m, \rho \mathbf{u}_m \rangle = 1$, where ρ denotes the material density, and $\langle \cdot, \cdot \rangle$ denotes an overlap integral over the waveguide cross-section. We can see from Eq. (2.11) that the Brillouin interaction is determined by the overlap integral of the optical force, which can be written as the linear sum of its components $\mathbf{f} = \mathbf{f}^{\mathrm{ES}} + \mathbf{f}^{\mathrm{RP}}$, and the acoustic mode profiles, each with Lorentzian frequency response, where Ω is the frequency of the optical forcing functions. Additionally, it is interesting to note that Brillouin gain grows with a longer acoustic-mode lifetime ($\propto 1/\Gamma_m$) and lower optical group velocities, both of which can be optimized for stronger Brillouin interactions [168, 169].

2.2 Phase matching and energy conservation

It is convenient to separate the analysis of Brillouin scattering into different cases, depending on the scattering geometry and the modes taking part in the process. In the following sections, we will consider three scattering processes relevant for guided systems, where the optical fields are all co-propagating or counter-propagating along the same axis:

1. **Backward stimulated Brillouin scattering:** *Counter-propagating* optical fields coupled to a *longitudinal* acoustic mode.

2. **Forward stimulated inter-modal Brillouin scattering:** *Co-propagating* optical fields in *distinct* modes (i.e., different polarizations or spatial modes) coupled to a *guided* acoustic mode.

3. **Forward stimulated intra-modal Brillouin scattering:** *Co-propagating* optical fields in the *same* optical mode coupled to a guided acoustic *transverse* mode.

As we shall see next, these different types of interactions have different properties and can lead to vastly different dynamics.

2.2.1 Backward stimulated Brillouin scattering

In the case of backward stimulated Brillouin scattering, all fields (optical and acoustic) propagate parallel to the same axis. As a first analysis, to help us gain some intuition, we assume the periodic perturbations caused by the acoustic wave act as a propagating Bragg mirror, traveling at the sound velocity in the material v_{ac} and reflecting light impinging on it. Since this mirror is moving, the reflected light will experience a Doppler-shift in frequency, given by

$$\Delta\omega = \pm 2\frac{v_{\mathrm{ac}}}{c/n}\omega_0 = \pm 2nv_{\mathrm{ac}}\frac{2\pi}{\lambda_0}, \tag{2.12}$$

where n is the refractive index of the medium and ω_0 the optical frequency, which can also be expressed in terms of wavelength $\lambda_0 = 2\pi c/\omega_0$. The frequency shift can be to a lower frequency, a redshift which is commonly referred to as a *Stokes* process, as well as to a higher frequency, a blueshift known as an *anti-Stokes* process. In these two cases, the acoustic field is propagating in a different direction with respect to the incident field, as illustrated in Fig. 2.2.

The scattering process can also be interpreted in a particle-like picture. The Stokes process can be described as an optical photon losing a quantum of energy, creating a phonon, resulting in a lower frequency photon. In contrast, in an anti-Stokes process the photon absorbs a quantum of energy, annihilating a phonon, resulting in a higher frequency photon.

While Eq. (2.12) gives us the frequency shift experienced by the scattered light, it is not the full picture, as we need to consider the fields' wavevectors to account for phase-matching conditions. Using the intuition from the particle analogy, we can think of an input photon with wavevector k_{p} decaying into a phonon with wavevector q_{s} and a counter-propagating Stokes photon with wavevector k_{s}, such that a phase-matched process requires $k_{\mathrm{p}} = q_{\mathrm{s}} - k_{\mathrm{s}}$. For an anti-Stokes process, a phonon with wavevector q_{as} is absorbed by the incoming photon to produce an anti-Stokes photon with wavevector k_{as}, requiring $k_{\mathrm{p}} + q_{\mathrm{as}} = -k_{\mathrm{as}}$.

Rearranging, we have

$$q_{\mathrm{s}} = k_{\mathrm{p}} + k_{\mathrm{s}} \approx 2k_{\mathrm{p}}, \qquad q_{\mathrm{as}} = -\left(k_{\mathrm{p}} + k_{\mathrm{as}}\right) \approx -2k_{\mathrm{p}}, \tag{2.13}$$

where we have used the approximation that the optical wavevector does not change substantially over the Brillouin frequency shift, i.e., $k_{\mathrm{p}} \approx k_{\mathrm{s}} \approx k_{\mathrm{as}}$. We can see that the wavevectors of the phonons taking part in the Stokes and anti-Stokes processes have different signs, corresponding to propagating and counter-propagating waves with respect to the input optical field, and consistent with our 'moving mirror' analogy from Eq. (2.12).

Using these phase-matching condition together with the acoustic dispersion relation $\Omega_i = v_{\mathrm{ac}}|q_i|$ $(i = \{\mathrm{s}, \mathrm{as}\})$ and optical dispersion relations $\omega_i = (c/n)|k_i|$ $(i = \{\mathrm{s}, \mathrm{p}, \mathrm{as}\})$, we

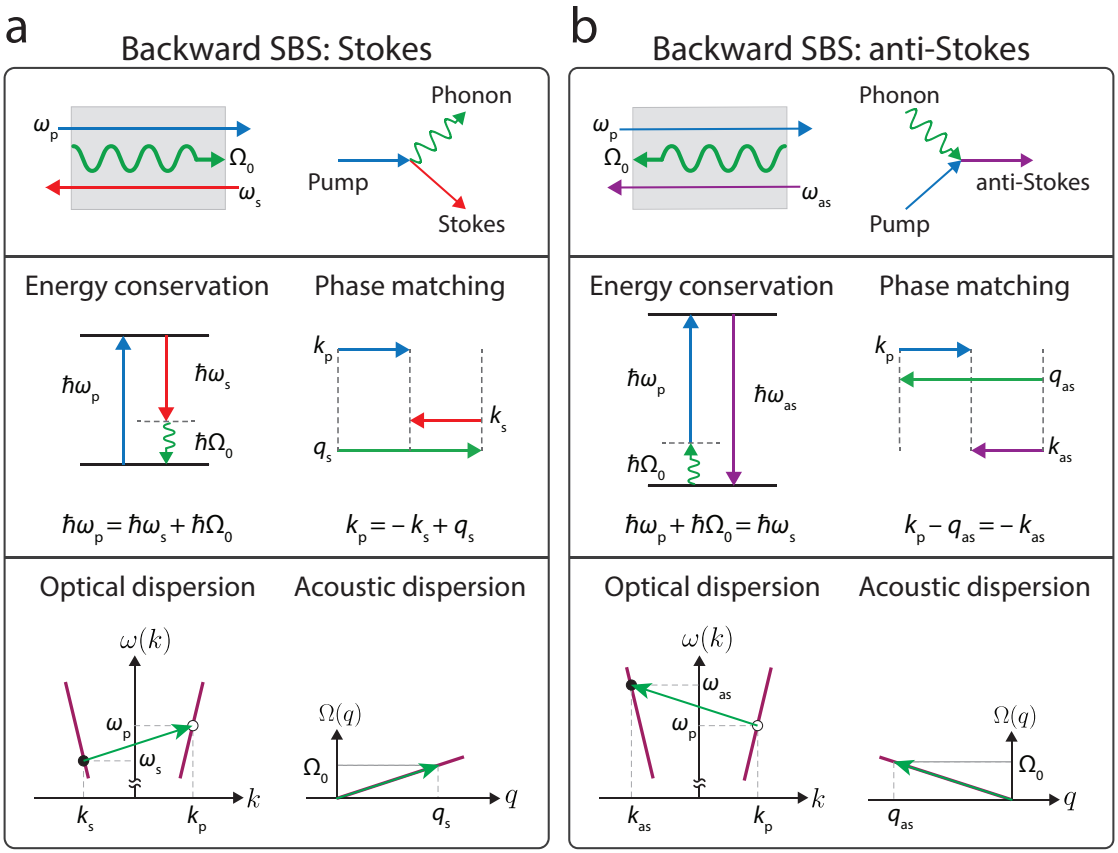

Figure 2.2: Phase matching and energy conservation conditions for backward SBS. **(a)** Stokes scattering and **(b)** anti-Stokes scattering. Top: particle analogy, where a phonon is created (Stokes process) or annihilated (anti-Stokes process). Middle: energy conservation and phase-matching conditions. Bottom: Optical and acoustic dispersion diagrams.

can find the frequency of the phonon taking part in the Stokes interaction

$$\Omega_{\mathrm{s}} = v_{\mathrm{ac}} q_{\mathrm{s}} = v_{\mathrm{ac}} \left(k_{\mathrm{p}} + k_{\mathrm{s}}\right) = v_{\mathrm{ac}} \frac{n}{c} \left(\omega_{\mathrm{p}} + \omega_{\mathrm{s}}\right) = v_{\mathrm{ac}} \frac{n}{c} \left(2\omega_{\mathrm{p}} - \Omega_{\mathrm{s}}\right), \tag{2.14}$$

where in the last step we have used energy conservation to write $\Omega_{\mathrm{s}} = \omega_{\mathrm{p}} - \omega_{\mathrm{s}}$. Solving for the Brillouin frequency, we have

$$\Omega_{\mathrm{s}} = 2\frac{v_{\mathrm{ac}}}{c/n} \left(\frac{1}{1 + \frac{v_{\mathrm{ac}}}{c/n}}\right) \omega_{\mathrm{p}} \approx 2\frac{v_{\mathrm{ac}}}{c/n}\omega_{\mathrm{p}}, \tag{2.15}$$

where the approximation assumes that the sound velocity is much smaller than the optical velocity ($v_{\mathrm{ac}} \ll c/n$), yielding a result in agreement with Eq. (2.12). An identical calculation can be done for anti-Stokes scattering, resulting in a similar expression to Eq. (2.15) with a minus sign in the denominator. We see that in the case of backward Brillouin scattering, the frequency shift is determined by the optical and acoustic wave velocities, as well as the optical wavelength $\lambda_{\mathrm{p}} = 2\pi c/\omega_{\mathrm{p}}$.

2.2.2 Forward inter-modal stimulated Brillouin scattering

In the previous section, we have analyzed backward Brillouin scattering, where we could describe an intuitive picture of three interacting scalar waves (two optical fields and one acoustic field), as is the case of a single-mode fiber for example. However, Brillouin interactions can also occur between distinct optical modes, such as different polarization states [30] or spatial modes [65]. Additionally, scattering can take place between two optical modes co-propagating along the same axis. Such *forward inter-modal* scattering processes can be a result of both electrostriction and radiation pressure [44], and can be the dominant form of scattering when, for example, the photoelastic tensor mediates strong Brillouin interaction in the forward direction, such as in silicon.

In the forward inter-modal case, the wavevector of each optical mode is described by a different dispersion relation, as shown in Fig. 2.3. Now, the phase-matching condition for the Stokes process is given by $q_{\mathrm{s}}(\Omega_{\mathrm{s}}) = k_1(\omega_{\mathrm{p}}) - k_2(\omega_{\mathrm{s}})$, where $k_1(\omega)$ and $k_2(\omega)$ are the functions describing the wavevector as a function of frequency for the modes in which the

pump and Stokes waves are propagating, respectively. At the same time, energy conservation requires $\hbar\Omega_0 = \hbar\omega_\mathrm{p} - \hbar\omega_\mathrm{s}$, illustrated in Fig. 2.3. Similarly, for an anti-Stokes process, the phase matching condition is given by $q_\mathrm{as}(\Omega_\mathrm{as}) = k_2(\omega_\mathrm{as}) - k_1(\omega_\mathrm{p})$, where now $k_2(\omega)$ and $k_1(\omega)$ describe the dispersion relations of the anti-Stokes and pump modes, respectively, and energy conservation is given by $\hbar\Omega_0 = \hbar\omega_\mathrm{as} - \hbar\omega_\mathrm{p}$.

The wavevector of the phase-matched phonon taking part in the process is usually small and necessitates guided acoustic modes with a cut-off frequency. This allows for modes with a small wavevector while supporting a non-vanishing frequency, as shown in Fig. 2.3. Additionally, we can see that the Stokes and anti-Stokes phonons travel in opposite

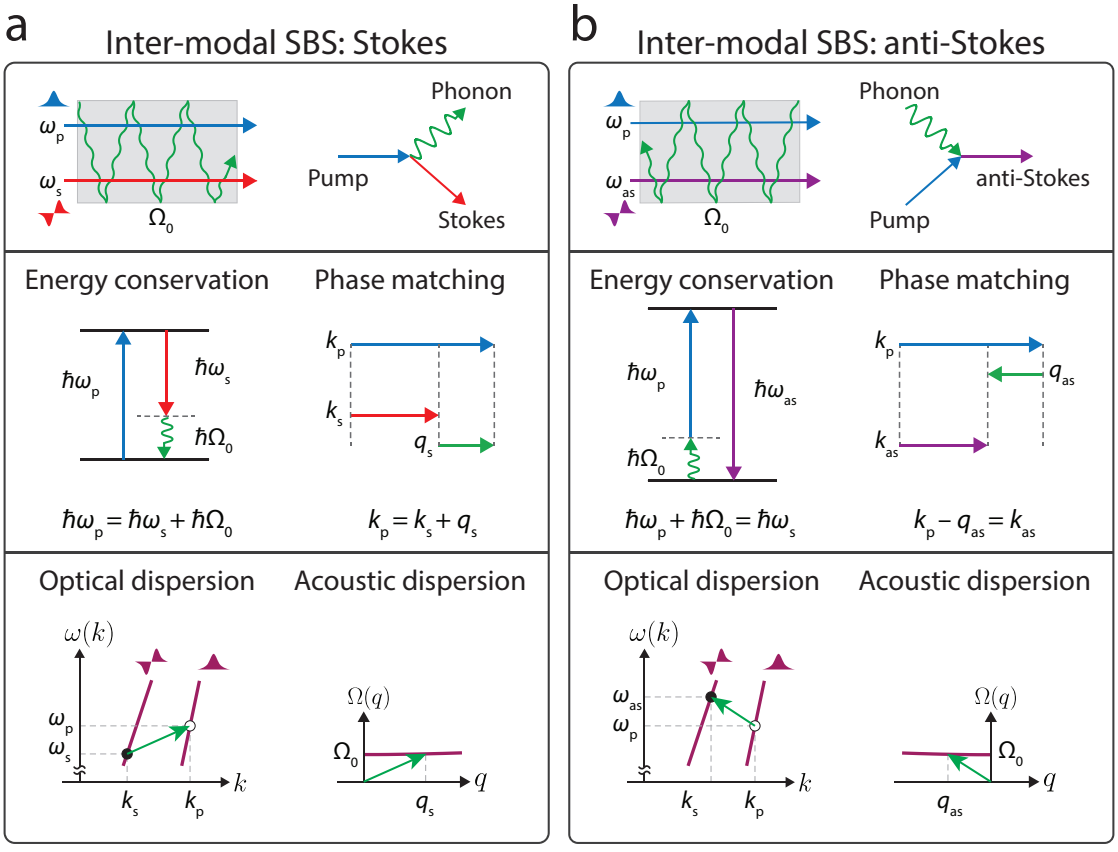

Figure 2.3: Phase matching and energy conservation conditions for forward inter-modal SBS. **(a)** Stokes scattering and **(b)** anti-Stokes scattering. Top: particle analogy, where a phonon is created (Stokes process) or annihilated (anti-Stokes process). Middle: energy conservation and phase-matching conditions. Bottom: Optical and acoustic dispersion diagrams. In this example, we considered the pump wave propagating in the fundamental optical spatial mode, and the Stokes/anti-Stokes in the first anti-symmetric mode, however, different configurations are possible.

directions.

2.2.3 Forward intra-modal stimulated Brillouin scattering

Finally, we consider Brillouin scattering between optical waves co-propagating in the same spatial and polarization mode, known as forward *intra-modal* scattering

In contrast to inter-modal scattering, and in the absence of strong dispersion, a single acoustic mode scatters the optical field to both the Stokes and ant-Stokes sidebands. Furthermore, the scattering can cascade further to multiple sidebands, as shown in Fig. 2.4. This scattering process is qualitatively different from inter-modal and backward Brillouin scattering, as multiple optical tones are coupled by a single phonon mode, and as we shall soon see, this results in a form of self-phase modulation.

Here, the phase matching requirements are $q_\mathrm{s} = k_\mathrm{p} - k_\mathrm{s} \approx 0$ for a Stokes process, and $q_\mathrm{as} = k_\mathrm{as} - k_\mathrm{p} \approx 0$ for the anti-Stokes case, where we have used the fact that the wavevector of a given optical mode does not change much over the acoustic frequency scale ($k_\mathrm{p} \approx k_\mathrm{s} \approx k_\mathrm{as}$). We can see that the phonons taking part in this process have a vanishingly-small wavevector. Additionally, assuming linear dispersion for the optical mode over this frequency range $k = (n_\mathrm{eff}/c)\omega$ together with energy conservation, we have

$$q_\mathrm{s} = \frac{n_\mathrm{eff}}{c}\left(\omega_\mathrm{p} - \omega_\mathrm{s}\right) = \frac{n_\mathrm{eff}}{c}\Omega_0 = \frac{n_\mathrm{eff}}{c}\left(\omega_\mathrm{as} - \omega_\mathrm{p}\right) = q_\mathrm{as}, \tag{2.16}$$

showing that the phonons mediating the Stokes and anti-Stokes process have the exact same wavevector, and that it is in fact the same acoustic mode taking part in both scattering processes.

2.3 Dynamics of Brillouin scattering processes

2.3.1 Hamiltonian framework

Now that we have presented the necessary energy and phase-matching conditions for the different types of Brillouin scattering processes, we will proceed to derive the dynamics

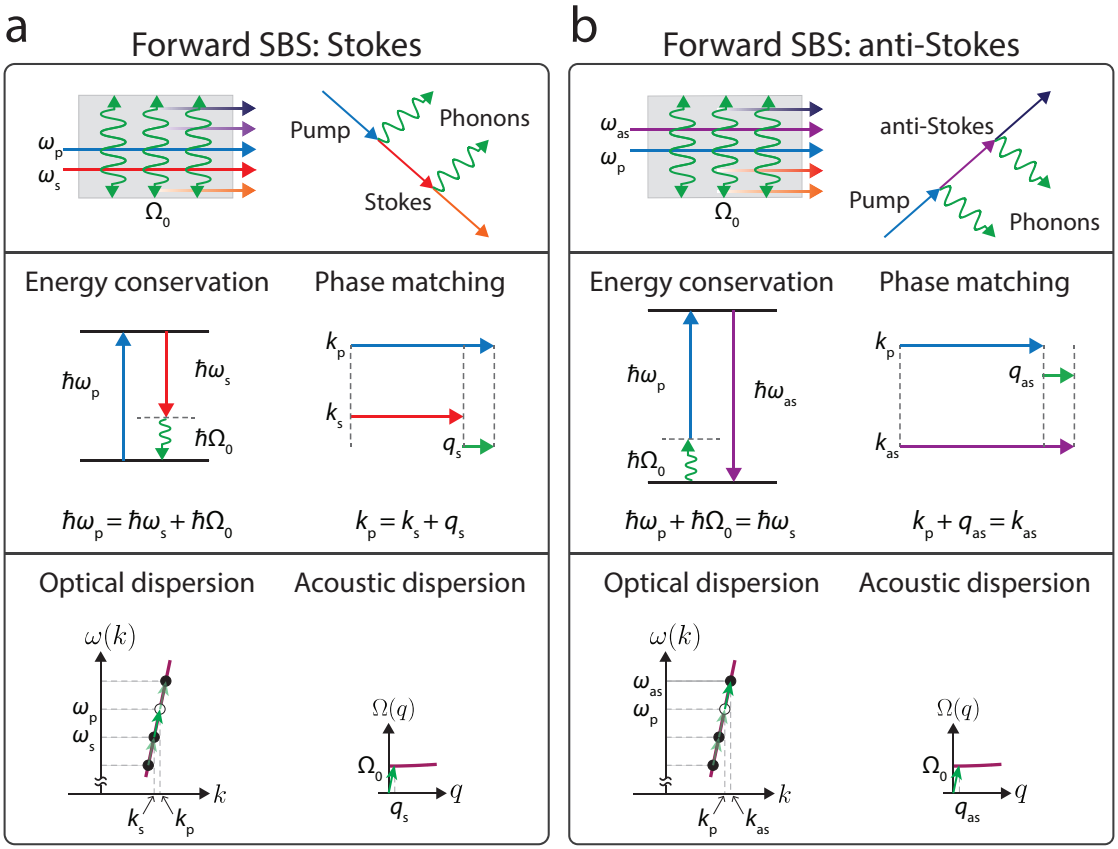

Figure 2.4: Phase matching and energy conservation conditions for forward intra-modal SBS. **(a)** Stokes scattering and **(b)** anti-Stokes scattering. Top: particle analogy, where phonons are created (Stokes process) or annihilated (anti-Stokes process). Middle: energy conservation and phase-matching conditions, showing how the same phonon mode takes part in both Stokes and anti-Stokes processes. Bottom: Optical and acoustic dispersion diagrams, which are essentially identical in Stokes and anti-Stokes processes.

of the optical and acoustic fields taking part in these interactions. We will use a traveling wave Hamiltonian formalism [170–172] which enables the treatment of both inter-modal and intra-modal scattering. Additionally, this approach enables a smooth connection to other fields such as optomechanics and quantum optics [170, 171, 173]. While we are choosing to present this formulation using quantum operators, the correspondence principle (or the canonical quantization procedure) guarantees that the basic structure of the equations of motion will be identical when examined in the classical domain. Alternative derivations, using classical fields, can be found for example in Refs. [29, 71, 154, 159, 163].

We start by describing a waveguide supporting both optical and acoustic modes, which

is translationally invariant along the z axis. The Hamiltonian of this system consists of terms describing the optical fields, the acoustic fields, and their interaction

$$H = H_{\text{opt}} + H_{\text{ac}} + H_{\text{int}}. \tag{2.17}$$

The optical and acoustic terms can be written as a sum over all spatial and polarization modes (indexed using n for optical fields and m for acoustic fields), and integrated over all possible wavevectors (denoted k for optical fields and q for acoustic fields)

$$\begin{aligned} H_{\text{opt}} &= \sum_n \int dk\ \hbar\omega_n(k) A_n^\dagger(k,t) A_n(k,t), \\ H_{\text{ac}} &= \sum_m \int dq\ \hbar\Omega_m(q) B_m^\dagger(q,t) B_m(q,t). \end{aligned} \tag{2.18}$$

Here, the mode amplitude $A_n(k,t)$ is unit-less such that its modulus squared represents the number of photons in mode n with wavevector k, and similarly, the modulus squared of $B_m(q,t)$ represents the number of phonons in mode m with wavevector q.

We are interested in analyzing travelling wave systems, and it is convenient to define new operators describing wave packet envelopes, by using a linear combination of modes with different wavevectors

$$a_n(z,t) = \frac{1}{\sqrt{2\pi}} \int dk\ A_n(k,t) e^{i(k-k_n)z}, \qquad b_m(z,t) = \frac{1}{\sqrt{2\pi}} \int dq\ B_m(q,t) e^{i(q-q_m)z}, \tag{2.19}$$

where the amplitude operators $a_n(z,t)$ and $b_m(z,t)$, describe optical and acoustic modes, respectively. Note that we are defining the operators around carrier wavevectors (k_n and q_m for the optical and acoustic waves, respectively), such that we are factoring out the fast spatial oscillations of the operators. These operators are time dependent, as we are working in the Heisenberg picture, and have units of [length$^{-1/2}$], such that their modulus squared represents the number of photons or phonons per unit length, and obey the commutation relations

$$\left[a_n(z,t), a_{n'}^\dagger(z',t)\right] = \delta\left(z-z'\right)\delta_{n,n'}, \qquad \left[b_m(z,t), b_{m'}^\dagger(z',t)\right] = \delta\left(z-z'\right)\delta_{m,m'}. \tag{2.20}$$

We can express the Hamiltonian using these spatial operators substituting Eq. (2.19) into Eq. (2.18), yielding

$$\begin{aligned} H_{\text{opt}} &= \sum_n \hbar \int dz\ a_n^\dagger(z,t)\hat{\omega}_n a_n(z,t), \\ H_{\text{ac}} &= \hbar \int dz\ b^\dagger(z,t)\hat{\Omega}_m b(z,t). \end{aligned} \tag{2.21}$$

The wavevector-dependent frequencies $\omega_n(k)$ and $\Omega_m(q)$ from Eq. (2.18) are now written as spatial operators $\hat{\omega}_n$ and $\hat{\Omega}_m$, by expanding them in a power series around their central wavevectors (k_n and q_m, respectively) and replacing the wavevector by a spatial derivative (as they are a Fourier pair). This yields [172]

$$\begin{aligned} \hat{\omega}_n &= \omega(k_n) + \partial_k\omega(k_n)\cdot k + \frac{1}{2!}\partial_k^2\omega(k_n)\cdot k^2 + \frac{1}{3!}\partial_k^3\omega(k_n)\cdot k^3 + \dots \\ &= \omega(k_n) + \partial_k\omega(k_n)\cdot(-i\partial_z) + \frac{1}{2!}\partial_k^2\omega(k_n)\cdot(-i\partial_z)^2 + \frac{1}{3!}\partial_k^3\omega(k_n)\cdot(-i\partial_z)^3 \dots \end{aligned} \tag{2.22}$$

for the optical modes, and similarly, for the acoustic modes we have

$$\hat{\Omega}_m = \Omega(q_m) + \partial_q\Omega(q_m)\cdot(-i\partial_z) + \frac{1}{2!}\partial_q^2\Omega(q_m)\cdot(-i\partial_z)^2 + \frac{1}{3!}\partial_q^3\Omega(q_m)\cdot(-i\partial_z)^3 + \dots \tag{2.23}$$

where we have used the notation ∂_x to denoted a derivative with respect to the variable x.

It is important to note, that since we are using a power series —which we will soon truncate for practical calculations— this approach assumes that the fields we are analyzing are sharply peaked around their central wavevector, consistent with a slowly varying envelope approximation, which is commonly used in nonlinear optics analyses [157, 172]. To first order, these operators are given by

$$\hat{\omega}_n \approx \omega_n - iv_n\frac{\partial}{\partial z}, \qquad \hat{\Omega}_m \approx \Omega_m - iV_m\frac{\partial}{\partial z}, \tag{2.24}$$

where we have denoted the center frequencies $\omega_n = \omega(k_n)$ and $\Omega_m = \Omega(q_m)$, and have used the fact that the derivative of the dispersion relation is the group velocity, i.e., $v_n = \partial_k\omega(k_n)$ and $V_m = \partial_q\Omega(q_m)$.

To capture the nonlinear response of the system, we introduce an interaction term of the form

$$H_{\text{int}} = \sum_{n}\sum_{n'}\sum_{m}\hbar\int dz\; g^{*}_{n,n',m}\; a_n(z,t)a^{\dagger}_{n'}(z,t)b^{\dagger}_{m}(z,t)e^{-i(q_m-k_n+k_{n'})z} + \text{H.C.}, \tag{2.25}$$

where the acousto-optic coupling $g_{n,n',m}$ describes the coupling between two optical modes n and n' interacting with a phonon mode m, with units of [length$^{1/2}\cdot$time^{-1}]. This can have both photoelastic (electrostrictive) and radiation pressure contributions, [171]

$$g_{n,n',m} = g^{\text{PE}}_{n,n',m} + g^{\text{RP}}_{n,n',m}, \tag{2.26}$$

which can be calculated using an overlap integral of the cross section of the modes taking part in the interaction [171, 172]

$$\begin{aligned} g^{\text{PE}}_{n,n',m} &= \sqrt{\frac{\hbar\omega_n\omega'_n\Omega_m}{8\epsilon_0^2}}\int dxdy\; D^{i\,*}_{n}D^{j}_{n'}\; p_{ijkl}\;\frac{\partial u^k_m}{\partial r^l}, \\ g^{\text{RP}}_{n,n',m} &= \sqrt{\frac{\hbar\omega_n\omega'_n\Omega_m}{8\epsilon_0^2}}\int dxdy\left[\epsilon_0^2\mathbf{E}^{\parallel\,*}_{n}\mathbf{E}^{\parallel}_{n'}\nabla\epsilon(x,y) - \mathbf{D}^{\perp\,*}_{n}\mathbf{D}^{\perp}_{n'}\nabla\epsilon^{-1}(x,y)\right]\cdot\mathbf{u}_m, \end{aligned} \tag{2.27}$$

where summation is implicit over identical indices. In these expressions, $\mathbf{E}$ and $\mathbf{D}$ are the electric field and the electric displacement field, respectively, $\mathbf{u}_m$ is the elastic displacement profile of phonon mode m and ϵ_r is the waveguide dielectric constant, all functions of the cross-section (x, y) over which the integration is carried out. For the radiation pressure term, which models boundary forces, we have separated the field components into those parallel ($\parallel$) and perpendicular ($\perp$) to the boundaries. The photoelastic term is an overlap integral of the electric displacement field components with the photoelastic tensor (p_{ijkl}) and the strain profile of the acoustic mode ($\partial u^k/\partial r^l = S_{kl}$). When the waveguide dimensions are not sub-optical wavelength, which will be most of the cases we are interested in throughout this work, we can usually neglect the radiation pressure term, as it is much smaller than that of the electrostrictive forces. However, when analyzing nanostructures with dimensions smaller than the wavelengths, radiation pressure has to be taken into account [161].

With this Hamiltonian, we can now examine the dynamics of the optical and acoustic fields in the system. Using the Heisenberg equations of motion

$$\frac{\partial}{\partial t}a_n(z,t) = \frac{1}{i\hbar}\left[a_n(z,t), H\right], \qquad \frac{\partial}{\partial t}b_m(z,t) = \frac{1}{i\hbar}\left[b_m(z,t), H\right], \tag{2.28}$$

together with the commutators from Eq. (2.20), we have

$$\begin{aligned}\frac{\partial}{\partial t}a_n &= -i\omega_n a_n - v_n\frac{\partial}{\partial z}a_n - i\sum_{n'}\sum_{m}\Big[g_{n,n',m}\ a_{n'}b_m e^{i(q_m-k_n+k_{n'})z} \\ &\qquad + g^*_{n',n,m}\ a_{n'}b^\dagger_m e^{-i(q_m-k_{n'}+k_n)z}\Big], \\ \frac{\partial}{\partial t}b_m &= -i\Omega_m b_m - V_m\frac{\partial}{\partial z}b_m - i\sum_{n}\sum_{n'}g^*_{n',n,m}\ a_n a^\dagger_{n'}\ e^{-i(q_m-k_n+k_{n'})z},\end{aligned} \tag{2.29}$$

where we have used the operators from Eq. (2.24), and we suppress the notation of the space and time arguments (z,t) of the operators for clarity. Next, we will use these equations of motion to analyze the dynamics of the different types of Brillouin scattering.

2.3.2 Backward stimulated Brillouin scattering

As we have discussed earlier, in the case of Backwards Brillouin scattering, the Stokes and anti-Stokes processes are mediated by separate phonons and are decoupled, such that we can analyze them separately. Here, we will focus on the Stokes process; the anti-Stokes process can be calculated similarly. We consider three fields: a pump propagating in the $+z$ direction, a Stokes field propagating in the $-z$ direction, and an acoustic field propagating in the $+z$ direction (see Fig. 2.2(a)). Using Eq. (2.29), we now have

$$\begin{aligned}\frac{\partial}{\partial t}a_{\mathrm{p}} &= -i\omega_{\mathrm{p}}a_{\mathrm{p}} - v_{\mathrm{p}}\frac{\partial}{\partial z}a_{\mathrm{p}} - i\left[g_{\mathrm{p,s}}\ a_{\mathrm{s}}b\ e^{i(q-k_{\mathrm{p}}-k_{\mathrm{s}})z} + g^*_{\mathrm{s,p}}\ a_{\mathrm{s}}b^\dagger\ e^{-i(q+k_{\mathrm{s}}+k_{\mathrm{p}})z}\right], \\ \frac{\partial}{\partial t}a_{\mathrm{s}} &= -i\omega_{\mathrm{s}}a_{\mathrm{s}} + v_{\mathrm{s}}\frac{\partial}{\partial z}a_{\mathrm{s}} - i\left[g_{\mathrm{s,p}}\ a_{\mathrm{p}}b\ e^{i(q+k_{\mathrm{s}}+k_p)z} + g^*_{\mathrm{p,s}}\ a_{\mathrm{p}}b^\dagger\ e^{-i(q-k_{\mathrm{p}}-k_{\mathrm{s}})z}\right], \\ \frac{\partial}{\partial t}b &= -i\Omega_0 b - V_0\frac{\partial}{\partial z}b - i\left[g^*_{\mathrm{s,p}}\ a_{\mathrm{p}}a^\dagger_{\mathrm{s}}\ e^{-i(q-k_{\mathrm{p}}-k_{\mathrm{s}})z} + g^*_{\mathrm{p,s}}\ a_{\mathrm{s}}a^\dagger_{\mathrm{p}}\ e^{-i(q+k_{\mathrm{s}}+k_{\mathrm{p}})z}\right],\end{aligned} \tag{2.30}$$

where we have a negative group velocity for the Stokes wave, as well as a negative wavevector, since it is counter-propagating compared to the other fields. From the phase-matching

conditions necessary for backward scattering, we know that a Stokes process requires $q = k_\mathrm{p} + k_\mathrm{s}$, such that

$$\begin{aligned}
\frac{\partial}{\partial t}a_\mathrm{p} &= -i\omega_\mathrm{p}a_\mathrm{p} - v_\mathrm{p}\frac{\partial}{\partial z}a_\mathrm{p} - i\left[g_\mathrm{p,s}\ a_\mathrm{s}b + g^*_\mathrm{s,p}\ a_\mathrm{s}b^\dagger\ e^{-2i(k_\mathrm{s}+k_\mathrm{p})z}\right], \\
\frac{\partial}{\partial t}a_\mathrm{s} &= -i\omega_\mathrm{s}a_\mathrm{s} + v_\mathrm{s}\frac{\partial}{\partial z}a_\mathrm{s} - i\left[g_\mathrm{s,p}\ a_\mathrm{p}b\ e^{2i(k_\mathrm{s}+k_p)z} + g^*_\mathrm{p,s}\ a_\mathrm{p}b^\dagger\ \right], \\
\frac{\partial}{\partial t}b &= -i\Omega_0 b - V_0\frac{\partial}{\partial z}b - i\left[g^*_\mathrm{s,p}\ a_\mathrm{p}a^\dagger_\mathrm{s} + g^*_\mathrm{p,s}\ a_\mathrm{s}a^\dagger_\mathrm{p}\ e^{-2i(k_\mathrm{s}+k_\mathrm{p})z}\right].
\end{aligned} \tag{2.31}$$

The oscillatory terms $e^{\pm 2i(k_\mathrm{s}+k_\mathrm{p})z}$ in these equations will average out when integrated over a propagation distance $z \gg [2(k_\mathrm{s}+k_\mathrm{p})]^{-1}$, and can typically be neglected.

At this point, we will also take into account that the system we are analyzing is an open system, and we introduce dissipation terms into our equations by adding an imaginary part to the modes' frequencies, i.e., $\omega \to \omega - i\,(\gamma/2)$ and $\Omega_0 \to \Omega_0 - i\,(\Gamma/2)$. As required by the fluctuation-dissipation theorem, to maintain thermal equilibrium we must consider the fluctuations introduced by the thermal bath each mode interacts with [174], which we denote ζ for the optical fields and η for the acoustic field

$$\begin{aligned}
\frac{\partial}{\partial t}a_\mathrm{p} &= -i\omega_\mathrm{p}a_\mathrm{p} - \frac{\gamma_\mathrm{p}}{2}a_\mathrm{p} - v_\mathrm{p}\frac{\partial}{\partial z}a_\mathrm{p} - ig_\mathrm{p,s}\ a_\mathrm{s}b + \zeta_\mathrm{p}, \\
\frac{\partial}{\partial t}a_\mathrm{s} &= -i\omega_\mathrm{s}a_\mathrm{s} - \frac{\gamma_\mathrm{s}}{2}a_\mathrm{s} + v_\mathrm{s}\frac{\partial}{\partial z}a_\mathrm{s} - ig^*_\mathrm{p,s}\ a_\mathrm{p}b^\dagger + \zeta_\mathrm{s}, \\
\frac{\partial}{\partial t}b &= -i\Omega_0 b - \frac{\Gamma}{2}b - V_0\frac{\partial}{\partial z}b - ig^*_\mathrm{s,p}\ a_\mathrm{p}a^\dagger_\mathrm{s} + \eta.
\end{aligned} \tag{2.32}$$

Next, we analyze the operators in the rotating frame in order to remove their fast oscillatory component and gain more insight into the field envelopes in their steady-state. We do this by first factoring out the fast oscillating terms of each operator

$$\begin{aligned}
a_\mathrm{p} &\to a_\mathrm{p}e^{-i\omega_\mathrm{p}t}, \qquad a_\mathrm{s} \to a_\mathrm{s}e^{-i\omega_\mathrm{s}t}, \qquad b \to be^{-i\Omega t}, \\
\zeta_\mathrm{p} &\to \zeta_\mathrm{p}e^{-i\omega_\mathrm{p}t}, \qquad \zeta_\mathrm{s} \to \zeta_\mathrm{s}e^{-i\omega_\mathrm{s}t}, \qquad \eta \to \eta e^{-i\Omega t},
\end{aligned} \tag{2.33}$$

where $\Omega = \omega_\mathrm{p} - \omega_\mathrm{s}$, followed by setting the time derivative to zero, leaving us with

$$\begin{aligned} v_\mathrm{p}\frac{\partial}{\partial z}a_\mathrm{p} &= -\frac{\gamma_\mathrm{p}}{2}a_\mathrm{p} - ig_{\mathrm{p,s}}\, a_\mathrm{s}b + \zeta_\mathrm{p}, \\ -v_\mathrm{s}\frac{\partial}{\partial z}a_\mathrm{s} &= -\frac{\gamma_\mathrm{s}}{2}a_\mathrm{s} - ig^*_{\mathrm{p,s}}\, a_\mathrm{p}b^\dagger + \zeta_\mathrm{s}, \\ V_0\frac{\partial}{\partial z}b &= -i\left(\Omega_0 - \Omega\right)b - \frac{\Gamma}{2}b - ig^*_{\mathrm{s,p}}\, a_\mathrm{p}a_\mathrm{s}^\dagger + \eta. \end{aligned} \tag{2.34}$$

For now, we will neglect the noise terms, as they are not important for the calculation of the power transfer between the fields in a driven process.

In the case where the spatial decay length of the acoustic field (given by V_0/Γ) is much shorter than the length scale over which the fields propagate, as well as much shorter than the optical decay length, we can adiabatically eliminate its spatial dynamics. This is a valid assumption in many systems, where the decay length of the acoustic waves is typically 10–100 μm at room temperature, hence the acoustic field has no 'spatial memory' and only couples to the optical fields locally at each point. More rigorously, we can solve the equation for the phonon field

$$b(z) = -\frac{i}{V_0}g^*_{\mathrm{s,p}}\int_0^z dz'\; a_\mathrm{p}(z')a_\mathrm{s}^\dagger(z')\exp\left[-i\left(\frac{\Omega_0-\Omega}{V_0}\right)\left(z-z'\right)\right]\exp\left[-\frac{\Gamma}{2V_0}\left(z-z'\right)\right], \tag{2.35}$$

and since the optical fields don't change much over the decay length V_0/Γ, we can pull them out of the integration

$$\begin{aligned} b(z) &\approx -\frac{i}{V_0}g^*_{\mathrm{s,p}}a_\mathrm{p}(z)a_\mathrm{s}^\dagger(z)\int_0^z dz'\;\exp\left[-i\left(\frac{\Omega_0-\Omega}{V_0}\right)\left(z-z'\right)\right]\exp\left[-\frac{\Gamma}{2V_0}\left(z-z'\right)\right] \\ &= -i\left(\frac{1}{i\left(\Omega_0-\Omega\right)+\Gamma/2}\right)g^*_{\mathrm{s,p}}a_\mathrm{p}(z)a_\mathrm{s}^\dagger(z)\left(1-\exp\left[-i\left(\frac{\Omega_0-\Omega}{V_0}\right)z\right]\exp\left[-\frac{\Gamma}{2V_0}z\right]\right) \\ &\approx -i\left(\frac{1}{i\left(\Omega_0-\Omega\right)+\Gamma/2}\right)g^*_{\mathrm{s,p}}a_\mathrm{p}(z)a_\mathrm{s}^\dagger(z), \end{aligned} \tag{2.36}$$

where in the last step, we have used the fact that for propagation distances larger than the acoustic decay length ($z \gg 2V_0/\Gamma$) the last term can be dropped[8].

8. We can see that this approximation has resulted in the elimination of the spatial derivative of the acoustic field in Eq. (2.34).

Substituting this result back into Eq. (2.34), and denoting the acoustic frequency response

$$\chi = \frac{1}{i\left(\Omega_0 - \Omega\right) + \Gamma/2}, \tag{2.37}$$

results in a system of coupled differential equations given by

$$\begin{aligned} \frac{\partial}{\partial z} a_\mathrm{p} &= -\frac{\gamma_\mathrm{p}}{2v_\mathrm{p}} a_\mathrm{p} - \frac{1}{v_\mathrm{p}} \chi \left|g_\mathrm{p,s}\right|^2 \; a_\mathrm{s} a_\mathrm{s}^\dagger a_\mathrm{p}, \\ \frac{\partial}{\partial z} a_\mathrm{s} &= +\frac{\gamma_\mathrm{s}}{2v_\mathrm{s}} a_\mathrm{s} - \frac{1}{v_\mathrm{s}} \chi^* \left|g_\mathrm{p,s}\right|^2 \; a_\mathrm{p} a_\mathrm{p}^\dagger a_\mathrm{s}, \end{aligned} \tag{2.38}$$

which have the same form as other third-order nonlinear optical processes, such as Kerr and Raman nonlinearities [157]. We can rewrite these equations in terms of optical power [172]

$$P_\mathrm{p} = \hbar\omega_\mathrm{p} v_\mathrm{p} a_\mathrm{p}^\dagger a_\mathrm{p}, \qquad P_\mathrm{s} = \hbar\omega_\mathrm{s} v_\mathrm{s} a_\mathrm{s}^\dagger a_\mathrm{s}, \tag{2.39}$$

giving us the coupled equations

$$\begin{aligned} \frac{\partial}{\partial z} P_\mathrm{p} &= -\frac{\gamma_\mathrm{p}}{v_\mathrm{p}} P_\mathrm{p} - G_\mathrm{B} \left(\frac{\Gamma}{2}\right)^2 \left|\chi\right|^2 P_\mathrm{s} P_\mathrm{p}, \\ \frac{\partial}{\partial z} P_\mathrm{s} &= +\frac{\gamma_\mathrm{s}}{v_\mathrm{s}} P_\mathrm{s} - G_\mathrm{B} \left(\frac{\Gamma}{2}\right)^2 \left|\chi\right|^2 P_\mathrm{p} P_\mathrm{s}, \end{aligned} \tag{2.40}$$

where we have defined the Brillouin gain [172]

$$G_\mathrm{B} = \frac{4\left|g_\mathrm{p,s}\right|^2}{\hbar\omega_\mathrm{p} v_\mathrm{p} v_\mathrm{s} \Gamma}, \tag{2.41}$$

which has units of [power^{-1} $\cdot$ length^{-1}] and is a useful measure of the Brillouin interaction strength, equivalent to the gain we introduced earlier in Eq. (2.11).

In many practical systems, the pump field is much stronger than the Stokes field (as is the case of an amplifier for example), and we can approximate the pump as having constant power, known as the *undepleted pump* approximation. In this case, we can solve Eq. (2.40)

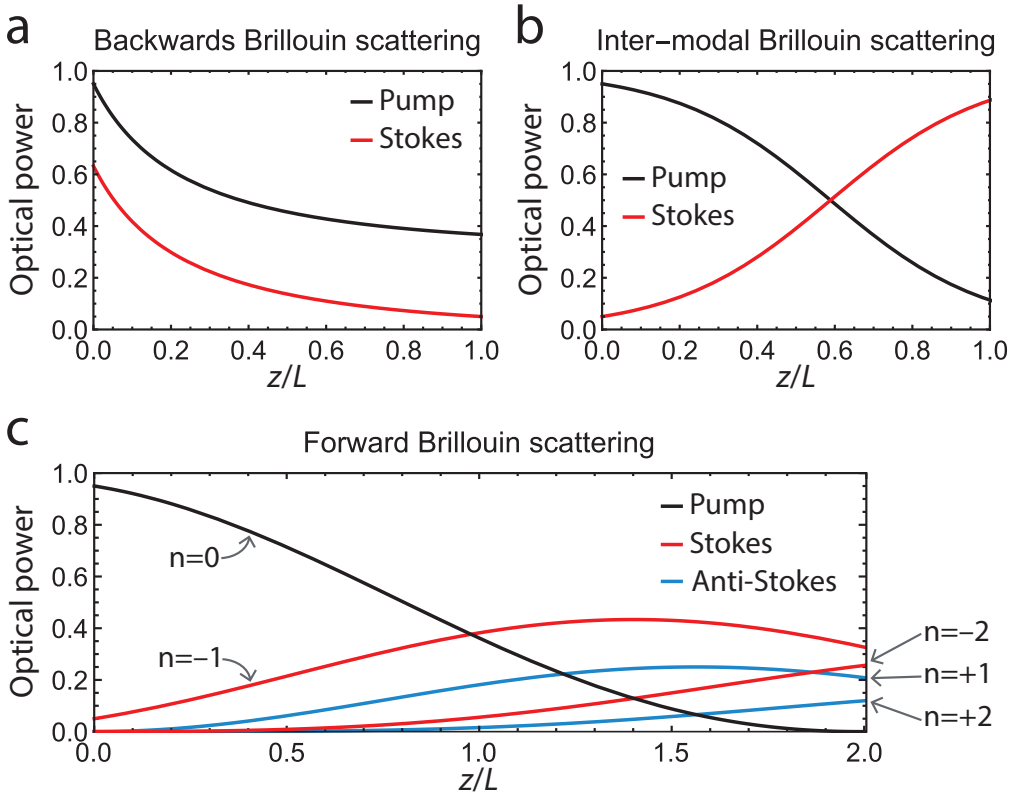

Figure 2.5: Optical power evolution for different types of Brillouin scattering processes. **(a)** Stimulated backward Brillouin scattering, following Eq. (2.40), showing the power transfer from the pump wave to a counter-propagating Stokes wave. **(b)** In a stimulated forward inter-modal scattering process, energy is transferred from the pump to a co-propagating Stokes wave, following Eq. (2.47). **(c)** Stimulated forward intra-modal scattering shows very different spatial dynamics, with multiple optical tones appearing as the field propagates, which can be described as a form of self-phase modulation. In all three calculations, we assume $G_{\mathrm{B}} = 5$ and optical losses were neglected.

to find the power evolution of the Stokes wave

$$P_{\mathrm{s}}(z) = P_{\mathrm{s}}(L) \exp\left[-\frac{\gamma_{\mathrm{s}}}{v_{\mathrm{s}}}\left(L - z\right)\right] \exp\left[\left(\frac{\Gamma}{2}\right)^2 |\chi|^2 \; G_{\mathrm{B}} P_{\mathrm{p}}\left(L - z\right)\right], \tag{2.42}$$

where we have assumed an active-Brillouin waveguide of length L. We can see that the Stokes wave experiences exponential amplification as it propagates. Fig. 2.5(a) shows a calculation of the optical power evolution of the optical fields, where we can see the power transfer from the pump to the Stokes wave.

Spontaneous backward Brillouin scattering

Next, we will analyze the contribution of the thermal fluctuations in the acoustic mode, which lead to spontaneous scattering of pump light to the Stokes tone. We return to Eq. (2.32), now keeping the stochastic term modeling the acoustic mode fluctuations. For simplicity, we will neglect optical loss and we assume the undepleted pump regime. We model the thermal fluctuations as a random variable with zero mean, $\langle \eta(z,t) \rangle = 0$, a correlation function $\langle \eta^\dagger(z,t)\eta(z',t') \rangle = n_{\mathrm{th}}\Gamma\delta(t-t')\delta(z-z')$, and a commutator $[\eta(z,t), \eta^\dagger(z,t)] = 1$ [172]. We have denoted n_{th} as the average number of thermally excited phonons at the Brillouin frequency, following a Bose-Einstein distribution $n_{\mathrm{th}} = [\exp(\hbar\Omega_0/k_{\mathrm{B}}T) - 1]^{-1}$, where k_{B} is the Boltzmann constant and T the temperature.

We transform the equations into the rotating frame (Eq. (2.33)), and neglect the spatial derivative of the phonon field (see Eq. (2.36)), leaving us with

$$\begin{aligned} \frac{\partial}{\partial t}a_{\mathrm{s}} &= v_{\mathrm{s}}\frac{\partial}{\partial z}a_{\mathrm{s}} - ig^*_{\mathrm{p,s}}\, a_{\mathrm{p}}b^\dagger, \\ \frac{\partial}{\partial t}b &= -i(\Omega_0 - \Omega)b - \frac{\Gamma}{2}b - ig^*_{\mathrm{s,p}}\, a_{\mathrm{p}}a_{\mathrm{s}}^\dagger + \eta. \end{aligned} \tag{2.43}$$

By writing the equations in the frequency domain (using a Fourier transform $\partial_t \to -i\omega$), we have

$$\begin{aligned} -i\omega a_{\mathrm{s}} &= v_{\mathrm{s}}\frac{\partial}{\partial z}a_{\mathrm{s}} - ig^*_{\mathrm{p,s}}\, a_{\mathrm{p}}b^\dagger, \\ b &= \widetilde{\chi}\left(-ig^*_{\mathrm{s,p}}\, a_{\mathrm{p}}a_{\mathrm{s}}^\dagger + \eta\right), \end{aligned} \tag{2.44}$$

where $\widetilde{\chi} = [i(\Omega_0 - \Omega - \omega)]^{-1}$. Solving for the Stokes tone leaves us with

$$a_{\mathrm{s}}(z,\omega) = \int_0^L dz\ \frac{i}{v_{\mathrm{s}}}g^* a_{\mathrm{p}}\eta^\dagger\widetilde{\chi}^* \exp\left[\frac{-i}{v_{\mathrm{s}}}\omega - \frac{1}{v_{\mathrm{s}}}|g|^2|a_{\mathrm{p}}|^2\,\widetilde{\chi}\,(L-z)\right], \tag{2.45}$$

where we have assumed no Stokes light at the input, i.e., $a_{\mathrm{s}}(0,\omega) = 0$, as we are only interested in spontaneous scattering. The power spectral density of the scattered light

$S_{\mathrm{s}}(\omega) = \hbar\omega_{\mathrm{s}} v_{\mathrm{s}} \langle a_{\mathrm{s}}^{\dagger}(L,\omega) a_{\mathrm{s}}(L,\omega)\rangle$ is given by

$$S_{\mathrm{s}}(\omega) = \hbar\omega_{\mathrm{s}} \left(n_{\mathrm{th}}+1\right) \left(\exp\left[G_{\mathrm{B}} P_{\mathrm{p}} L \, \frac{(\Gamma/2)^2}{\left(\Omega_0 - \Omega - \omega\right)^2 + (\Gamma/2)^2} \right] - 1 \right), \tag{2.46}$$

where we have expressed the spectrum in terms of the Brillouin gain and pump power using Eqs. (2.39) and (2.41). The total scattered optical power is given by integrating the spectrum $P_{\mathrm{s}} = 1/(2\pi) \int d\omega S_{\mathrm{s}}(\omega)$. The same analysis can be performed for anti-Stokes spontaneous scattering, yielding a similar result with $(n_{\mathrm{th}}+1) \rightarrow n_{\mathrm{th}}$. The lineshape we have obtained in Eq. (2.46) can be approximated as a Lorentzian when the Brillouin interaction is weak ($G_{\mathrm{B}} P_{\mathrm{p}} L \ll 1$) and as a Gaussian for strong interactions. Additionally, at a high temperature or low Brillouin frequency (when $\hbar\Omega_0 \ll k_{\mathrm{B}} T$) the thermal occupation number can be approximated as $n_{\mathrm{th}} = k_{\mathrm{B}} T/\hbar\Omega_0$, such that $S_{\mathrm{s}} \propto k_{\mathrm{B}} T \omega_{\mathrm{s}}/\Omega_0$.

For strong enough interactions, the Stokes scattered light can initiate a stimulated process. For example, in situations where we have large Brillouin gain, spontaneously scattered Stokes photons can seed the Brillouin amplification process [157, 158]. If the Brillouin gain reaches a critical value (typically when $G_{\mathrm{B}} P_{\mathrm{p}} L \sim$30 [157, 175]), this can lead to appreciable energy transfer between the pump and Stokes fields. Furthermore, this mechanism can cascade to further red-shifted Stokes tones [149].

2.3.3 Forward inter-modal stimulated Brillouin scattering

Next, we analyze the case of inter-modal Brillouin scattering between two optical waves co-propagating in two different spatial or polarization modes. This case is reminiscent of the backward Brillouin process, and we can rely on many of the calculations we have already done, with the difference that now all fields, optical and acoustic, are co-propagating in the $+z$ direction (for the Stokes scattering process). Following the same steps as before, taking into account the relevant phase-matching conditions for forward inter-modal scattering (i.e.,

$q_{\mathrm{s}}(\Omega_{\mathrm{s}}) = k_1(\omega_{\mathrm{p}}) - k_2(\omega_{\mathrm{s}}))$, we arrive at

$$\begin{aligned}\frac{\partial}{\partial z}a_{\mathrm{p}} &= -\frac{\gamma_{\mathrm{p}}}{2v_{\mathrm{p}}}a_{\mathrm{p}} - \frac{1}{v_{\mathrm{p}}}\chi\left|g_{\mathrm{p,s}}\right|^2\ a_{\mathrm{s}}a_{\mathrm{s}}^{\dagger}a_{\mathrm{p}},\\ \frac{\partial}{\partial z}a_{\mathrm{s}} &= -\frac{\gamma_{\mathrm{s}}}{2v_{\mathrm{s}}}a_{\mathrm{s}} + \frac{1}{v_{\mathrm{s}}}\chi^{*}\left|g_{\mathrm{p,s}}\right|^2\ a_{\mathrm{p}}a_{\mathrm{p}}^{\dagger}a_{\mathrm{s}}.\end{aligned} \tag{2.47}$$

These equations are equivalent to Eq. (2.38), with a positive group velocity for the Stokes wave, as it is co-propagating with the pump. In this case, under the undepleted pump approximation, the Stokes power is given by

$$P_{\mathrm{s}}(z) = P_{\mathrm{s}}(0)\exp\left[-\frac{\gamma_{\mathrm{s}}}{v_{\mathrm{s}}}z\right]\exp\left[\left(\frac{\Gamma}{2}\right)^2\left|\chi\right|^2 G_{\mathrm{B}}P_{\mathrm{p}}z\right], \tag{2.48}$$

showing exponential growth, similar to the backward Brillouin case. Fig. 2.5(b) shows the calculated power evolution of the optical fields, demonstrating how most of the pump power can be transferred to the Stokes wave. Comparing with the backward Brillouin case in Fig. 2.5(a) shows the difference in the power distribution over the propagation length. Whereas in the backward case, both pump and Stokes fields had the highest power at $z = 0$, in the forward inter-modal case the Stokes wave power grows as it propagates, while the pump is depleted. In fact, if we neglect optical loss, the total optical power does not change along the waveguide as it is transferred from pump to Stokes, i.e., $\partial_z[P_{\mathrm{p}}(z) + P_{\mathrm{s}}(z)] = 0$.

Analyzing the spontaneous scattering in an inter-modal Brillouin interaction follows the same steps as we have derived in the backward Brillouin case (see Eqs. (2.43)–(2.46)), and will also result in exponential amplification of the noise [56].

2.3.4 Forward intra-modal stimulated Brillouin scattering

The dynamics of forward intra-modal Brillouin scattering —where all optical waves co-propagate in the same optical mode— are very different from the backward and inter-modal cases we have just seen. In the intra-modal case, the same Brillouin-active phonon couples to both Stokes and anti-Stokes fields, and we cannot only take into account two optical fields in our analysis (such as we have done earlier with the pump and Stokes waves). Additionally, the same phonon can scatter light into further red- and blue-shifted sidebands, as seen in

Fig. 2.4. As we will show in this section, this leads to a form of Brillouin-induced self-phase modulation, with vastly different characteristics compared to the previous cases we have analyzed. This analysis will also be the basis for the next chapters, where we will show how the unique properties of forward intra-modal scattering can be utilized for processing signals within photonic devices.

To fully capture the dynamics of the electric and acoustic fields in this system, we use Eq. (2.29), keeping multiple optical modes in our analysis, all interacting with a single phonon mode. In this case, all of the optical modes (indexed n) lie on the same dispersion curve, which we assume is linear within the spectral region of interest. Adjacent modes will couple through the Brillouin process, i.e., $g_{n,n',m} = g_n\delta_{n,n'+1} + g_{n+1}\delta_{n,n'-1}$, leaving us with

$$\begin{aligned}\frac{\partial}{\partial t}a_n = -i\omega_n a_n - v_n\frac{\partial}{\partial z}a_n - i\Big[&g_n\ a_{n-1}b\ e^{i(q-k_n+k_{n-1})z} + g_{n+1}\ a_{n+1}b\ e^{i(q-k_n+k_{n+1})z} \\ &+ g_n^*\ a_{n-1}b^\dagger\ e^{-i(q-k_{n-1}+k_n)z} + g_{n+1}^*\ a_{n+1}b^\dagger\ e^{-i(q-k_{n+1}+k_n)z}\Big], \\ \frac{\partial}{\partial t}b = -i\Omega_0 b - V_0\frac{\partial}{\partial z}b - i\sum_n &\left[g_n a_n a_{n-1}^\dagger\ e^{-i(q-k_n+k_{n-1})z} + g_{n+1}\ a_n a_{n+1}^\dagger\ e^{-i(q-k_n+k_{n+1})z}\right].\end{aligned} \tag{2.49}$$

Keeping only the phase-matched terms ($q = k_n - k_{n-1}$), we have

$$\begin{aligned}\frac{\partial}{\partial t}a_n &= -i\omega_n a_n - v_n\frac{\partial}{\partial z}a_n - i\Big[g_n\ a_{n-1}b + g_{n+1}^*\ a_{n+1}b^\dagger\Big], \\ \frac{\partial}{\partial t}b &= -i\Omega_0 b - V_0\frac{\partial}{\partial z}b - i\sum_n g_n^*\ a_n a_{n-1}^\dagger,\end{aligned} \tag{2.50}$$

showing the contributions from multiple stokes and anti-Stokes scattering processes, occurring between all neighboring optical modes.

As we did in our earlier Brillouin scatting analyses, we remove the spatial derivative from the equation describing the phonon field using adiabatic elimination (see Eq. (2.36)). Furthermore, the phonon mode is practically at its cut-off frequency, with a vanishing wavevector and close-to-zero group velocity ($V_0 \to 0$) [44], as illustrated in the acoustic dispersion diagram in Fig. 2.4, hence the spatial-derivative term can easily be neglected.

To find the steady-state spatial evolution of the field envelopes, we follow the same steps

as Eqs. (2.31)–(2.38), arriving at

$$\begin{aligned}\frac{\partial}{\partial z}a_n &= -\frac{\gamma_n}{2v_n}a_n - \frac{i}{v_n}\Big[g_n\ a_{n-1}b + g_{n+1}^*\ a_{n+1}b^\dagger\Big],\\ b &= -i\chi\sum_n g_n^*\ a_n a_{n-1}^\dagger,\end{aligned} \tag{2.51}$$

where we have again denoted the acoustic frequency response χ (Eq. (2.37)) and the optical loss of the optical waves γ_n. To simplify our analysis, we drop the optical loss terms (a valid approximation for low-loss, short devices), and assume that all optical coupling rates and group velocities are equal, i.e., $v_n = v$ and $g_n = g$ for all n, which is a good approximation as the Brillouin frequency shifts are orders-of-magnitude smaller than the optical frequency scale, hence all optical modes have similar optical properties.

At this point, it is useful to examine how the phonon field evolves in space, by calculating the spatial derivative

$$\begin{aligned}\frac{\partial}{\partial z}b &= -i\chi g^*\sum_n\Big[\Big(\partial_z a_n\Big)a_{n-1}^\dagger + a_n\Big(\partial_z a_{n-1}^\dagger\Big)\Big]\\ &= \frac{i}{v}\chi g^*\sum_n\Big[\Big(g\ a_{n-1}b + g^*\ a_{n+1}b^\dagger\Big)a_{n-1}^\dagger - a_n\Big(g^*\ a_{n-2}^\dagger b^\dagger + g\ a_n^\dagger b\Big)\Big]\\ &= \frac{i}{v}\chi g^*\sum_n\Big[g\ b\Big(\ |a_{n-1}|^2 - |a_n|^2\ \Big) - g^*\ b^\dagger\Big(a_{n+1}a_{n-1}^\dagger - a_n a_{n-2}^\dagger\Big)\Big] = 0.\end{aligned} \tag{2.52}$$

We can see that the spatial derivative is zero when we sum over all of the optical modes, such that the acoustic mode envelope is constant in space. Hence, we can evaluate the phonon field at any point, and we can do so at the waveguide input ($z = 0$) where we know the values of the optical fields. Intuitively, we can think of the phonon creation and annihilation rates balancing each other, leading to a steady state. This result teaches us that in the limit of small optical dissipation, the magnitude of the phonon field remains stationary throughout the waveguide. Furthermore, the phonon field amplitude is a reflection of the magnitude of the local forcing function, since the phonons decay within a very short length (see Eq. (2.36)). This shows us that in essence, the forcing field produced by light remains unchanged along the length of the waveguide, despite the spectral evolution of the optical field as it propagates.

To draw some further insights from this results we consider the dynamics produced for an input pump and Stokes fields, with indices $n = 0$ and $n = -1$, and using Eq. (2.51) we have

$$\begin{aligned} \frac{\partial}{\partial z} a_n &= -\frac{1}{v} |g|^2 \left[a_{n-1} \chi a_0(0) a_{-1}^{\dagger}(0) - \ a_{n+1} \chi^* a_0^{\dagger}(0) a_{-1}(0) \right], \\ b &= -i \chi g^* \ a_0(0) a_{-1}^{\dagger}(0). \end{aligned} \tag{2.53}$$

We see that the Brillouin interaction has the form of a $\chi^{(3)}$ nonlinear optical process, such as four-wave mixing [157]. Rearranging Eq. (2.53), we have

$$\frac{\partial}{\partial z} a_n = -\frac{1}{v} |g|^2 |\chi| \, |a_0(0) a_{-1}(0)| \left[a_{n-1} e^{i(\phi+\Lambda)} - \ a_{n+1} e^{-i(\phi+\Lambda)} \right], \tag{2.54}$$

where we have defined the relative phase between the two tones at the input using $\Lambda = \arg(a_{-1}^{(\mathrm{A})\dagger}(0) a_0^{(\mathrm{A})}(0))$, and the phase of the frequency response is denoted $\phi = \arg(\chi)$. This differential equation has the solution

$$a_n(z) = a_0(0) J_{-n}(\xi \ z) \, e^{i(\phi+\Lambda)n} + a_{-1}(0) J_{-(n+1)}(\xi \ z) \, e^{i(\phi+\Lambda)(n+1)}, \tag{2.55}$$

where $J_n(\cdot)$ denotes the n^{th} order Bessel function. We have defined the parameter $\xi = G_{\mathrm{B}} (P_0^{(\mathrm{A})} P_{-1}^{(\mathrm{A})})^{1/2} (\Gamma/2) |\chi|$, using Eqs. (2.39) and (2.41) to express the fields in terms of input optical power and Brillouin gain (more details of this derivation can be found in Section 3.2). We can see that even though there were only two tones at the input of the system, multiple sidebands appear through the forward Brillouin process, as seen in Fig. 2.5(c).

The spectral evolution of the otical felds can be seen as a form Brillouin-driven self-phase modulation. We can show this by reintroducing the fast oscillating terms to the operators

we have derived, and calculating the total field amplitude by summing all optical tones

$$\begin{aligned} s(z,t) &\propto \sum_n a_n(z) e^{-i(\omega_0 + n\Omega)t} \\ &= \underbrace{\left(a_0(0) e^{-i\omega_0 t} + a_{-1}(0) e^{-i(\omega_0 - \Omega)t} \right)}_{\text{input fields}} \underbrace{\exp\left[i \frac{\Gamma}{2} |\chi| \, G_{\mathrm{B}} \sqrt{P_0 P_{-1}} \; z \sin\Big(\Omega t - (\phi + \Lambda) \Big) \right]}_{\text{phase modulation}}. \end{aligned} \tag{2.56}$$

Examining the optical power (as would be measured by a photodetector) yields

$$|s(z,t)|^2 \propto P_0 + P_{-1} + 2\sqrt{P_0 P_{-1}} \cos\left(\Omega t - \Lambda\right), \tag{2.57}$$

revealing that the optical power within the system is not varying in space and that the Brillouin scattering process does not affect the intensity beat note between the two tones at the device input.

At this stage, it is useful to examine small-signal optical amplification produced by forward intra-modal scattering to compare it with other Brillouin processes. We begin by using Eq. (2.55) to write the exact solution valid for all powers (i.e., including pump depeltion). The gain experienced by a Stokes signal ($n = -1$) as it propagates through the device along with a strong pump wave ($n = 0$) is given by

$$a_{-1}(z) = a_{-1}(0) \left(\left| \frac{a_0(0)}{a_{-1}(0)} \right| J_1\left(\xi z\right) e^{-i\phi} + J_0\left(\xi z\right) \right), \tag{2.58}$$

and in terms of optical powers $P_n \propto |a_n|^2$ this yields

$$P_{-1}(z) = P_{-1}(0) \left| \sqrt{\frac{P_0(0)}{P_{-1}(0)}} J_1\left(\xi z\right) e^{-i\phi} + J_0\left(\xi z\right) \right|^2. \tag{2.59}$$

To explore the small-signal limit, we assume that $(\xi z) \ll 1$, which is consistent with the undepleted pump approximation. By expanding the Bessel functions to first order ($J_0(x) \approx$

1, $J_1(x) \approx x/2$), we have

$$P_{-1}(z) = P_{-1}(0)\left|1 + \frac{1}{2}G_{\mathrm{B}}P_0\frac{\Gamma}{2}\chi z\right|^2. \tag{2.60}$$

We see that the gain experienced by the small Stokes signal grows quadratically with Brillouin gain, pump power, and propagation length. This is in contrast with the exponential amplification we saw for Backward and inter-modal Brillouin scattering (see Eqs. (2.42) and (2.48)), which can also be seen in Fig. 2.5.

When examining the spectral evolution using normalized mode amplitudes (that represent photon number density), our result looks like a phase-modulation process that conserves photon number (Eq. (2.56)). However, when expressing the fields as optical power, we see that it is a nonconservative process, in which the phonon field represents a loss channel that dissipates energy from the system. We can see this by summing the optical power in all optical waves, taking into account the different frequencies of each tone, following Eq. (2.39)

$$P_{\mathrm{tot}}(z) = \hbar v \sum_n (\omega_0 + n\Omega)\left|a_n(z)\right|^2, \tag{2.61}$$

and plugging in the mode amplitudes from Eq. (2.55)

$$P_{\mathrm{tot}}(z) = \underbrace{\hbar\omega_0 v\left|a_0(0)\right|^2 + \hbar\left(\omega_0 - \Omega\right)v\left|a_{-1}(0)\right|^2}_{P_{\mathrm{tot}}(0)} - \underbrace{\frac{\Omega}{\omega_0}G_{\mathrm{B}}P_0P_{-1}z\frac{\Gamma}{2}\,\mathrm{Re}\left(\chi\right)\left[1-\left(\Omega/\omega_0\right)\right]^{-1/2}}_{\text{redshift}}. \tag{2.62}$$

The first two terms are the power of the tones at the input (pump and Stokes, respectively), and the third term reveals a redshift, scaling linearly with the propagation length z. We can also express this redshift in terms of the number of phonons in the system and the Brillouin gain by using Eqs. (2.41) and (2.53), resulting in

$$P_{\mathrm{tot}}(z) = P_{\mathrm{tot}}(0) - \underbrace{\hbar\Omega\left|b\right|^2\Gamma z}_{\text{redshift}}, \tag{2.63}$$

where we have used $\mathrm{Re}\left(\chi\right) = (\Gamma/2)|\chi|^2$ for $\chi = [i(\Omega_0 - \Omega) + \Gamma/2]^{-1}$. We can now see that

the redshift can be described as the energy in the phonon field ($\hbar\Omega\,|b|^2$) with a constant dissipation rate Γ over a length z. This redshift can also be seen in Fig.(2.5)(c), showing higher optical power in the lower sidebands (rather than symmetric scattering to both upper and lower sidebands). Interestingly, since the phonon number is larger for high-Q acoustic modes ($|b|^2 \propto \Gamma^{-2}$) the redshift is inversely proportional to the dissipation rate $P_{\mathrm{tot}} \propto \Gamma^{-1}$. This effect is very small, as seen from the factor Ω_0/ω_0 for the redshift term in Eq. (2.62), which is typically on the order of $\sim 10^{-5}$. We note, that this analysis is consistent with previous studies as well as an experimental demonstration in optical fiber [29, 176].

Spontaneous forward Brillouin scattering

Finally, we turn to analyze spontaneous forward intra-modal Brillouin scattering, which is qualitatively different than the backward and inter-modal cases. We will assume a strong pump tone (with amplitude a_{p}) at the input of a forward Brillouion-active medium, and analyze the scattering to the Stokes (a_{s}) and anti-Stokes sidebands (a_{as}). As we did earlier, we will treat the pump as constant (undepleted) and we will also neglect scattering to higher-order sidebands. Using Eq. (2.50), and introducing a stochastic term η describing the fluctuations of the phonon mode, we have

$$\begin{aligned}
\frac{\partial}{\partial t}a_{\mathrm{s}} &= -v_{\mathrm{s}}\frac{\partial}{\partial z}a_{\mathrm{s}} - ig^*_{\mathrm{p,s}}\; a_{\mathrm{p}}b^\dagger, \\
\frac{\partial}{\partial t}a_{\mathrm{as}} &= -v_{\mathrm{as}}\frac{\partial}{\partial z}a_{\mathrm{as}} - ig_{\mathrm{as,p}}\; a_{\mathrm{p}}b, \\
\frac{\partial}{\partial t}b &= -i\left(\Omega_0 - \Omega\right)b - i\left(g^*_{\mathrm{p,s}}a_{\mathrm{p}}a^\dagger_{\mathrm{s}} + g^*_{\mathrm{as,p}}a_{\mathrm{as}}a^\dagger_{\mathrm{p}}\right) + \eta.
\end{aligned} \tag{2.64}$$

Solving for the Stokes field yields [172, 175]

$$a_{\mathrm{s}}(L,t) = -\frac{i}{v_{\mathrm{s}}}g^* a_{\mathrm{p}}\int_0^t dt' \int_0^L dz\eta^\dagger(z,t')\exp\left[-\frac{\Gamma}{2}\left(t-t'\right)\right], \tag{2.65}$$

where we have assumed equal coupling rates to the Stokes and anti-Stokes sidebands ($g^*_{\mathrm{p,s}} = g^*_{\mathrm{as,p}} = g$). We can calculate the spectral density of spontaneous scattering using the

Wiener–Khinchin theorem

$$S_{\mathrm{s}}(\omega) = \lim_{t\to\infty} \hbar\omega_{\mathrm{s}} v_{\mathrm{s}} \int dt' \langle a_{\mathrm{s}}^{\dagger}(L, t+t') a_{\mathrm{s}}(L,t)\rangle e^{-i\omega t'}, \tag{2.66}$$

resulting in [172]

$$S_{\mathrm{s}}(\omega) = \hbar\omega \left(n_{\mathrm{th}}+1\right) G_{\mathrm{B}} P_{\mathrm{p}} L \, \frac{(\Gamma/2)^2}{\left(\Omega_0 - \Omega - \omega\right)^2 + (\Gamma/2)^2}, \tag{2.67}$$

showing a Lorentzian lineshape. As we have see earlier, the total scattered optical power can be calculated by integrating this spectrum $P_{\mathrm{s}} = 1/(2\pi)\int d\omega S_{\mathrm{s}}(\omega)$, and similar expressions can be derived for anti-Stokes spontaneous scattering (the result is similar, with $(n_{\mathrm{th}}+1) \to n_{\mathrm{th}}$). We see that there is no exponential amplification in this case, and the scattered field shows linear growth with device length and pump power. Interestingly, noise cannot initiate a stimulated process through forward intra-modal scattering [172]. One way to interpret this result is that phonons created in the Stokes process are annihilated in the anti-Stokes interaction, and cannot build up energy to provide feedback. This is also consistent with the fact that forward Brillouin scattering results in phase modulation, rather than energy transfer and amplification.

2.4 Conclusion

In this chapter, we have presented the theory of Brillouin scattering and analyzed the necessary phase-matching and energy-conservation conditions for such processes. We have seen how the presence of acoustic fields in a medium can result in light scattering, through photoelastic and moving-boundary effects, resulting in Stokes (red-shifted) and anti-Stokes (blue-shifted) processes. In a stimulated scattering process, we have shown how optical forces, namely electrostriction and radiation pressure, can drive the acoustic fields, leading to an overall third-order ($\chi^{(3)}$) optical nonlinearity.

Using a Hamiltonian framework, we have examined different geometries of Brillouin scattering, namely Backward, forward inter-modal, and forward intra-modal processes, which

have vastly different properties. We have seen how forward intra-modal scattering results in a form of self-phase modulation, while backward and inter-modal scattering showed exponential power transfer between two optical tones. Understanding the dynamics produced by the different types of Brillouin scattering processes will become important when we utilize such effects within photonic devices. For example, in later chapters we will see how forward intra-modal scattering can be utilized to produce multi-pole narrowband filters, while the unique phase-matching conditions necessary for inter-modal scattering can be used to achieve nonreciprocal optical transmission.

The formalism presented here will be the basis for further analysis, where we will proceed to study more complex photonic systems that utilize Brillouin scattering to perform signal-processing operations. Additionally, the spontaneous scattering processes we have described here can be a source of noise in many Brillouin-based applications, and their analysis will be important when trying to examine the practical and fundamental limits of Brillouin-based technologies.

Chapter 3

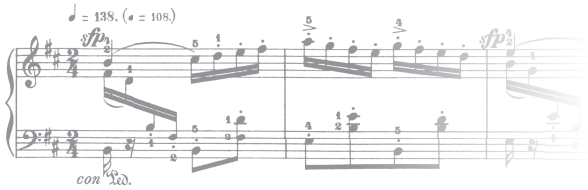

Nonlocal forward Brillouin interactions

3.1 Introduction

Optical nonlinear processes such as four-wave mixing and harmonic generation are usually described in terms of a spatially local susceptibility. Namely, the optical fields in one location do not alter the nonlinear response in another point in space [157]. In Raman scattering, for example, the short mean free path of the THz-frequency optical phonons participating in the nonlinear process also results in a local susceptibility. By comparison, nonlocal nonlinearities require a mechanism by which the optical fields in one location affect the optical response in another location. Nonlocal response has been studied in the context of thermally induced effects [177–179], as well as more exotic systems such as nematic liquid crystals [180], trapped atoms [181], Rydberg gases [182], plasmonic systems [183, 184], and graphene [185]. All of these interactions are the result of transport mechanisms, such as heat, electric charge, or atoms, which mediate the optical response over an extended distance.

The acoustic phonons that participate in a Brillouin scattering process can also mediate long-range interactions. These elastic modes can be long-lived and propagate many optical wavelengths before decaying, yielding nonlocal dynamics [44, 64, 168]. This acousto-optic coupling is a three-wave mixing process producing a coherent interaction of optical waves and acoustic phonons [35, 157, 173]. More specifically, in a forward Brillouin scattering

process, the optical fields are co-propagating, while the phonons produced by the scattering process are emitted perpendicular to the direction of optical wave propagation [44, 63, 64]. The transverse nature of the phonons, combined with their long lifetime, enables them to explore a space that is much larger than the acousto-optic overlap region [44]. This allows the design of structures where the acoustic fields extend the distance between distinct optical guided waves, which are otherwise optically decoupled [186, 187].

Such nonlocal Brillouin interactions have been recently demonstrated both in optical fiber and in chip-scale photonic devices. In multi-core fibers, light propagating within spatially distinct cores can be coupled to acoustic modes occupying the entire fiber cross-section [188]. By comparison, integrated photonic systems allow additional structural degrees of freedom which can be used to tailor both the optical and acoustic modes that participate in the nonlocal interaction [186]. Devices utilizing these interactions can be the basis for new signal processing schemes such as filters [187], oscillators [189], and modulators [139], for both optical and microwave applications.

In this chapter, we analyze these nonlocal interactions in the context of Brillouin-active superstructures supporting acoustic modes extending multiple optical waveguides. Because the phonon mode participating in the Brillouin interaction has an overlap with multiple optical fields, the scattering processes in the different waveguides are no longer independent. Hence, the light scattering in one waveguide will affect the dynamics in another, resulting in a nonlocal susceptibility between the two spatially separated waveguides. We show that the intensity envelope of light propagating in one waveguide of the device results in pure phase modulation of light in a spatially separate optical guided wave, determined by the acoustic and optical properties of both waveguides, revealing the nonlocal nature of the interaction. We further extend our analysis to the case of multiple acoustic modes participating in the acousto-optic process and show that coupling multiple acoustic modes results in phonon 'super-modes', all occupying the extended space and interacting with the optical fields. The coherent interference of these phonon super-modes yields a multi-pole frequency response for the nonlocal susceptibility, showing a faster frequency roll-off compared to the typical Lorentzian lineshape of a single acoustic resonance.

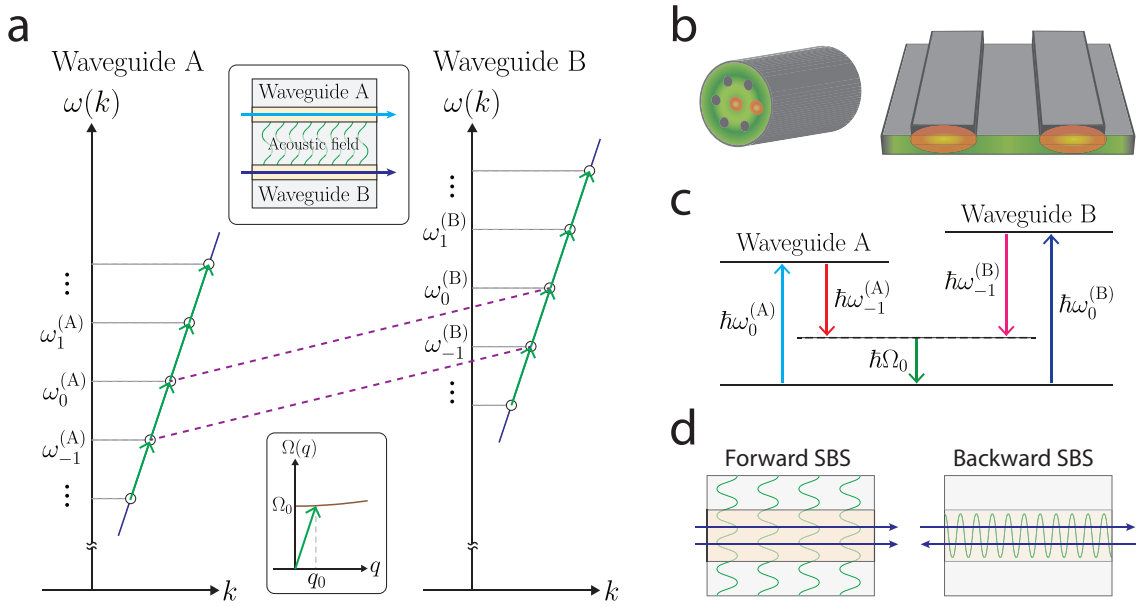

Figure 3.1: **(a)** Dispersion diagrams of an optical mode in each of the two waveguides. The phonon coupling between optical tones (green arrow) is phase-matched in both waveguides. The phonon couples multiple tones spaced by frequency Ω_0, as long as the dispersion relation is linear. Bottom inset: The acoustic dispersion diagram, illustrating the acoustic mode taking part in the interaction is near its cutoff frequency with a vanishing axial wavevector. Top inset: A schematic illustration of the system, where two guided optical modes are both coupled to an extended acoustic mode. **(b)** Left: An illustration of a multi-core optical fiber, where optical modes are spatially separated (orange), and a transverse acoustic mode (green) is supported by the entire cladding cross-section, such as described in Ref. [188]. Right: An illustration of a chip-scale device with two optical waveguides, each supporting an optical mode (orange), and a single spatially-extended acoustic mode (green), as discussed in Refs. [139,187]. **(c)** Energy level diagram illustrating two optical tones in each waveguide interacting with a spatially extended nonlocal acoustic mode. **(d)** Schematic comparison between forward and backward Brillouin processes. In a forward geometry, the transverse nature of the acoustic modes enables them to explore a large space, extending well beyond the acousto-optic overlap region, whereas in a backward process utilizing a bulk acoustic mode, the acoustic and optical waves are confined to a similar space. Reproduced from Ref. [154]

3.2 Theoretical analysis

We begin our analysis by considering an optomechanical system consisting of two independent optical waveguides that also supports a single guided acoustic mode. While the two waveguides are optically decoupled, the light in each waveguide is acousto-optically coupled to the acoustic mode through a forward stimulated Brillouin scattering (FSBS) process. We assume that all of the optical fields are co-propagating and that the photon-phonon coupling is a consequence of electrostrictive forces and radiation pressure [161, 171], which can be tailored through the design of the device geometry [44, 162]. Examples of chip-scale and fiber-based device geometries that can produce such interactions are illustrated in Fig. 3.1(b).

The FSBS process in each of the waveguides can be described as a three-wave interaction involving two photons and a phonon, as illustrated in the phase-matching diagrams in Fig. 3.1(a). As we have seen in Chapter 2, the phase-matching condition required in both waveguides is $q(\Omega_0) = k(\omega_0) - k(\omega_{-1})$, where $k(\omega)$ is the optical wavevector at optical frequencies ω_0 and ω_{-1}, and $q(\Omega_0)$ is the wavevector of the acoustic wave at frequency Ω_0. Since the optical waves have similar wavevectors, this requires a cut-off phonon mode, with a vanishing axial wavevector, such that the acoustic wave is nearly perpendicular to the direction of the optical wave propagation [29, 163, 172]. The transverse nature of these phonons enables them to extend much further than the optical waveguide cross-section. This is in contrast with backward-Brillouin scattering processes utilizing bulk acoustic modes, where the phonon typically occupies a similar region as the optical waves, as illustrated in Fig. 3.1(d). The wavelengths of the light in the two optical waveguides, which we denote A and B, can be different as long as energy is conserved in the process, as seen in Fig. 3.1(c). This requires $\hbar\Omega_0 = \hbar\omega_0^{(\mathrm{A})} - \hbar\omega_{-1}^{(\mathrm{A})}$ and $\hbar\Omega_0 = \hbar\omega_0^{(\mathrm{B})} - \hbar\omega_{-1}^{(\mathrm{B})}$, such that the phonon frequency matches the frequency difference of the two optical tones in both waveguides. Additionally, phase matching and energy conservation together require that the optical modes in both waveguides have similar optical group velocities [44].

As was discussed in Chapter 2, in the absence of strong optical dispersion, an FSBS

process enables light to be cascaded to multiple optical frequencies [29,64,170,172], and we describe the optical fields in each waveguide as a sum of discrete tones with field amplitude a_n that are spaced by frequency Ω such that $\omega_n - \omega_{n-1} = \Omega$. Building on the analysis of forward Brillouin scattering from Section 2.3.4, we write a Hamiltonian describing two optical waveguides, which are both coupled to a single acoustic mode. We can separate the Hamiltonian into terms describing the optical fields in each waveguide, the acoustic field, and the acousto-optic interactions in each waveguide

$$H = H_{\text{opt}}^{(\text{A})} + H_{\text{opt}}^{(\text{B})} + H_{\text{ac}} + H_{\text{int}}^{(\text{A})} + H_{\text{int}}^{(\text{B})}. \tag{3.1}$$

We denote the steady-state optical field amplitudes in the two waveguides as $a_n^{(\text{A})}$ and $a_n^{(\text{B})}$ with frequencies $\omega_n^{(\text{A})}$ and $\omega_n^{(\text{B})}$, and the steady-state acoustic field amplitude as b, with an acoustic dissipation rate Γ. We assume a constant optical group velocity over the frequency range of interest, such that the optical tones can cascade to an arbitrary number of sidebands. Following the discussion in Section 2.3.4, the different terms are given by

$$\begin{aligned}
H_{\text{opt}}^{(\text{A})} &= \sum_n \hbar \int dz\ {a_n^{(\text{A})}}^\dagger(z)\hat{\omega}_n^{(\text{A})} a_n^{(\text{A})}(z), \\
H_{\text{opt}}^{(\text{B})} &= \sum_n \hbar \int dz\ {a_n^{(\text{B})}}^\dagger(z)\hat{\omega}_n^{(\text{B})} a_n^{(\text{B})}(z), \\
H_{\text{ac}} &= \hbar \int dz\ b^\dagger(z)\hat{\Omega}_0 b(z), \\
H_{\text{int}}^{(\text{A})} &= \sum_n \hbar \int dz\ g_n^{(\text{A})*} a_n^{(\text{A})}(z) {a_{n-1}^{(\text{A})}}^\dagger(z) b^\dagger(z) e^{-i\Delta k_n^{(\text{A})} z} + \text{H.C.}, \\
H_{\text{int}}^{(\text{B})} &= \sum_n \hbar \int dz\ g_n^{(\text{B})*} a_n^{(\text{B})}(z) {a_{n-1}^{(\text{B})}}^\dagger(z) b^\dagger(z) e^{-i\Delta k_n^{(\text{B})} z} + \text{H.C.},
\end{aligned} \tag{3.2}$$

where $\Delta k_n^{(\text{A})} = q_0 - (k_n^{(\text{A})} - k_{n-1}^{(\text{A})})$ and $\Delta k_n^{(\text{B})} = q_0 - (k_n^{(\text{B})} - k_{n-1}^{(\text{B})})$ describe the phase mismatch between the phonon and the photons in each of the two waveguides. We assume each waveguide supports a single optical spatial mode, and the index n sums over all optical tones coupled through the acousto-optic interaction. The coupling rate g can have both photo-elastic and radiation pressure components, which can be evaluated using Eq. (2.27).

We can readily explore the dynamics of the acoustic field from the total Hamiltonian

H, using the Heisenberg equations of motion

$$\frac{\partial}{\partial t}a_n^{(\mathrm{A})}(t) = \frac{1}{i\hbar}\left[a_n^{(\mathrm{A})}(t), H\right], \qquad \frac{\partial}{\partial t}a_n^{(\mathrm{B})}(t) = \frac{1}{i\hbar}\left[a_n^{(\mathrm{B})}(t), H\right], \qquad \frac{\partial}{\partial t}b(t) = \frac{1}{i\hbar}\left[b(t), H\right]. \tag{3.3}$$

Using the commutation relations

$$\begin{aligned} \left[a_n^{(\mathrm{A})}(z,t), {a_m^{(\mathrm{A})}}^{\dagger}(z',t)\right] &= \delta\left(z-z'\right)\delta_{n,m}, \qquad \left[a_n^{(\mathrm{A})}(z,t), {a_m^{(\mathrm{B})}}^{\dagger}(z',t)\right] = 0, \\ \left[a_n^{(\mathrm{B})}(z,t), {a_m^{(\mathrm{B})}}^{\dagger}(z',t)\right] &= \delta\left(z-z'\right)\delta_{n,m}, \qquad \left[b(z,t), b^{\dagger}(z',t)\right] = \delta\left(z-z'\right), \end{aligned} \tag{3.4}$$

we find

$$\begin{aligned} \frac{\partial}{\partial t}a_n^{(\mathrm{A})} &= -i\hat{\omega}_n a_n^{(\mathrm{A})} - i\left(g_n^{(\mathrm{A})}a_{n-1}^{(\mathrm{A})}be^{i\Delta k_n^{(\mathrm{A})}z} + {g^{(\mathrm{A})}}_{n+1}^{*}a_{n+1}^{(\mathrm{A})}b^{\dagger}e^{-i\Delta k_{n+1}^{(\mathrm{A})}z}\right), \\ \frac{\partial}{\partial t}a_n^{(\mathrm{B})} &= -i\hat{\omega}_n a_n^{(\mathrm{B})} - i\left(g_n^{(\mathrm{B})}a_{n-1}^{(\mathrm{B})}be^{i\Delta k_n^{(\mathrm{B})}z} + g_{n+1}^{(\mathrm{B})*}a_{n+1}^{(\mathrm{B})}b^{\dagger}e^{-i\Delta k_{n+1}^{(\mathrm{B})}z}\right), \\ \frac{\partial}{\partial t}b &= -i\hat{\Omega}_0 b - i\sum_n\left(g_n^{(\mathrm{A})*}a_n^{(\mathrm{A})}{a_{n-1}^{(\mathrm{A})}}^{\dagger}e^{-i\Delta k_n^{(\mathrm{A})}z} + g_n^{(\mathrm{B})*}a_n^{(\mathrm{B})}{a_{n-1}^{(\mathrm{B})}}^{\dagger}e^{-i\Delta k_n^{(\mathrm{B})}z}\right). \end{aligned} \tag{3.5}$$

For brevity of notation, we have suppressed the arguments (z,t) for all operators.

We keep the dispersion operators to first order for the optical and acoustic fields, $\hat{\omega}_n \approx \omega_n - iv_n\partial_z$, $\hat{\Omega}_0 \approx \Omega_0 - iv_{\mathrm{ac}}\partial_z$, and add the phonon dissipation by including an imaginary part to the acoustic frequency, $\Omega_0 \to \Omega_0 - i\left(\Gamma/2\right)$. At this stage, it is convenient to rewrite the equations in the rotating frame by factoring out the fast oscillating terms $a_n \to a_n e^{-i\omega_n t}$ and $b \to be^{-i\Omega t}$ (where $\Omega = \omega_n - \omega_{n-1}$), which results in

$$\begin{aligned} \frac{\partial}{\partial t}a_n^{(\mathrm{A})} + v_n^{(\mathrm{A})}\frac{\partial}{\partial z}a_n^{(\mathrm{A})} &= -i\left(g_n^{(\mathrm{A})}a_{n-1}^{(\mathrm{A})}be^{i\Delta k_n^{(\mathrm{A})}z} + {g_{n+1}^{(\mathrm{A})}}^{*}a_{n+1}^{(\mathrm{A})}b^{\dagger}e^{-i\Delta k_{n+1}^{(\mathrm{A})}z}\right), \\ \frac{\partial}{\partial t}a_n^{(\mathrm{B})} + v_n^{(\mathrm{B})}\frac{\partial}{\partial z}a_n^{(\mathrm{B})} &= -i\left(g_n^{(\mathrm{B})}a_{n-1}^{(\mathrm{B})}be^{i\Delta k_n^{(\mathrm{B})}z} + {g_{n+1}^{(\mathrm{B})}}^{*}a_{n+1}^{(\mathrm{B})}b^{\dagger}e^{-i\Delta k_{n+1}^{(\mathrm{B})}z}\right), \\ \frac{\partial}{\partial t}b + v_{\mathrm{ac}}\frac{\partial}{\partial z}b &= -i\left(\Omega_0 - \Omega - i\Gamma/2\right)b \\ &\quad - i\sum_n\left(g_n^{(\mathrm{A})*}a_n^{(\mathrm{A})}{a_{n-1}^{(\mathrm{A})}}^{\dagger}e^{-i\Delta k_n^{(\mathrm{A})}z} + g_n^{(\mathrm{B})*}a_n^{(\mathrm{B})}{a_{n-1}^{(\mathrm{B})}}^{\dagger}e^{-i\Delta k_n^{(\mathrm{B})}z}\right). \end{aligned} \tag{3.6}$$

In the case of forward Brillouin scattering (FSBS) the phonon field $b(z)$ is close to its

cut-off frequency, as illustrated in Fig. 3.1(a), with a small axial wavevector and vanishing group velocity[1] [172], such that we can set $v_{\mathrm{ac}} \to 0$. We further assume that the optical mode has a constant group velocity in the frequency range of interest for each of the two waveguides, equivalent to no optical group velocity dispersion (GVD), such that $v_n = v$ and $\Delta k_n = \Delta k = 0$ [162, 172]. We also set the optomechanical coupling rates to be equal for all of the optical frequencies, $g_n = g$, a valid assumption since the optical field properties do not change much over the acoustic frequency range. The steady-state phonon field envelope now has the form

$$b = -i\chi \sum_n \left(g^{(\mathrm{A})*} a_n^{(\mathrm{A})} {a_{n-1}^{(\mathrm{A})}}^\dagger + g^{(\mathrm{B})*} a_n^{(\mathrm{B})} {a_{n-1}^{(\mathrm{B})}}^\dagger \right), \tag{3.7}$$

where we have denoted the frequency response of the acoustic field

$$\chi = \frac{1}{i\left(\Omega_0 - \Omega\right) + \Gamma/2}, \tag{3.8}$$

and the optical fields envelopes are given by

$$\begin{aligned} \frac{\partial}{\partial z} a_n^{(\mathrm{A})} &= -\frac{i}{v^{(\mathrm{A})}} \left(g^{(\mathrm{A})} a_{n-1}^{(\mathrm{A})} b + g^{(\mathrm{A})*} a_{n+1}^{(\mathrm{A})} b^\dagger \right), \\ \frac{\partial}{\partial z} a_n^{(\mathrm{B})} &= -\frac{i}{v^{(\mathrm{B})}} \left(g^{(\mathrm{B})} a_{n-1}^{(\mathrm{B})} b + g^{(\mathrm{B})*} a_{n+1}^{(\mathrm{B})} b^\dagger \right). \end{aligned} \tag{3.9}$$

Calculating the spatial derivative of the phonon field in Eq. (3.7) results in

$$\begin{aligned} \frac{\partial}{\partial z} b = -i\chi \sum_n \Bigg[& g^{(\mathrm{A})*} \frac{\partial a_n^{(\mathrm{A})}}{\partial z} {a_{n-1}^{(\mathrm{A})}}^\dagger + g^{(\mathrm{A})*} a_n^{(\mathrm{A})} \frac{\partial {a_{n-1}^{(\mathrm{A})}}^\dagger}{\partial z} \\ & + g^{(\mathrm{B})*} \frac{\partial a_n^{(\mathrm{B})}}{\partial z} {a_{n-1}^{(\mathrm{B})}}^\dagger + g^{(\mathrm{B})*} a_n^{(\mathrm{B})} \frac{\partial {a_{n-1}^{(\mathrm{B})}}^\dagger}{\partial z} \Bigg], \end{aligned} \tag{3.10}$$

1. For example, in real-world systems with an acoustic quality factor $Q \sim 1000$, the phonons decay after traveling a distance of ~ 10 nm [44]. This implies that negligible phonon transport occurs over the lifetime of the mode, and we can view the phonon as localized with respect to the direction of propagation.

and substituting into Eq. (3.9)

$$\frac{\partial}{\partial z}b = -\chi \sum_n \Bigg[g^{(\mathrm{A})*} \Bigg(g^{(\mathrm{A})} b \left(\left| a_{n-1}^{(\mathrm{A})} \right|^2 - \left| a_n^{(\mathrm{A})} \right|^2 \right) + g^{(\mathrm{A})*} b^\dagger \left(a_{n+1}^{(\mathrm{A})} a_{n-1}^{(\mathrm{A})\,\dagger} - a_n^{(\mathrm{A})} a_{n-2}^{(\mathrm{A})\,\dagger} \right) \Bigg) + g^{(\mathrm{B})*} \Bigg(g^{(\mathrm{B})} b \left(\left| a_{n-1}^{(\mathrm{B})} \right|^2 - \left| a_n^{(\mathrm{B})} \right|^2 \right) + g^{(\mathrm{B})*} b^\dagger \left(a_{n+1}^{(\mathrm{B})} a_{n-1}^{(\mathrm{B})\,\dagger} - a_n^{(\mathrm{B})} a_{n-2}^{(\mathrm{B})\,\dagger} \right) \Bigg) \Bigg] = 0, \tag{3.11}$$

we can see how the spatial derivative vanishes when we sum over all n for which the field operators are non-zero. Hence, the phonon field is constant in space and can be determined by its value at $z = 0$

$$b = -i\chi \sum_n \left(g^{(\mathrm{A})*} a_n^{(\mathrm{A})\dagger} a_{n+1}^{(\mathrm{A})} + g^{(\mathrm{B})*} a_n^{(\mathrm{B})\dagger} a_{n+1}^{(\mathrm{B})} \right) \Big|_{z=0}. \tag{3.12}$$

Next, to study the dynamics of the system, we analyze the effect of light scattering in waveguide A on the spectral evolution of a separate optical wave propagating in waveguide B. To do this, we assume two tones in the input of waveguide A at frequencies $\omega_0^{(\mathrm{A})}$ and $\omega_{-1}^{(\mathrm{A})} = \omega_0^{(\mathrm{A})} - \Omega$, with amplitudes $a_0^{(\mathrm{A})}$ and $a_{-1}^{(\mathrm{A})}$, which will drive the acoustic mode through a forward-Brillouin interaction, as seen from Eq. (3.12). Assuming a single tone in the input of waveguide B, the second term of Eq. (3.12) does not contribute, and we are left with

$$b = -i\chi g^{(\mathrm{A})*} a_{-1}^{(\mathrm{A})\dagger}(0)\; a_0^{(\mathrm{A})}(0). \tag{3.13}$$

Substituting into Eq. (3.9) yields the spatial evolution of the optical fields

$$\begin{aligned} \frac{\partial}{\partial z} a_n^{(\mathrm{A})} &= -\frac{1}{v^{(\mathrm{A})}} \left| g^{(\mathrm{A})} \right|^2 \left[a_{n-1}^{(\mathrm{A})} \chi a_{-1}^{(\mathrm{A})\dagger}(0) a_0^{(\mathrm{A})}(0) - a_{n+1}^{(\mathrm{A})} \chi^* a_{-1}^{(\mathrm{A})}(0) a_0^{(\mathrm{A})\dagger}(0) \right], \\ \frac{\partial}{\partial z} a_n^{(\mathrm{B})} &= -\frac{1}{v^{(\mathrm{B})}} \left[g^{(\mathrm{B})} g^{(\mathrm{A})*} a_{n-1}^{(\mathrm{B})} \chi a_{-1}^{(\mathrm{A})\dagger}(0) a_0^{(\mathrm{A})}(0) - g^{(\mathrm{B})*} g^{(\mathrm{A})} a_{n+1}^{(\mathrm{B})} \chi^* a_{-1}^{(\mathrm{A})}(0) a_0^{(\mathrm{A})\dagger}(0) \right]. \end{aligned} \tag{3.14}$$

To understand the nonlinear susceptibility produced by the forward-Brillouin process we examine the small-signal limit, by focusing on the dynamics of the $n = -1$ tone in each

waveguide (i.e., the Stokes wave). Neglecting higher-order ($|n| \geq 2$) tones, we have

$$\frac{\partial}{\partial z}a_{-1}^{(\mathrm{A})} = i\gamma^{(\mathrm{A})}a_0^{(\mathrm{A})}a_{-1}^{(\mathrm{A})}(0)a_0^{(\mathrm{A})\dagger}(0), \qquad \frac{\partial}{\partial z}a_{-1}^{(\mathrm{B})} = i\gamma^{(\mathrm{B})}a_0^{(\mathrm{B})}a_{-1}^{(\mathrm{A})}(0)a_0^{(\mathrm{A})\dagger}(0), \tag{3.15}$$

where we have defined the susceptibilities in the two waveguides

$$\gamma^{(\mathrm{A})} = -\frac{i}{v^{(\mathrm{A})}}\left|g^{(\mathrm{A})}\right|^2\chi^*, \qquad \gamma^{(\mathrm{B})} = -\frac{i}{v^{(\mathrm{B})}}g^{(\mathrm{B})*}g^{(\mathrm{A})}\chi^*. \tag{3.16}$$

Eq. (3.15) has the form of a third-order nonlinear optical process, where three field amplitudes produce field amplification, similar to the form derived for four-wave mixing, Raman scattering, and backward stimulated Brillouin scattering [157]. Examining the equation for waveguide B reveals the nonlocal nature of the susceptibility, where field amplitudes in waveguide A determine the response in the optically decoupled, spatially separated waveguide B. Furthermore, the susceptibility $\gamma^{(\mathrm{B})}$ depends on the Brillouin coupling rates in both waveguides A and B. Similar expressions can be written for the anti-Stokes ($n = 1$) tone in the waveguides.

For simplicity, we assume the two waveguides are identical[2] by setting $v^{(\mathrm{A})} = v^{(\mathrm{B})} = v$ and $g^{(\mathrm{A})} = g^{(\mathrm{B})} = g$, which is a good approximation in many physical systems [139,186,187]. The equations describing the fields in waveguides A and B are now

$$\begin{aligned}
\frac{\partial}{\partial z}a_n^{(\mathrm{A})} &= -\frac{1}{v}|g|^2\left|a_{-1}^{(\mathrm{A})}(0)\ a_0^{(\mathrm{A})}(0)\right||\chi|\left(a_{n-1}^{(\mathrm{A})}\ e^{i\phi}e^{i\Lambda} - a_{n+1}^{(\mathrm{A})}\ e^{-i\phi}e^{-i\Lambda}\right), \\
\frac{\partial}{\partial z}a_n^{(\mathrm{B})} &= -\frac{1}{v}|g|^2\left|a_{-1}^{(\mathrm{A})}(0)\ a_0^{(\mathrm{A})}(0)\right||\chi|\left(a_{n-1}^{(\mathrm{B})}\ e^{i\phi}e^{i\Lambda} - a_{n+1}^{(\mathrm{B})}\ e^{-i\phi}e^{-i\Lambda}\right),
\end{aligned} \tag{3.17}$$

where we denote the relative phase between the two tones at the input to waveguide A as $\Lambda = \arg(a_{-1}^{(\mathrm{A})\dagger}(0)\ a_0^{(\mathrm{A})}(0))$ and the phase of the frequency response $\phi = \arg(\chi)$. We now solve the differential equation by rotating the field operators $\bar{a}_n = a_n e^{-i(\phi+\Lambda)n}$, giving us

2. In the case where the two waveguides have a different coupling rate $g^{(\mathrm{A})} \neq g^{(\mathrm{B})}$ the results presented here will be only slightly modified, changing the effective Brillouin gain and potentially adding a global phase shift. However, note that the optical group velocities of the two waveguides cannot vary much to ensure phase-matching conditions (see Fig. 3.1(a) and Section 3.2.1).

the form

$$\frac{\partial}{\partial z}\bar{a}_n = -\frac{1}{2}G_{\mathrm{B}}\sqrt{P_0^{(\mathrm{A})}P_{-1}^{(\mathrm{A})}}\;\frac{\Gamma}{2}\,|\chi|\,(\bar{a}_{n-1}-\bar{a}_{n+1})\,, \tag{3.18}$$

for both waveguides, and we have expressed the input fields in terms of optical power, using $P_n = \hbar\omega_n v a_n^\dagger a_n$, and the acousto-optic coupling in terms of Brillouin gain $G_{\mathrm{B}} = 4|g|^2/(\hbar\omega v^2\Gamma)$ [172, 173]. This recurrence relation is consistent with the Bessel function identity $J_n' = \frac{1}{2}(J_{n-1} - J_{n+1})$, such that the optical fields can be written as a linear combination $\bar{a}_n(z) = \sum_m c_{n,m}J_m(-\xi\ z)$, where $\xi = G_{\mathrm{B}}(P_0^{(\mathrm{A})}P_{-1}^{(\mathrm{A})})^{1/2}(\Gamma/2)|\chi|$. We can find the coefficients $c_{n,m}$ using $J_m(0) = \delta_{m,0}$ such that $c_{n,m} = \bar{a}_{n-m}(0)$, and using the identity $J_n(-x) = J_{-n}(x)$, we arrive at

$$a_n(z) = \sum_m a_{n+m}(0)J_m\left(\xi\ z\right)e^{-i(\phi+\Lambda)m}, \tag{3.19}$$

where we have rotated the operators back to the field envelope frame. Substituting in the initial conditions for each waveguide gives us

$$\begin{aligned} a_n^{(\mathrm{A})}(z) &= a_0^{(\mathrm{A})}(0)J_{-n}\left(\xi\ z\right)e^{i(\phi+\Lambda)n} + a_{-1}^{(\mathrm{A})}(0)J_{-(n+1)}\left(\xi\ z\right)e^{i(\phi+\Lambda)(n+1)}, \\ a_n^{(\mathrm{B})}(z) &= a_0^{(\mathrm{B})}(0)J_{-n}\left(\xi\ z\right)e^{i(\phi+\Lambda)n}, \end{aligned} \tag{3.20}$$

where we have denoted the field amplitude at the input to waveguide B as $a_0^{(\mathrm{B})}$, with optical frequency $\omega_0^{(\mathrm{B})}$. Evaluating the optical field amplitude at the output of waveguide B, i.e., the sum of the amplitudes at equally spaced frequencies $s_{\mathrm{out}}^{(\mathrm{B})}(t) \propto \sum_n a_n^{(\mathrm{B})}e^{-i(\omega_0^{(\mathrm{B})}+n\Omega)t}$, we arrive at

$$s_{\mathrm{out}}^{(\mathrm{B})}(t) = \sqrt{P_0^{(\mathrm{B})}}e^{-i\omega_0^{(\mathrm{B})}t}\sum_n J_n\left(\frac{\Gamma}{2}\,|\chi|\,G_{\mathrm{B}}\sqrt{P_0^{(\mathrm{A})}P_{-1}^{(\mathrm{A})}}\ z\right)e^{-i\Big(\Omega t-(\phi+\Lambda)+\pi\Big)n}, \tag{3.21}$$

where we have used the identity $J_{-n} = (-1)^n J_n$, and neglected a global phase of the input field. The field amplitudes are normalized such that the total power entering waveguide B is $P_0^{(\mathrm{B})}$. Using the Jacobi-Anger expansion, $\sum_n J_n(z)e^{in\varphi} = e^{iz\sin\varphi}$, we can directly see

that the field is purely phase modulated

$$s_{\text{out}}^{(\text{B})}(t) = \sqrt{P_0^{(\text{B})}}\; e^{-i\omega_0^{(\text{B})}t}\; \exp\left[i\frac{\Gamma}{2}\,|\chi|\,G_{\text{B}}\sqrt{P_0^{(\text{A})}P_{-1}^{(\text{A})}}\; z\sin\Big(\Omega t-(\phi+\Lambda)\Big)\right], \tag{3.22}$$

where the modulation depth is determined by the Brillouin gain, the optical powers in waveguide A and the propagation length. The frequency response $\chi(\Omega)$ of this phase-modulated field follows a Lorentzian lineshape, determined by the acoustic resonant frequency and dissipation rate, with a magnitude given by $|\chi|^2 = [(\Omega_0-\Omega)^2+(\Gamma/2)^2]^{-1}$.

Summarizing the results of this section, we see how the optical intensity envelope generated by the two tones in waveguide A drives the acoustic mode, as seen in Eq. (3.13) and illustrated in Fig. 3.2(a). This acoustic field modulates an optical tone in waveguide B as it propagates through the device (see Fig. 3.2(e)), resulting in pure phase modulation, as seen in Fig. 3.2(f). The optical field in waveguide A also experiences phase modulation as a result of the forward Brillouin scattering process, seen in Figs. 3.2(b,c), however, the intensity envelope remains unchanged, as was discussed in Section 2.3.4.

Our analysis shows an overall redshift of the light in waveguide A as it propagates, as seen in the calculations presented in Figs. 3.2(b,c) and consistent with previous forward-Brillouin scattering studies [176]. The phonons generated through the Brillouin process have a finite lifetime, and their dissipation removes energy from the system, which in the absence of optical dissipation represents the only loss mechanism. The red-shift can be derived from the mode amplitudes (Eq. (3.20)), yielding a power-loss given by $P_{\text{RS}}^{(\text{A})}(z) = \hbar\Omega|b(z)|^2\Gamma z$, showing the energy dissipated from the phonon field, as was discussed in Section 2.3.4.

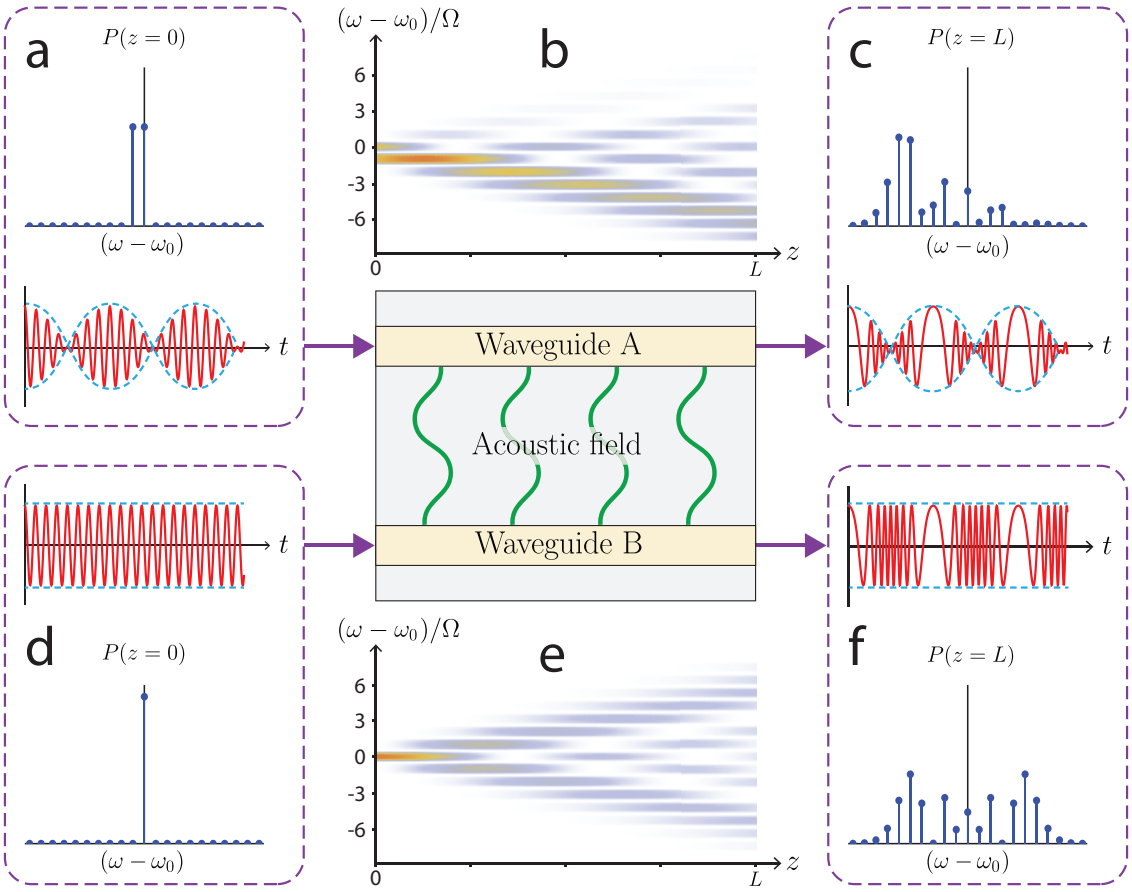

Figure 3.2: Simulation of the nonlocal transduction using an FSBS-active device. **(a)** The input to waveguide A is comprised of two tones, illustrated both in the frequency and time domain, showing the resulting envelope modulation. **(b)** The optical fields drive a phonon field, scattering light into multiple sidebands as they propagate along the device. **(c)** The field at the output of waveguide A shows phase modulation of the input wave, however, the intensity envelope is unaffected. The same steps are illustrated for waveguide B: **(d)** A single tone is launched into the waveguide, **(e)** is scattered by the acoustic field as it propagates along the device, and **(f)** shows phase modulation side-bands at the output. The time-domain illustrations in these figures are schematic, and not shown to scale. Reproduced from Ref. [154].

3.2.1 Effects of optical dispersion

Our results up to this point have relied on our assumption of vanishing optical group velocity dispersion (GVD) in the frequency range over which the optical tones are cascaded. Within this idealized system, we saw that the beat note produced between the pump and the signal wave is transferred over to the adjacent waveguide as pure phase modulation. However, this isn't necessarily the case if we include higher-order effects such as optical dispersion. Neglecting dispersion is a valid approximation in many practical systems [29, 64, 172] and GVD can be further avoided through dispersion engineering of optical waveguides [190,191]. However, in systems with non-negligible dispersion, the field dynamics will deviate from our derivation, such that the light in waveguide B will no longer be purely phase modulated, and will exhibit some residual intensity modulation [170].

To understand the impact of GVD, we rewrite the equations describing the field envelopes, keeping the second-order term of the optical dispersion operator (Eq. (2.22)) in both waveguides A and B

$$\begin{aligned} b &= -i\chi \sum_n \left(g_n^* a_n^{(\mathrm{A})} {a_{n-1}^{(\mathrm{A})}}^\dagger e^{-i\Delta k_n z} + g_n^* a_n^{(\mathrm{B})} {a_{n-1}^{(\mathrm{B})}}^\dagger e^{-i\Delta k_n z} \right), \\ \left[v_n \frac{\partial}{\partial z} - \frac{i}{2} \left(\frac{\partial^2 \omega}{\partial k^2} \right) \frac{\partial^2}{\partial z^2} \right] a_n &= -i \left(g_n a_{n-1} b e^{i\Delta k_n z} + g_{n+1}^* a_{n+1} b^\dagger e^{-i\Delta k_{n+1} z} \right). \end{aligned} \tag{3.23}$$

Now, we have frequency dependent optical group velocity $v_n = \partial_k \omega\big|_{\omega=(\omega_0+n\Omega)}$ and a phase mismatch term $\Delta k_n = q_0 - (k_n - k_{n-1}) \approx \Omega(v_0^{-1} - v_n^{-1})$. The dispersion leads to non-symmetric sidebands around the carrier, such that the phase-modulated wave also acquires some intensity modulation which we refer to as residual amplitude modulation (RAM). We quantify the RAM by looking at the components of the intensity at frequency Ω, normalized to the total scattered power

$$\mathrm{RAM} = \frac{\sum_n \left({a_{n-1}^{(\mathrm{B})}}^\dagger a_n^{(\mathrm{B})} + a_{n-1}^{(\mathrm{B})} {a_n^{(\mathrm{B})}}^\dagger \right)}{\sum_{n\neq 0} a_n^{(\mathrm{B})} {a_n^{(\mathrm{B})}}^\dagger}. \tag{3.24}$$

Numerically simulated RAM is shown in Figs. 3.3, where the dispersion is given both in

terms of GVD, and a commonly used dispersion parameter D, defined by

$$\mathrm{GVD} = \left.\frac{\partial^2 k}{\partial \omega^2}\right|_{\omega=\omega_0}, \qquad \mathrm{D} = -\frac{2\pi c}{\lambda^2}\mathrm{GVD}. \tag{3.25}$$

When using parameter values consistent with common materials and waveguide design, the simulation results in residual intensity modulation on the order of -50 dB. In a practical experimental context, the frequency response of other optical elements in the system (such as optical fiber components) can easily yield larger values of RAM compared with the RAM produced by the Brillouin-active device.

Another point to note is that throughout our analysis, we have studied the case where the modes in both waveguides A and B have the same group velocity, based on the assumption that they are similar in design and operating at similar wavelengths. However, when using vastly different optical wavelengths in waveguides A and B, the group velocity in each wavelength range may be different and can lead to a phase mismatch between the phonons driven in waveguide A and those needed for efficient phase modulation in waveguide B. This phase mismatch can be expressed in terms of the driving frequency Ω and the frequency-dependent group velocity $v(\omega)$

$$\Delta q = \Omega \left[\frac{1}{v\left(\omega_0^{(\mathrm{A})}\right)} - \frac{1}{v\left(\omega_0^{(\mathrm{B})}\right)} \right], \tag{3.26}$$

where we assume that the optical dispersion is identical in both waveguides A and B. For the phase mismatch to be small over the device length, i.e., $|\Delta q L| < \pi$, we have the condition

$$\left| \frac{1}{v\left(\omega_0^{(\mathrm{A})}\right)} - \frac{1}{v\left(\omega_0^{(\mathrm{B})}\right)} \right| < \frac{\pi}{\Omega L}. \tag{3.27}$$

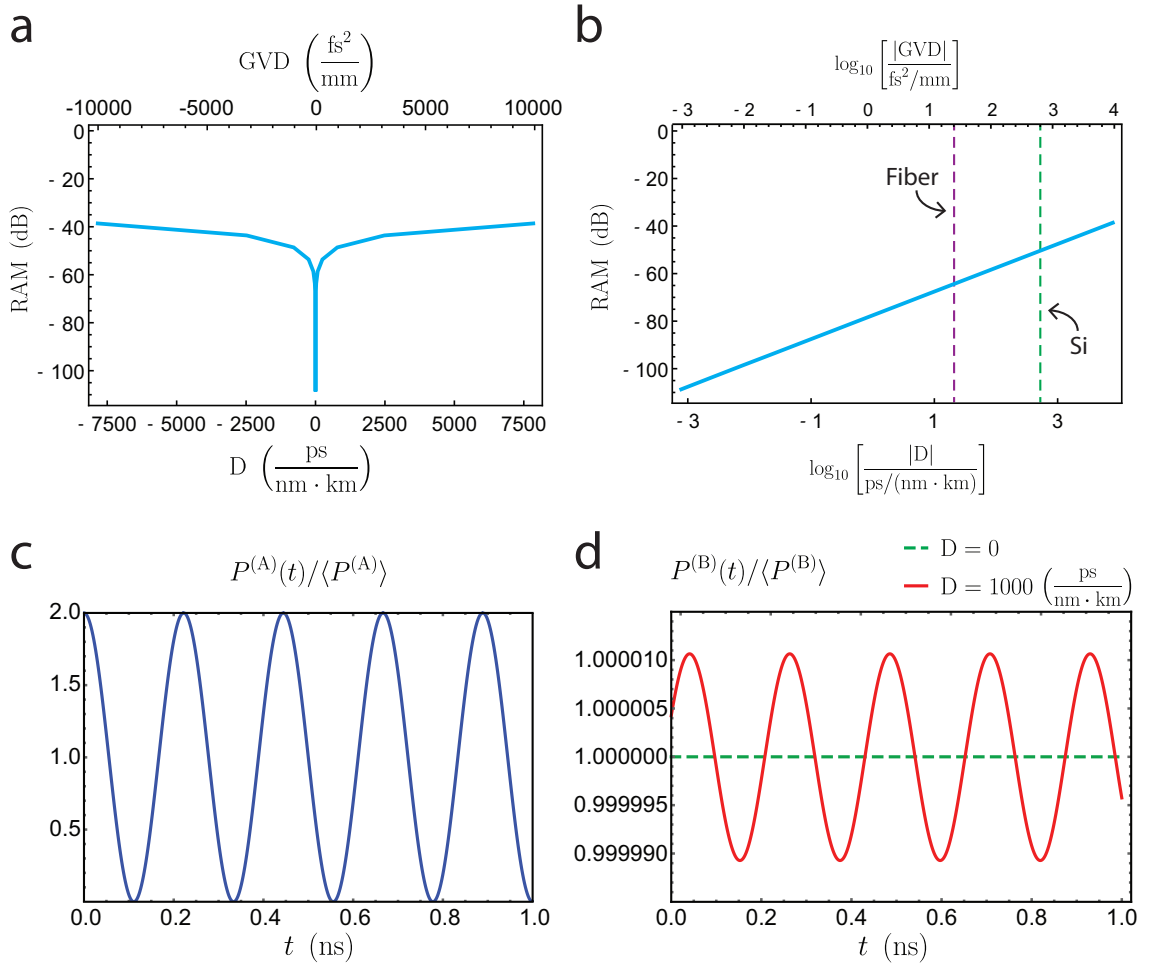

Figure 3.3: **(a)** Numerically calculated residual amplitude modulation (RAM) as a function of group velocity dispersion (GVD) for a 2.5 cm long device with Brillouin gain $G_{\text{B}} = 700\ (\text{Wm})^{-1}$ and an acoustic Q-factor of 1000. The input powers are 100 mW in each of the two tones into waveguide A and 100 mW into a single tone in waveguide B. The parameters have been chosen similar to those in a practical system, demonstrated in Ref. [187]. **(b)** The same results plotted on a logarithmic scale. Values of GVD in bulk silicon and optical fiber are shown for reference. **(c)** Normalized optical field envelope in waveguide A as a function of time shows the intensity modulation that drives an acoustic field at 4.5 GHz. **(d)** The normalized optical field envelope in waveguide B shows a constant envelope in the absence of dispersion (green, dashed). When some dispersion is taken into account, a small intensity modulation can be seen (red). Adapted from Ref. [154].

3.3 Coupling mediated by multiple phonon modes

As we have seen in the previous section, the frequency response of the Brillouin-induced nonlinear susceptibility is determined by the properties of the acoustic mode participating in the interaction. This response can be further engineered by utilizing multiple acoustic modes, such that they all contribute to the susceptibility. An example of such a device, implementing the acoustic coupling using a phononic crystal design, was demonstrated in Ref. [186]. In this section, we will analyze systems utilizing multiple acoustic modes, and show how the presence of multiple coherent phonons alters the frequency response of the Brillouin-induced susceptibility.

3.3.1 Second order frequency response

We start by looking at a system consisting of two identical spatially separated Brillouin-active waveguides. We assume that each waveguide supports an optical mode, as well as a phonon mode with a resonant frequency Ω_0, and we denote the amplitudes of the phonon modes $b^{(\mathrm{A})}$, $b^{(\mathrm{B})}$ for waveguides A and B, respectively. The structure is designed such that the two optical waveguides are optically separated while the two acoustic fields are coupled with a rate μ, as illustrated in Fig. 3.4(a).

The acoustic Hamiltonian from Eq. (3.2) is now

$$H_{\mathrm{ac}} = \hbar \int dz \ \left({b^{(\mathrm{A})}}^{\dagger} \hat{\Omega}_0 b^{(\mathrm{A})} + {b^{(\mathrm{B})}}^{\dagger} \hat{\Omega}_0 b^{(\mathrm{B})} - {b^{(\mathrm{A})}}^{\dagger} \mu b^{(\mathrm{B})} - b^{(\mathrm{A})} \ \mu \ {b^{(\mathrm{B})}}^{\dagger} \right), \tag{3.28}$$

which can also be written in matrix form

$$H_{\mathrm{ac}} = \hbar \int dz \ \begin{pmatrix} {b^{(\mathrm{A})}}^{\dagger} & {b^{(\mathrm{B})}}^{\dagger} \end{pmatrix} \begin{pmatrix} \hat{\Omega}_0 & -\mu \\ -\mu & \hat{\Omega}_0 \end{pmatrix} \begin{pmatrix} b^{(\mathrm{A})} \\ b^{(\mathrm{B})} \end{pmatrix}. \tag{3.29}$$

Assuming phase-matching conditions are satisfied, the interaction Hamiltonian terms are

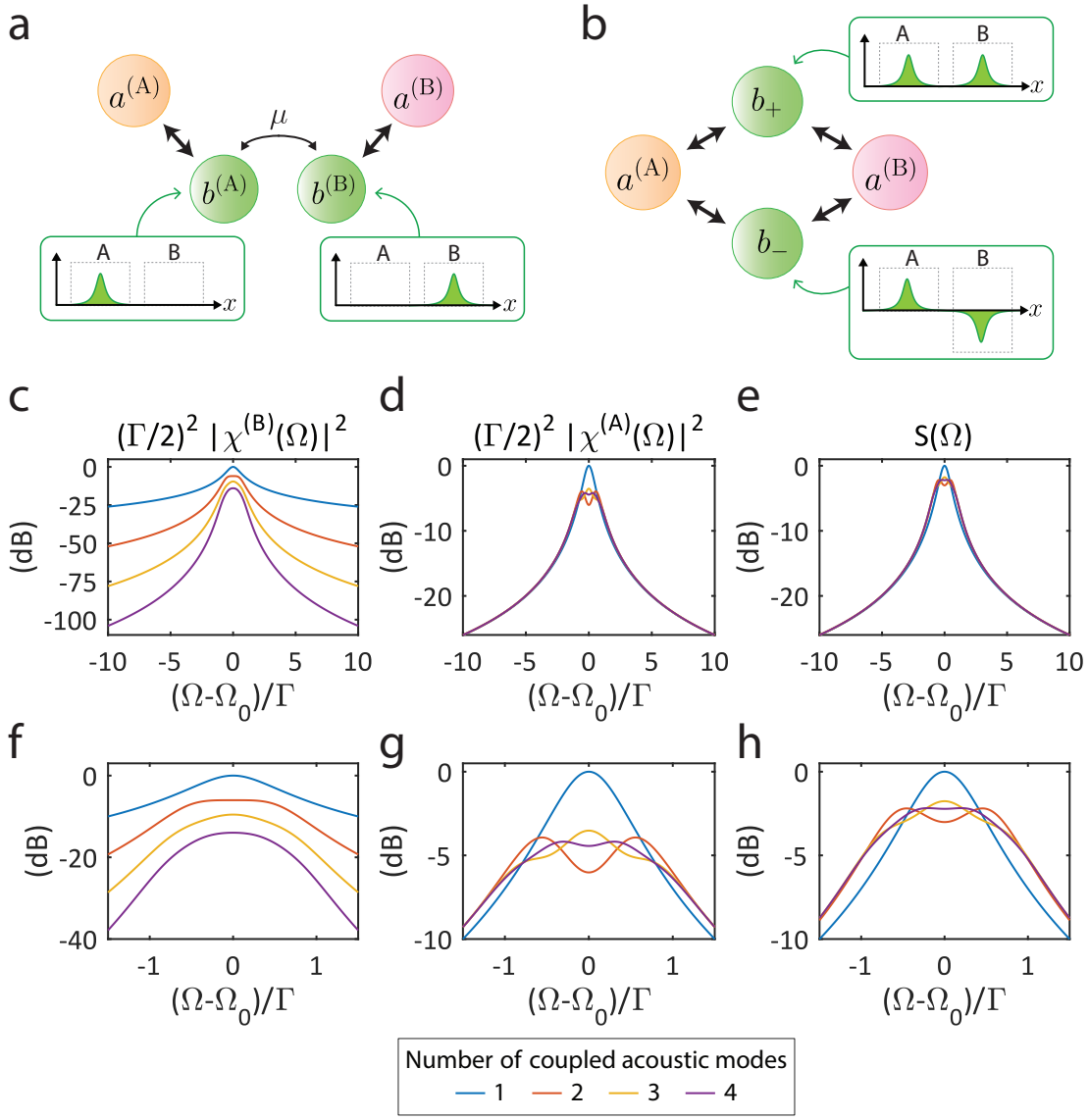

Figure 3.4: **(a)** The optical field in each waveguide ($a^{(A)}$, $a^{(B)}$) is coupled to an acoustic mode ($b^{(A)}$, $b^{(B)}$) through a forward Brillouin process. The two spatial acoustic modes are coupled to each other with a rate μ. **(b)** The same system can be described in the acoustic 'super-mode' basis, using symmetric and anti-symmetric combinations of the spatial acoustic modes. The two acoustic super-modes are acoustically decoupled, each interacting with both optical fields. **(c)** Calculated frequency response of the nonlocal susceptibility in waveguide B, for a different number of coupled acoustic modes, following Eq. (3.50). **(d)** Calculated frequency response of the local susceptibility in waveguide A. **(e)** Normalized spectrum of a spontaneous-scattering sideband, for a different number of coupled acoustic modes, following Eq. (3.59). **(f–h)**. Magnified view of panels (c–e), respectively. All of the simulated frequency responses were calculated assuming $\mu = \Gamma/2$. Adapted from Ref. [154].

given by

$$\begin{aligned} H_{\text{int}}^{(\text{A})} &= \sum_n \hbar \int dz\ g_n^{(\text{A})*} a_n^{(\text{A})} {a_{n-1}^{(\text{A})}}^{\dagger} b^{(\text{A})\dagger} + \text{H.C.}, \\ H_{\text{int}}^{(\text{B})} &= \sum_n \hbar \int dz\ g_n^{(\text{B})*} a_n^{(\text{B})} {a_{n-1}^{(\text{B})}}^{\dagger} b^{(\text{B})\dagger} + \text{H.C.}, \end{aligned} \tag{3.30}$$

where we see the three-wave process, between two optical tones and an acoustic mode, in each of the waveguides. We assume that the optical Hamiltonian terms remain unchanged. We can now calculate the equations of motion of the phonons using Eq. (3.3), yielding

$$\begin{aligned} \frac{\partial}{\partial t} b^{(\text{A})} &= -i\hat{\Omega}_0 b^{(\text{A})} + i\mu b^{(\text{B})} - i \sum_n g_n^{(\text{A})*} a_n^{(\text{A})} {a_{n-1}^{(\text{A})}}^{\dagger}, \\ \frac{\partial}{\partial t} b^{(\text{B})} &= -i\hat{\Omega}_0 b^{(\text{B})} + i\mu b^{(\text{A})} - i \sum_n g_n^{(\text{B})*} a_n^{(\text{B})} {a_{n-1}^{(\text{B})}}^{\dagger}. \end{aligned} \tag{3.31}$$

This result is consistent with a temporal coupled-mode theory approach such as described in Refs. [186, 192].

Alternatively, we can diagonalize Eq. (3.29), to the eigenbasis where we have two decoupled phonon modes

$$H_{\text{ac}} = \hbar \int dz\ \begin{pmatrix} b_+^\dagger & b_-^\dagger \end{pmatrix} \begin{pmatrix} \hat{\Omega}_+ & 0 \\ 0 & \hat{\Omega}_- \end{pmatrix} \begin{pmatrix} b_+ \\ b_- \end{pmatrix}. \tag{3.32}$$

These phonon 'super-modes' extend spatially to both waveguides, and can be written as a linear combination of the spatial phonon modes $b_\pm = \left(b^{(\text{A})} \pm b^{(\text{B})}\right)/\sqrt{2}$, and their respective frequencies $\hat{\Omega}_\pm = \hat{\Omega}_0 \mp \mu$, which retain the commutation relations $[b_\pm(z,t), b_\pm^\dagger(z',t)] = \delta(z-z')$ and $[b_\pm(z',t), b_\mp^\dagger(z',t)] = 0$. The interaction Hamiltonian terms in this basis are given by

$$\begin{aligned} H_{\text{int}}^{(\text{A})} &= \sum_n \hbar \int dz\ \left(g_+^{(\text{A})*} a_n^{(\text{A})} {a_{n-1}^{(\text{A})}}^{\dagger} b_+^\dagger + g_-^{(\text{A})*} a_n^{(\text{A})} {a_{n-1}^{(\text{A})}}^{\dagger} b_-^\dagger \right) + \text{H.C.}, \\ H_{\text{int}}^{(\text{B})} &= \sum_n \hbar \int dz\ \left(g_+^{(\text{B})*} a_n^{(\text{B})} {a_{n-1}^{(\text{B})}}^{\dagger} b_+^\dagger + g_-^{(\text{B})*} a_n^{(\text{B})} {a_{n-1}^{(\text{B})}}^{\dagger} b_-^\dagger \right) + \text{H.C.}, \end{aligned} \tag{3.33}$$

where $g_{\pm}^{(l)}$ is the coupling rate between a phonon super-mode and the optical tones in waveguide l ($l = \{\mathrm{A,B}\}$).

Next, we calculate the equations of motion using Eq. (3.3) and keep the dispersion operator to first order for the optical modes, and zero order for the acoustic modes. Additionally, we factor out the fast oscillating terms and add a dissipation rate Γ to the phonon modes

$$\begin{aligned}
&\frac{\partial}{\partial t}a_n^{(\mathrm{A})} + v\frac{\partial}{\partial z}a_n^{(\mathrm{A})} = -i\Big(g_+^{(\mathrm{A})}a_{n-1}^{(\mathrm{A})}b_+ + g_+^{(\mathrm{A})^*}a_{n+1}^{(\mathrm{A})}b_+^\dagger + g_-^{(\mathrm{A})}a_{n-1}^{(\mathrm{A})}b_- + g_-^{(\mathrm{A})^*}a_{n+1}^{(\mathrm{A})}b_-^\dagger\Big),\\
&\frac{\partial}{\partial t}a_n^{(\mathrm{B})} + v\frac{\partial}{\partial z}a_n^{(\mathrm{B})} = -i\Big(g_+^{(\mathrm{B})}a_{n-1}^{(\mathrm{B})}b_+ + g_+^{(\mathrm{B})^*}a_{n+1}^{(\mathrm{B})}b_+^\dagger + g_-^{(\mathrm{B})}a_{n-1}^{(\mathrm{B})}b_- + g_-^{(\mathrm{B})^*}a_{n+1}^{(\mathrm{B})}b_-^\dagger\Big),\\
&\frac{\partial}{\partial t}b_\pm + i\left(\Omega_\pm - \Omega - i\frac{\Gamma}{2}\right)b_\pm = -i\sum_n\left(g_\pm^{(\mathrm{A})^*}a_n^{(\mathrm{A})}{a_{n-1}^{(\mathrm{A})}}^\dagger + g_\pm^{(\mathrm{B})^*}a_n^{(\mathrm{B})}{a_{n-1}^{(\mathrm{B})}}^\dagger\right).
\end{aligned} \tag{3.34}$$

At steady-state, we have

$$\begin{aligned}
b_\pm &= -i\left(\frac{1}{i(\Omega_\pm - \Omega) + \Gamma/2}\right)\sum_n\left(g_\pm^{(\mathrm{A})^*}a_n^{(\mathrm{A})}{a_{n-1}^{(\mathrm{A})}}^\dagger + g_\pm^{(\mathrm{B})^*}a_n^{(\mathrm{B})}{a_{n-1}^{(\mathrm{B})}}^\dagger\right),\\
\frac{\partial}{\partial z}a_n^{(\mathrm{A})} &= -\frac{i}{v^{(\mathrm{A})}}\Big(g_+^{(\mathrm{A})}a_{n-1}^{(\mathrm{A})}b_+ + g_+^{(\mathrm{A})^*}a_{n+1}^{(\mathrm{A})}b_+^\dagger + g_-^{(\mathrm{A})}a_{n-1}^{(\mathrm{A})}b_- + g_-^{(\mathrm{A})^*}a_{n+1}^{(\mathrm{A})}b_-^\dagger\Big),\\
\frac{\partial}{\partial z}a_n^{(\mathrm{B})} &= -\frac{i}{v^{(\mathrm{B})}}\Big(g_+^{(\mathrm{B})}a_{n-1}^{(\mathrm{B})}b_+ + g_+^{(\mathrm{B})^*}a_{n+1}^{(\mathrm{B})}b_+^\dagger + g_-^{(\mathrm{B})}a_{n-1}^{(\mathrm{B})}b_- + g_-^{(\mathrm{B})^*}a_{n+1}^{(\mathrm{B})}b_-^\dagger\Big).
\end{aligned} \tag{3.35}$$

By projecting the '$\pm$' super-modes on waveguides A and B we see that $g_\pm^{(\mathrm{A})} = g/\sqrt{2}$, and $g_\pm^{(\mathrm{B})} = \pm g/\sqrt{2}$, a result of the symmetries of the super-modes. Since we assume that the waveguides are identical, we set the optical group velocities to the same value $v = v^{(\mathrm{A})} = v^{(\mathrm{B})}$, such that

$$\begin{aligned}
b_\pm &= -\frac{i}{\sqrt{2}}\left(\frac{1}{i(\Omega_\pm - \Omega) + \Gamma/2}\right)g^*\sum_n\left(a_n^{(\mathrm{A})}{a_{n-1}^{(\mathrm{A})}}^\dagger \pm a_n^{(\mathrm{B})}{a_{n-1}^{(\mathrm{B})}}^\dagger\right),\\
\frac{\partial}{\partial z}a_n^{(\mathrm{A})} &= -\frac{i}{\sqrt{2}}\frac{1}{v}\Big(ga_{n-1}^{(\mathrm{A})}b_+ + g^*a_{n+1}^{(\mathrm{A})}b_+^\dagger + ga_{n-1}^{(\mathrm{A})}b_- + g^*a_{n+1}^{(\mathrm{A})}b_-^\dagger\Big),\\
\frac{\partial}{\partial z}a_n^{(\mathrm{B})} &= -\frac{i}{\sqrt{2}}\frac{1}{v}\Big(ga_{n-1}^{(\mathrm{B})}b_+ + g^*a_{n+1}^{(\mathrm{B})}b_+^\dagger - ga_{n-1}^{(\mathrm{B})}b_- - g^*a_{n+1}^{(\mathrm{B})}b_-^\dagger\Big).
\end{aligned} \tag{3.36}$$

These equations have the same form as Eq. (3.12), where we saw that $\partial_z b_\pm = 0$, such that the phonon super-modes only depend on the initial conditions of the optical fields.

Similar to our earlier analysis, we consider the case of where the optical input fields

consist of two tones into waveguide A, separated in frequency by Ω, and a single tone in waveguide B, giving us

$$b_{\pm} = -\frac{i}{\sqrt{2}}\left(\frac{1}{i\left(\Omega_{\pm}-\Omega\right)+\Gamma/2}\right) g^{*} a_{0}^{(\mathrm{A})}(0)\; a_{-1}^{(\mathrm{A})\dagger}(0). \tag{3.37}$$

Substituting the phonon fields into the optical equations of motion yields

$$\begin{aligned}
\frac{\partial}{\partial z} a_{n}^{(\mathrm{A})} &= -\frac{|g|^{2}}{v}\left|a_{-1}^{(\mathrm{A})\dagger}(0)\; a_{0}^{(\mathrm{A})}(0)\right|\left|\chi^{(\mathrm{A})}\right|\left(a_{n-1}^{(\mathrm{A})} e^{i\phi^{(\mathrm{A})}} e^{i\Lambda} - a_{n+1}^{(\mathrm{A})} e^{-i\phi^{(\mathrm{A})}} e^{-i\Lambda}\right), \\
\frac{\partial}{\partial z} a_{n}^{(\mathrm{B})} &= -\frac{|g|^{2}}{v}\left|a_{-1}^{(\mathrm{A})\dagger}(0)\; a_{0}^{(\mathrm{A})}(0)\right|\left|\chi^{(\mathrm{B})}\right|\left(a_{n-1}^{(\mathrm{B})} e^{i\phi^{(\mathrm{B})}} e^{i\Lambda} - a_{n+1}^{(\mathrm{B})} e^{-i\phi^{(\mathrm{B})}} e^{-i\Lambda}\right),
\end{aligned} \tag{3.38}$$

where we have defined the frequency response in each waveguide

$$\begin{aligned}
\chi^{(\mathrm{A})} &= \frac{1/2}{i\left(\Omega_{+}-\Omega\right)+\Gamma/2} + \frac{1/2}{i\left(\Omega_{-}-\Omega\right)+\Gamma/2}, \\
\chi^{(\mathrm{B})} &= \frac{1/2}{i\left(\Omega_{+}-\Omega\right)+\Gamma/2} - \frac{1/2}{i\left(\Omega_{-}-\Omega\right)+\Gamma/2},
\end{aligned} \tag{3.39}$$

and phases

$$\phi^{(\mathrm{A})} = \arg\left(\chi^{(\mathrm{A})}\right), \qquad \phi^{(\mathrm{B})} = \arg\left(\chi^{(\mathrm{B})}\right), \qquad \Lambda = \arg\left(a_{-1}^{(\mathrm{A})\dagger}(0)\; a_{0}^{(\mathrm{A})}(0)\right). \tag{3.40}$$

The frequency response $\chi^{(\mathrm{B})}$ of the nonlocal susceptibility induced in waveguide B by the optical fields in waveguide A is dramatically changed in this multi-phonon case, a result of the phase difference between the two complex terms. As seen in Fig. 3.4(c), the coupling of multiple acoustic fields yields a high-order frequency response, showing a sharp frequency roll-off. This can also be understood from the interference of the two phonon super-modes, shown in Fig. 3.4(b), resulting in a multi-pole function. The susceptibility in waveguide A is also slightly altered around the acoustic resonance, as seen in Fig. 3.4(d), but decays as a Lorentzian away from the center frequency, similar to the single-phonon case. Following the steps described in the previous section, we can solve for the field amplitude at the output

of waveguide B

$$s_{\text{out}}^{(\text{B})}(t) = \sqrt{P_0^{(\text{B})}}\; e^{-i\omega_0^{(\text{B})}t}\; \exp\left[i\frac{\Gamma}{2}\left|\chi^{(\text{B})}\right|\; G_B\sqrt{P_0^{(\text{A})}P_{-1}^{(\text{A})}}\; z\sin\Big(\Omega t-(\phi+\Lambda)\Big)\right], \quad (3.41)$$

which now has the modified frequency response $\chi^{(\text{B})}$. Practically, this enables the design of acousto-optic filter responses with a high-order lineshape, which can have applications in high-performance microwave-photonics applications [193].

3.3.2 Multi-pole frequency response

We can extend our analysis further, considering an arbitrary number of phonons taking part in the transduction. Assuming N identical waveguides and nearest-neighbor acoustic coupling, the acoustic Hamiltonian is given by

$$H_{\text{ac}} = \hbar\int dz\; \begin{pmatrix} b^{(\text{A})\dagger} & b^{(\text{B})\dagger} & \dots & b^{(N)\dagger}\end{pmatrix} \begin{pmatrix} \hat{\Omega}_0 & \mu & & & \\ \mu^* & \hat{\Omega}_0 & \mu & & \\ & \ddots & \ddots & \ddots & \\ & & \mu^* & \hat{\Omega}_0 & \mu \\ & & & \mu^* & \hat{\Omega}_0 \end{pmatrix} \begin{pmatrix} b^{(\text{A})} \\ b^{(\text{B})} \\ \vdots \\ b^{(N)}\end{pmatrix}, \quad (3.42)$$

where $\mu = |\mu|e^{i\theta}$, and we assume that all matrix entries not on the three main diagonals are zero. The interaction Hamiltonian of the ℓ^{th} waveguide is now

$$H_{\text{int}}^{(\ell)} = \sum_n \hbar\int dz\; g^* a_n^{(\ell)} {a_{n-1}^{(\ell)}}^{\dagger} b^{(\ell)\dagger} + \text{H.C.} \quad (3.43)$$

The tridiagonal matrix from Eq. (3.42) can be diagonalized [194], yielding N distinct eigenvalues

$$\hat{\Omega}_m = \hat{\Omega}_0 + 2\,|\mu|\cos\left(\frac{\pi m}{N+1}\right), \quad (3.44)$$

and the phonon fields can be decomposed into phonon eigenmodes

$$b^{(\ell)} = \sum_{m=1}^{N} V_m^{(\ell)}\; b_m, \qquad V_m^{(\ell)} = \sqrt{\frac{2}{N+1}}\sin\left(\frac{\pi m\ell}{N+1}\right)e^{im\theta}. \quad (3.45)$$

Here, we have chosen the notation such that the index m denotes phonon super-modes, ℓ enumerates the different waveguides, and n sums the different optical tones spaced by frequency Ω. We can now rewrite the acoustic and interaction terms of the Hamiltonian

$$\begin{aligned} H_{\text{ac}} &= \sum_{m=1}^{N} \hbar \int dz\ b_m^{\dagger} \hat{\Omega}_m b_m, \\ H_{\text{int}}^{(\ell)} &= \sum_{m=1}^{N} \sum_{n} \hbar \int dz\ g_m^{(\ell)*} a_n^{(\ell)} {a_{n-1}^{(\ell)}}^{\dagger} b_m^{\dagger} + \text{H.C.}, \end{aligned} \tag{3.46}$$

where the rate $g_m^{(\ell)}$, denoting the coupling of the m^{th} phonon eigenmodes to the optical tones in the ℓ^{th} waveguide, can be described in terms of the single-phonon coupling rate ($g_m^{(\ell)} = gV_m^{(\ell)}$) using Eq. (3.45).

Calculating the equations of motion using Eq. (3.3), under the same assumptions as in the previous section, we can write the field envelopes for the phonon eigenmodes and the optical fields in the ℓ^{th} membrane

$$\begin{aligned} b_m &= -i \left(\frac{1}{i\Delta_m + \Gamma_m/2} \right) \sum_{n} \sum_{\ell=1}^{N} g_m^{(\ell)*} a_n^{(\ell)} {a_{n-1}^{(\ell)}}^{\dagger}, \\ \frac{\partial}{\partial z} a_n^{(\ell)} &= -\frac{i}{v} \sum_{m=1}^{N} \left(g_m^{(\ell)} a_{n-1}^{(\ell)} b_m + g_m^{(\ell)*} a_{n+1}^{(\ell)} b_m^{\dagger} \right). \end{aligned} \tag{3.47}$$

Assuming two tones at the input of waveguide A with a frequency separation Ω, and a single tone in the input of waveguide B, the phonon field from Eq. (3.47) is now

$$b_m = -i \left(\frac{1}{i\Delta_m + \Gamma_m/2} \right) g_m^{(\text{A})*} a_0^{(\text{A})}(0)\ {a_{-1}^{(\text{A})}}^{\dagger}(0), \tag{3.48}$$

where $\Delta_m = \Omega_m - \Omega$ and Γ_m are the detuning and the loss of the m^{th} phonon eigenmode, respectively. Following the same steps as described in Section 3.3, we can find the equation of motion for the optical tones in waveguide ℓ

$$\frac{\partial}{\partial z} a_n^{(\ell)} = -\frac{1}{v} |g|^2 \left| {a_{-1}^{(\text{A})}}^{\dagger}(0)\ a_0^{(\text{A})}(0) \right| \left| \chi^{(\ell)} \right| \left(a_{n-1}^{(\ell)} e^{i\phi^{(\ell)}} e^{i\Lambda} - a_{n+1}^{(\ell)} e^{-i\phi^{(\ell)}} e^{-i\Lambda} \right), \tag{3.49}$$

where the multi-pole frequency response is given by

$$\chi^{(\ell)} = \sum_{m=1}^{N} V_m^{(\ell)} V_m^{(\mathrm{A})*} \left(\frac{1}{i\Delta_m + \Gamma_m/2} \right), \tag{3.50}$$

where $\phi^{(\ell)} = \arg(\chi^{(\ell)})$, and $\Lambda = \arg(a_{-1}^{(\mathrm{A})\dagger}(0)\ a_0^{(\mathrm{A})}(0))$. Eq. (3.49) has an identical form to Eq. (3.17), and following the steps from Section 3.2 we can find the optical field envelopes

$$\begin{aligned} a_n^{(\mathrm{A})}(z) &= a_0^{(\mathrm{A})}(0) J_{-n}\left(\xi^{(\mathrm{A})} z\right) e^{i\left(\phi^{(\mathrm{A})}+\Lambda\right)n} + a_{-1}^{(\mathrm{A})}(0) J_{-(n+1)}\left(\xi^{(\mathrm{A})} z\right) e^{i\left(\phi^{(\mathrm{A})}+\Lambda\right)(n+1)}, \\ a_n^{(\mathrm{B})}(z) &= a_0^{(\mathrm{B})}(0) J_{-n}\left(\xi^{(\mathrm{B})} z\right) e^{i\left(\phi^{(\mathrm{B})}+\Lambda\right)n}, \end{aligned} \tag{3.51}$$

where $\xi^{(\mathrm{A})} = (\Gamma/2)|\chi^{(\mathrm{A})}|G_{\mathrm{B}}(P_0^{(\mathrm{A})}P_{-1}^{(\mathrm{A})})^{1/2}z$ and $\xi^{(\mathrm{B})} = (\Gamma/2)|\chi^{(\mathrm{B})}|G_{\mathrm{B}}(P_0^{(\mathrm{A})}P_{-1}^{(\mathrm{A})})^{1/2}z$. We note that in this case, waveguides A and B do not have to be in specific spatial positions along the coupled waveguide array, and are defined only by the optical inputs (i.e., we can analyze this for any value of ℓ). The field amplitude at the output of waveguide B is now given by

$$s_{\mathrm{out}}^{(\mathrm{B})}(t) = \sqrt{P_0^{(\mathrm{B})}}\ e^{-i\omega_0^{(\mathrm{B})}t}\ \exp\left[i\,\frac{\Gamma}{2}\left|\chi^{(\mathrm{B})}\right|\ G_{\mathrm{B}}\sqrt{P_0^{(\mathrm{A})}P_{-1}^{(\mathrm{A})}}\ z\sin\left(\Omega t - \left(\phi^{(\mathrm{B})}+\Lambda\right)\right)\right]. \tag{3.52}$$

The frequency response of the system (Eq. (3.50)) yields a sharper frequency roll-off with the addition of coupled acoustic modes, as seen in Fig. 3.4(c). We will examine the first few cases, starting with a single acoustic mode, which will follow a Lorentzian function

$$\chi^{(\mathrm{B})} = \frac{1}{\Omega - (\Omega_0 - i\Gamma/2)}, \tag{3.53}$$

which has a single pole, and a maximum amplitude at frequency $\Omega = \Omega_0$. Two coupled acoustic modes will have the response

$$\chi^{(\mathrm{B})} = \frac{i\mu}{[\Omega - (\Omega_+ - i\Gamma/2)]\,[\Omega - (\Omega_- - i\Gamma/2)]}, \tag{3.54}$$

where $\Omega_\pm = \Omega_0 \mp \mu$, which has two poles, with a maximum amplitude at $\Omega = \Omega_0 \pm$

$\sqrt{\mu^2 - (\Gamma/2)^2}$ when $\mu > \Gamma/2$. For $\mu \leq \Gamma/2$ the function will have a single peak at $\Omega = \Omega_0$. Three coupled acoustic modes will have the frequency response

$$\chi^{(\mathrm{B})} = \frac{-\mu^2}{[\Omega - (\Omega_+ - i\Gamma/2)]\,[\Omega - (\Omega_0 - i\Gamma/2)]\,[\Omega - (\Omega_- - i\Gamma/2)]} \tag{3.55}$$

where $\Omega_\pm = \Omega_0 \mp \sqrt{2}\mu$, which has three poles, and for $\mu > \sqrt{6}\Gamma$ has local amplitude maxima at $\Omega = \Omega_0$ and $\Omega = \Omega_0 \pm \sqrt{\frac{4}{3}\mu^2 + \frac{2}{3}\mu\sqrt{\mu^2 - 6(\Gamma/2)^2} - (\Gamma/2)^2}$, otherwise showing a single maximum at $\Omega = \Omega_0$.

Interestingly, calculating the frequency response at the output of waveguide A, given by the function $\chi^{(\mathrm{A})}$, always has $N-1$ zeros and N poles, regardless of the number of acoustic modes. Such functions behave overall similar to the single-pole case, decaying as a Lorentzian function, as seen in Fig. 3.4(d).

3.3.3 Spontaneous scattering

Up to this point, we have considered acousto-optic scattering from coherently driven phonons produced in waveguide A. However, the thermal occupation of the acoustic modes will result in spontaneous Brillouin scattering in the system [157, 172]. This can also be understood as the noise associated with the dissipation of the acoustic mode, through the fluctuation-dissipation theorem [175,195]. If we seek to utilize such nonlocal susceptibilities to transduce information, as the basis for new signal processing technologies [139,186–188], it is essential to understand how this noise is imparted from the elastic field onto the optical fields.

Starting from a single acoustic mode with frequency Ω_0, an optical tone at frequency ω_0 with a field amplitude a_0 will be scattered to sidebands at frequencies $\omega_0 \pm \Omega_0$. The amplitudes of the spontaneously scattered light are given by [172, 175]

$$\begin{aligned} a_{-1}(z,\tau) &= -i\frac{g^*}{v}a_0 \int_0^\tau d\tau' \int_0^z dz' \eta^\dagger(z',\tau') e^{-\frac{\Gamma}{2}(\tau-\tau')}, \\ a_1(z,\tau) &= -i\frac{g}{v}a_0 \int_0^\tau d\tau' \int_0^z dz' \eta(z',\tau') e^{-\frac{\Gamma}{2}(\tau-\tau')}, \end{aligned} \tag{3.56}$$

where η is the Langevin force corresponding to the phonon dissipation rate, with statistics $\langle \eta \rangle = 0$ and $\langle \eta^\dagger(z,t)\eta(z',t') \rangle = \bar{n}\Gamma\delta(z-z')\delta(t-t')$ when evaluating the ensemble aver-

ages [172]. We denote n_{th} as the average number of thermally occupied phonons, following a Bose-Einstein distribution $n_{\mathrm{th}} = [\exp(\hbar\Omega/k_{\mathrm{B}}T) - 1]^{-1}$, with T denoting the temperature, and k_{B} the Boltzmann constant. These expressions apply for the scattering in both waveguides A and B. As we have seen in Chapter 2, these equations can be used to calculate the spectral density of the spontaneous scattering

$$S(\omega) = \hbar\omega_0 G_{\mathrm{B}} P z \left(\frac{\Gamma}{2}\right)^2 \left(\frac{n_{\mathrm{th}}+1}{(\omega-(\omega_0-\Omega_0))^2+(\Gamma/2)^2} + \frac{n_{\mathrm{th}}}{(\omega-(\omega_0+\Omega_0))^2+(\Gamma/2)^2}\right), \tag{3.57}$$

showing a Lorentzian lineshape with a full-width at half-maximum Γ (see Section 2.3.4).

In the case of coupled acoustic modes, as discussed in the previous section, Eq. (3.56) can be generalized

$$\begin{aligned} a_{-1}^{(\ell)}(z,\tau) &= -i\frac{g^*}{v}a_0 \sum_{m=1}^{N} V_m^{(\ell)*} \int_0^\tau d\tau' \int_0^z dz' \eta_m^\dagger(z',\tau') e^{-\frac{\Gamma}{2}(\tau-\tau')}, \\ a_{1}^{(\ell)}(z,\tau) &= -i\frac{g}{v}a_0 \sum_{m=1}^{N} V_m^{(\ell)} \int_0^\tau d\tau' \int_0^z dz' \eta_m(z',\tau') e^{-\frac{\Gamma}{2}(\tau-\tau')}, \end{aligned} \tag{3.58}$$

where η_m is the Langevin force associated with the m^{th} phonon super-mode, and $V_m^{(\ell)}$ is the coefficient used in Eq. (3.50). Since the acoustic super-modes are orthogonal, we use the fact that the thermal phonons in each eigenmode are uncorrelated and follow $\langle\eta_m\rangle = 0$ and $\langle\eta_m^\dagger(z,t)\eta_{m'}(z',t')\rangle = n_m\Gamma\delta_{m,m'}\delta(z-z')\delta(t-t')$. The spectral density is now given by

$$\begin{aligned} S(\omega) =& \hbar\omega_0 G_{\mathrm{B}} P z \left(\frac{\Gamma}{2}\right)^2 \\ &\times \sum_{m=1}^{N} |V_m^{(l)}|^2 \left(\frac{n_m+1}{(\omega-(\omega_0-\Omega_m))^2+(\Gamma/2)^2} + \frac{n_m}{(\omega-(\omega_0+\Omega_m))^2+(\Gamma/2)^2}\right), \end{aligned} \tag{3.59}$$

where n_m is the average thermal phonon occupation of the m^{th} phonon super mode. We see that the spontaneous scattering results in a noise spectrum that is comprised of a sum of Lorentzian lineshapes. This is distinct from the multi-pole response observed for a transduced signal (Eq. (3.50)), which results from coherent interference. In the case of weakly coupled acoustic modes, we can readily see how the noise spectrum takes a

Lorentzian form. In this case, the frequency differences of the super-modes will be small and we can approximate $n_m \approx n_{\text{th}}$ and $\omega_0 \pm \Omega_m \approx \omega_0 \pm \Omega_0$. Using the fact that $\sum_{m=1}^{N} |V_m^{(l)}|^2 = 1$, we see that the spontaneous spectrum is consistent with a Lorentzian frequency response obtained from a single acoustic mode, given by Eq. (3.57).

Interestingly, the presence of spontaneously scattered photons in either waveguide has no impact on the driven acoustic field[3] [172]. The scattering produced from the thermally occupied phonons only adds phase fluctuations which do not change the forcing function driving the coherent acoustic fields, as it is determined only by the intensity envelope of the light field. This can be seen directly from Eq. (3.9) where the contribution to the driven phonon field is the sum of terms $(a_{-1}^{(\text{A})\dagger} a_0^{(\text{A})} + a_0^{(\text{A})\dagger} a_1^{(\text{A})} + a_{-1}^{(\text{B})\dagger} a_0^{(\text{B})} + a_0^{(\text{B})\dagger} a_1^{(\text{B})})$, which equals zero when plugging in the mode amplitudes from Eq. (3.56).

3.4 Conclusion

The theoretical model presented in this chapter describes the nonlinear dynamics of forward Brillouin active devices which utilize the nonlocal nature of the acoustic modes participating in the process. This nonlocal susceptibility is enabled by the long lifetime of the phonons, which allows them to propagate a large distance —spanning many optical wavelengths— to mediate coupling between optically-decoupled regions of the device.

We have shown that the optical intensity envelope of light in waveguide A induces a nonlinear response in the spatially-separated waveguide B, resulting in a phase modulation set by the Brillouin gain, acoustic properties, interaction length, and optical powers. This phenomenon can be readily measured within integrated-photonic devices, where the tight confinement of the optical and acoustic fields to micrometer-scale waveguides yields high Brillouin gain [139, 186, 187]. Multi-core optical fibers can also demonstrate nonlocal susceptibility between the separated cores, where the long interaction length and high-power handling can produce strong nonlinear effects [188].

We have seen that this nonlocal susceptibility can be mediated by multiple coupled

3. This analysis focuses on forward intra-modal Brillouin processes. The effects of spontaneous scattering will be different in backward and inter-modal scattering.

phonons, which can be treated as acoustic super-modes, all interacting with the optical fields. The coherent interference of these acoustic super-modes yields a nonlocal susceptibility corresponding to a multi-pole frequency response, which offers a sharp frequency roll-off and high out-of-band suppression. When using these optical nonlinearities for signal processing, such hybrid photonic-phononic strategies yield transfer functions that would be challenging to realize using all-optical techniques, providing technological value in many microwave and photonics applications [193, 196]. In the next chapters, we will see how this nonlocal response can be utilized to produce multi-pole microwave-photonic filters. Additionally, the analysis presented in this work can be readily adapted to describe nonlocal susceptibilities involving other scattering processes such as inter-modal Brillouin scattering [30, 65], which will be discussed further in Chapter 9.

Chapter 4

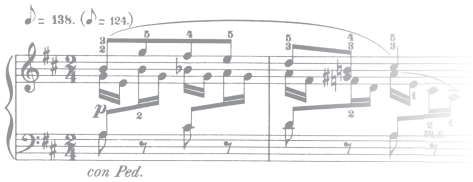

Microwave photonics

4.1 Introduction

As we seek to utilize an ever-increasing portion of the electromagnetic spectrum for next-generation communications and radar systems, microwave-photonic signal processing platforms show great promise for their ability to manipulate signals at high frequencies and over extremely wide bandwidths [193, 197]. The advantages offered by optical platforms include low-loss propagation in optical fibers, immunity to radio-frequency interference, and extremely large bandwidth. These properties have enabled the development of devices that would be very challenging to implement in conventional microwave systems. Furthermore, when considering the field of integrated photonics, the footprint of devices can be made much smaller than their microwave counterparts, as the optical wavelength is $\sim 10^5$ times smaller than that of microwaves.

In its simplest form, a microwave-photonic link is comprised of an electro-optic modulator, encoding a microwave signal onto an optical carrier wave at the link input, and a demodulation scheme and photodetection to convert the signal back to the microwave domain at the link output. While in the optical domain, the signal can be transmitted over a large distance thanks to optical fiber and optical amplification technology, and additionally, signal processing operations can be performed, as will be discussed in Section 4.5.

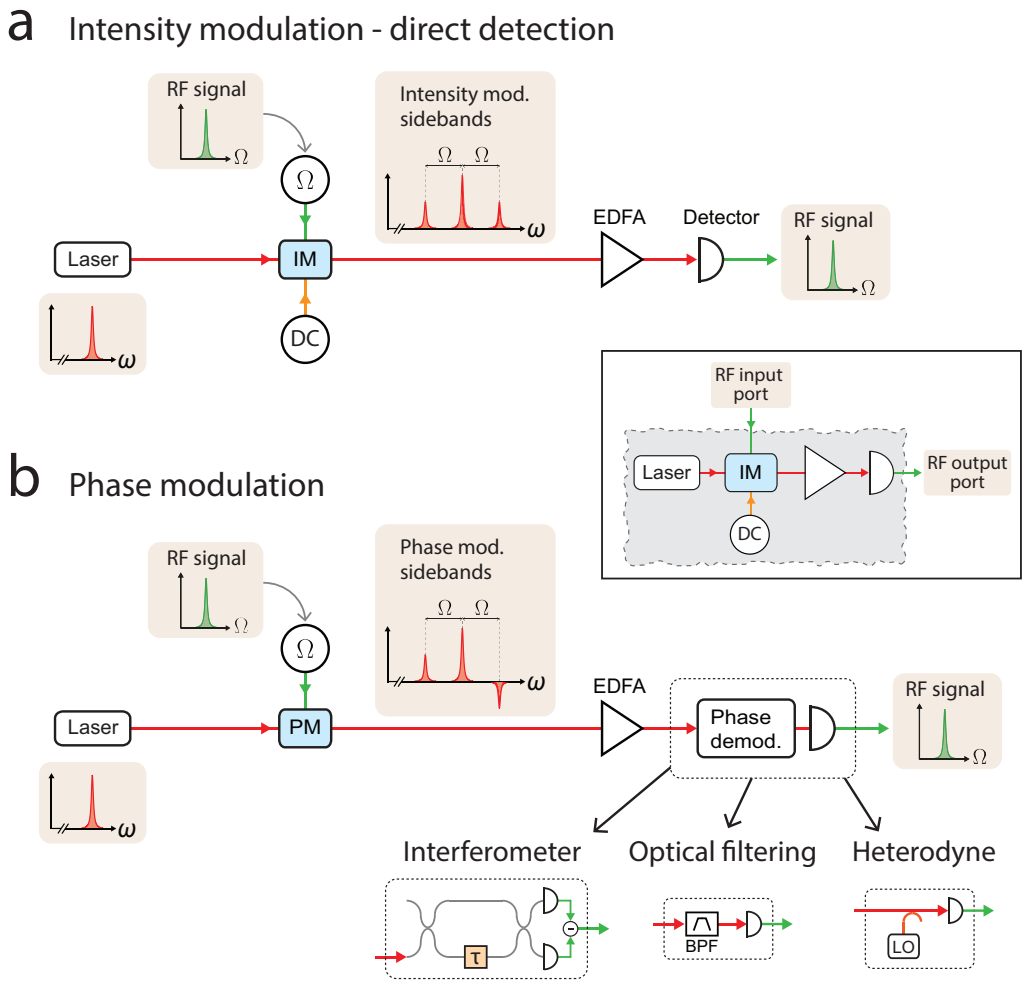

Figure 4.1: Schematic illustration of different microwave-photonic links. **(a)** Intensity-modulated: an optical tone is modulated by a microwave signal using an intensity modulator (IM), producing optical sidebands. The optical signal can be amplified using an optical amplifier (EDFA) and directly detected at the link output to retrieve the microwave signal. **(b)** Phase-modulated: The microwave signal is encoded into the optical carrier's phase using a phase modulator (PM). As phase cannot be directly detected, a demodulator needs to be implemented. This can be achieved using an interferometer and balanced detection, optical filtering, or heterodyne detection. The inset illustrates the analysis of the microwave-photonic link as a 'black box' microwave system, where we only have access to the input and output ports.

The microwave signal can be modulated using multiple different schemes onto an optical carrier. The two fundamental analog modulations are *intensity modulation*, where a microwave signal is encoded in the power of the optical carrier, and *phase modulation* in which the microwave signal induces phase shifts to the carrier wave. Fig. 4.1(a) illustrates a microwave-photonic link using an intensity modulation scheme, showing an intensity modulator (typically requiring a DC biasing voltage source), and direct detection, since a photodetector is sensitive to optical intensity and does not require additional demodulation. In contrast, the phase-modulated microwave-photonic link shown in Fig. 4.1(b) utilizes a phase modulator. Now, phase demodulation needs to be implemented, as optical detectors are not sensitive to the phase of the detected field.

In the following sections, we will analyze an example of an intensity modulation based microwave-photonic link, and study its performance. Additionally, we will examine possible sources of noise and signal distortion, which must be considered when designing practical systems and applications. This tutorial will introduce the concepts used in microwave-photonic design and analysis and will be the basis for our discussion of Brillouin-based microwave-photonic systems in the next chapters.

4.2 Microwave-photonic link example

We start by examining the operation of the intensity modulator at the RF-photonic link input, as seen in Fig. 4.1(a). In this link, an intensity modulator is used at the link input to encode the RF signal onto an optical signal. At the link output, direct detection using a photodetector retrieves the signal back to the RF domain in the form of photocurrent.

4.2.1 Intensity modulation using a Mach-Zehnder interferometer

An intensity modulator is commonly implemented using a Mach-Zehnder modulator (MZM), where an interferometer has sections made of a material with a strong electro-optic effect, such as $LiNbO_3$, GaAs, and InP. By applying an electric voltage across these sections, the optical path length is modulated, inducing a relative phase shift between optical waves

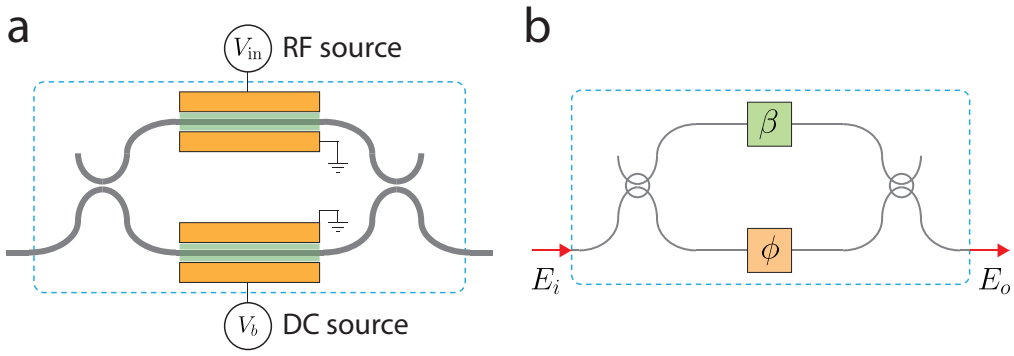

Figure 4.2: **(a)** Schematic illustration of a Mach-Zehnder intensity modulator (MZM). **(b)** An equivalent optical circuit diagram, where the effect of the electric fields is represented as phase shifts. One of the optical paths has a DC phase shift ϕ, while the other arm has a phase modulator inducing a time-dependent phase shift β. The interference of the two arms at the modulator output yields an intensity-modulated signal.

propagating in the two interferometer arms, and resulting in an intensity modulation at the modulator output. Typically, there is also a DC port, where a biasing voltage can be used to set the operating point of the modulator, as illustrated in Fig. 4.2.

We define the modulator half-wave voltage V_π as the applied voltage at which a phase shift of π is produced. These can be different for the RF port and the DC port, and can be used to write the phase shifts in terms of voltages

$$\beta = \pi \frac{V_{\text{in}}}{V_\pi^{\text{RF}}}, \qquad \phi = \pi \frac{V_b - V_{\text{offset}}}{V_\pi^{\text{DC}}}. \tag{4.1}$$

Here, V_{in} is the input RF voltage, V_b is the DC biasing voltage, and V_{offset} is the bias voltage necessary to set the DC phase to $\phi = 0$. To simplify notation, we will assume $V_{\text{offset}} = 0$ in the rest of our analysis, however, it needs to be taken into account in practice.

One often views the intensity modulator as a linear device that perfectly converts signals from the electrical to the optical domain, however, this notion is only valid for in the small-signal limit, when $V_{\text{in}} \ll V_\pi^{\text{RF}}$. More generally, the output optical field amplitude from a modulator, driven by an input RF voltage at frequency Ω, is given by

$$E_o = E_i \; e^{-i\omega t} \left[\alpha^2 \; e^{-i\phi} + \left(1 - \alpha^2\right) e^{i\beta \sin(\Omega t)} \right], \tag{4.2}$$

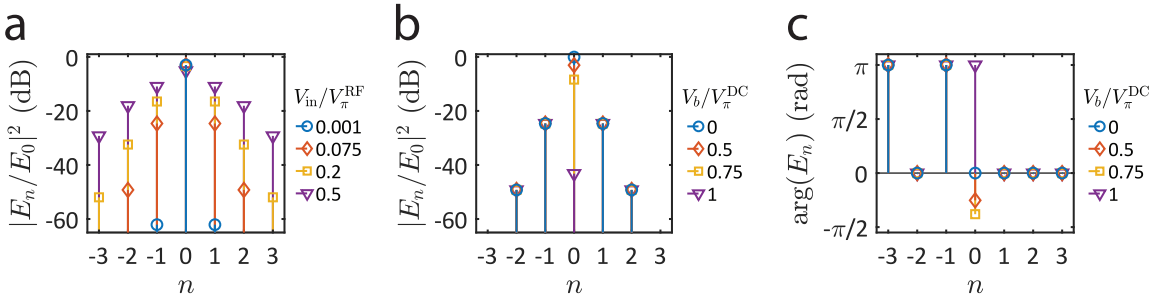

Figure 4.3: **(a)** The optical power in each of the tones generated by the modulation, where E_n denotes the component of the optical field oscillating at frequency $\omega + n\Omega$. The stronger the input voltage, the more power is transferred from the carrier ($n = 0$) to the sidebands. This calculation is for the case when the modulator is biased at quadrature, i.e., $V_b/V_\pi^{\mathrm{DC}} = 0.5$. **(b)** The optical power in the optical tones, for different biasing voltages. The input RF voltage in this calculation is set to $V_{\mathrm{in}}/V_\pi^{\mathrm{RF}} = 0.075$ **(c)** The phase of the optical tones corresponding to panel (b). The change in the biasing point only shifts the phase of the carrier ($n = 0$) relative to the sidebands.

where the parameter α accounts for the splitting ratios of the interferometer, and we have assumed that the modulator is lossless[1]. Using the Jacobi-Anger expansion, this can also be expressed as

$$E_o = E_i\, e^{-i\omega t}\left[\alpha^2\, e^{-i\phi} + \left(1-\alpha^2\right)\sum_{n=-\infty}^{\infty} J_n(\beta)e^{-in\Omega t}\right], \tag{4.3}$$

where $J_n(\cdot)$ denotes the n^{th} order Bessel function. We will assume the power is equally split within the interferometer, setting $\alpha = \sqrt{1/2}$, leaving us with

$$E_o = \frac{1}{2}E_i\, e^{-i\omega t}\left[e^{-i\phi} + \sum_{n=-\infty}^{\infty} J_n(\beta)e^{-in\Omega t}\right], \tag{4.4}$$

which has multiple optical tones separated by frequency Ω, as shown in Fig. 4.3.

Ultimately, we will be interested in optical power, as it is what is observable on a power-law detector. Examining the output power, $P_o = |E_o|^2$, we have

$$P_o = \frac{1}{2}P_i\left[1 + \cos\left(\beta\sin\left(\Omega t\right) - \phi\right)\right], \tag{4.5}$$

1. Loss is typically accounted for by multiplying Eq. (4.2) by a constant [198].

which can be rearranged to explicitly show the different frequency components

$$P_o = \frac{1}{2}P_i \left[\overbrace{1 + \cos(\phi)\, J_0(\beta)}^{\text{DC}} + \underbrace{2\cos(\phi) \sum_{n=1}^{\infty} J_{2n}(\beta) \cos\Big(2n\Omega t\Big)}_{\text{even sidebands}} + \underbrace{2\sin(\phi) \sum_{n=1}^{\infty} J_{2n-1}(\beta) \sin\Big((2n-1)\,\Omega t\Big)}_{\text{odd sidebands}} \right]. \tag{4.6}$$

This optical power represents the envelope of the field, which oscillates as a result of the interference between optical tones after modulation. We will limit our attention to the first few terms, which will become important in later analyses of signal distortion and noise sources. We can identify the DC term, and the first few RF components, at multiples of Ω

$$\begin{aligned} P_{\text{DC}} &= \frac{1}{2}P_i \Big[1 + \cos(\phi)\, J_0(\beta)\Big], & P_{2\Omega} &= P_i \cos(\phi)\, J_2(\beta) \cos(2\Omega t)\,, \\ P_{\Omega} &= P_i \sin(\phi)\, J_1(\beta) \sin(\Omega t)\,, & P_{3\Omega} &= P_i \sin(\phi)\, J_3(\beta) \sin(3\Omega t)\,, \end{aligned} \tag{4.7}$$

noting that the DC component is equivalent to the average power integrated over a time much longer than the RF frequency, $P_{\text{DC}} = (1/T)\int_0^T dt\; P_o(t)$ (where $T \gg 2\pi/\Omega$). We see that although the input RF signal was monochromatic, the optical intensity-modulated signal has multiple frequency components, including all integer multiples of the input frequency, as well as a DC term, as seen in Fig. 4.4. Interestingly, we see that the biasing point ϕ changes the power in the different frequency components, but does not affect the phase of the oscillations.

To see the relation between the input voltage and the optical power, it is useful to analyze the small-signal limit (i.e., $V_{\text{in}} \ll V_\pi^{\text{RF}}$). In this case, we can linearize the Bessel function to first order ($J_1(x) \approx x/2$), such that at the input frequency Ω, we have

$$P_{\Omega} = P_i \sin(\phi) \left(\frac{\pi}{2}\frac{V_{\text{in}}}{V_\pi^{\text{RF}}}\right) \sin(\Omega t)\,, \tag{4.8}$$

where we see that the 'effective' linear half-wave voltage is $V_{\text{eff}}^{\text{RF}}(\phi) = V_\pi^{\text{RF}}/\sin(\phi)$. We can see that the intensity-modulated output power at the fundamental frequency P_Ω is

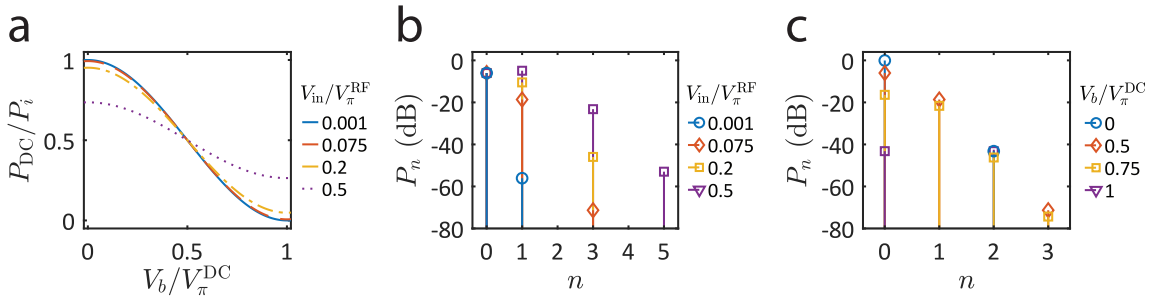

Figure 4.4: **(a)** The DC optical power at the modulator output, as a function of the biasing voltage. **(b)** Frequency components of the optical power for different values of RF voltages. This calculation is for the case when the modulator is biased at quadrature, i.e., $V_b/V_\pi^{\mathrm{DC}} = 0.5$, and we can see that the even sidebands are suppressed. **(c)** Frequency components of the optical power for different biasing voltages. The input RF voltage in this calculation is $V_{\mathrm{in}}/V_\pi^{\mathrm{RF}} = 0.075$

maximized when operating at $\phi = \pi/2$, corresponding to the biasing voltage $V_b = V_\pi^{\mathrm{DC}}/2$, which is referred to as the 'quadrature point'. At this biasing point, the optical power (Eq. (4.6)) is given by

$$P_o = \frac{1}{2}P_i\left[1 + 2\sum_{n=1}^{\infty} J_{2n-1}(\beta)\sin\Big((2n-1)\,\Omega t\Big)\right], \tag{4.9}$$

leaving us with odd sidebands only, as seen in Figs. 4.4(b,c).

4.2.2 Intensity modulation using optical filtering

An alternative method to produce an intensity-modulated optical field is by using a phase modulator and an optical filter to convert the phase modulation to intensity modulation. Interestingly, also in the case of the Mach-Zehnder modulator we analyzed earlier, the RF signal was phase-modulated onto an optical carrier, and the interference between the two interferometer paths yielded an intensity-modulated field (see Fig. 4.2). Now, we assume that an optical filter removes all but two optical frequencies, namely the optical carrier and a single sideband

$$E_o^{\mathrm{SSB}} = E_i\; e^{-i\omega t}\left[J_0\left(\beta\right) + J_1\left(\beta\right)e^{-i\Omega t}\right]. \tag{4.10}$$

Analyzing the small-signal limit, we expand the Bessel function to first order ($J_0(x) \approx 1$, $J_1(x) \approx x/2$), leaving us with

$$E_o^{\mathrm{SSB}} = E_i \; e^{-i\omega t}\left[1 + \frac{\beta}{2}e^{-i\Omega t}\right], \tag{4.11}$$

and examining the power $P_o = |E_o|^2$, isolating the term oscillating at frequency Ω, we have

$$P_\Omega^{\mathrm{SSB}} = P_i\left(\pi\frac{V_{\mathrm{in}}}{V_\pi^{\mathrm{RF}}}\right)\cos\left(\Omega t\right). \tag{4.12}$$

We see how the optical filter, selecting two tones from the phase modulator output, results in the optical power oscillating at the input voltage frequency[2]. However, implementing such optical filtering can be challenging, and in many cases, such as fiber-optic systems and integrated photonics, intensity modulation is implemented using the interferometric scheme discussed earlier (using an MZM).

4.2.3 Direct detection

At the link output, the microwave signal is retrieved from the optical domain back to the microwave domain, which in the case of intensity modulation can be achieved using direct detection. A photodetector generates photocurrent proportional to the optical power $I = \eta P_o$, where η is the responsivity of the detector.

To continue our analysis, it is useful to express the input and output RF signals in terms of their power, given by [198]

$$P_{\mathrm{in}} = \frac{\langle V_{\mathrm{in}}^2\rangle}{R_{\mathrm{in}}}, \qquad P_{\mathrm{out}} = \langle I^2\rangle R_{\mathrm{out}}|H_{\mathrm{pd}}|^2. \tag{4.13}$$

Here, $\langle\cdot\rangle$ denotes a time average, R_{in} is the input impedance to the modulator, R_{out} the output impedance of the detector, and H_{pd} is the detector circuit efficiency parameter, which can be frequency dependent.

2. More generally, we can analyze the interference between two tones with optical powers P_1 and P_2, separated by a frequency Ω and relative phase θ. The field amplitude, given by $E = e^{-i\omega t}(\sqrt{P_1}e^{i\theta} + \sqrt{P_2}e^{-i\Omega t})$, will result in a beat note with a power given by $P_\Omega = 2\sqrt{P_1 P_2}\cos(\Omega t + \theta)$.

We can treat the microwave-photonic link as a 'black box', and analyze the relationship between the microwave signals at the input and output ports. Assuming the input signal is a single sinusoidal tone at frequency Ω, such that $P_{\text{in}}^{(\Omega)} = V_{\text{in}}^2/(2R_{\text{in}})$, we can calculate the output RF power at different frequencies, using Eqs. (4.7) and (4.13), resulting in

$$\begin{aligned}
P_{\text{out}}^{(\text{DC})} &= \frac{P_i^2}{4}\left[1+\cos(\phi)\,J_0\left(\frac{\pi}{V_\pi^{\text{RF}}}\sqrt{2R_{\text{in}}P_{\text{in}}^{(\Omega)}}\right)\right]^2\eta^2 R_{\text{out}}|H_{\text{pd}}|^2,\\
P_{\text{out}}^{(\Omega)} &= \frac{P_i^2}{2}\sin^2(\phi)\,{J_1}^2\left(\frac{\pi}{V_\pi^{\text{RF}}}\sqrt{2R_{\text{in}}P_{\text{in}}^{(\Omega)}}\right)\eta^2 R_{\text{out}}|H_{\text{pd}}|^2,\\
P_{\text{out}}^{(2\Omega)} &= \frac{P_i^2}{2}\cos^2(\phi)\,{J_2}^2\left(\frac{\pi}{V_\pi^{\text{RF}}}\sqrt{2R_{\text{in}}P_{\text{in}}^{(\Omega)}}\right)\eta^2 R_{\text{out}}|H_{\text{pd}}|^2,\\
P_{\text{out}}^{(3\Omega)} &= \frac{P_i^2}{2}\sin^2(\phi)\,{J_3}^2\left(\frac{\pi}{V_\pi^{\text{RF}}}\sqrt{2R_{\text{in}}P_{\text{in}}^{(\Omega)}}\right)\eta^2 R_{\text{out}}|H_{\text{pd}}|^2.
\end{aligned} \tag{4.14}$$

It is important to note that the power described in Eq. (4.14) is the RF power after detection, such as would be measured on an RF-spectrum analyzer, and should not be confused with the optical power $P_{n\Omega}$ from Eq. (4.7), which describes optical power. The two are related through $P_{\text{out}}^{(n\Omega)} = \langle {P_{n\Omega}}^2\rangle \eta^2 R_{\text{out}}|H_{\text{pd}}|^2$, showing the square-law of photodetection.

4.3 Noise sources

When analyzing a microwave-photonic link we must consider noise that may accompany the detected signal, taking into account noise sources from both the microwave and the optical domains. While the noise analysis is system-specific, here we will mention a few of the noise sources that are relevant in most microwave-photonic links.

4.3.1 Laser intensity noise

The photodetector converts the optical intensity into an electrical current, hence intensity fluctuations of the optical carrier will induce current fluctuations, and will result in RF noise with a spectral density given by [198]

$$N_{\text{RIN}} = P_o^2\eta^2 R_{\text{out}}|H_{\text{pd}}|^2 \cdot \text{RIN}. \tag{4.15}$$

Here, RIN denotes 'relative intensity noise', given by RIN $= \langle P_o^2 \rangle / \langle P_o \rangle^2$. In many cases, these noise sources are band limited, and are strongly suppressed when operating at frequencies above ∼1 GHz.

4.3.2 Thermal noise

Any resistive conductor displays random voltage fluctuations across its terminals, such that it is kept in thermal equilibrium, in a manner consistent with the fluctuation-dissipation theorem. These fluctuations are referred to as 'Johnson–Nyquist' noise [174], with a power spectral density (PSD) given by [198]

$$N_{\text{J-N}} = \hbar\Omega \left[\frac{1}{\exp\left(\hbar\Omega / k_{\text{B}} T\right) - 1} + \frac{1}{2} \right], \tag{4.16}$$

which at the high temperature limit, when $T \gg \hbar\Omega / k_{\text{B}}$, simplifies to the well known expression[3] $N_{\text{J-N}} \approx k_{\text{B}} T$. This noise is present at any resistor, and in the microwave-photonic link we are analyzing here, we need to take into account two resistors —one within the detector and another at the RF input port of the intensity modulator— which both contribute to the noise measured at the link output. The noise produced at the detector is given by Eq. (4.16), however, the noise from the intensity modulator propagates through the microwave-photonic link, and we need to account for amplification or loss which we describe using the link gain parameter g. These two noise sources are uncorrelated, such that we can add their contributions to the power spectral density $(N_{\text{J-N}} + g N_{\text{J-N}})$, and we define

$$N_{\text{th}} = \hbar\Omega \left[\frac{1}{\exp\left(\hbar\Omega / k_{\text{B}} T\right) - 1} + \frac{1}{2} \right] (1 + g), \tag{4.17}$$

as the total microwave thermal-noise spectral density.

3. This can be derived by treating the electromagnetic field as an oscillator with two degrees of freedom (electric and magnetic), and from the equipartition theorem we know that each degree of freedom will have an average energy of $k_{\text{B}} T/2$ [199].

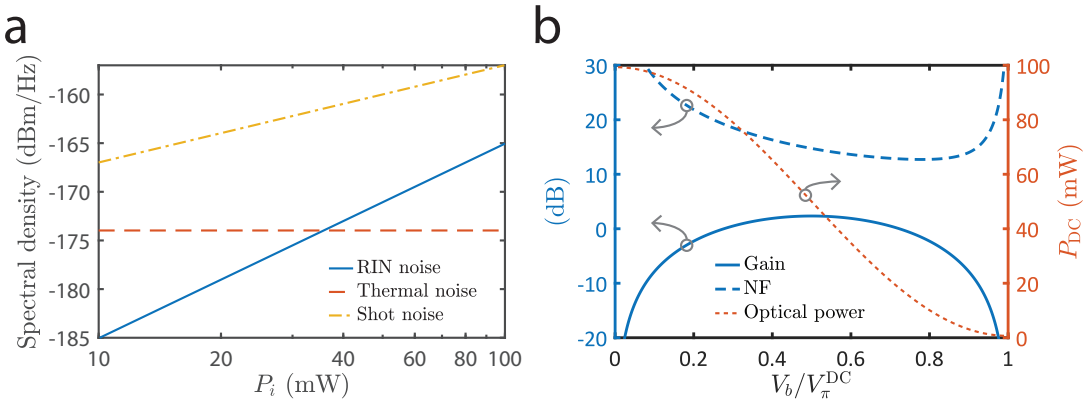

Figure 4.5: **(a)** Calculated spectral density of typical noise sources, assuming operation at the quadrature point ($V_b/V_\pi^{DC} = 0.5$), and $V_{in}/V_\pi^{RF} = 0.075$. **(b)** Microwave-photonic link gain and noise figure as a function of the modulator biasing voltage. While maximum gain is achieved at the quadrature point ($V_b = 0.5V_\pi^{DC}$), noise figure is minimized at $V_b = 0.77V_\pi^{DC}$. The DC optical power on the detector is also shown (dashed, right axis).

4.3.3 Shot noise

In the absence of technical noise, light emitted by a laser can be described as a coherent state, such that the photon arrival times at the detector are random and described by a Poisson distribution[4]. These fluctuations result in a power spectral density given by [198]

$$N_{shot} = 2I_{DC}\, qR_{out}|H_{pd}|^2, \tag{4.18}$$

where q is the electron charge, and I_{DC} is the DC photocurrent in the detector. Using Eqs. (4.7) and (4.13) we can express the photocurrent in terms of optical power and the modulator parameters, such that the shot noise spectral density as

$$N_{shot} = P_i\left[1 + \cos(\phi)\, J_0\left(\pi\frac{V_{in}}{V_\pi^{RF}}\right)\right]\eta qR_{out}|H_{pd}|^2, \tag{4.19}$$

showing linear scaling with optical power. While there can be other noise sources at the detector, we will consider shot noise as the dominant noise source associated with the detection process [198]. In fact, in many cases, shot noise dominates the link noise floor,

4. At frequencies larger than ~1 GHz this is a good assumption. However, for systems working at lower frequencies, other technical noise sources should be examined.

as shown in Fig. 4.5(a), where realistic microwave-photonic link parameters are used to calculate the spectral density of the different noise sources.

4.3.4 EDFA noise

Just as in microwave systems, low-noise amplification is extremely valuable in microwave-photonic applications, where amplification can be introduced in the optical domain. This can be achieved using erbium-doped fiber amplifiers (EDFA), which are utilized in many photonic systems, and here we consider additional noise sources resulting from the amplification process. Amplified spontaneous emission (ASE) results in three noise contributions in the RF domain; spontaneous emission beating with itself, spontaneous emission beating with the signal, and the shot noise associated with the randomness of the emission. In most microwave-photonic applications, the spontaneous-signal scattering is the dominant noise source, given by [198]

$$N_{\mathrm{EDFA}} = 4P_o n_{\mathrm{sp}} \hbar\omega \left(g_0 - 1\right) \eta^2 R_{\mathrm{out}} |H_{\mathrm{pd}}|^2, \tag{4.20}$$

where g_0 is the EDFA gain, and ω the optical angular frequency. The parameter n_{sp} is the spontaneous emission factor and is typically of order unity[5].

4.4 Microwave link performance metrics

In this section, we will use the expressions we have derived for the RF power and noise sources to analyze important RF figures of merit, and quantify the microwave-photonic link performance. For this example, we consider a full microwave-photonic link, with a Mach-Zehnder modulator used to convert the input microwave signal to the optical domain, and at the link output, direct detection converts the modulated optical field back to the microwave domain.

5. The spontaneous emission factor is given by $n_{\mathrm{sp}} = (\sigma_2 N_2)/(\sigma_2 N_2 - \sigma_1 N_1)$, where N_1 (N_2) is the density of atoms in the lower (upper) state of the amplifier transition, and σ_1 (σ_2) denotes the absorption (emission) cross-section [164, 198].

4.4.1 Link gain

We focus on the linear RF response of the system, i.e., the output signal oscillating at the same frequency as the input signal. We analyze the small-signal regime, such that $V_{\text{in}} \ll V_{\pi}^{\text{RF}}$, and by expanding Eq. (4.14) to first order (i.e., $J_1(x) \approx x/2$) we find a linear relationship between the input and output RF powers at frequency Ω

$$g = \frac{P_{\text{out}}^{(\Omega)}}{P_{\text{in}}^{(\Omega)}} = \frac{P_i^2}{4} \sin^2(\phi) \left(\frac{\pi}{V_{\pi}^{\text{RF}}} \right)^2 R_{\text{in}} \eta^2 R_{\text{out}} |H_{\text{pd}}|^2, \tag{4.21}$$

which is defined as the small-signal gain. When expressing the gain on a log-scale (in units of dB) it is typically denoted G. We can see that the half-wave voltage of the modulator V_{π}^{RF} determines the link gain, as it essentially describes the efficiency of the electro-optic conversion, and the development of low-voltage modulators are an active area of research [53, 200].

While link gain is an important parameter, describing the overall amplification or loss experienced by an RF signal propagating through the system, in many cases it can be improved by simply adding amplifiers (either in the optical or in the microwave domain). However, amplification will lead to higher noise and signal distortion, and it is important to analyze the noise figure and dynamic range when characterizing a microwave link.

4.4.2 Noise figure

An important metric for microwave link performance is the noise figure, quantifying the noise added by the system, defined as the ratio of the input to output signal-to-noise ratios

$$F = \frac{\text{SNR}_{\text{in}}}{\text{SNR}_{\text{out}}} = \frac{P_{\text{in}}^{(\Omega)}/N_{\text{in}}}{P_{\text{out}}^{(\Omega)}/N_{\text{out}}} \approx \frac{P_{\text{in}}^{(\Omega)}/N_{\text{in}}}{g P_{\text{in}}^{(\Omega)}/N_{\text{out}}} = \frac{N_{\text{out}}}{N_{\text{in}}} \frac{1}{g}. \tag{4.22}$$

The approximation assumes the small-signal limit, such that we could express the output power in terms of the input power and linear link gain. Using the link gain we calculated

in Eq. (4.21), we have

$$F = \frac{N_{\text{out}}}{N_{\text{in}}} \frac{4\left(V_\pi^{\text{RF}}/\pi\right)^2}{P_i^2 \sin^2(\phi) R_{\text{in}} \eta^2 R_{\text{out}} |H_{\text{pd}}|^2}. \tag{4.23}$$

The noise at input (N_{in}) and output (N_{out}) of the link is specific to the system, however, it is convention to use the Johnson-Nyquist thermal noise as the input noise source, with spectral density $N_{\text{in}} = k_{\text{B}}T$ at the high-temperature limit (valid at room temperature). It is important to note that in Eqs. (4.22) and (4.23) we have assumed the noise spectral density is constant over the measured bandwidth, such that the bandwidth is canceled in the final expression. In the case of a nonuniform spectral density, the noise power needs to be calculated by integrating the spectral density over the bandwidth of interest. We can see that modulators with a low half-wave voltage will lead to better performance, reducing the noise figure. When expressing the noise figure on a log-scale (in units of dB) it is commonly denoted 'NF' rather than F (the linear measure of the noise figure F is sometimes referred to as 'noise factor').

When considering a biasing voltage for the modulator at the link input, the quadrature point ($\phi = \pi/2$) will yield the highest link gain, as seen from Eq. (4.21) where $g \propto \sin^2(\phi/2)$. However, this might not be the case for optimizing the noise figure [198], as the link noise floor can have a different scaling with the biasing point, as is the case with shot noise. Using Eqs. (4.6) and (4.19), we have $N_{\text{shot}} \propto [1 + \cos(\phi)]$, and in the case of a shot-noise dominated link, the noise floor will decrease as we approach the half-wave voltage of the modulator. Fig. 4.5(b) shows the link gain and noise figure as a function of the biasing point, taking into account RIN (Eq. (4.15)), thermal noise (Eq. (4.17)), and shot noise (Eq. (4.19)). We can see that for the parameters used in this calculation, the optimal biasing voltage to minimize the noise figure is $V_b = 0.77V_\pi^{\text{DC}}$, compared to the maximum gain point, where $V_b = 0.5V_\pi^{\text{DC}}$ (the quadrature point). While this method improves the noise figure of the microwave-photonic link, it will limit its dynamic range, as we will see in the next section. Additionally, this operation point results in lower optical power at the modulator output, which needs to be considered in the system design.

4.4.3 Dynamic range

In the small-signal limit, we saw that the microwave-photonic link shows a linear response, described by the link gain. However, other frequency components can be generated in the link due to the nonlinear response of various components in the system, which distort the output signal. In the simple example we are analyzing here, we will consider the nonlinearity resulting from the intensity modulation process, as can be seen from Eq. (4.7), where additional frequency components are generated[6]. Furthermore, when the small-signal limit is not valid, the output signal will deviate from the linear trend we have described. Due to these effects, it is important to quantify the range over which we have linear, distortion-free operation.

Spur-free dynamic range

We start by describing the spur-free dynamic range of order n, defined as the range of input powers between the minimum detectable power (i.e., the noise floor) up to to the appearance of the n^{th} order spurious tone ($P_{\text{out}}^{(n\Omega)}$), as shown in Fig. 4.6. This dynamic range can be calculated using [198]

$$\text{SFDR}_n = \left(\frac{P_{\text{OIP}_n}^{(\Omega)}}{P_N} \right)^{(n-1)/n}, \tag{4.24}$$

where P_N is the noise spectral density integrated over some RF bandwidth B_{RF} (i.e., $P_N = N_{\text{out}} B_{\text{RF}}$), and OIP_n denotes the output intercept point of the signal and spur (see Fig. 4.6).

For this example, we will calculate the second- and third-order intercept points by equating the expressions from Eq. (4.7), approximating the Bessel functions to their first

6. Nonlinearities can also be present in other parts of the link, such as the detector, however, in many practical cases the modulator is the dominant source of signal distortion.

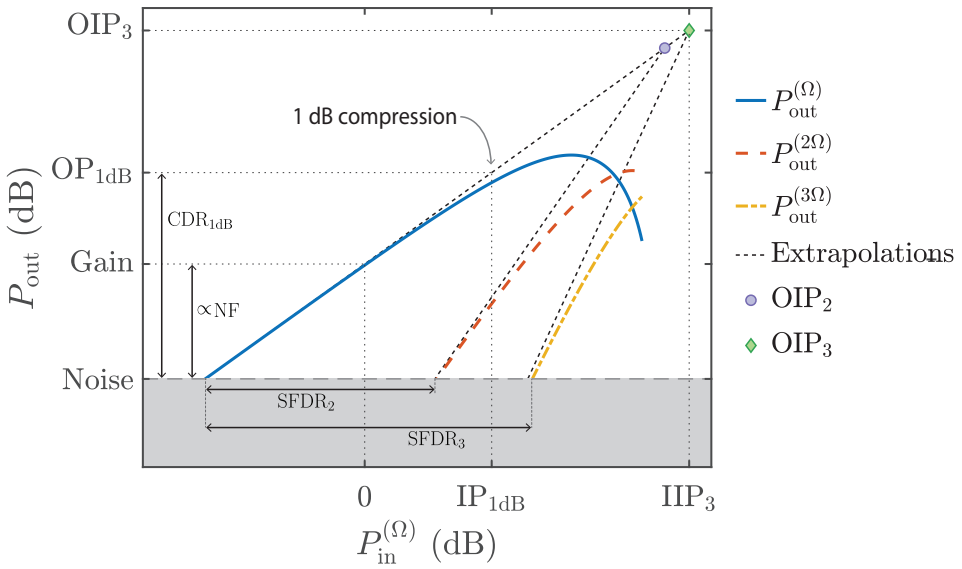

Figure 4.6: RF figures of merit at a given frequency can be graphically evaluated from a plot of the RF output power as a function of the input RF power. Linear extrapolations are used to find the intercept points of the spurious tones.

non-vanishing order ($J_1(x) \approx x/2$, $J_2(x) \approx x^2/8$, $J_3(x) \approx x^3/48$), such that

$$\begin{aligned} \frac{1}{4}\sin^2(\phi)\left(\frac{\pi}{V_\pi^{\mathrm{RF}}}\sqrt{2R_{\mathrm{in}}P_{\mathrm{IIP}_2}^{(\Omega)}}\right)^2 &= \frac{1}{64}\cos^2(\phi)\left(\frac{\pi}{V_\pi^{\mathrm{RF}}}\sqrt{2R_{\mathrm{in}}P_{\mathrm{IIP}_2}^{(\Omega)}}\right)^4, \\ \frac{1}{4}\left(\frac{\pi}{V_\pi^{\mathrm{RF}}}\sqrt{2R_{\mathrm{in}}P_{\mathrm{IIP}_3}^{(\Omega)}}\right)^2 &= \frac{1}{2304}\left(\frac{\pi}{V_\pi^{\mathrm{RF}}}\sqrt{2R_{\mathrm{in}}P_{\mathrm{IIP}_3}^{(\Omega)}}\right)^6. \end{aligned} \tag{4.25}$$

Solving for the input power results in

$$\begin{aligned} P_{\mathrm{IIP}_2}^{(\Omega)} &= \frac{8}{R_{\mathrm{in}}}\left(\frac{V_\pi^{\mathrm{RF}}}{\pi}\right)^2\tan^2(\phi), \\ P_{\mathrm{IIP}_3}^{(\Omega)} &= \frac{12}{R_{\mathrm{in}}}\left(\frac{V_\pi^{\mathrm{RF}}}{\pi}\right)^2. \end{aligned} \tag{4.26}$$

Using the small-signal link gain (Eq. (4.21)) we can find the output intercept point (OIP) $P_{\mathrm{OIP}_n}^{(\Omega)} = gP_{\mathrm{IIP}_n}^{(\Omega)}$, given by

$$\begin{aligned} P_{\mathrm{OIP}_2}^{(\Omega)} &= 2P_i^2\tan^2(\phi)\sin^2(\phi)\eta^2 R_{\mathrm{out}}|H_{\mathrm{pd}}|^2, \\ P_{\mathrm{OIP}_3}^{(\Omega)} &= 3P_i^2\sin^2(\phi)\eta^2 R_{\mathrm{out}}|H_{\mathrm{pd}}|^2, \end{aligned} \tag{4.27}$$

and finally arrive at the spur-free dynamic range

$$\begin{aligned} \mathrm{SFDR}_2 &= \left(2\, \frac{P_i^2 \tan^2(\phi) \sin^2(\phi)\, \eta^2 R_{\mathrm{out}} |H_{\mathrm{pd}}|^2}{N_{\mathrm{out}} B_{\mathrm{RF}}} \right)^{1/2}, \\ \mathrm{SFDR}_3 &= \left(3\, \frac{P_i^2 \sin^2(\phi)\, \eta^2 R_{\mathrm{out}} |H_{\mathrm{pd}}|^2}{N_{\mathrm{out}} B_{\mathrm{RF}}} \right)^{2/3}. \end{aligned} \tag{4.28}$$

In many applications, the third-order spur-free dynamic range will be the limiting factor of the link. First, when biasing the intensity modulator close to quadrature, the second-order spur is strongly suppressed, and will not limit the system operation[7]. Additionally, unless the system operates over an octave-spanning bandwidth, the second-order nonlinearity will result in frequency components well outside the bandwidth of interest. In contrast, the third-order nonlinearity can result in frequency mixing products well within the system bandwidth.

It is important to note that we have derived the spur-free dynamic ranges caused by the second and third harmonics, i.e., the system response at double and triple the input frequency. These nonlinearities can also be quantified using a two-tone test, where two frequencies are introduced at the link input and their mixing products are measured at the output, yielding an intermodulation dynamic range smaller by a factor $\sim$2 ($-$3 dB) compared to the expressions derived here.

Linear dynamic range

We turn to analyze the RF power range over which the output signal follows the linear, small-signal link gain. We quantify this by calculating the range starting at the minimum detectable power up to the point where the output deviates from the small-signal linear trend, commonly defined at 1 dB of deviation, i.e., $gP_{\mathrm{in}}^{(\Omega)}/P_{\mathrm{out}}^{(\Omega)} = 10^{0.1}$. We compare the

7. This can be seen in Eq. (4.28) where $\mathrm{SFDR}_2 \propto \tan^2(\phi)$ which diverges as we approach the quadrature point $\phi = \pi/2$.

the linear trend from Eq. (4.21) to the exact expression derived in Eq. (4.7)

$$\left(\frac{1}{4}\right)\frac{\left(\pi/V_{\pi}^{\mathrm{RF}}\right)^{2}\left(2R_{\mathrm{in}}P_{\mathrm{in}_{1\mathrm{dB}}}^{(\Omega)}\right)}{{J_1}^{2}\left(\left(\pi/V_{\pi}^{\mathrm{RF}}\right)\sqrt{2R_{\mathrm{in}}P_{\mathrm{in}_{1\mathrm{dB}}}^{(\Omega)}}\right)}=10^{0.1}, \tag{4.29}$$

and solving[8] for $P_{\mathrm{in}}^{(\Omega)}$ yields the input RF power where the output RF power deviates from the linear trend by 1 dB

$$P_{\mathrm{in}_{1\mathrm{dB}}}^{(\Omega)}=\frac{0.045765}{R_{\mathrm{in}}}\left(V_{\pi}^{\mathrm{RF}}\right)^{2}. \tag{4.30}$$

Defining the compression dynamic range as $\mathrm{CDR}_{1\mathrm{dB}}=gP_{\mathrm{in}_{1\mathrm{dB}}}^{(\Omega)}/P_N$, we arrive at

$$\mathrm{CDR}_{1\mathrm{dB}}=0.11292\,\frac{P_i^2\sin^2\left(\phi\right)\eta^2R_{\mathrm{out}}|H_{\mathrm{pd}}|^2}{N_{\mathrm{out}}B_{\mathrm{RF}}}, \tag{4.31}$$

which is maximized when the modulator is biased at quadrature ($\phi=\pi/2$).

As an example, Fig. 4.7 presents the calculated output RF power in the fundamental frequency, as well as the second- and third-order spurs as a function of input RF power, for different modulator biasing points. The corresponding RF link parameters are given in Table 4.1. We can see that in this example, as is the case in many systems, the spur-free dynamic range is the limiting factor for distortion-free operation, and the compression dynamic range will not limit performance. In our analysis, the limiting factor of the dynamic range is the intensity modulator, as is the case in many systems, and linearization schemes enhancing the dynamic range of electro-optic modulators will enhance the performance of microwave-photonic links [201].

4.4.4 Optical amplification

Next, we introduce an optical amplifier (EDFA) into the microwave-photonic link and show how the nonlinearity of the amplifier alters the link performance in a non-trivial way. We will consider a simple scenario, where the amplifier is fully saturated[9], assuming the amplifier

8. This can be calculated numerically.

9. A similar analysis can be performed when taking into account the saturation profile of the amplifier [202].

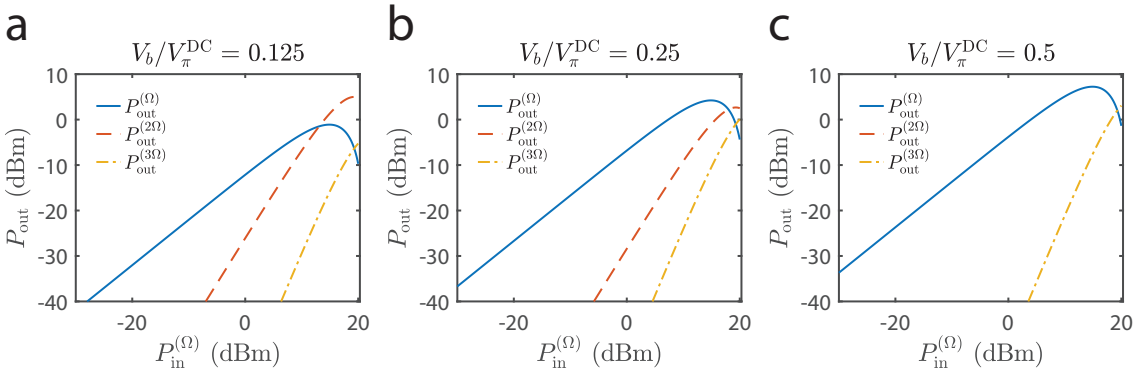

Figure 4.7: Calculated microwave-photonic link performance for a modulator with a DC half wave voltage of $V_\pi^{\mathrm{DC}} = 3$ V, biased at different voltages such that the DC phase is **(a)** $\phi = \pi/8$, **(b)** $\phi = \pi/4$, and **(c)** $\phi = \pi/2$ (the quadrature point). We can see that at quadrature, the second-order spurious tone vanishes, consistent with the fact that even-order sidebands are suppressed. In this example, we assume $P_i = 50$ mW of optical power, $\eta = 1$ (A/W) and $|H_{\mathrm{pd}}| = 0.5$, and impedances $R_{\mathrm{in}} = R_{\mathrm{out}} = 50\ \Omega$. The RF figures of merit corresponding to these plots are shown in Table 4.1.

Table 4.1: Calculated RF figures of merit at different biasing points, corresponding to Fig. 4.7.

Biasing angle (rad)	$\phi = \pi/8$	$\phi = \pi/4$	$\phi = \pi/2$	$\phi = \pi V_b/V_\pi^{\mathrm{DC}}$
G (dB)	-12.0	-6.7	-3.7	RF link gain
NF (dB)	26.0	20.7	17.7	Noise figure[1]
OIP_2 (dBm)	2.0	14.9	342.2	2nd order output intercept point[2]
$\mathrm{SFDR}_2\left(\mathrm{dB\ Hz}^{1/2}\right)$	81.0	87.5	251.1	2nd order spur-free dyn. range[3]
OIP_3 (dBm)	11.4	16.7	19.7	3rd order output intercept point[4]
$\mathrm{SFDR}_3\left(\mathrm{dB\ Hz}^{2/3}\right)$	114.3	117.8	119.8	3rd order spur-free dyn. range[5]
$\mathrm{OP}_{1\mathrm{dB}}$ (dBm)	-2.9	2.5	5.5	1 dB compression point
$\mathrm{CDR}_{1\mathrm{dB}}$ (dB Hz)	157.1	162.5	165.5	Linear dynamic range

In this example, we assume $P_i = 50$ mW of optical power, $\eta = 1$ (A/W) and $|H_{\mathrm{pd}}| = 0.5$, and impedances $R_{\mathrm{in}} = R_{\mathrm{out}} = 50\ \Omega$. The noise floor considered in this calculation is -160 dBm/Hz, corresponding to shot noise (see Fig. 4.5(a)).

[1] N_{in} is assumed to be thermal noise at room temperature ($T = 290$ K), such that $N_{\mathrm{in}} = k_{\mathrm{B}}T = -174$ dBm/Hz.

[2] Intermodulation OIP_2 is 6 dB lower.

[3] Intermodulation SFDR_2 is 3 dB lower.

[4] Intermodulation OIP_3 is 4.8 dB lower.

[5] Intermodulation SFDR_3 is 3.2 dB $\mathrm{Hz}^{2/3}$ lower.

has constant output power P_{EDFA}. In this example, we are neglecting other properties of the amplifier —such as additional noise when operating above the saturation point— and treating the EDFA simply as a nonlinear gain element to demonstrate how additional components can affect the link.

For a given optical power P_o, the gain provided by the amplifier is $\gamma = P_{\mathrm{EDFA}}/P_{\mathrm{DC}}$, such that the amplified RF signal is $P_{\Omega}^{\mathrm{amp}} = \gamma P_{\Omega}$, or equivalently, $P_{\Omega}^{\mathrm{amp}} = P_{\mathrm{EDFA}} P_{\Omega}/P_{DC}$. Using Eq. (4.7), this gives us

$$P_{\Omega}^{\mathrm{amp}} = P_{\mathrm{EDFA}} \frac{2J_1(\beta)\sin(\phi)}{1 + J_0(\beta)\cos(\phi)} \sin(\Omega t). \tag{4.32}$$

For a small-signal input, we have

$$P_{\Omega}^{\mathrm{amp}} = P_{\mathrm{EDFA}} \beta \tan(\phi/2) \sin(\Omega t), \tag{4.33}$$

where we have used the identity $\tan(x/2) = \sin(x)/[1 + \cos(x)]$, which grows as the phase ϕ approaches π. The divergence is a result of our (unrealistic) assumption that the EDFA is saturated, and has the same output power, regardless of the input power[10]. Fig. 4.8(a) shows the optical power at frequency Ω (Eq. (4.33)) as a function of the biasing voltage. We can see the optimal biasing point is dependent on the input RF voltage.

Fig. 4.8(b) shows the calculated RF noise power spectral density added in the amplification process (Eq. (4.20)), showing how changing the biasing point affects the noise spectral density. It is important to remember that this calculation assumes only noise generated by the beat note of the spontaneous emission with the signal, which is the dominant term in most practical cases. However, for low-power optical signals, the spontaneous-spontaneous scattering and the spontaneously-induced shot noise should not be neglected, as well as the fact that the assumption that the EDFA is saturated needs to be examined carefully.

We can calculate the output RF signal in this case of utilizing an optical amplifier,

10. At the limit of $\phi \to \pi$ the average optical power vanishes and our analysis clearly will not hold.

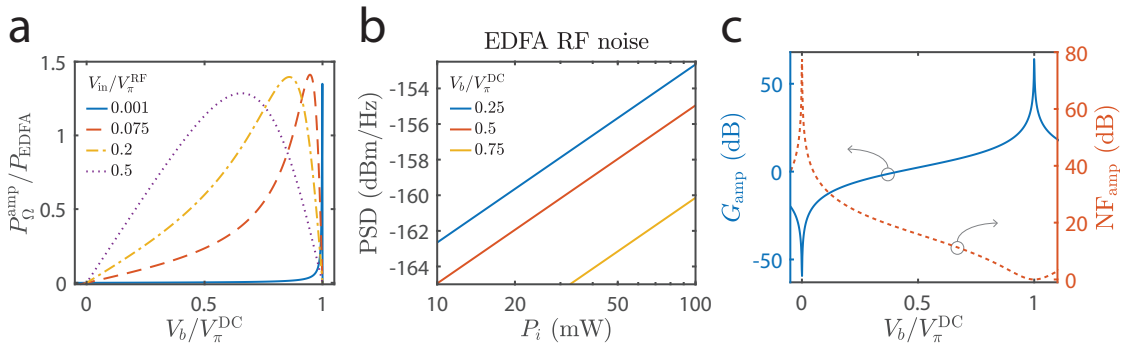

Figure 4.8: **(a)** The optical power of the beat-note at frequency Ω, normalized to the output power of a saturated EDFA, P_{EDFA}. We can see that for small input voltages, the beat-note will be enhanced when biasing off-quadrature, when the carrier power is suppressed. **(b)** Calculated EDFA noise for different optical powers and biasing points, following Eq. (4.20). **(c)** Calculated RF link gain and noise figure for a microwave-photonic link using an EDFA, assuming $V_\pi^{\text{DC}} = 3$. In these calculations, the EDFA gain is 27 dB, with a constant optical output power of 50 mW.

$P_{\text{out,amp}}^{(\Omega)}$, and the RF small-signal gain $g_{\text{amp}} = P_{\text{out,amp}}^{(\Omega)}/P_{\text{in}}^{(\Omega)}$, given by

$$g_{\text{amp}} = P_{\text{EDFA}}^2 \left(\frac{\pi}{V_\pi^{\text{RF}}}\right)^2 R_{\text{in}} \tan^2(\phi/2)\, \eta^2 R_{\text{out}} |H_{\text{pd}}|^2, \tag{4.34}$$

is shown in Fig. 4.8(c), as well as the noise figure from Eq. (4.22). We see that as the modulator biasing voltage is increased above the quadrature point, the link gain grows while the noise figure is decreased. As we have seen earlier, the limit of biasing close to the half-wave voltage (i.e., $V_b \to V_\pi^{(\text{DC})}$) should be examined carefully, as some of the assumptions we have made do not apply. For the noise figure calculation, we have assumed thermal noise at room temperature at the link input ($N_{\text{in}} = k_{\text{B}}T$) and the contributions of shot noise (Eq. (4.19)), thermal noise (Eq. (4.17)) and EDFA noise[11] (Eq. (4.20)) at the output (i.e., $N_{\text{out}} = N_{\text{shot}} + N_{\text{th}} + N_{\text{EDFA}}$).

11. We have neglected certain noise properties that can change the noise properties of the EDFA, such as the effects of saturation on the spontaneous emission factor.

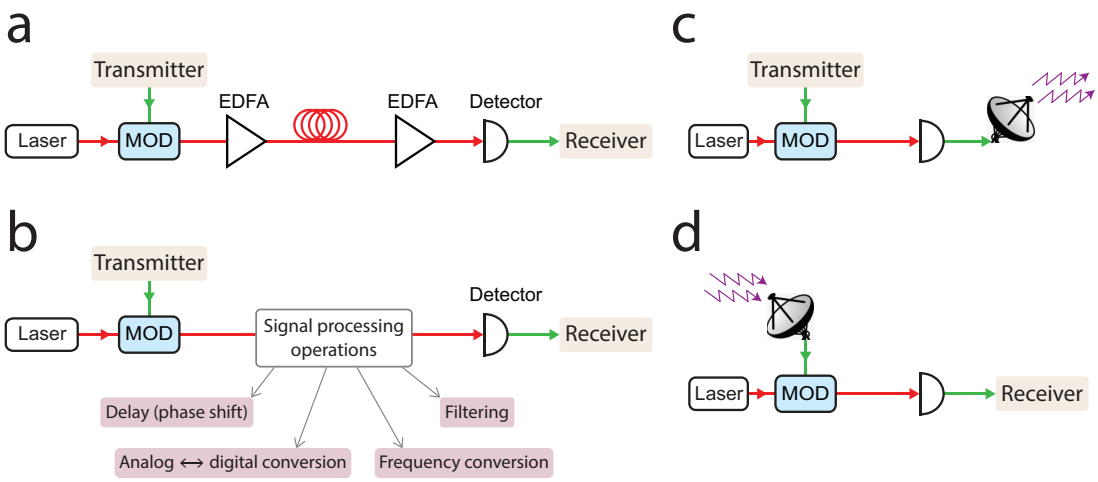

Figure 4.9: Examples of microwave-photonic link applications. **(a)** The low-loss platform provided by optical fibers, in combination with low-noise optical amplifiers, enables the transmission of RF signals over a long distance. **(b)** Signal processing operations can be introduced in the optical domain, expanding the capabilities of microwave-photonic links. These can be implemented in optical fibers or integrated-chip platforms. **(c)** Illustration of a microwave-photonic link between an RF transmitter and an antenna. **(d)** Illustration of a microwave-photonic link between an RF antenna and an RF receiver.

4.5 Applications of microwave-photonic links

Up to this point, we have analyzed a link that is not designed to perform any signal processing operations on the RF signal. This can be the case where the photonic link is used to transmit RF signals over long distances, utilizing the low propagation losses in optical fibers and the availability of low-noise amplifiers in the form of erbium-doped fiber amplifiers (EDFA), as shown schematically in Fig 4.9(a). In this scenario, all signal processing (besides amplification) is implemented directly on the RF signal, before or after the photonic link.

Alternatively, signal processing operations can be implemented in the optical domain within the microwave-photonic link. These operations may include phase shifting [203–205], analog to digital conversion (ADC and DAC) [206, 207], frequency conversion [208] and filtering operations [209], illustrated schematically in Fig. 4.9(b). A microwave photonic link can also be utilized within an RF transmitter or receiver, as illustrated in Figs. 4.9(c) and (d), respectively. These can be utilized, for example, in cellular network antenna remoting [210, 211], and radar technologies [212, 213].

An important application in which microwave-photonics can enable new technological capabilities is filtering microwave signals [209]. Microwave filtering is a crucial operation in many systems, such as channelization of multiplexed signals, and suppression of interfering signals and background noise. By performing filtering operations in the optical domain, the advantages of the optical platform —such as its wideband operation capabilities— enable the design of systems that would be challenging to implement in the microwave domain alone [214, 215]

Within an RF-photonic link, filtering operations can be implemented using multi-tap architectures [216–218], splitting and combining the signal with different delays, achieving finite-impulse response (FIR) filters. Alternatively, resonant structures can be used to produce filtering directly in the optical domain. These can be implement using Bragg gratings [219, 220], or ring resonators [221, 222]. However, the optical and microwave domains have vastly different frequency ranges (typically by a factor $\sim 10^5$), and realizing narrowband optical filters can be challenging. For example, filters with ∼MHz spectral resolution require resonators with ultrahigh quality factors ($Q \sim 10^8$), which demands ultralow-loss waveguides (∼0.1 dB/m). In the context of silicon photonics, there have been demonstrations of narrowband optical resonators [223], however, these require a large footprint, as well as sub-millikelvin temperature stability [51], and narrow-linewidth laser sources. Furthermore, many of these demonstrations have been shown in the optical domain, but have yet to be fully characterized in the context of a microwave-photonic link processing RF signals. A thorough review of integrated microwave photonics can be found in Ref. [196], and Ref. [209] reviews the field of integrated microwave-photonic filtering.

With the advancement of integrated photonics, the advantages of integrating photonics and electronics on the same platform have also led to the development of programmable photonic circuits, in which arrays of interferometers and resonators can be externally controlled and programmed [224]. By routing the optical paths on-chip, a single device can be programmed to perform multiple signal processing operations, including filtering, beamforming, and sensing [225, 226]. In the context of microwave photonics, reconfigurable filters performing bandpass and notch filtering operations have been demonstrated using

such strategies [227, 228].

4.5.1 Utilizing Brillouin scattering in microwave photonics

The seemingly endless appetite for high bandwidth, rapid reconfigurability, and high spectral resolution in modern communications is an impetus for new signal processing technologies that expand the capabilities offered by conventional RF circuits. One way to meet these challenges is to harness the complementary benefits offered by optical and acoustic wave signal processing technologies. Acoustic wave signal processing has long been a crucial part of modern RF systems [140, 229]. Signal operations requiring narrowband filtering and long delays invariably rely on electro-mechanical transduction to access slow-moving and long-lived acoustic waves, which are necessary to realize such operations within a small footprint [140, 230, 231].

When considering integrated photonic devices, accessing acoustic waves is typically implemented in piezoelectric material platforms using inter-digitated transducers (IDT) to electrically drive surface acoustic waves [232–235]. However, the lack of piezoelectric coupling in silicon makes the design of such silicon devices challenging, necessitating the integration of additional material layers [236], or utilizing thermoelastic effects [237].

Alternatively, Brillouin scattering —namely the coupling of light and acoustic phonons— enables direct access to the narrowband acoustic-wave properties, within the large-bandwidth optical domain [34, 35, 238]. Brillouin-based filters, sensors, and oscillators were first demonstrated using discrete-component optical fiber technologies [68, 69, 91, 129], and more recently, have been developed on-chip through the progress made in Brillouin-active waveguide design [35, 56, 144, 239]. The long-lived acoustic waves that mediate Brillouin interactions yield narrow spectral features, similar to the role played by acoustic waves in microwave filters [140, 229], with frequencies in the microwave range, and are further tunable through optical wavelength and device geometry [69, 100, 240]. These features make Brillouin-based devices a promising candidate for microwave-photonic applications such as filters [144, 241], delay lines [129, 135], oscillators [38, 242] and spectral analysis [243, 244]. Further, the recent demonstrations of Brillouin scattering in silicon [63–65] could facilitate low-cost,

high-volume production using CMOS-compatible fabrication techniques, and enable the integration of photonic and electronic components on the same platform [46, 47, 245].

When considering microwave-photonic filters, Brillouin-based technologies offer many advantages compared to other strategies, as the acoustic resonances are in the microwave range, and are directly accessible from the optical domain. Stimulated Brillouin scattering can result in the energy transfer from a strong pump tone to a Stokes tone, given that the phase-matching conditions are met, as was discussed in Chapter 2. The fact that the scattering occurs only around a narrow band —determined by the acoustic mode lifetime— enables the design of microwave-photonic filters with a spectral resolution of <10 MHz. Such filters were first demonstrated in optical fiber [69, 100, 248], where the long interaction length enables strong Brillouin scattering, and more recently in chip-integrated platforms, in which the tight confinement of the optical and acoustic fields to a small cross-section results in a strong interaction [144, 247, 249]. A recent review of the field of integrated Brillouin photonics is presented in Ref. [35], and a discussion of recent advances in Brillouin-based microwave-photonic subsystems, such as filters and phase shifters can be found in Ref. [250].

The underlying concept in the vast majority of Brillouin-based microwave-photonic filtering schemes includes modulation of the RF signal onto an optical carrier, resulting in optical sidebands. By introducing another strong optical tone to serve as a 'Brillouin pump' wave, stimulated scattering can be used to amplify or suppress a specific spectral region of an optical sideband. At the detector, the beat note of the optical carrier and the processed sidebands results in the suppression or enhancement of a narrow spectral band that is determined by the Brillouin bandwidth. Examples of such schemes are presented in Fig. 4.10. In these filters, backward Brillouin scattering is typically used, enabling the tuning of the filter center frequency and bandwidth by shifting the wavelength of the Brillouin pump and tailoring its spectral characteristics [246, 251]. It is important to note that the introduction of Brillouin gain also results in spontaneous scattering, adding excess noise within the Brillouin bandwidth. In the case of notch-filtering operations, the noise is in the stop-band of the filter and may not be a problem. However, in the case of bandpass filters, the Brillouin noise must be taken into account when analyzing the filter noise figure and

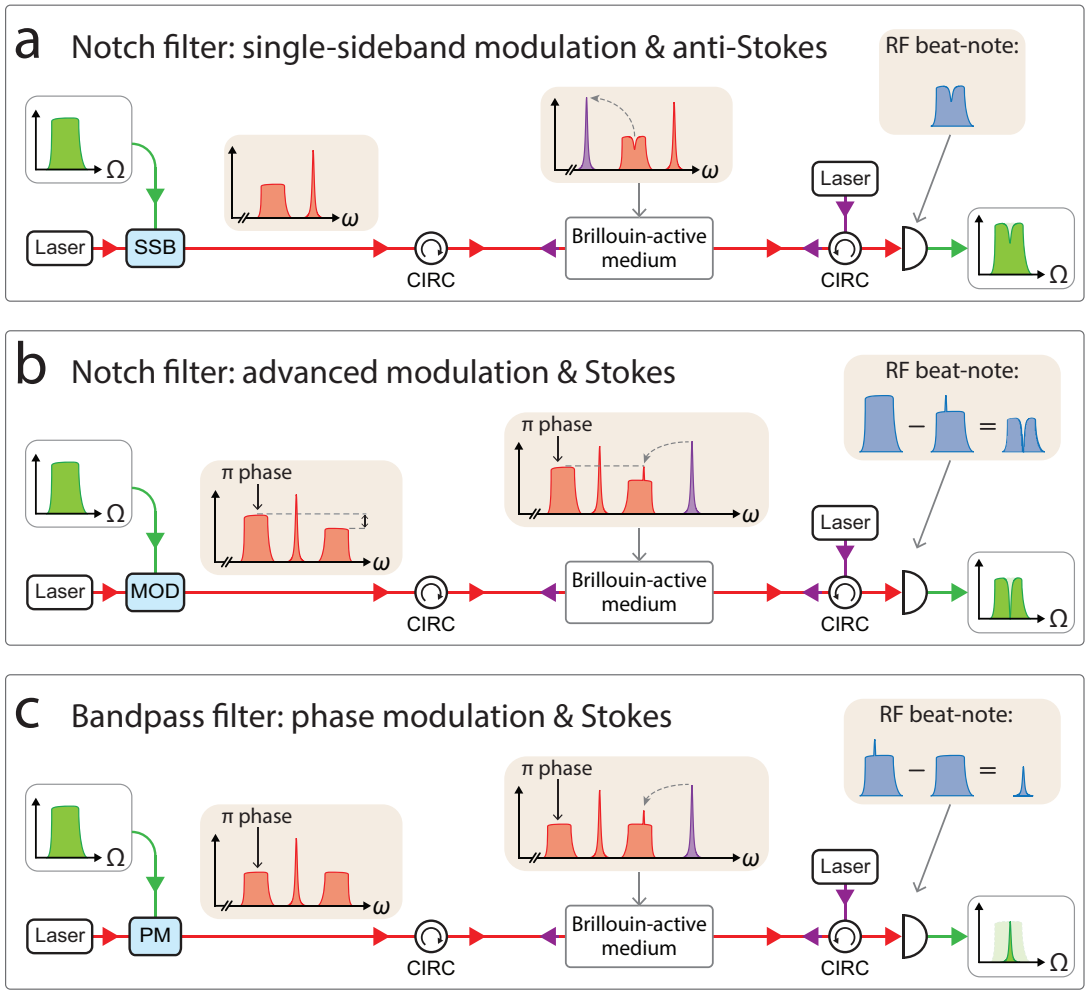

Figure 4.10: Three examples utilizing backward Brillouin scattering in a microwave-photonic filtering scheme: **(a)** The RF signal is modulated onto an optical carrier using a single-sideband modulator. By introducing a red-detuned Brillouin pump, an anti-Stokes Brillouin process scatters light out of the sideband around a narrow spectral band. At the detector, the RF beat note between the carrier and the sideband takes on the spectral shape of the sideband, showing a dip at the Brillouin frequency, essentially performing a notch-filtering operation [246]. **(b)** The RF signal is modulated onto the carrier using an advanced modulation technique such that the two sidebands around the optical carrier are out of phase, and are unequal in amplitude. By introducing a blue-detuned Brillouin pump, a narrow band of the weaker sideband is amplified, such that the beat notes produced by the two sidebands cancel out at the Brillouin frequency, resulting in strong suppression of the RF signal [142, 246]. **(c)** The RF signal is modulated onto the optical carrier using a phase modulator, resulting in sidebands equal in amplitude and out of phase. Using a Stokes process, a narrow spectral band within one of the sidebands is amplified. At the detector, the beat notes of the two sidebands with the carrier cancel each other out (as they are out of phase) except for the narrow band that was amplified, resulting in a bandpass frequency response [247]. CIRC: circulator, SSB: single-sideband modulator, MOD: advanced modulator, PM: phase modulator.

dynamic range, as it may determine the link noise floor.

An alternative approach to performing Brillouin-based microwave-photonic filtering utilizes the nonlocal optical response enabled by forward Brillouin scattering, which was presented in Chapter 3. Using a photonic-phononic emit-receive (PPER) scheme, a modulated microwave signal can be transduced between the optical and acoustic domains, taking on the spectral shape of the acoustic modes in the process. Additionally, this strategy enables the design of multi-pole filters with sharper frequency response, and higher out-of-band suppression [186]. Such filters have recently demonstrated ∼MHz wide filtering in a silicon platform [187] and can be utilized for both bandpass, as well as notch filtering operations, as will be discussed in the next chapters.

4.6 Conclusion

In this chapter, we have introduced the concept of an analog microwave-photonic link and derived some of the important figures of merit that characterize its performance. We have seen how the modulator parameters, namely the half-wave voltage, are crucial for the performance of a microwave-photonic link as it will determine the link gain and noise figure, and the development of high-performance modulators will directly enhance the capabilities of future microwave-photonic systems. Additionally, we have seen that in the case of an intensity modulator, the biasing point can play an important role in the dynamic range of the link and should be considered when analyzing a system. While we have examined an intensity modulator based link, a similar analysis can be done in the case of phase modulation [198], however, the analysis method and the figures of merit that were presented here are general.

We have discussed possible noise sources present in microwave-photonic systems, from both the optical and the microwave domains, as well as excess noise that accompanies optical amplification. While we have examined typical noise sources, an analysis should be performed for any system of interest, as additional system-specific noise can be present. For example, in many Brillouin-based microwave-photonic filters, scattering of light from

thermally excited acoustic waves is the dominant noise source, as we shall see in the next chapter.

Finally, we have discussed how additional functionalities can be implemented in the optical domain, processing the RF signals within the photonic link. The opportunities offered by the optical platform have enabled the development of multiple devices and systems that could be very challenging to achieve with typical microwave components. In this context, utilizing Brillouin scattering is a promising strategy, as the acoustic waves taking part in the process are in the microwave range, have sharp spectral features, and can be tailored to accommodate multiple applications such as filtering and sensing. Additionally, with the advances in integrated photonics, chip-scale systems including both optical and electrical circuits can be integrated within a small footprint.

Chapter 5

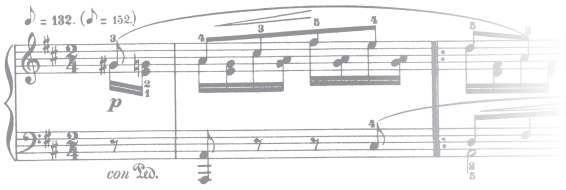

Using photonic-phononic emit-receive devices for microwave filtering

5.1 Introduction

Microwave filtering is a crucial component in radio-frequency systems, used to suppress unwanted interference and noise from signals of interest, as well as separating wideband signals into different spectral components [209]. Microwave photonic systems offer many capabilities that are difficult to achieve using typical RF components, such as wideband operation, large range tunability, and low loss. Furthermore, rapid progress in the field of silicon photonics has enabled the integration of high-speed modulators [50, 53], amplifiers [54,64,252] and detectors [49] with electronic and photonic circuitry [46,57,59,245], opening the door to miniaturization of radio-frequency photonic circuits having signal-processing performance that is competitive with established microwave technologies [45,214]. However, it remains challenging to implement narrowband filtering using all-optical techniques, as ultralow-loss waveguides are needed to store signals for long periods of time [253–255].

Narrowband filtering operations can also be realized by accessing long-lived acoustic phonons through stimulated Brillouin scattering (SBS), a nonlinear three-wave interaction that produces coupling between two optical waves and a GHz-frequency elastic wave. While

Brillouin interactions have been used to implement an array of filtering and delay operations [68, 135, 142, 144, 246, 249, 256], in this chapter we focus on bandpass filtering.

Brillouin-based bandpass filtering operations are conventionally achieved by making use of the narrowband optical amplification supplied by the stimulated Brillouin scattering process [141, 247]. While such amplification-based filtering strategies have been used to synthesize highly desirable response functions [142, 246, 256], the high levels of Brillouin gain necessary to implement these schemes also enhance unwanted noise sources that can degrade the performance of the RF link [144]. Other filtering schemes have demonstrated bandpass filtering by utilizing Brillouin-induced loss on both sides of the desired pass-band, achieving a lower noise figure at the expense of the filter bandwidth, out-of-band rejection, and stop-band range [144]. In many cases, the noise figure, dynamic range, and out-of-band rejection of such filters do not meet the increasingly stringent requirements of numerous applications [196, 257].

Alternatively, Brillouin interactions can produce narrowband filtering without using an amplification process by using a photonic-phononic emit-receive (PPER) device. Within a PPER device, the signal is converted to an acoustic wave that transfers information between two spatially distinct waveguides over a narrow spectral band, utilizing the nonlocal nature of forward Brillouin interactions, as was described in Chapter 3. This scheme yields a different design space from other Brillouin-based microwave-photonic filters, which may prove advantageous for many practical applications. For example, the spatial separation of the optical waves decouples the input signal propagating in the 'emit' waveguide from spontaneous scattering within the 'receive' waveguide, which is a fundamental noise source in Brillouin-based devices. In order to design and improve PPER-based filters, it is necessary to identify system parameters that will provide the greatest opportunity to achieve high performance.

In this chapter, we present a systematic analysis of a microwave-photonic filter designed around a PPER device and identify the key characteristics of the system that dictate the link performance. Building on the analysis that was presented in Chapter 4, our model of the system includes the effects of noise associated with the laser sources and optical detection,

as well as excess noise produced by spontaneous Brillouin scattering within the PPER device. Our analysis reveals that the spontaneous Brillouin scattering from thermally-populated acoustic phonons is the dominant noise source within the system over a range of operating conditions. Nevertheless, we show that this strategy holds the potential for high performance based on commercially available modulators and detector technologies. Furthermore, with the development of new electro-optic modulator technologies [53,200,258] and high power handling capabilities [254,259,260], we show how PPER based filters with a high RF-link gain (>45 dB), a large dynamic range (>110 dB $Hz^{2/3}$) and a low noise figure (<10 dB) are possible.

5.2 Operation scheme

Throughout this chapter, we consider the operation of a PPER device within a microwave-photonic link of the type seen in the block diagram of Fig. 5.1(a). This system is used to filter a wideband microwave signal that enters through the input RF port and exits at the output RF port after taking on the spectral characteristics produced by the acoustic transfer function of the device.

5.2.1 Dynamics of the optical and acoustic fields

We begin by describing how the input RF signal is shaped as it is converted between the microwave, optical, and acoustic domains when passing through the system depicted in Fig. 5.1(a). The incident RF signal, seen in panel (i), is encoded on an optical carrier produced by Laser A, panel (ii), using an intensity modulator (IM), as shown in panel (iii). The modulated field is injected into the 'emit' waveguide of the device, denoted waveguide A. As the laser field traverses the device, a portion of the signal wave is transduced as acoustic waves with microwave frequency over a narrow spectral band, determined by the device geometry [44, 161, 162], as seen in panel (iv). A second laser field produced by Laser B, seen in panel (v), is injected into a spatially separated 'receive' waveguide (waveguide B) that is used to sense the transduced acoustic wave. This spectrally-filtered replica of the

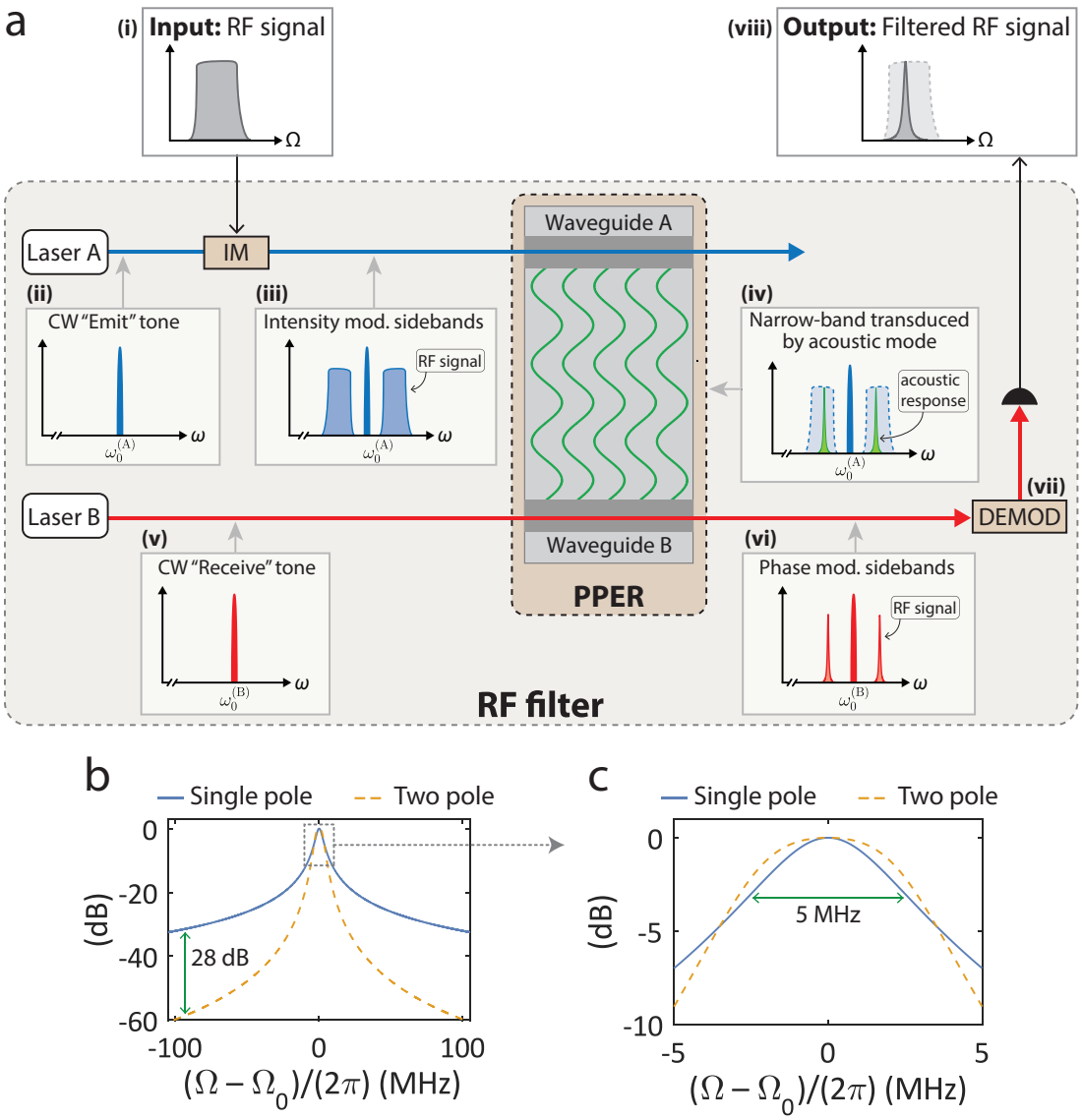

Figure 5.1: **(a)** Operation scheme of a PPER-based microwave-photonic filter. The RF input (i) is used to modulate a laser tone (ii), such that the RF information is in the optical sidebands (iii) and directed into waveguide A of the PPER. A narrowband acoustic field (iv) mediates the information to waveguide B and modulates a separate optical tone (v) in the form of phase modulation (vi). The phase modulation sidebands are demodulated (vii) and the filtered RF information is retrieved at the filter output (viii). IM: intensity modulator, DEMOD: phase demodulation. **(b)** Normalized frequency response of a PPER-based filter, for both a single- and two-pole design. The two-pole filter yields a sharper frequency roll-off, with an improvement of 28 dB out-of-band rejection at frequencies 100 MHz from the pass-band center. **(c)** Magnified view of the pass-band center shows a flat-top frequency response, closer to an ideal bandpass filter. The filter parameters used for the calculations are presented in Table 5.2. Adapted from Ref. [155] © 2020 IEEE.

microwave signal is encoded on the light propagating in the 'receive' waveguide as pure phase modulation, illustrated in panel (vi). The phase-modulated signal wave exiting the 'receive' waveguide is then passed through a demodulator (vii) that converts phase modulation into intensity modulation and is converted back to the microwave domain at the output (viii). The resulting output RF signal is filtered, taking on the shape of the acoustic transfer function. The PPER device can be designed to produce single-pole acoustic frequency response, as well as mutli-pole response (see Section 3.3), as shown in Figs. 5.1(b,c).

Next, we outline the analytical form of the signal wave as it traverses the microwave-photonic filter, which allows us to identify key parameters of the system. At the input port, an RF voltage with amplitude V_{in} and frequency Ω modulates an optical carrier with power $P^{(\text{A})}$ and optical frequency $\omega_0^{(\text{A})}$. The intensity-modulated optical field can be described by [198]

$$E_{\text{in}}^{(\text{A})}(t) = \sqrt{P^{(\text{A})}} e^{-i\omega_0^{(\text{A})} t} \left(\frac{i}{\sqrt{2}} + \frac{1}{\sqrt{2}} \exp\left[-i \left(\pi \frac{V_{\text{in}}}{V_\pi} \right) \sin(\Omega t) \right] \right), \tag{5.1}$$

where V_π is the half-wave voltage of the modulator, which is assumed to be biased at quadrature. Using the Jacobi-Anger expansion this can be expressed as

$$E_{\text{in}}^{(\text{A})}(t) = \sqrt{P^{(\text{A})}} e^{-i\omega_0^{(\text{A})} t} \left(\frac{i}{\sqrt{2}} + \frac{1}{\sqrt{2}} \sum_n J_n \left(\pi \frac{V_{\text{in}}}{V_\pi} \right) e^{-in\Omega t} \right), \tag{5.2}$$

where $J_n(\cdot)$ denotes an n^{th} order Bessel function. Since the field is comprised of an array of optical tones spaced apart by frequency Ω, we write the amplitude of each tone as $a_n^{(\text{A})}(z)$ and $a_n^{(\text{B})}(z)$, oscillating with frequency $\omega_0^{(\text{A})} + n\Omega$ and $\omega_0^{(\text{B})} + n\Omega$ for waveguides A and B, respectively, and normalized using $E_{\text{out}}(t) = \sqrt{\hbar\omega_0 v} \sum_n a_n e^{-i(\omega_0 + n\Omega)t}$, such that the optical power is given by $P^{(\text{A})} = \langle |E_{\text{out}}|^2 \rangle$ [172]. By collecting terms with similar time dependence, the intensity-modulated field at the input to waveguide A (Eq. (5.2)) can be expressed in terms of the field amplitudes

$$a_n^{(\text{A})}(0) = \begin{cases} a_0^{(\text{A})}(0) \left[\frac{i}{\sqrt{2}} + \frac{1}{\sqrt{2}} J_0 \left(\pi \frac{V_{\text{in}}}{V_\pi} \right) \right] & n = 0 \\ a_0^{(\text{A})}(0) \frac{1}{\sqrt{2}} J_n \left(\pi \frac{V_{\text{in}}}{V_\pi} \right) & n \neq 0. \end{cases} \tag{5.3}$$

This field drives a coherent acoustic mode through forward Brillouin scattering [44], with a displacement amplitude determined by the acoustic resonance properties, the Brillouin coupling rate, and the input optical power.

A second optical source is directed into waveguide B with optical power $P^{(\mathrm{B})}$ and optical frequency $\omega_0^{(\mathrm{B})}$, such that $E_{\mathrm{in}}^{(\mathrm{B})}(t) = \sqrt{P^{(\mathrm{B})}} e^{-i\omega_0^{(\mathrm{B})} t}$. In terms of field amplitudes, this is given by

$$a_0^{(\mathrm{B})}(0) = \sqrt{\frac{P^{(\mathrm{B})}}{\hbar\omega_0^{(\mathrm{B})} v}}, \qquad a_{n\neq 0}^{(\mathrm{B})}(0) = 0. \tag{5.4}$$

As we have seen in Chapter 3, the equations of motion of the optical and acoustic field amplitudes propagating through a PPER device (parallel to the z axis) can be described by

$$\begin{aligned} \frac{\partial}{\partial z} a_n^{(\mathrm{A})} &= -\frac{i}{v}\left(gba_{n-1}^{(\mathrm{A})} + g^* b^\dagger a_{n+1}^{(\mathrm{A})}\right), \\ \frac{\partial}{\partial z} a_n^{(\mathrm{B})} &= -\frac{i}{v}\left(gba_{n-1}^{(\mathrm{B})} + g^* b^\dagger a_{n+1}^{(\mathrm{B})}\right), \\ b &= -i\left(\frac{1}{i(\Omega_0 - \Omega) + \Gamma/2}\right) \sum_n g^* \left(a_n^{\dagger(\mathrm{A})} a_{n+1}^{(\mathrm{A})} + a_n^{\dagger(\mathrm{B})} a_{n+1}^{(\mathrm{B})}\right)\Big|_{z=0}, \end{aligned} \tag{5.5}$$

where b denotes the acoustic field, with a resonant frequency Ω_0 and dissipation rate Γ, g is the acoust-optic coupling rate, and v is the optical group velocity, which is assumed equal in both waveguides A and B. In our analysis, we neglect optical loss in the waveguides, and the fluctuations associated with the loss of the acoustic mode will be treated in Section 5.3.

Substituting the initial conditions from Eqs. (5.3) and (5.4) into Eq. (5.5) gives us the phonon field

$$b = -\left(\frac{1}{i(\Omega_0 - \Omega) + \Gamma/2}\right) g^* \left|a_0^{(\mathrm{A})}(0)\right|^2 J_1\left(\pi \frac{V_{\mathrm{in}}}{V_\pi}\right), \tag{5.6}$$

and using this expression together with Eq. (5.5) yields

$$\frac{\partial}{\partial z} a_n = \frac{i}{v} |\chi| \, |g|^2 \left|a_0^{(\mathrm{A})}(0)\right|^2 J_1\left(\pi \frac{V_{\mathrm{in}}}{V_\pi}\right)\left(a_{n-1} e^{i\phi} + a_{n+1} e^{-i\phi}\right), \tag{5.7}$$

for each of the waveguides A and B. Here, we have defined the frequency response $\chi = [i(\Omega_0 - \Omega) + \Gamma/2]^{-1}$, and $\phi = \arg(\chi)$. In terms of Brillouin gain and optical power, we can

express this as

$$\frac{\partial}{\partial z}a_n = i\frac{\Gamma}{4}\,|\chi|\,G_{\mathrm{B}}P^{(\mathrm{A})}J_1\left(\pi\frac{V_{\mathrm{in}}}{V_\pi}\right)\left(a_{n-1}e^{i\phi}+a_{n+1}e^{-i\phi}\right), \tag{5.8}$$

where $G_{\mathrm{B}} = 4|g|^2/(\hbar\omega v^2\Gamma)$ and $P = \hbar\omega v|a|^2$, as was discussed in Section 2.3.1.

The recurrence relation obtained in Eq. (5.8) is consistent with a modified Bessel function following $I_n' = \frac{1}{2}(I_{n-1}+I_{n+1})$, such that the optical fields can be written as a linear combination $a_n(z) = e^{i\phi n}\sum_m c_{n,m}I_m\left(i(\Gamma/2)|\chi|G_{\mathrm{B}}P^{(\mathrm{A})}J_1(\pi V_{\mathrm{in}}/V_\pi)z\right)$. We can find the coefficients $c_{n,m}$ by using the identity $I_m(0) = \delta_{m,0}$, such that $c_{n,m} = a_{n-m}(0)e^{-i\phi(n-m)}$, and by using the relation $I_m(x) = i^{-m}J_m(ix)$ we have

$$a_n(z) = \sum_m a_{n+m}(0)i^m J_m\left(\beta_{\mathrm{in}}\right)e^{-i\phi m}, \tag{5.9}$$

for both waveguides A and B, where we have defined $\beta_{\mathrm{in}} = (\Gamma/2)|\chi|G_{\mathrm{B}}P^{(\mathrm{A})}J_1(\pi V_{\mathrm{in}}/V_\pi)z$. We can now plug in the initial conditions from Eq. (5.4) to calculate the spatial evolution of the field amplitude in waveguide B

$$a_n^{(\mathrm{B})}(z) = a_0^{(\mathrm{B})}(0)\,(-i)^n\,J_{-n}\left(\beta_{\mathrm{in}}\right)e^{i\phi n}. \tag{5.10}$$

Fig. 5.2 shows the power of the different optical tones in the two waveguides as a function of β_{in}, following Eq. (5.9) and the initial conditions (Eqs. (5.3) and (5.4)), where we can see the power oscillating in the different tones, as described by the Bessel functions.

Summing all the mode amplitudes in waveguide B,

$$E_{\mathrm{out}}^{(\mathrm{B})}(t) = \sqrt{\hbar\omega_0^{(\mathrm{B})}v}\sum_n a_n^{(\mathrm{B})}e^{-i\left(\omega_0^{(\mathrm{B})}+n\Omega\right)t}, \tag{5.11}$$

and using the Jacobi-Anger expansion $\sum_n i^n J_n(z)e^{ixn} = e^{iz\cos x}$ we can rewrite the field at the output

$$E_{\mathrm{out}}^{(\mathrm{B})}(t) = \sqrt{P^{(\mathrm{B})}}\;e^{-i\omega_0^{(\mathrm{B})}t}\;\exp\Big[i\;\beta_{\mathrm{in}}\cos\left(\Omega t-\phi\right)\Big], \tag{5.12}$$

showing a pure phase modulation of the optical tone. The modulation index is determined

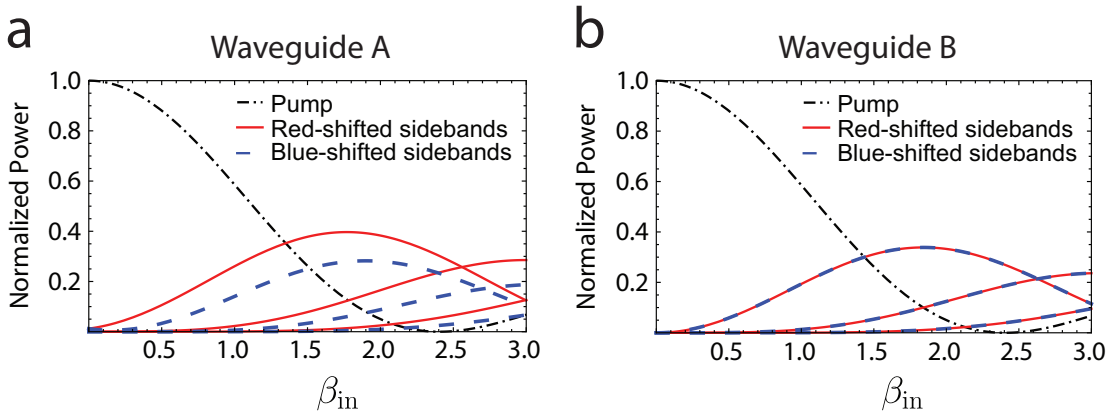

Figure 5.2: Normalized power of the optical tones, given an intensity-modulated input into waveguide A, and a single tone input into waveguide B. In each waveguide, the pump tone is denoted in black, Stokes (red-shifted) tones in red, and anti-Stokes (blue-shifted) tones are shown in blue. Adapted from Ref. [155] © 2020 IEEE.

by the system and device parameters, given by

$$\beta_{\text{in}} = \frac{\Gamma}{2} |\chi(\Omega)| J_1 \left(\pi \frac{V_{\text{in}}}{V_\pi} \right) G_{\text{B}} P^{(\text{A})} L, \tag{5.13}$$

where Γ is the acoustic dissipation rate, $\chi(\Omega)$ is the frequency response of the acoustic resonance, and $J_1(\cdot)$ denotes a Bessel function of the first order, describing the power in the first sidebands of the intensity-modulated input field. The Brillouin gain G_{B} is a metric for the strength of the light-sound interaction, and L the length of the region where the Brillouin coupling takes place.

The same analysis can be repeated for PPER devices utilizing two coupled acoustic modes, as was discussed in Chapter 3. In this case, the frequency response follows a two-pole lineshape $\chi^{(2\text{ pole})} = ([i(\Omega_0 - \mu - \Omega) + \Gamma/2]^{-1} - [i(\Omega_0 + \mu - \Omega) + \Gamma/2]^{-1})/2$, where μ denotes the coupling rate between the two acoustic modes taking part in the Brillouin process. This scheme results in a response with sharp frequency roll-off, as shown in Figs. 5.1(b,c), and strong out-of-band suppression. The ability to achieve two-pole Brillouin-based filters is unique to the PPER scheme, and could also enable higher-order multi-pole filtering (see Section 3.3.2).

We can also analyze the field at the output of waveguide A by substituting in the input

mode amplitudes from Eq. (5.3) into Eq. (5.9), giving us

$$a_n^{(\mathrm{A})}(z) = a_0^{(\mathrm{A})}(0) \sum_m i^m J_m\left(\beta_{\mathrm{in}}\right) e^{-i\phi m} \left[\frac{1}{\sqrt{2}} J_{n+m}\left(\pi \frac{V_{\mathrm{in}}}{V_\pi}\right) + \frac{i}{\sqrt{2}} \delta_{n+m,0}\right], \tag{5.14}$$

where $\delta_{i,j}$ denotes the Kronecker delta. Summing all the mode amplitudes (see Eq. (5.11)), and using a similar derivation to the one we had for waveguide B, we arrive at

$$E_{\mathrm{out}}^{(\mathrm{A})}(t) = \underbrace{\sqrt{P^{(\mathrm{A})}}\; e^{-i\omega_0^{(\mathrm{A})} t} \sum_n e^{-in\Omega t} \left[\frac{1}{\sqrt{2}} J_n\left(\pi \frac{V_{\mathrm{in}}}{V_\pi}\right) + \frac{i}{\sqrt{2}} \delta_{n,0}\right]}_{E_{\mathrm{in}}^{(\mathrm{A})}(t)} \exp\left[i\ \beta_{\mathrm{in}} \cos\left(\Omega t - \phi\right)\right], \tag{5.15}$$

showing that the input (Eq. (5.2)) undergoes pure phase-modulation. Calculating the beatnote at frequency Ω reveals that it is unchanged as the field propagates in waveguide A, i.e., $\sum_n {a_n^{(\mathrm{A})}}^\dagger(z)\ a_{n+1}^{(\mathrm{A})}(z) = |a_0^{(\mathrm{A})}(0)|^2 J_1(\pi V_{\mathrm{in}}/V_\pi)$.

The forward Brillouin dynamics utilized in these devices have interesting advantages when considering noise and scalability. The acousto-optic interaction results in phase modulation, such that the intensity envelope of the light propagating through the system remains unchanged, regardless of the strength of the nonlinear interaction. Similarly, the scattering produced by thermally-excited phonons results in phase fluctuations alone, which do not affect the intensity envelope and the driven coherent phonon field. This results in no degradation of information encoded in the form of optical intensity modulation when the light field propagates through the device [187]. These properties can enable cascading of multiple devices in series without losing signal fidelity, further broadening their technological impact.

5.2.2 Signal demodulation using balanced detection

Next, we turn to analyze the conversion of the signal from the optical domain back to the microwave domain. As we have just seen, the PPER output encodes the signal in the form of phase modulation, and since a photodetector is not sensitive to the phase of light, a phase demodulation scheme needs to be used to retrieve the RF signal. Numerous schemes can be used for demodulation [198, 261, 262], and we will start by considering the use of

an unbalanced Mach-Zehnder interferometer (MZI), illustrated schematically in Fig. 5.3(a). The MZI is composed of a directional coupler, a time delay τ on one of the two interferometer arms, and a second coupler, and is followed by a pair of balanced photodetectors. This can be described in terms of matrix operations on the input field amplitudes [198]

$$\begin{pmatrix} E_1(t) \\ E_2(t) \end{pmatrix} = \frac{1}{2} \begin{pmatrix} 1 & i \\ i & 1 \end{pmatrix} \begin{pmatrix} \hat{\Gamma}(\tau) & 0 \\ 0 & 1 \end{pmatrix} \begin{pmatrix} 1 & i \\ i & 1 \end{pmatrix} \begin{pmatrix} E_{\text{out}}(t) \\ 0 \end{pmatrix}, \tag{5.16}$$

where we assume ideal lossless couplers with an equal splitting ratio (50:50), and $\hat{\Gamma}(\tau)$ is a time-delay operator, such that $\hat{\Gamma}(\tau) E(t) = E(t-\tau)$. The input to the MZI is the field from the output of waveguide B, denoted $E_{\text{out}}(t)$ and given in Eq. (5.12), such that at the output of the MZI we have

$$E_1 = \frac{1}{2}\Big(E_{\text{out}}(t-\tau) - E_{\text{out}}(t)\Big), \qquad E_2 = \frac{i}{2}\Big(E_{\text{out}}(t-\tau) + E_{\text{out}}(t)\Big). \tag{5.17}$$

Each of the two MZI output fields is directed to photodetector, as illustrated in Fig. 5.3(a), and the photocurrent generated in each of the detectors $I(t) = \eta|E(t)|^2$ is subtracted $I_{\text{bal}}(t) = \eta\left(|E_2(t)|^2 - |E_1(t)|^2\right)$, where we assume the two detectors have equal responsivities

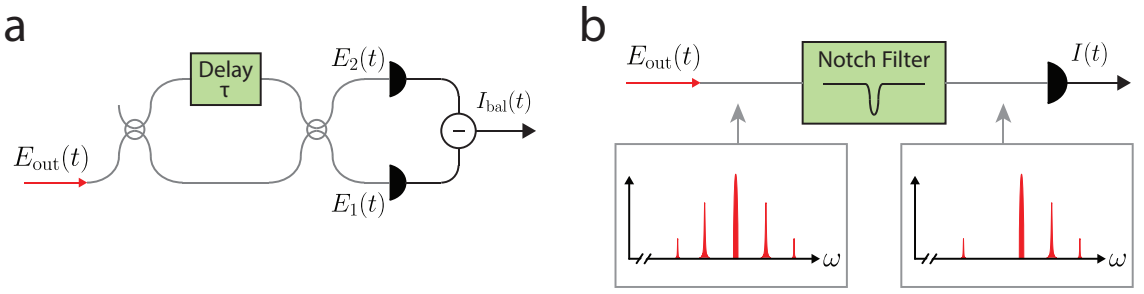

Figure 5.3: **(a)** An unbalanced MZI splits the input field and adds a phase shift corresponding to a time delay τ to one of the two arms. The two interferometer arms are then combined using another coupler and detected using two photodetectors. The photocurrent of the detectors is subtracted from each other for balanced detection. **(b)** An alternative phase demodulation scheme, using a narrowband notch filter to eliminate one of the optical sidebands. Adapted from Ref. [155] © 2020 IEEE.

η. Using Eq. (5.17), this gives us the photocurrent

$$I_{\text{bal}}(t) = \frac{1}{2}\eta\Big(E^*_{\text{out}}(t-\tau)E_{\text{out}}(t) + E_{\text{out}}(t-\tau)E^*_{\text{out}}(t)\Big) = \eta\,\text{Re}\left(E^*_{\text{out}}(t-\tau)E_{\text{out}}(t)\right), \quad (5.18)$$

and plugging in the output field from the device, (Eq. (5.12)) yields

$$I_{\text{bal}}(t) = \eta P^{(\text{B})}\,\text{Re}\left(e^{-i\omega_0\tau}\exp\left[i\;\beta_{\text{in}}\Big(\cos\left(\Omega t-\phi\right) - \cos\left(\Omega(t-\tau)-\phi\right)\Big)\right]\right). \quad (5.19)$$

Using trigonometric and Bessel-function identities, we can rewrite the expression above as

$$I_{\text{bal}}(t) = \eta P^{(\text{B})}\,\text{Re}\left(e^{-i\omega_0\tau}\sum_n J_n\Big(2\beta_{\text{in}}\sin\left(\Omega\tau/2\right)\Big)e^{-in(\Omega t-\Omega\tau/2-\phi)}\right), \quad (5.20)$$

which is the general form for the photocurrent after demodulation.

Next, we analyze the photocurrent component oscillating at frequency Ω, as this is the frequency of the signal at the input to the system. We isolate this frequency component by keeping only the $n = \pm 1$ terms in the sum from Eq. (5.20), and using the Bessel function property $J_1(x) = -J_{-1}(x)$, we have

$$\begin{aligned} I^{\Omega}_{\text{bal}}(t) = \eta P^{(\text{B})} J_1\Big(2\beta_{\text{in}}\sin\left(\Omega\tau/2\right)\Big) \\ \times\Big(\cos\left(\Omega t-\Omega\tau/2-\phi+\omega_0\tau\right) - \cos\left(\Omega t-\Omega\tau/2-\phi-\omega_0\tau\right)\Big), \end{aligned} \quad (5.21)$$

which can also be expressed as

$$I^{\Omega}_{\text{bal}}(t) = -2\eta P^{(\text{B})} J_1\Big(2\beta_{\text{in}}\sin\left(\Omega\tau/2\right)\Big)\sin\left(\Omega t-\Omega\tau/2-\phi\right)\sin\left(\omega_0\tau\right). \quad (5.22)$$

We can see from this expression that the MZI time-delay τ needs to be chosen with respect to both the optical frequency ω_0 as well as the RF input frequency Ω. For the rest of our analysis, we will assume that $\omega_0\tau$ is set to maximize the photocurrent, such that $\omega_0\tau = \pi(m+1/2)$ (where m is an integer).

Finally, we can calculate the output RF power at frequency Ω

$$P_{\text{out}}^{\text{RF}}(\Omega) = 2\left[\eta P^{(\text{B})} J_1\left(\Gamma\left|\chi(\Omega)\right| J_1\left(\pi\frac{V_{\text{in}}}{V_\pi}\right) G_{\text{B}} P^{(\text{A})} L \sin\left(\Omega\tau/2\right)\right)\right]^2 R_{\text{out}}|H_{\text{pd}}|^2, \quad (5.23)$$

where we have used $P_{\text{out}}^{\text{RF}} = \langle I_\Omega^2\rangle R_{\text{out}}|H_{\text{pd}}|^2$, and R_{out}, H_{pd} denote the output impedance and the photodiode circuit efficiency, respectively, and we have expressed β_{in} explicitly using Eq. (5.12). We see that the demodulated RF signal at the output of the microwave-photonic link is determined by the optical powers, the Brillouin-active device length, and the properties of the intensity modulator and the detector. We also notice that the frequency dependence of the output RF signal is determined by the acoustic frequency response $\chi(\Omega)$, as well as the time-delay τ.

5.3 Possible noise sources

Now we turn to examine possible noise sources in the PPER-based microwave-photonic link, which ill be necessary for our analysis of its performance metrics. Since our filtering scheme utilizes the optical, acoustic, and microwave domains to implement filtering, a full description of the link properties requires us to consider noise sources from all these different domains. Following the standard convention in microwave photonics [198], we express the noise power per unit frequency as

$$\begin{aligned} N_{\text{out}} = k_{\text{B}}T + g k_{\text{B}}T + 2q\eta P^{(\text{B})} R_{\text{out}}|H_{\text{pd}}|^2 \\ + \left(\eta P^{(\text{B})}\right)^2 R_{\text{out}}|H_{\text{pd}}|^2\Big(\text{RIN} + \text{RIN}_{\text{phase}} + \text{RIN}_{\text{B}}\Big). \end{aligned} \quad (5.24)$$

The first term in Eq. (5.24) is the RF thermal noise ('Johnson–Nyquist' noise) at the detector, where T denotes the temperature and k_{B} is the Boltzmann constant. The second term is the RF thermal noise at the link input after propagating through the filter, with an RF link gain g (g will be analyzed in the next section). The third term is due to shot noise, where q is the electron charge and scales linearly with the optical power incident on the detector. The first relative intensity noise (RIN) term accounts for intensity fluctuations

from the optical sources, which are usually negligible at frequencies over a few GHz. The next term $\mathrm{RIN}_{\mathrm{phase}}$ accounts for the demodulation at the device output, turning phase fluctuations into intensity, such that phase noise from the laser source is converted to intensity noise. Assuming the phase noise has a Lorentzian spectral lineshape with full-width at half-maximum γ, it has been shown that detection using an MZI will result in a noise power spectral density given by [198, 263, 264]

$$\mathrm{RIN}_{\mathrm{phase}}^{\mathrm{bal}} = e^{-\gamma\tau}\left(\frac{2\gamma}{\gamma^2+\Omega^2}\right)\Big(\cosh(\gamma\tau)-\cos(\Omega\tau)\Big). \tag{5.25}$$

The last term in Eq. (5.24) is the result of the thermal occupation of the acoustic modes participating in the Brillouin scattering process. At non-zero temperature, thermally driven fluctuations will add phase noise to the optical field in the 'receive' waveguide, which can also be described in terms of spontaneous forward Brillouin scattering [157, 172]. More specifically, the thermally occupied phonon population results in light scattering to sidebands spaced Ω_0 around the optical frequency ω_0 [172]. Assuming a single-tone input into the waveguide, the optical field at the output can be described by

$$E_{\mathrm{out}}(t) = \sqrt{\hbar\omega_0 v}\left(a_{-1}e^{-i(\omega_0-\Omega_0)t} + a_0 e^{-i\omega_0 t} + a_1 e^{-i(\omega_0+\Omega_0)t}\right), \tag{5.26}$$

where the amplitudes a_{-1} and a_1 are the sidebands generated by the spontaneous scattering. The sidebands' field amplitudes are given by [172, 175, 195]

$$\begin{aligned} a_{-1}(z,\tau) &= -i\frac{g^*}{v}a_0\int_0^\tau d\tau'\int_0^z dz'\eta^\dagger(z',\tau')e^{-\frac{\Gamma}{2}(\tau-\tau')},\\ a_1(z,\tau) &= -i\frac{g}{v}a_0\int_0^\tau d\tau'\int_0^z dz'\eta(z',\tau')e^{-\frac{\Gamma}{2}(\tau-\tau')}, \end{aligned} \tag{5.27}$$

where $\eta(z,t)$ is the Langevin force corresponding to the phonon dissipation, such that $\langle\eta(z,t)\rangle = 0$ and $\langle\eta^\dagger(z,t)\eta(z',t')\rangle = n_{\mathrm{th}}\Gamma\delta(z-z')\delta(t-t')$, where n_{th} is the mean thermal phonon occupation number. At room temperature, when $n_{\mathrm{th}} \gg 1$, this thermal occupation can be approximated using $n_{\mathrm{th}} \approx (k_{\mathrm{B}}T)/(\hbar\Omega_0)$, where T denotes the temperature, and k_{B} is the Boltzmann constant.

Spontaneous Brillouin scattering taking place in the 'receive' waveguide (waveguide B) will be detected at the link output, and contribute to the noise of the microwave-photonic link. For the case of the MZI balanced detection scheme described here, we can calculate the photocurrent generated by this noise source $I_{\mathrm{N}}(t)$ by substituting Eqs. (5.26) and (5.27) into Eq. (5.18), and using the Wiener-Khinchin theorem to find the power spectral density

$$S_{\mathrm{N}}^{\mathrm{RF}}(\Omega) = R_{\mathrm{out}}|H_{\mathrm{pd}}|^2 \int dt' e^{-i\Omega t'} \langle I_{\mathrm{N}}(t+t') I_{\mathrm{N}}(t) \rangle. \tag{5.28}$$

Keeping terms oscillating around frequency Ω_0 yields

$$\begin{aligned} S_{\mathrm{N}_{\mathrm{bal}}}^{\mathrm{RF}}(\Omega) = 4\eta^2 \frac{\omega_0}{\Omega_0} G_{\mathrm{B}} {P^{(\mathrm{B})}}^2 L k_{\mathrm{B}} T R_{\mathrm{out}} |H_{\mathrm{pd}}|^2 \\ \times \left[\sin^2 (\Omega\tau/2) \left(\frac{(\Gamma/2)^2}{(\Gamma/2)^2 + (\Omega - \Omega_0)^2} + \frac{(\Gamma/2)^2}{(\Gamma/2)^2 + (\Omega + \Omega_0)^2} \right) \right. \\ \left. - \frac{\Omega_0 \Gamma e^{-(\Gamma/2)\tau} \left((\Gamma/2)^2 - \Omega^2 + \Omega_0^2 \right) \sin(\Omega_0 \tau)}{\left[(\Gamma/2)^2 + (\Omega - \Omega_0)^2 \right] \left[(\Gamma/2)^2 + (\Omega + \Omega_0)^2 \right]} \right], \end{aligned} \tag{5.29}$$

where we have used the fact that the MZI is operating at quadrature ($e^{-2i\omega_0\tau} = -1$).

As we will see in the next section, maximum link gain is achieved when the time delay is set such that $\Omega_0\tau/2 = \pi(m+1/2)$, and will be the operating point of the microwave-photonic link. At this setting, the spectral density will be

$$\begin{aligned} S_{\mathrm{N}_{\mathrm{bal}}}^{\mathrm{RF}}(\Omega) = 4\eta^2 \frac{\omega_0}{\Omega_0} G_{\mathrm{B}} {P^{(\mathrm{B})}}^2 L k_{\mathrm{B}} T R_{\mathrm{out}} |H_{\mathrm{pd}}|^2 \sin^2(\Omega\tau/2) \\ \times \left[\frac{(\Gamma/2)^2}{(\Gamma/2)^2 + (\Omega - \Omega_0)^2} + \frac{(\Gamma/2)^2}{(\Gamma/2)^2 + (\Omega + \Omega_0)^2} \right]. \end{aligned} \tag{5.30}$$

Integrating a narrow RF bandwidth B_{RF} centered around Ω, will yield the noise power

$$P_{\mathrm{N\,bal}} = 8\eta^2 \frac{\omega_0}{\Omega_0} G_{\mathrm{B}} {P^{(\mathrm{B})}}^2 L k_{\mathrm{B}} T B_{\mathrm{RF}} R_{\mathrm{out}} |H_{\mathrm{pd}}|^2 \sin^2(\Omega\tau/2) \left(\frac{\Gamma}{2} \right)^2 |\chi_N(\Omega)|^2, \tag{5.31}$$

where B_{RF} is in units of Hz, and we have denoted the frequency spectrum of the spontaneous

Brillouin scattering as $\chi_N(\Omega)$. In terms of RIN, this can by expressed by

$$\mathrm{RIN}_{\mathrm{B}}^{\mathrm{bal}} = 8\frac{\omega_0}{\Omega_0} G_{\mathrm{B}} L k_{\mathrm{B}} T \sin^2(\Omega\tau/2) \left(\frac{\Gamma}{2}\right)^2 |\chi_N(\Omega)|^2 , \tag{5.32}$$

to be consistent with Eq. (5.24).

For a sigle-pole filter, utilizing a single acoustic mode in the PPER, the spontaneous scattering follows a Lorentzian lineshape $|\chi_N|^2 = \left[(\Omega-\Omega_0)^2 + (\Gamma/2)^2\right]^{-1}$. When analyzing high-order filters, all of the acoustic modes participating in the filtering process contribute to the spontaneous scattering, as was discussed in Chapter 3. In the case of two identical acoustic modes with a coupling rate μ, this will yield $|\chi_N^{(2\text{ pole})}|^2 = ([(\Omega-\Omega_0+\mu)^2 + (\Gamma/2)^2]^{-1} + [(\Omega-\Omega_0-\mu)^2 + (\Gamma/2)^2]^{-1})/2$, which exhibits a modified frequency response as a result of the two resonances, but decays as a single-pole Lorentzian away from the pass-band (see Section 3.3.3).

While spontaneous Brillouin scattering does occur in the 'emit' waveguide as well, it does not degrade the signal-to-noise of the system. This is because only intensity-modulated light fields contribute to the coherent transduction of information, while the spontaneous scattering results only in phase modulation, independent of the driving field in the 'emit' waveguide.

Considering typical experimental conditions, the dominant contribution to the microwave-photonic link noise floor is from spontaneous Brillouin scattering, as can be seen in Fig. 5.4(c), and consistent with experimental demonstrations [187]. Importantly, this noise is centered around the center frequency and does not contribute excess noise out-of-band. For the rest of our analysis, we will assume that Brillouin noise is the dominant noise source in the system, such that it solely determines the noise floor measured at the output of the link.

5.4 Microwave-photonic link performance

With a description of the output signal and noise from the PPER-based filter in hand, we can now proceed to analyze the link performance of the system, examining its gain, noise figure,

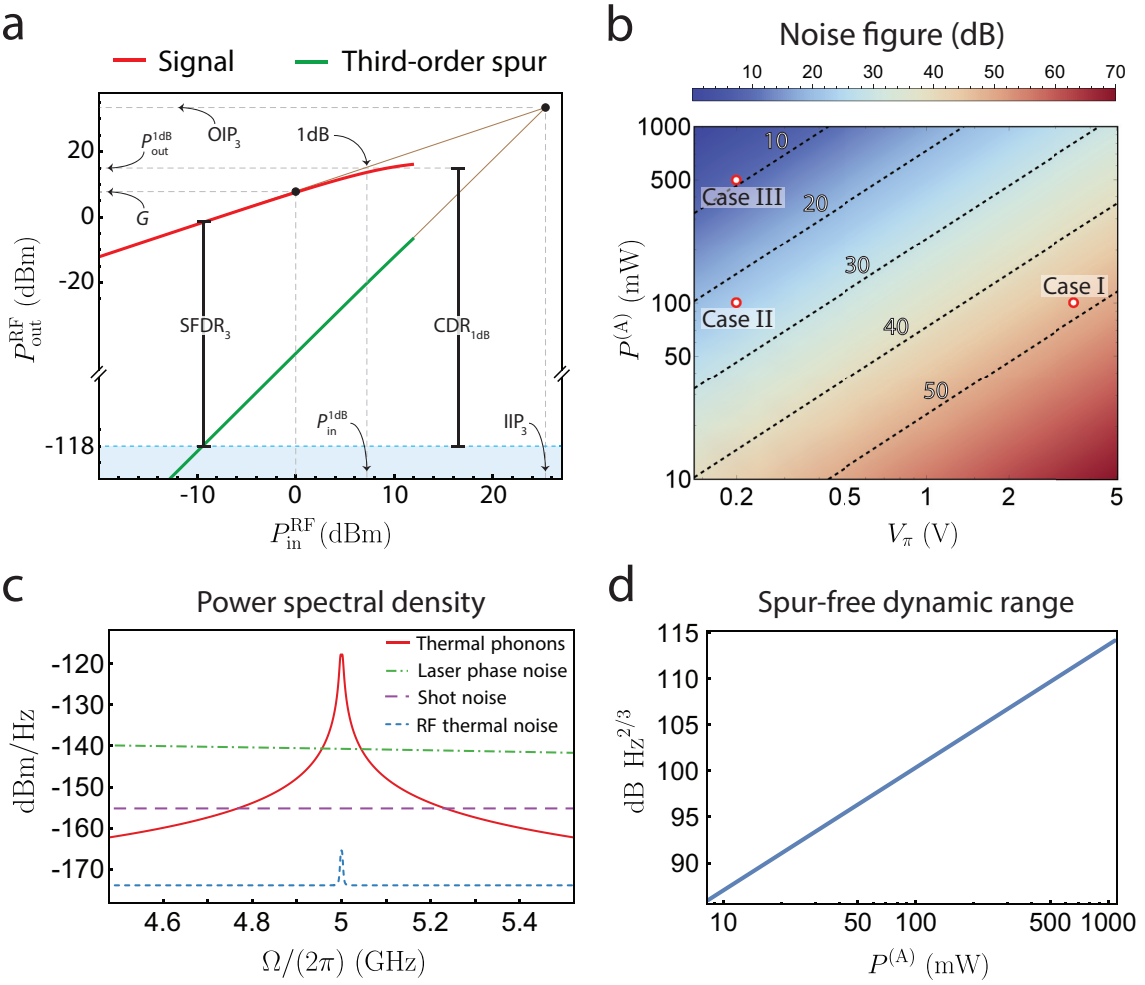

Figure 5.4: **(a)** Calculated RF output power as a function of RF input power using the parameters from Table 5.2, illustrating the signal (red), the third-order spur (green), and the link noise-floor (blue). **(b)** Calculated noise figure of a PPER-based microwave-photonic link, as a function of optical power in waveguide A and the intensity modulator V_π, using the parameters given in Table 5.2. The three cases examined in Table 5.1 are shown here for reference. **(c)** Calculated spectral density of the noise sources in a PPER-based microwave-photonic link, using the device parameters given in Table 5.2. **(d)** Calculated SFDR_3 as a function of optical power in waveguide A, using $V_\pi = 3.5$ V, and the parameters detailed in Table 5.2. Adapted from Ref. [155] © 2020 IEEE.

and dynamic range, as were discussed in Chapter 4. The analysis of these performance metrics will be important for practical deployment of such filters, and interfacing them with other components and systems.

5.4.1 Link gain

We start by calculating the link gain, describing the linear relation between the input and output RF power. First, we take the small-signal limit ($V_{\text{in}} \ll V_\pi$), and linearize the Bessel functions in Eq. (5.23) ($J_1(x) \approx x/2$), leaving us with

$$P_{\text{out}}^{\text{RF}}(\Omega) = \frac{1}{2} R_{\text{out}} |H_{\text{pd}}|^2 \left[\eta P^{(\text{B})} \frac{\Gamma}{2} |\chi| \frac{\pi V_{\text{in}}}{V_\pi} G_{\text{B}} P^{(\text{A})} L \sin(\Omega\tau/2) \right]^2 . \tag{5.33}$$

Expressing the input signal in terms of power, i.e., $P_{\text{in}}^{\text{RF}} = V_{\text{in}}^2/(2R_{\text{in}})$, where R_{in} is the input impedance of the intensity modulator [198], we arrive at the linear link gain

$$g = \frac{P_{\text{out}}^{\text{RF}}}{P_{\text{in}}^{\text{RF}}} = R_{\text{in}} R_{\text{out}} |H_{\text{pd}}|^2 \left[\eta P^{(\text{B})} \frac{\Gamma}{2} |\chi(\Omega)| \frac{\pi}{V_\pi} G_{\text{B}} P^{(\text{A})} L \sin(\Omega\tau/2) \right]^2 , \tag{5.34}$$

showing that the link gain improves quadratically with the optical powers, Brillouin gain, and device length. We can also see that for maximum signal output, we need the time-delay of the MZI that is used for phase demodulation to satisfy $\Omega_0\tau/2 = \pi(m + 1/2)$. Together with the expression for the output noise (Eq. (5.32)), we can look at the signal-to-noise ratio (SNR) for a given RF input signal

$$\text{SNR} = \frac{P_{\text{out}}^{\text{RF}}}{P_{\text{N}}} = \frac{1}{8} P_{\text{in}}^{\text{RF}} \left(\frac{\pi}{V_\pi} \right)^2 \frac{\Omega_0}{\omega_0^{(\text{B})}} \frac{G_{\text{B}} \left(P^{(\text{A})} \right)^2 L}{k_{\text{B}} T B_{\text{RF}}} \frac{|\chi(\Omega)|^2}{|\chi_N(\Omega)|^2} R_{\text{in}}, \tag{5.35}$$

which can be improved by using a low V_π modulator, as well as high optical power and long devices.

5.4.2 Linear dynamic range

The link gain we have derived is valid at the small-signal limit, however, the output power can deviate from this linear function at higher input powers. To assess the nonlinearity of

the link, we first calculate the 1 dB compression point, i.e., the RF input power at which the output power is 1 dB lower than the linear response predicts. Setting the ratio between Eqs. (5.23) and (5.34) to 1 dB (i.e., $10^{0.1}$), we can solve numerically to find the input RF power

$$P_{\text{in}}^{\text{1dB}} = \frac{0.183}{R_{\text{in}}} \left[\frac{V_\pi}{\Gamma \left|\chi(\Omega)\right| G_{\text{B}} P^{(\text{A})} L \sin\left(\Omega\tau/2\right)} \right]^2. \tag{5.36}$$

The linear dynamic range, defined as $\text{CDR}_{\text{1dB}} = gP_{\text{in}}^{\text{1dB}}/P_{\text{N}}$ (see Fig. 5.4(a)), is given by

$$\text{CDR}_{\text{1dB}} = 0.226 \frac{\Omega_0}{\omega_0^{(\text{B})}} \frac{1}{k_{\text{B}} T B_{\text{RF}}} \frac{1}{\Gamma^2 \left|\chi(\Omega)\right|^2 G_{\text{B}} L \sin^2\left(\Omega\tau/2\right)}, \tag{5.37}$$

where the noise power (P_{N}) is assumed to be Brillouin-noise dominated, (see Eq. (5.31)). In this calculation, we have assumed that the compression is a result of the intensity modulator at the link input, consistent with the parameters of recent demonstrations [187]. A similar expression can be derived for the distortion resulting from the Brillouin process in the case of very strong nonlinear optical interactions.

5.4.3 Spur-free dynamic range

As we have discussed in Chapter 4, another important measure of the performance of a microwave system is the third-order intercept point, describing the power at which the linear signal is equal to the third-order spurious tone [198], illustrated in Fig. 5.4(a). In the PPER-based system we are analyzing here, the spurious tone is a result of the intensity modulator not having a perfectly linear response, producing unwanted spurious signals, as was discussed in Section 4.4.3.

To quantify this distortion, we assume that the input RF signal is oscillating at frequency $\Omega/3$ and analyze the propagation of the third-order modulation through the device. In this case, Eq. (5.13) transforms into $\beta_{\text{in}}^{3\Omega/3} = (\Gamma/2) \left|\chi(\Omega)\right| J_3\left(\pi V_{\text{in}}/V_\pi\right) G_{\text{B}} P_0^{(\text{A})} L$, where the Bessel function is of third order, as we are interested in the third harmonic. Substituting into Eq. (5.23) and expanding the Bessel functions to the first non-vanishing order ($J_3(x) \approx$

$x^3/48$) we have

$$P_{\text{out}}^{3\Omega/3} = \frac{1}{144}\left(P_{\text{in}}^{\text{RF}}\right)^3 R_{\text{in}}^3 R_{\text{out}} |H_{\text{pd}}|^2 \left[\eta P^{(\text{B})} \frac{\Gamma}{2} |\chi(\Omega)| \left(\frac{\pi}{V_\pi}\right)^3 G_{\text{B}} P^{(\text{A})} L \sin\left(\Omega\tau/2\right)\right]^2 . \quad (5.38)$$

To find the third-order intercept point, we equate Eqs. (5.34) and (5.38), and solve for the input RF power, giving the input intercept point (IIP_3)

$$\text{IIP}_3 = 12\frac{V_\pi^2}{\pi^2 R_{\text{in}}}, \quad (5.39)$$

and plugging back into Eq. (5.34), we have the output intercept point (OIP_3)

$$\text{OIP}_3 = 12\left[\eta P^{(\text{B})} \frac{\Gamma}{2} |\chi(\Omega)| \, G_{\text{B}} P^{(\text{A})} L \sin\left(\Omega\tau/2\right)\right]^2 R_{\text{out}} |H_{\text{pd}}|^2. \quad (5.40)$$

We can now calculate the spur-free dynamic range, describing the range of RF powers between the minimum detectable signal up to the appearance of the third-order spur (see Fig. 5.4(a)), given by $\text{SFDR}_3 = (\text{OIP}_3/P_{\text{N}})^{2/3}$. Using Eqs. (5.40) and (5.31) we have

$$\text{SFDR}_3 = \left[\frac{3}{2}\frac{\Omega_0}{\omega_0^{(\text{B})}} \frac{G_{\text{B}}\left(P^{(\text{A})}\right)^2 L}{k_{\text{B}} T B_{\text{RF}}} \frac{|\chi(\Omega)|^2}{|\chi_N(\Omega)|^2}\right]^{2/3}, \quad (5.41)$$

showing higher dynamic range with higher optical power, longer device length, and higher Brillouin gain. Interestingly, we see that the spur-free dynamic range does not depend on the value of the modulator half-wave voltage. This is because both the signal and the third-order spur are generated at the modulator and a different value of V_π will affect both the signal and the spur in the same way, such that overall, their intercept point is unaffected (see Eq. (5.40)).

5.4.4 Noise figure

Finally, we analyze the noise figure of the link, quantifying the noise added by the microwave-photonic system, by calculating the ratio of the input and output signal-to-noise ratios (SNR), $F = \text{SNR}_{\text{in}}/\text{SNR}_{\text{out}}$. Using the output SNR from Eq. (5.35), and assuming thermal

noise at the RF input port ($k_{\mathrm{B}}TB_{\mathrm{RF}}$), we have

$$F = \frac{P_{\mathrm{in}}^{\mathrm{RF}}/\left(k_{\mathrm{B}}TB_{\mathrm{RF}}\right)}{gP_{\mathrm{in}}^{\mathrm{RF}}/P_{\mathrm{N}}} = \frac{8}{R_{\mathrm{in}}}\left(\frac{V_\pi}{\pi}\right)^2\left(\frac{\omega_0^{(\mathrm{B})}}{\Omega_0}\right)\frac{1}{G_{\mathrm{B}}\left(P^{(\mathrm{A})}\right)^2 L}\frac{\left|\chi_N(\Omega)\right|^2}{\left|\chi(\Omega)\right|^2}. \tag{5.42}$$

Examining a two-pole filter using realistic system parameters (see Table 5.2), we calculate a noise figure of 48 dB and a spur-free dynamic range of 100 dB $\mathrm{Hz}^{2/3}$. The system parameters chosen here are similar to those used in recent experiments [186, 187], and the theoretical analysis is consistent with experimental results. For example, using the experimental parameters described in Ref. [187] with no further calibration, we predict the measured gain, noise-figure, and spur-free dynamic range to within a few dB.

5.4.5 Potential performance of PPER-based filtering

As we seek higher performance systems of this type, it is instructive to explore a broader parameter space to inform future generations of PPER device design and RF links. Analyzing the design space of the system, illustrated in Figs. 5.4(b,d), reveals that we can further improve the performance of the RF link by using a low half-wave voltage (V_π) modulator and higher optical powers. Lower V_π corresponds to higher efficiency in the optical intensity modulation for the same input RF voltage [265]. This results in a stronger acoustic field transducing the RF signal, while not adding noise to the link. We demonstrate the link parameter space by comparing three scenarios: recently demonstrated systems (denoted Case I), a PPER-based link employing a low half-wave voltage modulator (Case II), and a link utilizing a low-V_π modulator, as well as higher optical power (Case III), presented in Table 5.1 and shown in Fig. 5.4(b). For example, using an optical power of 500 mW in waveguide A and a modulator with $V_\pi = 0.2$ V will result in a noise figure of 9 dB, and a dynamic range of 110 dB $\mathrm{Hz}^{2/3}$. Additional improvement to the dynamic range can be achieved by using linearized modulators, as modulator-induced distortion is the limiting factor for linearity in this microwave link [201,266]. As was discussed in Chapter 4, a simple microwave-photonic link yields a noise figure on the order of 20 dB (see Section 4.4), and when considering a microwave-photonic link implementing narrowband filtering, the noise

figure is typically even higher [144]. The possibility of achieving a noise figure under 10 dB with a PPER-based filter shows its potential for high-performance narrow-band filtering.

5.4.6 Alternative demodulation scheme using optical filtering

In our analysis up to this point, we have assumed an MZI-based phase demodulation scheme to retrieve the filtered RF signal at the PPER output, however, alternative demodulation schemes are possible. Here, we describe the performance of a PPER-based microwave-photonic link implementing a different demodulation scheme, using optical filtering, such as was demonstrated in Ref. [187]. In this demodulation scheme, the first sideband of the phase-modulated PPER output is suppressed by using an optical filter, resulting in the conversion of phase modulation into an intensity signal that can be detected using a single photodetector, as illustrated in Fig. 5.3(b). The output field is now given by $E_{\text{out}}^{(\text{B})}(t) = \sqrt{\hbar\omega_0^{(\text{B})} v}\sum_{n\neq -1} a_n^{(\text{B})} e^{-i\left(\omega_0^{(\text{B})}+n\Omega\right)t}$, which results in a photocurrent $I = \eta|E_{\text{out}}^{(\text{B})}(t)|^2$ when using a photodiode with responsivity η. Plugging in Eq. (5.12), keeping terms oscillating around frequency Ω, yields

$$I_\Omega = 2\eta P^{(\text{B})} \cos\left(\Omega t + \pi/2 - \phi\right)\left[J_0\left(\beta_{\text{in}}\right) J_1\left(\beta_{\text{in}}\right) - J_1\left(\beta_{\text{in}}\right) J_2\left(\beta_{\text{in}}\right)\right], \tag{5.43}$$

and the average RF output power ($P_{\text{out}}^{\text{RF}} = \langle I_\Omega^2\rangle R_{\text{out}}|H_{\text{pd}}|^2$) is now

$$P_{\text{out}}^{\text{RF}}(\Omega) = 2R_{\text{out}}|H_{\text{pd}}|^2\Big(\eta P^{(\text{B})}\left[J_0\left(\beta_{\text{in}}\right) J_1\left(\beta_{\text{in}}\right) - J_1\left(\beta_{\text{in}}\right) J_2\left(\beta_{\text{in}}\right)\right]\Big)^2. \tag{5.44}$$

In the small-signal linear regime, we expand the Bessel functions to first order, leaving us with

$$P_{\text{out}}^{\text{RF}}(\Omega) = \frac{1}{8}\left[\eta P^{(\text{B})}\frac{\Gamma}{2}\left|\chi\right|\frac{\pi V_{\text{in}}}{V_\pi} G_{\text{B}} P^{(\text{A})} L\right]^2 R_{\text{out}}|H_{\text{pd}}|^2, \tag{5.45}$$

showing a four-fold reduction in power when compared to the interferometer-based demodulation analyzed earlier (compare to Eq. (5.33)). This also implies that the RF link gain $g = P_{\text{out}}^{\text{RF}}/P_{\text{in}}^{\text{RF}}$ will be four times lower (-6 dB). The reduction in optical power should not surprise us, as in the optical filtering process we are discarding some of the signal power.

Table 5.1: Calculated microwave-photonic link properties of a two-pole PPER-based filter, assuming phase demodulation using an MZI and using the parameters from Table 5.2. Adapted from Ref. [155] © 2020 IEEE.

Parameter	Case I	Case II	Case III	Description
G (dB)	7.8	32.7	46.7	RF link gain ($P_{\mathrm{out}}/P_{\mathrm{in}}$)
$\mathrm{OIP_3}$ (dBm)	32.6	32.6	46.5	Output intercept point
$\mathrm{SFDR_3}$ (dB $\mathrm{Hz}^{2/3}$)	100.4	100.4	109.9	Spur-free dyn. range $(\mathrm{OIP_3}/P_{\mathrm{N}})^{2/3}$
$P_{\mathrm{out}}^{\mathrm{1dB}}$ (dBm)	9	9	9	1 dB compression point
$\mathrm{CDR_{1dB}}$ (dB Hz)	127	127	127	Linear dyn. range $\left(P_{\mathrm{out}}^{\mathrm{1dB}}/P_{\mathrm{N}}\right)$
NF (dB)	48.2	23.3	9.3	Noise figure $(\mathrm{SNR_{in}}/\mathrm{SNR_{out}})$
SNR (dB Hz)	135.8	160.7	174.6	Signal to noise ratio ($P_{\mathrm{out}}/P_{\mathrm{N}}$)

Case I: $V_\pi = 3.5$ V, $P^{(\mathrm{A})} = 100$ mW, Case II: $V_\pi = 0.2$ V, $P^{(\mathrm{A})} = 100$ mW, Case III: $V_\pi = 0.2$ V, $P^{(\mathrm{A})} = 500$ mW.

Table 5.2: Parameters used in the microwave link analysis. Adapted from Ref. [155] © 2020 IEEE.

Parameter	Value	Description
$P^{(\mathrm{A})}$ (mW)	100	Optical power in waveguide A
$P^{(\mathrm{B})}$ (mW)	100	Optical power in waveguide B
$\lambda^{(\mathrm{B})}$ (nm)	1550	Optical wavelength
Ω_0 (2π GHz)	5	Acoustic resonant frequency
Q	1000	Acoustic Q-factor
μ (2π MHz)	2	Acoustic coupling between phonons[1]
L (mm)	30	Active length
G_{B} ($\mathrm{W^{-1}m^{-1}}$)	1000	Brillouin gain
$P_{\mathrm{in}}^{\mathrm{RF}}$ (dBm)	10	Input RF power
V_π (V)	3.5	Intensity modulator half-wave voltage
η (A/W)	0.75	Photodiode responsivity
R_{in} (Ω)	50	Input impedance
R_{out} (Ω)	50	Output impedance
H_{pd}	0.5	Photodiode response
τ (ps)	100	Interferometer time delay for demodulation
B_{RF} (Hz)	1	RF bandwidth
T (K)	290	Temperature
γ (2π kHz)	5	Laser linewidth

[1] Applies only to multi-pole filters.

Next, we analyze the noise floor, taking into account the optical-filtering demodulation scheme. We can describe the spontaneous-Brillouin scattered light using Eq. (5.26), which now has only one sideband due to the optical filtering

$$E_{\text{out}}(t) = \sqrt{\hbar\omega_0 v}\left(a_0 e^{-i\omega_0 t} + a_1 e^{-i(\omega_0+\Omega_0)t}\right). \tag{5.46}$$

Calculating the photocurrent generated by this spontaneous scattering $I_{\text{N}}(t) = \eta\left|E_{\text{out}}(t)\right|^2$ gives us

$$I_{\text{N}}(t) = \eta\hbar\omega_0 v\left[|a_0|^2 + |a_1|^2 + 2\,\text{Re}\left(a_0^\dagger a_1 \cos\left(\Omega_0 t\right)\right)\right], \tag{5.47}$$

and keeping terms oscillating around Ω_0, we can derive the spectral density using Eq. (5.28)

$$S_{\text{N}}^{\text{RF}}(\Omega) = \eta^2\frac{\omega_0}{\Omega_0}G_{\text{B}}P^2 L k_{\text{B}}T R_{\text{out}}|H_{\text{pd}}|^2\left[\frac{(\Gamma/2)^2}{(\Gamma/2)^2+(\Omega-\Omega_0)^2} + \frac{(\Gamma/2)^2}{(\Gamma/2)^2+(\Omega+\Omega_0)^2}\right]. \tag{5.48}$$

Integrating a narrow bandwidth B_{RF} around frequency Ω, the single-sideband power spectral density is given by

$$P_{\text{N}}(\Omega) = 2\eta^2\frac{\omega_0}{\Omega_0}G_{\text{B}}P^2 L k_{\text{B}}T B_{\text{RF}} R_{\text{out}}|H_{\text{pd}}|^2\left(\frac{\Gamma}{2}\right)^2|\chi_N(\Omega)|^2, \tag{5.49}$$

which is four times smaller than the balanced detection result shown earlier in Eq. (5.31). This is consistent with the calculation of the output signal power (Eq. (5.45)), which also shows a four-fold reduction, resulting in the same signal-to-noise ratio, regardless of the demodulation scheme.

We also note that the filtering of the optical sideband turns the phase fluctuations into intensity, resulting in the laser phase noise being converted into intensity noise, with a RIN given by

$$\text{RIN}_{\text{phase}} = \frac{2}{\pi}\int_{-B/2}^{B/2} d\Omega'\left(\frac{\gamma}{(\gamma/2)^2+(\Omega')^2}\right)\left(\frac{\gamma}{(\gamma/2)^2+(\Omega'-\Omega)^2}\right), \tag{5.50}$$

where B is the bandwidth of the optical filter used to reject one of the sidebands, and γ is the laser linewidth resulting from its phase fluctuations. As with the MZI demodulation

case, using typical values, the thermal phonon scattering contribution is still the dominant noise source [187].

Next, we quantify the usable dynamic range of the microwave-photonic filter with the alternative demodulation scheme. We start by calculating the 1 dB compression point. Setting the ratio between Eqs. (5.44) and (5.45) to 1 dB, and solving for the input power, we have

$$P_{\mathrm{in}}^{\mathrm{1dB}} = \frac{0.245}{R_{\mathrm{in}}} \left(\frac{V_\pi}{\Gamma \left| \chi \right| G_{\mathrm{B}} P^{(\mathrm{A})} L} \right)^2, \tag{5.51}$$

showing the same scaling with system parameters as we had with the MZI-based demodulation scheme (see Eq. 5.36). We calculate the third-order intercept point [198], by assuming the input RF signal is at frequency $\Omega_0/3$ and analyzing the propagation of the third-order modulation through the microwave-photonic link. In this case we have $\beta_{\mathrm{in}}^{3\Omega/3} = (\Gamma/2)|\chi| J_3(\pi V_{\mathrm{in}}/V_\pi) G_{\mathrm{B}} P_0^{(\mathrm{A})} L$, and plugging into Eq. (5.44), expanding the Bessel functions to the first non-vanishing orders, we have

$$P_{\mathrm{out}}^{3\Omega/3} = \frac{1}{576} R_{\mathrm{in}}^3 R_{\mathrm{out}} |H_{\mathrm{pd}}|^2 \left(P_{\mathrm{in}}^{\mathrm{RF}} \right)^3 \left(\eta P^{(\mathrm{B})} \frac{\Gamma}{2} \left| \chi \right| \left(\frac{\pi}{V_\pi} \right)^3 G_{\mathrm{B}} P^{(\mathrm{A})} L \right)^2. \tag{5.52}$$

To find the third-order intercept point, we equate Eqs. (5.45) and (5.52), and solve for the input RF power, giving the input intercept point (IIP_3)

$$\mathrm{IIP}_3 = 12 \frac{V_\pi^2}{\pi^2 R_{\mathrm{in}}}. \tag{5.53}$$

Substituting into Eq. (5.45), we find the output intercept point (OIP_3)

$$\mathrm{OIP}_3 = 3 \left[\eta P^{(\mathrm{B})} \frac{\Gamma}{2} \left| \chi \right| G_{\mathrm{B}} P^{(\mathrm{A})} L \right]^2 R_{\mathrm{out}} |H_{\mathrm{pd}}|^2, \tag{5.54}$$

showing a four-fold reduction when comparing to the MZI-based demodulation scheme (see Eq. (5.40)).

We can see that when using the alternative phase demodulation scheme, the signal and the noise both change by the same factor, such that the noise figure and spur-free dynamic range do not change. However, different demodulation schemes may have different signal

compression, yielding a difference in the linear dynamic range.

5.5 Enhanced performance at cryogenic temperatures

Up to this point, we have analyzed the performance of a PPER-based microwave-photonic filter at room temperature, where thermally-occupied phonons dominate the link noise floor. In this section we will consider operating such microwave links at lower temperatures, where the phonon occupation is reduced, resulting in lower spontaneous Brillouin scattering noise. Additionally, we expect the phonon lifetime (τ_{ac}) in the device to increase at lower temperatures, as internal sources of phonon dissipation are suppressed [168, 267, 268]. This corresponds to a higher phonon quality factor ($Q \propto \tau_{ac}$) and results in a larger Brillouin gain, which scales linearly with the Q-factor ($G_B \propto 1/\Gamma \propto Q$). Additional effects of low temperature could be reduced two-photon absorption, enabling higher optical power handling of the devices, however, these are not considered in the following analysis. Operating optomechanical devices at cryogenic temperatures has been frequently performed over the past decade [268–270], and could be adapted to the types of Brillouin-active devices discussed here.

Throughout this section, the calculations use the parameters presented in Table 5.4, all of which are similar to recent experimental demonstrations [64, 187], and we consider a two-pole PPER-based filter and an MZI balanced-detection phase demodulation scheme.

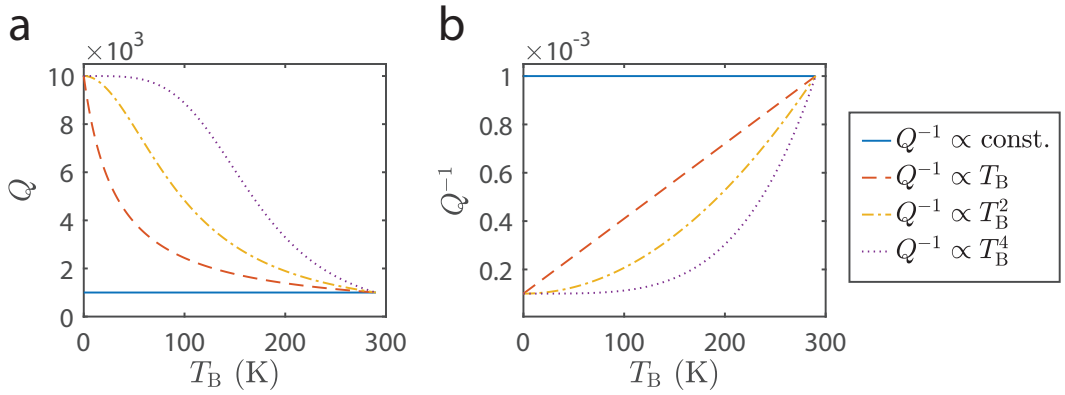

Figure 5.5: **(a)** Different scenarios of the acoustic Q-factor as a function of temperature. **(b)** Inverse Q-factor, proportional to the phonon dissipation rate ($Q^{-1} \propto \Gamma$).

To consider the uncertainty of the acoustic mode lifetime as a function of temperature, we analyze four different cases for the dependence of the acoustic Q-factor on temperature, as shown in Fig. 5.5. This includes the case where the acoustic mode does not change with temperature and three cases where we assume the phonon Q-factor grows from $Q = 10^3$ at room temperature ($T = 290$ K) to $Q = 10^4$ in the limit $T \to 0$, each with different scaling.

The first observation we note is the change in the two-pole filter lineshape at different temperatures. Since the phonon dissipation rate determines the pass-band width, lower temperatures will result in sharper filters, as seen in Fig. 5.6. In our calculations, we are scaling the acoustic coupling rate μ as the temperature is changed, resulting in a constant peak in all lineshapes, and the change is seen only in the bandwidth and sharpness of the filter. We note that the case of a constant Q-factor (not depending on temperature) can be used to compare the operation of filters with the same bandwidth at different temperatures, which could be achieved through device geometry. Practically, this implies that the devices are designed with the target operating temperature in mind and fabricated accordingly.

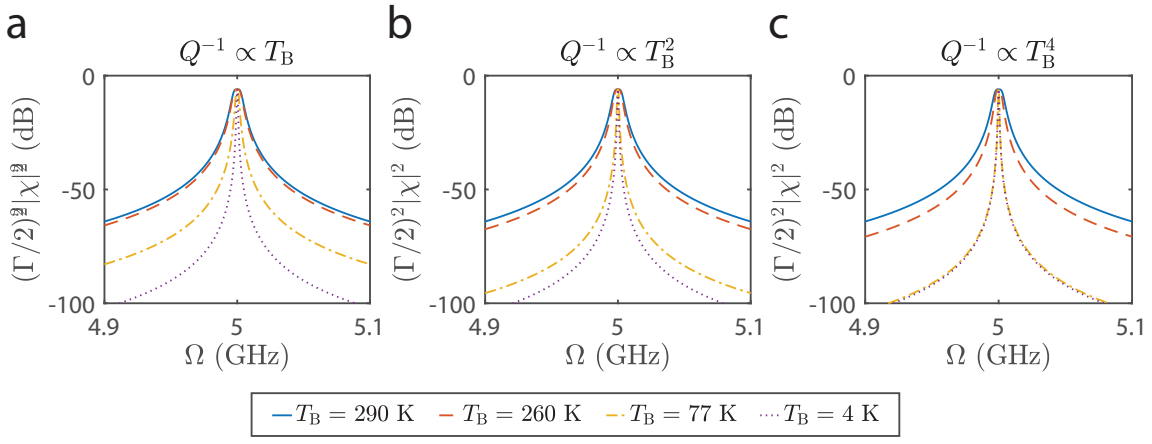

Figure 5.6: Filter lineshape as a function of temperature.

5.5.1 Noise sources

Next, we examine the dependence of the different noise sources on the device temperature. Restating Eq. (5.24), the noise sources we consider in our analysis are given by

$$N_{\mathrm{tot}} = N_{\mathrm{th}} + N_{\mathrm{shot}} + N_{\mathrm{phase}} + N_{\mathrm{B}}. \tag{5.55}$$

The first term accounts for thermal microwave noise ('Johnson–Nyquist' noise), at the link input and output, given by

$$N_{\mathrm{th}} = \hbar\Omega \left[\frac{1}{\exp\left(\hbar\Omega/k_{\mathrm{B}}T\right) - 1} + \frac{1}{2}\right]\left(1 + g\right), \tag{5.56}$$

where g is the link gain. In the high temperature limit ($k_{\mathrm{B}}T \gg \hbar\Omega$) the expression reduces to $N_{\mathrm{th}} = k_{\mathrm{B}}T\left(1 + g(\Omega)\right)$, which we have used earlier in the room-temperature analysis. It is important to note that the temperature T in Eq. (5.56) refers to the environment of the input and output of the link (intensity modulator and detector), which we will assume is at room temperature regardless of the temperature of the device. The second and third terms in Eq. (5.55) take into account shot noise and laser phase noise, which do not depend on the device temperature and were given in Eqs. (5.24) and (5.25). The last contribution is that of thermal Brillouin noise, a consequence of the occupation of the acoustic modes at thermal equilibrium, given by

$$N_{\mathrm{B}} = 8\left(\eta P^{(\mathrm{B})}\right)^2 R_{\mathrm{out}}|H_{\mathrm{pd}}|^2 \left[\hbar\omega_0 G_{\mathrm{B}} L n_{\mathrm{th}} \sin^2\left(\Omega\tau/2\right)\left(\frac{\Gamma}{2}\right)^2 |\chi_N(\Omega)|^2\right], \tag{5.57}$$

where $n_{\mathrm{th}} = [(\exp\left(\hbar\Omega/k_{\mathrm{B}}T_{\mathrm{B}}\right) - 1)^{-1}]$ is the mean phonon occupation at the device temperature T_{B}. The frequency response reduces to $|\chi_N|^2 = 2/\Gamma^2$ at the filter center. We note that Eq. (5.57) is equivalent to the earlier Eq. (5.31), without assuming the high temperature limit.

Fig. 5.7 shows the power spectral density (PSD) of the different noise sources at different device temperatures, assuming different scalings of the acoustic Q-factor with temperature.

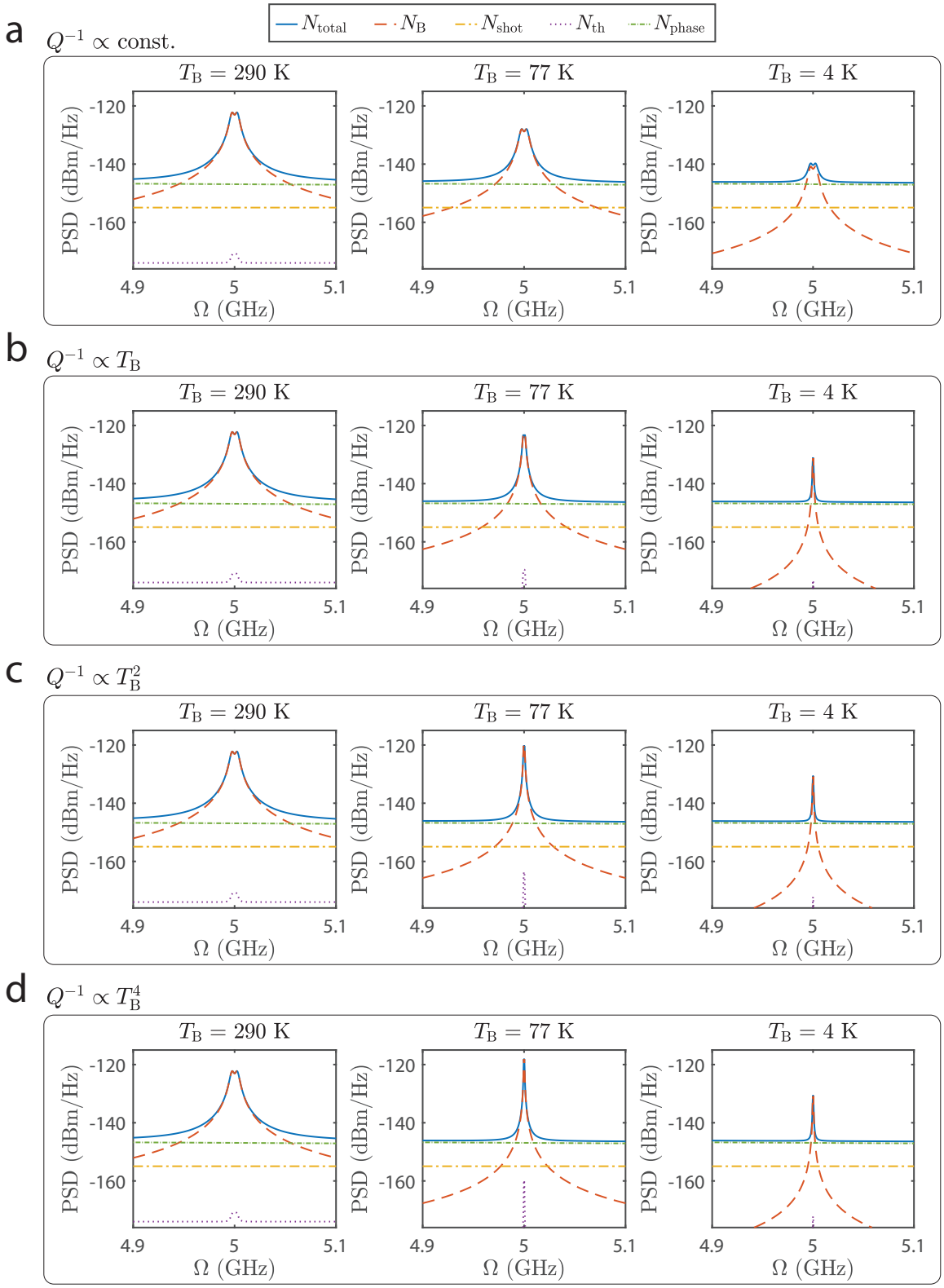

Figure 5.7: Power spectral density for different device temperatures.

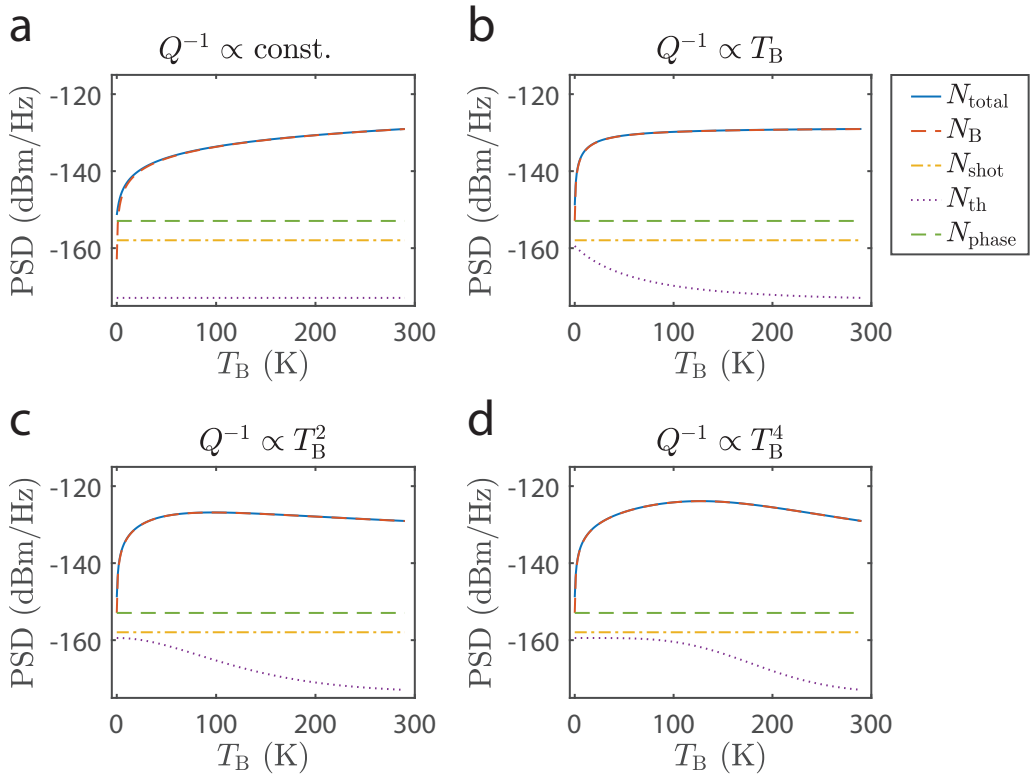

Figure 5.8: Peak power spectral density at the center of the passband ($\Omega = \Omega_0$) as a function of device temperature.

In Fig. 5.8, the PSD at the center of the filter pass-band ($\Omega = \Omega_0$) is plotted as a function of temperature. We can see the reduction in Brillouin noise at lower temperatures, as there is a smaller population of thermal phonons. Interestingly, the thermal noise increases as the temperature drops, as a result of the higher link gain due to the longer lifetime of the acoustic modes.

5.5.2 RF-link performance

We turn to estimate the potential microwave-link performance metrics at low temperatures. We can identify a number of possible advantages of low-temperature operation when considering the potential performance of the microwave-photonic link.

Starting with the link gain, we use Eq. (5.34), however, now the phonon dissipation rate Γ, the Brillouin gain G_B, and the frequency response $\chi(\Omega)$ are temperature dependent. In this case, lower temperature will result in longer phonon lifetimes, yielding higher Brillouin

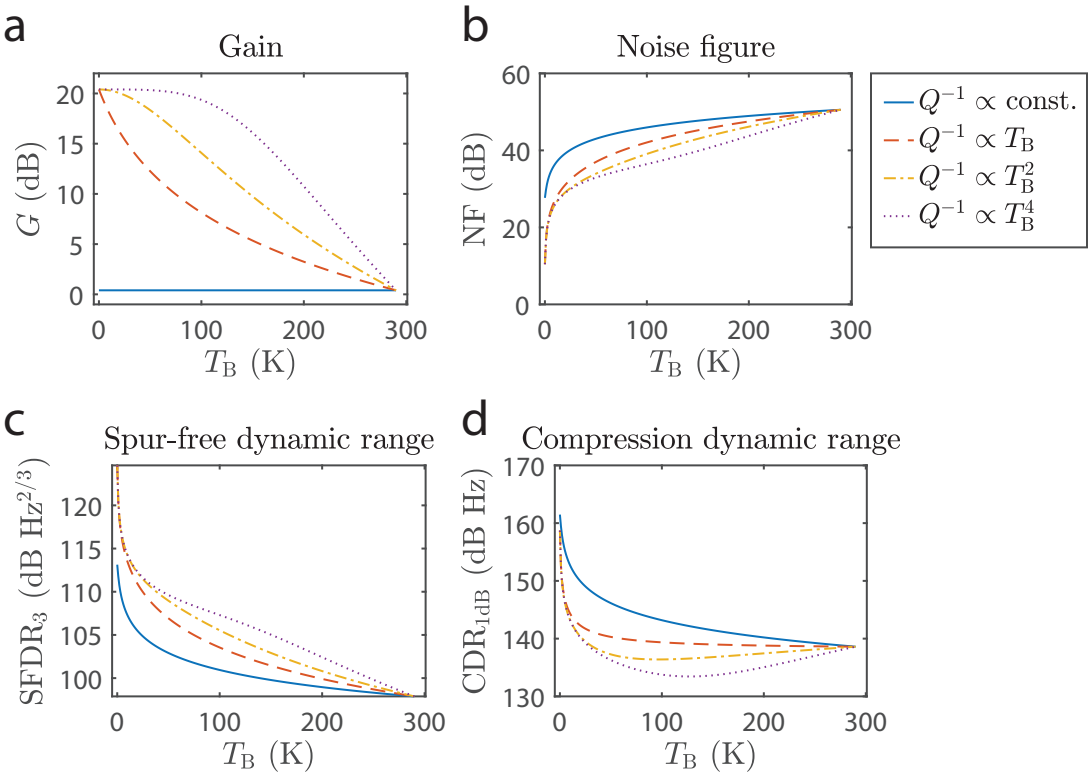

Figure 5.9: Calculated microwave-photonic link performance as a function of temperature.

Table 5.3: Calculated microwave link performance at four different device temperatures, assuming $Q \propto T_B^4$.

T_B (K)	290	260	77	4	Temperature
G (dB)	0.4	3.7	20	20.4	RF link gain
NF (dB)	50.6	48.4	35	22.1	Noise figure[1]
$SFDR_3$ (dB $Hz^{2/3}$)	97.9	99.3	108.3	116.9	Spur-free dynamic range
CDR_{1dB} (dB Hz)	138.6	137.4	134.6	147.1	Linear dynamic range

[1] N_{in} is assumed to be thermal noise at room temperature ($T = 290$ K), such that $N_{in} = k_B T = -174$ dBm/Hz.

gain and a higher RF link gain, as shown in Fig. 5.9(a). Next, we calculate the noise figure as a function of temperature. We consider the input noise spectral density to be room temperature thermal noise $N_{\text{in}} = k_{\text{B}}T$, and in the linear gain regime, we can write the noise figure as $F = N_{\text{tot}}/(gk_{\text{B}}T)$, where N_{tot} was given in Eq. (5.55). As could be expected, the reduction in the Brillouin noise due to the lower temperature results in a lower noise figure, as seen in Fig. 5.9(b). The spur-free dynamic range is calculated by evaluating the third-order intercept point OIP_3 from Eq. (5.40), and using $\text{SFDR}_3 = (\text{OIP}_3/P_N)^{2/3}$. As seen in Fig. 5.9(c), we expect a sharp increase in the dynamic range as the temperature drops, a consequence of the lower noise floor. Finally, we calculate the 1 dB compression-free dynamic range $\text{CDR}_{1\text{dB}} = gP_{\text{in}_{1\text{dB}}}/P_N$, where $P_{\text{in}_{1\text{dB}}}$ is given by Eq. (5.36), as shown in Fig. 5.9(d). We can see that the linear dynamic range is still much larger than the spur-free dynamic range, and will not limit system operation within its distortion-free range. We summarize the RF link properties at four different temperatures in Table 5.3, for the case of $Q^{-1} \propto T_{\text{B}}^4$, demonstrating the enhanced performance as the temperature is reduced.

Table 5.4: Parameters used in the low temperature analysis.

Parameter	Value	Description
$\lambda^{(\text{B})}$ (nm)	1550	Optical wavelength ($2\pi c/\omega^{(\text{B})}$)
Ω_0 (2π GHz)	5	Phonon frequency
Q_0	1000	Acoustic Q-factor at room temperature
μ	$\Omega_0/(2Q)$	Acoustic coupling rate
$P^{(\text{A})}$ (mW)	100	Optical power in the 'emit' waveguide
$P^{(\text{B})}$ (mW)	100	Optical power on the 'receive' detector
G_{B} ($\text{W}^{-1}\text{m}^{-1}$)	1000	Brillouin gain at room temperature
L (mm)	10	Active-Brillouin interaction length
V_π (V)	3	Half-wave modulation voltage
η (A/W)	0.8	Photodioide responsivity
R_{out} (Ω)	50	Output impedance
H_{pd}	0.5	Photodiode response
R_{in} (Ω)	50	Input impedance
τ (ps)	100	Interferometer time delay for demodulation
γ (2π kHz)	1	Laser linewidth

5.6 Conclusion

In this chapter, we have analyzed a microwave-photonic link that utilizes a Brillouin-active PPER device, and have shown how this system can be used to implement narrowband bandpass filtering. In our analysis, we have described the output RF signal in terms of the optical, microwave, and acoustic parameters of the system. The PPER device in the heart of this microwave-photonic link provides the acousto-optic interaction that enables the RF-link to achieve narrowband filtering and directly affects link performance. For example, designing PPER devices with a lower acoustic dissipation rate can yield sub-MHz filter lineshapes, and further improvements to the link performance can be achieved through mode-engineering of the optical waveguides to achieve stronger Brillouin gain. Additionally, increasing the interaction length, by designing longer devices or utilizing resonant structures [66], will improve filter performance. The separation of optical tones to spatially separated waveguides reduces the effects of optical nonlinearity such as four-wave mixing, which can be detrimental to filter performance. This also reduces the effects of spurious optical tones such as from unwanted reflections [247], degrading filter response, and avoids the use of circulators which may be challenging to integrate on-chip.

The ability to design a multi-pole frequency response using the PPER scheme is unique when comparing to other Brillouin-based filtering methods. Additionally, an all-optical filter with a similar frequency response would be very challenging to realize. For example, an equivalent filter using two coupled ring-resonators would require each resonator to have a Q-factor on the order of $\sim 10^8$, with precise control over the coupling rates between the rings and to the bus waveguides [192]. Moreover, the lasers used in such a filtering scheme would need to be frequency-stabilized relative to the resonances used for the filtering operation. In contrast, the PPER scheme does not rely on optical resonances, avoiding these limitations, with the benefit of being optically transparent over large bandwidths.

Analyzing the noise sources of a PPER-based RF link, we have seen that the dominant noise is the result of thermally-excited phonons when operating at room temperature, and we have shown how Brillouin noise can be reduced by decreasing the operating temperature of

the device. Since the dynamic range of this system is limited by distortions originating from the electro-optic modulator, significant enhancement of the spur-free dynamic range can be possible with the availability of linearized intensity modulators [201, 266], possibly yielding SFDR_3 >135 dB. An important parameter for a low noise figure is a low half-wave voltage of the intensity modulator. Using newly developed low V_π modulators [53, 258] in conjunction with higher optical powers, a noise figure of <10 dB becomes feasible. Alternatively, through the use of an RF low-noise amplifier (LNA) to amplify the microwave signals entering the intensity modulator, this PPER filter system can yield an overall lower noise figure. The use of an LNA at the input of a PPER-based filter is further discussed and demonstrated in Chapter 7.

This new type of microwave-photonic link offers a variety of strategies for trimming and tuning the bandpass frequency and can be used in multiple frequency multiplexing schemes. The resonant frequency of the PPER can be tuned through the geometry of the device, as it sets the boundary conditions for the acoustic modes taking part in the signal transduction [44]. Furthermore, by implementing different modulation schemes at the filter input, the filter bandpass frequency can be tuned optically, as illustrated in Fig. 5.10(a). In this scenario, the RF information is modulated on an optical carrier (optical frequency $\omega_0^{(\mathrm{A})}$) using a phase modulator, and a separate optical tone at optical frequency ω_{LO} is used as an optical local oscillator (LO) to drive the acoustic field and transduce the information onto the light in the 'receive' waveguide. As there are no optical resonances in the device, the optical tuning of the RF filter pass-band can be varied over a large spectral range [240], while maintaining a few MHz pass-band. Furthermore, the 'emit' and 'receive' waveguides can operate at different wavelengths, effectively frequency shifting the optical carrier when information is transduced in the device. The possibilities of frequency-response trimming and pass-band tunability using the PPER scheme will be discussed further in Chapters 6 and 7.

Another intriguing property of the PPER RF-filtering scheme is the ability to cascade multiple filters in series without degrading the RF signal modulated on the optical field. The phonon field generated in the device phase-modulates the 'emit' optical field as it prop-

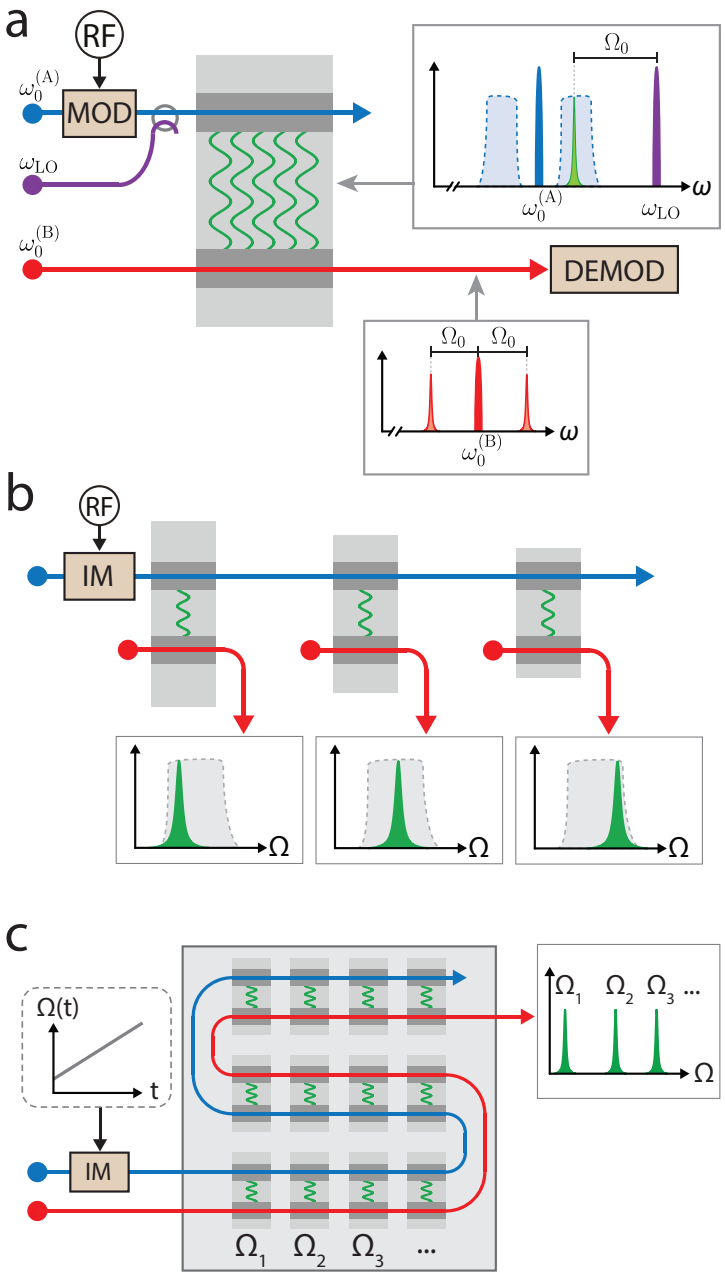

Figure 5.10: **(a)** An RF signal is modulated on an optical carrier (blue) and combined with a second optical tone (purple). By tuning the optical wavelength, the filter passband is shifted, as the acoustic resonance (green) overlaps with different spectral bands of the modulated RF information. **(b)** Cascading multiple filters in series enables the filtering of different frequency bands simultaneously, without the need to split the signal, and with no signal degradation. **(c)** Cascading multiple PPER devices with different resonant frequencies can be used as an on-chip sensor. A swept RF source allows spatial resolution of the different segments, enabling distributed sensing on-chip. Adapted from Ref. [155].

agates in waveguide A, but does not affect the intensity modulation that encodes the input RF signal, as was discussed in Chapter 3. Hence, the field coming out of waveguide A has an identical intensity modulation profile as the input field and can drive another PPER filter cascaded in the system exactly in the same manner. This is in contrast with a conventional RF filter array in which out-of-band spectral components are attenuated, leading to the need for splitting and amplifying the RF signal, resulting in lower signal power, degrading the SNR of the link, and adding to the complexity of the system. The ability to cascade multiple PPER filters in series can be of great practical use in applications such as spectral awareness and channelization [271, 272], where multiple bands of the RF spectrum are monitored simultaneously, as well as filter banks used frequently in communication systems. The scheme illustrated in Fig. 5.10(b) could enable us to filter out multiple spectral bands simultaneously using a single intensity modulator at the link input, and a separate 'receive' signal-path for each spectral channel. For example, by using millimeter-scale PPER segments, each filtering a 5 MHz spectral region, 1000 filters can be cascaded, with an overall length of a few centimeters, spanning a 5 GHz spectral range on a single chip. Additionally, since the dominant noise source is from spontaneous Brillouin scattering, it is centered around the center frequency of each filter and does not add out-of-band noise.

An alternative cascading scheme is illustrated in Fig. 5.10(c). In this scenario, a single optical tone propagates through the 'receive' waveguide in multiple cascaded PPER segments, while an RF signal generator performs a frequency sweep through the range of acoustic frequencies. By designing the geometry of each PPER segment to have a different resonant frequency, the swept RF source at the input will result in multiple peaks measured on an RF spectrum analyzer, corresponding to the different segments. The high-Q acoustic resonances, combined with the high SNR of the PPER scheme, make this an ideal candidate for on-chip sensing applications. For example, the Brillouin frequency is sensitive to nanometer-scale geometrical perturbations [64, 65], enabling the design of distributed sensors with micrometer spatial resolution, and a sensitivity to atomic-scale perturbations, proportional to the inverse of the Q-factor [273]. Brillouin scattering is widely used in fiber-optic sensors, as external perturbations such as strain and temperature result in a

measurable change of the acoustic resonance [87, 274]. More recently, chip-scale devices implementing Brillouin scattering have been demonstrated for sensing [239]. Furthermore, using forward-Brillouin scattering as the optomechanical coupling process enables interrogation of the device surface, as the transverse acoustic waves are set by the boundary conditions of the acoustic waveguide [94]. In chip-integrated devices, this property could be utilized by activating the device surfaces to bind to different chemical compounds [275,276].

While recent demonstrations of PPER devices were implemented in suspended silicon waveguides, the concept can be realized in other systems where distinct optical fields are coupled to mutual acoustic resonances. Potential systems include multi-core fiber [188], as well as systems where optical fields are guided in different spatial modes [139], or are separated in wavelength [44]. The modularity of the PPER system and the large design space enable numerous applications, ranging from high-performance microwave-photonic filters to high-resolution channelizers and distributed sensors.

Chapter 6

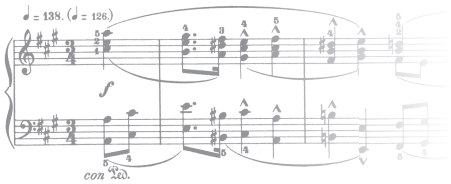

Multi-pole photonic-phononic emit-receive devices in silicon

6.1 Introduction

A promising strategy to utilize Brillouin scattering for microwave-filtering operations is using a photonic-phononic emitter-receiver (PPER), where information is transduced between the optical and acoustic domains, resulting in a narrowband frequency response [186, 187]. As we have shown in the previous chapter, this can be accomplished by encoding information on an optical carrier that drives spatially-extended coherent acoustic waves, which in turn induce a narrowband phase modulation onto light propagating in a separate optical waveguide. In contrast to the Lorentzian lineshape typical of Brillouin interactions, the PPER scheme enables us to produce a multi-pole filter response by utilizing multiple coherent acoustic modes in the transduction process [186].

Experimentally, PPER multi-pole response was demonstrated with devices fabricated from silicon and silicon nitride materials using a MEMS fabrication process that involved planarization through chemical-mechanical polishing (CMP) [186]. While these initial device studies demonstrated the feasibility of high-performance multi-pole response, dimensional nonuniformities produced during CMP-based planarization made it challenging to

consistently reproduce such multi-pole filters. Moreover, the technological impact of PPER-based filtering technology hinges on the nonlinear and noise characteristics of such devices within a microwave-photonic link, which were not explored in the earlier study. Recently, a PPER-based microwave-photonic link was demonstrated using a single-pole silicon device, showing the feasibility of such filtering schemes [64]. However, the single-pole nature of the filter yielded limited out-of-band suppression. Because this rudimentary single-pole device lacks an acoustic stop-band, numerous acoustic resonances supported in this system lead to high transmission of frequencies outside of the pass-band, degrading the filter performance. As we develop these nascent technologies for real-world applications, we seek microwave-photonic filters that have frequency-tunable operation, excellent filter lineshape and link performance, as well as robust foundry compatible fabrication [196].

In this chapter, we will expand on the design considerations of a practical device, utilizing a standard silicon-on-insulator (SOI) platform and standard CMOS-compatible fabrication steps. The layer structure of the SOI chips we will use is comprised of a 215 nm silicon layer on a 3 μm buried oxide (silica) and a silicon handle ($\sim$0.5 mm) under the oxide (see Fig. 6.1(a)). We will present the design of a device supporting two optical modes and two acoustic modes, with a strong forward Brillouin interaction between each pair of optical and acoustic modes. By utilizing a phononic crystal structure we introduce controlled coupling between the acoustic modes, achieving a two-pole frequency response and a wide stop-band of several GHz, suppressing unwanted acoustic modes. Furthermore, by tailoring the geometry of the device, we demonstrate how we can control the spectral features of the frequency response, and study the effects of fabrication imperfections.

The standard silicon-on-insulator (SOI) platform enables fabrication using standard CMOS lithography steps, and we will present results from devices fabricated using electron-beam lithography, as well as from a silicon-photonics photolithography facility. The use of well-established fabrication methods and standard materials results in high fabrication yield, reproducible results, and robust device performance over time.

6.2 Brillouin-active waveguide design

We start by designing a Brillouin-active waveguide (following Ref. [64]) which consists of a 215 nm silicon layer in which an optically guiding rib is defined by partially etching the silicon layer to a thickness of 130 nm. We use the fundamental TE-like optical mode guided in this waveguide, and the electric field is well localized in the rib region as shown in Fig. 6.1(c). In order to achieve acoustic guiding in the silicon device layer, the buried oxide is removed such that the waveguide is suspended, as shown in Figs. 6.1(a,b). This step is important, as the silica (SiO_2) layer has a slower sound velocity compared to silicon (Si), and acoustic energy can easily escape the waveguide if it is not removed.

To achieve a strong forward Brillouin interaction, the optical and acoustic fields must overlap within the waveguide with the correct phase-matching conditions. As we analyzed in Chapter 2, phase matching of a forward Brillouin process requires an acoustic mode with a cut-off frequency, hence the acoustic waveguide must have transverse confinement. This can be achieved by etching slots parallel to the waveguide [64], as shown in Fig. 6.1(b),

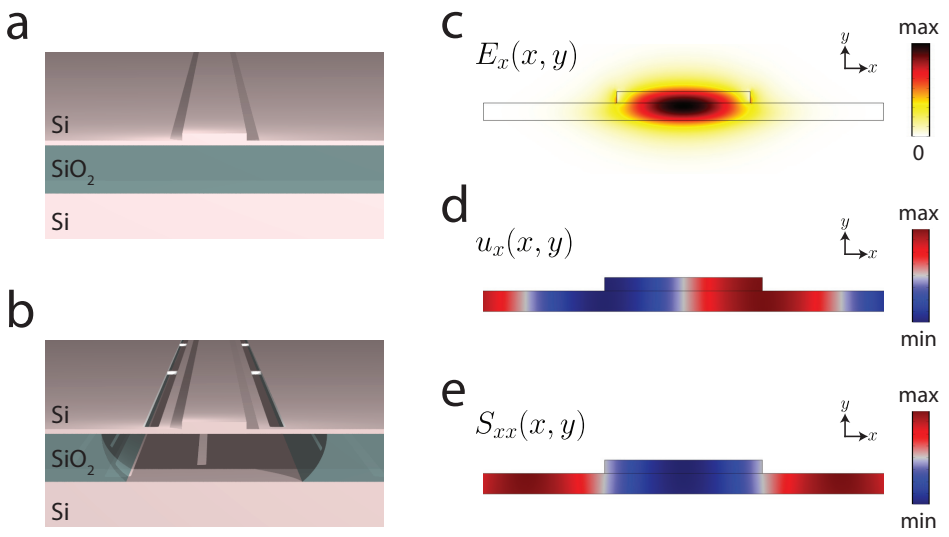

Figure 6.1: **(a)** Illustration of the silicon-on-insulator device layer structure with a rib waveguide etched into the device layer. **(b)** By etching slots parallel to the rib waveguide and removing the silica under the waveguide, a low-loss acoustic waveguide is defined. **(c)** The x component of the fundamental electric field guided by the rib structure. **(d)** The x component of the displacement profile of the acoustic eigenmode used in the forward Brillouin process. **(e)** The corresponding S_{xx} component of the strain profile.

yielding high-Q acoustic modes. Additionally, the symmetry of the spatial mode profiles of the acoustic and optical modes must be engineered to yield a large overlap integral. In silicon, the largest photo-elastic tensor component is p_{11}, and the dominant contribution to the coupling rate (see Section 2.3.1) is $g^{\mathrm{pe}} \propto \int dxdy\ |D_x|^2 p_{11} \partial_x u_x$, where D_x is the x component of the electric displacement field, and u_x is the x component of the mechanical displacement. We can see that the coupling occurs between the electric field polarized along the x axis (as satisfied by the TE-like mode) and the strain component along the x axis ($S_{xx} = \partial_x u_x$). As the function $|D_x|^2$ is symmetric in space with respect to the x axis (assuming the origin at the center of the waveguide), this requires the acoustic mode to have a symmetric strain profile and an anti-symmetric displacement profile. The displacement profile of forward Brillouin-active phonon mode is shown in Fig. 6.1(d), and the strain is shown in Fig. 6.1(e), where the desired symmetric function can be seen.

When designing a two-pole PPER device, we want to *acoustically* couple two of these waveguides, as discussed in Chapter 3. Since the slots provide a 'hard boundary', i.e., they completely stop the propagation of phonons, this does not allow their coupling to other devices. Hence, a different form of acoustic lateral confinement is required for multi-pole devices. We achieve this by using a phononic crystal structure, in which the acoustic energy is reflected (preserving the high-Q acoustic mode) while at the same time, it penetrates the crystal region, such that it can interact with other acoustic modes.

6.3 Acoustic mode engineering

We design a phononic crystal comprised of a cubic lattice of air holes in the silicon layer to achieve an acoustic stop-band that will reflect the acoustic mode taking part in the Brillouin process. The phononic crystal can be parametrized by the unit-cell pitch a and hole diameter d, which determine the acoustic dispersion of the phononic crystal. We analyze the acoustic properties of such structures using finite-element-method (FEM) simulations, shown in Fig. 6.2. First, we simulate the propagation of acoustic modes with displacement along the x axis through a phononic crystal region, demonstrating low acoustic transmission over a 2.5

GHz range, as seen in Fig. 6.2(a). In this analysis, we drive x-displacement modes which are similar to the acoustic modes coupled to in the forward Brillouin process (see Fig. 6.1(d)). Interestingly, once a ridge structure is added, as seen in Fig. 6.2(b), acoustic propagation is possible within this stop-band. This is because the out-of-plane ridge structure couples modes with displacement in the x and y directions.

Next, we simulate a single unit cell of the phononic crystal, and calculate the acoustic band structure for wavevectors along the k_x axis. Fig. 6.2(c) shows the band structure, setting boundary conditions such that there is no out-of-plane displacement. We can identify the stop-band from panel (a), noticing a band that does not participate in the propagation of x-displacement modes (denoted (iii)). When we remove the out-of-plane constraint and simulate the full band structure, as seen in Fig. 6.2(d), we can identify the modes responsible for the transmission window from panel (b). Examining the displacement components of the acoustic modes from different bands, as shown in Figs. 6.2(e,f), we see that most bands have a dominant displacement axis. While the structure does not have a complete acoustic bandgap, within the stop-bands there are modes with mostly y and z displacement, which do not participate in the forward Brillouin interaction. For example, the mode denoted (iii) in Figs. 6.2(c,e) has displacement primarily along the z axis, which is not driven through the forward Brillouin process [186].

We note that in measurements performed on such structures, we find a deviation from the frequencies obtained in the simulation, on the order of $\sim$10%. This could be a result of fabrication imperfections, the difference in geometry between the devices and simulation, as well as the effects of built-in stress in the suspended silicon layer [277, 278].

Utilizing this phononic crystal structure, we can now design a 'super-structure' comprised of two ridge waveguides, as shown in Fig. 6.3, where the acoustic modes of the two waveguides are coupled through the phononic crystal region. The optical rib waveguides are well separated by the central phononic crystal region, such that the optical modes do not interact, as seen in Fig. 6.4(a). The lateral width of the acoustic waveguides (W) is chosen to produce phonon modes with an acoustic frequency within the phononic crystal stop-band, such that the acoustic modes are confined by the phononic crystal regions on either side of

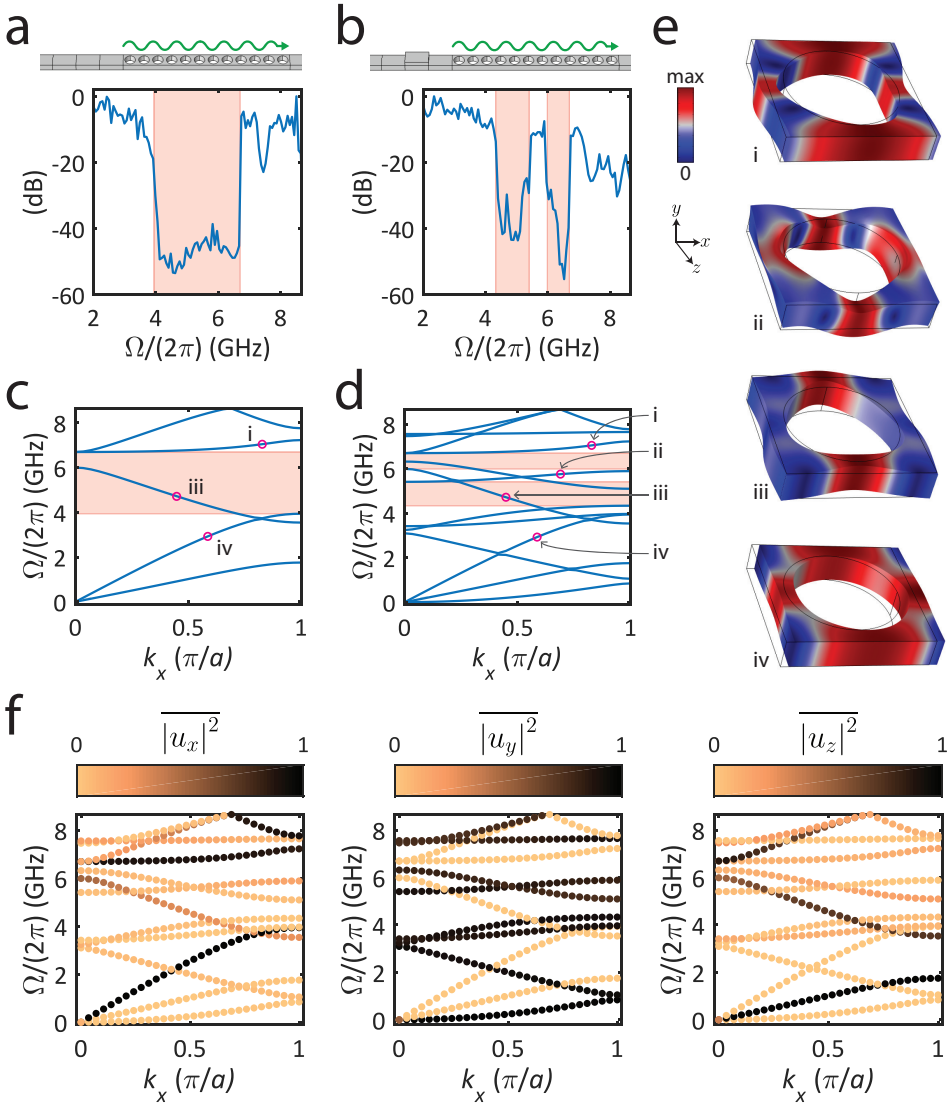

Figure 6.2: **(a)** Simulated acoustic transmission of an acoustic wave with x displacement through twelve rows of a phononic crystal, showing a 2.5 GHz stop-band. The cubic phononic crystal in the simulation has a pitch of $a = 650$ nm and a hole diameter of $d = 500$ nm. **(b)** Acoustic transmission after adding a ridge structure results in transmission within the stop-band. **(c)** Simulated 2D band structure of the phononic crystal, along the Γ–X line of the Brillouin zone. The structure is constrained to have no displacement out of the x–z plane. The stop-band region from panel (a) is shown for reference. **(d)** Acoustic band structure of the phononic crystal, without constraints. The stop-bands from panel (b) are shown for reference. **(e)** Simulated displacement of a unit cell in the cubic lattice, corresponding to the four points marked in panels (c) and (d). **(f)** The acoustic band structure from panel (d), showing the relative mean square displacement of the acoustic modes along the different axes, $\overline{|u_i|^2} = \int dx^3 |u_i|^2 / (\Sigma_i \int dx^3 |u_i|^2)$, $i = \{x, y, z\}$. Adapted from Ref. [156].

the device. Fig. 6.4(f) presents the measured frequency response of such a device, showing an acoustic resonance at 3.90 GHz within a ∼1.7 GHz acoustic stop-band. In Chapter 3 we have shown how the two coupled acoustic modes utilized in a second-order PPER device can be described as phononic 'super-modes' with symmetric and anti-symmetric profiles. In this acoustic structure, we can see these super-modes in the simulation results presented in Figs. 6.4(b–e). We can also see that the acoustic modes have the required symmetries for strong forward Brillouin interactions.

6.4 Multi-pole frequency response

Using two coupled acoustic modes results in second-order frequency response due to their coherent interaction, as was derived in Chapter 3. This can be directly seen from the two poles in the frequency response (see Section 3.3.1), given by

$$\left|\chi^{(2\text{ pole})}(\Omega)\right|^2 \propto \frac{\mu^2}{\left[(\Gamma/2)^2+(\Omega-\Omega_0+\mu)^2\right]\left[(\Gamma/2)^2+(\Omega-\Omega_0-\mu)^2\right]}, \tag{6.1}$$

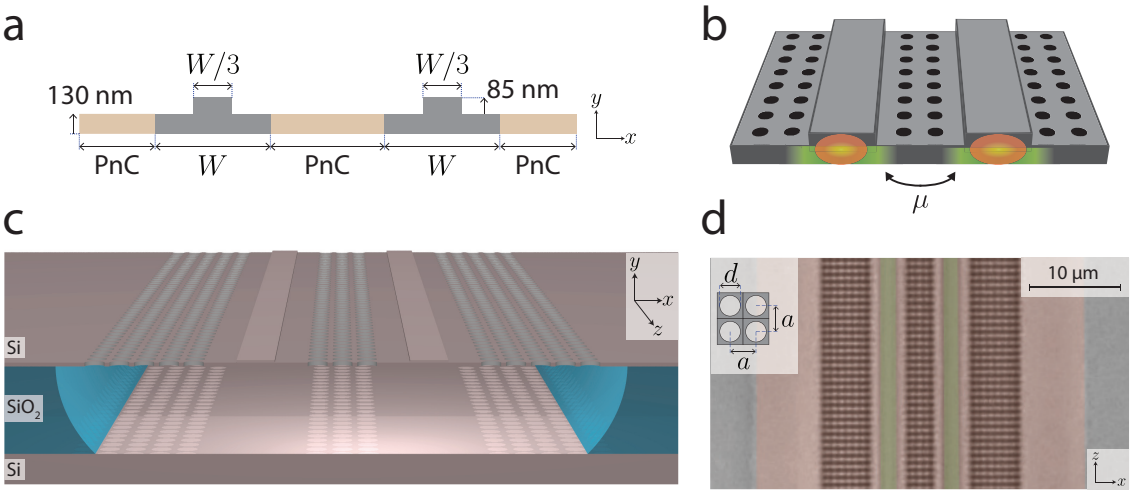

Figure 6.3: **(a)** Cross-section of a two-pole PPER device, consisting of two rib waveguides and phononic crystal (PnC) regions. **(b)** Illustration of the device, showing the optical modes in the rib waveguides (orange), and the acoustic modes (green) confined between the phononic crystal regions. **(c)** Artistic illustration of the device, showing the under etched region under the Brillouin-active waveguides. **(d)** Micrograph of a fabricated device, with enhanced colors to show the rib optical waveguides (green), and the phononic crystal regions. Adapted from Refs. [154] and [156].

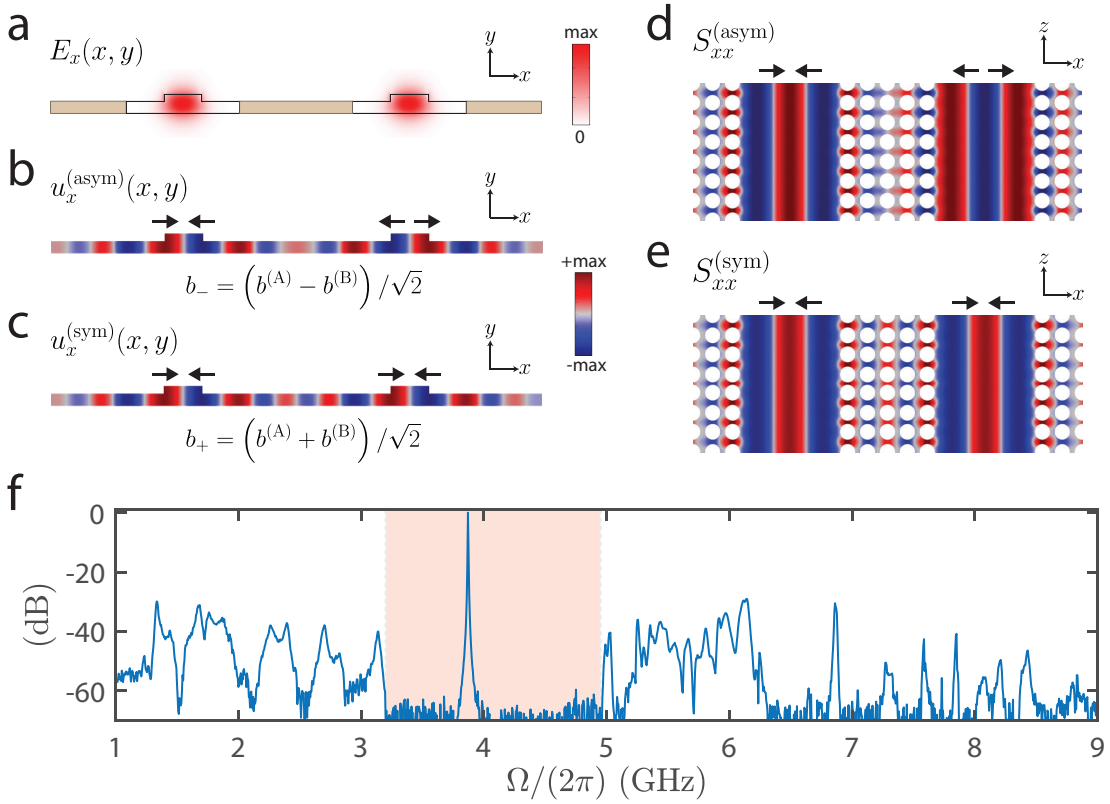

Figure 6.4: **(a)** FEM simulation of the x component of the electric fields in a two-pole PPER device. The shaded areas represent the phononic crystal regions. **(b)** Simulation of the x component of the displacement of the anti-symmetric acoustic super-mode, which can be interpreted as a linear combination of the two spatial acoustic modes. **(c)** Simulation of the x component of the displacement of the symmetric acoustic super-mode. **(d)** Simulation of the S_{xx} component of the strain tensor of the anti-symmetric acoustic super-mode. **(e)** Simulation of the S_{xx} component of the strain tensor of the symmetric acoustic super-mode. **(f)** Measured frequency response of a two-pole PPER device, showing the acoustic stop-band (shaded region) and an acoustic resonance at 3.9 GHz. Adapted from Refs. [154] and [156].

where μ is the coupling rate between the two acoustic modes, Γ the acoustic dissipation rate, and Ω_0 the resonant frequency of each of the two separate acoustic modes, which we assume are equal for both acoustic modes. The second-order response has very different characteristics compared to that of a single-pole PPER device, namely a fast frequency roll-off and high out-of-band suppression. This is demonstrated in Fig. 6.5(a), presenting the measured frequency response of a single-pole (top panel) and a two-pole PPER device (bottom panel). The resonances of the single-pole device follow a Lorentzian lineshape, and the structure supports multiple high-Q resonances. In contrast, the phononic crystal of the multi-pole device yields an acoustic stop-band, as well as suppression of out-of-band phonon modes. A comparison of the phonon lineshapes, seen in Fig. 6.5(b), shows the sharp frequency roll-off enabled by the multi-pole device, resulting in high out-of-band rejection, with >60 dB of suppression for frequencies >100 MHz from the filter center frequency, an improvement of 30 dB compared to an equivalent single-pole filter. This property is of great importance for applications such as channelizers, where different spectral bands may interfere in the absence of high out-of-band rejection [272]. Furthermore, the multi-pole pass-band can be designed to have a flatter frequency response when comparing to a typical Lorentzian lineshape, yielding a closer approximation of an ideal bandpass filter.

6.4.1 Tailoring frequency response through device geometry

In our design, the acoustic modes guided by the two waveguides are coupled in the central phononic crystal region, and we can control the coupling rate through the number of unit cells between the waveguide, i.e., the number of rows of holes. This is demonstrated experimentally in Figs. 6.6(a–c), showing the measured frequency response of three devices with a resonant frequency $\Omega_0/(2\pi) = 3.9$ GHz, with $N = 3, 4, 5$ rows of holes between the two acoustic waveguides, yielding fitted coupling rates $\mu/(2\pi) = 10.5, 5, 2$ MHz, respectively, and acoustic dissipation rates $\Gamma/(2\pi) = 4.6, 4.4, 5.1$ MHz. The two peaks in the frequency response are separated by $\delta\Omega = 2\mu[1 - (\Gamma/(2\mu))^2]^{1/2}$, which can be described as the frequency splitting resulting from the coupling of two degenerate acoustic modes, or equivalently, the frequencies of the two eigenmodes of the coupled system. When the

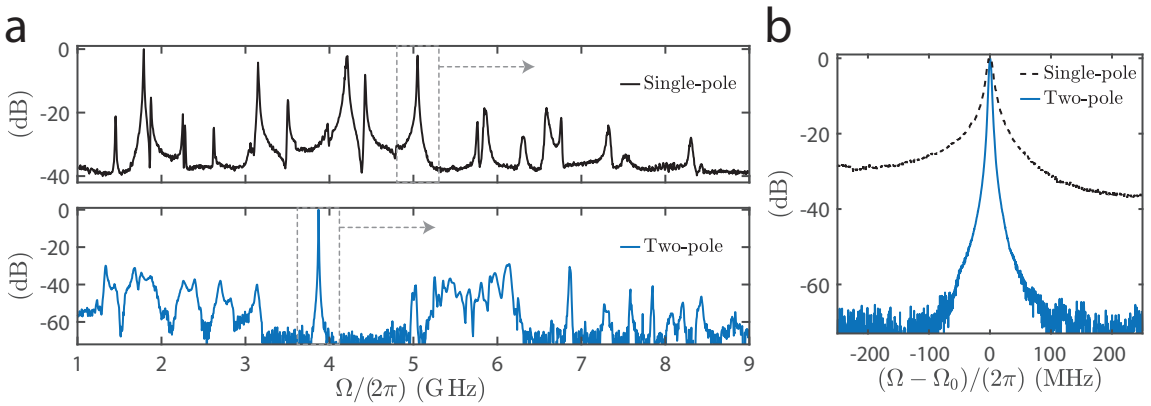

Figure 6.5: **(a)** Top: Measured frequency response of a single-pole PPER device, without a phononic crystal structure (such as was used in Ref. [187]), showing limited out-of-band suppression. Bottom: Measured frequency response of a two-pole PPER device using a phononic crystal structure, resulting in a stop-band, as well as suppression of spurious acoustic resonances. **(b)** Magnified view of the phonon resonances at 5 GHz of the single-pole device and 3.9 GHz of the two-pole device, shifted in frequency for comparison. Reproduced from Ref. [156].

coupling is smaller than half the dissipation rate ($\mu < \Gamma/2$), this yields a single-peaked line shape, as is the case for $N = 5$.

The forward Brillouin interaction can also be measured through spontaneous scattering, which occurs in the PPER devices as a result of the thermal occupation of the acoustic modes at room temperature, as was described in Chapter 3. The power spectrum of these fluctuations can be described by summing the contribution of the acoustic super-modes of the device (see Section 3.3.3), given by

$$|\chi_N(\Omega)|^2 = \frac{|V_+|^2}{(\Gamma/2)^2 + (\Omega - \Omega_0 + \mu)^2} + \frac{1 - |V_+|^2}{(\Gamma/2)^2 + (\Omega - \Omega_0 - \mu)^2}, \tag{6.2}$$

where V_+ is a parameter that takes into account possible asymmetry between the two phonon modes, which will be discussed in detail in Section 6.4.2. Figs. 6.6(d–f) show measured spontaneous Brillouin scattering of the three devices, demonstrating the frequency response for different coupling rates. The fitted coupling rates from the spontaneous measurements are $\mu/(2\pi) = 10.1, 4.6, 2$ MHz, in good agreement with the measurements from Figs. 6.6(a–c). Fig. 6.7(d) presents the measured acoustic coupling rates, showing how the coupling rate drops as hole rows are added, consistent with the decay of the acoustic field

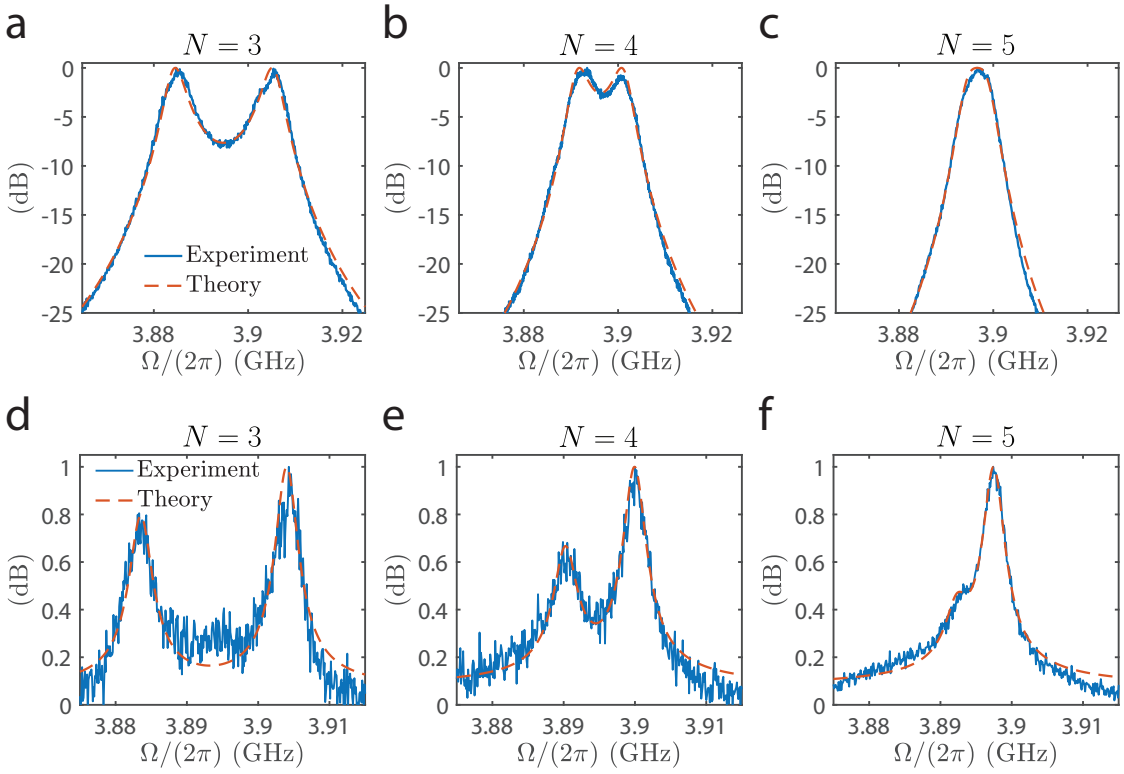

Figure 6.6: **(a–c)** Normalized measured frequency response of PPER filters with $N = 3, 4, 5$ rows of holes between the two acoustic defect regions, respectively. **(d–f)** Normalized measurements of spontaneous Brillouin scattering in the same three devices, revealing the thermal occupation of the two super-modes. The phononic crystal design used in these devices has a pitch of $a = 600$ nm and hole diameter of $d = 462$ nm, and the acoustic waveguides have a width of $W = 3.3$ μm. Reproduced from Ref. [156].

in the phononic crystal stop-band. The control over the coupling rate enables the design of different frequency responses, which will correspond to the filter lineshape, as shown in Figs. 6.7(e,f), where responses with two peaks and a single peak are demonstrated.

The acoustic resonant frequency can be tailored through the width of the acoustic waveguides, set by the distance between the phononic crystal regions, illustrated in Fig. 6.7(a). By fabricating devices with acoustic waveguide widths between 3–3.9 μm, the resonant frequency of the PPER operation was measured in the range 3.38–4.23 GHz, as shown in Fig. 6.7(b). The resonant frequency follows an inverse relation to the width ($\Omega_0 \propto W^{-1}$), seen in Fig. 6.7(c), demonstrating how the filter frequency can be tuned through the device geometry. We can see that the coupling rate is higher for wider waveguides, as seen in Fig 6.7(b), where the lower frequency resonances show a visible frequency splitting. These

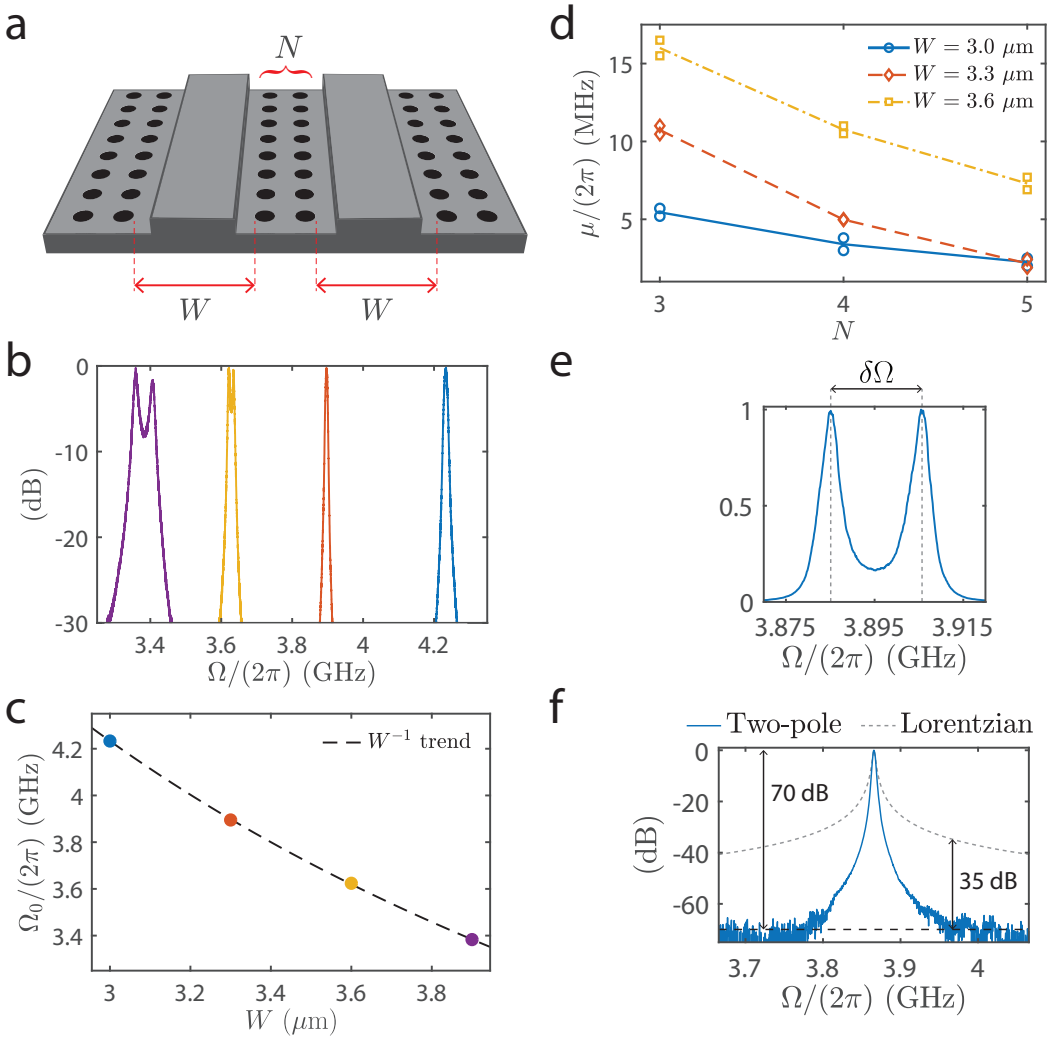

Figure 6.7: **(a)** A schematic illustration of a two-pole PPER device. The length W is the width of each waveguide, and N denotes the number of rows of holes in the center of the structure. **(b)** The measured resonant frequencies of devices fabricated with different waveguide widths. The difference in the filter lineshape is a result of the different coupling rates for different acoustic frequencies. The phononic crystal design used in these devices has a pitch of $a = 600$ nm and a hole diameter of $d = 462$ nm. **(c)** Measured Brillouin frequency, corresponding to the data in panel (b), showing an inverse relation between the frequency and width $\Omega_0 \propto W^{-1}$. **(d)** Fitted coupling rates (μ) for measured two-poles devices, with different numbers of rows of holes (N). The two data points at each value of N correspond to two different devices. **(e)** Measured frequency response of a device with $N = 3$ rows of holes, where the frequency splitting $\delta\Omega$ can be resolved, resulting in two peaks. **(f)** Measured frequency response of a device with $N = 5$ rows of holes, where the frequency splitting cannot be resolved, yielding a single peak. A single-pole Lorentzian lineshape is shown for reference. Adapted from Ref. [156].

correspond to lower frequency modes, having longer wavelengths, such that effectively the distance between the two waveguides is shorter.

6.4.2 Non-identical acoustic modes

In our analysis so far, we have considered the two acoustic modes to be identical, as the design of the two-pole PPER device is completely symmetric, i.e., we are coupling two identical structures. However, fabrication imperfections and material nonuniformity can lead to an asymmetry between the two acoustic modes. A deviation of a few nanometers, well below fabrication tolerances, can lead to ∼MHz shift in the acoustic resonance frequency, which can have a measurable effect.

To take possible asymmetry into account, we describe the acoustic modes of each of the two coupled waveguides using two different frequencies, $\Omega_0^{(\mathrm{A})}$ and $\Omega_0^{(\mathrm{B})}$. Following the description in Chapter 3 (see Section 3.3.3), we can write the acoustic part of the Hamiltonian describing two coupled acoustic modes with a coupling rate μ

$$H_{\mathrm{ac}} = \hbar \int dz \begin{pmatrix} b^{(\mathrm{A})\dagger} & b^{(\mathrm{B})\dagger} \end{pmatrix} \begin{pmatrix} \Omega_0^{(\mathrm{A})} & \mu \\ \mu^* & \Omega_0^{(\mathrm{B})} \end{pmatrix} \begin{pmatrix} b^{(\mathrm{A})} \\ b^{(\mathrm{B})} \end{pmatrix}. \tag{6.3}$$

The matrix in Eq. (6.3) is Hermitian, and we can diagonalize it using a unitary matrix V such that

$$\begin{pmatrix} \Omega_+ & 0 \\ 0 & \Omega_- \end{pmatrix} = V^\dagger \begin{pmatrix} \Omega_0^{(\mathrm{A})} & \mu \\ \mu^* & \Omega_0^{(\mathrm{B})} \end{pmatrix} V, \tag{6.4}$$

where $\Omega_\pm$ are the eigenfrequencies of the coupled system, and the eigenmodes are given by

$$\begin{pmatrix} b_+ \\ b_- \end{pmatrix} = V^\dagger \begin{pmatrix} b^{(\mathrm{A})} \\ b^{(\mathrm{B})} \end{pmatrix}. \tag{6.5}$$

The eigenfrequencies are given by

$$\Omega_\pm = \Omega_0 \pm \sqrt{\left(\frac{\Delta\Omega}{2}\right)^2 + |\mu|^2}, \tag{6.6}$$

where we have defined the average frequency $\Omega_0 = (\Omega_0^{(\mathrm{A})} + \Omega_0^{(\mathrm{B})})/2$ and the frequency difference $\Delta\Omega = \Omega_0^{(\mathrm{B})} - \Omega_0^{(\mathrm{A})}$. The elements of the unitary matrix V are given by

$$V_{\pm}^{(\mathrm{A})} = \frac{1}{\mathcal{N}_{\pm}} \left(-\frac{\Delta\Omega}{2\,|\mu|} \pm \sqrt{1 + \left(\frac{\Delta\Omega}{2\,|\mu|}\right)^2} \right), \qquad V_{\pm}^{(\mathrm{B})} = \frac{1}{\mathcal{N}_{\pm}} \arg(\mu), \tag{6.7}$$

with the normalization factor

$$\mathcal{N}_{\pm} = \sqrt{1 + \left| \frac{\Delta\Omega}{2|\mu|} \mp \sqrt{1 + \left(\frac{\Delta\Omega}{2|\mu|}\right)^2} \right|^2}. \tag{6.8}$$

Here, we have used the notation

$$V = \begin{pmatrix} V_+^{(\mathrm{A})} & V_-^{(\mathrm{A})} \\ V_+^{(\mathrm{B})} & V_-^{(\mathrm{B})} \end{pmatrix} \tag{6.9}$$

to refer to the different matrix elements.

Since the diagonalizing matrix V is unitary, the matrix elements follow the relations

$$\left|V_+^{(\mathrm{A})}\right|^2 + \left|V_-^{(\mathrm{A})}\right|^2 = 1, \qquad \left|V_+^{(\mathrm{B})}\right|^2 + \left|V_-^{(\mathrm{B})}\right|^2 = 1, \qquad V_{\pm}^{(\mathrm{B})} V_{\pm}^{(\mathrm{A})*} + V_{\mp}^{(\mathrm{B})} V_{\mp}^{(\mathrm{A})*} = 0, \tag{6.10}$$

which is equivalent to the orthonormality of the eigenbasis. Figs. 6.8(a,b) show the dependence of the eigenfrequencies and the coefficients $V_{\pm}^{(\ell)}$ on the asymmetry between the two acoustic modes. We can see that in the case of two identical modes, the frequency difference between the eigenmodes is exactly twice the coupling rate, and the coefficients are equal in magnitude $|V_{\pm}^{(\ell)}|^2 = 1/2$. When asymmetry is introduced, the frequency splitting grows, and the coefficients are no longer equal.

The equations of motion describing the optical and acoustic modes in the two waveguides

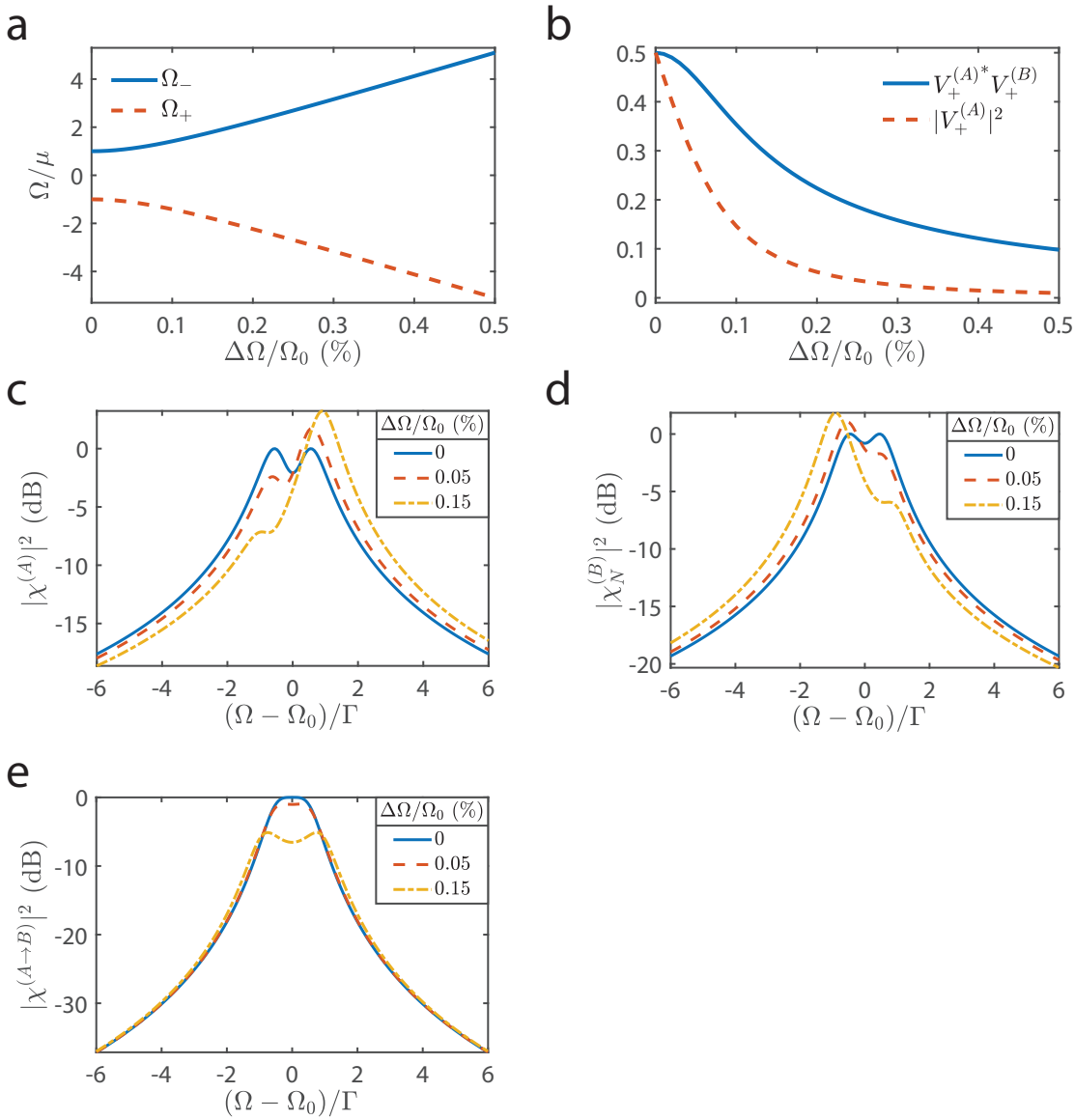

Figure 6.8: **(a)** Calculated acoustic eigenfrequencies of a PPER device, as a function of the asymmetry between the two acoustic modes. **(b)** The coefficients determining the frequency response (Eq. (6.7)) as a function of asymmetry between the acoustic modes. **(c)** The frequency response of the phase modulation experienced by the field propagating in the 'emit' waveguide, for different amounts of asymmetry. **(d)** The power spectrum of spontaneous Brillouin scattering in the 'receive' waveguide, for different amounts of asymmetry. **(e)** The filter shape of a PPER operation, for different amounts of asymmetry. The calculations assume $\Omega_0/\Gamma = 1000$ and $\mu = \Gamma/2$. Reproduced from Ref. [156].

of the PPER, as were derived in Chapter 3, are given by

$$\begin{aligned} b_{\pm} &= \left(\frac{1}{\Omega-\Omega_{\pm}+i\frac{\Gamma}{2}}\right)\sum_n\left(g_{\pm}^{(\mathrm{A})^*}a_n^{(\mathrm{A})}{a_{n-1}^{(\mathrm{A})}}^{\dagger}+g_{\pm}^{(\mathrm{B})^*}a_n^{(\mathrm{B})}{a_{n-1}^{(\mathrm{B})}}^{\dagger}\right),\\ \frac{\partial}{\partial z}a_n^{(\mathrm{A})} &= -\frac{i}{v}\Big(g_+^{(\mathrm{A})}a_{n-1}^{(\mathrm{A})}b_+ + g_+^{(\mathrm{A})^*}a_{n+1}^{(\mathrm{A})}b_+^{\dagger}+g_-^{(\mathrm{A})}a_{n-1}^{(\mathrm{A})}b_- + g_-^{(\mathrm{A})^*}a_{n+1}^{(\mathrm{A})}b_-^{\dagger}\Big),\\ \frac{\partial}{\partial z}a_n^{(\mathrm{B})} &= -\frac{i}{v}\Big(g_+^{(\mathrm{B})}a_{n-1}^{(\mathrm{B})}b_+ + g_+^{(\mathrm{B})^*}a_{n+1}^{(\mathrm{B})}b_+^{\dagger}+g_-^{(\mathrm{B})}a_{n-1}^{(\mathrm{B})}b_- + g_-^{(\mathrm{B})^*}a_{n+1}^{(\mathrm{B})}b_-^{\dagger}\Big). \end{aligned} \tag{6.11}$$

Here, A and B denote the 'emit' and 'receive' waveguides of the PPER, respectively, v is the optical group velocity of the guided optical modes, and we have absorbed the coefficients V into the acousto-optic coupling rates g, such that $g_{\pm}^{(\ell)} = g^{(\ell)}V_{\pm}^{(\ell)}$. Following the derivation presented earlier (see Section 3.3.1), the phonon fields in the PPER structure are given by

$$b_{\pm} \propto -i\chi_{\pm}g_{\pm}^{(\mathrm{A})^*}\left|a_0^{(\mathrm{A})}(0)\right|^2, \tag{6.12}$$

where we have defined the frequency responses $\chi_{\pm} = [i(\Omega_{\pm}-\Omega)+\Gamma/2]^{-1}$. Substituting this expression into the equations of motion of the optical fields yields

$$\begin{aligned} \frac{\partial}{\partial z}a_n^{(\mathrm{A})} \propto -\frac{1}{v}\left|a_0^{(\mathrm{A})}(0)\right|^2\Big[&a_{n-1}^{(\mathrm{A})}e^{i\Lambda}\left(\chi_+\left|g_+^{(\mathrm{A})}\right|^2+\chi_-\left|g_-^{(\mathrm{A})}\right|^2\right)\\ &-a_{n+1}^{(\mathrm{A})}e^{-i\Lambda}\left(\chi_+^*\left|g_+^{(\mathrm{A})}\right|^2+\chi_-^*\left|g_-^{(\mathrm{A})}\right|^2\right)\Big],\\ \frac{\partial}{\partial z}a_n^{(\mathrm{B})} \propto -\frac{1}{v}\left|a_0^{(\mathrm{A})}(0)\right|^2\Big[&a_{n-1}^{(\mathrm{B})}e^{i\Lambda}\left(\chi_+g_+^{(\mathrm{B})}g_+^{(\mathrm{A})^*}+\chi_-g_-^{(\mathrm{B})}g_-^{(\mathrm{A})^*}\right)\\ &-a_{n+1}^{(\mathrm{B})}e^{-i\Lambda}\left(\chi_+^*g_+^{(\mathrm{B})^*}g_+^{(\mathrm{A})}+\chi_-^*g_-^{(\mathrm{B})^*}g_-^{(\mathrm{A})}\right)\Big]. \end{aligned} \tag{6.13}$$

We factor out the coupling rate $g_{\pm}^{(l)} = g^{(l)}V_{\pm}^{(l)}$, leaving us with

$$\begin{aligned} \frac{\partial}{\partial z}a_n^{(\mathrm{A})} &\propto -\frac{1}{v}\left|a_0^{(\mathrm{A})}(0)\right|^2\left|g^{(\mathrm{A})}\right|^2\left|\chi^{(\mathrm{A})}\right|\left(a_{n-1}^{(\mathrm{A})}e^{i\phi^{(\mathrm{A})}}-a_{n+1}^{(\mathrm{A})}e^{-i\phi^{(\mathrm{A})}}\right),\\ \frac{\partial}{\partial z}a_n^{(\mathrm{B})} &\propto -\frac{1}{v}\left|a_0^{(\mathrm{A})}(0)\right|^2\left|g^{(\mathrm{B})}g^{(\mathrm{A})^*}\right|^2\left|\chi^{(\mathrm{A}\to\mathrm{B})}\right|\left(a_{n-1}^{(\mathrm{B})}e^{i\phi^{(\mathrm{A}\to\mathrm{B})}}-a_{n+1}^{(\mathrm{B})}e^{-i\phi^{(\mathrm{A}\to\mathrm{B})}}\right), \end{aligned} \tag{6.14}$$

where we have defined the frequency response in each waveguide

$$\chi^{(\mathrm{A})} = \left[\chi_+\left|V_+^{(\mathrm{A})}\right|^2+\chi_-\left|V_-^{(\mathrm{A})}\right|^2\right], \qquad \chi^{(\mathrm{A}\to\mathrm{B})} = \left[\chi_+V_+^{(\mathrm{B})}V_+^{(\mathrm{A})^*}+\chi_-V_-^{(\mathrm{B})}V_-^{(\mathrm{A})^*}\right], \tag{6.15}$$

and denoted the phase responses $\phi^{(\mathrm{A})} = \arg(\chi^{(\mathrm{A})})$, $\phi^{(\mathrm{A}\to\mathrm{B})} = \arg(\chi^{(\mathrm{A}\to\mathrm{B})})$. Using the unitary relations from Eq. (6.10) we can rewrite these frequency responses as

$$\chi^{(\mathrm{A})} = \left[\chi_+ \left|V_+^{(\mathrm{A})}\right|^2 + \chi_- \left(1 - \left|V_+^{(\mathrm{A})}\right|^2\right)\right], \qquad \chi^{(\mathrm{A}\to\mathrm{B})} = V_+^{(\mathrm{B})} V_+^{(\mathrm{A})*}\Big[\chi_+ - \chi_-\Big]. \tag{6.16}$$

The frequency response $\chi^{(\mathrm{A}\to\mathrm{B})}$ describes the filter lineshape obtained in the PPER operation (transducing information from waveguide A to B), whereas $\chi^{(\mathrm{A})}$ describes the frequency response of the phase modulation experienced by the optical field propagating through the 'emit' waveguide. We can also analyze the spectrum of spontaneous Brillouin scattering, calculated by an incoherent sum of the two acoustic super-modes. The resulting power spectrum of these thermal fluctuations in waveguide B (which can determine the noise floor of a PPER-based photonic filter, for example) is given by

$$\left|\chi_N^{(\mathrm{B})}\right|^2 = \left[|\chi_+|^2 \left|V_+^{(\mathrm{B})}\right|^2 + |\chi_-|^2 \left(1 - \left|V_+^{(\mathrm{B})}\right|^2\right)\right]. \tag{6.17}$$

Figs. 6.8(c–e) present calculated frequency responses for different amounts of asymmetry in the two acoustic modes using Eqs. (6.16) and (6.17), showing that $\chi^{(\mathrm{A}\to\mathrm{B})}$ stays symmetric around the pass-band center, even in the case of non-identical acoustic modes. In contrast, the functions $\chi^{(\mathrm{A})}$ and $|\chi_N^{(\mathrm{B})}|$ show increasing asymmetry for larger values of $\Delta\Omega$. Additionally, we see that $\chi^{(\mathrm{A})}$ and $\chi_N^{(\mathrm{B})}$ are mirrored across the center frequency when switching the roles of 'emit' and 'receive' waveguides, i.e., looking at the responses $\chi^{(\mathrm{B})}$ and $\chi_N^{(\mathrm{A})}$. The effects of this assymetry can be demonstrated experimentally, as seen in Fig. 6.9, showing the measured frequency response of spontaneous scattering (panels (a,b)), and forward Brillouin-induced phase modulation (panels (c,d)). As can be seen from the data, the asymmetric line shapes are mirrored through the center of the trace when switching between waveguides A and B, as expected from Eqs. (6.16) and (6.17). The measurements are consistent with an asymmetry of $\Delta\Omega = 2.65 \pm 0.5$ MHz, corresponding to a deviation of 0.03% per waveguide from the average frequency, which can be a result of variations on the order of ∼2 nm in the geometry of each of the two acoustic guiding structures. In contrast, Fig. 6.9(e) shows that the PPER filter response does not change when switching the roles of

'emit' and 'receive' between waveguides A and B (i.e., $\chi^{(\mathrm{A}\to\mathrm{B})} = \chi^{(\mathrm{B}\to\mathrm{A})}$), consistent with Eq. (6.16).

6.4.3 Effects of optical cross-talk

Up to this point, we have assumed that there is no optical cross-talk between the 'emit' and 'receive' waveguides. This is a good assumption, as the optical guiding regions of the waveguides are separated by a distance larger than the optical wavelength scale. A measurement of the optical cross-talk in a two-pole PPER device is presented in Fig. 6.10(f), showing −60 dB of optical cross-talk. However, residual coupling occurring in other parts of the chip could affect the filter lineshape obtained in a PPER operation and should be considered. Using Eq. (6.11), and assuming optical cross-talk ε from waveguide A to B, the phonon field can be described by

$$b_\pm \propto -i\chi_\pm \left(g_\pm^{(\mathrm{A})^*} + \varepsilon g_\pm^{(\mathrm{B})^*}\right) \left|a_0^{(\mathrm{A})}(0)\right|^2, \tag{6.18}$$

where we have assumed $|\varepsilon| \ll 1$ such that we can neglect the energy lost in waveguide A, and we have denoted the frequency response $\chi_\pm = [i(\Omega_\pm - \Omega) + \Gamma/2]^{-1}$. Plugging back into Eq. (6.11) gives us the equation of motion for the optical field in waveguide B

$$\begin{aligned}\frac{\partial}{\partial z} a_n^{(\mathrm{B})} \propto -\frac{1}{v}\left|a_0^{(\mathrm{A})}(0)\right|^2 \Bigg(& a_{n-1}^{(\mathrm{B})}\left[\chi_+\left(g_+^{(\mathrm{B})} g_+^{(\mathrm{A})^*} + \varepsilon\left|g_+^{(\mathrm{B})}\right|^2\right) + \chi_-\left(g_-^{(\mathrm{B})} g_-^{(\mathrm{A})^*} + \varepsilon\left|g_-^{(\mathrm{B})}\right|^2\right)\right] \\ & - a_{n+1}^{(\mathrm{B})}\left[\chi_+^*\left(g_+^{(\mathrm{B})^*} g_+^{(\mathrm{A})} + \varepsilon^*\left|g_+^{(\mathrm{B})}\right|^2\right) + \chi_-^*\left(g_-^{(\mathrm{B})^*} g_-^{(\mathrm{A})} \varepsilon^*\left|g_-^{(\mathrm{B})}\right|^2\right)\right]\Bigg).\end{aligned} \tag{6.19}$$

We factor out the rate g, yielding

$$\frac{\partial a_n^{(\mathrm{B})}}{\partial z} \propto -\frac{1}{v}|g|^2 \left|a_0^{(\mathrm{A})}(0)\right|^2 \left|\widetilde{\chi}^{(\mathrm{A}\to\mathrm{B})}\right| \left(a_{n-1}^{(\mathrm{B})} e^{i\widetilde{\phi}^{(\mathrm{B})}} - a_{n+1}^{(\mathrm{B})} e^{-i\widetilde{\phi}^{(\mathrm{B})}}\right), \tag{6.20}$$

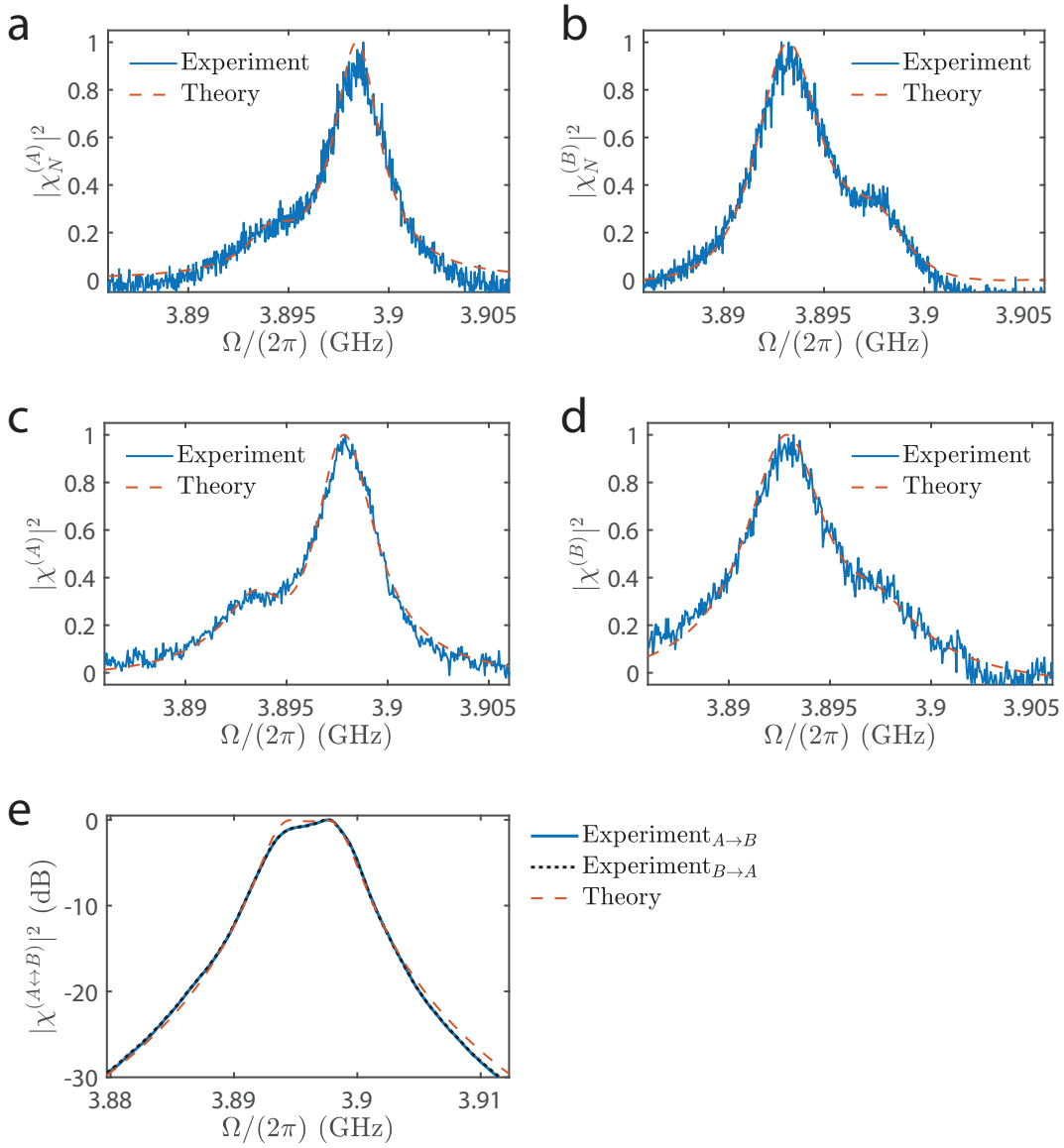

Figure 6.9: **(a)** Normalized power spectrum of spontaneous Brillouin scattering in the 'emit' waveguide. **(b)** Normalized power spectrum of spontaneous Brillouin scattering in the 'receive' waveguide, showing a mirrored lineshape. **(c)** Normalized frequency response of the phase modulation experienced by an optical field propagating in the 'emit' waveguide. **(d)** Normalized frequency response of the phase modulation experienced by an optical field propagating in the 'receive' waveguide, showing a mirrored lineshape. **(e)** The two-pole filter lineshape of a PPER operation is identical for both possible choices of 'emit' and 'receive' waveguides. Reproduced from Ref. [156].

where $\widetilde{\phi}^{(\mathrm{A}\to\mathrm{B})} = \arg(\widetilde{\chi}^{(\mathrm{A}\to\mathrm{B})})$ and the frequency response is given by

$$\widetilde{\chi}^{(\mathrm{A}\to\mathrm{B})} = \left[\left(V_+^{(\mathrm{B})} V_+^{(\mathrm{A})^*} + \varepsilon \left| V_+^{(\mathrm{B})} \right|^2 \right) \chi_+ - \left(V_+^{(\mathrm{B})} V_+^{(\mathrm{A})^*} - \varepsilon \left(1 - \left| V_+^{(\mathrm{B})} \right|^2 \right) \right) \chi_- \right]. \quad (6.21)$$

We can see that even in the case of two identical acoustic modes, such that $V_+^{(\mathrm{B})} V_+^{(\mathrm{A})^*} = |V_+^{(\mathrm{B})}|^2 = 1/2$, we have

$$\widetilde{\chi}^{(\mathrm{A}\to\mathrm{B})} = \frac{1}{2}\Big[(1+\varepsilon)\,\chi_+ - (1-\varepsilon)\,\chi_- \Big], \quad (6.22)$$

revealing the asymmetric response as a result of the non-negligible cross-talk, seen in Fig. 6.10(a). This line shape can be slightly altered when considering a phase shift induced in the coupling, equivalent to a complex-valued ε.

6.4.4 Effects of Kerr nonlinearities

When optical cross-talk occurs in the device, we should consider the effects of Kerr-induced four-wave-mixing in the 'receive' waveguide, which also occurs in the silicon waveguides [64]. The interplay between Kerr and forward Brillouin nonlinearities alters the lineshape of the Brillouin frequency response [176, 279], and needs to be taken into account for practical applications [280]. Analyzing one of the optical sidebands ($n = -1$ in this example), we can write the contribution of both Brillouin and Kerr nonlinearities [44]

$$\frac{\partial}{\partial z} a_{-1}^{(\mathrm{B})} \propto -i \left[\frac{G_\mathrm{B}\Gamma}{4} \widetilde{\chi}^{(\mathrm{A}\to\mathrm{B})} + 2\varepsilon\gamma_\mathrm{Kerr} \right] \left| a_0^{(\mathrm{A})}(0) \right|^2 a_0^{(\mathrm{B})}, \quad (6.23)$$

where $G_\mathrm{B} = 4|g|^2/(\hbar\omega\Gamma v^2)$ is the Brillouin gain coefficient, Γ the acoustic dissipation rate, $\widetilde{\chi}^{(\mathrm{A}\to\mathrm{B})}$ the Brillouin frequency response from Eq. (6.22), and γ_Kerr is the Kerr coefficient. We assume that the Kerr nonlinearity has no frequency dependence over the bandwidth of interest, as it is typically a wideband effect (∼500 GHz) compared to the Brillouin frequency response (∼5 MHz). In the silicon structures we are studying here, the Kerr coefficient is an order of magnitude smaller than that of the Brillouin gain [64]. Figs. 6.10(b–e) show calculated filter line shapes when including optical cross-talk and four-wave-mixing,

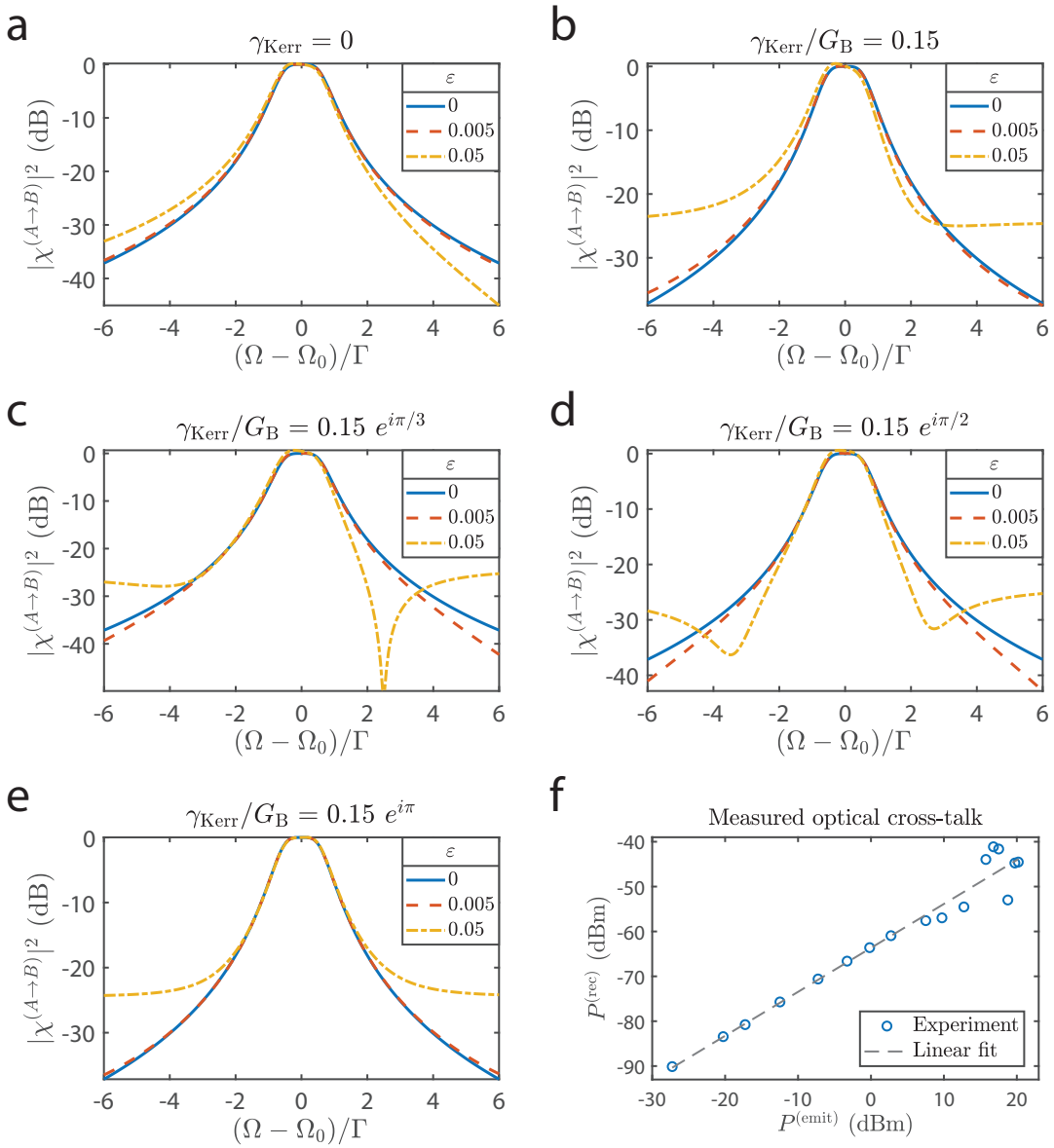

Figure 6.10: **(a)** Calculated two-pole filter lineshapes of a PPER operation, including different amounts of optical cross-talk ε. **(b–e)** Calculated two-pole filter lineshapes of a PPER operation including optical cross-talk and Kerr-induced four-wave-mixing, showing how different relative phases between the Brillouin and Kerr nonlinearities result in different lineshapes. The calculations assume $\Omega_0/\Gamma = 1000$ and $\mu = \Gamma/2$. **(f)** Measured cross-talk in a two-pole PPER device, showing -60 dB of optical power leaking from the 'emit' to the 'receive' waveguide. $P^{(\mathrm{emit})}$ is the optical power injected into waveguide A and $P^{(\mathrm{rec})}$ is the optical power measured at the output of waveguide B. Reproduced from Ref. [156].

assuming $|\gamma_{\mathrm{Kerr}}/G_{\mathrm{B}}| = 0.15$. Since these are coherent processes, varying the phase between the two nonlinear contributions will yield different line shapes. This phase difference can be a result of the optical coupling mechanism leading to the cross-talk, as well as the phase difference between the optical fields in waveguides A and B. The Kerr coefficient has a small magnitude compared to the Brillouin contribution, hence the four-wave-mixing results in a small change to the line shape at the center of the filter pass-band. Appreciable deviation is only seen at frequencies outside the half-maximum of the response and can be neglected in many practical cases (such as filtering).

6.4.5 Third-order filters

The PPER-based filtering scheme can be extended to higher-order filters by coupling more acoustic modes, as was discussed in Chapter 3. For example, when coupling three identical acoustic modes (b_{A}, b_{B}, b_{C}), with a resonant frequency Ω_0, dissipation rate Γ, and nearest-neighbor coupling rate μ, the frequency response is given by

$$\left|\chi^{(3\text{ pole})}(\Omega)\right|^2 \propto \frac{\mu^4}{\left[(\Gamma/2)^2+(\Omega-\Omega_-)^2\right]\left[(\Gamma/2)^2+(\Omega-\Omega_0)^2\right]\left[(\Gamma/2)^2+(\Omega-\Omega_+)^2\right]}. \tag{6.24}$$

The three super-modes of the coupled system are

$$b_- = \left(b_{\mathrm{A}} - \sqrt{2}\, b_{\mathrm{B}} + b_{\mathrm{C}}\right)/2, \qquad b_0 = \left(b_{\mathrm{A}} - b_{\mathrm{C}}\right)/\sqrt{2}, \qquad b_+ = \left(b_{\mathrm{A}} + \sqrt{2}\, b_{\mathrm{B}} + b_{\mathrm{C}}\right)/2, \tag{6.25}$$

with frequencies

$$\Omega_- = \Omega_0 + \sqrt{2}\mu, \qquad \Omega_0, \qquad \Omega_+ = \Omega_0 - \sqrt{2}\mu. \tag{6.26}$$

A three-pole PPER device is schematically illustrated in Fig. 6.11(a), where three acoustic waveguides of width W are coupled through N rows of holes. Simulation of the acoustic super-modes supported by the structure are presented in Fig. 6.11(b), consistent with Eq. (6.25).

We fabricate such three-pole PPER devices, with $N = 3, 4, 5$ rows of holes between each of the acoustic waveguides, an example of which is shown in Fig. 6.11(c). Measurements of

the frequency response are presented in Figs. 6.11(d–f), and the fitted parameters are consistent with a phonon frequency $\Omega_0/(2\pi) = 4.24$ GHz, coupling rates $\mu/(2\pi) = 7.5, 2.1, 1.8$ MHz, respectively, and acoustic dissipation rates $\Gamma/(2\pi) = 7, 7.7, 9.3$ MHz. The non-ideal lineshapes obtained in the measurements can be the consequence of the larger device structure, resulting in a wider suspended region, as well as the need to define more holes in the phononic crystal, which can lead to a larger degree of nonuniformity in the fabrication process, deviating from theory [281]. The devices presented in this work were all fabricated using a two-step electron-beam lithography process which can suffer from drift, however, implementation of these designs using photolithography may yield higher uniformity and

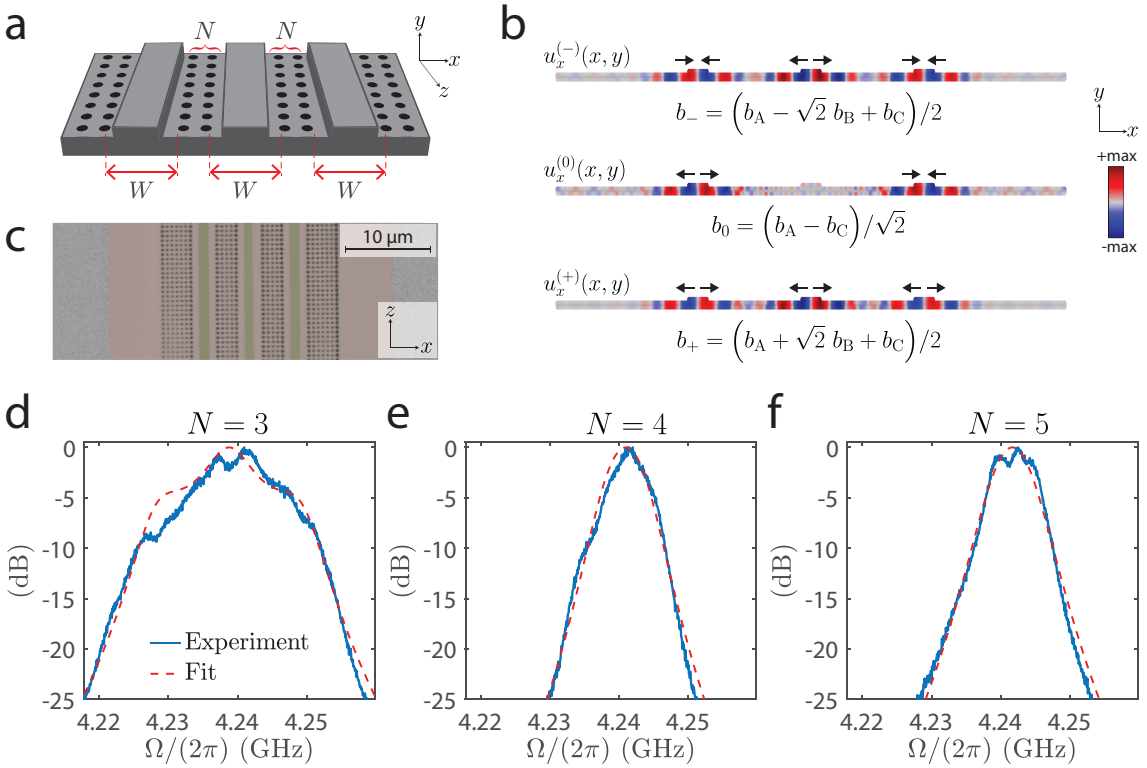

Figure 6.11: **(a)** An illustration of a three-pole device, showing the three waveguides of width W, with nearest-neighbor coupling through N rows of holes. **(b)** FEM simulation of the x component of the displacement (u_x) of the three acoustic super-modes taking part in the PPER operation. **(c)** Micrograph image with enhanced colors of a top-down view of a fabricated three-pole PPER device. **(d–f)** Normalized measured frequency response of three-pole PPER filters with $N = 3, 4, 5$ rows of holes between the acoustic waveguides, respectively. The phononic crystal design used in these devices had a pitch of $a = 600$ nm, hole diameter of $d = 462$ nm, and a waveguide width of $W = 3$ μm. Adapted from Ref. [156].

more ideal line shapes (see Section 6.6 for more details).

6.5 Spatially-distributed Brillouin-active segments

The control over the PPER frequency response through the device geometry, combined with the strong forward Brillouin scattering in silicon, enables us to measure the response from short active segments, with higher spatial resolution than previously demonstrated [239, 282]. This can be achieved by designing a PPER device with multiple active regions, each supporting a different resonant frequency. Through the design, we know which resonance corresponds to each segment, enabling us to monitor the frequency response of different regions on the chip, as illustrated in Fig. 6.12(a).

We demonstrate cascaded PPER sections experimentally by measuring four 50 μm long PPER segments with acoustic waveguide widths varying by 60 nm between segments (the active PPER region design follows Ref. [187]), as seen in Figs. 6.12(b,c). The measured frequency shifts by 1.18 MHz per nanometer, and the 20 dB signal-to-noise suggests that a measurable signal could be detected using sub-micron active-length segments. A second demonstration, seen in Figs. 6.12(d,e), shows measurement from four two-pole PPER segments, where the acoustic waveguide width is varied by 15 nm between segments, resulting in the resonant frequency shifting by 0.62 MHz per nanometer. Given the $\sim$3 MHz linewidths of the resonances, we can expect to resolve a change of acoustic waveguide dimensions on the order of single nanometers. As the acoustic response is affected by temperature, strain, and mass, devices of this type could be used as on-chip sensors, and could, for example, detect the bonding of different chemical compounds to the surface of the material [275,276].

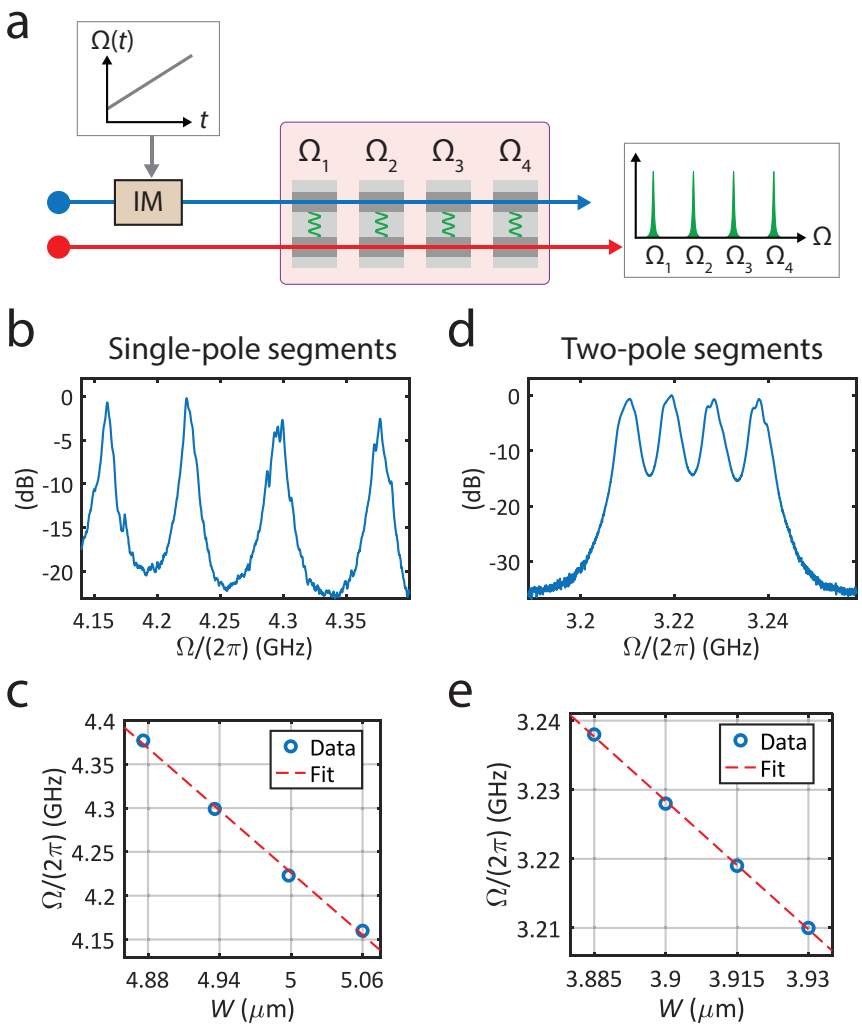

Figure 6.12: **(a)** Schematic illustration of the measurement scheme. An RF tone driving an intensity modulator is swept, and the demodulated output signal is measured using a spectrum analyzer. **(b)** Measurement of a PPER device with four active segments (following the device design from Ref. [187]). Each segment is 50 μm long, with an increase of 60 nm in acoustic waveguide width between segments, resulting in well-resolved peaks with a bandwidth of $\sim$4 MHz. **(c)** Fitting the acoustic resonant frequency (the peaks from panel (b)) as a function of waveguide width results in a linear slope of 1.1836 MHz/nm. **(d)** Measurement of a two-pole PPER device with four 500 μm long active segments. The acoustic waveguide width between segments is increased by 15 nm, resulting in peaks with a bandwidth of $\sim$3 MHz. **(e)** Fitting the peaks from panel (d) results in a slope of 0.62 MHz/nm. The factor $\sim$2 difference in the fitted slopes between panels (c) and (e) is a consequence of the different acoustic modes used in the single-pole PPER segments compared to the two-pole PPER segments.

6.6 Device fabrication

The Brillouin-active PPER devices presented in this chapter were fabricated in a standard silicon-on-insulator (SOI) material platform, using standard silicon processing methods. In this section, we will present devices fabricated using both electron-beam lithography and photolithography, demonstrating the repeatable results enabled by using these well-established fabrication methods.

6.6.1 Yale fabrication process

The measurements presented up until now were of devices fabricated using electron-beam lithography at Yale University in the Applied Physics Cleanroom[1] and the Yale Institute for Nanoscience and Quantum Engineering (YINQE)[2]. First, Cr/Au alignment markers were defined on a 6″ silicon-on-insulator (SOI) wafer using electron-beam lithography and a liftoff procedure, after which the wafer was diced into 35 × 22 mm rectangular chips. Next, an electron-beam lithography step defines the optical waveguide rib structures using hydrogen silsesquioxane (HSQ) electron-beam resist (XR1541 6%), development in MF-312, and a Cl_2 reactive ion etch (RIE), removing 80 nm of silicon. A second lithography step is used to define the array of holes and slots using either ZEP520A or CSAR electron-beam resist, followed by development in Xylenes. The remainder of the silicon is removed through another Cl_2 RIE, exposing the oxide. Finally, a wet-etch using 49% hydrofluoric (HF) acid removes the oxide under-cladding to suspended the Brillouin-active sections.

The fabricated devices exhibit highly repeatable and consistent results, which we demonstrate by fabricating 16 two-pole PPER devices on the same chip. All of the devices show good performance (100% yield), exhibiting a two-pole lineshape with a bandwidth of a few MHz, seen in 6.13(a). Fitted parameters are displayed in Fig. 6.13(b), demonstrating high consistency. The lineshapes vary slightly between devices, consistent with different design parameters in the geometry of each device such as the number of hole rows between the

1. https://cleanroom.yale.edu

2. https://nano.yale.edu

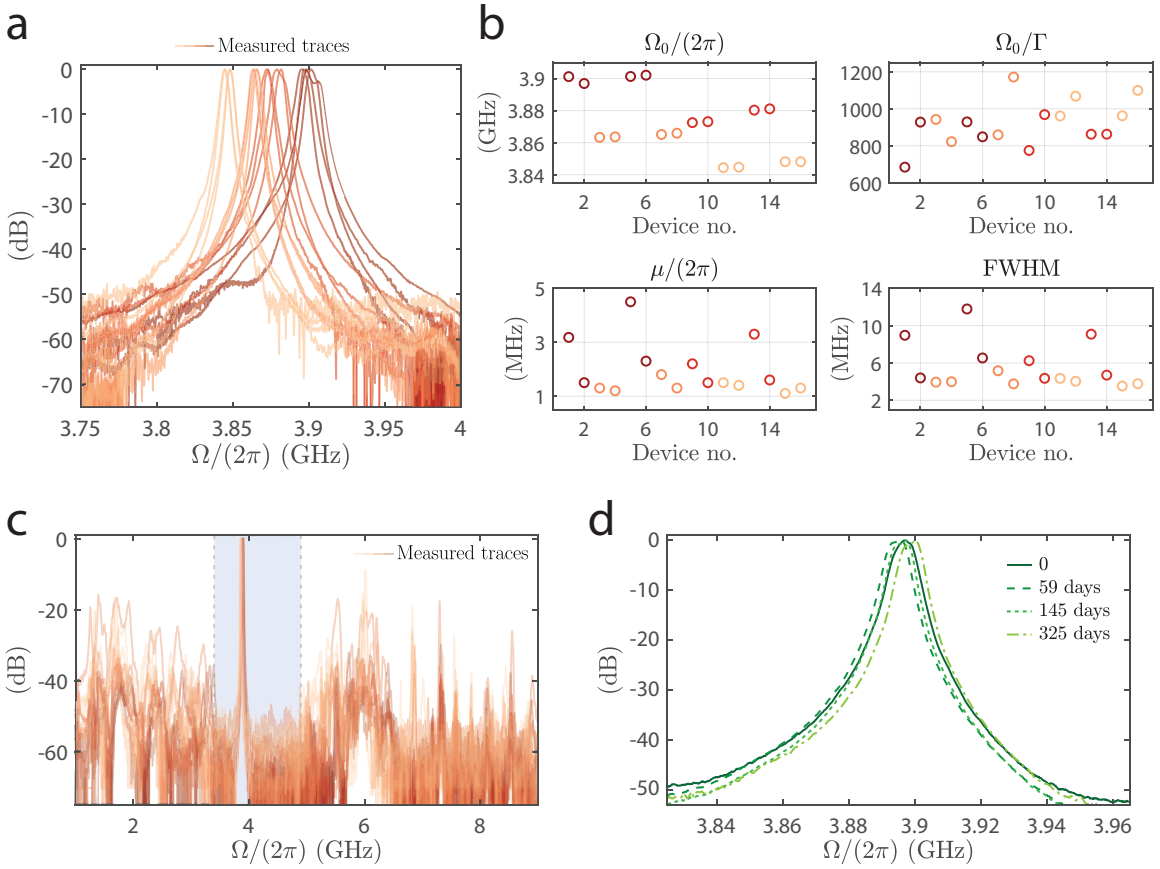

Figure 6.13: **(a)** Measurements of 16 devices fabricated on the same chip using electron-beam lithography, all showing a two-pole frequency response around 3.9 GHz. The variation of the center frequency and precise line shapes are the result of a slightly different geometry of each device. **(b)** Fitted parameters to the filter lineshapes, showing high consistency in the center frequency (Ω_0), Q-factor of the acoustic modes (Ω_0/Γ), acoustic coupling rate (μ), and full-width at half-maximum (FWHM) of the two-pole lineshape. **(c)** Analyzing a wider frequency span shows a stop-band width on the order of 1.5 GHz (shaded region). **(d)** Repeated measurements of a single device over a period of eleven months show no degradation of performance and no change in the two-pole lineshape. The center frequency shows a fluctuation of 0.1%, which can be the result of temperature variation between measurements. Adapted from Ref. [156].

waveguides, and waveguide width. A wider frequency sweep, seen in Fig. 6.13(c), shows that all devices have an acoustic stop-band of ∼1.5 GHz with >50 dB suppression, and acoustic modes in the range 3.85–3.90 GHz.

The devices show highly consistent results when used over long periods of time. Repeated measurements show no deterioration in performance, an important advantage of silicon when comparing to other materials used for integrated Brillouin-active devices [283,284]. This is demonstrated in Fig. 6.13(d), showing measurements of the frequency response of the same device, spanning eleven months. The lineshape is identical in all measurements, showing a full-width at half-maximum (FWHM) of 6.2 MHz at a center frequency of 3.90 GHz. The measurements were all performed at atmospheric pressure, without environmental control, and with no active stabilization. The variation of 0.1% (4 MHz) in the center frequency can be the result of ambient temperature fluctuations, or the amount of optical power on-chip at the time of the measurements, which can readily be stabilized. These results show the potential of these silicon-based devices to be good candidates for practical applications and field deployment.

6.6.2 Sandia Laboratories fabrication process

Brillouin-active devices can also be fabricated using CMOS-foundry photolithography [285], as they are implemented in a standard silicon-on-insulator (SOI) platform. We fabricated PPER devices using a well established CMOS silicon-photonic process developed at Sandia National Laboratories[3] MESA facilities[4], using a standard SOI processing, and patterned with stepper photolithography. As such, the fabrication of these devices should be compatible with any commercial CMOS foundry with the additional release step.

The devices were fabricated on 8″ wafers, with a 230 nm silicon layer structure atop a 3

3. Sandia National Laboratories is a multi-program laboratory managed and operated by National Technology and Engineering Solutions of Sandia, LLC., a wholly-owned subsidiary of Honeywell International, Inc., for the U.S. Department of Energy's National Nuclear Security Administration under contract DE-NA-0003525. This dissertation describes objective technical results and analysis. Any subjective views or opinions that might be expressed in this work do not necessarily represent the views of the U.S. Department of Energy, or the United States Government.

4. https://www.sandia.gov/mesa/

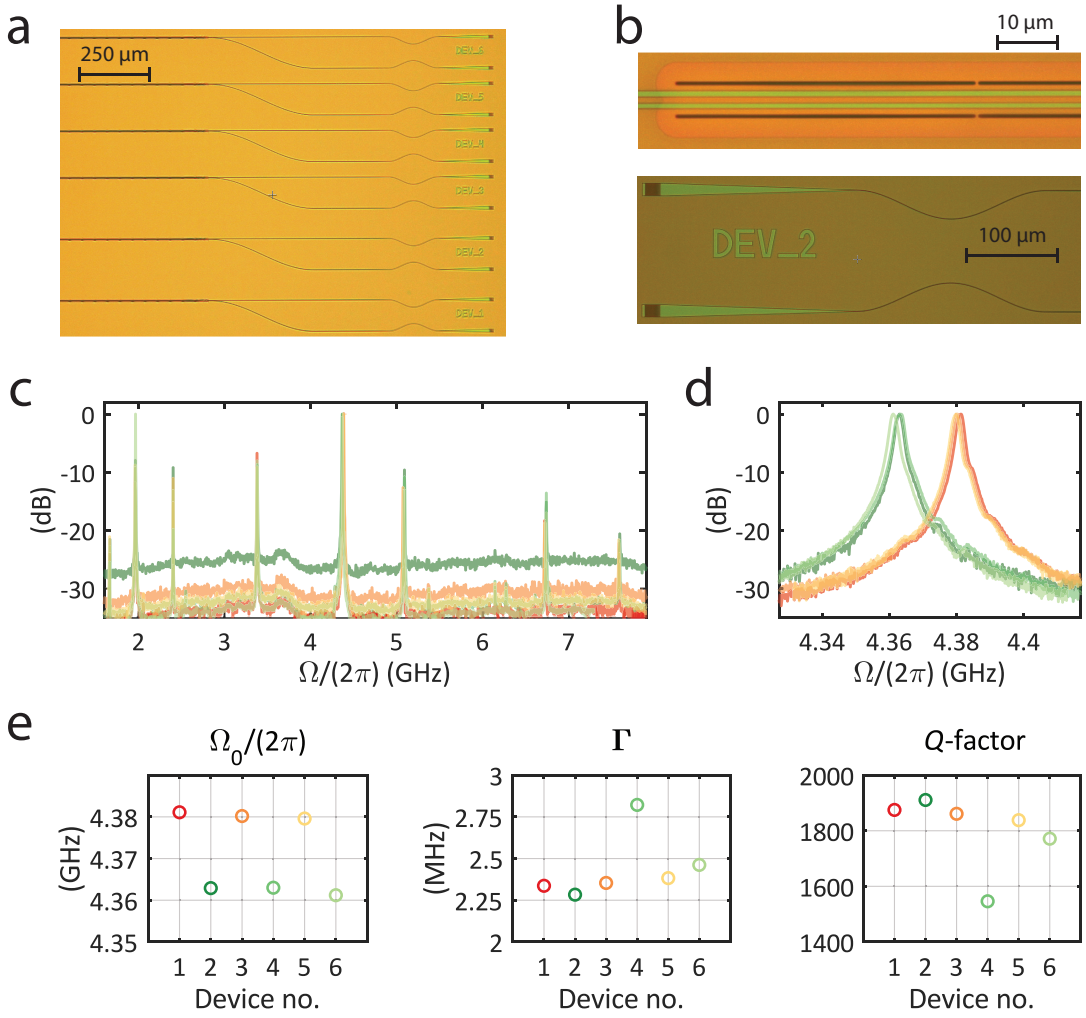

Figure 6.14: **(a)** Micrograph of six devices fabricated using standard photolithography in Sandia National Laboratories. **(b)** Top: Magnified view of the Brillouin-active region showing the two ridge waveguides and slots. Bottom: Magnified view of the integrated grating couplers used to couple light on and off the chip. **(c)** Measured frequency response of the PPER devices, showing highly repeatable results. **(d)** Magnified view of the peaks around 4.39 GHz. The green traces and orange traces correspond to slightly different device designs, resulting in a ∼20 MHz difference in the resonant frequency. **(e)** Fitted parameters to the frequency response center frequency (Ω_0), dissipation rate (Γ) and Q-factor.

μm buries oxide layer. The rib waveguides are defined by etching 80 nm of the silicon layer, and the holes and slots are achieved by fully etching the silicon layer, exposing the buried oxide. The devices were fabricated within 4×4 millimeter squares on the wafer. Finally, the active regions of the devices were suspended using a 49% hydrofluoric (HF) acid wet etch. Examples of fabricated devices are shown in Figs. 6.14(a,b).

The fabrication process yielded highly consistent results. Fig. 6.14(c) shows the measurement of six single-pole PPER devices (following the design from [187]), all having an identical frequency response. Examining the peaks around 4.37 GHz (Fig. 6.14(d)) shows the high acoustic quality-factor ($Q \sim$2000) of all the Brillouin-active modes (Fig. 6.14(e)). Two-pole PPER devices were also fabricated at the Sandia National Laboratories facility, demonstrating the feasibility of producing high-quality phononic crystal devices, as seen in Fig. 6.15(a). The frequency response of two of the fabricated devices is shown in Figs. 6.15(b,d), corresponding to devices with $N = 4$ and $N = 5$ rows of holes between the two waveguides, respectively. A measurement of a wider frequency span is shown in Figs. 6.15(c,e), where we can see a 1.5 GHz acoustic stop-band.

6.7 Conclusion

In this chapter, we have shown the design process of multi-pole PPER devices in a standard silicon-on-insulator platform and studies the possible frequency responses we can obtain from such devices, as well as the effects of fabrication imperfections. Through acoustic mode-engineering, utilizing coupled acoustic modes in a phononic crystal, we can produce lineshapes with an improvement of 40 dB in out-of-band rejection compared to earlier silicon PPER-based devices [187]. In contrast to previous multi-pole demonstrations, the devices were all fabricated using standard SOI wafers and CMOS compatible methods. We have demonstrated that the devices can be fabricated using CMOS-foundry photolithography, which can enable the scaling of production, yielding cheap, high-volume, and consistent results [48, 59]. Moreover, we have shown that silicon PPER devices are reproducible and that their performance is robust over time, crucial properties for practical technological

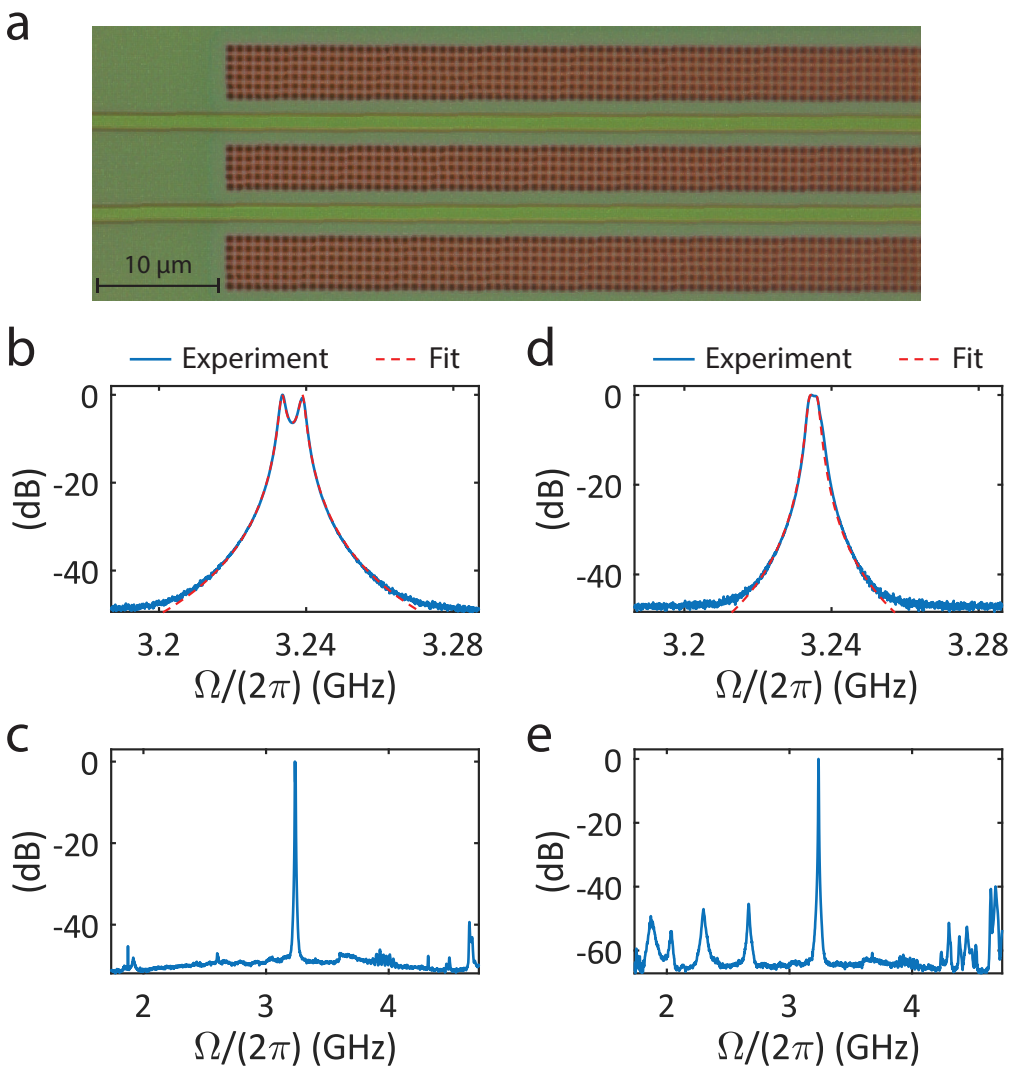

Figure 6.15: **(a)** Micrograph of a two-pole PPER device fabricated using photolithography in Sandia National Laboratories. **(b)** Two-pole frequency response of a device with $N = 4$ rows of holes between the waveguides. Fitting the frequency response is consistent with a center frequency of $\Omega_0/(2\pi) = 3.236$ GHz, an acoustic dissipation rate of $\Gamma/(2\pi) = 1.45$ MHz and an acoustic coupling rate of $\mu/(2\pi) = 2.83$ MHz. **(c)** Measurement of a wider frequency span of the device from panel (b). **(d)** Two-pole frequency response of a device with $N = 5$ rows of holes between the waveguides. Fitted parameters yield $\Omega_0/(2\pi) = 3.235$ GHz, $\Gamma/(2\pi) = 1.69$ MHz, and $\mu/(2\pi) = 1.10$ MHz. **(e)** Measurement of a wider frequency span of the device from panel (d).

applications.

The lineshape obtained by these devices stands out for its ability to produce multi-pole frequency responses with a narrow (∼MHz) pass-band, and excellent out-of-band suppression. Additionally, the devices exhibit a wide (∼GHz) stop-band around the pass-band, with spurious transmission peaks suppressed by more than 30 dB, which can be eliminated by the use of additional broadband filtering [52, 143]. Similar performance in the optical domain using ring resonators would require two ultrahigh-Q ($>10^8$) resonators, and ultralow-loss (∼0.1 dB/m) waveguides [52, 253, 254, 286]. Implementing such a device in silicon would demand a large footprint [223], as well as sub-millikelvin temperature stability [51] and narrow-linewidth laser sources. In contrast, the devices in this work have a footprint of ∼0.1 mm^2, which can facilitate integration for filter-bank and channelizing applications. The measurements presented here were performed with no active stabilization, as the resonant frequencies are determined in the acoustic domain. To avoid drift of the filter pass-band over longer time scales, the temperature needs to be stabilized on the order of ∼1 K. Additionally, we have shown how the PPER design can be extended to produce higher-order filters.

We have shown how the forward Brillouin process used in the devices demonstrated here has the advantage of scalability by cascading active segments in series. Multiple PPER devices could be integrated on the same chip, retaining fidelity as the input signal traverses the cascaded array, without the need of splitting and amplifying the signal in multiple stages, which degrade the noise figure of the system. These capabilities could enable channelizing applications, as well as sensing schemes with record-high spatial resolution.

Chapter 7

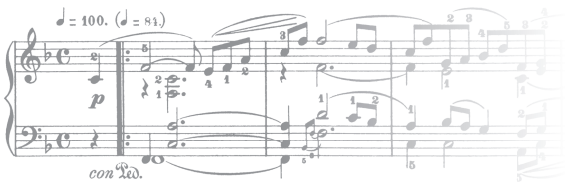

Narrowband microwave-photonic bandpass filtering

7.1 Introduction

In this chapter, we will utilize a two-pole PPER device to experimentally demonstrate narrowband filtering within a full microwave-photonic link. The device consists of the Brillouin-active suspended waveguides that were presented in Chapter 6, supporting both optical modes as well as long-lived acoustic modes. Using a phononic crystal design with an acoustic stop-band, enabling the coupling of acoustic modes in a controllable fashion, we demonstrate a second-order filter response with 3.5 MHz full-width at half-maximum (FWHM) at a center frequency of 3.87 GHz and 70 dB out-of-band suppression. The microwave-photonic link implementing this filter yields a link gain of $G = -17.3$ dB. We further show that the addition of an RF amplifier at the link input enables a larger-than-unity gain ($G = 0.6$ dB) and improves the link noise figure. Additionally, by introducing a tunable local oscillator, we demonstrate the tunability of the filter pass-band over multiple GHz, while maintaining the highly selective, narrow-bandwidth filter lineshape.

Comparable performance in the optical domain demands ultralow-loss ($\sim$0.1 dB/m) waveguides and ultrahigh-Q ($>10^8$) optical resonators [52, 223, 253, 254, 286, 287], which are

challenging to realize in silicon-photonic circuits. Narrowband (∼MHz) filtering and long (>100 ns) signal delays —of the type routinely performed in the acoustic domain— are not yet possible in silicon photonics, and the results presented here represent ∼100× higher spectral resolution than previously demonstrated by silicon multi-pole filters [52]. Based on a recent comprehensive survey of microwave-photonic filters [209], the link performance of the filter demonstrated here is on par with other microwave-photonic filtering schemes, while having a narrower bandwidth and higher out-of-band rejection.

7.2 Experimental demonstration

We use a silicon two-pole PPER device, as was described in Chapter 6, with two suspended rib waveguides, and phononic crystal regions comprised of a cubic lattice of air holes (see Fig. 6.3). The active region of the device is $L = 5$ mm long, with $N = 5$ lines of holes between the two waveguides, and phononic waveguide regions of width $W = 3.3$ μm. The phononic crystal pitch is $a = 650$ nm with a hole diameter $d = 500$ nm.

The microwave-photonic link follows our description in Chapter 5, and the experimental setup used to demonstrate the link is illustrated schematically in Fig. 7.1(a). An RF signal at frequency Ω modulates an optical tone with frequency ω_1 using an intensity modulator (Optilab IM-1550-20-A), yielding sidebands around the optical carrier. This modulated optical tone is amplified and injected into the 'emit' waveguide of the PPER device. When the modulation frequency approaches the Brillouin resonance, acoustic waves are emitted through a forward Brillouin process, resulting in time modulation of the effective refractive index of both waveguides through photoelastic coupling. A second optical source with frequency ω_2 is injected into the 'receive' waveguide of the device, where it experiences phase modulation by the transduced acoustic fields. Phase demodulation is implemented with optical filtering using a commercial bandpass filter (Alnair BVF-300CL), and the signal is detected on a high-power photodiode (Discovery Semiconductors, Inc. DSC100S, $V_{\text{bias}} = 7$ V).

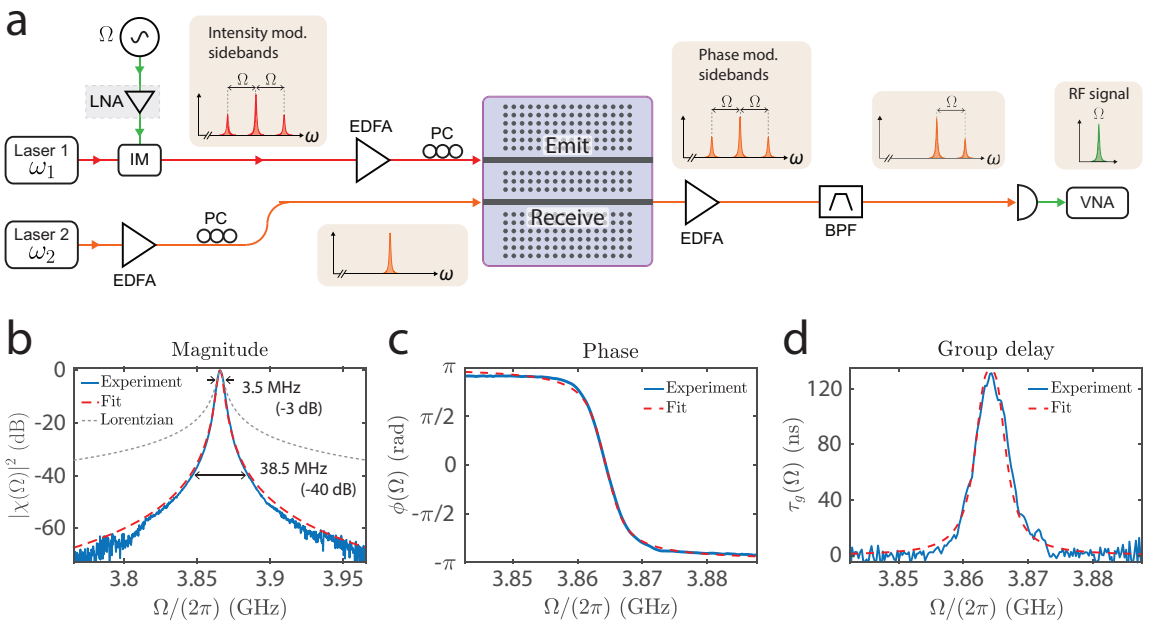

Figure 7.1: **(a)** Schematic illustration of the experimental setup used to characterize the PPER-based RF link. IM: intensity modulator, LNA: RF low-noise amplifier, EDFA: erbium-doped fiber amplifier, PC: polarization controller, BPF: optical band-pass filter, VNA: RF vector network analyzer. **(b)** Normalized magnitude of the filter frequency response, showing a two-pole lineshape with a FWHM of 3.5 MHz and a 40 dB bandwidth of 38.5 MHz. A Lorentzian (single-pole) lineshape with the same FWHM is shown for reference. **(c)** The measured phase response shows a 2π phase-shift over the filter bandwidth. **(d)** Measured group delay of the filter, showing $\tau_g = 131$ ns at the center of the pass-band. Reproduced from Ref. [156].

7.2.1 Filter frequency response

First, the frequency response of the filter was measured by sweeping the RF frequency Ω through the acoustic resonance Ω_0. The filter exhibits a center pass-band frequency of $\Omega_0/(2\pi) = 3.87$ GHz, seen in Fig. 7.1(b), with a 3 dB linewidth of $\Delta\Omega/(2\pi) = 3.5$ MHz, corresponding to a Q-factor of $\Omega_0/\Delta\Omega = 1106$. The second-order filter response shows a fast frequency roll-off of 3.7 dB/MHz, yielding a 40 dB bandwidth of 38.5 MHz, and 70 dB out-of-band suppression at frequencies 100 MHz from the center of the pass-band. In comparison to a Lorentzian lineshape with the same full-width at half-maximum (FWHM), this two-pole lineshape yields a 35 dB improvement in out-of-band suppression. The measured phase response is presented in Fig. 7.1(c), showing a 2π phase shift over the filter bandwidth, and the measured group delay of the filter ($\tau_g = -\partial\phi/\partial\Omega$) is $\tau_g = 131$ ns at the center of

the pass-band, as seen in Fig. 7.1(d). These measurements are consistent with a phonon dissipation rate of $\Gamma/(2\pi) = 3.7$ MHz and an acoustic coupling rate of $\mu/(2\pi) = 1$ MHz. The smooth phase response suggests that the RF signal propagates throughout the filter with minimal distortion.

7.3 Microwave-photonic link performance

Next, we analyze the performance of a full microwave link implementing a bandpass filtering operation using the PPER device, as was discussed in Chapter 5. Fig. 7.2(a) shows the aggregated measurements of single RF tones at the filter output, for an input RF power of -4 dBm, tuned to the center of the pass-band, and at frequencies 5 MHz and 10 MHz from the pass-band center. We can see the suppression of the signal as we tune it away from the center frequency, consistent with the two-pole frequency response. We can also see that the noise floor of the RF link is comprised of a Lorentzian-like peak —a result of spontaneous Brillouin scattering occurring in the 'receive' waveguide— and a wideband noise background (dominated by EDFA noise), seen in Figs. 7.2(a,b). The spontaneous Brillouin scattering is due to the thermal occupation of the phonon modes at room temperature, which has an average phonon number of $k_B T/(\hbar\Omega_0) = 1565$. [187].

The RF link performance was characterized by measuring the RF power at the output of the filter ($P_{\text{out}}^{\text{RF}}$) as a function of the input RF power ($P_{\text{in}}^{\text{RF}}$). Fig. 7.2(c) presents the link performance, with an 'emit' optical power of 105 mW and with 76 mW incident on the photodetector. The noise spectral density at the center of the pass-band was measured at $N = -134.6$ dBm/Hz. The RF link gain was measured at $G = -17.3$ dB, yielding a link noise figure of $\text{NF} = N - G - N_{\text{in}} = 56.7$ dB, where we have assumed thermal noise at the link input (i.e., $N_{\text{in}} = k_B T = -174$ dBm/Hz). The linear dynamic range of the link (up to 1 dB compression from a linear response) was measured at $\text{CDR}_{1\text{dB}} = 119.1$ dB Hz.

We study the nonlinearity of the microwave-photonic link by quantifying the third-order spurious tone generated in the link, which can lead to distortion of the filtered signal [198], as was discussed in Section 5.4.3. We inject an input RF tone at frequency $\Omega = \Omega_0/3$, and

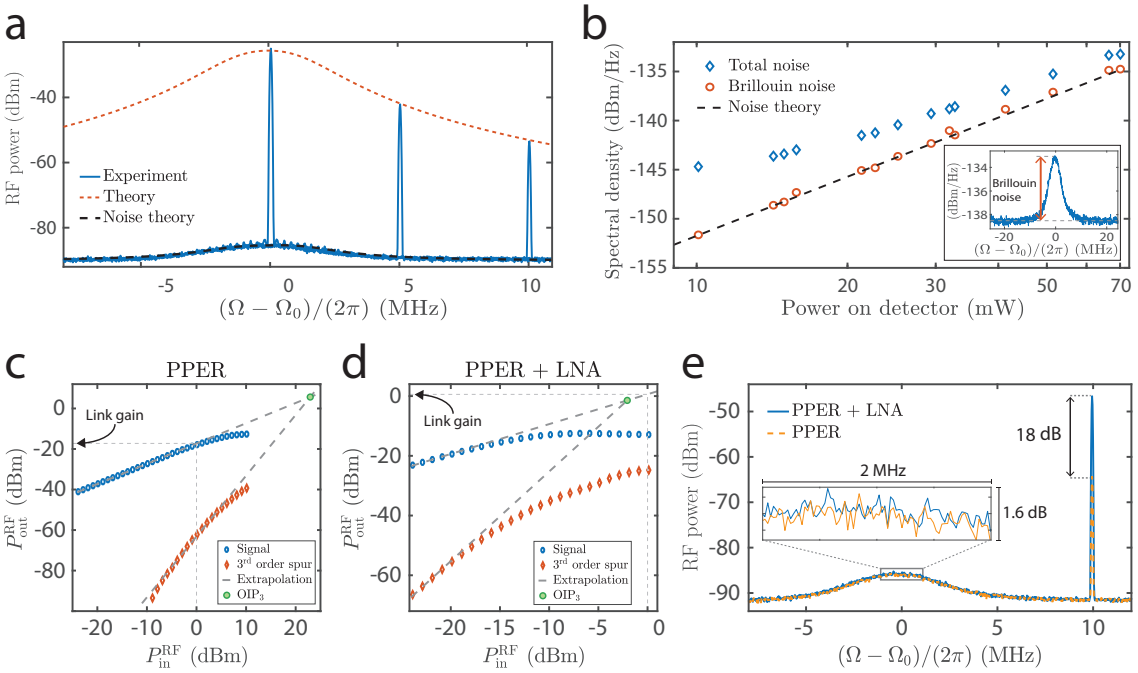

Figure 7.2: **(a)** Measured spectrum from the filter output, for input signals at the center of the filter pass-band, as well as frequencies 5 MHz and 10 MHz away from the center frequency. Parameters used for calculating the theoretical plots are presented in Table 7.2. **(b)** Measured peak value of the noise power spectral density, as a function of the optical power on the detector, and the extracted thermal-Brillouin contribution to the noise. Inset: Measured noise spectral density, when the optical power on the detector is 70 mW, showing the narrowband thermal Brillouin peak. **(c)** Measured RF output power as a function of RF input power for the fundamental (blue) and third harmonic (red) tones of the filter. Extrapolated linear trends, the third-order intercept point (OIP_3), and link gain are shown for reference. The bandwidth used in the measurement was 300 Hz. **(d)** Repeated measurement after adding an RF amplifier (LNA) at the filter input (see Fig. 7.1(a)). **(e)** Measured output spectrum of the RF link, with (blue) and without (orange) the LNA at the link input, when the input signal is 10 MHz from the center of the filter pass-band. The LNA amplifies the signal power by 18 dB, while the noise floor does not change (magnified in inset). The bandwidth used in the measurements was 50 kHz. Adapted from Ref. [156].

Table 7.1: Measured microwave link parameters, with and without an RF amplifier at the link input, corresponding to the data presented in Fig. 7.2(c,d). Adapted from Ref. [156].

Parameter	PPER	PPER+LNA	Description
G (dB)	-17.3	0.6	RF link gain
N (dBm/Hz)	-134.6	-134.2	Noise floor
NF (dB)	56.7	39.2	Noise figure[1]
$\mathrm{OIP_3}$ (dBm)	5.6	-1.5	Output intercept point[2]
$\mathrm{SFDR_3}$ $\left(\mathrm{dB\ Hz^{2/3}}\right)$	93.5	88.5	Spur-free dynamic range[3]
$P_{\mathrm{in}}^{\mathrm{1dB}}$ (dBm)	1.7	-15.2	1 dB compression point
$\mathrm{CDR_{1dB}}$ (dB Hz)	119.1	119.6	Linear dynamic range[4]

[1] Noise figure was calculated using $\mathrm{NF} = N - G - N_{\mathrm{in}}$ (with $N_{\mathrm{in}} = k_{\mathrm{B}}T = -174$ dBm/Hz).
[2] Inter-modulation $\mathrm{OIP_3}$ is 4.8 dBm lower.
[3] Spur-free dynamic range is given by $\mathrm{SFDR_3} = (2/3)(\mathrm{OIP_3} - N)$. Inter-modulation spur-free dynamic range is 3.2 dB $\mathrm{Hz^{2/3}}$ lower.
[4] Linear dynamic range was calculated using $\mathrm{CDR_{1dB}} = P_{\mathrm{in}}^{\mathrm{1dB}} + G - N$.

measure the output RF power at frequency Ω_0, as seen in Fig. 7.2(c), yielding a spurious-free dynamic range of $\mathrm{SFDR_3} = 93.5$ dB $\mathrm{Hz^{2/3}}$. The third-order spurious tone is a result of the intensity modulator used at the link input, which can be suppressed using linearization schemes [201]. The $\mathrm{SFDR_3}$, obtained here using a third-harmonic measurement, can be related to an inter-modulation distortion (IMD), as measured when implementing a two-tone test [198], yielding $\mathrm{SFDR_3^{(IMD)}} = 90.3$ dB $\mathrm{Hz^{2/3}}$. These results can be improved further by using higher optical powers, as well as using a modulator with a lower half-wave voltage [53], as was discussed in Chapter 5. A summary of the measured link parameters is presented in Table 7.1.

The high noise figure obtained from the microwave-photonic link —typical of Brillouin-based filtering [35, 144]— is a result of spontaneous Brillouin scattering generating noise in the link. However, the PPER-based filtering scheme offers a unique design space in which we can enhance the noise performance of the RF link, as was described in Chapter 5. More specifically, the noise figure can be improved by increasing the transduction strength in the 'emit' waveguide. Since the noise is set by thermal-Brillouin noise (spontaneous scattering) in the 'receive' path, the link gain will increase without affecting the noise floor, achieving a lower noise figure.

One way to improve the noise figure of a noisy system is to add a low-noise amplifier

Table 7.2: Parameters used for the theory trends of Figs. 7.1 and 7.2. Adapted from Ref. [156].

Parameter	Value	Description
λ (nm)	1530	Optical wavelength
T (K)	290	Temperature
Ω_0 (2π GHz)	3.86	Phonon frequency
Γ (2π MHz)	3.7	Acoustic dissipation rate
μ (2π MHz)	1	Acoustic coupling rate
V_+	$(0.48)^{1/2}$	Asymmetry parameter
$G_{\mathrm{B}}^{(\mathrm{emit})}$ ($\mathrm{W}^{-1}\mathrm{m}^{-1}$)	1300	'Emit' Brillouin gain
$G_{\mathrm{B}}^{(\mathrm{rec})}$ ($\mathrm{W}^{-1}\mathrm{m}^{-1}$)	915	'Receive' Brillouin gain
L (mm)	5	Brillouin interaction length
V_π (V)	6.94	Half-wave voltage
$\eta^2 R_{\mathrm{out}}\lvert H_{\mathrm{pd}}\rvert^2$ (W^{-1})	4.6	Calibrated detector response
R_{in} (Ω)	50	Iinput impedance
$P_{\mathrm{in}}^{\mathrm{RF}}$ (dBm)	10.1	Input RF power
N_{bg} (dBm/Hz)	-139.1	Background noise

at the input of the system (before the noisy elements), typically at the expense of dynamic range. To demonstrate this, an RF low-noise amplifier (MiniCircuits ZX60-V63+) was added before the modulator at the link input (see Fig. 7.1(a)). Fig. 7.2(e) shows how the addition of the low-noise amplifier (LNA) boosts a signal by 18 dB, without changing the noise floor of the link, which is still Brillouin-noise dominated. The RF power measurements were repeated, seen in Fig. 7.2(d), yielding a link gain of $G = 0.6$ dB and a noise figure of NF = 39.2 dB. We can see that the full amount of gain provided by the amplifier contributes to the reduction of the noise figure. The linear dynamic range is practically unchanged by the LNA, however, the measured spurious-free dynamic range is reduced, showing a trade-off between noise-figure and dynamic range, which is a common situation in many microwave-photonic links [265]. A summary of the measured link parameters with the LNA is presented in Table 7.1.

7.4 Bandpass tunability

In many practical microwave-photonic systems, we are interested in processing multiple frequency bands, requiring filters with different pass-band frequencies. This can be achieved by using multiple devices with geometries designed to filter different frequencies, as was demonstrated in Chapter 6. However, a more economical approach is to design a scheme that enables the tuning of the pass-band of a given PPER-based filter. Such tunability can be achieved by using a modified modulation scheme at the PPER 'emit' signal path, illustrated schematically in Fig. 7.3(a). To implement this, the input RF signal is first encoded onto the optical carrier using a phase modulator. Because phonons are generated by intensity modulation of light, this phase-modulated optical carrier alone does not drive a phonon field. To convert the phase-modulated sidebands into an intensity beat note that can be used to transduce acoustic waves, we introduce a second optical tone, used as an optical local oscillator (LO). The pass-band is set by the Brillouin frequency (Ω_0) and the LO frequency (ω_{LO}), which we use to select the spectral band that is transduced to the acoustic field. It is important to note that the acoustic field is driven around the Brillouin frequency Ω_0, regardless of the LO setting. The optical tone in the 'receive' waveguide is phase modulated by the driven acoustic field, and after demodulation and detection, the output RF signal has a power proportional to the input RF signal at the filtered frequency. Fig. 7.3(a) illustrates how tuning the LO frequency relative to the signal, seen in panels (1–3), changes the signal power at the filter output, seen in panels (4–6), respectively. Alternatively, this tuning scheme can be understood as a series of mixing and filtering operations, as illustrated in Fig. 7.3(b,c). In this analogy, the tuning of the LO frequency shifts the input signal relative to a static filter —set at the Brillouin frequency— and the demodulation and detection of the light at the PPER output perform a down-conversion from the optical domain to the Brillouin frequency.

Tunable PPER-based filtering is demonstrated using the experimental setup illustrated in Fig. 7.4(a). The RF input signal is modulated on an optical carrier with optical frequency ω_1 using a phase modulator (Thorlabs LN65S-FC). The optical LO was synthesized from the

same laser source, using an intensity modulator and an optical filter, yielding a single tone at optical frequency $\omega_{\mathrm{LO}} = \omega_1 + \Omega_{\mathrm{LO}}$. The two optical fields were combined and directed into the 'emit' waveguide of the PPER device, while a second optical tone at frequency ω_2 was injected into the 'receive' waveguide. The light from the 'receive' output was demodulated using a commercial optical filter, detected using a photodetector, and measured using an RF spectrum analyzer. The device used for this demonstration has an active-Brillouin length of $L = 3$ mm, and a phononic crystal structure with pitch $a = 600$ nm and hole diameter $d = 462$ nm, yielding a resonant acoustic frequency of $\Omega_0 = 3.90$ GHz and a 3 dB linewidth of 6.2 MHz.

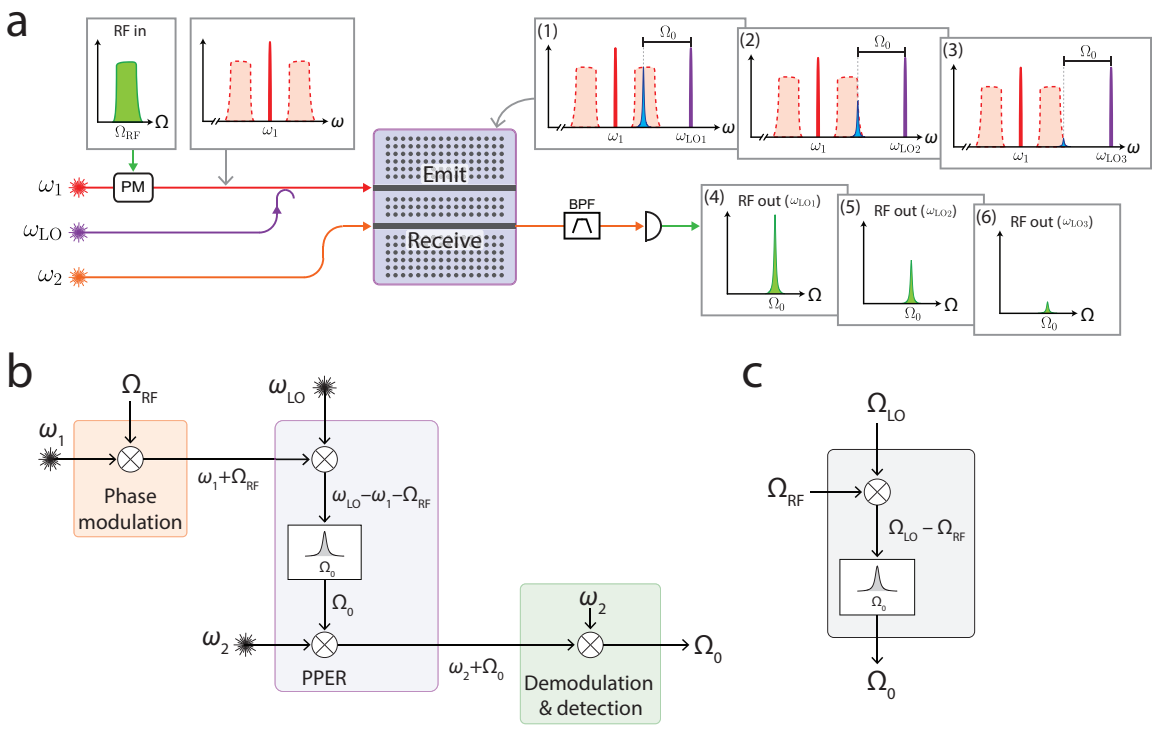

Figure 7.3: **(a)** Schematic illustration of a tunable PPER-based filter, where the LO frequency determines the spectral band of the input signal that drives the narrowband Brillouin process (illustrated in blue). The output of the filter is centered around the Brillouin frequency Ω_0, with power proportional to the signal at the filtered frequency. Panels (1,2,3) show the LO tuned to different frequencies, and the corresponding output power in panels (4,5,6). **(b)** The PPER-based tunable filter described in terms of mixing operations and a static filter at the Brillouin frequency. **(c)** A simplified equivalent circuit in the RF domain, after removing the optical carrier ω_1 at the input of the filter ($\Omega_{\mathrm{LO}} = \omega_{\mathrm{LO}} - \omega_1$), and ω_2 at the output. Adapted from Ref. [156].

First, we demonstrate the function of this high-resolution filter by using it to filter a complex RF signal, operating in essence as a spectrum analyzer, as illustrated schematically in Fig. 7.4(b). In this scenario, a wideband input RF signal is injected into the filter input. The LO frequency is tuned such that the filter pass-band sweeps across the bandwidth of the input signal. For each LO frequency, the output RF signal power is proportional to the input signal at the filtered frequency. The resulting output RF power as a function of the

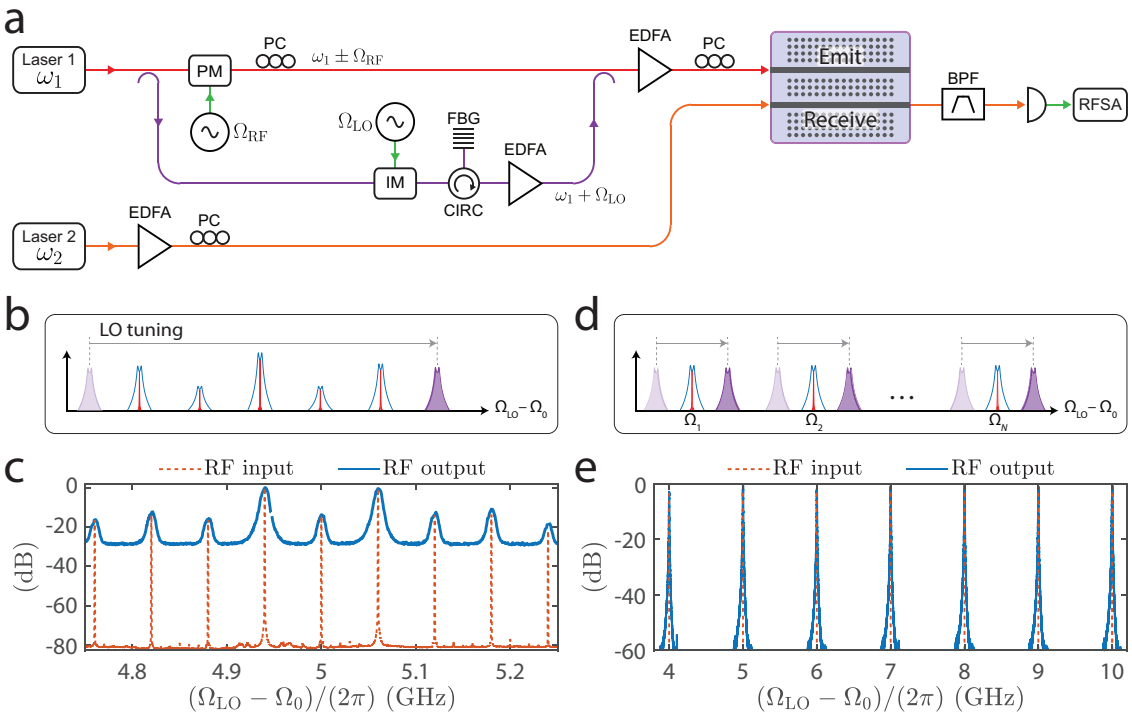

Figure 7.4: **(a)** Experimental setup used to demonstrate filter pass-band tunability. PM: phase modulator, IM: intensity modulator, FBG: fiber-Bragg-grating filter, CIRC: circulator, EDFA: optical amplifier, PC: polarization controller, BPF: optical bandpass filter, RFSA: RF spectrum analyzer. **(b)** Schematic illustration of the filter used as a spectrum analyzer. The input signal consists of an array of RF tones (red). By tuning the LO frequency, the two-pole filter pass-band (purple) is swept across the input signal, producing the output RF signal (blue). **(c)** Measurement corresponding to the scheme presented in panel (b). The input signal consists of RF tones spaced by 60 MHz. The PPER output reproduces the input, and the resolution is determined by the acoustic lineshape. **(d)** Schematic illustration of the demonstration of wideband tunability. The input signal (red) is set at Ω_1, and the LO (purple) is swept to yield the output signal (blue). The input tone is shifted to different frequencies $(\Omega_2 \dots \Omega_N)$ and the LO tuning is repeated at each step. **(e)** Measurements corresponding to the scheme presented in panel (d), demonstrating the tuning of the filter pass-band over 6 GHz. Reproduced from Ref. [156].

LO frequency is a convolution of the input signal with the two-pole filter lineshape. Fig. 7.4(c) shows a measurement demonstrating such a spectrum analyzer scheme. The input RF signal consists of a comb of tones separated by 60 MHz, centered around 5 GHz. The measured output RF power reproduces the input signal, and the spectral resolution is given by the lineshape of the acoustic mode. The noise floor of this measurement (SNR = 29 dB) was determined by the 100 MHz measurement bandwidth.

When processing wideband microwave signals, large-span filter tunability is an important feature of microwave-photonic systems. The photonic platform enables the design of systems that can operate over large bandwidths, which would be challenging to implement using microwave components alone. We demonstrate the wideband tunability possible with the PPER-based filter by shifting the pass-band over a spectral range spanning multiple-GHz. The measurement scheme is illustrated schematically in Fig. 7.4(d). An input signal is set at RF frequency Ω_1, and the LO sweeps the filter pass-band such that the output power reproduces the signal at the output. To demonstrate that this tunability can be reproduced at any number of frequencies over a wide range, we shift the frequency of the input signal to frequency Ω_2, and the LO tuning is repeated. This process is performed for multiple input frequencies, spanning a large frequency range, demonstrating the wide-band tunability of the filter. Experimentally, we set the input RF signal at frequencies between Ω_{RF} = 4–10 GHz (limited by the bandwidth of the phase modulator used in the experiment). For each input frequency, the filter pass-band swept a range of 250 MHz. Fig. 7.4(e) presents the aggregated measurements, showing the pass-band tuned over a 6 GHz range without changing its narrow-band multi-pole lineshape.

7.4.1 Bandwidth limitations

When considering the use of tunable PPER-based systems for practical applications it is important to analyze the bandwidth limitations of the system, namely the bandwidth over which we can expect distortion-free operation. Here, we expand on this point, starting our analysis by noting that the forward Brillouin scattering process used in the PPER-based filtering scheme is inherently double-sided, such that the Stokes (red-shifted) and anti-

Stokes (blue-shifted) processes are coupled, as was discussed in Chapter 2. In the static filter case (Fig. 7.1(a)) this results in the carrier beating with both sidebands in the 'emit' waveguide. However, in the frequency-tuning scheme presented here, this results in the optical local oscillator (LO) driving the acoustic field by beating with light spaced by the Brillouin frequency at both higher ($\omega_{\mathrm{LO}} + \Omega_0$) and lower ($\omega_{\mathrm{LO}} - \Omega_0$) frequencies. Fig. 7.5 illustrates the two sidebands (blue) where forward Brillouin scattering can occur around the LO (purple). The dual-sideband nature of the process is equivalent to an image frequency in heterodyne detection, where unwanted frequency components interfere with the desired signal [288]. As long as the input RF signal bandwidth Δ_{RF} is smaller than twice the Brillouin frequency $\Delta_{\mathrm{RF}} < 2\Omega_0$, there will not be distortion in the filter operation. As shown in Fig. 7.5(a), when tuning the LO, only the lower 'LO sideband' overlaps with the modulated information. It is important to note that this RF bandwidth corresponds to the spectral content of the signal, i.e., $\Delta_{\mathrm{RF}} = \max(\Omega_{\mathrm{RF}}) - \min(\Omega_{\mathrm{RF}})$, and does not constrain the highest frequency at the filter input.

In contrast, when the input signal bandwidth limitation is not satisfied, such that $\Delta_{\mathrm{RF}} > 2\Omega_0$, the measured output signal will not always be proportional to the filtered input RF signal. This is illustrated in Fig. 7.5(b), showing that as the LO approaches the center of the RF sideband it drives the acoustic field through two scattering processes whose contributions will be summed. This distortion can be avoided by using an image-rejection filter, common in many homodyne RF receiver schemes [288], ensuring single-sideband filtering. Alternatively, this bandwidth limitation can be lifted by using inter-modal Brillouin scattering that is inherently a single-sideband process [65, 139], which will be discussed further in Chapter 9.

We note that throughout this discussion we are assuming the small-signal regime, such that the RF-modulation sidebands are much smaller than the optical carrier and the local oscillator. This enables us to neglect the beat note generated between different spectral components within and between the RF sidebands, as their contribution will be much smaller than that of the beat note generated by the strong LO.

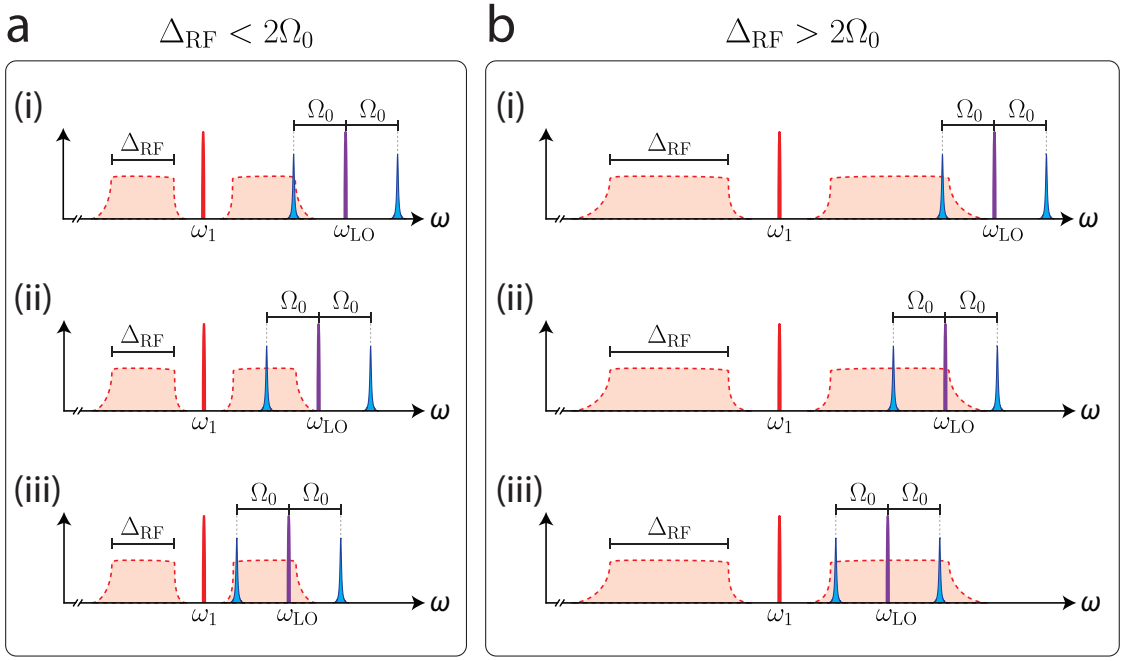

Figure 7.5: Tuning of the optical local oscillator (LO) across the RF-modulated sideband enables the filtering of different spectral bands. **(a)** When the total bandwidth of the RF sideband is smaller than twice the Brillouin frequency ($\Delta_{RF} < 2\Omega_0$), there is no overlap of the higher LO sideband with the RF-modulated signal, and the filter output corresponds to the transfer function of the acoustic mode with no distortion. **(b)** If the bandwidth limitation is not satisfied ($\Delta_{RF} > 2\Omega_0$), as we tune the pass-band of the filter, both sidebands of the LO can overlap with the RF signal (panel (iii)), yielding distortion at the filter output, equivalent to image-frequency interference. Reproduced from Ref. [156].

7.4.2 Alternative tuning schemes

Up to this point, we have discussed the use of both static and tunable PPER-based filters for spectral analysis, which result in the conversion of the output RF signal to be centered around the Brillouin frequency, summarized in Fig. 7.6. This downconversion can be advantageous in systems where frequency conversion is necessary, simplifying system design by performing both operations. However, in some applications, where the filter is part of a larger microwave-photonic system, complementary strategies could be needed, in which we can control the frequency of the output RF signal. Such control can be achieved by employing optical heterodyne demodulation at the output of the PPER device, as illustrated in Fig. 7.7(a). By using an optical tone at frequency ω_{DM} for demodulation, the resulting RF signal is at frequency $\Omega_{out} = \omega_{DM} - \omega_2 - \Omega_0$, which can be determined by tuning ω_{DM}

and ω_2.

Additionally, microwave-photonic filters could be utilized in place of microwave filters (which can operate at arbitrarily-high frequencies), where the output microwave frequency is not changed compared to the input frequency. Such frequency-neutral tunable filtering can be achieved in PPER-based systems by using an alternative demodulation scheme, in which the optical local oscillator that is used to tune the filter pass-band is also utilized to perform heterodyne detection. This demodulation scheme results in an output microwave frequency that follows the filtered input microwave signal, as illustrated in Fig. 7.7(b). The input into the microwave-photonic link is the same as in the tunable frequency-shifting

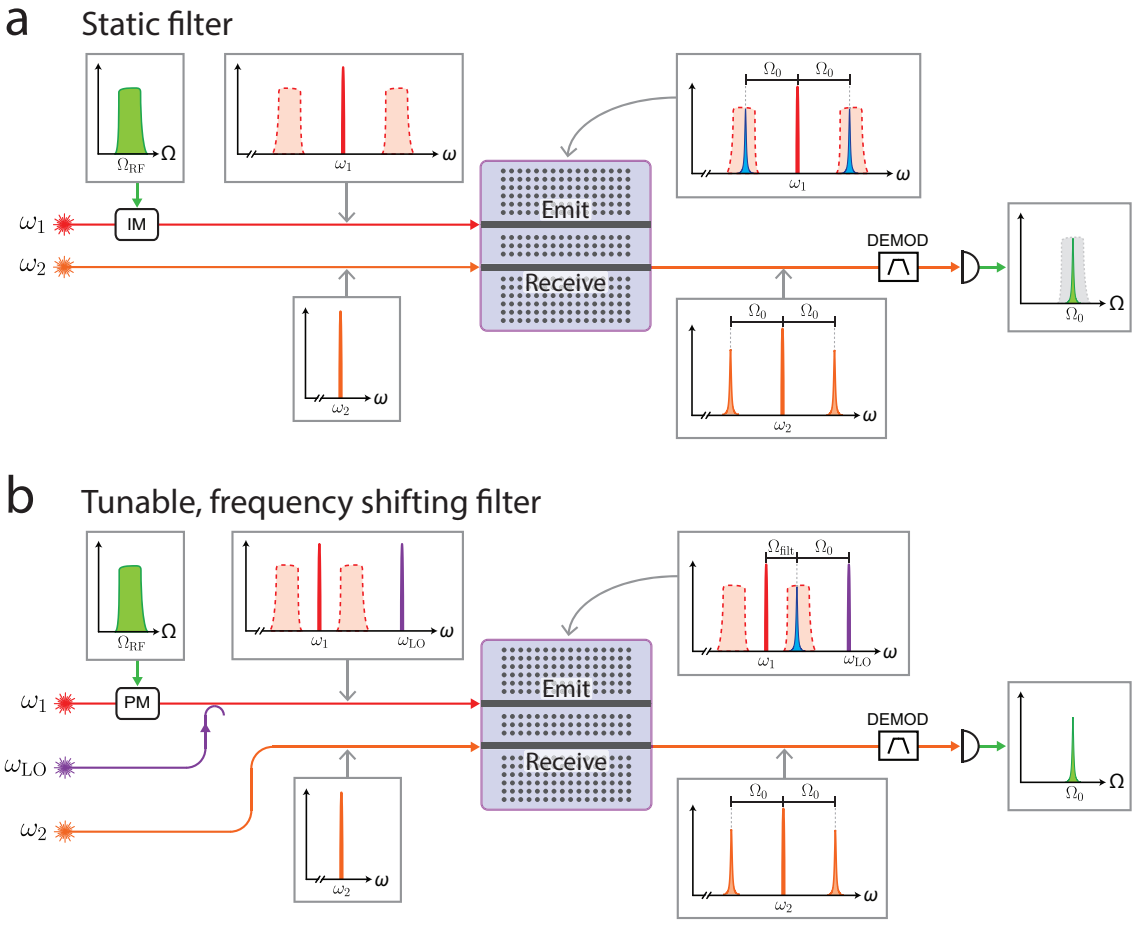

Figure 7.6: **(a)** Schematic illustration of a PPER-based microwave-photonic filter with a set frequency Ω_0, determined by the device geometry. **(b)** By adding a frequency-tunable optical local oscillator (LO) at the link input, the filter pass-band Ω_{filt} can be shifted, however, the output RF signal is still around the Brillouin frequency.

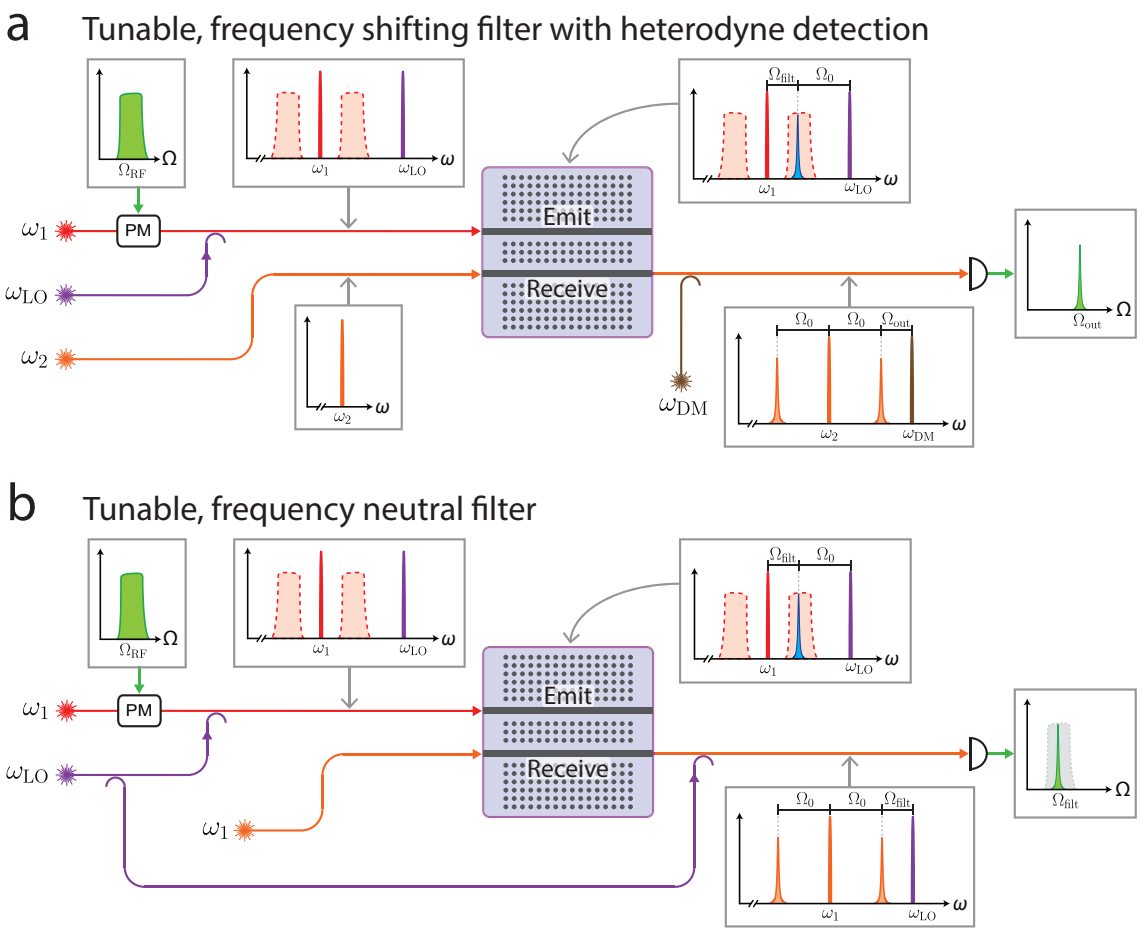

Figure 7.7: **(a)** Optical heterodyne demodulation, using an optical tone at frequency ω_{DM}, shifts the output RF signal to $\Omega_{\mathrm{out}} = \omega_{\mathrm{DM}} - \omega_2 - \Omega_0$. **(b)** Using the LO to perform heterodyne detection at the link output and setting the 'emit' and 'receive' tones to the same frequency ($\omega_2 = \omega_1$) yields a frequency neutral filter, where the output RF signal is at the same frequency as the filter pass-band. Reproduced from Ref. [156].

case, such that a pass-band centered around $\Omega_{\mathrm{filt}} = \omega_{\mathrm{LO}} - \omega_1 - \Omega_0$ yields phase modulation at the Brillouin frequency Ω_0. By combining the phase-modulated 'receive' tone with the LO, a beat note is produced, yielding an RF signal after detection. In the example from Fig. 7.7(b), the output RF tone will have frequency $\Omega_{\mathrm{out}} = \omega_{\mathrm{LO}} - \omega_2 - \Omega_0$, where ω_2 is the 'receive' optical carrier. By setting $\omega_2 = \omega_1$, i.e., using the same optical frequency in the 'emit' and 'receive' waveguides, we obtain a frequency neutral filter, where $\Omega_{\mathrm{out}} = \Omega_{\mathrm{filt}}$. Similarly, a constant offset can be chosen, when $\omega_2 \neq \omega_1$.

7.5 Conclusion

In this chapter, we have presented a PPER-based multi-pole microwave-photonic filter, and studied its frequency response and performance within an RF link, showing an improvement of two orders of magnitude in the resolution of silicon-photonic multi-pole filters. We have also demonstrated how a PPER-based filter can be tuned over a wide spectral range, for the first time. The device yields a narrow pass-band and excellent out-of-band suppression, surpassing the performance of available silicon-photonic technologies [52], as well as other integrated microwave-photonic demonstrations, as seen in Fig. 7.8. Additionally, the device is fabricated in a standard silicon platform, using well-established CMOS-compatible fabrication techniques.

The RF link performance demonstrated using the silicon PPER device is competitive with other microwave-photonic schemes [196], such as ring-resonators [309], interferometers [310], Brillouin-based filtering [35, 144], and pulse shaping [311]. The spatial separation of 'emit' and 'receive' waveguides reduces the effects of optical nonlinearities such as four-wave mixing, which can be detrimental to the filter performance. Additionally, the use of forward Brillouin scattering in the filtering process reduces the effects of unwanted reflections and eliminates the use of circulators and isolators which are challenging to integrate on-chip.

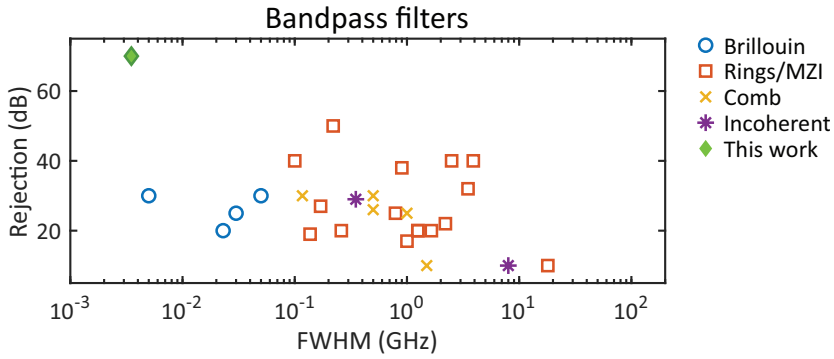

Figure 7.8: Summary of recently demonstrated integrated microwave-photonic bandpass filters, showing out-of-band rejection and spectral resolution (FWHM: full-width at half-maximum). Surveyed work includes Brillouin-based filtering [144, 187, 247, 251], filters using ring resonators and interferometers [52, 227, 287, 289–295, 295–301], comb-generation and spectral shaping [302–306], and incoherent multi-tap filters [307, 308].

The PPER-based filtering scheme utilizes the optical, microwave, and acoustic domains —each with vastly different and complementary properties— which can all be optimized for further improvement of the device performance, as was discussed in Chapter 5. Longer devices will result in higher gain, lower noise figure, and a larger dynamic range. For example, by using a PPER device with an active length of 5 cm (while preserving the acoustic lineshape) the link gain will increase by 20 dB, and the noise figure will be reduced by 10 dB compared to the results shown in this work, which were obtained from a 5 mm long device. Higher optical power in the 'emit' waveguide will yield a higher link gain, without adding noise in the process. Dispersion engineering of the optical waveguides can enable stronger Brillouin coupling [169], resulting in a larger spur-free dynamic range and lower noise figure. Additionally, an interferometric phase demodulation scheme will result in a higher link gain [198]. In the acoustic domain, stronger acousto-optic coupling can be achieved by longer-lived acoustic modes, which will also result in a narrower filter lineshape. For example, this can be accomplished by optimizing the phononic crystal design, achieving a complete acoustic band-gap [312]. Improvement of the phononic crystal can also yield a wider acoustic stop-band [313], decreasing signal distortion and averting the need for further filtering.

In the microwave domain, using improved electro-optic modulators will directly enhance the performance of the link. In the scheme we have demonstrated, the third-order spurious tone is a result of the nonlinerity of the intensity modulator at the filter input, and using linearized modulation schemes [198, 201] will yield a larger dynamic range. Furthermore, modulators with a lower half-wave voltage [53] will result in a lower noise figure. For instance, by using a modulator with a half-wave voltage of 1 V, a 5 cm long device could yield a link gain of 26 dB and a noise figure of 30 dB (see Section 5.4). Alternatively, a microwave low-noise amplifier (LNA) can be used at the input to the modulator, yielding a lower noise figure, as we have demonstrated here.

With the advancement of integrated silicon light sources [56, 259], amplifiers [54, 187], modulators [314] and detectors [49], PPER-based filtering schemes can be a step towards foundry-compatible, fully integrated microwave-photonic systems.

Chapter 8

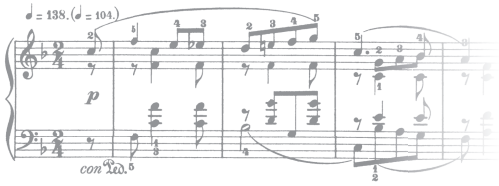

Narrowband microwave-photonic notch filtering

8.1 Introduction

In the previous chapters, we have shown how the nonlocal nature of forward Brillouin interactions can be used to design photonic-phononic emit-receive (PPER) devices, which can be used in microwave-photonic filtering operations. Experimentally, we have demonstrated narrowband, tunable microwave-photonic bandpass filters in a silicon platform, with ∼MHz spectral resolution. In this chapter, we will show how PPER devices can also be used to implement notch-filtering operations, strongly suppressing a narrow spectral band of a microwave signal. Notch filters are an important building block in many microwave systems. For example, in the case of an interfering signal within the operation bandwidth of an RF system, a notch filter is needed to suppress the interferer with minimum distortion to the signal, as illustrated in Fig. 8.1. The interfering signal may be a result of other components in the system, such as RF local oscillators used for signal processing, or external narrowband noise sources. When the interfering tone is close in frequency to a signal of interest, a narrowband notch filter is required, such that the signal is minimally affected in the filtering process.

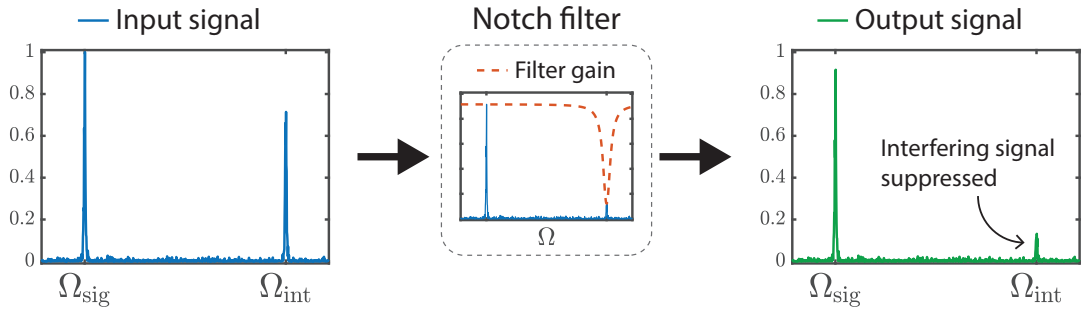

Figure 8.1: An example of a spectrum showing a signal at frequency Ω_{sig} and an unwanted interfering tone at frequency Ω_{int}. By passing the signal through a notch filter, the interfering signal can be suppressed before detection or further signal processing.

In this context, microwave-photonic notch filters are attractive for their ability to be tuned over large frequency ranges and their immunity to electromagnetic interference. Microwave-photonic notch filters have been demonstrated using optical fiber, utilizing delay lines [315] and Bragg gratings [316]. For narrowband applications, Brillouin scattering [317, 318] and Brillouin dynamic gratings [99, 100] have been used to produce narrowband filters, thanks to the unique properties of the acoustic waves taking part in the filtering process. In chip-integrated systems, microwave-photonic filtering has been demonstrated using micro-ring resonators [221, 309, 319, 320], which are typically limited in their ability to produce a narrow spectral response [209] and require ultralow-loss waveguides to achieve ∼MHz spectral features [223, 254]. Other chip-scale narrowband photonic filtering demonstrations have included whispering-gallery modes in microspheres [321] and gas absorption [322], however, the integration of such devices may be challenging.

Alternatively, Brillouin scattering has been a promising strategy to achieve narrowband filtering in integrated-photonic platforms, similar to its use in optical fiber [35, 41, 64]. The long lifetime of the acoustic modes participating in the interaction produces narrow spectral features, which can be used to synthesize microwave-photonic filters, analogous to the role played by SAW and BAW devices in RF signal processing [140]. Specifically, Brillouin-based notch filtering has been demonstrated by utilizing Brillouin-induced loss or gain to shape the spectrum of optical sidebands which encode an RF signal in the optical domain. In order to implement notch filtering operations, advanced modulation schemes are necessary

to translate the shaped optical spectrum into a filtered microwave signal [240, 246, 247], as was discussed in Chapter 4 (see Fig. 4.10).

We have seen in previous chapters that an alternative intriguing method for utilizing Brillouin interactions is by using a photonic-phononic emitter-receiver (PPER) [186]. In this scheme, we use forward Brillouin scattering to transduce information between two spatially separated waveguides, resulting in a narrow bandpass frequency response set by the acoustic modes.

Here, we will demonstrate how a PPER process can be used to produce flexible narrowband notch-filtering operations, offering new design degrees of freedom relative to prior Brillouin-based microwave-photonic filters. The filtering scheme is based on the destructive interference of the input signal with the narrowband output of a PPER device, achieving notch filters with a bandwidth of 3 MHz and 60 dB of signal rejection. Additionally, we show how single-pole filters, as well as two-pole filters, can be achieved using this strategy. Such narrowband response enables the suppression of an interfering signal, without degrading information encoded on an optical carrier only a few MHz away, as we demonstrate experimentally. Furthermore, we show how the notch frequency can be shifted over multiple GHz by using an optical local oscillator at the filter input. Importantly, the narrowband ($\sim$MHz) resolution of the notch filter does not degrade when tuning it over a wide frequency range. We characterize a full microwave-photonic link implementing a PPER-based filter, demonstrating a link gain of -3.6 dB. These results are competitive with other microwave-photonic filtering schemes [209], showing the feasibility of these filters to be integrated within larger microwave-photonic systems. Moreover, the devices used in this work are fabricated in a standard silicon-on-insulator (SOI) platform, using well-established fabrication methods, opening the door to wafer-scale integration of additional system components on the same platform.

8.2 Operation scheme

The notch-filtering operation in our scheme is achieved through the design of an interferometer, in which a narrow bandpass filter is implemented on one of the interferometer paths, illustrated schematically in Fig. 8.2(a). By adjusting the delay (τ) between the two signal paths, such that they are out of phase, the signals destructively interfere at a frequency set by the bandpass filter, resulting in a notch frequency response, shown in Figs. 8.2(b–e). In this way, the frequency response of the bandpass filter is effectively inverted to achieve the desired notch filter response. In the filter presented here, a PPER device is used to implement the bandpass operation within the interferometer, resulting in ∼MHz spectral resolution.

Next, we describe how the interferometric scheme utilizing a PPER device, as illustrated in Fig. 8.3, yields a microwave-photonic notch-filtering operation. First, the input RF signal is encoded on an optical carrier with frequency ω_1 using an intensity modulator, yielding a field amplitude given by [198]

$$E^{\mathrm{IM}}(t) = \sqrt{\frac{\widetilde{P}^{(\mathrm{A})}}{2}} e^{-i\omega_1 t}\left(e^{i\theta} + \sum_n J_n\left(\frac{\pi V_{\mathrm{in}}}{V_\pi}\right) e^{-in\Omega t}\right). \tag{8.1}$$

Here, $\widetilde{P}^{(\mathrm{A})}$ denotes the optical power, the input voltage V_{in} oscillates at frequency Ω, and the half-wave voltage of the modulator is denoted V_π. The angle θ is determined by the biasing point of the modulator, and for the rest of our analysis, we will assume that it is biased at quadrature (i.e., $\theta = \pi/2$). The field is split using a directional coupler, and one branch is directed into the 'emit' waveguide of a PPER device, while the other bypasses the device completely, and is directed to a photodetector. A separate laser source with frequency ω_2 is used for the 'receive' path of the PPER, and as we have derived in Chapter 5, at the output of the PPER this results in a phase-modulated signal

$$E^{\mathrm{PPER}}(t) = \sqrt{\widetilde{P}^{(\mathrm{B})}}\; e^{-i\omega_2 t}\; e^{i\beta_{\mathrm{in}}\cos(\Omega t - \phi)}. \tag{8.2}$$

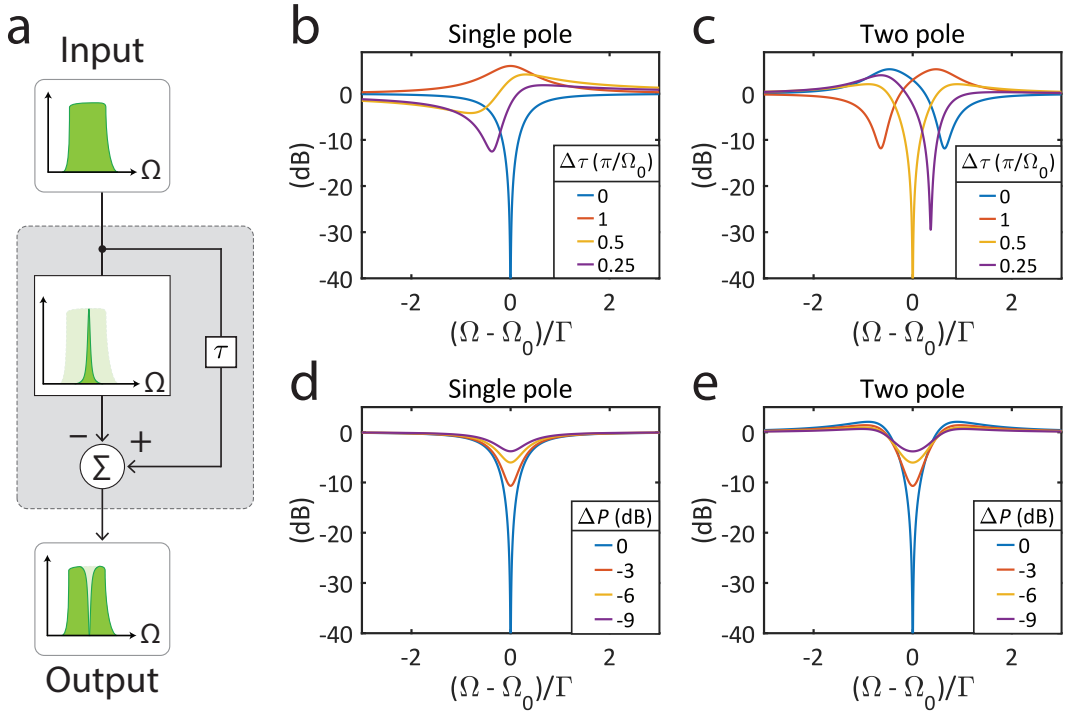

Figure 8.2: **(a)** Operation scheme of the notch-filter. The signal is split into two paths, and one of the paths is bandpass filtered. By setting the appropriate time-delay τ, the signals from the two interferometer paths are out of phase, and a notch filter frequency response is obtained. **(b)** Calculated frequency response of the notch filter scheme, for the case of a single-pole filter, showing different values of time-delay between the two interferometer paths. **(c)** Equivalent calculation for the case of a two-pole filter. **(d)** Calculated frequency response for different cases of power difference between the two interfering signals. To achieve perfect signal cancellation, the two signals need to be power balanced, i.e., $\Delta P = 0$. **(e)** Equivalent calculation for the case of a two-pole filter.

Here, $\widetilde{P}^{(\mathrm{B})}$ is the 'receive' optical power, and the modulation index is given by

$$\beta_{\mathrm{in}} = G_{\mathrm{B}} P^{(\mathrm{E})} L J_1 \left(\frac{\pi V_{\mathrm{in}}}{V_\pi} \right) \frac{\Gamma}{2} \left| \chi(\Omega) \right| , \tag{8.3}$$

where G_{B} is the Brillouin gain, $P^{(\mathrm{E})}$ is the optical power in the 'emit' waveguide, L the length of the active region of the device, and $J_n(\cdot)$ is an n^{th} order Bessel function. Above, the phonon lifetime is given by Γ, $\chi(\Omega)$ is the acoustic frequency response, and we have denoted the phase $\phi(\Omega) = \arg(\chi(\Omega))$. Using the Jacobi-Anger expansion, Eq. (8.2) can also

be expressed as

$$E^{\mathrm{PPER}}(t) = \sqrt{\widetilde{P}^{(\mathrm{B})}}\; e^{-i\omega_2 t} \sum_n i^{-n} J_{-n}\left(\beta_{\mathrm{in}}\right) e^{-in(\Omega t - \phi)}. \tag{8.4}$$

The phase of the optical field from Eq. (8.4) is demodulated using an optical filter (see Section 5.4.6), such that we are left with an optical carrier and a single sideband

$$\overline{E}^{\mathrm{PPER}}(t) = \sqrt{\widetilde{P}^{(\mathrm{B})}} e^{-i\omega_2 t}\left(J_0\left(\beta_{\mathrm{in}}\right) + iJ_1\left(\beta_{\mathrm{in}}\right) e^{-i(\Omega t - \phi)}\right). \tag{8.5}$$

In our analysis, we have assumed that the demodulation is performed using an ideal filter, such that there is no attenuation for the transmitted carrier and sideband, while all other optical sidebands are completely suppressed.

The demodulated PPER output field is directed to the photodetector, such that the

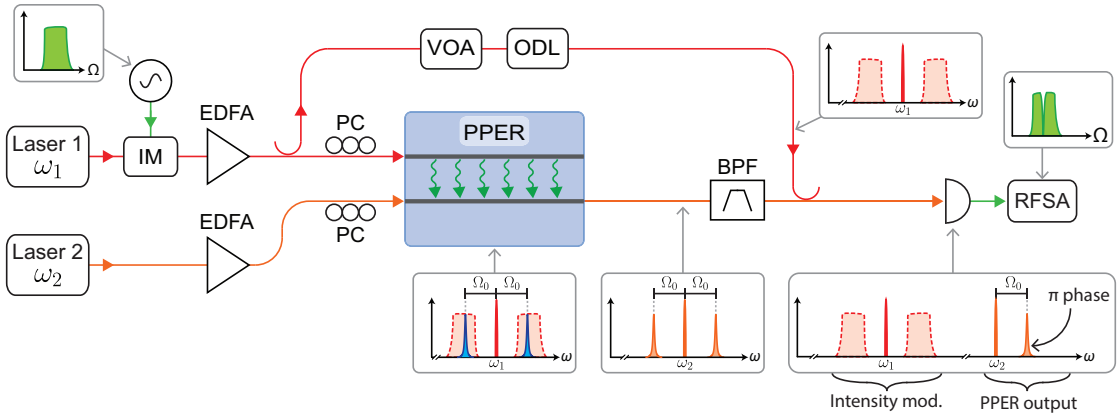

Figure 8.3: Schematic illustration of the experimental setup used to demonstrate PPER-based notch filtering. An RF tone is modulated onto an optical carrier using an intensity modulator (IM) and is split into two paths. One is directed into the 'emit' port of the PPER device, while the other is combined with the output of the PPER. A separate optical wave propagates in the 'receive' waveguide. BPF: bandpass filter, VOA: variable optical attenuator, ODL: optical delay line, EDFA: erbium-doped fiber amplifier, PC: polarization controller, RFSA: RF spectrum analyzer.

total detected field is given by

$$E(t) = \sqrt{\frac{P^{(\mathrm{A})}}{2}} e^{-i\omega_1\left(t-\tau^{(\mathrm{A})}\right)} \left(i + \sum_n J_n \left(\frac{\pi V_{\mathrm{in}}}{V_\pi} \right) e^{-in\Omega\left(t-\tau^{(\mathrm{A})}\right)} \right) + i\sqrt{P^{(\mathrm{B})}} e^{-i\omega_2\left(t-\tau^{(\mathrm{B})}\right)} \left(J_0\left(\beta_{\mathrm{in}}\right) + iJ_1\left(\beta_{\mathrm{in}}\right) e^{-i\left(\Omega\left(t-\tau^{(\mathrm{B})}\right)-\phi\right)} \right), \tag{8.6}$$

where the first line represents the optical field amplitude from the intensity modulator (bypassing the PPER device) and the second line is the demodulated PPER output. Here, $\tau^{(\mathrm{A})}$, $\tau^{(\mathrm{B})}$ are the time delays experienced by the fields in each of the optical paths. The relation between $\{\widetilde{P}^{(\mathrm{A})}, \widetilde{P}^{(\mathrm{B})}\}$ and $\{P^{(\mathrm{A})}, P^{(\mathrm{B})}\}$ is determined by the splitting ratio of the directional coupler used before detection (for example, a 50:50 coupler would yield $P^{(\mathrm{A})} = \widetilde{P}^{(\mathrm{A})}/2$ and $P^{(\mathrm{B})} = \widetilde{P}^{(\mathrm{B})}/2$), and the factor i is a result of the phase imparted in the directional coupling. The photocurrent at the detector is given by $I = \eta P$, where η is the detector responsivity, and the fields are normalized such that $P = |E|^2$. Isolating the current oscillating at frequency Ω, we are left with

$$I^{(\Omega)}(t) = 2\eta \Bigg[P^{(\mathrm{B})} J_0\left(\beta_{\mathrm{in}}\right) J_1\left(\beta_{\mathrm{in}}\right) \sin\left(\Omega\left(t - \tau^{(\mathrm{B})} \right) - \phi \right) - P^{(\mathrm{A})} J_1\left(\frac{\pi V_{\mathrm{in}}}{V_\pi} \right) \sin\left(\Omega\left(t - \tau^{(\mathrm{A})} \right) \right) \Bigg]. \tag{8.7}$$

We note that the two optical wavelengths from the two lasers are chosen such that the beat note between the carriers is well beyond the detector bandwidth, and does not contribute to the RF signal. This is easily implemented, as a difference as small as $\Delta\lambda = 1$ nm ($\Delta\lambda = |2\pi c/\omega_1 - 2\pi c/\omega_2|$) corresponds to $\Delta\omega/(2\pi) \approx 125$ GHz ($\Delta\omega = |\omega_1 - \omega_2|$), well beyond the bandwidth of typical detectors.

In the small-signal limit, when $V_{\mathrm{in}} \ll V_\pi$, we can expand the Bessel functions to first order ($J_0(x) \approx 1$, $J_1(x) \approx x/2$), and ignoring an overall phase, this leaves us with the RF signal

$$I^{(\Omega)}(t) = \eta \left(\frac{\pi V_{\mathrm{in}}}{V_\pi} \right) \left[P^{(\mathrm{A})} \sin\left(\Omega t\right) - \left(\frac{1}{2} P^{(\mathrm{B})} G_{\mathrm{B}} P^{(\mathrm{E})} L \frac{\Gamma}{2} \left|\chi(\Omega)\right| \right) \sin\left(\Omega t + \Omega\Delta\tau - \phi\right) \right], \tag{8.8}$$

where we have substituted β_{in} from Eq. (8.3), and denoted the time difference between the two optical paths as $\Delta\tau = \tau^{(\text{A})} - \tau^{(\text{B})}$. Rearranging this expression, we arrive at

$$I^{(\Omega)}(t) = \eta \left(\frac{\pi V_{\text{in}}}{V_\pi}\right) \text{Im}\left[e^{-i\Omega t}\left(P^{(\text{A})} - \frac{1}{2}P^{(\text{B})}G_{\text{B}}P^{(\text{E})}L\frac{\Gamma}{2}\left|\chi(\Omega)\right| e^{-i(\Omega\Delta\tau-\phi)}\right)\right]. \tag{8.9}$$

We note that $P^{(\text{A})}$ and $P^{(\text{B})}$ are the optical power on the detector from the unfiltered interferometer path, and the PPER path, respectively, while $P^{(\text{E})}$ represents the optical power in the 'emit' waveguide of the PPER device. From Eq. (8.9) we can see how complete cancellation of the RF signal can be achieved at the Brillouin frequency Ω_0 by setting the power ($P^{(\text{A})}$) and time delay ($\Delta\tau$) such that $P^{(\text{A})} = P^{(\text{B})}G_{\text{B}}P^{(\text{E})}L\Gamma|\chi(\Omega_0)|/4$ and $\Omega_0\Delta\tau = \phi(\Omega_0) + 2\pi m$ (where m is an integer). These conditions are dependent on the frequency response of the PPER device $\chi(\Omega)$, as were discussed in Chapter 3.

We begin by examining the case of a single-pole PPER response, given by

$$\chi(\Omega) = \frac{1}{i(\Omega_0 - \Omega) + \Gamma/2}, \tag{8.10}$$

such that at the Brillouin frequency (Ω_0) we have

$$|\chi(\Omega_0)| = \frac{2}{\Gamma}, \qquad \phi(\Omega_0) = 0. \tag{8.11}$$

From Eq. (8.9) we see that in order of achieve signal cancellation at Ω_0 we need to set $P^{(\text{A})} = P^{(\text{B})}G_{\text{B}}P^{(\text{E})}L/2$ and $\Delta\tau = 2\pi m/\Omega_0$, yielding

$$I^{(\Omega)}(t) = \eta \left(\frac{\pi V_{\text{in}}}{V_\pi}\right)\left(\frac{1}{2}P^{(\text{B})}G_{\text{B}}P^{(\text{E})}L\right) \text{Im}\left[e^{-i\Omega t}\underbrace{\left(1 - \frac{\Gamma}{2}\chi(\Omega)e^{-i(2\pi m\Omega/\Omega_0)}\right)}_{\xi(\Omega)}\right]. \tag{8.12}$$

Here, we have denoted the frequency response of the notch filter $\xi(\Omega)$.

In the case of a two-pole PPER device, the frequency response from Eq. (8.9) is replaced with

$$\chi^{(\text{2-pole})}(\Omega) = \frac{1/2}{i(\Omega_0 - \mu - \Omega) + \Gamma/2} - \frac{1/2}{i(\Omega_0 + \mu - \Omega) + \Gamma/2}, \tag{8.13}$$

where μ is the coupling rate between the two acoustic modes participating in the filtering process, and at the Brillouin frequency we have

$$\left|\chi^{(\text{2-pole})}(\Omega_0)\right| = \frac{\mu}{\mu^2 + (\Gamma/2)^2}, \qquad \phi^{(\text{2-pole})}(\Omega_0) = \frac{\pi}{2} + \arg(\mu) - \arg\left(\mu^2 + (\Gamma/2)^2\right). \quad (8.14)$$

For this analysis we will assume $\mu = \Gamma/2$, where signal cancellation at the notch frequency requires setting the optical power ($P^{(\text{A})}$) and the time delay ($\Delta\tau$) such that $P^{(\text{A})} = P^{(\text{B})} G_{\text{B}} P^{(\text{E})} L/4$ and $\Delta\tau = (\pi/2 + 2\pi m)/\Omega_0$. Substituting these parameters into Eq. (8.9) yields

$$I^{(\Omega)}(t) = \eta \left(\frac{\pi V_{\text{in}}}{V_\pi}\right) \left(\frac{1}{4} P^{(\text{B})} G_{\text{B}} P^{(\text{E})} L\right) \times \text{Im}\left[e^{-i\Omega t} \underbrace{\left(1 - \frac{\Gamma}{2}\chi^{(\text{2-pole})}(\Omega) e^{-i\left[(\pi/2+2\pi m)(\Omega/\Omega_0)\right]}\right)}_{\xi^{(\text{2-pole})}(\Omega)}\right], \quad (8.15)$$

where we have identified the frequency response of the two-pole notch filter $\xi^{(\text{2-pole})}(\Omega)$, showing signal suppression at $\Omega = \Omega_0$.

Finally, we analyze the DC photocurrent at the detector, which is important for designing practical systems that have power-handling limitations, and for estimating the noise floor of the microwave-photonic link. Calculating the DC terms of the photocurrent, we have

$$I^{(\text{DC})} = \eta\Big(P^{(\text{A})} + P^{(\text{B})}\left[J_0^2(\beta_{\text{in}}) + J_1^2(\beta_{\text{in}})\right]\Big) \approx \eta\Big(P^{(\text{A})} + P^{(\text{B})}\Big), \quad (8.16)$$

where in the last step used a small-signal approximation, consistent with our earlier analysis.

8.3 Experimental demonstration

The first PPER device used to demonstrate narrowband notch filtering was fabricated at the Sandia National Laboratories[1] MESA facilities using a standard SOI process and

1. Sandia National Laboratories is a multi-program laboratory managed and operated by National Technology and Engineering Solutions of Sandia, LLC., a wholly-owned subsidiary of Honeywell International, Inc., for the U.S. Department of Energy's National Nuclear Security Administration under contract DE-NA-0003525. This dissertation describes objective technical results and analysis. Any subjective views or

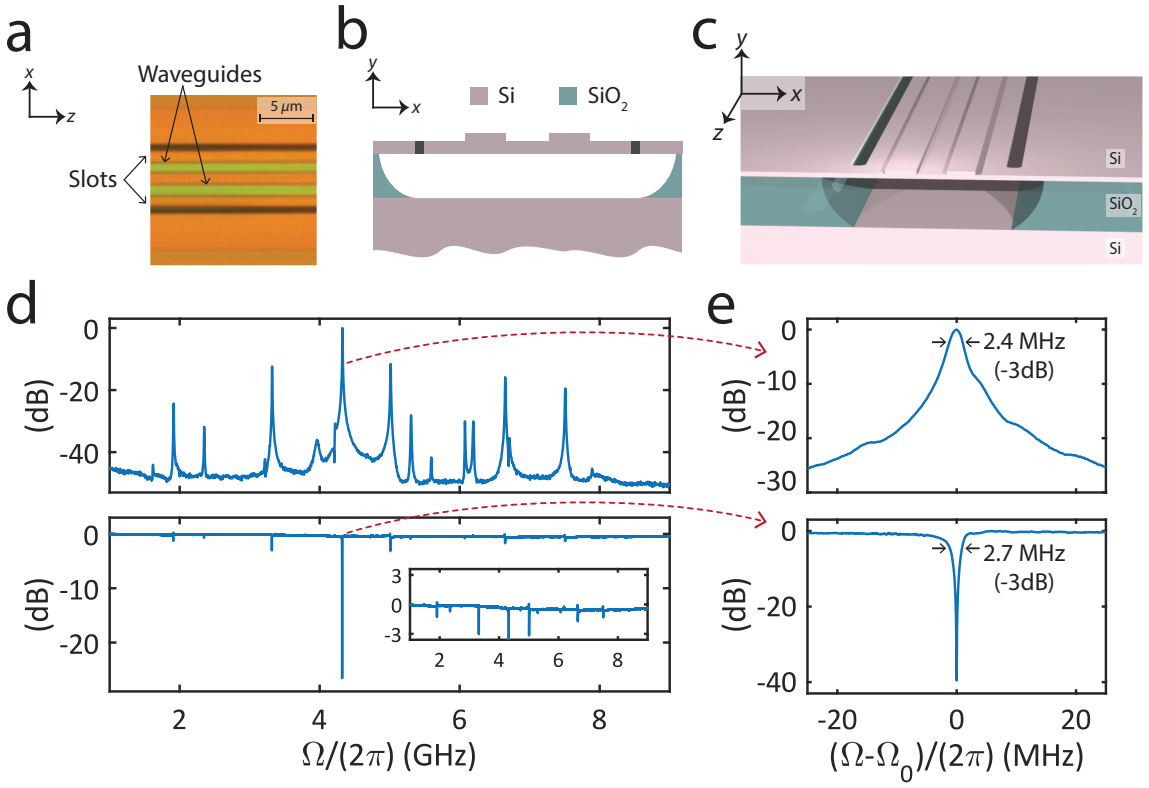

Figure 8.4: **(a)** Top-down micrograph of a PPER device, showing the two ridge waveguides, and the slots used to suspend the device and confine the acoustic modes. **(b)** Illustration of the silicon-on-insulator PPER device cross section. **(c)** Artistic illustration of the suspended device. **(d)** Top: Measured frequency response of the PPER device, showing multiple acoustic modes. Bottom: The corresponding notch filter frequency response. Inset: Magnified view of the pass-band ripple. **(e)** Magnified view of the frequency response around 4.32 GHz. Top: PPER band-pass response. Bottom: Corresponding notch filter response.

patterned with stepper photolithography. As shown in Figs. 8.4(a–c), the active region of the device consists of two ridge-waveguides, which are suspended by removing the oxide under-cladding, with an active length $L = 1.48$ mm. Each of the rib waveguides supports a TE-like optical mode, while the suspended region supports high-Q acoustic modes, which are confined laterally using etched slots in the silicon layer. The overlap of the optical and acoustic fields in the device results in strong forward Brillouin coupling (more details about the device design can be found in Ref. [187]). All measurements were conducted at telecom wavelengths, and light was coupled on and off the chip using integrated grating couplers.

opinions that might be expressed in this work do not necessarily represent the views of the U.S. Department of Energy, or the United States Government.

The frequency response of the filter is measured using the experimental setup illustrated schematically in Fig. 8.3, by sweeping an RF tone Ω at the input to the intensity modulator and measuring the output RF power at the same frequency. The PPER alone produces a bandpass filter response, revealing multiple acoustic resonances (determined by the device geometry [44]), as shown in the top panel Fig. 8.4(d). Focusing on the resonance at $\Omega_0/(2\pi) = 4.32$ GHz, we see that the acoustic response has a Lorentzian lineshape with a full-width at half-maximum (FWHM) of 2.4 MHz, seen in the top panel of Fig. 8.4(e), corresponding to a Q-factor of $Q = 1722$.

To achieve a notch filter response, we utilize the interferometric scheme described earlier, and tune the optical power and delay to cancel the signal at Ω_0, achieving signal suppression of 47 dB at the notch frequency. Outside the filtered notch, the frequency response is flat over a span of 1.6 GHz, as seen in Figs. 8.4(d,e). Using a vector network analyzer (VNA), we measure the phase response of the filter, seen in Fig. 8.5, showing a flat response with a π phase discontinuity at the notch frequency, consistent with theory, and demonstrating that the PPER-based filtering scheme does not degrade the fidelity of RF signals traversing the system.

In our experimental demonstrations, the interferometer was balanced using a variable optical delay line and a variable optical attenuator (VOA), with no active stabilization. Fluctuations in the phase and polarization of the fields in the interferometer set a limit to the suppression we could demonstrate, and active stabilization could enhance the performance of the filter. It is important to note, that many of the components utilized in the laboratory proof-of-concept presented here would not be necessary when integrated on-chip. Additionally, a chip-integrated system would result in a higher level of stability and high-performance filtering.

When analyzing a wider frequency range of the notch filter, the effect of spurious acoustic modes can be seen, yielding pass-band ripple on the order of $\sim$3 dB, as seen in the inset of the bottom panel of Fig. 8.4(d). These spectral features correspond to acoustic resonances which are not perfectly balanced in the interferometric scheme, such that the signal is distorted. In certain applications, the distortion can hinder filter operation and a ripple-

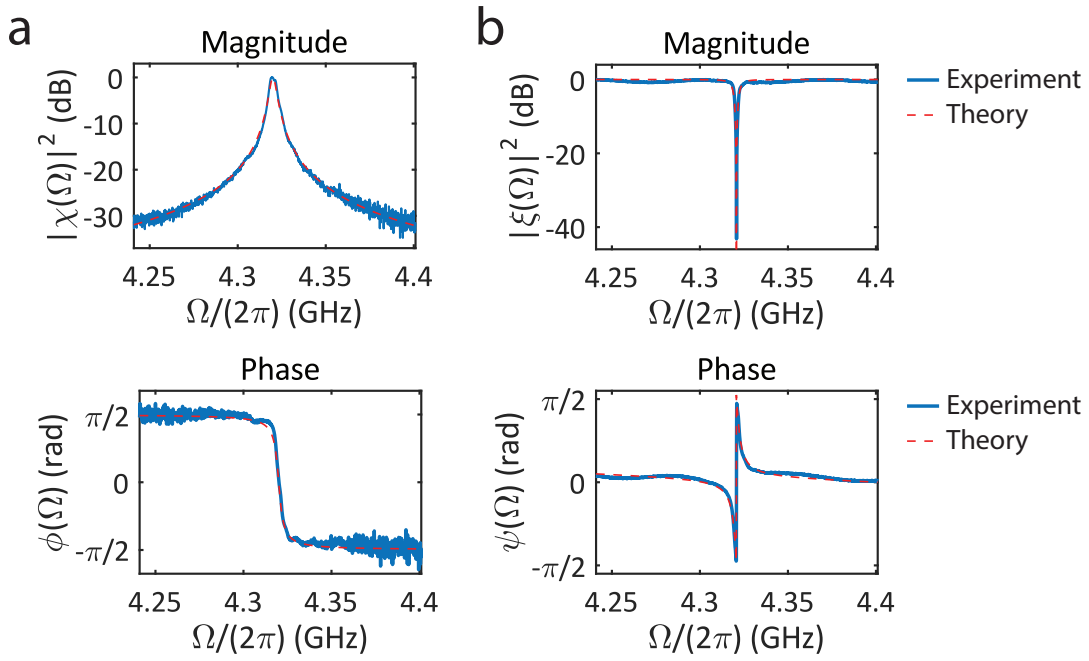

Figure 8.5: **(a)** Measurements of the frequency response of a single-pole PPER-based filter, top: magnitude, bottom: phase. **(b)** Measurements of the corresponding notch filter response. The theoretical trends follow Eqs. (8.10) and (8.12).

free pass-band is required. This can be achieved through phononic-band engineering, as we proceed to demonstrate.

8.3.1 Ripple suppression

Next, we use a different PPER device, which has phononic crystal regions in place of the slots, designed to provide acoustic confinement while suppressing spurious acoustic modes, removing the distortion in the notch filter pass-band. One such device is shown in Figs. 8.6(a–c), where the phononic crystal region —a cubic lattice of air holes with a pitch $a = 0.6$ μm and hole diameter $d = 0.5$ μm— result in a phononic stop-band over a $\sim$2 GHz spectral range, as was discussed in Chapter 6. The phononic crystal devices were fabricated with standard electron-beam lithography, as was detailed in 6.6. When utilizing a phononic crystal to confine acoustic modes, phonon modes with frequencies outside the acoustic stop-band readily pass through the phononic crystal regions, resulting in low-Q modes and weak acousto-optic interaction. The PPER frequency response is seen in Fig.

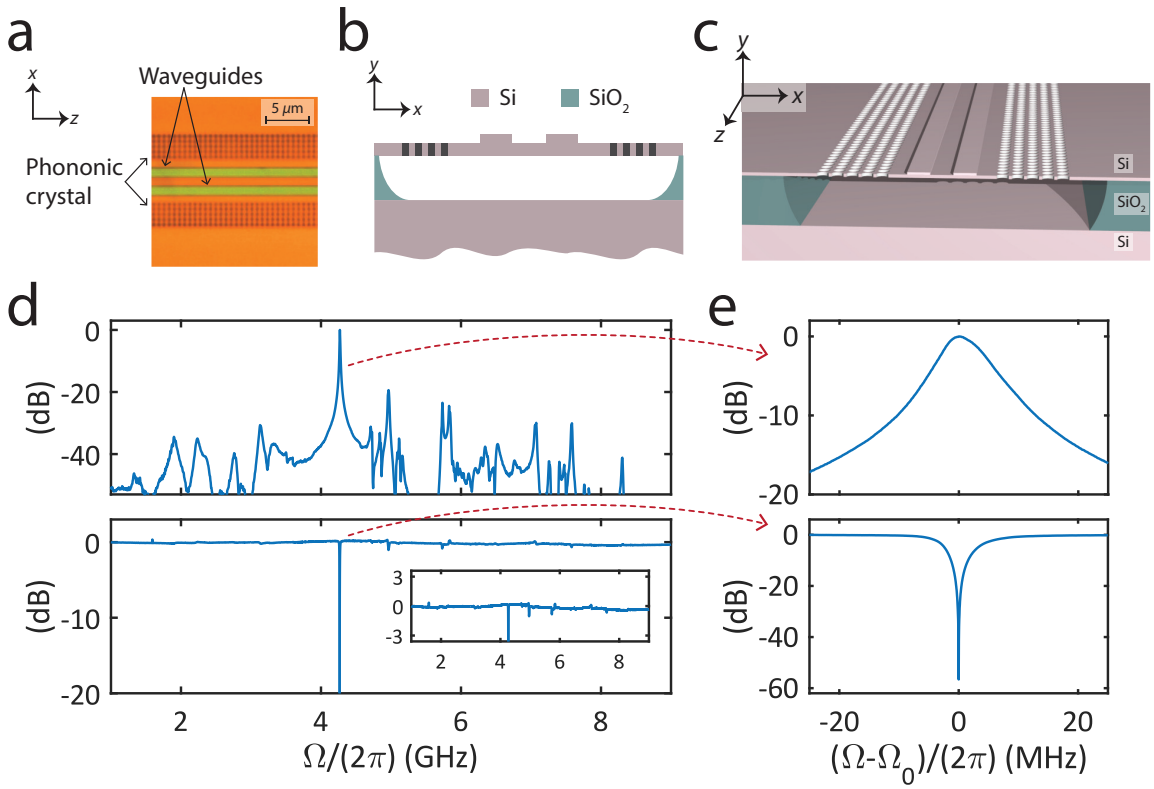

Figure 8.6: **(a)** Top-down micrograph of a PPER device, utilizing a phononic crystal structure. **(b)** Illustration of the device cross section. **(c)** Artistic illustration of the suspended device. **(d)** Top: Measured frequency response of the PPER device. Bottom: Corresponding notch filter frequency response. Inset: Magnified view of pass-band ripple. **(e)** Magnified view of the frequency response around 4.3 GHz. Top: PPER band-pass response. Bottom: Corresponding notch filter response.

8.6(d), showing a sharp peak at $\Omega_0/(2\pi) = 4.3$ GHz (within the acoustic stop-band), while acoustic modes outside this region are suppressed by more than 20 dB. When used as a notch filter, we can see that the distortions in the pass-band are reduced, and over an 8 GHz range, the filter pass-band is flat to within 1 dB. At the notch frequency Ω_0, the filter shows signal suppression of 57 dB (see Fig. 8.6(e)). This demonstration shows how acoustic mode engineering is a powerful tool to shape the PPER-based notch filter response.

8.3.2 Second-order filtering

The modularity of the notch filtering scheme enables us to use different PPER devices in the filtering process, as we have just shown. Now, we proceed to demonstrate the

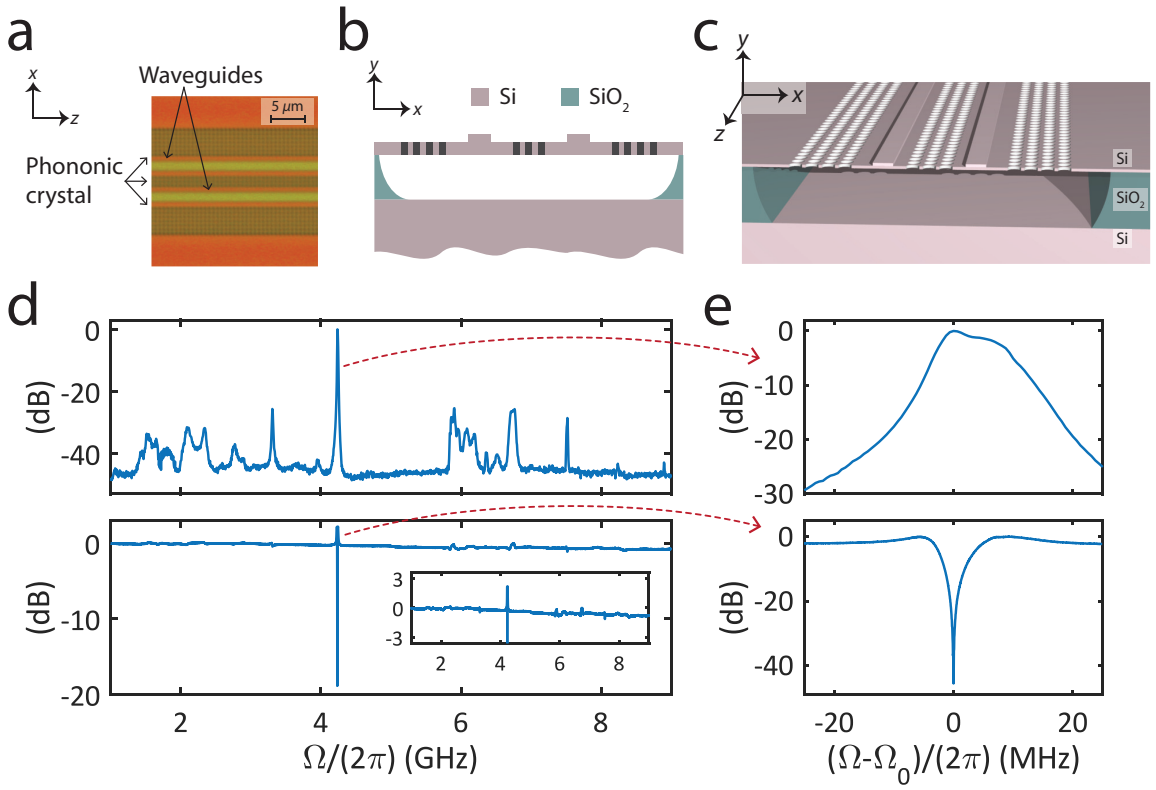

Figure 8.7: **(a)** Top-down micrograph of a two-pole PPER device, utilizing a phononic crystal structure. **(b)** Illustration of the device cross section. **(c)** Artistic illustration of the suspended device. **(d)** Top: Measured frequency response of the PPER device. Bottom: Corresponding notch filter frequency response. Inset: Magnified view of pass-band distortion. **(e)** Magnified view of the frequency response around 4.2 GHz. Top: PPER band-pass response. Bottom: Corresponding notch filter response.

use of a two-pole PPER device, such as was described in Chapter 6, within the notch-filtering scheme. The device used in these measurements is shown in Figs. 8.7(a–c), where a phononic-crystal region between the two waveguides enables controlled coupling of two Brillouin-active acoustic modes. The frequency response obtained by such a device exhibits a two-pole lineshape, with a sharp frequency roll-off compared to the typical Lorentzian response obtained from a single acoustic resonance, as was discussed in Section 6.4.

We use a two-pole PPER device with four lines of holes between the two waveguides, yielding the frequency response seen in Fig. 8.7(d), showing a two-pole response at frequency $\Omega_0/(2\pi) = 4.2$ GHz, and strong suppression of other acoustic modes, which are outside the phononic crystal stop-band. When using the two-pole device within the notch-filter scheme,

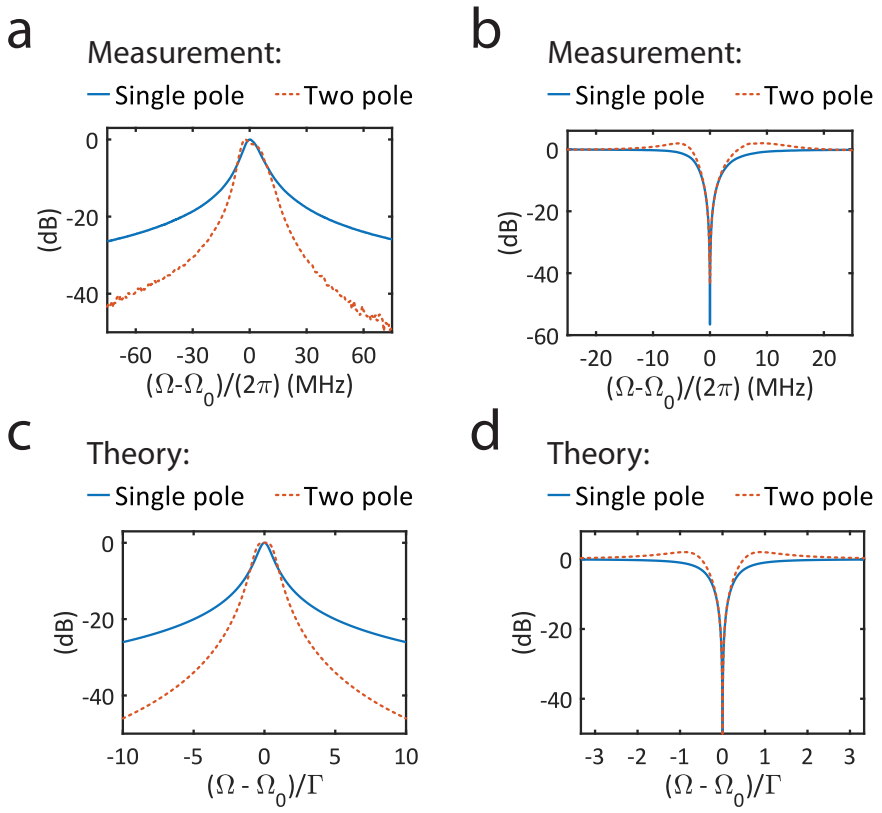

Figure 8.8: **(a)** Measurements of the frequency response of a PPER-based filter, for both single-pole (blue) and two-pole (red, dashed) filters. **(b)** Measurements of the corresponding notch filter response. **(c)** Calculation of the expected frequency response, following Eqs. (8.10) and (8.13). **(d)** Calculation of the frequency response of the corresponding notch filters, following Eqs. (8.12) and (8.15). In the calculations, we have assumed a time delay with $m = 0$, and for the two-pole filter case, we have used $\mu = \Gamma/2$.

as shown in the bottom panel of Figs. 8.7(d,e), we see 46 dB of RF signal suppression at the notch frequency Ω_0 and less than 1 dB of ripple over an 8 GHz range. The measured filter lineshapes are consistent with theory (Eqs. (8.13) and (8.15)), as seen in Fig. 8.8.

8.4 Notch-frequency tunability

In this section, we demonstrate how the wideband optical platform can be utilized to tune the notch frequency of the filter over a large spectral range. This is achieved by using an optical local oscillator (LO) to tune the input signal with respect to the Brillouin frequency, similar to the demonstrations that were presented in Chapter 7. The experimental scheme

used for the filter tuning demonstrations is illustrated in Fig. 8.9(a). In this configuration, the input RF signal is encoded onto an optical carrier using a phase modulator. In the absence of the LO, the phase modulation does not drive an acoustic field in the device, because there is no modulation of the optical power that is required for the stimulated Brillouin process in the PPER. However, the introduction of the optical LO produces intensity modulation through the beat note between the LO and the phase-modulation sideband. By tuning the LO frequency, different spectral components of the phase modulation sideband participate in the signal transduction and get encoded onto the phase of the light in the 'receive' waveguide. In our demonstration, the optical LO is synthesized from the same laser source, using an intensity modulator driven at frequency Ω_{LO} and a commercial optical bandpass filter, such that the LO is at optical frequency $\omega_{\mathrm{LO}} = \omega_1 + \Omega_{\mathrm{LO}}$. We note that the detected RF signal at the filter output is determined by the same beat note that is driving the acoustic field, which is set by the LO. Hence, the output RF signal will be shifted in frequency compared to the input RF signal, such that the filtered frequency will always be at the Brillouin frequency, similar to the bandpass filter tuning scheme that was analyzed in Section 7.4 (see Fig. 7.3(b)).

First, we demonstrate the shifting of the notch filter over a large spectral range. Fig. 8.9(b) shows aggregated data from multiple measurements, in which the notch frequency is shifted in 2 GHz increments while maintaining its narrowband lineshape. Each trace was acquired by setting the LO frequency (Ω_{LO}), which effectively determines the notch frequency, and sweeping the input RF signal (Ω_{RF}) over a 1 GHz range. In all of the measurements, the output RF signal was measured around the Brillouin frequency ($\Omega_0 = |\Omega_{\mathrm{RF}} - \Omega_{\mathrm{LO}}|$), such that demodulation and detection stay identical to that of the static filter case. For example, the notch response around 8.2 GHz (see green trace in Fig. 8.9(b)) was obtained by setting the LO frequency at $\Omega_{\mathrm{LO}} = 4$ GHz, sweeping the input RF signal in the range $\Omega_{\mathrm{RF}} = 7.7$–$8.7$ GHz, and measuring the output RF signal in the range 3.7–4.7 GHz (centered around the Brillouin frequency $\Omega_0 = 4.32$ GHz). All measurements show a flat RF response over the sweeping range, and $\sim$40 dB of signal suppression at the notch frequency.

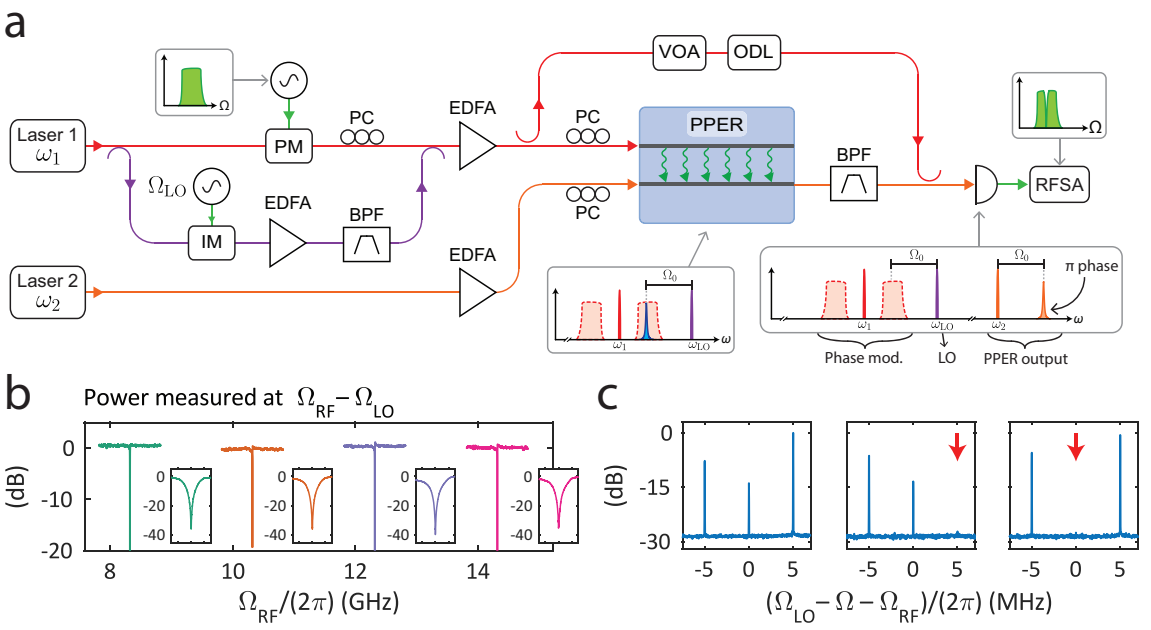

Figure 8.9: **(a)** Schematic illustration of the experimental setup used to tune the notch filter frequency. The input RF signal is modulated using a phase modulator (PM), and an optical local oscillator (LO) tone is synthesized using an intensity modulator (IM) and an optical bandpass filter (BPF). VOA: variable optical attenuator, ODL: optical delay line, EDFA: erbium-doped fiber amplifier, PC: polarization controller, RFSA: RF spectrum analyzer. **(b)** Aggregated data from four measurements demonstrating the shifting of the filter frequency over a wide range. For each measurement, the LO was set and the input signal swept a 1 GHz span around the notch frequency. The insets show a magnified view (6 MHz span) of the filter stop-band at each LO setting, demonstrating ∼40 dB extinction. **(c)** Experimental demonstration of high-resolution filtering. The input RF signal consists of three tones, separated in frequency by 5 MHz (left panel). By tuning the notch filter to the frequency indicated by the red arrow (middle and right panels), one of the input tones can be suppressed, without affecting the other tones.

Next, we proceed to show how the narrow bandwidth of the filter enables selective suppression of RF tones with ∼MHz frequency resolution. We synthesize an input signal consisting of RF tones separated in frequency by 5 MHz, seen in Fig. 8.9(c). While keeping the input RF signal unchanged, we tune the LO such that the notch frequency is shifted, suppressing specific input frequency components, without affecting nearby signals. Together, these demonstrations show wideband tunability while maintaining high resolution, a result of the combination of the photonic platform and the unique properties of acoustic waves.

8.5 Microwave-photonic link performance

In this section, we analyze the RF performance metrics of a microwave-photonic link implementing narrowband notch-filtering operations using the PPER-based scheme, showing their potential technological impact. Furthermore, the analysis of RF link metrics is important when considering these microwave-photonic filters as part of larger, more complex RF signal-processing systems. First, we will present the experimentally measured microwave link parameters, including link gain, noise figure, and dynamic range. Then, we will theoretically model the RF link figures of merit in order to analyze the potential performance of such notch-filtering schemes, following the previous discussions in Chapters 4 and 5.

8.5.1 Experimental results

We characterize the PPER-based notch filter RF link using the experimental scheme shown in Fig. 8.3, with an additional optical amplifier (EDFA) at the output of the PPER device to offset fiber-chip coupling losses. The RF link measurements were performed in the notch filter pass-band, 30 MHz away from the notch frequency (Ω_0), with an optical power of $P^{(\mathrm{B})} = 79$ mW on the detector, and we estimate the optical power in the 'emit' waveguide of the PPER device at $P^{(\mathrm{A})} = 50$ mW. The device used for the measurement was a single-pole, phononic-crystal PPER (see Fig. 8.6(a–c)) with an active length of $L = 17$ mm. In our measurements, the dominant noise source was amplified spontaneous emission from the optical amplifiers, with a measured noise floor of $N = -125.1$ dBm/Hz.

We proceed to measure the microwave-photonic link parameters, including link gain, noise figure, and dynamic range, following the same methods that were used in Chapter 7. First, an input RF tone at frequency $\Omega_{\mathrm{in}} = \Omega_0 + \delta\Omega$ (where $\delta\Omega/(2\pi) = 30$ MHz) is injected into the link input and the RF power at the link output is measured at the same RF frequency, showing a linear response, seen in Fig. 8.10(a). The RF link gain was measured at $G = -3.6$ dB, such that the microwave-photonic link has a noise figure of NF = 52.5 dB (where the input noise is assumed to be $N_{\mathrm{in}} = k_{\mathrm{B}}T = -174$ dBm/Hz). At high input RF powers, the output power is compressed, deviating from the linear trend,

with a measured linear dynamic range of $\mathrm{CDR}_{1\mathrm{dB}} = 125.6$ dB Hz. To quantify the spur-free dynamic range of the microwave-photonic link, we measure the propagation of a third-harmonic distortion through the link, similar to the measurement presented in Section 7.3. More specifically, the input RF signal frequency was set to $\Omega_{\mathrm{in}} = (\Omega_0 + \delta\Omega)/3$, and the RF power at frequency $\Omega_{\mathrm{out}} = 3\Omega_{\mathrm{in}}$ was measured at the link output. As can be seen in Fig. 8.10(a), the output power follows a cubic trend, as expected from a third-harmonic measurement. Extrapolating the linear and nonlinear measurements, we calculate a spur-free dynamic range of $\mathrm{SFDR}_3 = 93.6$ dB $\mathrm{Hz}^{2/3}$. The corresponding inter-modulation SFDR_3, such as would be obtained from a two-tone measurement, is 3.2 dB $\mathrm{Hz}^{2/3}$ lower [198]. A summary of the measured RF link parameters is presented in Table 8.1.

The performance of the PPER device is determined by the strength of the forward Brillouin interaction, which is given by the product of the optical power in the 'emit' waveguide ($P^{(\mathrm{E})}$), the active-region length (L), and the Brillouin gain (G_{B}), as was discussed in Chapter 3. These will in turn affect the link performance of microwave-photonic systems using the PPER device, such as the notch filters we are studying here. To demonstrate the potential of the presented filtering scheme, we show how the link parameters scale with optical power and device length. First, we repeat the RF link measurements using different optical powers in the 'emit' waveguide of the PPER device, presented in Figs. 8.10(b–d). By tuning the optical power injected into the 'emit' waveguide of the device, we can see the enhancement of the link gain, which scales as $G \propto (G_{(\mathrm{B})}P^{(\mathrm{E})}L)^2$, the reduction of the noise figure, which scales as $\mathrm{NF} \propto (G_{\mathrm{B}}P^{(\mathrm{E})}L)^{-2}$, and the improvement in dynamic range, which scales as $\mathrm{SFDR} \propto (G_{\mathrm{B}}P^{(\mathrm{E})}L)^{4/3}$, with higher optical power. The measurements were repeated with a shorter PPER device, having an active-region length of $L = 1.5$ mm. As can be seen from Fig. 8.10(b–d), the device yields a lower link gain, has a higher noise figure, and a smaller dynamic range, a result of the reduction in the Brillouin interaction strength ($G_{\mathrm{B}}P^{(\mathrm{E})}L$). This degradation in performance is expected since the Brillouin interaction strength is $\sim$10 times weaker for the shorter device.

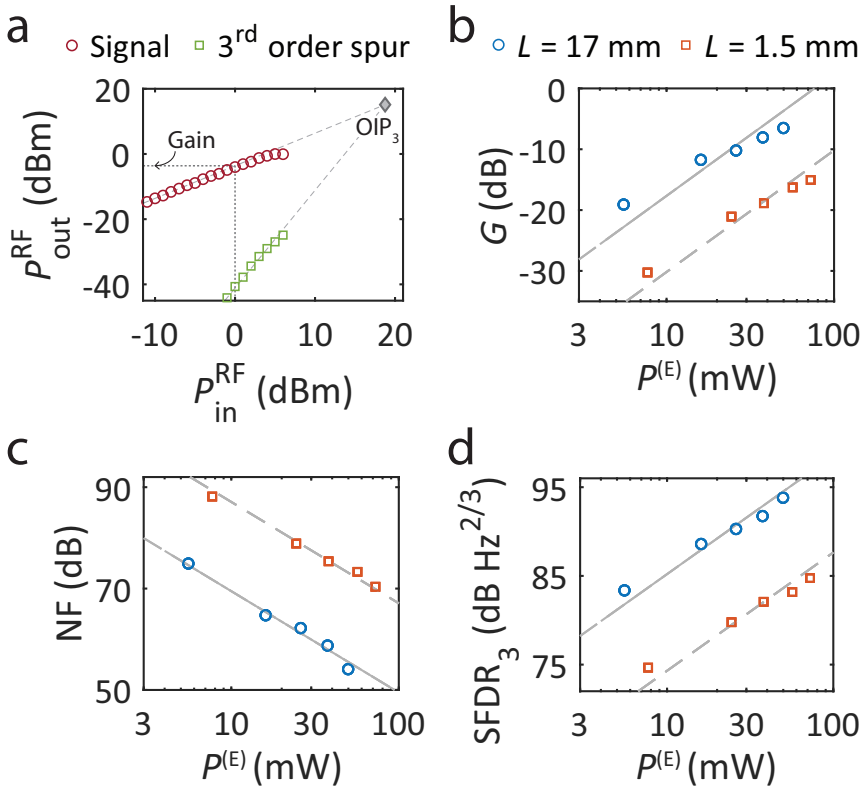

Figure 8.10: **(a)** Measured RF output power as a function of RF input power, showing the fundamental tone (circles) and the third harmonic (squares) of the microwave-photonic link. Extrapolated linear trends and the third-order intercept point are shown for reference. **(b)** RF link gain as a function of optical power in the 'emit' waveguide, measured using two PPER devices, with active lengths of $L = 17$ mm (blue) and $L = 1.5$ mm (red). **(c)** Corresponding noise figure and **(d)** third-order spurious-free dynamic range. The intermodulation $SFDR_3$ is 3.2 dB $Hz^{2/3}$ lower than the results shown here which were measured using the third harmonic. The trends expected from theory are shown for reference: slope 2 for link gain (panel (b)), slope -2 for noise figure (panel (c)), and slope 4/3 for dynamic range (panel (d)).

8.5.2 Potential link performance

Next, we use the results developed in Section 8.2 to calculate key RF link metrics and to explore potential performance as a function of system parameters. We return to Eq. (8.12), and calculate the average output RF power, using $P^{(\Omega)}_{out} = \langle I^2 \rangle R_{out} |H_{pd}|^2$, where R_{out} is the output impedance of the detector and H_{pd} is the photodiode circuit efficiency [198]. Expressing the input signal in terms of RF power, using $P^{(\Omega)}_{in} = V^2_{in}/(2R_{in})$, where R_{in} is

Table 8.1: Measured microwave-photonic link parameters, corresponding to the data presented in Fig. 8.10(a).

Parameter	Value	Description
G (dB)	-3.6	RF link gain
N (dBm/Hz)	-125.1	Noise floor
NF (dB)	52.5	Noise figure[1]
$\mathrm{OIP_3}$ (dBm)	15.1	Output intercept point[2]
$\mathrm{SFDR_3}$ $\left(\mathrm{dB\ Hz^{2/3}}\right)$	93.6	Spur-free dynamic range[3]
$P_{\mathrm{in}}^{\mathrm{1dB}}$ (dBm)	4.1	1 dB compression point
$\mathrm{CDR_{1dB}}$ (dB Hz)	125.6	Linear dynamic range

[1] Assuming $N_{\mathrm{in}} = k_{\mathrm{B}}T = -174$ (dBm/Hz).
[2] Inter-modulation $\mathrm{OIP_3}$ is 4.8 dB lower.
[3] Inter-modulation $\mathrm{SFDR_3}$ is 3.2 dB $\mathrm{Hz^{2/3}}$ lower.

the intensity modulator input impedance, we have

$$P_{\mathrm{out}}^{(\Omega)} = \frac{1}{4} P_{\mathrm{in}}^{(\Omega)} \eta^2 R_{\mathrm{out}} |H_{\mathrm{pd}}|^2 R_{\mathrm{in}} \left(\frac{\pi}{V_\pi}\right)^2 \left(P^{(\mathrm{B})} G_{\mathrm{B}} P^{(\mathrm{E})} L\right)^2 \left|\xi(\Omega)\right|^2, \tag{8.17}$$

from which we can calculate the link gain $g = P_{\mathrm{out}}^{(\Omega)} / P_{\mathrm{in}}^{(\Omega)}$ in the filter pass-band (where $\xi(\Omega) \to 1$)

$$g = \frac{1}{4} \eta^2 R_{\mathrm{out}} |H_{\mathrm{pd}}|^2 R_{\mathrm{in}} \left(\frac{\pi}{V_\pi}\right)^2 \left(P^{(\mathrm{B})} G_{\mathrm{B}} P^{(\mathrm{E})} L\right)^2. \tag{8.18}$$

We can see that the link gain increases with higher optical powers, device length, and Brillouin gain, consistent with the measurements shown in Fig. 8.10(b). Furthermore, a lower half-wave voltage of the intensity modulator at the link input (V_π) results in higher gain, as shown in the calculations presented in Fig. 8.11(a).

Next, we consider possible noise sources in the systems, with a noise spectral density given by [144, 198]

$$N = \underbrace{(1+g)\, k_{\mathrm{B}} T}_{\text{Thermal noise}} + \underbrace{2qR_{\mathrm{out}} \left|H_{\mathrm{pd}}\right|^2 I^{(\mathrm{DC})}}_{\text{Shot noise}} + \underbrace{4\eta n_{\mathrm{sp}} \hbar\omega \left(g_{\mathrm{EDFA}} - 1\right) R_{\mathrm{out}} \left|H_{\mathrm{pd}}\right|^2 I^{(\mathrm{DC})}}_{\text{EDFA noise}}, \tag{8.19}$$

where the DC current $I^{(\mathrm{DC})}$ was given in Eq. (8.16). The first term accounts for Johnson-Nyquist noise at the link input and output, proportional to the link gain. The second term is shot noise, where q is the electron charge. The third term considers the noise from an

optical erbium-doped fiber amplifier (EDFA), where we assume the main contribution is the beating of spontaneous emission with the signal [198], where n_{sp} is the spontaneous emission factor (of order unity), and g_{EDFA} is the amplifier gain. Fig. 8.11(b) shows the scaling of these noise sources with optical power and device length, for different cases of modulator half-wave voltage values. We can see that the noise added when using an EDFA is the dominant term and determines the noise floor of the microwave link.

We calculate the noise factor (F) of the microwave-photonic link, a measure of the degradation of signal-to-noise, given by

$$F = \frac{\mathrm{SNR}_{\mathrm{in}}}{\mathrm{SNR}_{\mathrm{out}}} = \frac{P_{\mathrm{in}}^{(\Omega)}/N_{\mathrm{in}}}{P_{\mathrm{out}}^{(\Omega)}/N_{\mathrm{out}}} = \frac{N_{\mathrm{out}}}{gN_{\mathrm{in}}}, \tag{8.20}$$

where we typically assume thermal noise at the link input (i.e., $N_{\mathrm{in}} = k_{\mathrm{B}}T = -174$ dBm/Hz). Using Eqs. (8.18) and (8.19) for the gain and output noise, we can calculate the expected noise figure of the link ($\mathrm{NF} = 10\log_{10}(F)$), as shown in Fig. 8.11(c) for the case of a link using an EDFA, and in Fig. 8.11(e) for a link without an EDFA. In both cases, we see the reduction in noise figure for stronger Brillouin interactions, consistent with our experimental results (see Fig. 8.10(c)).

The main source of nonlinearity in the microwave-photonic link is the intensity modulator at the link input. When operating the modulator at quadrature, the third-order nonlinearity is the dominant source of distortion. Following the derivation presented in Chapter 5, we can calculate the third-order output intercept point (OIP_3)

$$\mathrm{OIP}_3 = 3\eta^2 R_{\mathrm{out}}|H_{\mathrm{pd}}|^2\Big(P^{(\mathrm{B})}G_{\mathrm{B}}P^{(\mathrm{E})}L\Big)^2, \tag{8.21}$$

from which we can derive the third-order spur-free dynamic range, given by $\mathrm{SFDR}_3 = (\mathrm{OIP}_3/(NB_{\mathrm{RF}}))^{2/3}$, where B_{RF} is the RF bandwidth measured at the link output. Figs. 8.11(d,f) show the calculated dynamic range, with and without optical amplification. These results show an increase of the dynamic range with stronger Brillouin interactions, consistent with our earlier experimental demonstration (see Fig. 8.10(d)).

The calculations presented here show the potential of PPER-based notch filters to yield

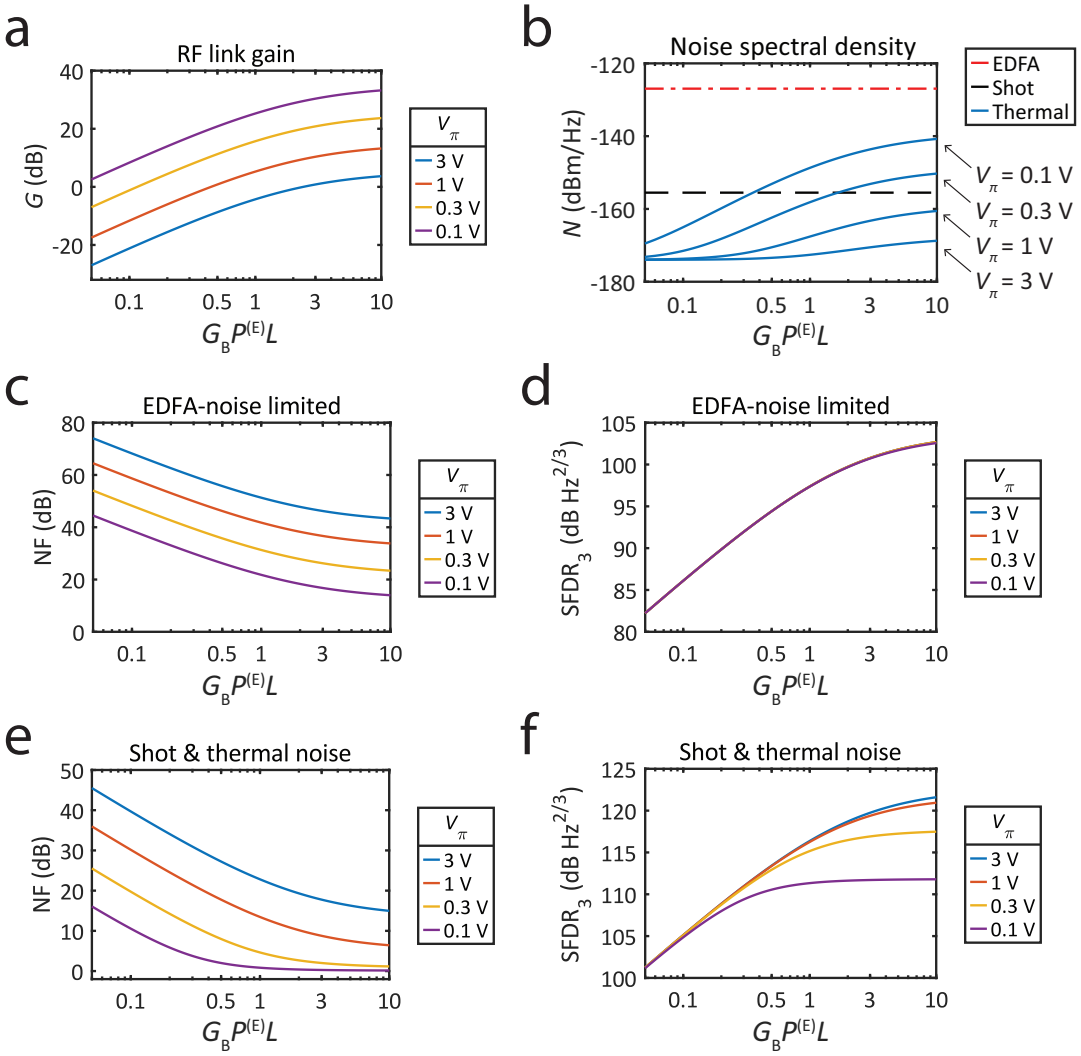

Figure 8.11: Calculated RF link performance as a function of the acousto-optic interaction strength in the PPER device ($G_B P^{(E)} L$). The values used for the calculations are typical to the device and link demonstrated in this work, assuming 100 mW of optical power on the detector. **(a)** RF link gain, for different values of modulator half-wave voltages. **(b)** Noise spectral density of the noise sources considered in Eq. (8.19). **(c)** Noise figure, assuming all three noise sources are present. **(d)** Spur-free dynamic range, assuming all three noise sources are present. **(e)** Noise figure, in the case of a system without an optical amplifier (EDFA). **(f)** Spur-free dynamic range, in the case of a system without an optical amplifier.

a link gain of 20 dB, a noise figure of ∼20 dB, and a spur-free dynamic range >100 dB $\mathrm{Hz}^{2/3}$, as can be seen in Figs. 8.11(c,d). Furthermore, full integration of the filter on-chip could eliminate the need for optical amplification, which will reduce the noise floor (see Fig. 8.11(b)). The lower noise will enhance system performance, potentially improving the noise figure by 10 dB, and the dynamic range by 20 dB $\mathrm{Hz}^{2/3}$, as can be seen in Figs. 8.11(e,f).

8.6 Notch-frequency selection

The cancellation of the microwave signal at the notch frequency is a result of the coherent destructive interference between the signals from the two interferometer paths. To achieve strong suppression, both the phase and amplitude of the signals have to be balanced (see Fig. 8.2). In the case of a PPER device supporting multiple acoustic modes, the frequency at which the cancellation occurs can be selected by matching the power and time-delay in the reference arm of the interferometer to that of different signals from the PPER output, which correspond to different acoustic modes. Multiple acoustic modes can be present in the same device, as seen in Fig. 8.4(d), or could be a result of multiple PPER segments designed to have different resonant frequencies, as was discussed earlier in Chapter 6.

As an example, we consider a single-pole PPER with two acoustic resonances at frequencies $\Omega_0^{(1)}$ and $\Omega_0^{(2)}$, with Brillouin gains $G_\mathrm{B}^{(1)}$ and $G_\mathrm{B}^{(2)}$, respectively. Following our derivation in the previous section, the output RF power can be written as

$$P_\mathrm{out}^{(\Omega)} = P_\mathrm{in}^{(\Omega)}\eta^2 R_\mathrm{out}|H_\mathrm{pd}|^2 R_\mathrm{in}\left(\frac{\pi}{V_\pi}\right)^2 \times \left|P^{(\mathrm{A})} - \frac{1}{2}P^{(\mathrm{B})}P^{(\mathrm{E})}L\left(G_\mathrm{B}^{(1)}\frac{\Gamma}{2}\chi^{(1)}(\Omega) + G_\mathrm{B}^{(2)}\frac{\Gamma}{2}\chi^{(2)}(\Omega)\right)\right|^2, \tag{8.22}$$

where we have assumed the path lengths are matched, such that $\Delta\tau = 0$. We can use the difference in Brillouin gain to select the frequency at which strong signal suppression will occur. If we set the power $P^{(\mathrm{A})}$ to balance the first resonance, i.e., $P^{(\mathrm{A})} = P^{(\mathrm{B})}G_\mathrm{B}^{(1)}P^{(\mathrm{E})}L/2$,

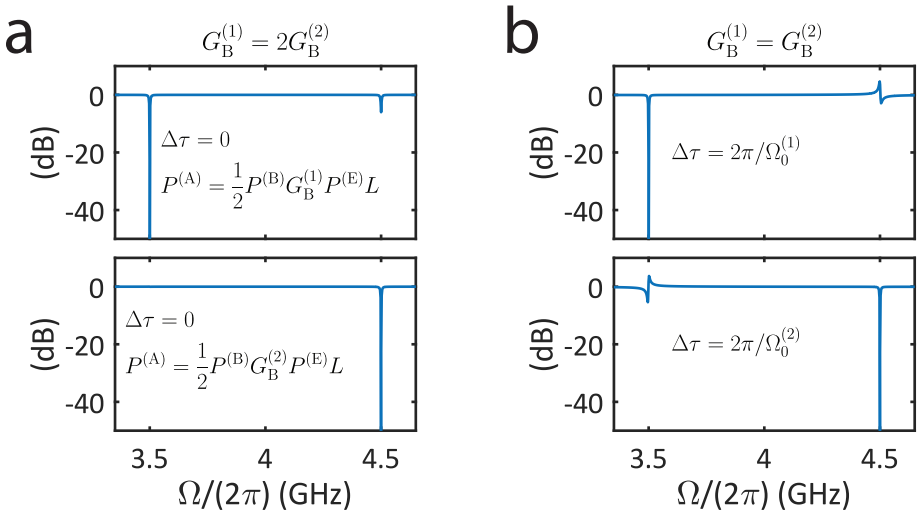

Figure 8.12: **(a)** The notch frequency can be switched between two resonances with different Brillouin gains by matching the power to each resonance, assuming no time-delay in the two interferometer paths. **(b)** In the case of two resonances with identical gain, the phase induced by the time-delay between the two interferometer paths can be used to select the notch frequency.

we will get cancellation of the signal at $\Omega_0^{(1)}$, while at frequency $\Omega_0^{(2)}$ we will have

$$P_{\text{out}}^{(\Omega)}\left(\Omega_0^{(2)}\right) = \frac{1}{4}P_{\text{in}}^{(\Omega)}\eta^2 R_{\text{out}}|H_{\text{pd}}|^2 R_{\text{in}}\left(\frac{\pi}{V_\pi}\right)^2\left(P^{(B)}G_B^{(1)}P^{(E)}L\right)^2\left|1-\frac{G_B^{(2)}}{G_B^{(1)}}\right|^2. \tag{8.23}$$

Here, we have assumed that the two acoustic modes are well separated, such that $\chi^{(1)}(\Omega_0^{(2)}) = \chi^{(2)}(\Omega_0^{(1)}) = 0$. Alternatively, if we set the optical power to match the second resonance, such that $P^{(A)} = P^{(B)}G_B^{(2)}P^{(E)}L/2$, we will get perfect cancellation at frequency $\Omega_0^{(2)}$, while at frequency $\Omega_0^{(1)}$ the power is given by

$$P_{\text{out}}^{(\Omega)}\left(\Omega_0^{(1)}\right) = \frac{1}{4}P_{\text{in}}^{(\Omega)}\eta^2 R_{\text{out}}|H_{\text{pd}}|^2 R_{\text{in}}\left(\frac{\pi}{V_\pi}\right)^2\left(P^{(B)}G_B^{(2)}P^{(E)}L\right)^2\left|1-\frac{G_B^{(1)}}{G_B^{(2)}}\right|^2, \tag{8.24}$$

As an example, we assume that the Brillouin gain of two modes differs by 3 dB, i.e., $G_B^{(1)} = 2G_B^{(2)}$, and that they are separated in frequency by 1 GHz. When the signal is fully suppressed at frequency $\Omega_0^{(1)} = 3.5$ GHz, there will be a 6 dB dip at $\Omega_0^{(2)} = 4.5$ GHz, as seen in the calculation in Fig. 8.12(a). In this example, when the amplitude is matched to cancel the signal at $\Omega_0^{(2)}$, there will be no ripple in the frequency response at $\Omega_0^{(1)}$.

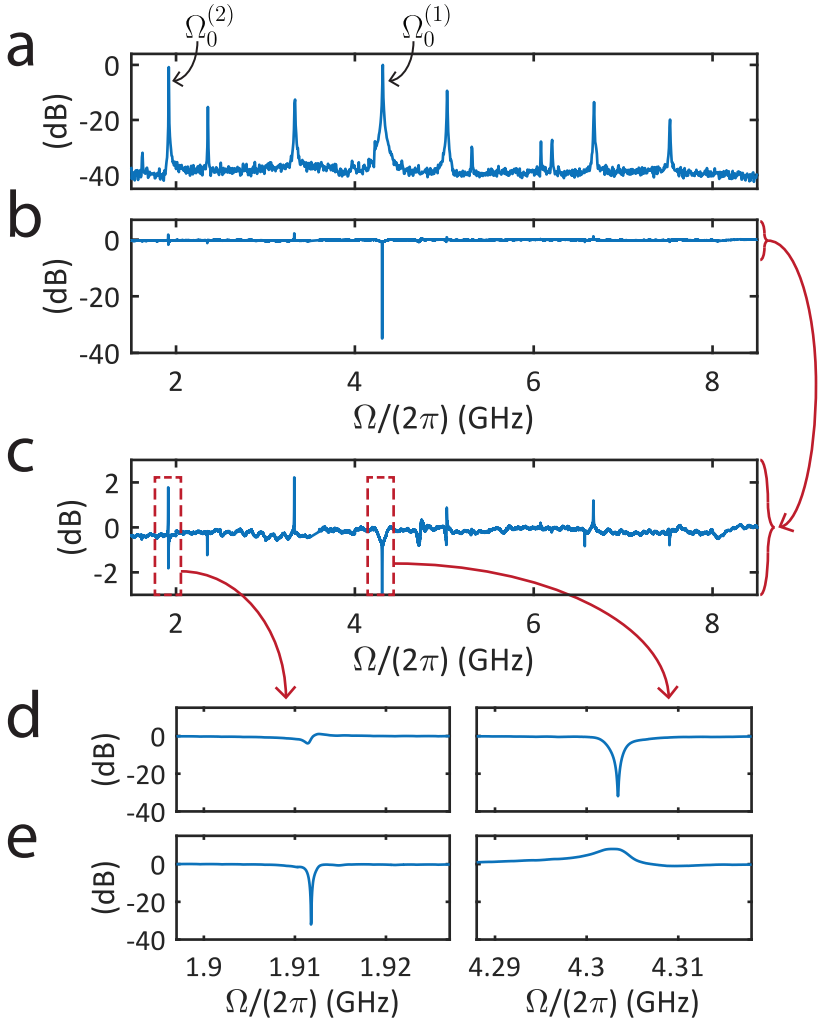

Figure 8.13: **(a)** Measured frequency response of a PPER device showing multiple acoustic modes. **(b)** The corresponding notch filter response, when the interferometer is set to achieve cancellation of the signal at frequency $\Omega_0^{(1)} = 4.3$ GHz. **(c)** A magnified view shows spurs at frequencies corresponding to other acoustic modes. **(d)** Magnified view, showing the ripple around frequency $\Omega_0^{(2)} = 1.9$ GHz and ∼40 dB of cancellation at frequency $\Omega_0^{(1)} = 4.3$ GHz. **(e)** By tuning the interferometer, using a variable optical amplifier (VOA), we shift the notch filter to achieve signal cancellation at frequency $\Omega_0^{(2)} = 1.9$ GHz.

We demonstrate the selection of the notch frequency experimentally, using a PPER device with multiple acoustic resonances, seen in Fig. 8.13(a). By balancing the power of the resonance at frequency $\Omega_0^{(1)} = 4.3$ GHz, we achieve a notch filter with ∼40 dB rejection (Fig. 8.13(b)), while the other resonances produce a ripple of a few dB, as shown in the magnified view in Figs. 8.13(c,d). By tuning the power $P^{(\mathrm{A})}$, matching it to the resonance at frequency $\Omega_0^{(2)} = 1.9$ GHz, we shift the ∼40 dB notch response to $\Omega_0^{(2)}$, leaving a distortion of 8 dB at $\Omega_0^{(1)}$, seen in Fig. 8.13(e). While this demonstration utilized acoustic modes within the same PPER device that have different Brillouin gain, a similar calculation can be carried out for the case of multiple PPER segments. In this case, the active segments can be designed to have different active lengths L, resulting in an amplitude difference between their corresponding signals, which can be used for notch frequency selection in a similar way.

An alternative strategy for notch-frequency selection is to utilize the different phase shift accumulated by different frequency components for a given time-delay. We consider a system with two well-separated acoustic modes, which we now assume to have equal Brillouin gain, and match the optical powers of the two interferometer paths, such that

$$P_{\mathrm{out}}^{(\Omega)} = \frac{1}{4} P_{\mathrm{in}}^{(\Omega)} \eta^2 R_{\mathrm{out}} |H_{\mathrm{pd}}|^2 R_{\mathrm{in}} \left(\frac{\pi}{V_\pi}\right)^2 \left(P^{(\mathrm{B})} G_{\mathrm{B}} P^{(\mathrm{E})} L\right)^2 \times \left| 1 - \left(\frac{\Gamma}{2}\chi^{(1)}(\Omega) + \frac{\Gamma}{2}\chi^{(2)}(\Omega)\right) e^{-i\Omega\Delta\tau} \right|^2 . \tag{8.25}$$

Here, we can use the time-delay $\Delta\tau$ to select the frequency at which perfect signal cancellation occurs. By setting $\Delta\tau = 2\pi m/\Omega_0^{(1)}$ (for integer m), strong signal suppression will occur at frequency $\Omega_0^{(1)}$. By changing the time delay, such that $\Delta\tau = 2\pi m/\Omega_0^{(2)}$, we can shift the notch frequency to $\Omega_0^{(2)}$. This is demonstrated numerically in Fig. 8.12(b), where we have chosen the value $m = 1$, showing the shifting of the notch filter between two frequencies, with a distortion of a few dB at the unsuppressed resonance.

8.6.1 Inverting the frequency response

As we have seen in the previous sections, the frequency response of the notch filter is set by the phase relation between the two interferometer arms. When the signals are exactly out of phase, we achieve a notch filter response, assuming both signals have equal powers. If, however, the signals add in phase, by setting the time delay such that $\Delta\tau = \pi/\Omega_0 + 2\pi m$ (for integer m), the resulting frequency response will show a peak of 6 dB at the resonance frequency (see Fig. 8.2(b)). The ability to manipulate the frequency response using a phase shift can be utilized for switching applications, where the notch filter can be effectively turned on and off through control of a time-delay.

The change in the relative phase between the two signals can also be controlled through the demodulation scheme we are implementing at the PPER output. The demodulation we have used in our demonstration utilizes optical filtering of the light exiting the 'receive' waveguide of the PPER, such that only the optical carrier ω_2 and the first upper sideband (indices $n = 0, 1$ from Eq. (8.4)) are transmitted. However, if we use the optical filter to select the carrier and the first lower sideband (indices $n = -1, 0$) and repeat the steps of the derivation from the previous section, the photocurrent at the detector will be given by

$$I^{(\Omega)}(t) = -\eta \left(\frac{\pi V_{\text{in}}}{V_\pi}\right) \text{Im}\left[e^{-i\Omega t}\left(P^{(\text{A})} + \frac{1}{2}P^{(\text{B})}G_{\text{B}}P^{(\text{E})}L\frac{\Gamma}{2}\left|\chi(\Omega)\right| e^{-i(\Omega\Delta\tau-\phi)}\right)\right]. \quad (8.26)$$

When the power $P^{(\text{A})}$ is set to the value needed for notch filtering and the time-delays of the two optical paths are matched ($\Delta\tau = 0$), the output RF power will be

$$P_{\text{out}}^{(\Omega)} = \frac{1}{4}P_{\text{in}}^{(\Omega)}\eta^2 R_{\text{out}}|H_{\text{pd}}|^2 R_{\text{in}}\left(\frac{\pi}{V_\pi}\right)^2\left(P^{(\text{B})}G_{\text{B}}P^{(\text{E})}L\right)^2\left|1+\frac{\Gamma}{2}\chi(\Omega)\right|^2. \quad (8.27)$$

On resonance ($\Omega = \Omega_0$), this yields a combined power that is four times larger than the power off-resonance, since $(\Gamma/2)\chi(\Omega_0) = 1$ and $\chi(\Omega \neq \Omega_0) \to 0$. Hence, by switching the sideband selected in the PPER demodulation, the notch filter response can be transformed into a 6 dB peak in transmission. We demonstrate this experimentally, switching between a ~40 dB dip and a 6 dB peak, as seen in Fig. 8.14.

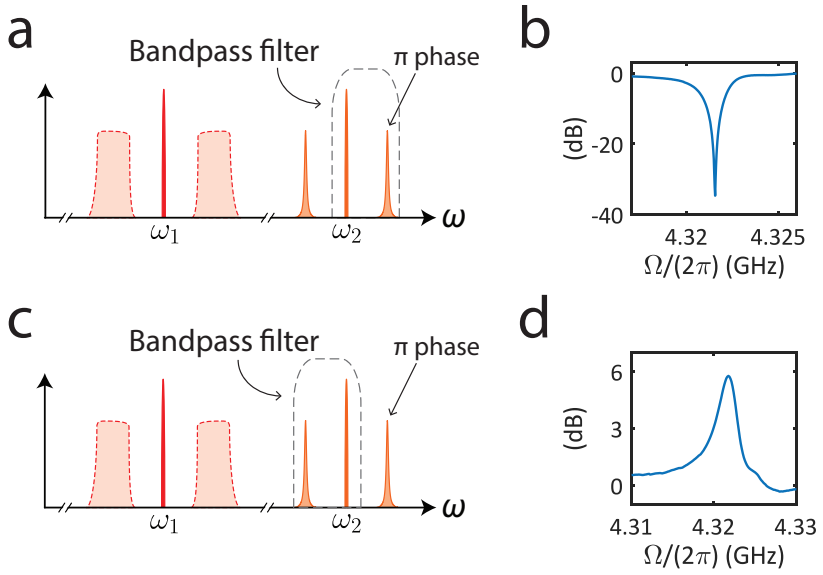

Figure 8.14: **(a)** When the beat note produced by the intensity modulator (red) is out of phase with the demodulated PPER output (orange), we achieve cancellation at the Brillouin frequency. **(b)** Measured frequency response showing cancellation at the notch frequency. **(c)** By tuning the bandpass filter, the demodulated signal is in-phase with the one produced by the intensity modulator. **(d)** Measured response of the filter after tuning the bandpass filter, showing a 6 dB peak as a result of the signals adding in phase.

8.7 Alternative notch-filtering implementations

In the notch-filtering scheme we have presented, the signals from the two interferometer paths were combined in the optical domain before detection. However, there was no optical interference in this scheme, as the wavelengths of the two fields were well separated, and the interference was achieved in the microwave domain (i.e., the photocurrent in the detector). In this section, we will consider alternative implementations of PPER-based notch filters, using balanced detection, as well as optical interference, which both result in a narrowband notch frequency response set by the PPER device.

8.7.1 Balanced detection

A possible variation to the PPER-based notch filter we have presented is to use two photodetectors, each detecting the light from one of the interferometer paths. By combining the photocurrents from the two detectors out of phase, we can achieve signal cancellation,

as is typically implemented in balanced detection schemes. One such scheme is presented in Fig. 8.15(a), where each path of the optical interferometer is detected separately, and the signals from the two photodetectors are combined using an RF hybrid (i.e., RF directional coupler) to achieve the desired notch filter response.

Analyzing this scenario, the field impinging on the first photodetector is the output of the intensity modulator, which was described in Eq. (8.1). The photocurrent produced by this detector at the RF input frequency (Ω) is given by

$$I_{\mathrm{A}}^{(\Omega)} = -2\eta^{(\mathrm{A})}\widetilde{P}^{(\mathrm{A})}J_1\left(\frac{\pi V_{\mathrm{in}}}{V_\pi}\right)\sin\Omega t, \tag{8.28}$$

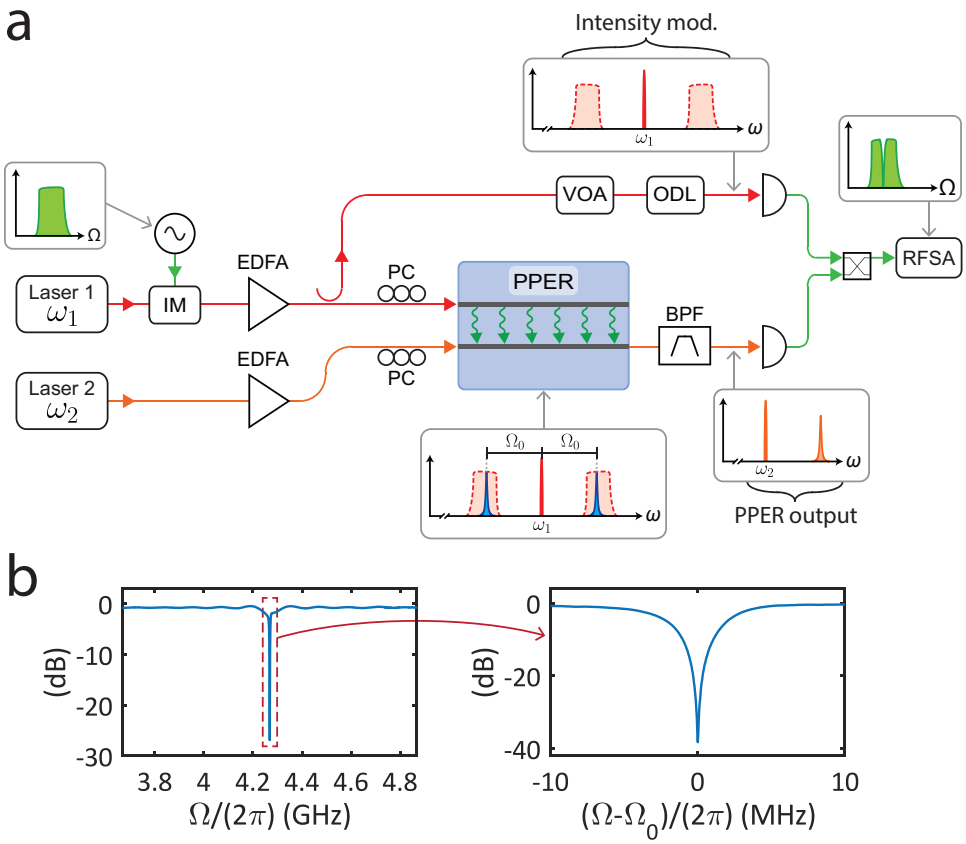

Figure 8.15: **(a)** Schematic illustration of the experimental setup used to demonstrate PPER-based notch filtering using two photodetectors. IM: intensity modulator, VOA: variable optical attenuator, ODL: optical delay line, BPF: optical bandpass filter, RFSA: RF spectrum analyzer. EDFA: erbium-doped fiber amplifier, PC: polarization controller. **(b)** Left: Measured frequency response of the notch filter. Right: Magnified view around the filter notch frequency, showing 40 dB of signal suppression.

where $\eta^{(\mathrm{A})}$ is the responsivity of the detector. The photocurrent produced by the second detector is a result of the demodulated PPER output, which was described in Eq. (8.5), and calculating the photocurrent at frequency Ω gives us

$$I_{\mathrm{B}}^{(\Omega)} = 2\eta^{(\mathrm{B})}\widetilde{P}^{(\mathrm{B})}J_0\left(\beta_{\mathrm{in}}\right)J_1\left(\beta_{\mathrm{in}}\right)\sin\left(\Omega t-\phi\right), \tag{8.29}$$

where $\eta^{(\mathrm{B})}$ is the responsivity of the second detector. Combining the currents from Eqs. (8.28) and (8.29) yields

$$\begin{aligned} I^{(\Omega)}(t) = 2\Bigg[&\eta^{(\mathrm{B})}P^{(\mathrm{B})}J_0\left(\beta_{\mathrm{in}}\right)J_1\left(\beta_{\mathrm{in}}\right)\sin\left(\Omega\left(t-\tau^{(\mathrm{B})}\right)-\phi\right) \\ &-\eta^{(\mathrm{A})}P^{(\mathrm{A})}J_1\left(\frac{\pi V_{\mathrm{in}}}{V_\pi}\right)\sin\left(\Omega\left(t-\tau^{(\mathrm{A})}\right)\right)\Bigg], \end{aligned} \tag{8.30}$$

which has a similar form to Eq. (8.7) we had in our previous filtering scheme. The time-delays $\tau^{(\mathrm{A})}$ and $\tau^{(\mathrm{B})}$ correspond to the time-delays of the two signal paths, which can be adjusted in the optical or in the RF domain. The relation between the powers $\{\widetilde{P}^{(\mathrm{A})},\widetilde{P}^{(\mathrm{B})}\}$ and $\{P^{(\mathrm{A})},P^{(\mathrm{B})}\}$ is determined by the ratios in which the currents are combined. Analyzing the performance of this scheme is equivalent to that presented in the previous section, where a possible difference in the responsivity of the two detectors needs to be taken into account. An experimental demonstration of filtering using this scheme is presented in Fig. 8.15(b), showing the measurement of a PPER-based notch filter with 40 dB of signal suppression at the notch frequency.

8.7.2 Signal interference in the optical domain

Alternatively, signal cancellation can be achieved directly in the optical domain, rather than through RF signal interference. This filtering scheme is shown schematically in Fig. 8.16(a), illustrating the cancellation of the optical sidebands at the notch frequency before detection. By using the same laser source for both the 'emit' and 'receive' waveguides of the PPER, all signals can be optically coherent, and the optical sidebands carrying the RF information can directly interfere in the optical domain, resulting in the cancellation of the optical signal at an optical frequency spaced by the Brillouin frequency from the carrier. After detection,

this corresponds to suppression of the RF signal at the Brillouin frequency. In this case, the interference occurs in the optical domain, and implementing such a microwave-photonic filter requires a higher level of stabilization, which could be achieved by a fully integrated device [310].

Using the expression for the combined field at the detector from Eq. (8.6), and assuming

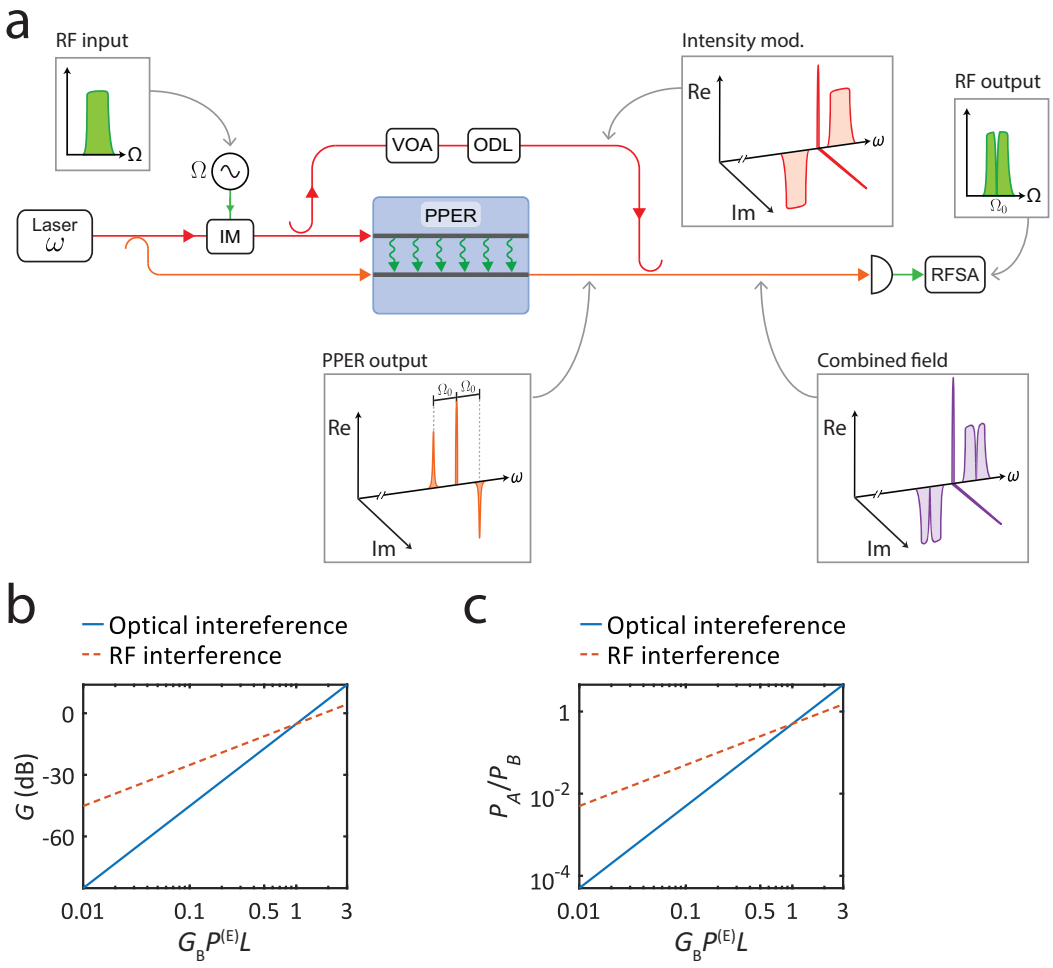

Figure 8.16: **(a)** PPER-based notch filtering using optical interference. IM: intensity modulator, VOA: variable optical attenuator, ODL: optical delay line, RFSA: RF spectrum analyzer **(b)** Calculated RF link gain and **(c)** optical power needed to achieve signal cancellation as a function of the Brillouin interaction strength (solid blue line). The equivalent calculation for the RF-interference notch-filtering scheme (see Section 8.2) is shown for reference (dashed red line).

both fields have the same optical carrier frequency ω, we have

$$E(t) = \sqrt{\frac{P^{(\mathrm{A})}}{2}} e^{-i\omega t} \left(i + \sum_n J_n \left(\frac{\pi V_{\mathrm{in}}}{V_\pi} \right) e^{-in\Omega t} \right) + i\sqrt{P^{(\mathrm{B})}}\ e^{-i\omega(t+\Delta\tau)} \sum_n i^{-n} J_{-n}\left(\beta_{\mathrm{in}}\right) e^{-in(\Omega(t+\Delta\tau)-\phi)}, \tag{8.31}$$

where we have defined the time delay between the two signals $\Delta\tau$. Next, we set the time delay such that $\omega\Delta\tau = \pi/2 + 2\pi m$ (fo integer m), resulting in

$$E(t) = \sqrt{\frac{P^{(\mathrm{A})}}{2}} e^{-i\omega t} \left(i + \sum_n J_n \left(\frac{\pi V_{\mathrm{in}}}{V_\pi} \right) e^{-in\Omega t} \right) + \sqrt{P^{(\mathrm{B})}}\ e^{-i\omega t} \sum_n J_{-n}\left(\beta_{\mathrm{in}}\right) e^{-in(\Omega(t+\Delta\tau)-\phi+\pi/2)}. \tag{8.32}$$

For small RF signals (i.e., $V_{\mathrm{in}} \ll V_\pi$), we can expand the Bessel functions to first order ($J_0(x) \approx 1$, $J_{\pm1}(x) \approx \pm x/2$), neglecting higher order terms. Substituting $\beta_{\mathrm{in}} \approx G_{\mathrm{B}} P^{(\mathrm{E})} L(\pi V_{\mathrm{in}}/V_\pi)|\chi(\Omega)|\Gamma/4$ (see Eq. (8.3)), we have

$$\begin{aligned} E(t) =& e^{-i\omega t}\left[\left(i\sqrt{\frac{P^{(\mathrm{A})}}{2}} + \sqrt{\frac{P^{(\mathrm{A})}}{2}} + \sqrt{P^{(\mathrm{B})}} \right) \right. \\ &\left. + i\left(\frac{\pi V_{\mathrm{in}}}{V_\pi} \right) \mathrm{Im}\left[e^{-i\Omega t} \left(\sqrt{\frac{P^{(\mathrm{A})}}{2}} - \frac{1}{2}\sqrt{P^{(\mathrm{B})}} G_{\mathrm{B}} P^{(\mathrm{E})} L \frac{\Gamma}{2} |\chi(\Omega)| e^{-i(\Omega\Delta\tau-\phi+\pi/2)} \right) \right] \right]. \end{aligned} \tag{8.33}$$

To achieve cancellation at the Brillouin frequency, we set the optical power $P^{(\mathrm{A})}$ such that $P^{(\mathrm{A})} = P^{(\mathrm{B})}(G_{\mathrm{B}} P^{(\mathrm{E})} L)^2/2$, yielding

$$\begin{aligned} E(t) =& \sqrt{P^{(\mathrm{B})}} e^{-i\omega t}\left[\left(1 + \frac{1}{2} G_{\mathrm{B}} P^{(\mathrm{E})} L + \frac{i}{2} G_{\mathrm{B}} P^{(\mathrm{E})} L \right) \right. \\ &\left. + i\left(\frac{\pi V_{\mathrm{in}}}{V_\pi} \right) \left(\frac{1}{2} G_{\mathrm{B}} P^{(\mathrm{E})} L \right) \mathrm{Im}\left[e^{-i\Omega t} \left(1 - \frac{\Gamma}{2} |\chi(\Omega)| e^{-i(\Omega\Delta\tau-\phi+\pi/2)} \right) \right] \right]. \end{aligned} \tag{8.34}$$

Calculating the photo-current at a detector ($I = \eta|E|^2$), keeping the terms oscillating at

frequency Ω, we have

$$I^{(\Omega)}(t) = 2\eta \left(\frac{\pi V_{\text{in}}}{V_\pi}\right) P^{(\text{B})} \left(\frac{1}{2} G_{\text{B}} P^{(\text{E})} L\right)^2 \text{Im}\left[e^{-i\Omega t}\left(1 - \frac{\Gamma}{2}|\chi(\Omega)|e^{-i(\Omega\Delta\tau - \phi + \pi/2)}\right)\right]. \tag{8.35}$$

Assuming a single-pole PPER device[2] (see Eqs. (8.10) and (8.11)) we set the time delay $\Omega_0\Delta\tau = -\pi/2 + 2\pi m$ (for integer m), giving us

$$\begin{aligned} I^{(\Omega)}(t) = 2\eta \left(\frac{\pi V_{\text{in}}}{V_\pi}\right) P^{(\text{B})} \left(\frac{1}{2} G_{\text{B}} P^{(\text{E})} L\right)^2 \\ \times \text{Im}\left[e^{-i\Omega t}\left(1 - \frac{\Gamma}{2}\chi(\Omega) e^{-i\left[(\pi/2)(1-\Omega/\Omega_0) + 2\pi m(\Omega/\Omega_0)\right]}\right)\right], \end{aligned} \tag{8.36}$$

which has a similar form to Eq. (8.12). We can calculate the output RF power ($P_{\text{out}}^{(\Omega)} = \langle I^2 \rangle R_{\text{out}} |H_{\text{pd}}|^2$), yielding

$$P_{\text{out}}^{(\Omega)} = \frac{1}{4} P_{\text{in}}^{(\Omega)} \eta^2 R_{\text{out}} |H_{\text{pd}}|^2 R_{\text{in}} \left(\frac{\pi}{V_\pi}\right)^2 {P^{(\text{B})}}^2 \left(G_{\text{B}} P^{(\text{E})} L\right)^4 \left|1 - \frac{\Gamma}{2}\chi(\Omega) e^{-i\left[(\pi/2)(1-\Omega/\Omega_0)\right]}\right|^2, \tag{8.37}$$

where we have expressed the input RF signal in terms of power ($P_{\text{in}}^{(\Omega)} = V_{\text{in}}^2/(2R_{\text{in}})$). The RF link gain in the filter pass-band (i.e., $\chi(\Omega) \to 0$) is given by

$$g = \frac{1}{4} \eta^2 R_{\text{out}} |H_{\text{pd}}|^2 R_{\text{in}} \left(\frac{\pi}{V_\pi}\right)^2 {P^{(\text{B})}}^2 \left(G_{\text{B}} P^{(\text{E})} L\right)^4. \tag{8.38}$$

We see that in this case, the RF link gain scales with the fourth power of the Brillouin interaction strength ($G_{\text{B}} P^{(\text{E})} L$), rather than the quadratic scaling we saw earlier. Fig. 8.16(b) shows the calculated RF link gain as a function of $G_{\text{B}} P^{(\text{E})} L$ and compares it to that obtained for the RF-interference notch-filtering scheme discussed in Section 8.2. Fig. 8.16(c) presents the required optical power $P^{(\text{A})}$ needed to achieve signal cancellation at the notch frequency. We can calculate the DC current at the detector when the power $P^{(\text{A})}$

2. A similar analysis can be performed for a two-pole PPER response, as was detailed in Section 8.2.

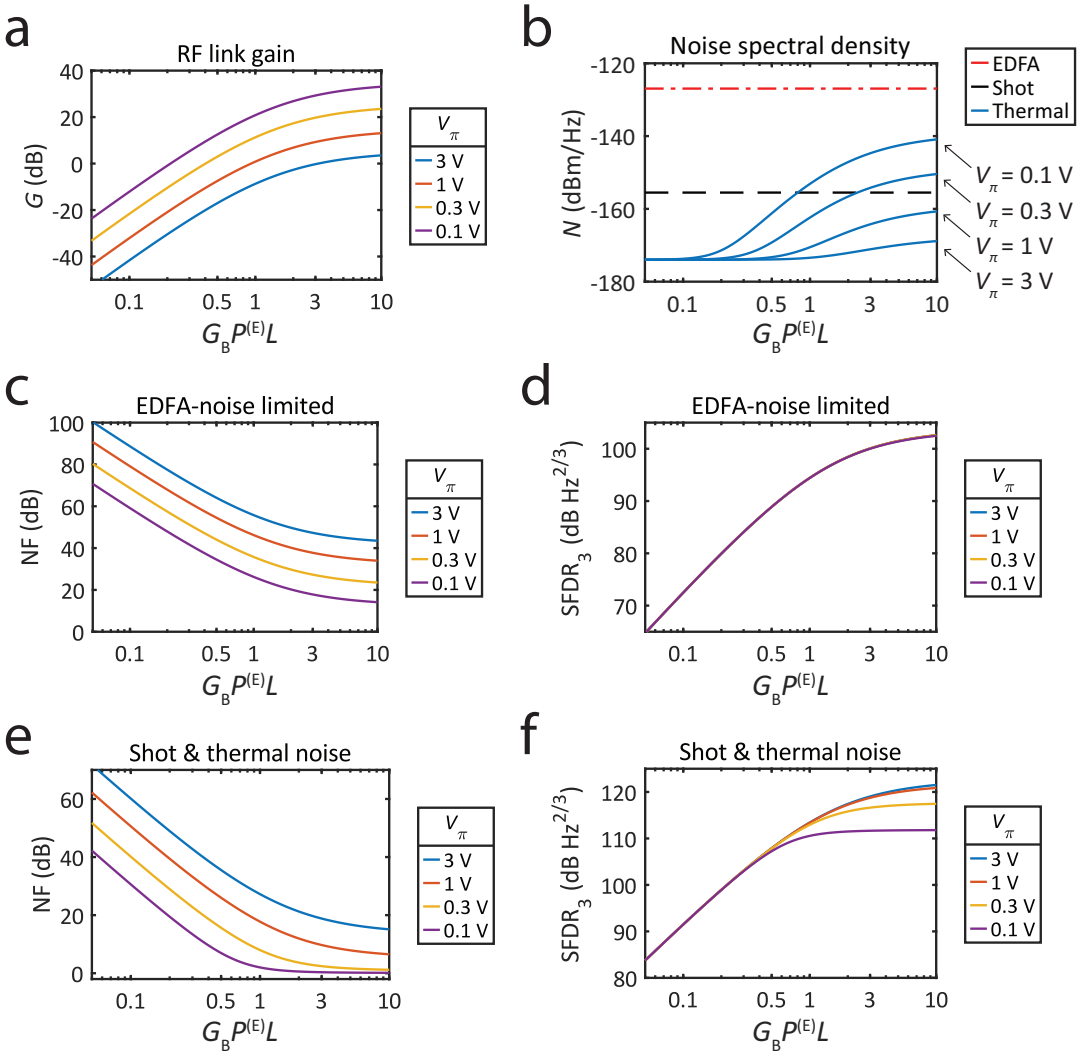

Figure 8.17: Calculated RF link performance for the optical interference scheme (see Fig. 8.16) as a function of the acousto-optic interaction strength in the PPER device ($G_B P^{(E)} L$). The values used for calculations are typical to the device and link demonstrated in this work, assuming 100 mW of optical power on the detector. **(a)** RF link gain, for different values of modulator half-wave voltages. **(b)** Noise spectral density of the noise sources considered in Eq. (8.19). **(c)** Noise figure, assuming all three noise sources are present. **(d)** Spur-free dynamic range, assuming all three noise sources are present. **(e)** Noise figure, in the case of a system without an optical amplifier (EDFA). **(f)** Spur-free dynamic range, in the case of a system without an optical amplifier.

is set for notch filtering

$$I^{(\mathrm{DC})} = \eta\Big(P^{(\mathrm{A})} + P^{(\mathrm{B})} + \sqrt{2P^{(\mathrm{A})}P^{(\mathrm{B})}}\Big), \tag{8.39}$$

from which we can derive the noise at the microwave-photonic link output using Eq. (8.19), as well as the noise figure and dynamic range (Eqs. (8.20) and (8.21)), seen in Fig. 8.17. We can see enhanced performance when increasing the Brillouin interaction strength, showing higher gain, lower noise figure, and a larger dynamic range.

8.8 Conclusion

In this chapter, we have an presented an important application of the photonic-phononic emit-receive (PPER) device scheme, implementing narrowband, tunable microwave-photonic notch filters in a standard silicon platform. By designing an interferometer with a narrowband PPER-based filter in one of the optical paths, we can transform the narrow bandpass response of the PPER device into a notch filter, achieving a high level of signal suppression at the notch frequency. When comparing to other recently demonstrated integrated microwave-photonic filters, this filter stands out for its high spectral resolution (∼MHz) while maintaining high signal rejection, as seen in Fig. 8.18. We have demonstrated how the filter can be tuned over a wide spectral range utilizing the wideband photonic platform while maintaining a narrowband notch response determined by the acoustic properties of the device. Furthermore, we have shown how the unique properties of the PPER scheme enable the design of multi-pole filters, as well as the suppression of unwanted acoustic resonances through phononic band engineering.

We have demonstrated PPER devices that were fabricated with standard photolithography methods, with an additional wet-etch step to suspend the active regions of the devices, which could also be incorporated into foundry production in the future. The use of mature fabrication technologies and a CMOS-compatible platform enables high-yield production and robust performance, as was shown in Chapter 6. Additionally, it enables the possibility of integrating electronic components on the same chip [48]. By integrating phase

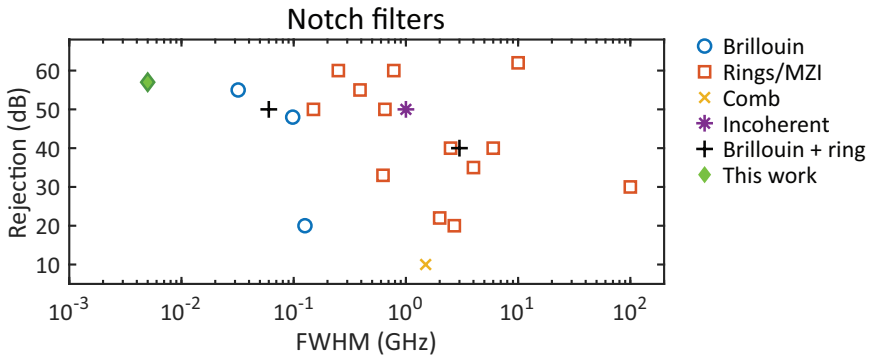

Figure 8.18: Summary of recently demonstrated integrated microwave-photonic notch filters, showing filter rejection and spectral resolution (FWHM: full-width at half-maximum). Surveyed work includes Brillouin-based filtering [142, 240, 246], filters using ring resonators and interferometers [221, 222, 227, 291, 295, 296, 309, 310, 319, 320, 323–326], comb-generation and spectral shaping [303], incoherent multi-tap filtering [308], and Brillouin scattering combined with resonators [241, 256].

shifters [327], optical attenuators [47], and filters [52] in the silicon platform, all of the components of a PPER-based filter can be implemented on-chip. Fig. 8.19 presents an artistic illustration of how a PPER device could be integrated, including all of the optical and electrical components needed for the filtering scheme.

In our experimental demonstrations, all measurements were performed with no active stabilization and with free-running laser sources. The fluctuations in power and phase of the signals in the two interferometer paths set the limit on the signal rejection we could demonstrate experimentally. By fully integrating the filter on-chip, the stability of the interferometer can be greatly enhanced, reducing fluctuations and yielding higher stop-band rejection.

Using a PPER device for microwave-photonic filtering has several advantages when considering their integration into larger microwave-photonic systems. The spatial separation of 'emit' and 'receive' paths eliminates unwanted reflections and reduces the effects of other optical nonlinearities such as Kerr-induced four-wave-mixing. Furthermore, the forward-Brillouin geometry obviates the need for circulators or isolators, facilitating the path to full integration, as these components can be challenging to implement on-chip. Additionally, this filtering scheme uses a conventional intensity or phase modulator and does not require advanced modulation methods or additional signal preparation.

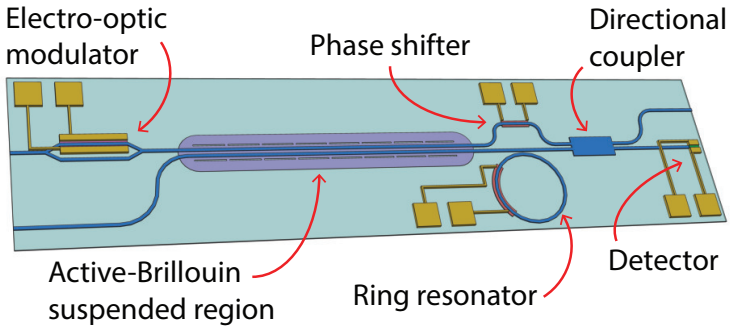

Figure 8.19: Schematic illustration of a fully integrated PPER-based notch filter, including an electro-optic modulator, an active-Brillouin suspended section performing the PPER operation, and a detector. Other integrated components can include ring resonators, phase shifters, and directional couplers.

The low-loss waveguides used in the PPER devices, with a typical linear loss of ∼0.2 dB/cm [64, 187], can enable the design of filter arrays with minimal degradation of the signal as it propagates through the system. More specifically, the notch frequency of each filter can be determined through its geometry, and by cascading filters in series, we can achieve multiple notch frequencies, as illustrated in Fig. 8.20. The presence of multiple acoustic modes could also be used to shift the notch frequency response, by balancing the interferometer to strongly suppress a specific mode, without much distortion to other frequencies. A proof-of-concept has been demonstrated here utilizing multiple Brillouin-active modes within a single PPER segment, however, this can also be performed between resonances of separate PPER sections. Additionally, we have discussed how the time delay between the interferometer paths could also be used for notch frequency selection.

Another possible notch filtering scheme consisting of multiple PPER devices is illustrated in Fig. 8.21. Here, the PPER devices are set in parallel, and in each device, an optical local oscillator is used to select the spectral region that is being filtered, similar to the scheme presented in Section 8.4. By combining the demodulated outputs of all the PPER devices, along with the output of an intensity modulator, multiple notch frequencies can be obtained, each separately tunable using an optical local oscillator. While such a system requires more components compared with other schemes presented here, all of the necessary elements, namely modulators, filters, and directional couplers, can be integrated on-chip and

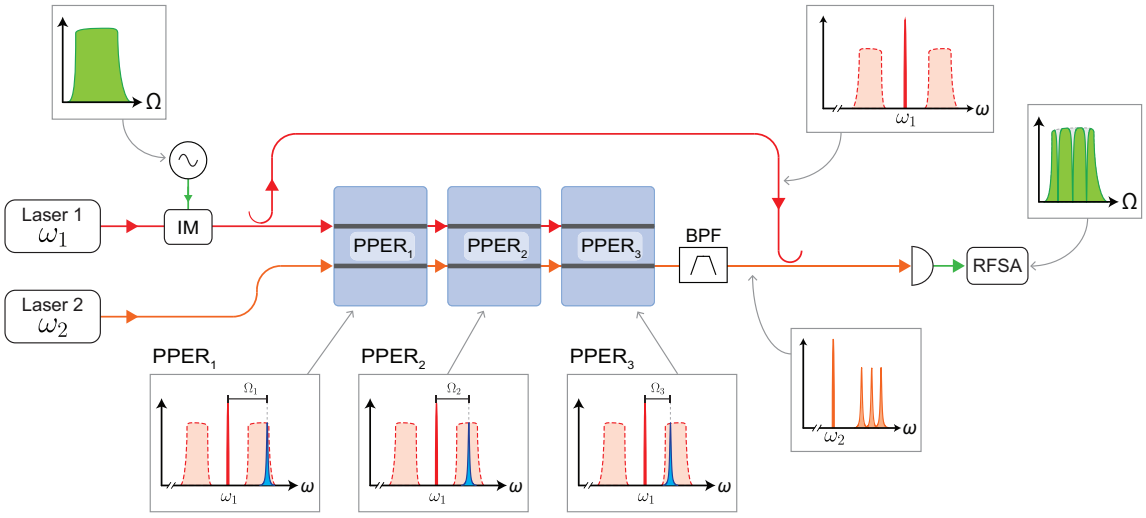

Figure 8.20: Schematic illustration of three cascaded PPER filters used to produce three notch frequencies. In this scheme, the geometry of each PPER segment is designed to have a different Brillouin frequency. IM: intensity modulator, BPF: optical bandpass filter, RFSA: RF spectrum analyzer.

are compatible with processes in existing silicon-photonic foundries.

The performance of PPER-based microwave-photonic notch filters is determined by the strength of the Brillouin interaction in the device, as well as the properties of the electro-optic modulator at the filter input. The RF link performance presented here, using a centimeter-scale device, is comparable to many other filtering schemes [196, 209]. At the pass-band of the notch filter, the performance of the PPER-based filter is determined by the modulator at the filter input, and by using modulators with a low half-wave voltage [53,200], as well as linearization schemes [201], lower noise figure and a larger dynamic range could be possible. Additionally, cascading the filter with a microwave low-noise amplifier can improve the noise figure, as was demonstrated in Chapter 7.

The Brillouin interaction in the device is proportional to its length (L), the optical power in the 'emit' waveguide ($P^{(\mathrm{E})}$), and the Brillouin gain (G_{B}), which is determined by the material properties, waveguide design, and the acoustic dissipation rate. Improving any of these parameters will enhance the RF performance of the filter. For example, we can expect a device of length $L = 5$ cm (keeping all other properties constant) to improve the link gain by 10 dB compared to the measurements we have presented here. In our demonstrations, the

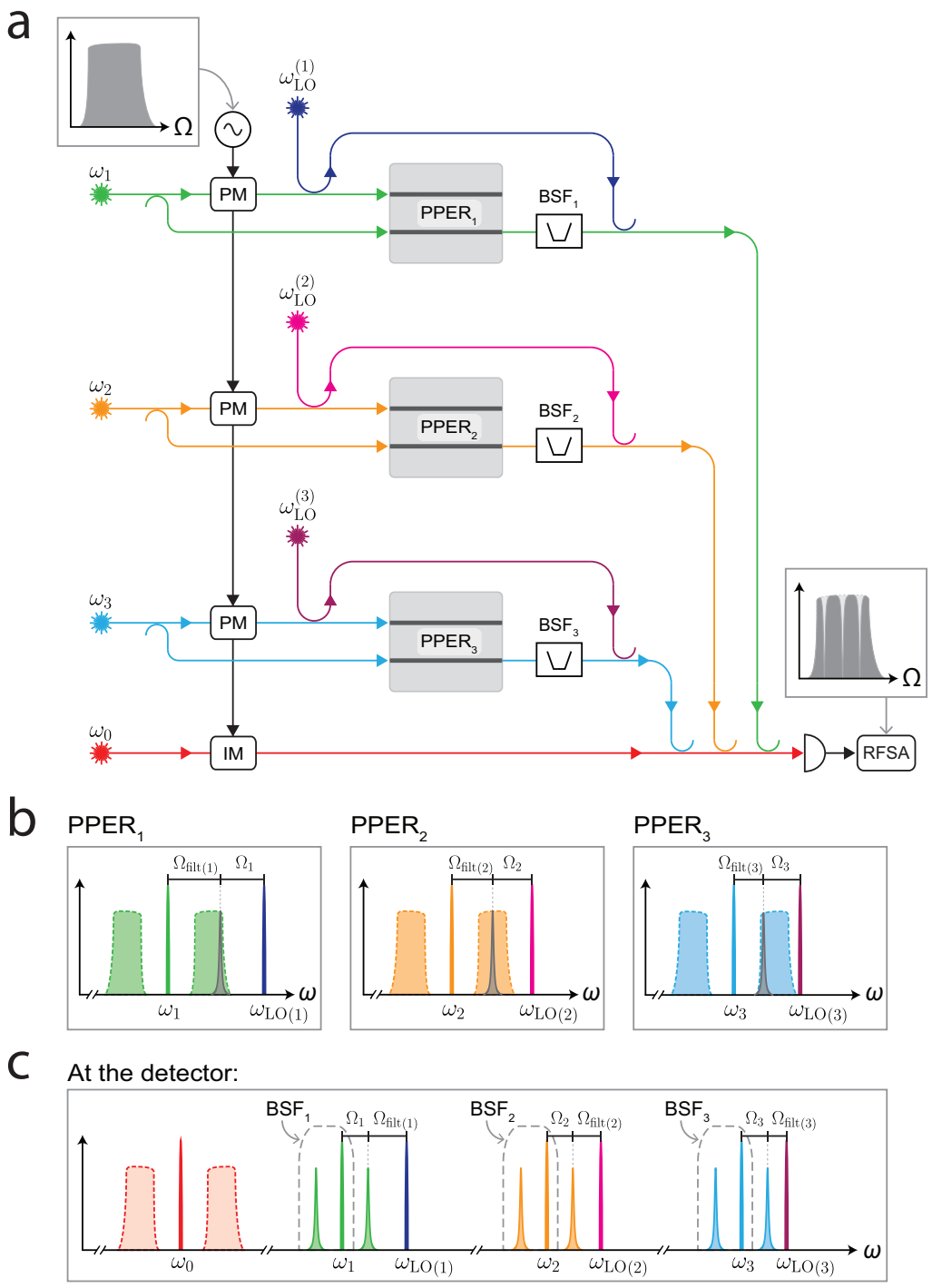

Figure 8.21: **(a)** Schematic illustration of three PPER-based filters used to achieve independently tunable notch frequencies. PM: phase modulator, IM: intensity modulator, BSF: optical bandstop filter, RFSA: RF spectrum analyzer. **(b)** In each of the PPER devices, an optical local oscillator selects the spectral band that is transduced in the device. **(c)** At the detector, the signals from the different segments are combined, and their interference with the output of an intensity modulator results in the multiple-notch frequency response.

noise floor was set by the optical amplifiers (EDFA) used in the experiments. By integrating more of the filter components on-chip, fiber-chip coupling losses could be avoided (such that amplifiers may not be needed), vastly decreasing the noise floor and improving the noise figure and dynamic range of the RF link. It is important to note that the Brillouin process adds noise, however, only around a narrow band centered at the Brillouin frequency. In the notch filtering scheme presented here, the Brillouin frequency is in the stop-band of the filter, and Brillouin noise does not affect signals a few MHz away, leaving the pass-band of the filter unaffected.

Chapter 9

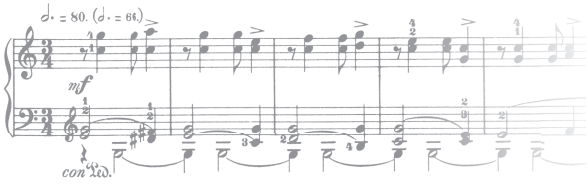

Using inter-modal Brillouin scattering in emit-receive operations

9.1 Introduction

In the previous chapters, we have focused on photonic-phononic emit-receive (PPER) devices utilizing *intra-modal* forward Brillouin scattering, studying their properties and showing how they can be used for filtering operations. More specifically, in the devices we have considered so far, all of the optical tones in each waveguide were guided in the same spatial and polarization mode, and described by the same dispersion relation. In this chapter, we will analyze devices utilizing the nonlocal properties of forward Brillouin scattering between different optical modes, i.e., *inter-modal* Brillouin scattering. Building on the theoretical analysis presented in Chapter 3, we will describe nonlocal susceptibilities produced by inter-modal Brillouin scattering, focusing on the case where light is scattered between two different guided spatial modes. Similar to the intra-modal case, the acoustic modes that mediate the interaction are mostly transverse and can extend a large space beyond the optical-guiding region. The extended nature of these phonons enables interaction with spatially separated optical waveguides, yielding a nonlocal effect, and can be used to design PPER structures.

When utilizing scattering processes between distinct guided modes, the field dynamics are vastly different compared to the forward intra-modal Brillouin scattering we have analyzed thus far. An intriguing property of inter-modal scattering is the ability to achieve a nonreciprocal response thanks to the unique phase-matching conditions of the system [137, 328]. Such optical nonreciprocity is an active area of research [329–331], as it is a promising strategy to be implemented in chip-integrated devices [136, 138]. Recently, an inter-modal PPER scheme has been used to demonstrate nonreciprocity in a standard silicon platform [139]. This nonlocal inter-band Brillouin scattering (NIBS) device demonstrated up to 38 dB of isolation and a transmission bandwidth of 1 nm (125 GHz). In the following sections, we will explore strategies to enhance the capabilities of such nonreciprocal NIBS devices. We will show how optical dispersion engineering could potentially increase the bandwidth of NIBS devices by an order of magnitude, and that varying the spatial distribution of Brillouin gain in the device could be used to enhance the nonreciprocal contrast. Additionally, we will examine the possibilities of resonantly enhancing the efficiency of NIBS devices, which may enable the design of low-loss optical isolators.

Another important feature of inter-modal Brillouin scattering is its single-sideband nature [30, 65], which can provide opportunities in the context of optical and microwave-photonic filtering. As we have seen in Chapter 7, intra-modal forward Brillouin PPER-based filters are limited in the maximum signal bandwidth they can process without distortion (see Fig. 7.5). This limitation is a result of the dual-sideband nature of the intra-modal Brillouin process, similar to the distortion from an image frequency in heterodyne receivers [288]. By using inter-modal scattering in PPER-based microwave-photonic filters, the bandwidth limitation could be avoided, enabling the design of filters that could be translated over terahertz frequency ranges. Utilizing the design strategies presented in Chapter 6, we will present a two-pole inter-modal PPER device achieving a narrow bandwidth of 4.4 MHz, a sharp frequency roll-off, and a stopband of 4 GHz, while demonstrating 22 dB of single-sideband contrast. Such devices could potentially implement filtering operations with ∼MHz resolution and be tunable over optical-wavelength scales (∼THz) to perform optical and microwave signal processing operations within an integrated silicon platform.

9.2 Inter-modal scattering analysis

We use the theory presented in Section 2.3.3 to analyze a photonic-phononic emit-receive (PPER) scheme utilizing inter-modal Brillouin interactions. There are multiple configurations in which the device can be operated, choosing different combinations of spatial modes and Stokes or anti-Stokes processes [139]. For our discussion here, we consider the interaction between four optical fields. These include pump and Stokes tones in the 'emit' waveguide, and pump and Stokes tones in the 'receive' waveguide. In each waveguide, we assume that the pump and Stokes waves are propagating in two different spatial modes, and a single extended acoustic mode supported by the device interacts with the fields in both waveguides through inter-modal Brillouin scattering. Other configurations can be examined similarly.

We consider traveling wave interactions between the pump tone ($a_{\mathrm{p}}^{(\mathrm{A})}$) and the Stokes tone ($a_{\mathrm{s}}^{(\mathrm{A})}$) in the 'emit' waveguide (denoted A), described by

$$\frac{\partial}{\partial z}a_{\mathrm{p}}^{(\mathrm{A})} = -\frac{i}{v_{\mathrm{p}}^{(\mathrm{A})}}g^{(\mathrm{A})}a_{\mathrm{s}}^{(\mathrm{A})}b, \qquad \frac{\partial}{\partial z}a_{\mathrm{s}}^{(\mathrm{A})} = -\frac{i}{v_{\mathrm{s}}^{(\mathrm{A})}}g^{(\mathrm{A})*}a_{\mathrm{p}}^{(\mathrm{A})}b^{\dagger}, \tag{9.1}$$

where we have assumed that the process is phase matched, and we have neglected optical loss. Here, the acoustic field amplitude is denoted b, $g^{(\mathrm{A})}$ is the acousto-optic coupling rate in waveguide A, and $v_{\mathrm{p}}^{(\mathrm{A})}$ and $v_{\mathrm{s}}^{(\mathrm{A})}$ are the optical group velocities of the pump and Stokes, respectively, which are different as they are guided in different modes, as seen in Fig. 9.1(a). We note that unlike the intra-modal case, cascading to other optical tones does not occur in inter-modal scattering, and we do not need to consider additional optical fields.

In the 'receive' waveguide (denoted B), the pump and Stokes optical modes (with amplitudes $a_i^{(\mathrm{B})}$ and group velocities $v_i^{(\mathrm{B})}$, $i = \{\mathrm{p}, \mathrm{s}\}$) are given by

$$\frac{\partial}{\partial z}a_{\mathrm{p}}^{(\mathrm{B})} = -\frac{i}{v_{\mathrm{p}}^{(\mathrm{B})}}g^{(\mathrm{B})}a_{\mathrm{s}}^{(\mathrm{B})}b\ e^{i\Delta qz}, \qquad \frac{\partial}{\partial z}a_{\mathrm{s}}^{(\mathrm{B})} = -\frac{i}{v_{\mathrm{s}}^{(\mathrm{B})}}g^{(\mathrm{B})*}a_{\mathrm{p}}^{(\mathrm{B})}b^{\dagger}\ e^{-i\Delta qz}, \tag{9.2}$$

where $g^{(\mathrm{B})}$ is the acousto-optic coupling rate in waveguide B. Notice that we have introduced a phase-mismatch term Δq, which can be the consequence of different dispersion relations

between waveguides A and B, or a difference in the optical frequency of the light in each waveguide, as illustrated in 9.1(b).

Finally, the phonon mode participating in the interaction is described by

$$b = -i\chi\Big[g^{(\mathrm{A})*}a_{\mathrm{p}}^{(\mathrm{A})}a_{\mathrm{s}}^{(\mathrm{A})\dagger} + g^{(\mathrm{B})*}a_{\mathrm{p}}^{(\mathrm{B})}a_{\mathrm{s}}^{(\mathrm{B})\dagger}\ e^{-i\Delta qz}\Big], \tag{9.3}$$

showing the interaction with the optical fields in both waveguides, where χ denotes the acoustic frequency response with a Lorentzian lineshape (i.e., $\chi = [i(\Omega - \Omega_0) + \Gamma/2]^{-1}$, where Ω_0 is the Brillouin frequency and Γ is the phonon dissipation rate). To simplify our analysis, we will assume at this point that the phonons are driven primarily in waveguide A, and neglect the effects of scattering in waveguide B on the acoustic field. This is the case, for example, when $a_{\mathrm{p}}^{(\mathrm{A})}a_{\mathrm{s}}^{(\mathrm{A})\dagger} \gg a_{\mathrm{p}}^{(\mathrm{B})}a_{\mathrm{s}}^{(\mathrm{B})\dagger}$, leaving us with

$$b \approx -i\chi g^{(\mathrm{A})*}a_{\mathrm{p}}^{(\mathrm{A})}a_{\mathrm{s}}^{(\mathrm{A})\dagger}. \tag{9.4}$$

We can see that under this assumption, the phonon field is fully determined by the optical fields and the acousto-optic coupling in the 'emit' waveguide.

9.2.1 Transmission bandwidth

We analyze the optical transmission through the 'receive' waveguide, examining the optical bandwidth over which efficient inter-modal Brillouin scattering occurs, as illustrated in Fig. 9.1(c). Focusing on the Stokes field in waveguide B, we use Eqs. (9.2) and (9.4) to write the field amplitude

$$\frac{\partial}{\partial z}a_{\mathrm{s}}^{(\mathrm{B})} = \frac{1}{v_{\mathrm{s}}^{(\mathrm{B})}}\chi^* g^{(\mathrm{B})*}g^{(\mathrm{A})}a_{\mathrm{p}}^{(\mathrm{B})}a_{\mathrm{p}}^{(\mathrm{A})\dagger}a_{\mathrm{s}}^{(\mathrm{A})}\ e^{-i\Delta qz}, \tag{9.5}$$

showing nonlocal susceptibility, where the 'receive' waveguide is affected by the fields in the spatially-separated 'emit' waveguide. To gain insight into the effects of the phase mismatch on the optical transmission, we assume that all of the input fields ($a_{\mathrm{p}}^{(\mathrm{B})}$, $a_{\mathrm{p}}^{(\mathrm{A})\dagger}$, and $a_{\mathrm{s}}^{(\mathrm{A})}$)

are undepleted, such that they are constant throughout the device, leaving us with

$$a_{\mathrm{s}}^{(\mathrm{B})}(z) = \frac{1}{v_{\mathrm{s}}^{(\mathrm{B})}} \chi^* g^{(\mathrm{B})^*} g^{(\mathrm{A})} a_{\mathrm{p}}^{(\mathrm{B})} a_{\mathrm{p}}^{(\mathrm{A})^\dagger} a_{\mathrm{s}}^{(\mathrm{A})} \int_0^z dz' \; e^{-i\Delta q z'}. \tag{9.6}$$

The optical power, after a propagation length L, is given by

$$P_{\mathrm{s}}(L) \propto \left| a_{\mathrm{s}}^{(\mathrm{B})}(L) \right|^2 = \left| \frac{1}{v_{\mathrm{s}}^{(\mathrm{B})}} \chi^* g^{(\mathrm{B})^*} g^{(\mathrm{A})} a_{\mathrm{p}}^{(\mathrm{B})} a_{\mathrm{p}}^{(\mathrm{A})^\dagger} a_{\mathrm{s}}^{(\mathrm{A})} L \right|^2 \mathrm{sinc}^2 \left(\frac{\Delta q L}{2} \right). \tag{9.7}$$

We can see that the phase mismatch and interaction length determine the transmission of light through the device. Evaluating the full-width at half-maximum (FWHM) of the sinc function from Eq. (9.7) (i.e., $\mathrm{sinc}^2(1.39) = 0.5$), we can define the 3 dB phase-matched bandwidth

$$\Delta q = \frac{5.56}{L}. \tag{9.8}$$

This response is similar to that of $\chi^{(2)}$ optical nonlinearities, describing a three-wave interaction with undepleted pumps [157]. In our case, the three waves include two photon modes and one phonon mode.

We have seen that the optical transmission bandwidth is determined by the wavevector mismatch. The phase-matched bandwidth Δq can be expressed in terms of system parameters which are more practical in device design and experiments, namely optical dispersion and wavelength. We start from the driven phonon in the system, with a wavevector determined by the optical modes in the 'emit' waveguide

$$\begin{aligned} q_0 &= k_+^{(\mathrm{A})} \left(\omega_{\mathrm{p}}^{(\mathrm{A})} \right) - k_-^{(\mathrm{A})} \left(\omega_{\mathrm{s}}^{(\mathrm{A})} \right) \\ &= k_+^{(\mathrm{A})} \left(\omega_{\mathrm{p}}^{(\mathrm{A})} \right) - k_-^{(\mathrm{A})} \left(\omega_{\mathrm{p}}^{(\mathrm{A})} - \Omega_0 \right), \end{aligned} \tag{9.9}$$

where we have assumed that the pump wave propagates in a symmetric spatial mode, with a dispersion relation $k_+^{(\mathrm{A})}(\omega)$, while the Stokes wave is in the anti-symmetric mode, with dispersion $k_-^{(\mathrm{A})}(\omega)$. We have also used energy conservation, i.e., $\omega_{\mathrm{s}}^{(\mathrm{A})} = \omega_{\mathrm{p}}^{(\mathrm{A})} - \Omega_0$, where Ω_0 is the phonon frequency (see Fig. 9.1(a)).

In the 'receive' waveguide, we assume that the input pump wave is propagating in the

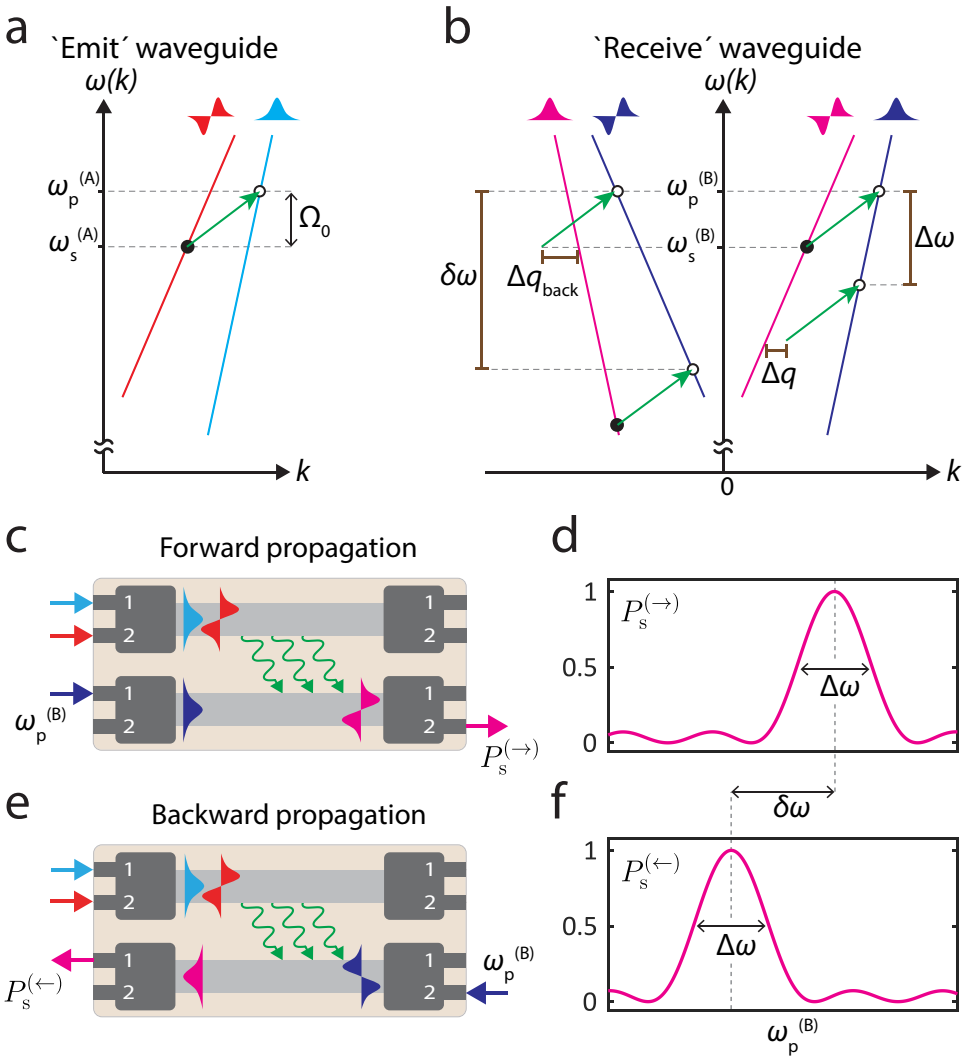

Figure 9.1: **(a)** Dispersion diagram of the optical modes in the 'emit' waveguide. A pump tone at frequency $\omega_{\mathrm{p}}^{(\mathrm{A})}$ and a Stokes tone at frequency $\omega_{\mathrm{s}}^{(\mathrm{A})}$ drive an inter-modal Brillouin-active acoustic mode with frequency Ω_0. **(b)** Dispersion diagram of the optical modes in the 'receive' waveguide. In the forward direction (positive k vectors), the driven acoustic mode couples an input pump tone in the symmetric mode to a Stokes tone in the anti-symmetric mode. This process is efficient over a bandwidth $\Delta\omega$, after which the phase mismatch Δq suppresses scattering. In the backward direction (negative k vectors), an input pump tone in the anti-symmetric will no experience efficient scattering, as there is a phase mismatch Δq_{back}. At a different optical frequency, separated by $\delta\omega$, the process is phase-matched in the backward direction. **(c)** Illustration of the device operating in the forward direction, where all fields are co-propagating. **(d)** Illustration of the output power as a function of optical frequency in the 'receive' waveguide in the forward direction. **(e)** In the backward direction, optical fields in the 'receive' waveguide counter-propagate compared to the fields in the 'emit' waveguide. **(f)** Illustration of the output power as a function of optical frequency in the 'receive' waveguide in the backward direction, showing that the process is phase-matched at a different frequency.

symmetric mode, with dispersion $k_+^{(\mathrm{B})}(\omega)$, and analyze the scattering into the asymmetric mode, $k_-^{(\mathrm{B})}(\omega)$, which will be red-shifted in frequency, as seen in Fig. 9.1(b). The phase mismatch is given by

$$\begin{aligned}\Delta q &= q_0 - \left[k_+^{(\mathrm{B})}\left(\omega_\mathrm{p}^{(\mathrm{B})}\right) - k_-^{(\mathrm{B})}\left(\omega_\mathrm{s}^{(\mathrm{B})}\right)\right] \\ &= \left[k_+^{(\mathrm{A})}\left(\omega_\mathrm{p}^{(\mathrm{A})}\right) - k_+^{(\mathrm{B})}\left(\omega_\mathrm{p}^{(\mathrm{B})}\right)\right] - \left[k_-^{(\mathrm{A})}\left(\omega_\mathrm{p}^{(\mathrm{A})} - \Omega_0\right) - k_-^{(\mathrm{B})}\left(\omega_\mathrm{p}^{(\mathrm{B})} - \Omega_0\right)\right],\end{aligned} \tag{9.10}$$

where we have used Eq. (9.9) and energy conservation in the 'receive' waveguide, i.e., $\omega_\mathrm{s}^{(\mathrm{B})} = \omega_\mathrm{p}^{(\mathrm{B})} - \Omega_0$. For this discussion, we will assume that the dispersion curves in the 'emit' and the 'receive' waveguides are identical ($k_+^{(\mathrm{A})} = k_+^{(\mathrm{B})}$ and $k_-^{(\mathrm{A})} = k_-^{(\mathrm{B})}$), such that perfect phase matching occurs when $\omega_\mathrm{p}^{(\mathrm{A})} = \omega_\mathrm{p}^{(\mathrm{B})}$. When the two waveguides have different dispersion properties, the phase-matched frequency will be shifted, however, the analysis remains similar [139].

Assuming the dispersion curves are approximately linear over the frequency range of interest[1], we can express the dispersion relations in terms of the group velocity ($v_g = \partial_k \omega$), or equivalently, the group index ($n_g = c/v_g$) of the two optical modes

$$k_+(\omega) = k_+^{(0)} + \frac{n_+}{c}\omega, \qquad k_-(\omega) = k_-^{(0)} + \frac{n_-}{c}\omega, \tag{9.11}$$

where $k_+^{(0)}$ and $k_-^{(0)}$ are constants around which we are expanding the dispersion functions, and we have denoted the group velocities and group indices as $v_\pm$ and $n_\pm$, respectively. From Eqs. (9.10) and (9.11) we see that the phase mismatch is given by

$$\Delta q = \frac{n_+ - n_-}{c}\Delta\omega, \tag{9.12}$$

where $\Delta\omega$ is the frequency measured from the phase-matched frequency. Using Eq. (9.8),

1. This is a valid assumption since the Brillouin frequency is typically <10 GHz, much smaller than the optical frequencies in the system (∼100 THz).

this gives us the transmission bandwidth

$$\Delta\omega = \frac{c}{L}\frac{5.56}{|n_+ - n_-|}, \tag{9.13}$$

illustrated in Fig. 9.1(d), which can also be expressed in terms of optical wavelength

$$\Delta\lambda = \frac{2.78}{\pi}\left(\frac{\lambda_0^2}{L}\right)\frac{1}{|n_+ - n_-|}. \tag{9.14}$$

We can see that the bandwidth is inversely proportional to the device length, as well as the difference in group indices of the two optical modes.

9.2.2 Nonreciprocal optical propagation

Next, we consider the case of light propagating in the 'receive' waveguide in the opposite direction, as illustrated in Fig. 9.1(e). The phase mismatch is now given by

$$\begin{aligned}\Delta q &= q_0 + \left[k_-^{(\mathrm{B})}\left(\omega_\mathrm{p}^{(\mathrm{B})}\right) - k_+^{(\mathrm{B})}\left(\omega_\mathrm{s}^{(\mathrm{B})}\right)\right] \\ &= \left[k_+^{(\mathrm{A})}\left(\omega_\mathrm{p}^{(\mathrm{A})}\right) - k_+^{(\mathrm{B})}\left(\omega_\mathrm{p}^{(\mathrm{B})} - \Omega_0\right)\right] - \left[k_-^{(\mathrm{A})}\left(\omega_\mathrm{p}^{(\mathrm{A})} - \Omega_0\right) - k_-^{(\mathrm{B})}\left(\omega_\mathrm{p}^{(\mathrm{B})}\right)\right],\end{aligned} \tag{9.15}$$

where we have switched the signs of the wavevectors and the spatial modes of the pump and Stokes in the 'receive' waveguide. Assuming the two waveguides are identical, and using the first order approximation of the dispersion relations from Eq. (9.11), we have

$$\Delta q = \frac{n_+}{c}\left[\omega_\mathrm{p}^{(\mathrm{A})} - \omega_\mathrm{p}^{(\mathrm{B})} + \Omega_0\right] - \frac{n_-}{c}\left[\omega_\mathrm{p}^{(\mathrm{A})} - \Omega_0 - \omega_\mathrm{p}^{(\mathrm{B})}\right], \tag{9.16}$$

and to find the optical frequency at which there is perfect phase matching in the backwards direction, we set $\Delta q = 0$, resulting in

$$\delta\omega = \left(\frac{n_+ + n_-}{n_+ - n_-}\right)\Omega_0. \tag{9.17}$$

Here, $\delta\omega = \omega_\mathrm{p}^{(\mathrm{emit})} - \omega_\mathrm{p}^{(\mathrm{rec})}$, which is also the frequency spacing between the forward and backwards phase-matched optical frequencies, as illustrated in Fig. 9.1. In terms of wave-

length, this separation is given by

$$\delta\lambda = -\lambda_0^2 \frac{\Omega_0}{2\pi c}\left(\frac{n_+ + n_-}{n_+ - n_-}\right), \tag{9.18}$$

and we see that the dispersion relations, namely the difference in group indices, will determine this wavelength separation.

We have seen that phase-matched mode conversion in the 'receive' waveguide occurs at different wavelengths for forward and backward propagation (assuming that the fields in the 'emit' are unchanged), showing the nonreciprocal nature of optical transmission through the device. Another way we examine the nonreciprocity of this process is to set the pump wavelength in the 'receive' waveguide for perfect phase matching in the forward direction and calculate the phase mismatch at the same optical frequency when operating in the backward direction. Using Eqs. (9.12) and (9.17), this 'backward' phase mismatch is given by

$$\Delta q_{\text{back}} = \frac{\Omega_0}{c}\left(n_+ + n_-\right). \tag{9.19}$$

Practically, a nonreciprocal response will be observed when the active length over which the interaction is taking place is large enough, such that $\Delta q_{\text{back}} L > \pi$, which requires a minimum length $L \sim 10$ mm for the silicon devices we are studying in this work. This is equivalent to the requirement $|\delta\lambda| > \Delta\lambda$ in terms of wavelengths (see Eqs. (9.14) and (9.18)). In other words, the separation between the $\text{sinc}^2(\cdot)$ functions describing the transmission in the forward and backward directions needs to be larger than their bandwidth (see Figs. 9.1(d,f)). Experimental data showing the measurement of a NIBS device is presented in Fig. 9.2, demonstrating nonreciprocal optical transmission, with a difference in power of up to 30 dB between forward- and backward-propagating waves. The forward and backward phase-matched optical wavelengths are separated by $\delta\lambda = 3.2$ nm, and the transmission bandwidth is $\Delta\lambda = 1.4$ nm.

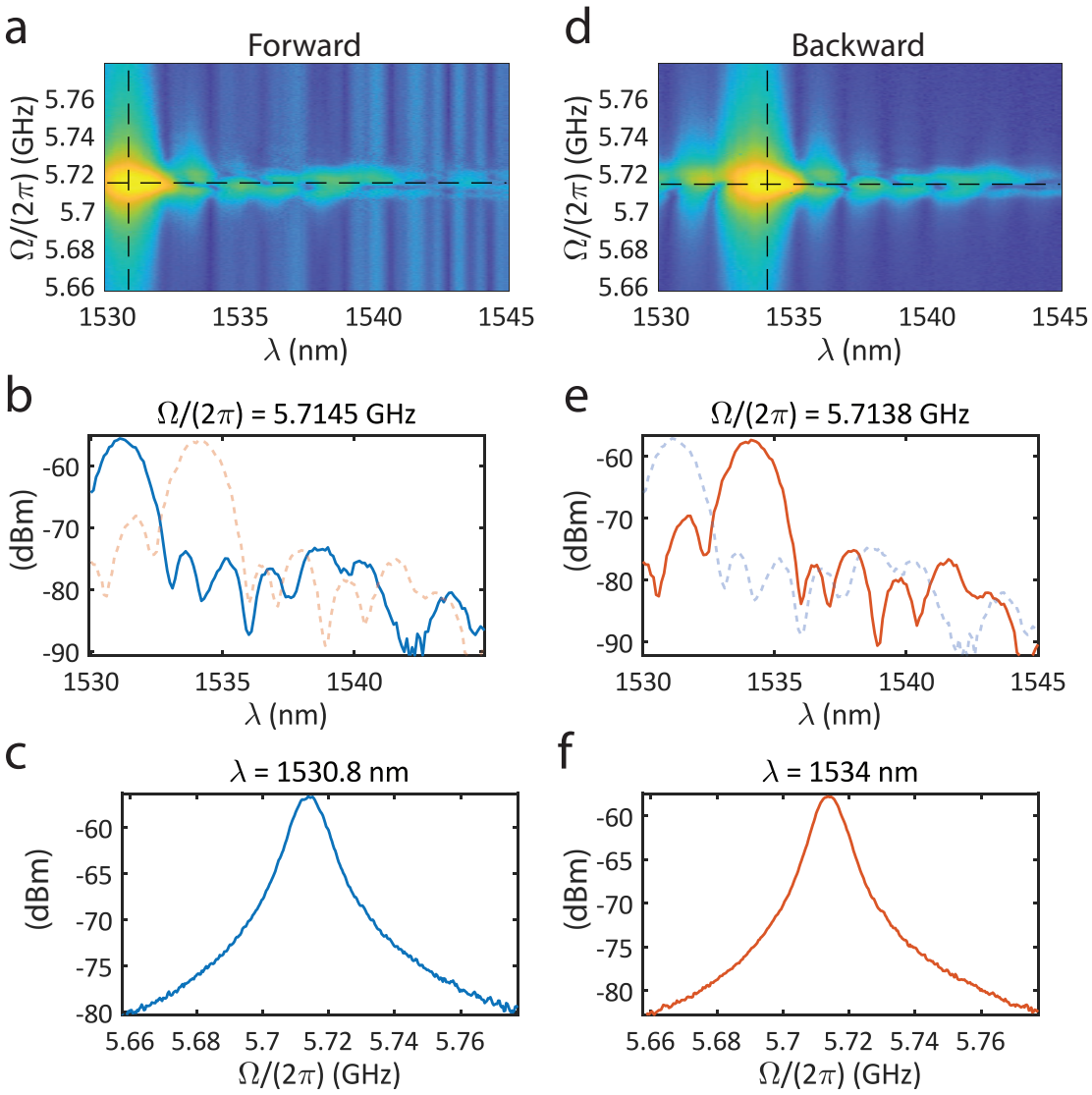

Figure 9.2: Characterization of a NIBS nonreciprocal modulator, with a device similar to the design from Ref. [139], and an active length of $L = 12$ mm. **(a)** Forward optical transmission, sweeping the driven phonon frequency Ω, and the optical wavelength in the 'receive' waveguide (λ). **(b)** Optical power, corresponding to the dashed horizontal line from panel (a), with peak transmission at 1530.8 nm, and a 3 dB bandwidth of $\Delta\lambda = 1.40$ nm. The dashed red line shows the backward optical transmission for reference. **(c)** Acoustic frequency response, corresponding to the dashed vertical line from panel (a), showing a Lorentzian lineshape with a 3 dB bandwidth of 8.4 MHz. **(d)** Backward optical transmission in the same device. **(e)** Optical power, demonstrating the nonreciprocal response, where peak transmission is shifted by $\delta\lambda = 3.2$ nm (dashed horizontal line from panel (d)). The dashed blue line shows the forward optical transmission for reference. **(f)** Acoustic frequency response (dashed horizontal line from panel (d)). The experimental setup used to measure the data is illustrated in Fig. 9.11.

9.3 Implementing an optical isolator

We have seen that under the right conditions, a NIBS device demonstrates nonreciprocal optical transmission, and can be utilized as an optical isolator. There are many configurations in which these devices can be operated, depending on the modes and nonlinear processes that are used. Here, we will focus on two schemes based on the discussion from the previous section. As we did in our earlier analyses, we will neglect the effect of the 'receive' waveguide on the acoustic field, which we will still treat as a constant (i.e., undepleted). However, we will not assume the pump field in the 'receive' waveguide is constant, and analyze the spatial evolution and power exchanged between the pump and Stokes modes. Solving Eqs. (9.2) and (9.3), we have

$$\begin{aligned} a_{\mathrm{p}}^{(\mathrm{B})}(z) &= e^{i(\Delta q/2)z}\Bigg[a_{\mathrm{p}}^{(\mathrm{B})}(0)\left(\cos(\beta z) - i\frac{\Delta q/2}{\beta}\sin(\beta z)\right) \\ &\qquad - ia_{\mathrm{s}}^{(\mathrm{B})}(0)\left(\frac{\pi/2}{\beta\ell_c}\sqrt{\frac{v_{\mathrm{s}}^{(\mathrm{B})}}{v_{\mathrm{p}}^{(\mathrm{B})}}}\right)e^{i\phi}\sin(\beta z)\Bigg], \\ a_{\mathrm{s}}^{(\mathrm{B})}(z) &= e^{-i(\Delta q/2)z}\Bigg[a_{\mathrm{s}}^{(\mathrm{B})}(0)\left(\cos(\beta z) + i\frac{\Delta q/2}{\beta}\sin(\beta z)\right) \\ &\qquad - ia_{\mathrm{p}}^{(\mathrm{B})}(0)\left(\frac{\pi/2}{\beta\ell_c}\sqrt{\frac{v_{\mathrm{p}}^{(\mathrm{B})}}{v_{\mathrm{s}}^{(\mathrm{B})}}}\right)e^{-i\phi}\sin(\beta z)\Bigg], \end{aligned} \tag{9.20}$$

where we have defined the parameters

$$\beta = \sqrt{\left(\frac{\Delta q}{2}\right)^2 + \left(\frac{\pi/2}{\ell_c}\right)^2}, \qquad \ell_c = \frac{\pi}{2}\frac{\sqrt{v_{\mathrm{p}}^{(\mathrm{B})}v_{\mathrm{s}}^{(\mathrm{B})}}}{\left|b\ g^{(\mathrm{B})}\right|}, \qquad \phi = \arg\left(bg^{(\mathrm{B})}\right). \tag{9.21}$$

Using these equations, we can analyze the light scattered between the pump and Stokes waves in the 'receive' waveguide, each propagating in a separate spatial mode, as a function of the phase mismatch Δq.

We start from the case of perfect phase matching, i.e., $\Delta q = 0$. In this case, we can see

from Eq. (9.21) that β takes the value $\beta = \pi/(2\ell_c)$, leaving us with

$$\begin{aligned} a_{\mathrm{p}}^{(\mathrm{B})}(z) &= a_{\mathrm{p}}^{(\mathrm{B})}(0)\cos\left(\frac{\pi}{2}\frac{z}{\ell_c}\right) - ia_{\mathrm{s}}^{(\mathrm{B})}(0)\sqrt{\frac{v_{\mathrm{s}}^{(\mathrm{B})}}{v_{\mathrm{p}}^{(\mathrm{B})}}}e^{i\phi}\sin\left(\frac{\pi}{2}\frac{z}{\ell_c}\right), \\ a_{\mathrm{s}}^{(\mathrm{B})}(z) &= a_{\mathrm{s}}^{(\mathrm{B})}(0)\cos\left(\frac{\pi}{2}\frac{z}{\ell_c}\right) - ia_{\mathrm{p}}^{(\mathrm{B})}(0)\sqrt{\frac{v_{\mathrm{p}}^{(\mathrm{B})}}{v_{\mathrm{s}}^{(\mathrm{B})}}}e^{-i\phi}\sin\left(\frac{\pi}{2}\frac{z}{\ell_c}\right). \end{aligned} \tag{9.22}$$

Assuming that we have an input field into the pump mode ($a_{\mathrm{p}}^{(\mathrm{B})}(0) \neq 0$, $a_{\mathrm{s}}^{(\mathrm{B})}(0) = 0$), the power evolution of each mode is given by

$$P_p^{(\rightarrow)}(z) = P_{\mathrm{p}}^{(\rightarrow)}(0)\cos^2\left(\frac{\pi}{2}\frac{z}{\ell_c}\right), \qquad P_{\mathrm{s}}^{(\rightarrow)}(z) = P_{\mathrm{p}}^{(\rightarrow)}(0)\sin^2\left(\frac{\pi}{2}\frac{z}{\ell_c}\right), \tag{9.23}$$

where we have used $P(z) = \hbar\omega v\,|a(z)|^2$ to calculate the power from the field amplitudes [172], and we have used '$(\rightarrow)$' to denote 'forward' (phase-matched) propagation. We can see that full conversion between the two spatial modes is achieved after a propagation length ℓ_c, as seen in Fig. 9.3(a), which depends inversely on the amplitude of the acoustic field ($\ell_c \propto |b|^{-1}$). In the case of optical driving (i.e., with a PPER scheme), the acoustic field amplitude is proportional to the optical powers in the 'emit' waveguide, $\ell_c \propto (a_{\mathrm{p}}^{(\mathrm{A})}a_{\mathrm{s}}^{(\mathrm{A})})^{-1}$, as seen from Eq. (9.4). However, our description here can also describe other transduction mechanisms. For example, in the case of piezoelectric acoustic driving [236, 330], the conversion length will be determined by the RF power, as $\ell_c \propto (P_{\mathrm{RF}})^{-1/2}$.

Next, we turn to analyze the case where the process is not phase-matched, such that $\Delta q\ell_c \gg \pi$. In this limit, Eq. (9.21) can be simplified to $\beta \approx \Delta q/2$, leaving us with negligible mode conversion

$$P_{\mathrm{p}}^{(\leftarrow)}(z) \approx P_{\mathrm{p}}^{(\leftarrow)}(0), \qquad P_{\mathrm{s}}^{(\leftarrow)}(z) \approx P_{\mathrm{s}}^{(\leftarrow)}(0). \tag{9.24}$$

Here, we have used '$(\leftarrow)$' to denote 'backward' propagation, where the process is not phase matched.

Examining cases of intermediate phase mismatch, we see from Eq. (9.21) that $\Delta q\ell_c$ is a key parameter that governs mode conversion. Fig. 9.3 shows the calculated power evolution in the two optical modes for different cases of phase mismatch, showing that the

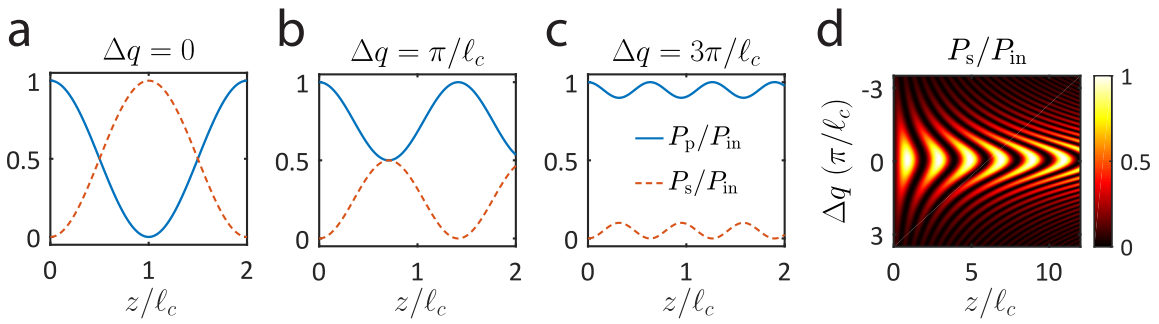

Figure 9.3: **(a)** In the case of perfect phase matching, after a propagating length of ℓ_c, all of the pump power will be mode converted. **(b)** For a phase mismatch of $\Delta q_{\text{back}} = \pi/\ell_c$, only 50% of the power can be converted. **(c)** For a large phase mismatch, the conversion efficiency will be very low, showing small deviations from the input power. **(d)** Calculated mode-converted power for different values of phase mismatch.

phase mismatch must be small to achieve efficient mode conversion. For example, $\Delta q \ell_c < \pi$ is required to achieve at least 50% of power transfer.

We can see that the inter-modal process, implemented using the NIBS device, enables the necessary phase-matching conditions to achieve mode conversion only in one propagation direction. Choosing the input frequency to be phase-matched in the forward direction (for a given acoustic drive and system parameters), the forward conversion efficiency of a device of length L will be $\eta_{\text{f}}^2 = \sin^2(\pi L/(2\ell_c))$. In the backward direction, the conversion efficiency η_{b}^2 will be determined by the phase mismatch Δq, using Eqs. (9.19) and (9.20). With this notation, we can write the output power of the mode-converted light as $P_{\text{s}}^{(\rightarrow)}(L) = \eta_{\text{f}}^2 P_{\text{p}}^{(\rightarrow)}(0)$, and $P_{\text{s}}^{(\leftarrow)}(L) = \eta_{\text{b}}^2 P_{\text{p}}^{(\leftarrow)}(0)$. A system with a substantial nonreciprocal response ($\eta_{\text{f}} \gg \eta_{\text{b}}$) can be used to implement an optical isolator, as illustrated in Figs. 9.4(a,b).

An important practical consideration in the design of isolators based on mode conversion, is the performance of mode multiplexers used to interface the two spatial modes in the active regions of the device. Using the mode multiplexer design from Ref. [65] as an example, we model non-ideal mode multiplexing with a transmission parameter (t) for the anti-symmetric mode, where power conversion from the initial to the final mode is given by t^2 (an ideal mode multiplexer implies $t = 1$). We assume that the fundamental (symmetric) mode does not suffer significant loss in the multiplexing process (see Figs. 9.4(a,b)).

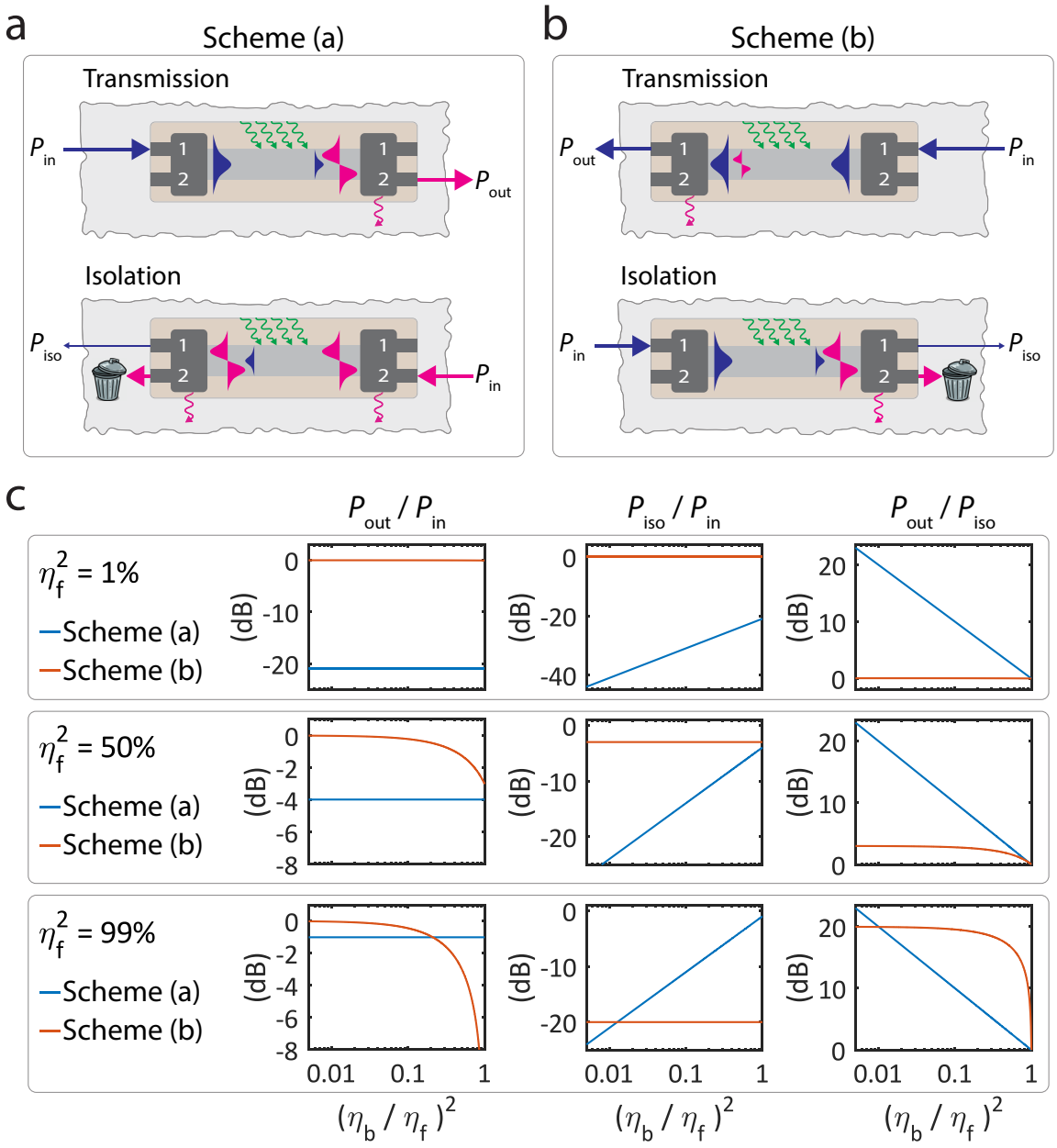

Figure 9.4: Using a NIBS device for optical isolation. We assume the acoustic field is driven externally, and analyze the optical transmission through the 'receive' waveguide, at an optical frequency that is phase-matched only in the forward direction. **(a)** Scheme (a): Mode-converted light is used for forward transmission (top). The low conversion efficiency in the backward direction results in optical isolation (bottom). **(b)** Scheme (b): Non-converted light is used for transmission (top). In the isolation direction, mode conversion removes the optical field from the signal path. **(c)** Calculated performance of the two isolation schemes as a function of the nonreciprocal efficiency contrast, for three cases of mode-conversion efficiency: 1% (top), 50% (middle), and 99% (bottom). We assume mode multiplexers with $t^2 = 80\%$ mode-multiplexing efficiency in this calculation.

9.3.1 Isolation schemes

We will analyze the performance of two different optical isolation schemes utilizing a NIBS device. To facilitate our discussion, we will denote the input optical power into the isolator P_{in}, and the output powers when operating in the forward and backward direction as P_{out} and P_{iso}, respectively, as illustrated in Figs. 9.4(a,b). Two important figures of merit for an optical isolator are the insertion loss ($P_{\text{out}}/P_{\text{in}}$) and isolation ration ($P_{\text{out}}/P_{\text{iso}}$) [136]. An ideal isolator will have unity transmission $P_{\text{out}}/P_{\text{in}} = 1$ and a high isolation ratio $P_{\text{out}}/P_{\text{iso}} \to \infty$ (equivalent to no backward transmission $P_{\text{iso}} = 0$).

The first isolation scheme we will consider, denoted 'Scheme (a)', uses the mode-converted light for transmission, as seen in Fig. 9.4(a), such that the transmitted optical power in the forward and backward directions are given by $P_{\text{out}} = \eta_{\text{f}}^2 t^2 P_{\text{in}}$ and $P_{\text{iso}} = \eta_{\text{b}}^2 t^2 P_{\text{in}}$, respectively. Another possible isolation scheme, denoted 'Scheme (b)' and shown in Fig. 9.4(b), uses the unconverted light in the transmission direction, and uses the mode-conversion process for isolation. In this case, the forward and backward transmission are given by $P_{\text{out}} = \left(1 - \eta_{\text{b}}^2\right) P_{\text{in}}$ and $P_{\text{iso}} = \left(1 - \eta_{\text{f}}^2\right) P_{\text{in}}$, respectively. The insertion loss and isolation ratio of the two schemes are given by

$$\begin{aligned} &\text{Scheme (a):} \quad \frac{P_{\text{out}}}{P_{\text{in}}} = \eta_{\text{f}}^2 t^2, \qquad \frac{P_{\text{out}}}{P_{\text{iso}}} = \left(\frac{\eta_{\text{f}}}{\eta_{\text{b}}}\right)^2, \\ &\text{Scheme (b):} \quad \frac{P_{\text{out}}}{P_{\text{in}}} = 1 - \eta_{\text{b}}^2, \qquad \frac{P_{\text{out}}}{P_{\text{iso}}} = \frac{1 - \eta_{\text{b}}^2}{1 - \eta_{\text{f}}^2}. \end{aligned} \tag{9.25}$$

Fig. 9.4(c) shows the calculated transmission and isolation for three cases of mode-conversion efficiency ($\eta_{\text{f}} = 1\%$, 50%, and 99%) for the two isolation schemes. We can see that for low efficiency (such as was demonstrated in Ref. [139]) Scheme (a) can yield a high isolation ratio (as long as $\eta_{\text{f}} \gg \eta_{\text{b}}$), while Scheme (b) is not feasible, as the isolation ratio is very low. However, assuming higher mode-conversion efficiency could be achieved, Scheme (b) can be utilized for isolation and may outperform the first in the case of non-negligible backward mode conversion. Additionally, Scheme (b) does not require mode converters, as the device is interfaced only through the fundamental mode (see Fig. 9.4(b)), which can drastically

simplify the design and reduce footprint. In this case, the necessary mode filtering of the anti-symmetric mode can be achieved by tapering the width of the multi-mode waveguide to the point that it is single-mode, and does not require additional components.

Finally, we note that throughout this section, our objective was to spatially separate the forward and backward propagating fields to achieve a practical scheme for nonreciprocal operation. However, if we analyze the basic form of the scattering matrix associated with inter-modal scattering, spatial separation is not necessary to have nonreciprocity. Using a generalized scattering matrix formalism [136, 332, 333], waves with different frequencies are assigned separate ports, even in the case that they are propagating in the same spatial mode. Within this framework, a time-modulated system is considered reciprocal only if any two modes i and j, which may differ by their spatial mode, polarization, or oscillation frequency, are related by symmetric scattering matrix elements (i.e., $s_{ji} = s_{ij}$ for any i and j). Applying this definition, we see that any form of inter-modal scattering breaks reciprocity.

For example, we consider the case of a NIBS device with phase matching conditions satisfied in both propagation directions (i.e., $\Delta q_{\text{back}} L < \pi$, or equivalently, $\eta_{\text{f}} \approx \eta_{\text{b}}$), which can be the case for a device with a short active length. In this scenario, an input tone at frequency ω_i results in an output field shifted in frequency $\omega_j = \omega_i - \Omega_0$, which we define as modes i and j, respectively. In the reverse direction, mode j will also be frequency-shifted through the inter-modal scattering process to frequency $\omega_j - \Omega_0 \neq \omega_i$. We can see from this example that the generalized scattering matrix is not symmetric ($s_{ji} \neq s_{ij}$), such that the system is not reciprocal under this generalized definition. To utilize such a nonreciprocal system practically, additional filters are required to separate the different frequency components to different physical ports [330]. This can be challenging, especially when the frequency separation between modes is small.

In our discussion of optical isolation throughout this chapter, we have considered nonreciprocity as determined by the total power entering and exiting the different ports, regardless of their frequency. Hence, for this more practical definition, a substantial phase mismatch between forward and backward propagation is crucial for the type of isolator that

we are analyzing. In the next sections, we will explore possible strategies to enhance the potential performance of isolators based on the schemes we have been discussing so far.

9.3.2 Dispersion engineering

In the previous section, we have seen that optical mode conversion is determined by the phase-matching conditions in a NIBS device and that the optical transmission approximately follows a $\mathrm{sinc}^2(\cdot)$ function (see Eq. (9.7)). The operation bandwidth of the device ($\Delta\lambda$) is inversely proportional to the difference in group indices $\Delta n_g = |n_+ - n_-|$ (or equivalently, the dispersion properties of the modes), as can be seen from Eq. (9.14). The optical dispersion is determined by the waveguide material and geometry, and minimizing Δn_g can be achieved by modifying the waveguide design and material properties [334–340]. Analyzing the optical dispersion relations (see for example Fig. 9.1(b)), minimizing Δn_g is equivalent to the requirement that the dispersion curves of the two optical modes have similar slopes[2]. Furthermore, since the bandwidth is inversely proportional to the active length $\Delta\lambda \propto 1/L$ (see Eq. (9.14)), long devices (which may be needed to achieve high efficiency) may require the enhancement of the bandwidth through dispersion engineering to produce a useful operation bandwidth.

We demonstrate the possible bandwidth enhancement by comparing the bandwidth of a device similar to the one demonstrated experimentally in Ref. [139], and an alternative waveguide design with a lower group-index mismatch. Fig. 9.5(a) shows the waveguide design from Ref. [139], and the symmetric and anti-symmetric TE-like optical mode profiles, simulated using a mode solver. The simulation results give a difference of group indices $\Delta n_g = 0.11$, in good agreement with measurements. The calculated transmission of this NIBS device in the forward and backward directions is shown in Fig. 9.5(b), showing similar features to the measured nonreciprocal response of such devices. An alternative waveguide design is illustrated in Fig. 9.5(c), where the dimensions of the guiding ridge are smaller and the ridge sidewalls have a 65° angle. Simulating this geometry, the difference

2. The slopes of the dispersion curves are described by the group velocities. The operation bandwidth is increased when the group velocities of the two modes are similar, since $\Delta\lambda \propto c/[n_+ - n_-| = (v_+ v_-)/|v_+ - v_-|$, where $n_\pm$ and $v_\pm$ denote group indices and ground velocities, respectively.

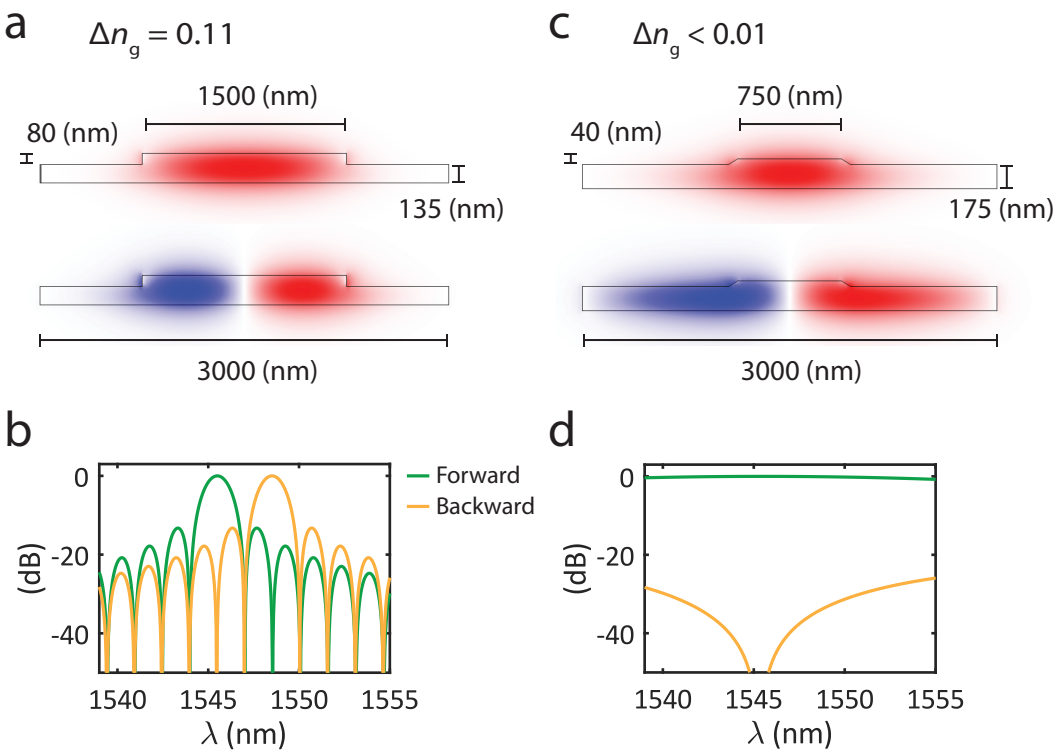

Figure 9.5: **(a)** Dimensions of the ridge waveguides used in NIBS measurements, and simulated x component of the electric field for the first two optical modes supported by the waveguide. **(b)** Calculated transmission as a function of wavelength shows the phase-matching $\mathrm{sinc}^2(\cdot)$ response in the forward and backwards directions. **(c)** An alternative ridge waveguide design with reduced ridge dimensions and angled sidewalls, resulting in a tenfold reduction in the difference of group indices (Δn_g). **(d)** Calculated transmission using the waveguide shown in panel (c). The reduction of Δn_g increases the bandwidth by a factor of 10. Adapted from Ref. [139].

in group indices is calculated to be $\Delta n_g = 0.01$, a tenfold reduction compared to the first device design. The calculated transmission response of the modified device is illustrated in Fig. 9.5(d), showing a tenfold increase in bandwidth, covering the entire telecom C-band wavelength range.

9.3.3 Gain apodization

We have seen how the optical transmission as a function of wavelength follows a $\mathrm{sinc}^2(\cdot)$ function due to the phase-matching conditions in the NIBS device. This response is characteristic of a uniform Brillouin coupling rate along the length of the device, as seen from Eqs. (9.6) and (9.7) and illustrated in Fig. 9.6(a). The optical transmission exhibits trans-

mission side-lobes 16 dB below maximum transmission that may limit the isolation of the device, as side-bands of the backward direction may coincide with the forward transmission bandwidth, seen in Fig. 9.6(b). Alternatively, by controlling the Brillouin gain along the propagation axis of the device, the phase-matched optical transmission can be manipulated. Following the derivation from Section 9.1, the scattered field is described by

$$a_{\mathrm{s}}^{(\mathrm{B})}(z) = \frac{1}{v_{\mathrm{s}}^{(\mathrm{B})}} \chi^* a_{\mathrm{p}}^{(\mathrm{B})} a_{\mathrm{p}}^{(\mathrm{A})\dagger} a_{\mathrm{s}}^{(\mathrm{A})} \int_0^L dz' \; g^{(\mathrm{A})}(z') \; g^{(\mathrm{B})*}(z') \; e^{-i\Delta q z'}, \tag{9.26}$$

where we have allowed for spatially varying Brillouin coupling rates in waveguide A and B, denoted $g^{(\mathrm{A})}$ and $g^{(\mathrm{B})}$, respectively. We can see that the mode-converted field is in fact the spatial Fourier transform of the product of the coupling rates. Hence, by varying the coupling rates in space we can engineer the phase-matched optical response to improve isolation and nonreciprocal contrast. This strategy is analogous to an apodization function in filter design, where a tapered window function is used to suppress side lobes of the filter response [341, 342].

As an example, we consider the case where the 'emit' waveguide has a constant coupling rate, while the 'receive' waveguide is designed to have a spatially varying coupling rate, as illustrated in Fig. 9.6(c). The calculated mode-converted transmission is shown in Fig. 9.6(d), where we can see a large reduction in the side-lobe amplitude, resulting in ∼60 dB of contrast between forward and backward transmission. Practically, the Brillouin gain may be modulated by changing the waveguide design along the optical propagation axis, however, the effect of these changes on the Brillouin frequency and optical dispersion —which we have assumed constant in this analysis— must be considered in the design.

9.4 Resonant enhancement

We have seen in Section 9.3 that the optical mode-conversion efficiency is determined by the acoustic field amplitude and acousto-optic coupling rate. In recent demonstrations, a mode-conversion efficiency of 1% was demonstrated using an optical drive (i.e., using a PPER device) and an active length of 2.39 cm [139]. Alternatively, piezoelectric transduction

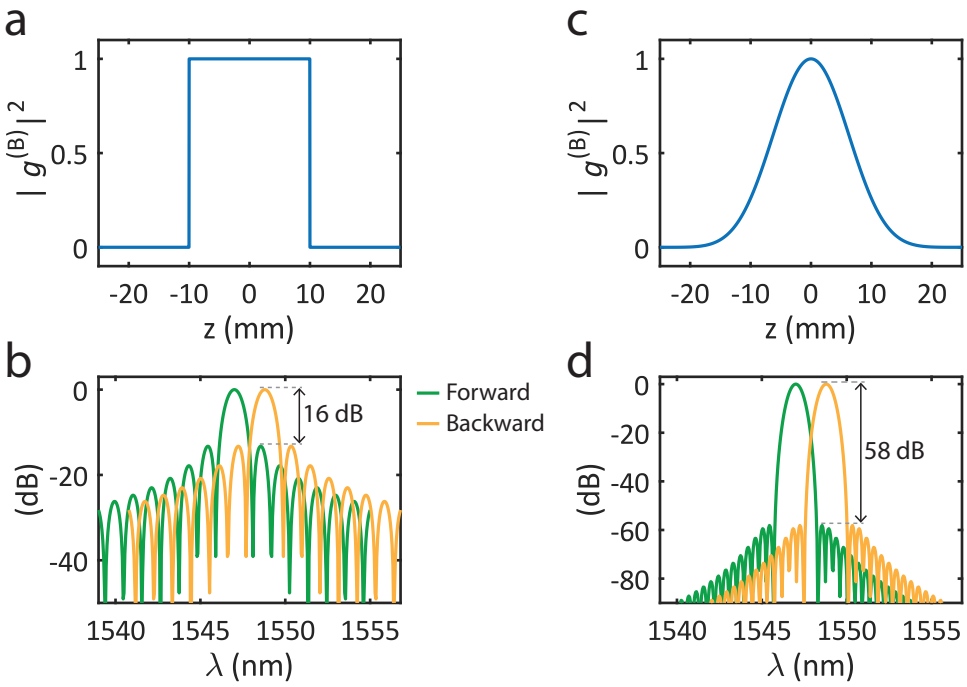

Figure 9.6: **(a)** Brillouin coupling rate $g^{(\mathrm{B})}$ along the optical propagation direction, in a 2 cm long NIBS device. **(b)** The corresponding transmission for forward and backward propagation through the 'receive' waveguide of the device. **(c)** In an apodized device, the coupling rate is modulated throughout the device length. **(d)** The resulting transmission response shows a reduction of the side lobes, enabling a larger nonreciprocal contrast between forward and backward transmission.

can be used to generate coherent acoustic waves with higher power. Early demonstrations using piezoelectric materials have shown TE–TM mode conversion [343–347], however, these devices required long acousto-optic interaction lengths and high electrical power to achieve high-performance mode conversion. More recently, 10% of mode conversion between two TE-like spatial modes was achieved by cascading multiple transduction section [236], and 18% was demonstrated in a lithium niobate platform [330]. In this section, we will explore the possibility of utilizing a doubly-resonant structure to enhance the effective interaction length of the optical and acoustic fields, and achieving higher mode-conversion efficiency. We have shown earlier how strong nonreciprocity is achieved for an active length $L \gg c/[\Omega_0(n_+ + n_-)]$, which in the silicon platform demonstrated in Ref. [139] results in a minimum length of $L \approx 3$ mm.

To achieve high mode-conversion efficiency (and nonreciprocal response) with low power

consumption and within a small-footprint device, resonant structures can be used to enhance performance [136]. Resonant inter-modal Brillouin devices in silicon have been used to demonstrate lasers [56] and amplifiers [66, 285], utilizing the resonant buildup of optical power within a ring resonator, suggesting the feasibility of this scheme. Additionally, nonreciprocal devices using resonant structures have been demonstrated in other material platforms, showing promising results when using this strategy [329, 348].

An example of a resonant device is illustrated schematically in Figs. 9.7(a,b), where a ring resonator is used as the 'receive' path of a NIBS device. In this example, a mode selective coupler (labeled '1' in the figure) is used to inject light into the symmetric mode of the resonator. In the active section, interaction with the acoustic field scatters light into the anti-symmetric mode, which then exits the ring through another mode-selective coupler (labeled '2' in the figure). In the reverse direction, phase mismatch results in inefficient inter-modal scattering, as we have analyzed in Section 9.1, suppressing transmission and achieving optical isolation. The acoustic field can be driven using the same 'emit' configuration as in Figs. 9.1(c,e), or alternatively, using an RF drive in combination with a piezoelectric material [236] or through thermo-elastic effects [237]. For the rest of our analysis, we will assume that a constant acoustic field drives the inter-modal scattering process; we will not concern ourselves with the details of phonon generation.

9.4.1 Mode-conversion efficiency

We start our analysis of the resonant structure by making the analogy to a system of two ring resonators, as illustrated in Fig. 9.7(c). In this analogy, each ring corresponds to a distinct spatial mode, and the optical properties, namely the effective index, group index, and optical loss of each ring, corresponds to the equivalent values of the spatial modes in the multi-mode system. The acousto-optic coupling produced within the active region (illustrated in green in Figs. 9.7(a,b)) is modeled by introducing optical coupling between the two ring resonators. We denote the round trip losses $a_j = \exp[-\alpha_j L_r/2]$, where α_j is the loss per unit length of mode $j = \{1, 2\}$, and L_r is the length of each of the ring resonators. Finally, each mode accumulates a round-trip phase $\phi_j = 2\pi n_e^{(j)} L_r/\lambda_j$, determined by the

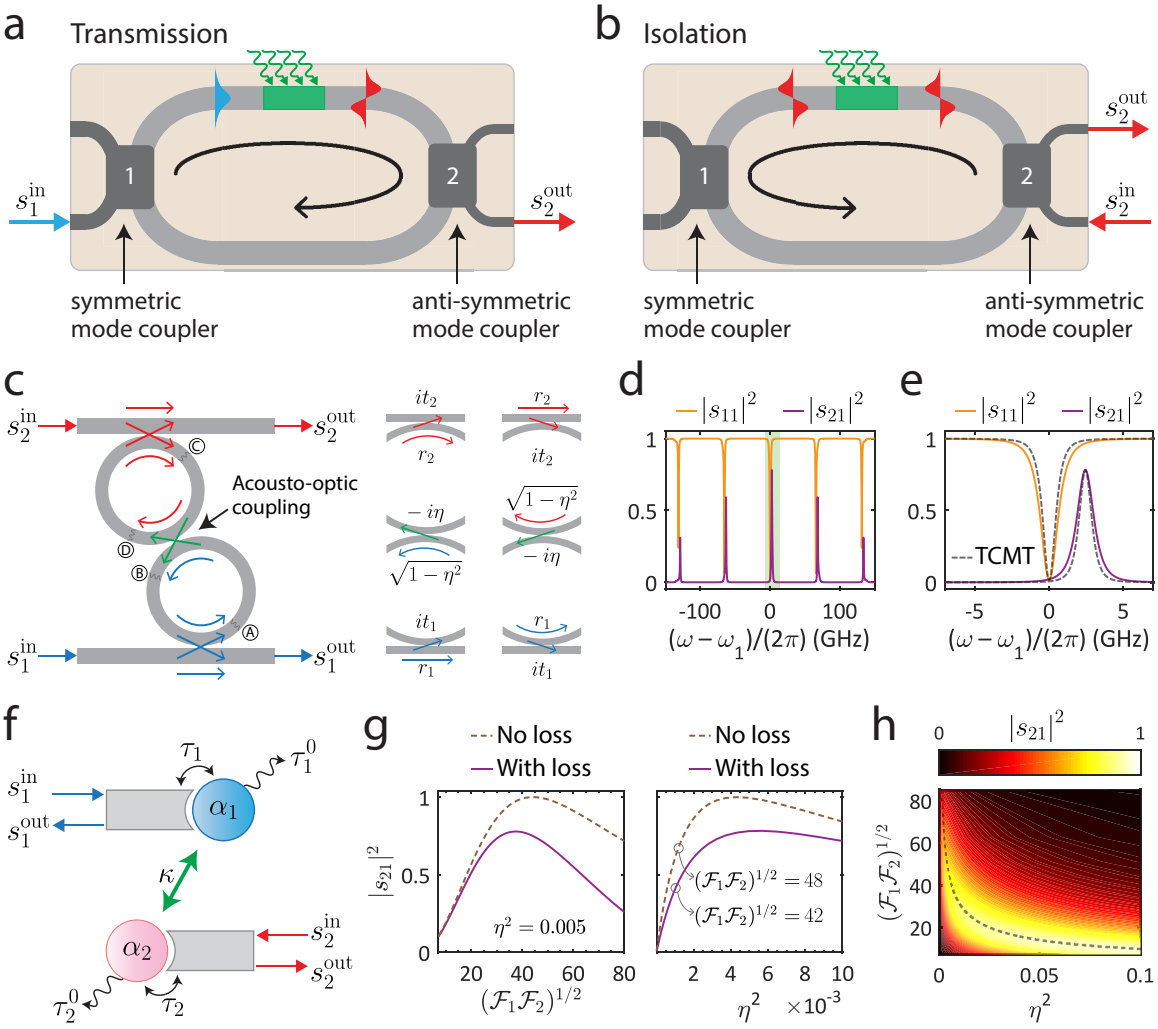

Figure 9.7: **(a)** Resonantly enhanced nonreciprocal mode converter in the transmission direction, where the acousto-optic process is phase matched. **(b)** In the reverse direction, there is no mode conversion, resulting in optical isolation. **(c)** Left: We can analyze the system as coupled ring resonators, each representing a different spatial mode. Right: The notation used to describe the coupling ratio of each directional coupler. **(d)** Calculation of the optical frequency response using typical system parameters. We use the notation $s_{11} = s_1^{\text{out}}/s_1^{\text{in}}$ and $s_{21} = s_2^{\text{out}}/s_1^{\text{in}}$. In this example, $\eta^2 = 0.005$, $\mathcal{F}_1 = 103$ and $\mathcal{F}_2 = 17$. The intrinsic losses of the ring resonators are $\alpha_1 = 6$ m^{-1}, $\alpha_2 = 15$ m^{-1}. **(e)** Magnified view of the shaded region from panel (d), showing 78% of power conversion through the system (-1 dB). Temporal coupled-mode theory (TCMT) calculations are in good agreement. **(f)** Temporal coupled-mode analysis, where α represents the energy stored in a mode, and s^{in} (s^{out}) is the power flowing into (out of) each mode. **(g)** Left: Mode-conversion efficiency as a function of resonator finesse. Right: Mode-conversion efficiency as a function of single-pass coupling. The case of no intrinsic loss (i.e., $\alpha_1 = \alpha_2 = 0$) is shown for reference. **(h)** Mode-conversion efficiency as a function of resonator finesse and single-pass coupling. The dashed line follows the function π/η, showing that maximum mode conversion occurs close to the condition $\eta^2 = \pi^2/(\mathcal{F}_1\mathcal{F}_2)$.

effective index ($n_e^{(j)}$) and wavelength (λ_j).

We can write a self-consistent set of equations describing the relations between the field amplitudes at different points in the coupled-ring system (see Fig. 9.7(c))

$$\begin{aligned} s_{\mathrm{A}} &= (it_1)\, s_1^{\mathrm{in}} + \left(r_1\sqrt{a_1 e^{i\phi_1}}\right) s_{\mathrm{B}}, \qquad & s_{\mathrm{B}} &= \left(\sqrt{1-\eta^2}\sqrt{a_1 e^{i\phi_1}}\right) s_{\mathrm{A}} + \left(-i\eta\sqrt{a_2 e^{i\phi_2}}\right) s_{\mathrm{C}}, \\ s_{\mathrm{C}} &= (it_2)\, s_2^{\mathrm{in}} + \left(r_2\sqrt{a_2 e^{i\phi_2}}\right) s_{\mathrm{D}}, \qquad & s_{\mathrm{D}} &= \left(\sqrt{1-\eta^2}\sqrt{a_2 e^{i\phi_2}}\right) s_{\mathrm{C}} + \left(-i\eta\sqrt{a_1 e^{i\phi_1}}\right) s_{\mathrm{A}}. \end{aligned} \tag{9.27}$$

Here, r and t denote the splitting ratio of the directional couplers interfacing the rings, assumed to be lossless ($r^2 + t^2 = 1$), and the acousto-optic conversion per round trip is denoted η. The field amplitudes at the two output ports are given by

$$s_1^{\mathrm{out}} = (r_1)\, s_1^{\mathrm{in}} + \left(it_1\sqrt{a_1 e^{i\phi_1}}\right) s_{\mathrm{B}}, \qquad s_2^{\mathrm{out}} = (r_2)\, s_2^{\mathrm{in}} + \left(it_2\sqrt{a_2 e^{i\phi_2}}\right) s_{\mathrm{D}}. \tag{9.28}$$

In the forward direction, we assume an input into mode 1 ($s_1^{\mathrm{in}} \neq 0$, $s_2^{\mathrm{in}} = 0$). Solving Eqs. (9.27) and (9.28), we have

$$\begin{aligned} s_1^{\mathrm{out}} &= s_1^{\mathrm{in}} \left[\frac{r_1 + p_2 a_1 e^{i\phi_1} - r_1\,(p_1+p_2)\sqrt{1-\eta^2} - a_1 e^{i\phi_1} t_1^2\sqrt{1-\eta^2}}{1-(p_1+p_2)\sqrt{1-\eta^2}+p_1 p_2}\right], \\ s_2^{\mathrm{out}} &= s_1^{\mathrm{in}} \left[\frac{i\eta t_1 t_2\sqrt{a_1 e^{i\phi_1} a_2 e^{i\phi_2}}}{1-(p_1+p_2)\sqrt{1-\eta^2}+p_1 p_2}\right], \end{aligned} \tag{9.29}$$

where we have grouped the terms

$$p_1 = r_1 a_1 \exp\left[i\phi_1\right], \qquad p_2 = r_2 a_2 \exp\left[i\phi_2\right]. \tag{9.30}$$

To gain insight into the resonantly-enhanced mode conversion, we simplify the expression by assuming that the internal losses are low compared to the coupling losses ($a \approx 1$). Additionally, we consider the case where both modes are on resonance with the ring resonators, i.e., the wavelengths λ_j ($j = \{1, 2\}$) are chosen such that $\phi_j = 2\pi m_j$, where m_j are integers, and that their frequency separation equals the Brillouin frequency[3] [56, 66]. We also

3. The frequency shift imparted by the inter-modal acousto-optic scattering process is the Brillouin fre-

assume that the single-pass mode-conversion efficiency is low ($\eta \ll 1$), as we are analyzing the resonant enhancement of weak acousto-optic coupling. Under these assumptions, the output power from port 2 has the form

$$\left|\frac{s_2^{\text{out}}}{s_1^{\text{in}}}\right|^2 = \left[\frac{\eta\, t_1 t_2}{(1-r_1)\,(1-r_2)}\right]^2 \approx \frac{4}{\pi^2}\eta^2 \mathcal{F}_1 \mathcal{F}_2, \tag{9.31}$$

where we have expressed the mode-converted power in terms of the finesse $\mathcal{F} = \pi r^{1/2}/(1-r)$ of each cavity modes, and used the approximation $(1+r)/r^{1/2} \approx 2$ for $r \approx 1$.

We see that for high-finesse resonators, i.e., structures in which the optical fields propagate multiple round trips before decaying, the conversion efficiency can be enhanced quadratically. Figs. 9.7(d,e) show the mode-converted power ($|s_2^{\text{out}}/s_1^{\text{in}}|^2$) exiting the output port, demonstrating 78% of mode conversion when using realistic system parameters[4]. For this case, Fig. 9.7(g) shows the mode-converted power as a function of cavity finesse ($\mathcal{F}$) and single-pass acousto-optic mode conversion (η). Interestingly, maximum mode conversion occurs when the coupling rate and cavity finesse are balanced, such that $\eta^2 \approx \pi^2/(\mathcal{F}_1\mathcal{F}_2)$, as seen in Fig. 9.7(h). It is important to note that the mode conversion in this example is limited due to the intrinsic loss within the resonators; in the case of lossless resonators (i.e., $\alpha_1 = \alpha_2 = 0$) the mode conversion can reach 100%, as seen from the dashed curves in Fig. 9.7(g).

9.4.2 Temporal coupled-mode theory

An alternative way to describe the system we are analyzing is using *temporal coupled-mode theory* [349, 350]. Here, the mode amplitudes α_j ($j = \{1, 2\}$), related to the stored energy in each of the resonators as $|\alpha_j|^2$, are completely described by coupling rates and resonant angular frequencies (these α_j should not be confused with the notation we had for loss in the previous section). The coupling of the two mode amplitudes, illustrated in Fig. 9.7(f),

quency Ω_0, i.e., $|\omega_1 - \omega_2| = \Omega_0$, where $\omega_j = 2\pi c/\lambda_j$.

4. In this calculation we have used $\alpha_1 = 6\ \text{m}^{-1}$, $\alpha_2 = 15\ \text{m}^{-1}$ and a single-pass mode conversion of $\eta = 0.5\%$.

is given by the following equations of motion

$$\begin{aligned}\frac{\partial}{\partial t}\alpha_1 &= -i\omega_1^0\alpha_1 - \left(\frac{1}{\tau_1}+\frac{1}{\tau_1^0}\right)\alpha_1 - i\kappa\alpha_2 + i\sqrt{\frac{2}{\tau_1}}s_1^{\text{in}}, \qquad s_1^{\text{out}} = s_1^{\text{in}} + i\sqrt{\frac{2}{\tau_1}}\alpha_1,\\ \frac{\partial}{\partial t}\alpha_2 &= -i\omega_2^0\alpha_2 - \left(\frac{1}{\tau_2}+\frac{1}{\tau_2^0}\right)\alpha_2 - i\kappa^*\alpha_1 + i\sqrt{\frac{2}{\tau_2}}s_2^{\text{in}}, \qquad s_2^{\text{out}} = s_2^{\text{in}} + i\sqrt{\frac{2}{\tau_2}}\alpha_2.\end{aligned} \tag{9.32}$$

Here, ω_j^0 denotes the resonant frequency, $1/\tau_j^0$, $1/\tau_j$ are the amplitude decay rates due to intrinsic loss and external coupling, and κ denotes the coupling rate between the two spatial modes due to the acousto-optic interaction. The waves flowing in and out of each mode are s_j^{in} and s_j^{out}, respectively, where $|s|^2$ represents power. Here, all parameter are given in terms of rates, whereas in our previous analysis (Section 9.4.1) the coupling parameters were unitless.

Analyzing the system in the frequency domain [350], considering optical fields at frequencies ω_1 and ω_2, we have[5]

$$\begin{aligned}\left[i\left(\omega_1^0-\omega_1\right)+\frac{1}{\tau_1}+\frac{1}{\tau_1^0}\right]\alpha_1 &= -i\kappa\alpha_2 + i\sqrt{\frac{2}{\tau_1}}s_1^{\text{in}}, \qquad s_1^{\text{out}} = s_1^{\text{in}} + i\sqrt{\frac{2}{\tau_1}}\alpha_1,\\ \left[i\left(\omega_2^0-\omega_2\right)+\frac{1}{\tau_2}+\frac{1}{\tau_2^0}\right]\alpha_2 &= -i\kappa^*\alpha_1 + i\sqrt{\frac{2}{\tau_2}}s_2^{\text{in}}, \qquad s_2^{\text{out}} = s_2^{\text{in}} + i\sqrt{\frac{2}{\tau_2}}\alpha_2.\end{aligned} \tag{9.33}$$

Considering the transmission through the system, with an input wave entering port 1 ($s_1^{\text{in}} \neq 0$, $s_2^{\text{in}} = 0$), we can solve Eq. (9.33), yielding

$$\begin{aligned}s_1^{\text{out}} &= s_1^{\text{in}}\left[1-\left(\frac{2}{\tau_1}\right)\frac{\chi_1}{1+|\kappa|^2\chi_1\chi_2}\right]\\ s_2^{\text{out}} &= s_1^{\text{in}}\left[i\left(\frac{2}{\sqrt{\tau_1\tau_2}}\right)\frac{\kappa^*\chi_1\chi_2}{1+|\kappa|^2\chi_1\chi_2}\right],\end{aligned} \tag{9.34}$$

where we have denoted

$$\chi_j = \left[i\left(\omega_j^0-\omega_j\right)+\frac{1}{\tau_j}+\frac{1}{\tau_j^0}\right]^{-1}, \qquad j=\{1,2\}. \tag{9.35}$$

We repeat the approximations we had in Section 9.4.1, assuming that the intrinsic loss

5. In the frequency domain, we have $\partial_t\alpha_1 \to -i\omega_1$ and $\partial_t\alpha_2 \to -i\omega_2$.

is much smaller than the coupling loss ($\tau_2^0 \gg \tau_2$, $\tau_1^0 \gg \tau_1$), and that the single-pass acousto-optic coupling is weak ($\tau_2\tau_1|\kappa|^2 \ll 1$). In this limit, we obtain[6]

$$\left|\frac{s_2^{\text{out}}}{s_1^{\text{in}}}\right|^2 = 4\,|\kappa|^2\,\tau_2\tau_1. \tag{9.36}$$

To compare this with our previous analysis (Eq. (9.31)), we relate the coupling coefficient η to the rate κ using $\kappa = \eta(v_1v_2)^{1/2}/L_r$, where v_j ($j = \{1, 2\}$) is the group velocity, and L_r the ring length. The factor $(v_j/L_r)^{-1}$ represents the round-trip time of each mode, and in this way, we relate the single-pass mode-conversion efficiency to a coupling rate. Finally, by using the definitions of the free spectral range (FSR), full-width at half-maximum bandwidth ($\Delta\omega$), and finesse ($\mathcal{F}$), given by

$$\text{FSR} = 2\pi\frac{v}{L_r}, \qquad \tau = \frac{2}{\Delta\omega}, \qquad \mathcal{F} = \frac{\text{FSR}}{\Delta\omega}, \tag{9.37}$$

we arrive at the same result as with the two-ring calculation, $|s_{21}|^2 = (4/\pi^2)\eta^2\mathcal{F}_1\mathcal{F}_2$.

With temporal coupled-mode theory, we have formulated the problem in the spirit of mean-field analysis where the modes are fully described in the time domain. We see that this treatment produces excellent agreement with our previous analysis (Section 9.4.1) in the limit when a mean-field analysis is appropriate (i.e., small acousto-optic scattering per round trip and low intrinsic losses). Fig. 9.7(e) presents calculations using temporal coupled-mode theory, showing good agreement with the two-ring model. This method yields fast results, accurate estimates, and is the method of choice for many of these types of calculations. However, it is restricted to the analysis around a limited bandwidth, as it does not take into account multiple resonator longitudinal modes (as seen in Fig. 9.7(d)). It is also important to note that coupled-mode theory assumes reasonably high quality-factor resonances, which should be considered when modeling the system.

6. This result is equivalent to the cooperativity between the two optical modes.

9.5 Second-order acoustic frequency response

In our discussion up to this point, we have only considered the optical transmission and mode conversion in an inter-modal PPER operation using a NIBS device. For these applications, the acoustic mode is used to scatter light between two optical spatial modes, and the acoustic frequency response does not play a substantial role in the process. In fact, this only requires a monochromatic acoustic drive, which can be designed to be on resonance with the acoustic mode to maximize efficiency. However, the NIBS device can be used for additional signal processing operations, such as the filtering and sensing applications we have discussed in previous chapters, with intriguing different properties. For example, the inter-modal process yields single-sideband scattering [65], as the phase-matching conditions result in a process involving the energy transfer between two optical tones.

In filtering applications, the single-sideband nature of the device eliminates the bandwidth limitations of a tunable PPER-based filter that were discussed in Chapter 7. In a tunable PPER-based filter utilizing this single-sideband process, an optical tone used as a local oscillator will select the filter pass-band frequency with no distortion from other unwanted frequency components, i.e., with no 'image' frequency [288] (see Section 7.4.1 and Fig. 7.5). The elimination of these limitations can enable the design of a filter that could process arbitrary input signals, and tuned over a large spectral range. Such a device could be used not only for wideband microwave spectral analysis but could also be utilized as an optical spectrum analyzer (OSA), as the pass-band frequency can be tuned over optical-scale ($\sim$THz) frequency ranges.

Utilizing Brillouin scattering for spectral analysis has had great success in providing high-resolution measurements over large wavelength ranges, typically using backward Brillouin scattering in long segments of optical fiber [351,352]. There have been demonstrations of tailoring the spectral response in backward Brillouin processes, utilizing multiple pump tones to induce both gain and loss at selected frequencies, achieving an order-of-magnitude enhancement in spectral resolution [353, 354]. Utilizing the vectorial nature of Brillouin scattering can further enhance the resolution and the dynamic range by using polarizers to

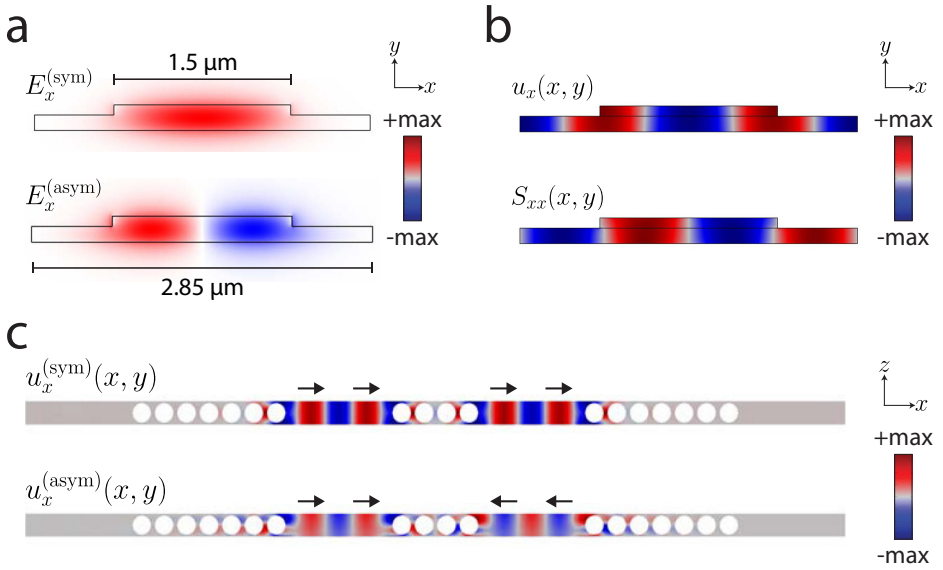

Figure 9.8: Simulations of the optical and acoustic fields in a two-pole PPER structure. **(a)** The x component of guided optical fields, showing the fundamental mode (top) and first anti-symmetric mode (bottom) supported by the rib waveguide. **(b)** The x component of the displacement profile of the Brillouin-active acoustic mode (top) and the corresponding S_{xx} strain tensor element (bottom). **(c)** The x component of the displacement profiles of the two acoustic 'super-modes' supported by the two-pole PPER structure. The phononic crystal is a cubic lattice of air holes, with pitch $a = 0.55$ μm and hole diameter $d = 0.43$ μm.

filter out noise [244,355]. The devices presented here could enable such high-resolution spectral analysis to be implemented in an integrated silicon platform, using sub-millimeter-long devices. Furthermore, designing devices with a multi-pole frequency response will have the advantage of a sharp frequency roll-off, enhancing the possible resolution of such filtering schemes without the need for additional components.

The design principle of the two-pole inter-modal device is similar to those discussed earlier in Chapter 6. We design a suspended rib waveguide, comprised of a 215 nm silicon layer in which 85 nm are etched to define a ridge structure. The ridge is designed to guide two optical TE-like modes, as seen in Fig. 9.8(a). The rib structure also supports a guided acoustic mode, seen in 9.8(b), with an anti-symmetric strain profile, needed to couple the two optical modes through forward inter-modal Brillouin scattering [65]. Using a phononic crystal structure, comprised of a cubic lattice of air holes in the silicon layer, we can acoustically couple the two acoustic waveguides, while keeping the optical modes

separated, as was described in Section 6.3. The acoustic coupling results in symmetric and anti-symmetric acoustic super-modes, shown in Fig. 9.8(c), consistent with the theoretical analysis presented in Chapter 3. The coherent interaction of the two acoustic modes yields a two-pole frequency response

$$\chi^{(2\text{ pole})}(\Omega) = \frac{i\mu}{[\Gamma/2 + i(\Omega_0 - \mu - \Omega)][\Gamma/2 + i(\Omega_0 + \mu - \Omega)]}, \tag{9.38}$$

where Ω_0 and Γ are the Brillouin frequency and phonon dissipation rate in each of the acoustic waveguides, respectively, and μ is the acoustic coupling rate. The two-pole frequency response results in a sharp frequency roll-off compared to a typical Lorentzain response which is obtained by a single acoustic mode.

Measurements of the frequency response of a two-pole device are presented in Fig. 9.9(c), showing a center frequency of 5.74 GHz and a full-width at half-maximum (FWHM) of 4.4 MHz. Comparing the two-pole frequency response to that of a single-pole device, seen in Fig. 9.9(e), shows an improvement of 20 dB in out-of-band rejection at frequencies 30 MHz from the center of the passband, thanks to the sharp roll-off of the multi-pole lineshape. Additionally, phononic band engineering enables the suppression of unwanted acoustic modes. When analyzing a wider frequency range, seen in Fig. 9.9(d), we can see that there are no spurious modes within a 4 GHz span around the pass-band, in contrast to the single-pole device which does not utilize a phononic crystal structure and shows multiple acoustic modes, as seen in Fig. 9.9(b). Additionally, the device shows 22 dB of sideband contrast, as shown in Fig. 9.9(f).

We characterize the device by performing both acoustic and optical frequency sweeps, presented in Fig. 9.10. In these measurements, the RF frequency Ω determines the frequency at which we are driving the acoustic modes through the 'emit' waveguide, and the wavelength λ refers to the optical wavelength of the light injected into the 'receive' waveguide. As seen in Figs. 9.10(b,e), the device demonstrates nonreciprocal optical transmission, with a bandwidth $\Delta\lambda = 3.1$ nm and a separation of $\delta\lambda = 2.8$ nm between the forward and backward phase-matched wavelengths. All together, the data shows how a two-pole line-

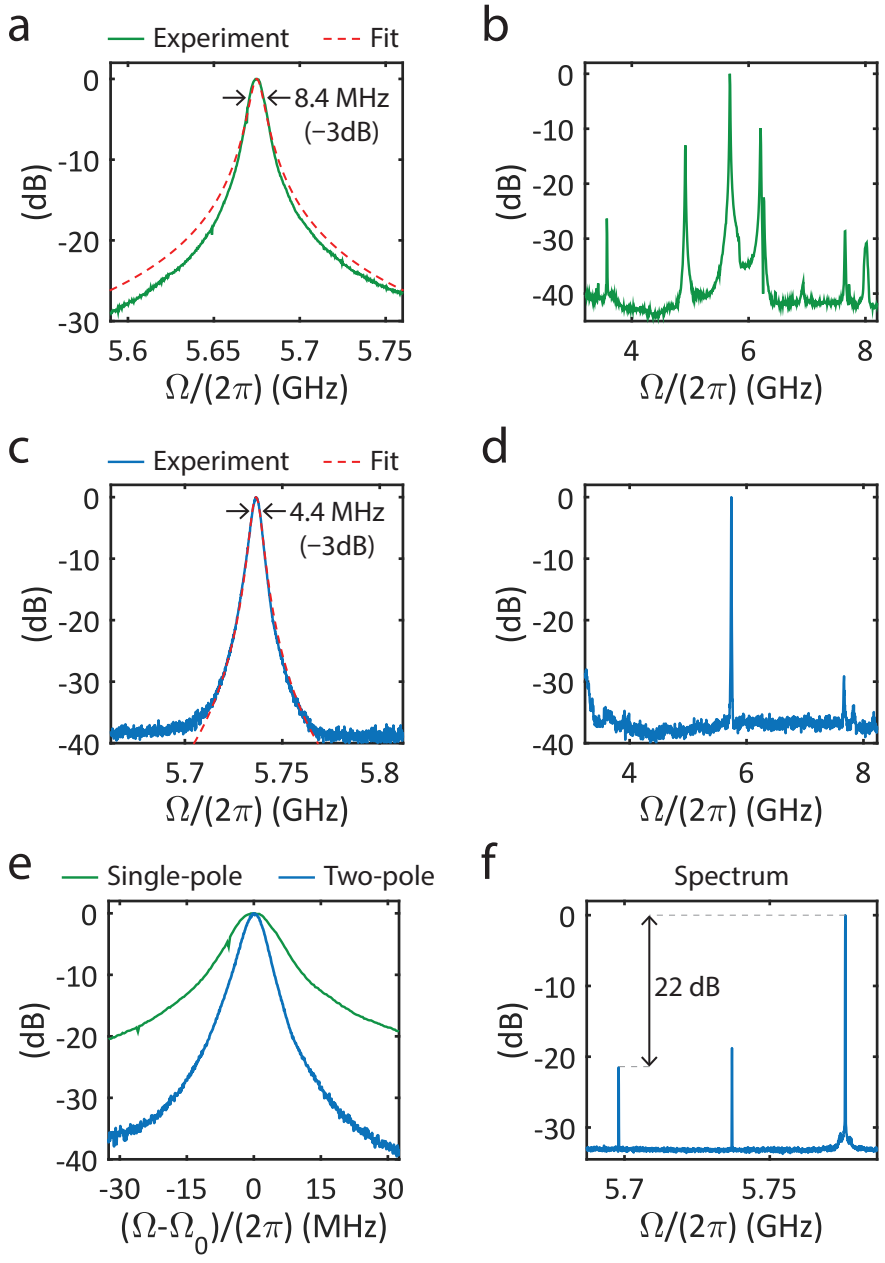

Figure 9.9: **(a)** Measured frequency response of a single-pole NIBS device, with a center frequency of $\Omega_0/(2\pi) = 5.68$ GHz and an acoustic dissipation rate $\Gamma/(2\pi) = 8.37$ MHz. **(b)** A wider frequency span reveals other strong inter-modal Brillouin-active acoustic modes within ~ 400 MHz of the main peak. **(c)** The frequency response of a two-pole device with a center frequency $\Omega_0/(2\pi) = 5.74$ GHz, acoustic dissipation rate of $\Gamma/(2\pi) = 6.12$ MHz and an acoustic coupling rate $\mu = 0.89$ MHz. **(d)** The two-pole device shows no spurious modes within a 4 GHz frequency span. **(e)** A comparison of the frequency response from panels (a) and (c), showing the fast frequency roll-off of the two-pole device. **(f)** Heterodyne measurement of the two-pole NIBS device shows 22 dB of sideband contrast.

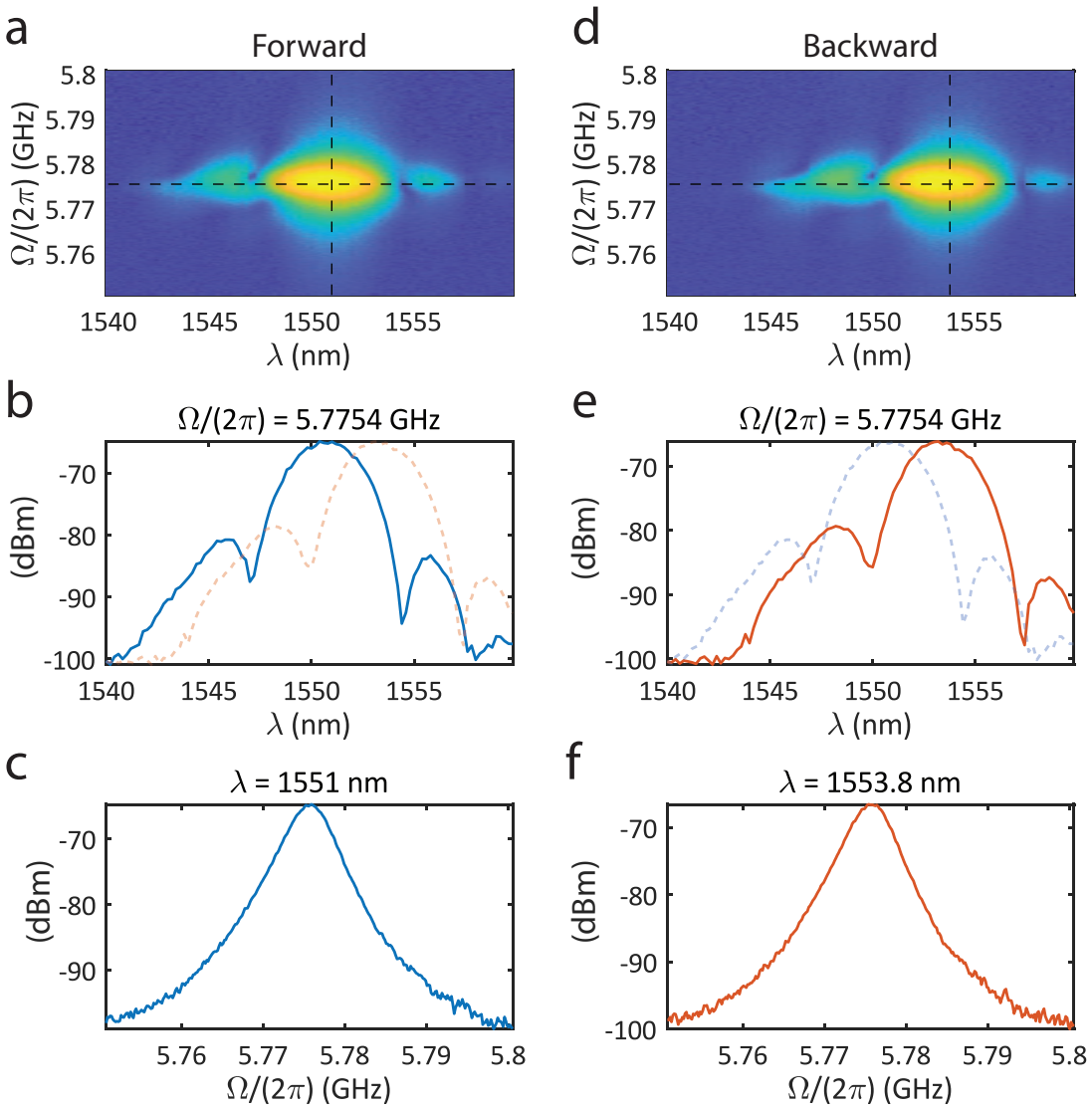

Figure 9.10: Characterization of a two-pole NIBS nonreciprocal modulator, with an active length of $L = 5.5$ mm. **(a)** Forward transmission, sweeping the driven phonon frequency Ω in the 'emit' waveguide, and the optical wavelength in the 'receive' waveguide (λ). **(b)** Optical power, corresponding to the dashed horizontal line from panel (a), with peak transmission at 1551 nm, and a bandwidth of $\Delta\lambda = 3.08$ nm. The dashed red line shows the backward optical transmission for reference. **(c)** Acoustic frequency response, corresponding to the dashed vertical line from panel (a), showing a two-pole lineshape with a full-width at half-maximum (FWHM) of 4.4 MHz. **(d)** Backward transmission measurement of the same device. **(e)** Optical power, demonstrating the nonreciprocal response, where peak transmission is shifted by $\delta\lambda = 2.8$ nm (dashed horizontal line from panel (d)). The dashed blue line shows the forward optical transmission for reference. **(f)** Acoustic frequency response (dashed horizontal line from panel (d)). The experimental setup used to measure the data is illustrated in Fig. 9.11.

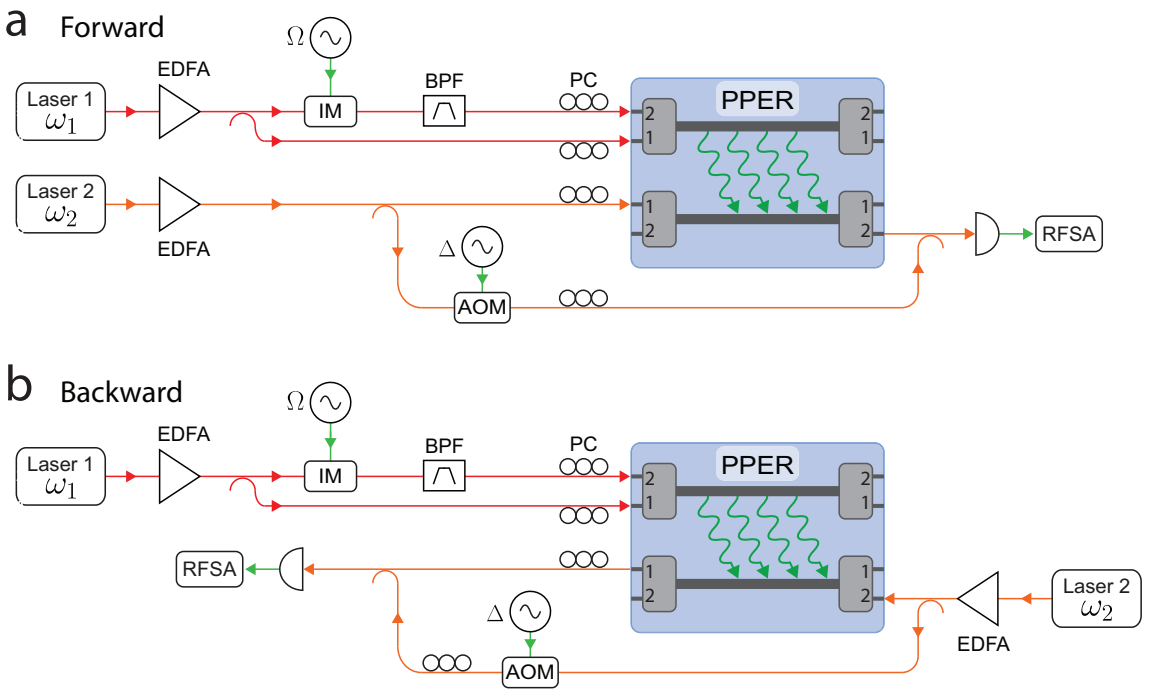

Figure 9.11: Schematic illustration of the experimental setup used for the characterization of the inter-modal nonreciprocal devices. **(a)** Forward transmission measurement. The pump and Stokes tones in the 'emit' waveguide are synthesized from the same laser at optical frequency ω_1. An RF frequency source driving an intensity modulator (IM) at frequency Ω, followed by an optical bandpass filter (BPF) to select a single sideband, is used to generate the Stokes tone at frequency $\omega_1 - \Omega$. Light from a second laser source at optical frequency ω_2 is directed to the fundamental mode of the 'receive' waveguide of the device, and the mode-converted field is collected at the output. The same light source is used to perform self-heterodyne detection, using an acousto-optic modulator (AOM). **(b)** In the backward direction, the input and output ports of the 'receive' waveguide are switched.

shape can be obtained using an inter-modal PPER device showing single-sideband scattering. This demonstrates the feasibility of designing filters which could potentially be tuned over a large spectral range to process both microwave and optical signals. The experimental setup used to measure the data presented in this section is illustrated in Fig. 9.11.

9.6 Conclusion

In this chapter, we have analyzed the dynamics of inter-modal photonic-phononic emit-receive (PPER) operations and studied the nonreciprocal response which can be achieved through their unique phase-matching conditions. Specifically, we have presented different

schemes in which the device can be used to implement optical isolation. By examining the dependence of optical transmission on the dispersion properties of the device, we identified potential designs that could increase the bandwidth and isolation ratio, making the non-local inter-band Brillouin scattering (NIBS) device a potential strategy for future technologies.

We have demonstrated the potential for high-efficiency mode conversion within a small-footprint device using the resonant enhancement of the optical fields within a multi-mode resonator. While this could potentially yield near-unity conversion efficiency, the trade-off of this scheme is the reduction in transmission bandwidth. This is because large enhancement requires high finesse cavities, which will have a narrow transmission band, and will restrict the operation bandwidth of the device. For example, a typical ring resonator in silicon may have a bandwidth of ∼500 MHz [66, 285], much narrower compared to the phase-matching limited bandwidth of a non-resonant device, which can be on the order of ∼100 GHz [139], or potentially even larger ($>$ 1 THz), as was shown in Section 9.3.2.

Alternatively, high-efficiency NIBS devices could be achieved by driving the acoustic field with an electromechanical transducer rather than using optical driving. For example, direct RF transduction can be achieved by using piezoelectric materials and interdigital transducers (IDT) to drive acoustic waves and achieve higher transduction efficiencies [236, 330]. Another intriguing concept for generating high-frequency phonons is by utilizing the thermoelastic expansion effect using metal gratings on the silicon layer [237]. The PPER scheme utilizing optical driving of the acoustic fields does however have advantages, such as wavelength-tunable phase matching, which would be difficult to obtain using IDTs with fixed geometry. The symmetry in the PPER design between the 'emit' and 'receive' waveguides also enables the design of devices with long interaction lengths, not limited by the finite aperture of an IDT. Since the driven optical field is proportional to the driving optical power, the design of high power-handling devices can be another potential direction to achieve high-performance isolators. In silicon photonics at telecom wavelengths, nonlinear loss limits the power-handling capabilities of devices. To achieve higher power handling, active free-carrier sweeping can be implemented [259]; alternatively, operation at longer optical wavelengths ($\lambda > 2.1$ μm) eliminates two-photon absorption (TPA), as well as TPA-induced free-carrier

absorption (FCA), which will drastically reduce nonlinear losses [356]. Another strategy to enable high Brillouin gain in silicon is through the design of new waveguide geometries, which are optimized for higher power handling, discussed further in Chapter 10.

We have experimentally demonstrated how we can design an inter-modal PPER device with multi-pole acoustic frequency response. The sharp frequency roll-off, together with the suppression of spurious modes through the use of a phononic stop-band, can enable filtering schemes with ∼MHz resolution. The single-sideband nature of the inter-modal scattering process could enable such filters to be tuned over wide spectral ranges for use in microwave-photonic systems, or for optical spectral analysis. In our proof-of-concept experiments, we have demonstrated 22 dB of single-sideband relative suppression, however, similar devices have shown that ∼40 dB of sideband contrast could be possible [139].

The dependence of the optical response on the dispersion parameters of the waveguides could potentially be utilized for sensing, where small perturbations to the waveguide geometry can be translated to measurable signals. As we have seen in our analysis, the optical dispersion properties of the waveguides directly affect the phase-matching conditions, which can result in large, measurable changes in the output signal. For example, a perturbation of 5 nm in the waveguide width of a NIBS device results in the shifting of the phase-matched optical wavelength by ∼10 nm [139]. This high sensitivity to perturbations, together with the high signal-to-noise ratio possible with the PPER scheme, may enable the design of sensors with high spatial resolution, which could be used to detect changes in material properties.

In conclusion, utilizing inter-modal Brillouin scattering —taking advantage of its non-local nature and unique phase-matching properties— may open the door to the design of novel devices and signal processing schemes. Future work in dispersion engineering techniques, power handling, and efficient acousto-optic interactions could potentially lead to high-impact filtering, isolation, and sensing technologies.

Chapter 10

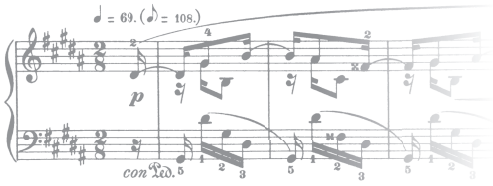

Towards power-scalable Brillouin-active devices

10.1 Introduction

Throughout the experimental demonstrations in this work, we have used a silicon-on-insulator (SOI) platform, enabling us to design versatile Brillouin-active devices while utilizing mature and robust fabrication methods. Silicon is one of the leading material platforms to implement integrated-photonic systems thanks to the well-developed infrastructure of CMOS fabrication facilities, the ability to integrate electronic circuits on the same chip. Additionally, the large refractive index contrast between the silicon and oxide layers, enables strong guiding of optical modes [46, 48, 62]. However, the nonlinear loss mechanisms in silicon limit the amount of power that can be processed on-chip, as the optical absorption increases at high intensities. Moreover, since high intensities are required to achieve strong nonlinearities, such as Brillouin scattering, the trade-off between gain and loss needs to be taken into account when designing devices that operate at high optical powers.

In this chapter, we focus on possible strategies to enable higher power-handling capabilities than currently available in Brillouin-active silicon devices. As we have seen in previous chapters, the performance of many Brillouin-based applications is determined by the amount

of power we can deliver to the device. For example, in Chapter 5 we saw how in the context of a microwave-photonic link, higher optical power results in a lower noise figure and larger dynamic range, and in Chapter 9 we showed that nonreciprocal behavior of devices utilizing inter-modal scattering is more efficient at higher optical powers. Additionally, higher power could enable high-gain amplifiers [64], and low-threshold lasers [56].

In the following sections, we will analyze waveguide designs that could enable higher power handling by utilizing geometries that have a larger optical mode area, reducing the field intensity and nonlinear loss. We analyze the trade-off between gain and nonlinear loss, and present waveguide designs that could potentially lead to high-performance Brillouin devices. Another strategy we consider is the distribution of Brillouin gain between multiple identical Brillouin-active sections, and coherently summing the processed signals. We show how this can be implemented by integrating Brillouin-active waveguides within a Mach-Zehnder interferometer (MZI). Such devices could potentially enable higher power handling, with the additional advantage that the pump and signal waves can be directed to separate ports, eliminating the need for pump-wave filtering.

10.2 Nonlinear loss in silicon devices

In silicon waveguides operating at telecom wavelengths (∼1550 nm), power handling is limited by nonlinear loss, restricting integrated optical circuits of the type presented in this work to maximum power handling of ∼100 mW [63–65,357]. The nonlinear loss mechanisms are two-photon absorption (TPA) and free-carrier absorption (FCA), with losses that scale with the square and the cube of optical intensity, respectively. In a two-photon absorption process, an electron is excited from the valence band to the conduction band by the absorption of two photons. This phenomenon is related to Kerr nonlinearity and can be described in terms of the imaginary part of the nonlinear refractive index [62, 356]. Free carrier absorption describes the process of intra-band transitions through light absorption, which depends on the steady-state free-carrier generation rate and lifetime [358].

Taking into account linear and nonlinear losses, the spatial evolution of the optical

intensity of a wave propagating in a silicon waveguide can be described by [359]

$$\frac{\partial}{\partial z}I = -\alpha I - \beta_{\mathrm{TPA}} I^2 - \gamma_{\mathrm{FCA}} I^3. \tag{10.1}$$

Here, α is the linear loss coefficient, β_{TPA} is the TPA loss coefficient of the material, and the FCA loss coefficient is given by $\gamma_{\mathrm{FCA}} = \sigma_{\mathrm{FCA}}\beta_{\mathrm{TPA}}\tau_0/(2\hbar\omega)$, where τ_0 is the carrier lifetime, σ_{FCA} is the electron scattering cross section, and ω is the optical frequency [359]. For a guided mode with an effective mode area A_{eff} [360], we can rewrite Eq. (10.1) in terms of optical power ($P \propto I/A_{\mathrm{eff}}$), such that

$$\frac{\partial}{\partial z}P = -\alpha P - \underbrace{\left(\frac{\beta_{\mathrm{TPA}}}{A_{\mathrm{eff}}}\right)}_{\beta} P^2 - \underbrace{\left(\sigma_{\mathrm{FCA}}\ \beta_{\mathrm{TPA}}\ \frac{\tau_0}{2\hbar\omega}\frac{1}{A_{\mathrm{eff}}^2}\right)}_{\gamma} P^3, \tag{10.2}$$

where we have defined normalized nonlinear loss coefficients (β and γ), showing how the effects of nonlinear loss are reduced for a larger effective mode area ($\beta \propto A_{\mathrm{eff}}^{-1}$ and $\gamma \propto A_{\mathrm{eff}}^{-2}$).

To analyze the effect of these loss mechanisms in the context of Brillouin-active systems, we will consider the example of small-signal Brillouin amplification, where a strong pump tone, with power P_{p}, is used to amplify a weak Stokes signal with power P_{s} (i.e., $P_{\mathrm{s}} \ll P_{\mathrm{p}}$). The Stokes wave spatial evolution can be described by [361]

$$\frac{\partial}{\partial z}P_{\mathrm{s}} = G_{\mathrm{B}}P_{\mathrm{s}}P_{\mathrm{p}} - \alpha P_{\mathrm{s}} - 2\beta P_{\mathrm{s}}P_{\mathrm{p}} - \gamma P_{\mathrm{s}}P_{\mathrm{p}}^2, \tag{10.3}$$

where we see the Brillouin gain G_{B} scales the same as TPA with optical power, as they are both $\chi^{(3)}$ optical nonlinearities. While this simple model does not take into account pump depletion and anti-Stokes scattering, it is sufficient to describe the process of small-signal Brillouin amplification [64]. By designing waveguides with a larger optical mode area, we can significantly decrease the effects of nonlinear loss, enabling higher pump powers and stronger Brillouin interactions. However, the increase in the mode area will also reduce the Brillouin gain and a careful analysis needs to be performed when designing high-power devices.

10.3 Multi-ridge waveguide design

As we explore structures that could yield improved performance, we begin by considering new Brillouin-active structures that distribute the optical field into multiple identical optical waveguide modes, which all couple to a common Brillouin-active phonon mode. By distributing the same phase-coherent light-field between these waveguides —which can also be viewed as the spatially-extended optical super-mode of the multi-waveguide structure— a larger effective mode area is achieved. Our objective is to investigate designs that produce larger effective mode areas without degrading the Brillouin gain. This can be achieved by placing the optical waveguides (i.e., the guiding ridges) in locations that maximize optomechanical coupling to an individual phonon mode. Throughout this chapter we consider similar ridge structures to the ones presented in Chapter 6, with a height of 85 nm on a single silicon membrane of thickness 130 nm (see Fig. 6.3), permitting Brillouin interactions with a common phonon mode supported by this system, as seen in Fig. 10.1.

As a first analysis, we will set the guiding acoustic membrane width to be constant, and estimate the performance of devices with a different number of ridge waveguides. To achieve strong Brillouin scattering, the symmetries of the acoustic and optical modes need to be considered. Here, we will analyze the case for forward intra-modal Brillouin scattering (FSBS) utilizing the fundamental optical mode (symmetric in space), which requires an acoustic mode with an anti-symmetric displacement profile. By placing the optical-guiding regions at locations where the optical forces interfere constructively (i.e., with the correct symmetry), it is possible to achieve a larger mode area, while leaving the Brillouin gain mostly unchanged. Fig. 10.1 shows the simulation results of the electric and acoustic fields for devices with a different number of optically-guiding ridges, while the width of the acoustic membrane is kept constant. Calculating the Brillouin gain expected for the different acoustic modes supported by the structures, we see that in all cases, the strongest interaction is with the same acoustic mode at a frequency around 4.45 GHz and a similar value for Brillouin gain.

Next, using the simulated electric field distributions, we calculate the expected nonlinear

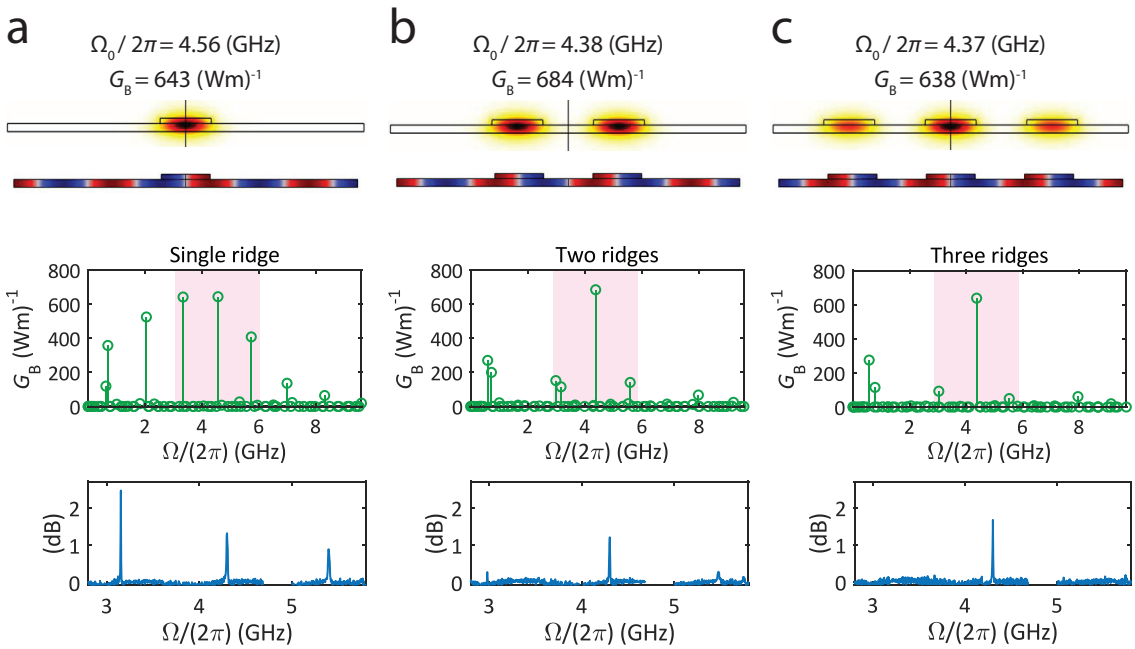

Figure 10.1: Simulations of Brillouin-active devices with multiple optical guiding ridges. In all cases, the acoustic-guiding membrane is 7 μm wide, and the optical ridges are 1 μm wide, with a separation of 1 μm between ridges. Panels **(a)**, **(b)** and **(c)** show devices with one, two and three ridges, respectively. Top: The optical field $|E|$ and the x component of the displacement profile (u_x) of the strongest Brillouin-active acoustic mode. Middle: Calculated Brillouin gain G_{B} of the simulated acoustic modes of the structure. Bottom: Brillouin gain measurements of fabricated devices. Calculated small-signal amplification as a function of pump power for these structures is shown in Fig. 10.2.

Table 10.1: Calculated nonlinear loss coefficients of multi-ridge waveguide designs.

Parameter	Single ridge	Two ridges	Three ridges	Four ridges	Description
α (m^{-1})	4.1	4.1	4.1	4.1	Linear loss [64]
β ($\mathrm{W}^{-1}\mathrm{m}^{-1}$)	49.9	24.9	18.4	18.1	TPA coefficient[1]
γ ($\mathrm{W}^{-2}\mathrm{m}^{-1}$)	2400	598	325	263	FCA coefficient[1]
A_{eff} ($\mu\mathrm{m}^2$)	0.236	0.472	0.640	0.779	Mode area

[1] See Table 10.2 for the parameters used to obtain these values.

loss coefficients for devices with different numbers of ridge waveguides, as seen in Table 10.1. Using Eqs. (10.1) and (10.3), we calculate the small-signal Brillouin amplification that such devices could yield, as seen in Fig. 10.2(f). We can see that these multi-ridge devices have the potential to yield a tenfold increase in small-signal amplification and power handling relative to the single-ridge device. The parameters used throughout the calculations in this chapter are on par with those of recent experimental demonstrations [64, 65], summarized in Table 10.2.

An intriguing feature of this design is that it also produces suppression of spurious acoustic modes. When confining acoustic modes in the suspended waveguides using slots (acting as 'acoustic mirrors'), multiple long-lived modes are supported by the structure, which can all have strong Brillouin gain. The spurious modes, seen in Fig. 10.1(a), can be a source of noise and loss in Brillouin-based applications. These can be suppressed by using a phononic crystal structure to engineer the acoustic modes in the system, as was discussed in Chapter 6. However, the multi-ridge structures presented here provide an alternative path towards such spur suppression. The effect of using multiple optical guiding ridges can be understood by analyzing the spatial profiles of the acoustic modes, and their overlap with the optical fields. The optical forces in the device, which are determined by the spatial distribution of the optical fields, interfere constructively when driving certain acoustic modes, and cancel out for others. Effectively, the number of spurious Brillouin-active modes in the system is reduced, as can be seen in the Brillouin-gain simulation

Table 10.2: Parameters used for nonlinear loss calculations.

Parameter	Value	Description
$P_{\mathrm{s}}(0)/P_{\mathrm{p}}$ (dB)	-30	Stokes to pump ratio at input
λ (nm)	1550	Optical wavelength
Q	500	Acoustic Q-factor
L (mm)	30	Device length[1]
β_{TPA} ($\mathrm{W^{-1}m}$)	$7.9 \cdot 10^{-12}$	TPA coefficient [362]
σ_{FCA} ($\mathrm{m^2}$)	$1.45 \cdot 10^{-21}$	FCA cross section [358]
τ_0 (ns)	2	Free-carrier lifetime [64]

[1] We assume that the Brillouin-active length is the same as the device length.

results presented in the middle row of Fig. 10.1. As a proof-of-concept, Brillouin gain measurements were carried out on such devices. We can see the suppression of spurious modes while retaining similar gain for an acoustic mode at 4.2 GHz, as seen in the bottom row of Fig. 10.1.

While the designs presented so far enabled the distribution of the optical power —with the added benefit of spur suppression— they require a wide acoustic membrane to support multiple optical ridges. The wider device results in a larger acoustic mode area, which

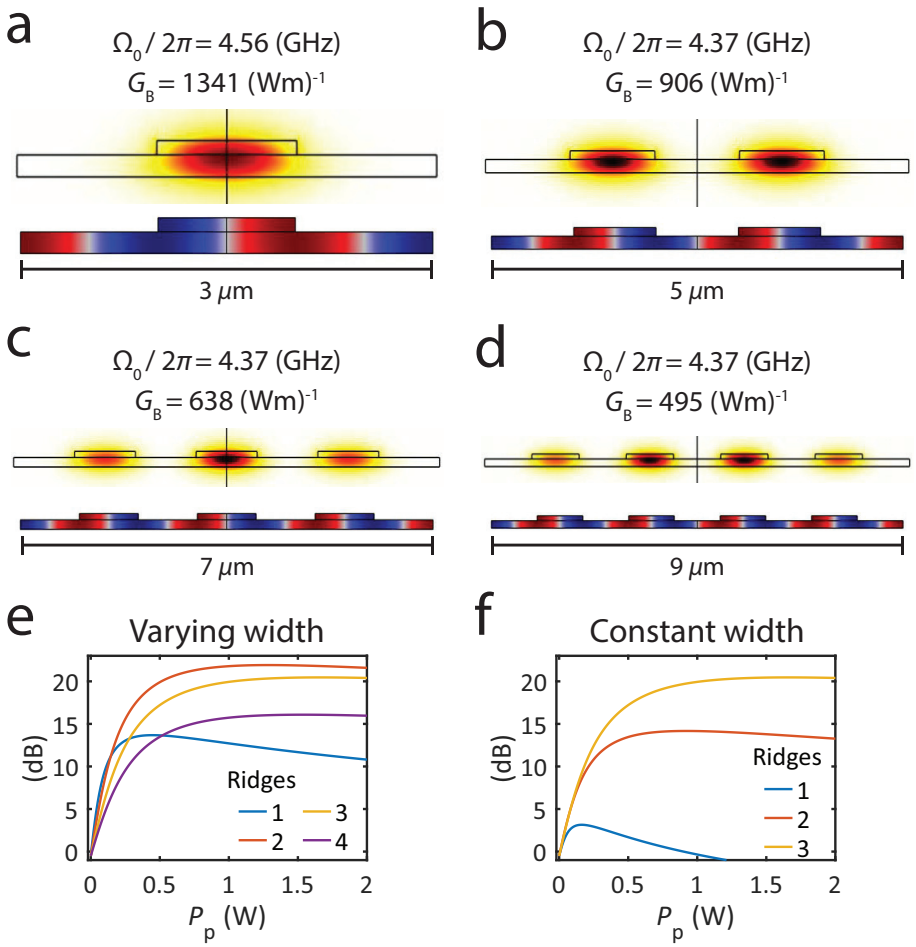

Figure 10.2: **(a–d)** Simulations of Brillouin-active devices with multiple optical guiding ridges. The optical ridges are 1 μm wide, with a separation of 1 μm between ridges for all devices. The acoustic membrane widths are 3 μm, 5 μm,7 μm, and 9 μm, respectively. **(e)** Calculated small-signal Brillouin gain for the four device designs as a function of pump power in the presence of linear and nonlinear loss. **(f)** Calculated small-signal Brillouin gain as a function of pump power in the presence of linear and nonlinear loss for the three devices from Fig. 10.1.

reduces the Brillouin gain, as the acoustic power of the phonon mode is spread out over a large region. As our next step, we estimate the Brillouin gain for multi-ridge devices, without the constraint of a constant acoustic membrane width, as shown in Fig. 10.2(a–d). Now, the devices that have fewer ridges also have a smaller acoustic membrane and exhibit higher Brillouin gain. We calculate the potential small-signal amplification of these devices using Eqs. (10.1) and (10.3), as shown in Fig. 10.2(e). We can see that out of the four designs, the two-ridge structure exhibits the largest small-signal amplification.

It is important to note, that these large-mode devices can be challenging to fabricate, as they require a large suspended region which can suffer from the built-in compressive stress in the SOI platform [277, 278], which can lead to deformations and even to devices breaking altogether. These challenges can potentially be addressed through the integration of materials with controllable stress to counteract the forces in the silicon layer [363, 364].

10.4 Brillouin-active Mach-Zehnder interferometers

An alternative strategy to enable high power-handling Brillouin devices is to split the optical power between several separate Brillouin-active waveguides in parallel and coherently combine the amplified signals. Such devices can be achieved by designing Brillouin-active regions within a balanced Mach-Zehnder interferometer (MZI). This interferometric scheme could enable higher power handling, as the optical power within each waveguide is lower, resulting in the reduction of nonlinear loss. An additional benefit from this design is the possibility to separate pump and signal waves into separate ports of the interferometer. The separation of pump and signal waves can be challenging in forward Brillouin devices, where both waves co-propagate in the same spatial mode, and are separated in frequency by only a few GHz, as illustrated in Fig. 10.3(a).

The Mach-Zehnder Brillouin-active device, illustrated schematically in Fig. 10.3(b), consists of three sections; a directional coupler at the input splitting the optical field into two separate paths, followed by a Brillouin gain region on each one of the branches of the interferometer, and a second directional coupler at the output, combining the amplified

fields. We start by describing the operation of a directional coupler, splitting the optical power equally between its two output ports, using the transfer matrix [198]

$$\begin{pmatrix} E'_{\text{top}} \\ E'_{\text{bot}} \end{pmatrix} = \frac{1}{\sqrt{2}} \begin{pmatrix} 1 & i \\ i & 1 \end{pmatrix} \begin{pmatrix} E^{(\text{in})}_{\text{top}} \\ E^{(\text{in})}_{\text{bot}} \end{pmatrix} = \frac{1}{\sqrt{2}} \begin{pmatrix} E^{(\text{in})}_{\text{top}} + iE^{(\text{in})}_{\text{bot}} \\ iE^{(\text{in})}_{\text{top}} + E^{(\text{in})}_{\text{bot}} \end{pmatrix}, \tag{10.4}$$

where the subscripts 'top' and 'bot' refer to the upper and lower branches of the interferometer. Here, E' denoted the field after the directional coupler and $E^{(\text{in})}$ denotes the input fields at the input ports of the coupler. Next, we can describe the Brillouin-active regions, where a small-signal Stokes tone with field amplitude $a_s(z)$ experiences amplification given

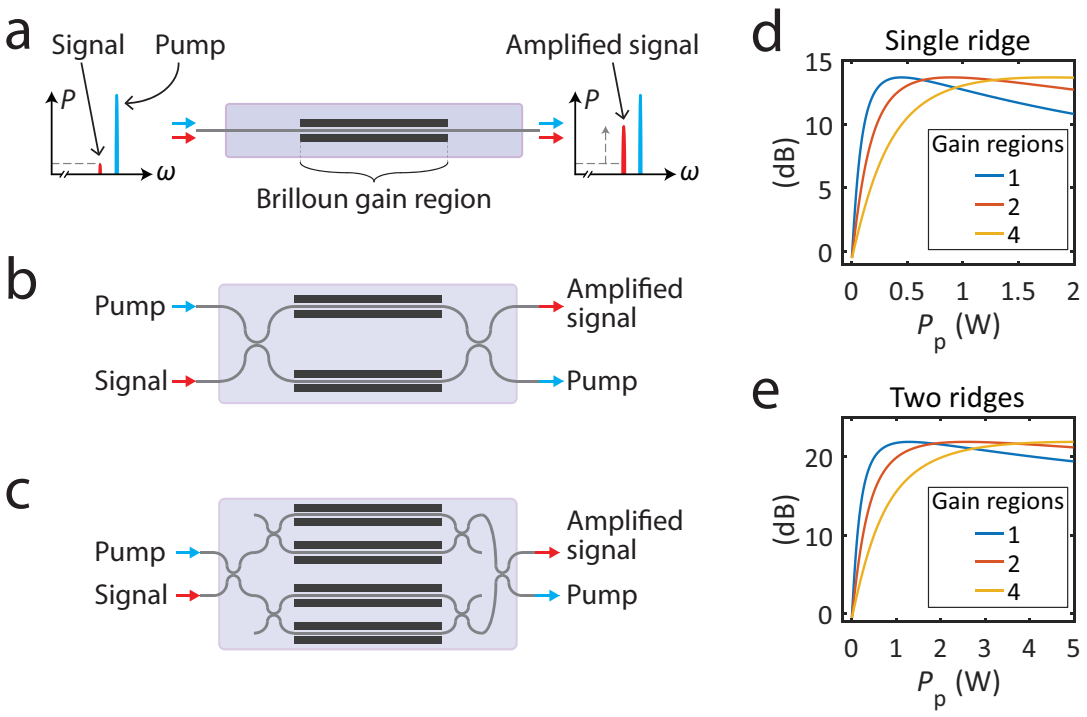

Figure 10.3: Comparing the potential performance of MZI Brillouin-active devices. **(a)** A single Brillouin-active region. **(b)** A Mach-Zehnder interferometer with two Brillouin-active regions in parallel. **(c)** Two Mach-Zehnder interferometers in parallel with four Brillouin-active regions. **(d)** Calculated small-signal Brillouin amplification for the three device schemes in panels (a–c) as a function of pump power, in the presence of linear and nonlinear loss. **(e)** Calculated small-signal Brillouin amplification for the same three devices, assuming each gain region is a two-ridge Brillouin-active section, as seen in Fig. 10.2(b).

by [172]

$$a_{\mathrm{s}}(L) = a_{\mathrm{s}}(0)\left(1 + \frac{1}{2}G_{\mathrm{B}}P_{\mathrm{p}}L\right). \tag{10.5}$$

Here, L is the length of the Brillouin-active gain region, G_{B} denotes the Brillouin gain, and we assume a strong, undepleted pump with power P_{p}.

Using Eqs. (10.4) and (10.5) we can analyze the field amplitudes in an MZI-Brillouin device, of the type shown in Fig. 10.3(b). We inject a strong pump tone (with a field amplitude a_{p}) into the top port of the device and a small Stokes signal into the bottom port

$$\begin{pmatrix} E_{\mathrm{top}}^{(\mathrm{in})} \\ E_{\mathrm{bot}}^{(\mathrm{in})} \end{pmatrix} = \begin{pmatrix} a_{\mathrm{p}} \\ a_{\mathrm{s}}(0)e^{i\Omega_0 t} \end{pmatrix}, \tag{10.6}$$

where Ω_0 denotes the Brillouin frequency, by which the two optical tones are separated. After the first directional coupler, these fields become

$$\begin{pmatrix} E'_{\mathrm{top}} \\ E'_{\mathrm{bot}} \end{pmatrix} = \frac{1}{\sqrt{2}} \begin{pmatrix} a_{\mathrm{p}} + ia_{\mathrm{s}}(0)e^{i\Omega_0 t} \\ ia_{\mathrm{p}} + a_{\mathrm{s}}(0)e^{i\Omega_0 t} \end{pmatrix}, \tag{10.7}$$

and after propagating through the gain regions (assuming an undepleted pump) we have

$$\begin{pmatrix} E''_{\mathrm{top}} \\ E''_{\mathrm{bot}} \end{pmatrix} = \frac{1}{\sqrt{2}} \begin{pmatrix} a_{\mathrm{p}} + ia_{\mathrm{s}}(L)e^{i\Omega_0 t} \\ ia_{\mathrm{p}} + a_{\mathrm{s}}(L)e^{i\Omega_0 t} \end{pmatrix}. \tag{10.8}$$

From Eq. (10.5) we know that $a_{\mathrm{s}}(L) = a_{\mathrm{s}}(0)[1 + G_{\mathrm{B}}P_{\mathrm{p}}L/4]$, where the reduction in the amplification (by a factor 2) is the result of having half the pump power in each of the Brillouin-active amplifying regions. Finally, we calculate the field amplitudes at the device output, after the second directional coupler

$$\begin{pmatrix} E_{\mathrm{top}}^{(\mathrm{out})} \\ E_{\mathrm{bot}}^{(\mathrm{out})} \end{pmatrix} = i \begin{pmatrix} a_{\mathrm{s}}(0)\left[1 + G_{\mathrm{B}}P_{\mathrm{p}}L/4\right]e^{i\Omega_0 t} \\ a_{\mathrm{p}} \end{pmatrix}, \tag{10.9}$$

revealing that the pump and signal waves now exit distinct ports of the interferometer. We note that the gain is half of that achieved by a Brillouin amplifier of the same length

(compare to Eq. (10.5)). This is a consequence of the fact that Brillouin amplification scales linearly with the pump power, and in the MZI structure, only half of the pump power propagates in each gain section. However, similar to the multi-ridge devices analyzed in Section 10.3, the reduction in power within each segment results in lower nonlinear losses, and overall enhanced power handling, as seen by the calculations presented in Fig. 10.3(d).

We can see that although the maximum gain does not change when comparing a single Brillouin-active waveguide (Fig. 10.3(a)) and the MZI-Brillouin device (Fig. 10.3(b)), however, the gain is achieved at a higher pump power. This is important when amplifying larger signals, where pump depletion will limit the amplifier operation[1]. For example, if our objective is to perform small-signal amplification, (e.g. boost a signal with power $P_{\mathrm{s}}^{(\mathrm{in})} = 1$ μW to $P_{\mathrm{s}}^{(\mathrm{out})} = 10$ μW), a single Brillouin-active waveguide could provide gain using a pump power of $P_{\mathrm{p}} \approx 100$ mW. In this case, the signal is much smaller than the pump throughout the amplification process (i.e., $P_{\mathrm{s}}^{(\mathrm{out})} \ll P_{\mathrm{p}}$). However, if we want to boost a signal from $P_{\mathrm{s}}^{(\mathrm{in})} = 5$ mW to $P_{\mathrm{s}}^{(\mathrm{out})} = 50$ mW, this cannot be accomplished using a single waveguide segment since much higher pump powers are necessary for amplification, requiring high power-handling Brillouin devices.

The Mach-Zehnder Brillouin-active scheme can be extended, implementing more gain regions in parallel by designing arrays of interferometers, as illustrated schematically in Fig. 10.3(c). Such designs could have the potential to support high optical powers ($P_{\mathrm{p}} > 1$ W), as splitting the power into multiple regions further reduces nonlinear loss[2]. Furthermore, using multi-ridge waveguides (such as were discussed in Section. 10.3) within the MZI scheme may enable even higher power handling and permit large Brillouin gain in silicon, as shown in the calculations seen in Fig. 10.3(e).

Finally, we note that throughout our analyses we have neglected complexities and addi-

1. For example, using the parameters presented in this chapter, a single Brillouin-active waveguide (Fig. 10.3(a)) will result in the amplified signal experiencing 1 dB of compression (compared to the case of an undepleted pump) when $P_{\mathrm{s}}/P_{\mathrm{p}} \approx 4\%$, where P_{s} and P_{p} are the signal and pump powers at the amplifier input.

2. As we have seen in the single MZI analysis (Eq. 10.9), splitting the pump power between more Brillouin-active sections will also result in a smaller small-signal gain for the device, as can be seen from the slopes of the calculated gain for the different devices in Fig. 10.3(d) at low pump power.

tional linear and nonlinear losses that can be produced by waveguides and couplers within this system. However, in practice, losses from other components such as directional couplers and grating couplers must be considered.

10.4.1 Spontaneous Brillouin scattering

We turn to analyze the spontaneous scattering occurring in such an MZI-Brillouin device. At non-zero temperature, the acoustic modes are occupied by thermally-excited phonons, which scatter the pump field into Stokes and anti-Stokes sidebands, as was described in Chapter 2. In practical applications, this is essentially excess noise added by the Brillouin process. Following the derivation from Chapter 2 and Ref. [172], the amplitude of the scattered pump into the Stokes sideband, after an interaction within a single Brillouin-active region of length L, is given by

$$a_s(L,t) = -\frac{i}{v} g^* a_p \int_0^t dt' \int_0^L dz\ \eta^\dagger(z,t') e^{-(t-t')\Gamma/2}, \tag{10.10}$$

where v is the optical group velocity, g is the acousto-optic coupling rate, and Γ is the acoustic dissipation rate. Here, $\eta(z,t)$ is a stochastic term to account for the thermal Brillouin fluctuations, with zero mean ($\langle \eta(z,t) \rangle = 0$) and a two-time correlation function given by $\langle \eta^\dagger(z,t)\eta(z',t') \rangle = n_{\text{th}}\Gamma\delta(z-z')\delta(t-t')$. The number of thermal phonons is denoted n_{th} and follows a Bose-Einstein distribution $n_{\text{th}} = [\exp(\hbar\Omega/k_{\text{B}}T) - 1]^{-1}$, where T is the temperature, and k_{B} is the Boltzmann constant. Calculating the total scattered power from a pump with power P_p into the Stokes sideband, we have

$$P_{\text{N}} = \hbar\omega v \langle a_s^\dagger a_s \rangle = \frac{1}{4} G_{\text{B}} P_p L \Gamma \hbar\omega (n_{\text{th}} + 1). \tag{10.11}$$

In an MZI-Brillouin device, we can calculate the Brillouin noise power using Eqs. (10.8)–(10.11), and follow a similar derivation to the one we did for the amplified signal. Alternatively, we can understand this directly by inspecting Eq. (10.11), and noting that the noise scales linearly with the pump power, such that in each of the two MZI optical paths, only half the noise power will be produced. Taking both Brillouin-active regions into account,

the same amount of spontaneous scattering will occur compared to a single Brillouin-active region. However, since spontaneous scattering is an incoherent process, and the thermal phonons in each active region are uncorrelated, the spontaneous-scattering induced sideband will be split evenly between the two outputs of the interferometer. The noise power at the interferometer output ports is given by

$$\begin{pmatrix} P_{\mathrm{N}}^{(\mathrm{top})} \\ P_{\mathrm{N}}^{(\mathrm{bot})} \end{pmatrix} = \begin{pmatrix} G_{\mathrm{B}} P_p L \Gamma \hbar \omega (n_{\mathrm{th}} + 1)/8 \\ G_{\mathrm{B}} P_p L \Gamma \hbar \omega (n_{\mathrm{th}} + 1)/8 \end{pmatrix}, \tag{10.12}$$

where we can see that at each of the ports, only have half the noise power will be measured compared to a single gain region of the same length (see Eq. (10.11)). Hence, for the same optical powers, the noise power exiting the signal output port (top port in Fig. 10.3(b)) will be half of that produced by a single Brillouin-active device (Fig. 10.3(a)). While the noise exiting the signal port is lower, the gain is also reduced (see Eq. (10.9)), and the noise figure of the amplifier should be analyzed carefully, taking into account all of the system parameters. A similar analysis can be carried out for the 4-port systems of the type seen in Fig. 10.3(c), resulting in another twofold reduction in the noise power exiting each of the four output ports.

10.4.2 Experimental proof-of-concept

As a proof-of-concept, we fabricated MZI Brillouin-active devices in a standard silicon-on-insulator platform, illustrated schematically in Fig. 10.4(a). The directional couplers were implemented using multi-mode interference (MMI) sections, seen in Figs. 10.4(b,c), where the coherent interference of multiple optical modes is used to achieve directional coupling with an equal power-splitting ratio. The MMI dimensions are 10 $\times$ 125 μm, and 1 μm wide waveguides are used as the input and output ports. A calculation of the field distribution within the MMI region is shown in Fig. 10.4(e). Further discussion of the MMI design process can be found in Appendix A. The Brillouin-active regions follow the design from Ref. [64], and are comprised of an 85 nm ridge defined in a 215 nm silicon layer, suspended over an active-region of $L = 7$ mm to enable strong forward Brillouin

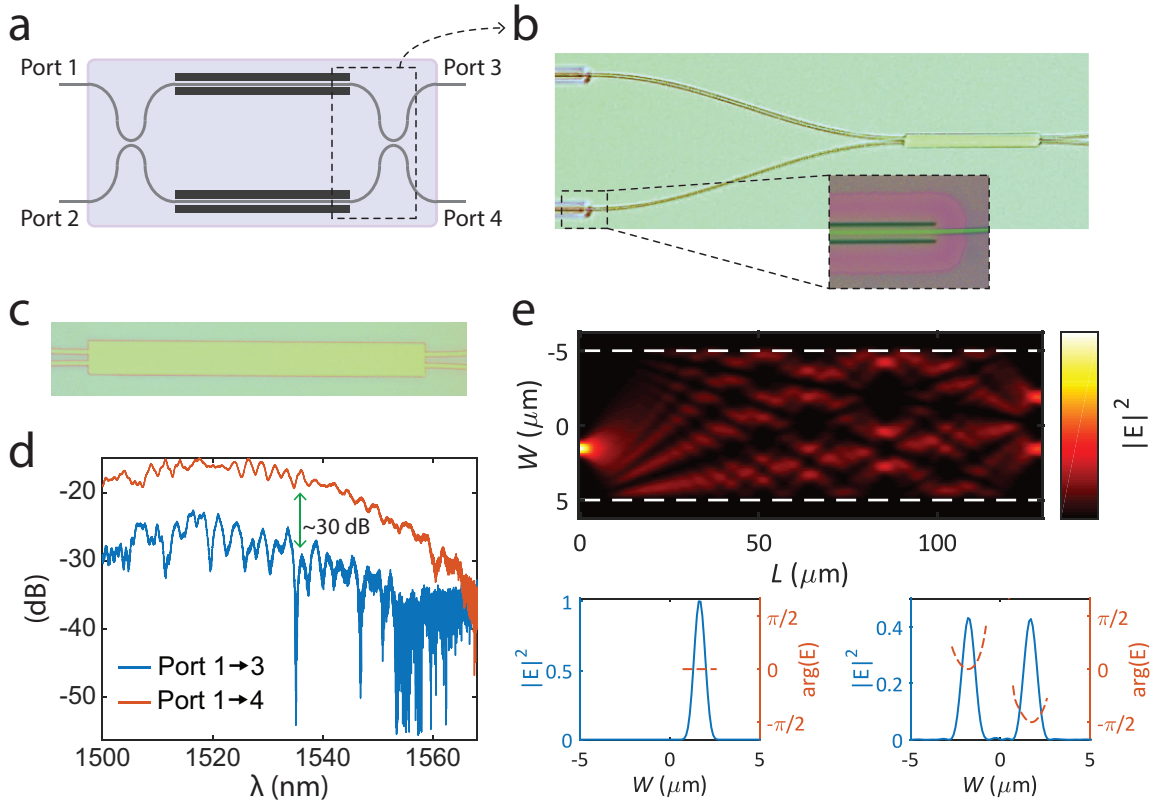

Figure 10.4: **(a)** A schematic illustration of the MZI-Brillouin device. The dark shaded regions represent the Brillouin-active sections of the waveguides. **(b)** Micrograph of a fabricated device, showing one of the directional couplers and part of the Brillouin-active regions. The inset shows a magnified view of the active region. **(c)** Magnified view of the MMI directional coupler. **(d)** Measured wavelength response of the MZI. **(e)** Top: Simulated electric field distribution within the MMI used for directional coupling. The dashed lines mark the edges of the device. Bottom: Simulated electric field at the input (left) and output (right) planes of the MMI, showing equal power distribution between the two output waveguides, and a $\pi/2$ relative phase.

interactions. Integrated grating couplers were used to couple light on and off the chip.

First, we analyze the performance of the balanced Mach-Zehnder interferometer. We direct a tunable laser into port 1 (as denoted in Fig. 10.4(a)), and measure the output power from ports 3 and 4 as a function of optical wavelength, as seen in Fig. 10.4(d). We see a 40 nm bandwidth with ∼15 dB of contrast between the two ports, and specific wavelengths showing >30 dB. This sweep was performed at low optical power (∼100 μW on-chip) such that nonlinear loss and heating effects are negligible.

Next, we perform a Brillouin gain measurement, using the experimental setup illustrated

in Fig. 10.5(a). A laser source is split and used as a pump directed into port 1, and a small signal (−30 dB lower power than the pump) is synthesized using an intensity modulator and an optical bandpass filter. Using an optical switch, the signal can be directed to either port 1 or 2, as illustrated in Figs. 10.5(b,c). A second optical switch is used to select the output light from either port 3 or 4, which is combined with an optical local oscillator to perform a self-heterodyne measurement.

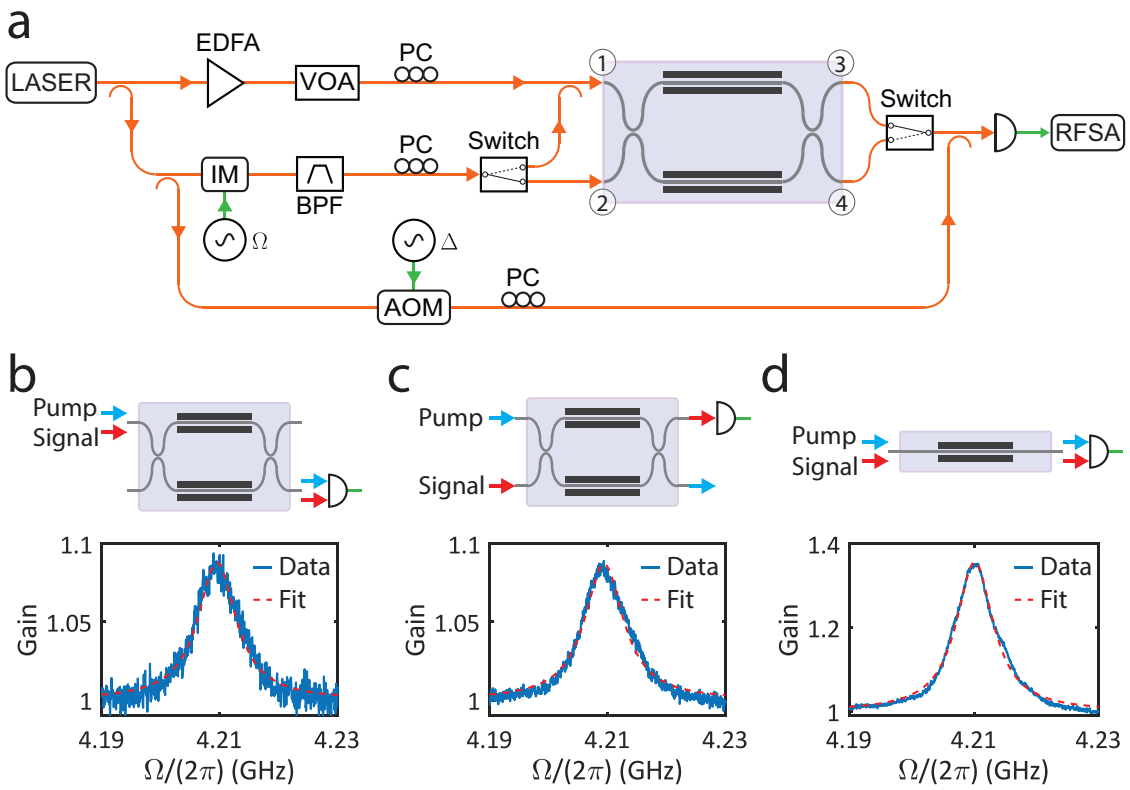

Figure 10.5: **(a)** Schematic illustration of the experimental setup used to measure the MZI-Brillouin device. VOA: variable optical attenuator, EDFA: erbium-doped fiber amplifier, RFSA: radio-frequency spectrum analyzer, PC: polarization controller, BPF: optical band-pass filter, IM: intensity modulator, AOM: acousto-optic frequency shifter. **(b)** Measurement of an MZI-Brillouin device, injecting the pump and signal into the same port. The Brillouin peak is centered around $\Omega_0/(2\pi) = 4.21$ GHz and has a linewidth of $\Gamma_0/(2\pi) = 7.91$ MHz. **(c)** Measurement of the same device, when injecting the pump and signal into separate input ports. The Brillouin peak is centered around $\Omega_0/(2\pi) = 4.21$ GHz and has a linewidth of $\Gamma_0/(2\pi) = 8.02$ MHz. The measured output optical power is 29 dB lower compared to that from panel (b). **(d)** Measurement of a single Brillouin gain region for reference, showing a Brillouin peak at $\Omega_0/(2\pi) = 4.21$ GHz and a linewidth of $\Gamma_0/(2\pi) = 7.22$ MHz.

We measure the Brillouin gain in two configurations. In the first configuration, the pump and signal are directed into the same port, as seen in Fig. 10.5(b). In the second configuration, the pump and signal are directed into separate input ports, as seen in Fig. 10.5(c). We see that in both cases the gain spectrum is practically identical, yielding 0.374 dB of amplification, at a frequency of 4.21 GHz and linewidth of 8 MHz. These measurements were done with an estimated pump power of 24 mW on-chip, and a Brillouin gain of 1000 $(\mathrm{Wm})^{-1}$ in each of the suspended regions, consistent with Ref. [64]. The measurements in Fig.10.5(b) are noisier, as our switching scheme resulted in a tenfold reduction in the signal input power for this configuration, however, we see the small-signal gain is unaffected. The measured output powers were 2.022 mW and 2.29 μW for the traces in Figs. 10.5(b) and 10.5(c), respectively, demonstrating 29 dB of power suppression when implementing the pump-separation scheme. We repeated the measurement with a higher pump power of 35 mW on-chip, yielding a small-signal gain of 0.55 dB. At these higher pump powers, the interferometer performance is degraded, reducing the pump suppression to 18 dB. For comparison, we measure a device consisting of a single gain region with the same Brillouin-active design on the same chip. As seen in Fig. 10.5(d), this device yields the same frequency response and higher gain, as expected from our earlier analysis, demonstrating that the Brillouin frequency response is not affected when utilizing gain regions within an interferometer.

This proof-of-concept experiment demonstrates the feasibility of the MZI Brillouin-active devices, showing how spatially separated Brillouin active regions can be used within an interferometer. The degradation in performance of the devices could be avoided by implementing phase shifters and tunable couplers to stabilize the interferometer. Actively-stabilized devices will result in strong pump suppression at higher optical powers and could achieve high-power Brillouin amplification with minimal signal distortion. Furthermore, the device presented here was fabricated using electron-beam lithography, which can suffer from drift, resulting in fabrication imperfections. Fabrication of these devices using photography, as was discussed in Chapter 6, could result in devices with better performance.

10.5 Conclusion

In this chapter, we have explored possible strategies to enable high power handling silicon devices through the design of waveguides with larger mode areas. We have analyzed this in the context of forward intra-modal Brillouin scattering, however, the same concepts can be used when considering other forms of nonlinear interactions in silicon, such as inter-modal Brillouin scattering, Kerr, and Raman nonlinearities. As we have seen, the larger mode area results in lower Brillouin gain as well as lower nonlinear losses. By analyzing this trade-off we were able to show potential higher power-handling performance compared with previous demonstrations. Furthermore, while we have examined small-signal amplification as an example where higher power handling enhances device performance —potentially achieving a tenfold increase in amplification— these capabilities can be highly advantageous to other Brillouin-based applications in silicon, including lasers, filters, and modulators.

Another strategy for high power-handling devices is processing signals in multiple Brillouin-active regions in parallel. We presented an amplifier design utilizing Brillouin-gain segments within a Mach-Zehnder interferometer, which also enables the separation of the pump and signal tones at the device output. The distribution of gain to multiple spatially separated regions reduces the optical power propagating in each waveguide, and while this reduces the amplifier linear gain, it also suppresses nonlinear loss and could enable overall higher power handling. Our proof-of-concept experimental demonstration shows the feasibility of such schemes, achieving 29 dB of pump suppression at the signal output port. Such high power-handling amplifiers could be used for the amplification of larger input optical signals, where pump depletion can degrade the linearity of the system. By using higher pump powers, which could be possible with this new class of devices, the amplified signal can remain much smaller than the pump power throughout the amplification process, yielding high-power, low-distortion amplification.

The use of a standard silicon platform could enable the integration of active electronics on-chip to achieve stronger pump suppression. The fluctuations in the passive balanced interferometer used in our demonstration limited the performance of the device. By in-

tegrating active heaters, for example, the interferometer could be stabilized and enable high pump suppression at higher optical powers. Additionally, other active elements, such as integrated P-I-N junctions to perform carrier sweeping, could further reduce nonlinear loss [365]. Such active devices have been fabricated at Sandia National Laboratories[3] MESA facilities and could be a path towards high-power silicon devices. Finally, these strategies could utilize resonantly-enhanced Brillouin gain regions to achieve higher gain and smaller device footprint [66]. These schemes could open the door to a new class of high-power amplifiers, lasers, filters, and isolators, expanding the possible capabilities of integrated silicon devices.

3. Sandia National Laboratories is a multi-program laboratory managed and operated by National Technology and Engineering Solutions of Sandia, LLC., a wholly-owned subsidiary of Honeywell International, Inc., for the U.S. Department of Energy's National Nuclear Security Administration under contract DE-NA-0003525. This dissertation describes objective technical results and analysis. Any subjective views or opinions that might be expressed in this work do not necessarily represent the views of the U.S. Department of Energy, or the United States Government.

Chapter 11

Conclusion

In this dissertation, we have set out to study the intriguing properties of forward Brillouin scattering, and how they can be utilized to develop novel photonic devices. The nonlocal nature of the scattering process enabled us to design systems where the interactions between multiple coherent acoustic waves give rise to multi-pole frequency responses, typically unattainable in Brillouin devices. Building on basic device physics, we have described the performance of microwave-photonic filtering schemes based on this principle, and studied the fundamental sources of noise and signal distortion that degrade signal fidelity in such systems. The narrowband acoustic frequency response, combined with the large-bandwidth optical platform, enables the design of high-resolution widely-tunable filters, difficult to obtain with optical or microwave technologies alone.

The theoretical analysis and experimental demonstrations presented in this work point at a new strategy for optical and microwave-photonic signal processing, with a vastly different design space compared to other schemes. For example, acoustic mode engineering, in combination with the long lifetime of acoustic waves, enables spectral resolution previously unattainable in integrated devices. The optical separation of the input signal and output signal, by using an 'emit-receive' scheme, leads to low-noise operation and avoids technical issues such as pump rejection and unwanted optical nonlinearities. Furthermore, the forward geometry of the scattering we have studied here enables the design of cascaded systems, without the need for circulators and isolators, which could enable novel signal-processing

and sensing schemes.

Experimentally, we designed and fabricated devices implementing these nonlocal interactions in a standard silicon platform, using standard CMOS-compatible fabrication methods, and demonstrated microwave-photonic bandpass and notch filtering operations with record-narrow spectral resolution and a wideband tunability. Additionally, we explored future directions for these signal-processing schemes, utilizing the unique properties of inter-modal Brillouin scattering, and enhancing the performance of silicon devices by enabling higher power handling.

The ability to integrate Brillouin-active waveguides in a standard silicon platform opens the door to the design of complex systems, utilizing a wide range of available photonic and electronic components, on the same chip. For example, light sources, detectors, modulators, and resonators can all be integrated together with Brillouin-active regions to produce high-performance devices within a small footprint. The use of active electronic control of the photonic circuits, using integrated heaters, for example, may enable further tailoring of the acoustic modes in the system. Moreover, the device schemes presented here can be combined with other recently developed Brillouin technologies such as lasers and amplifiers, to expand possible capabilities. It is also important to note that while our experimental demonstrations focused on silicon at telecom wavelengths, the concepts presented here could be implemented in other material platforms —as Brillouin interactions are present in practically any material— as well as different optical wavelengths.

One of the main limitations of Brillouin-based systems is the noise added by thermally-excited acoustic modes, resulting in spontaneous scattering of light. Designing devices operating at higher acoustic frequencies could reduce this noise source. Another strategy is to operate Brillouin devices in cryogenic temperatures, which will drastically reduce Brillouin noise and has the potential of vastly increasing Brillouin gain. Operating optomechanical devices in cryogenic conditions is routinely performed over the past decade and could be implemented with the devices presented here. Furthermore, recent demonstrations of quantum operations using optomechanical devices suggest that the schemes presented in this work could be used within the context of quantum measurement and quantum signal

processing.

The analyses and experiments presented here have enabled us to show a path towards low-noise and low-distortion performance for forward Brillouin-based signal-processing technologies. In addition to bringing greatly enhanced performance to silicon photonics, we demonstrated reliability and robustness, key milestones necessary to transition silicon-based optomechanical technologies from the scientific bench-top to field-deployable devices. The results presented in this dissertation are another step towards foundry-compatible, fully-integrated photonic systems, which can be the basis for new high-impact technologies.

Appendix A

Multi-mode interferometers

In this section, we will describe the principle of operation of multi-mode interference devices, and outline design strategies to utilize them in photonic devices. For example, the directional couplers demonstrated in Chapter 10 implemented such structures for the splitting and combining of light within a Brillouin-active Mach-Zehnder interferometer.

The basic concept of multi-mode interference (MMI) devices utilizes the propagation of coherent optical fields in multiple guided spatial modes —each with a different propagation constant— such that their interference pattern changes along the propagation axis. By carefully choosing the geometry of the multi-mode section and the location of input and output ports, we will show how many photonic devices can be implemented. MMI devices can be simulated using commercial software packages, with finite-difference methods especially suited for such calculations. However, it is useful to consider semi-analytical calculations, which yield fast results and give additional insight and intuition to the design process. While these calculations neglect some processes occurring in the device, such as reflections and loss, they give good estimates of device performance and can serve as a starting point for further optimization.

Multi-mode wave propagation

We begin our analysis by describing the structure illustrated in Fig. A.1(a), consisting of a narrow waveguide, used as in input port, connected to a wide waveguide, and followed by a

third narrow section, which is the output port of the system. We assume the length along the z axis of each section to be much larger than the optical wavelength in the material, such that we can treat each section separately as a waveguide with translation invariance. Throughout our analysis, we will consider a single polarization, such that we can treat the fields as scalar, defined by their spatial profile along the x axis. Finally, we assume the geometry of all sections is identical along the y axis (out-of-plane), which is the case in many integrated-photonic platforms.

As an example, we launch a monochromatic field in the first mode of the input port, denoted $E_{\text{in}}(x)$ and illustrated in red in Fig. A.1(a). The wide MMI section supports multiple guided modes, as illustrated in blue in the figure. We can treat the field from the input port as an initial condition exciting the modes of the MMI section, and decompose the input field into a linear combination of guided MMI modes and radiating modes

$$E_{\text{in}}(x) = \sum_{m=0}^{M-1} c_m \phi_m(x) + f_{\text{rad}}, \tag{A.1}$$

where $\phi_m(x)$ is the m^{th} guided mode of the MMI wide section, and we assume there are M such guided modes. The term f_{rad} accounts for the fact that the MMI modes are not a complete basis, and some of the field at the MMI input couples to non-guided modes and is practically lost. The coefficients c_m are given by the overlap integral of the input field distribution and each one of the normalized modes

$$c_m = \int dx\ \phi_m^*(x) E_{\text{in}}(x), \qquad \int dx\ |\phi_m(x)|^2 = 1. \tag{A.2}$$

Next, we can write the field within the MMI at a distance z from the input, using the propagation constant β_m corresponding to each of the guided modes

$$E(x,z) = \sum_{m=0}^{M-1} c_m \phi_m(x) e^{i\beta_m z}. \tag{A.3}$$

The output of the MMI, illustrated in green in Fig. A.1 (a), can be calculated by an overlap integral of the fields at the end of the MMI section (after propagating a distance L) and

the guided modes of the output waveguide

$$a_n = \int dx\ \varphi_n^*(x) E(x, L), \qquad \int dx\ |\varphi_n(x)|^2 = 1, \tag{A.4}$$

where we have denoted $\varphi_n(x)$ as the n^{th} mode of the output waveguide. Finally, the total field at the output will be given by summing over all guided modes in the output waveguide

$$E_{\text{out}}(x) = \sum_{n=0}^{N-1} a_n \varphi_n(x). \tag{A.5}$$

We see that in this simple model of propagation, in order to compute the fields propagating and interfering in the MMI we need to find the mode profiles in each one of the sections of the device and their corresponding propagation constants. This can be done using commercial mode solvers, however, in the spirit of numerical estimations, we will describe methods that can be calculated using common programming languages, yielding fast results and good estimates, after which further optimization can be performed.

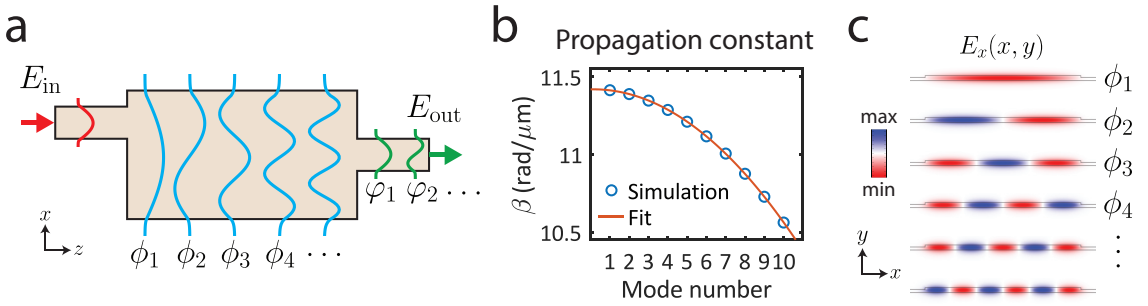

Figure A.1: **(a)** A schematic illustration of an MMI structure, showing a single mode at the input waveguide, a multi-mode region, and an output waveguide. **(b)** Simulated propagation constants of a 7 μm wide MMI device. The guiding region is 215 nm of silicon, while the 'cladding' is 130 nm thick, on a buried oxide layer. A quadratic function ($\propto m^2$) fits well to the simulated values. **(c)** Simulated mode profiles of the first six guided modes of the structure, corresponding to the propagation constants from panel (b).

Calculating guided modes as eigenstates of the geometry

We can describe the guided mode profiles in each translationally-invariant region of the device using the 1D Helmholtz equation [366]

$$\left[\frac{\partial^2}{\partial x^2} + n_{\text{eff}}^2(x)k_0^2\right]\phi_m(x) = \beta_m^2\phi_m(x), \tag{A.6}$$

where $n_{\text{eff}} = n_{\text{core}}$ in the guiding region, and $n_{\text{eff}} = n_{\text{clad}}$ outside of this region, in the effective 'cladding'. This one-dimensional 'effective index' model is useful for many photonics applications, where the full 3D geometry can be simplified and effectively projected into one dimension (not including the propagation axis). More details about the effective index method can be found in Appendix B.

Inspecting Eq. (A.6), we see that it is an eigenvalue problem, where we need to find the eigenvectors and eigenvalues of the operator $\hat{O} = \left[\partial_x^2 + n_{\text{eff}}^2(x)k_0^2\right]$. This can be done numerically by discretizing the x axis and writing the operator as a matrix. A numerical approximation of the second derivative can be written as

$$\frac{\partial^2}{\partial x^2}f(x) = \frac{f(x+h) - 2f(x) + f(x-h)}{h^2} + \mathcal{O}(h^2), \tag{A.7}$$

where h is the disretization step along the x axis, and we have used a central-difference scheme. We can use this to write the operator $\hat{O}$ in matrix form

$$\hat{O} = \frac{1}{h^2}\begin{pmatrix} -2 & 1 & & & \\ 1 & -2 & 1 & & \\ & & \ddots & & \\ & & 1 & -2 & 1 \\ & & & 1 & -2 \end{pmatrix} + k_0^2\begin{pmatrix} n_{\text{clad}}^2 & & & & \\ & \ddots & & & \\ & & n_{\text{core}}^2 & & \\ & & & \ddots & \\ & & & & n_{\text{clad}}^2 \end{pmatrix}, \tag{A.8}$$

where we assume all matrix elements that are not specified are zero. Now, we can numerically calculate the eigenvalues β_m and eigenfunctions $\psi_m(x)$ of the operator $\hat{O}$. Note that we will get more eigenmodes than the number of guided modes (as many as there are rows

or columns in the matrix), and we can use the criteria $\beta_m^2 \geq n_{\text{clad}}^2 k_0^2$ to find the indices (m) corresponding to guided mode. Since $\hat{O}$ is a Hermitian operator ($\hat{O}^\dagger = \hat{O}$), its eigenvalues β^2 will all be real numbers, as expected for lossless propagation constants, and the eigenfunctions $\phi_m(x)$ will be orthogonal. With these parameters in hand, we can now use Eqs. (A.1)–(A.4) to calculate the fields propagating in the structure.

Closed-form approximation

Alternatively, it is possible to approximate the modes and propagation constants analytically, which can make the calculation even faster, as well as give interesting observations into the interference of the fields as they propagate in the structure.

Assuming the modes are well-confined in the structures, the eigenmodes in the multimode region can be approximated as [367]

$$\phi_m(x) \approx \sqrt{\frac{2}{W_{\text{e}}}} \sin\left[\frac{\pi(m+1)}{W_{\text{e}}} x\right], \qquad m = 0, 1, 2 \ldots \tag{A.9}$$

in the region $x \in [0, W_{\text{e}}]$. Here, W_{e} is the effective width of the mode, given by [368]

$$W_{\text{e}} = W_{\text{core}} + \frac{\lambda}{\pi} \left(n_{\text{core}}^2 - n_{\text{clad}}^2\right)^{-1/2} \left(\frac{n_{\text{clad}}}{n_{\text{core}}}\right)^{2\sigma}, \tag{A.10}$$

where λ is the optical wavelength, and $\sigma = 1$ for TM modes and $\sigma = 0$ for TE modes.

We can identify the factor $\pi(m+1)/W_{\text{e}}$ in Eq. (A.9) as the transverse wave-vector component (k_x), such that in the guiding region we have

$$n_{\text{core}}^2 k_0^2 = k_z^2 + k_x^2 = \beta_m^2 + \left(\frac{\pi\,(m+1)}{W_{\text{e}}}\right)^2, \tag{A.11}$$

where $k_0 = 2\pi/\lambda$. Using the paraxial approximation ($n_{\text{core}}^2 k_0^2 \gg k_x^2$) we can write the propagation constants

$$\beta_m \approx \frac{2\pi}{\lambda} n_{\text{core}} - \left(\frac{m+1}{2W_{\text{e}}}\right)^2 \frac{\lambda\,\pi}{n_{\text{core}}}, \qquad m = 0, 1, 2 \ldots \tag{A.12}$$

showing a quadratic scaling of the propagation constants with mode number. This is demonstrated in Fig. A.1(b), showing a quadratic fit to simulated propagation constants of a device of the type used in this work (guiding silicon ridge on buried oxide). We can see excellent agreement between the quadratic approximation and the propagation constants obtained using a commercial mode solver. Simulations of the first six eigenmodes of the structure are presented in Fig. A.1(c), showing an approximate sine wave spatial distribution, as was expected from Eq. (A.9).

Directional coupler design

Next, we use the closed-form approximation we have derived to gain more insight into the field profiles in the MMI structure, and how they can be utilized for practical devices, following ideas presented in Refs. [367, 369, 370]. Specifically, we will show how multi-port directional couplers can be designed, splitting and combining optical fields in a controlled fashion.

First, we define the beat length as the inverse of the difference between the two closest

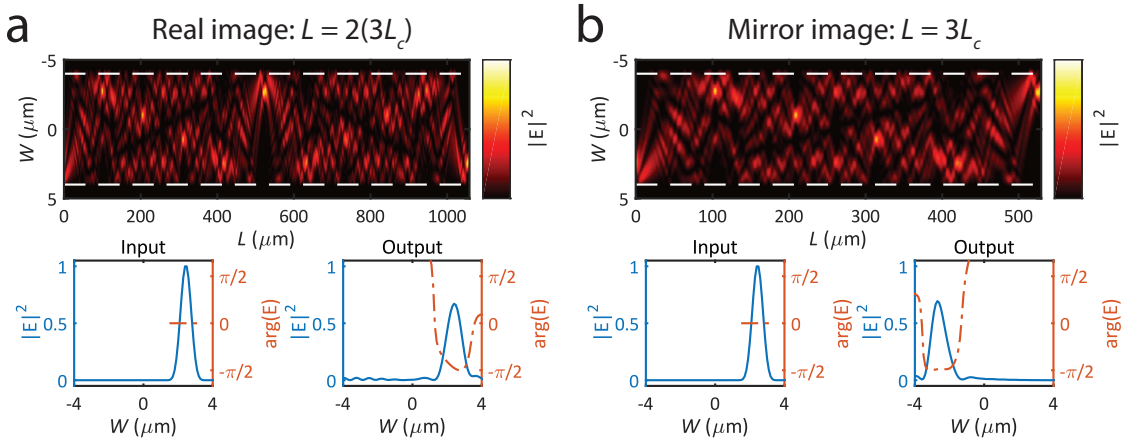

Figure A.2: **(a)** Simulation of an MMI of length $2(3L_C)$ resulting in a real image of the input at the output plane. **(b)** Simulation of an MMI of length $3L_C$ such that we have a mirror image of the input at the output plane. The MMI width in the calculations is 8 μm.

propagation constants ($m = 0, 1$)

$$L_c = \frac{\pi}{\beta_0 - \beta_1} = \frac{4}{3}\frac{W_e^2}{\lambda} n_{\text{core}}. \tag{A.13}$$

Next, we write the fields in the MMI (Eq. (A.3)) using this definition, and factor out the phase of the fundamental mode

$$E(x,z) = \sum_{m=0}^{M-1} c_m \phi_m(x) e^{i(\beta_m - \beta_0)z} = \sum_{m=0}^{M-1} c_m \phi_m(x) \exp\left[-i\pi \frac{m(m+2)}{3L_c} z\right]. \tag{A.14}$$

We separate this expression into two sums, grouping symmetric (even m) and anti-symmetric (odd m) spatial modes

$$\begin{aligned} E(x,z) = &\sum_{m=0,2,4\ldots}^{M-1} c_m \phi_m(x) \exp\left[-i\pi \frac{m(m+2)}{3L_c} z\right] \\ &+ \sum_{m=1,3,5\ldots}^{M-1} c_m \phi_m(x) \exp\left[-i\pi \frac{m(m+2)}{3L_c} z\right]. \end{aligned} \tag{A.15}$$

Using the fact that the term $m(m+2)$ is even for even m and odd for odd m, we see that after a propagation length of $z = 2p(3L_c)$ (for $p = 0, 1, 2\ldots$) both phase terms will give us a multiple integer of 2π, yielding a direct image of the input. When the propagation length is $z = (2p+1)(3L_c)$ the even phase terms will be a multiple of 2π, while the odd modes will have a phase of an odd multiple of π, yielding a mirrored image of the input, as demonstrated in Fig. A.2.

We can also define an intermediate-length $L_N^M = (M/N)3L_c$, where M and N are positive integers without a common denominator (not to confuse with the M we used earlier for the number of guided modes). It can be shown that N corresponds to the number of images, and M are possible device lengths (for a short device we can set $M = 1$). Following Ref. [369], the output can be written in the form

$$E(x,z) = \frac{1}{C} \sum_{q=0}^{N-1} E_{\text{in}}(x - x_q) e^{-i\varphi_q}, \tag{A.16}$$

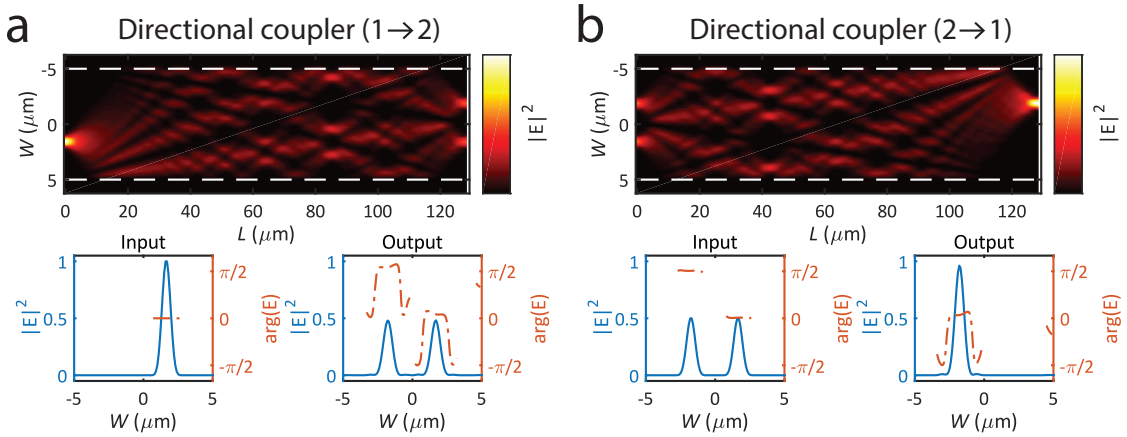

Figure A.3: MMI as a 50:50 directional coupler. **(a)** Input to one of the ports splits the power between the two output ports with a $\pi/2$ phase shift between them. **(b)** Input to both ports with the correct phase difference directs the light to a single output.

where the normalization, displacement and phase are given by

$$C = \exp\left[-i\beta_0 L_N^M\right] \sum_{q=0}^{N-1} \exp\left[i\pi \frac{x_q}{W_e} - i\varphi_q\right], \quad x_q = (2q-N)\frac{M}{N}W_e, \quad \varphi_q = q(N-q)\frac{M}{N}\pi. \tag{A.17}$$

This form reveals the occurrence of multiple copies of the input with different phases and positions as the field propagates in the device.

Using this insight, we can design an $N \times N$ port coupler by using an MMI of length $L = (1/N)3L_c$ and placing the input at an offset of $a = (W_e/2)(1 - 1/N)$ from the center

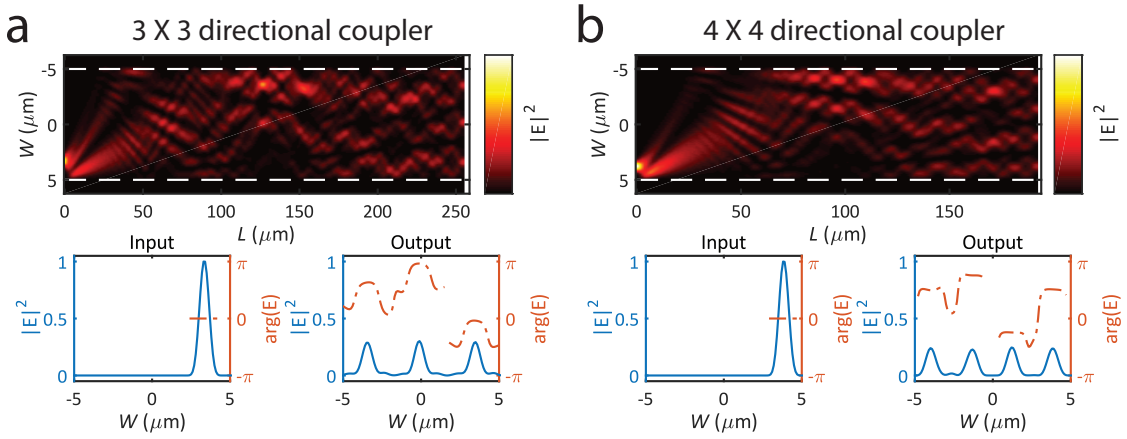

Figure A.4: An MMI used as a multi-port directional coupler with different numbers of ports. **(a)** 3×3 coupler. **(b)** 4×4 coupler.

[369]. The phases of the images can also be derived analytically under these assumptions, where we use the indices n and m for the input and output ports of the coupler [369]

$$\begin{aligned} m+n \text{ even:} \quad \theta_{n,m} &= -\left[\theta_0 + \pi + \frac{\pi}{4N}(m-n)(2N-m+n)\right], \\ m+n \text{ odd:} \quad \theta_{n,m} &= -\left[\theta_0 + \frac{\pi}{4N}(m+n-1)(2N-m-n+1)\right], \end{aligned} \tag{A.18}$$

and the constant phase term is defined as

$$\theta_0 = -\beta_0 L_N^1 - \frac{\pi}{N} - \frac{\pi}{4}(N-1). \tag{A.19}$$

Examples of directional couplers using this design strategy are simulated in Figs. A.3 and A.4.

The position of the input waveguide is an important degree of freedom that can yield different intensity and phase profiles at the output [368]. As an example, directional couplers with unequal power splitting can be designed. The power directed between ports, from input port n to output port m can be calculated [370]

$$\frac{P_m}{P_n} = \frac{4}{N}\cos^2\left[(N-m)\frac{\pi n}{2N} - \frac{\pi}{2}\right], \tag{A.20}$$

where the MMI length is L_N^1, the inputs are located at an offset $a = (W_e/2)(1-2n/N)$ from the MMI center, and we have assumed single-mode waveguides as input and output ports. Table A.1 gives some N and n values to achieve different power splitting ratios, and simulations of such couplers are presented in Fig. A.5.

Table A.1: Parameters for nonuniform power splitting in an MMI directional coupler [370], see Eq. (A.20).

N	n	Splitting ratio
2	1	100:0
3	1,2	100:0
4	1,3	85:15
4	2	100:0
5	1,2,3,4	72:28
6	1,5	62:33:5
6	2,4	50:50
6	3	33:33:33

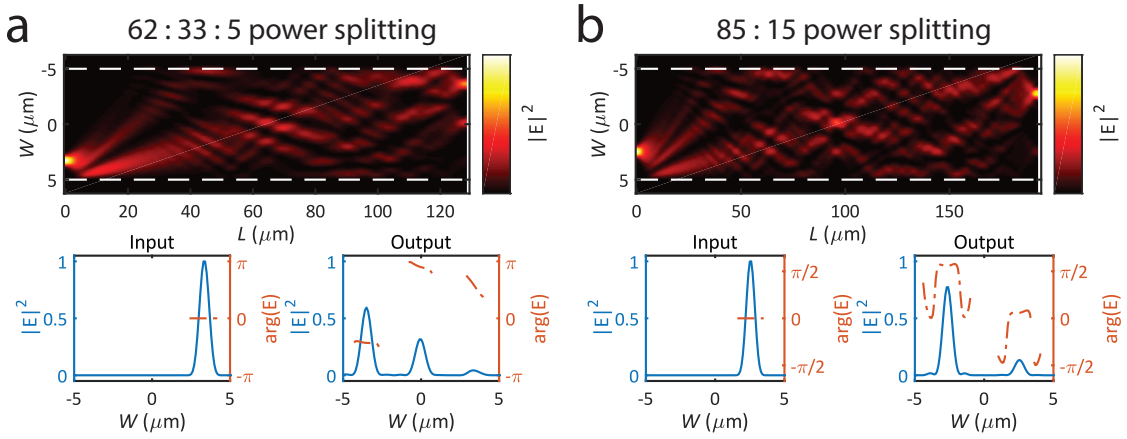

Figure A.5: MMI directional couplers with varying power-splitting ratios, following Eq. (A.20) and Table A.1. **(a)** 3×3 coupler with a 62:33:5 power splitting ratio, using $N = 6, n = 1$. **(b)** 2×2 coupler with a 85:15 power splitting ratio, using $N = 4, n = 1$.

Comparison with commercial software

We compare a calculation using the effective index method to solutions obtained using the FDTD solver *Lumerical*. We simulate a silicon ridge waveguide with a ridge height of 80 nm and a total silicon layer of 220 nm. The optical wavelength in the simulation is $\lambda = 1555$ nm and the discretization step is $h = 44.36$ nm. The effective indices obtained from Lumerical were $n_{\text{core}} = 2.81$ and $n_{\text{clad}} = 2.22$, which is a slightly larger index contrast compared with our numerical calculations.

Fig. A.6 presents the simulation of a 50:50 power splitter and compares it to a calculation using the approximation methods discussed in the previous sections. We see that the length of the simulated devices is slightly longer, due to the different refractive indexes. However, the results are similar and by adjusting the output plane position, the devices exhibit identical performance.

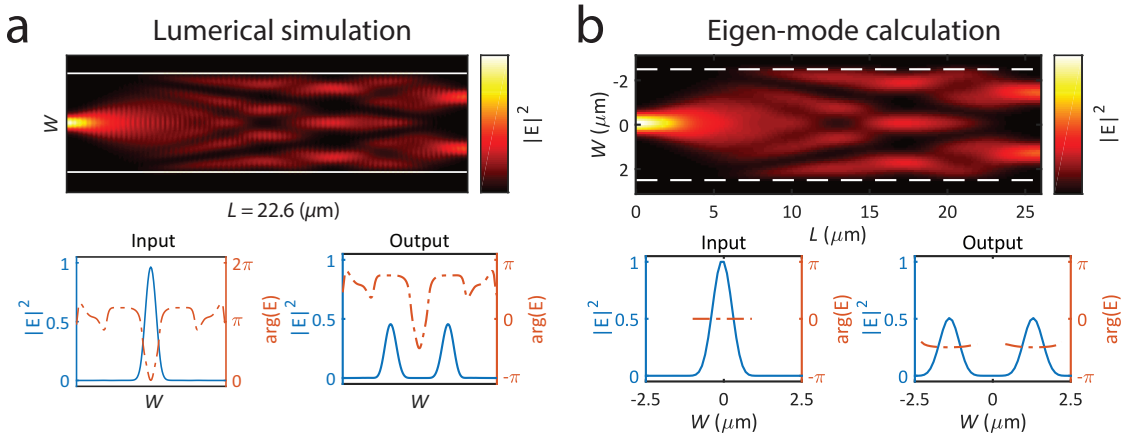

Figure A.6: **(a)** Simulation results of a 50:50 power splitter using a commercial FDTD solver (Lumerical). **(b)** Equivalent calculation using the methods described in this section. The discrepancy in the device length is a result of slightly different values for the effective indices used in the calculation.

Phase shifter

MMIs can be utilized to design additional integrated photonic components and devices. One example is an integrated phase shifter. Since the width of the MMI region is different than that of a narrower waveguide, the propagation constants of the modes it is guiding are different, as is seen in Eq. (A.12). Hence, we can couple into the MMI, and couple out at an image plane, where the field returns to the input spatial profile. The phase accumulated while propagating through the MMI will be different than that accumulated in a waveguide with no mode mixing. Fig. A.7(a) shows a 1 μm wide waveguide, demonstrating a $\pi/2$ phase shift over the propagation length. In contrast, an MMI section of the same length, seen in Fig. A.7(b) results in no phase shift, showing how the MMI effectively acts as a $\pi/2$ phase shifter.

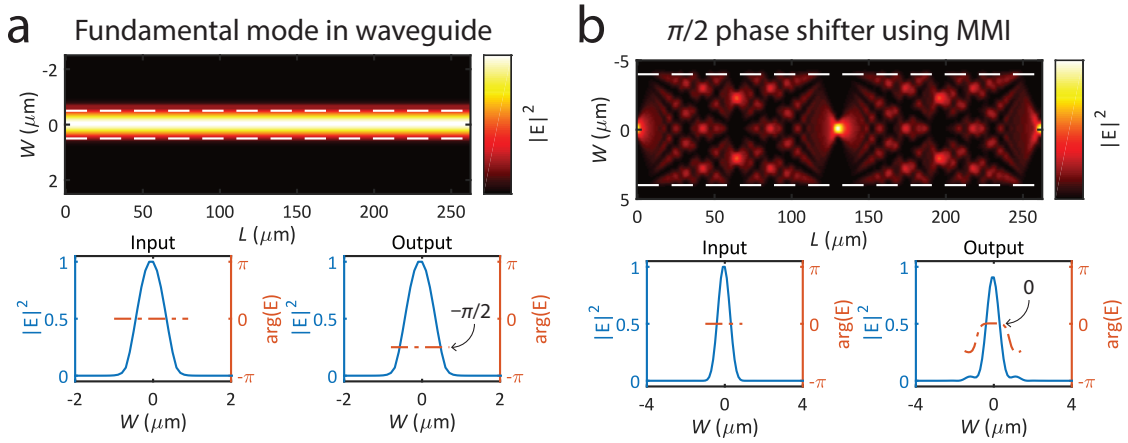

Figure A.7: **(a)** Propagation of the fundamental mode in a 1 μm wide waveguide. **(b)** Propagation through an MMI structure, demonstrating a $\pi/2$ relative phase shift.

Mode multiplexer

Another potential application of MMIs is in the design of spatial-mode multiplexers [371, 372]. As an example, we can use the MMI to design mode multiplexers with three ports: a common multi-mode waveguide on one side and two single-mode waveguides on the other. Ideally, the device directs each spatial mode to a separate port. When operating in the reverse direction, each port maps the field to a different spatial mode in the multimode waveguide. An example of such a design is shown in Fig. A.8, where we assume a multi-mode waveguide connected to the left side of the structure and two single-mode waveguides on the right. In panel (a), the fundamental mode is mapped to the upper output waveguide, and in panel (b) we see that the anti-symmetric mode is routed to the lower output. We can see that in the anti-symmetric case, there is residual cross-talk at the upper waveguide, however, the field profile in that region closely corresponds to an anti-symmetric mode, which could be spatially filtered.

We note that the examples shown here, and throughout this appendix, were calculated using the approximation methods to demonstrate design principles, and were not optimized further for performance.

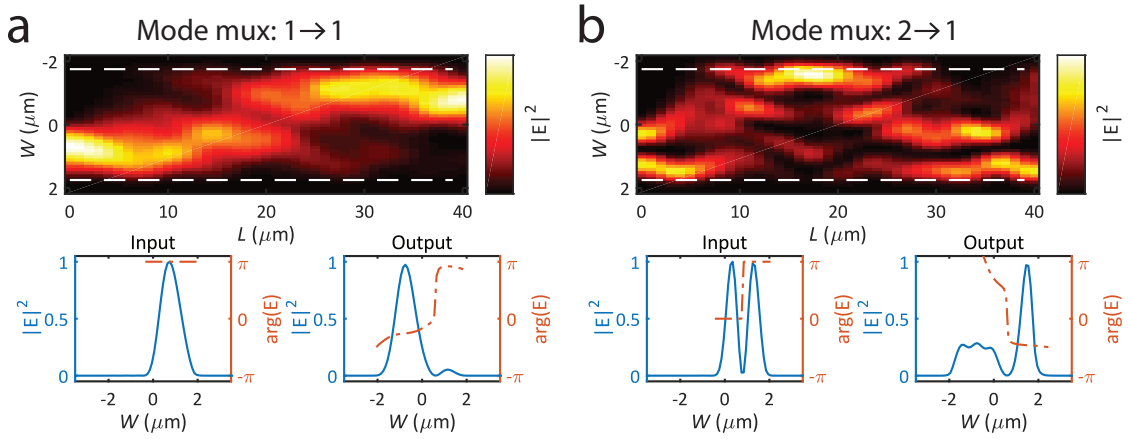

Figure A.8: Using an MMI as a spatial mode multiplexer. **(a)** Input from the fundamental mode of a 1.5 μm wide waveguide results in the optical power concentrated at the top of the device output plane. **(b)** Input from the first anti-symmetric mode of the input waveguide results in most of the optical power at the bottom of the output plane. By placing output waveguides at the proper locations, the two modes could be separated.

Appendix B

Effective index method

We present a short review of the effective index method for modeling 3D waveguides, as detailed in Refs. [373, 374]. This method enables us to simplify a three-dimensional waveguide structure, with translational invariance along the optical propagation axis, into an equivalent two-dimensional system. As an example, we will use the rib waveguide design of the type studied in this work. A waveguide section is illustrated in Fig. B.1(a), composed of a silicon guiding layer, in which a ridge has been defined for lateral optical confinement, over a silica layer. The propagation direction is defined along the z axis, where we assume translational invariance, and the cross-section is shown in Fig B.1(b).

We start by using the translation invariance property of the waveguide in the z direction

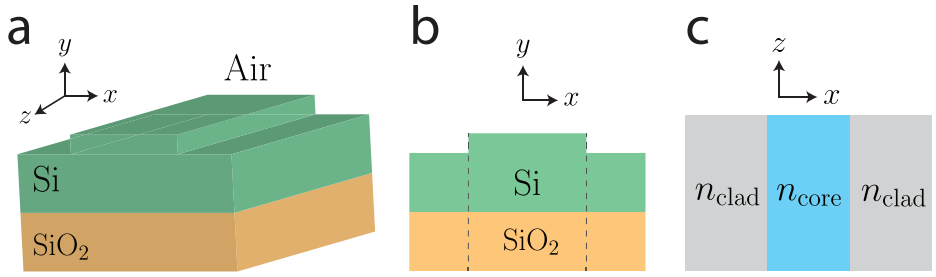

Figure B.1: The effective index method can be used to model a three-dimensional structure in two dimensions. **(a)** A three-dimensional illustration of a silicon (Si) on silica (SiO_2) ridge waveguide (not to scale). **(b)** Cross section of the ridge waveguide. **(c)** Using the effective index method, the waveguide can be reduced to a two-dimensional model with a guiding core and a cladding.

to write the field as

$$E(x,y,z,t) = \psi(x,y)e^{i\beta z}e^{-i\omega t}, \tag{B.1}$$

such that the Helmholtz equation now has the form [366]

$$\left[\frac{\partial^2}{\partial x^2} + \frac{\partial^2}{\partial y^2} + n^2(x,y)k_0^2 - \beta^2\right]\psi(x,y) = 0. \tag{B.2}$$

Here, $n(x,y)$ is the refractive index and $k_0 = \omega/c$, where ω and c are the optical frequency and the speed of light in vacuum, respectively. Assuming that $\psi(x,y)$ is separable [374], we can separate the function into x and y components $\psi(x,y) = \psi_x(x)\psi_y(y)$. Substituting this form into Eq. (B.2), we have

$$\frac{1}{\psi_x(x)}\frac{\partial^2}{\partial x^2}\psi_x(x) + \frac{1}{\psi_y(y)}\frac{\partial^2}{\partial y^2}\psi_y(y) + n^2(x,y)k_0^2 - \beta^2 = 0. \tag{B.3}$$

We can now define an effective index $n_{\text{eff}}(x)$, varying only along the x direction, which we add and subtract in Eq. (B.3). At this point, we can write separate equations for the x and y components

$$\begin{aligned}\left[\frac{\partial^2}{\partial y^2} + n^2(x,y)k_0^2 - n_{\text{eff}}^2(x)k_0^2\right]\psi_y(y) = 0,\\ \left[\frac{\partial^2}{\partial x^2} + n_{\text{eff}}^2(x)k_0^2 - \beta^2\right]\psi_x(x) = 0.\end{aligned} \tag{B.4}$$

Using these equations, we can find the effective index by solving a slab waveguide structure, infinite in the x direction, in each of the different regions of the waveguide. A detailed treatment of this method is found in [373].

For the silicon-on-silica ridge structure we are interested in —with a ridge height of 80 nm and a total silicon thickness of 215 nm— the effective indices obtained at an optical wavelength of $\lambda = 1550$ nm are $n_{\text{core}} = 2.76$ and $n_{\text{clad}} = 2.36$. Using these values, the problem can be simplified to the two-dimensional structure illustrated in Fig. B.1(c). We see that the effective index values obtained are between the refractive indices of bulk silicon ($n_{\text{Si}} = 3.48$) and silica ($n_{\text{SiO2}} = 1.44$).

Bibliography

[1] R. J. Strutt. Scattering of light by solid substances. *Proc. R. Soc. Lond. A*, 95(672):476–479, 1919.

[2] J. Larmor. The doppler effect in the molecular scattering of radiation. *Nature*, 103(2583):165–166, 1919.

[3] C. V. Raman. The doppler effect in the molecular scattering of radiation. *Nature*, 103(2583):165–165, May 1919.

[4] C. V. Raman. Optical observation of the thermal agitation of the atoms in crystals. *Nature*, 109(2724):42–42, 1922.

[5] L. Brillouin. Diffusion de la lumière et des rayons X par un corps transparent homogène. *Ann. Phys.*, 9:88–122, 1922.

[6] L. I. Mandelstam. Light scattering by inhomogeneous media. *Zh. Russ. Fiz-Khim. Ova*, 58:831, 1926.

[7] E. Gross. Change of wave-length of light due to elastic heat waves at scattering in liquids. *Nature*, 126(3171):201–202, 1930.

[8] E. Meyer and W. Ramm. Die Struktur der Rayleigh-Strahlung. *Phys. Zeitschr.*, 33:270, 1932.

[9] B. V. Raghavendra Rao. Examination of molecularly scattered light with a Fabry-Perot etalon. *Proc. Indian Acad. Sci. - Sect. A*, 1(5):261–268, Nov 1934.

[10] C. V. Raman and C. S. Venkateswaran. Optical observation of the Debye heat waves in crystals. *Nature*, 142(3588):250–250, 1938.

[11] P. Debye and F. Sears. On the scattering of light by supersonic waves. *Proc. Natl. Acad. Sci.*, 18(6):409, 1932.

[12] C. S. Venkateswaran. Interferometric studies of light scattering: Hypersonic velocities in liquids. *Proc. Indian Acad. Sci. - Sect. A*, 15(5):371–375, May 1942.

[13] A. Lawson and L. Meyer. Light scattering in liquid helium. *Phys. Rev.*, 93(2):259, 1954.

[14] R. S. Krishnan. Elastic constants of crystals from light scattering measurements. *Proc. Indian Acad. Sci. - Sect. A*, 41(3):91–97, Mar 1955.

[15] T. H. Maiman. Stimulated optical radiation in ruby. *Nature*, 187(4736):493–494, Aug 1960.

[16] R. Chiao, C. Townes, and B. Stoicheff. Stimulated Brillouin scattering and coherent generation of intense hypersonic waves. *Phys. Rev. Lett.*, 12(21):592, 1964.

[17] Y. R. Shen and N. Bloembergen. Theory of stimulated Brillouin and Raman scattering. *Phys. Rev.*, 137(6A):A1787, 1965.

[18] R. G. Brewer and K. E. Rieckhoff. Stimulated Brillouin scattering in liquids. *Phys. Rev. Lett.*, 13(11):334, 1964.

[19] E. Garmire and C. Townes. Stimulated Brillouin scattering in liquids. *Appl. Phys. Lett.*, 5(4):84–86, 1964.

[20] E. Hagenlocker and W. Rado. Stimulated Brillouin and Raman scattering in gases. *Appl. Phys. Lett.*, 7(9):236–238, 1965.

[21] E. Ippen and R. Stolen. Stimulated Brillouin scattering in optical fibers. *Appl. Phys. Lett.*, 21(11):539–541, 1972.

[22] R. G. Smith. Optical power handling capacity of low loss optical fibers as determined by stimulated Raman and Brillouin scattering. *Appl. Opt.*, 11(11):2489–2494, 1972.

[23] Y. Aoki, K. Tajima, and I. Mito. Input power limits of single-mode optical fibers due to stimulated Brillouin scattering in optical communication systems. *J. Lightwave Technol.*, 6(5):710–719, 1988.

[24] J. B. Coles, B.-P. Kuo, N. Alic, S. Moro, C.-S. Bres, J. C. Boggio, P. Andrekson, M. Karlsson, and S. Radic. Bandwidth-efficient phase modulation techniques for stimulated Brillouin scattering suppression in fiber optic parametric amplifiers. *Opt. Express*, 18(17):18138–18150, 2010.

[25] J. White, A. Vasilyev, J. Cahill, N. Satyan, O. Okusaga, G. Rakuljic, C. Mungan, and A. Yariv. Suppression of stimulated Brillouin scattering in optical fibers using a linearly chirped diode laser. *Opt. Express*, 20(14):15872–15881, 2012.

[26] K. Tei and S. Yamaguchi. Suppression of stimulated Brillouin scattering in optical fibers using a stepwise optical frequency pulse train. *Opt. Express*, 28(12):17793–17800, 2020.

[27] R. Shelby, M. Levenson, and P. Bayer. Guided acoustic-wave Brillouin scattering. *Phys. Rev. B*, 31(8):5244, 1985.

[28] P. S. J. Russell, D. Culverhouse, and F. Farahi. Experimental observation of forward stimulated Brillouin scattering in dual-mode single-core fibre. *Electron. Lett.*, 26(15):1195–1196, 1990.

[29] M. S. Kang, A. Nazarkin, A. Brenn, and P. S. J. Russell. Tightly trapped acoustic phonons in photonic crystal fibres as highly nonlinear artificial Raman oscillators. *Nat. Phys.*, 5(4):276, 2009.

[30] M. S. Kang, A. Brenn, and P. S. J. Russell. All-optical control of gigahertz acoustic resonances by forward stimulated interpolarization scattering in a photonic crystal fiber. *Phys. Rev. Lett.*, 105(15):153901, 2010.

[31] W. H. Renninger, R. O. Behunin, and P. T. Rakich. Guided-wave Brillouin scattering in air. *Optica*, 3(12):1316–1319, 2016.

[32] F. Yang, F. Gyger, and L. Thévenaz. Intense Brillouin amplification in gas using hollow-core waveguides. *Nat. Photonics*, 14(11):700–708, 2020.

[33] R. O. Behunin, Y.-H. Ou, and K. Kieu. Spontaneous forward Brillouin scattering in carbon disulfide. *Phys. Rev. A*, 99(6):063826, 2019.

[34] E. Garmire. Perspectives on stimulated Brillouin scattering. *New J. Phys.*, 19(1):011003, 2017.

[35] B. J. Eggleton, C. G. Poulton, P. T. Rakich, M. J. Steel, and G. Bahl. Brillouin integrated photonics. *Nat. Photonics*, 13(10):664–677, 2019.

[36] I. S. Grudinin, A. B. Matsko, and L. Maleki. Brillouin lasing with a CaF_2 whispering gallery mode resonator. *Phys. Rev. Lett.*, 102(4):043902, 2009.

[37] W. Loh, A. A. Green, F. N. Baynes, D. C. Cole, F. J. Quinlan, H. Lee, K. J. Vahala, S. B. Papp, and S. A. Diddams. Dual-microcavity narrow-linewidth Brillouin laser. *Optica*, 2(3):225–232, 2015.

[38] J. Li, H. Lee, and K. J. Vahala. Microwave synthesizer using an on-chip Brillouin oscillator. *Nat. Commun.*, 4:2097, 2013.

[39] G. Bahl, J. Zehnpfennig, M. Tomes, and T. Carmon. Stimulated optomechanical excitation of surface acoustic waves in a microdevice. *Nat. Commun.*, 2(1):1–6, 2011.

[40] C.-H. Dong, Z. Shen, C.-L. Zou, Y.-L. Zhang, W. Fu, and G.-C. Guo. Brillouin-scattering-induced transparency and non-reciprocal light storage. *Nat. Commun.*, 6(1):1–6, 2015.

[41] R. Pant, C. G. Poulton, D.-Y. Choi, H. Mcfarlane, S. Hile, E. Li, L. Thevenaz, B. Luther-Davies, S. J. Madden, and B. J. Eggleton. On-chip stimulated Brillouin scattering. *Opt. Express*, 19(9):8285–8290, 2011.

[42] F. Gyger, J. Liu, F. Yang, J. He, A. S. Raja, R. N. Wang, S. A. Bhave, T. J. Kippenberg, and L. Thévenaz. Observation of stimulated Brillouin scattering in silicon nitride integrated waveguides. *Phys. Rev. Lett.*, 124(1):013902, 2020.

[43] S. Gundavarapu, G. M. Brodnik, M. Puckett, T. Huffman, D. Bose, R. Behunin, J. Wu, T. Qiu, C. Pinho, N. Chauhan, et al. Sub-hertz fundamental linewidth photonic integrated Brillouin laser. *Nat. Photonics*, 13(1):60–67, 2019.

[44] H. Shin, W. Qiu, R. Jarecki, J. A. Cox, R. H. Olsson III, A. Starbuck, Z. Wang, and P. T. Rakich. Tailorable stimulated Brillouin scattering in nanoscale silicon waveguides. *Nat. Commun.*, 4:1944, 2013.

[45] B. Jalali and S. Fathpour. Silicon photonics. *J. Lightwave Technol.*, 24(12):4600–4615, December 2006.

[46] R. Soref. The past, present, and future of silicon photonics. *IEEE J. Sel. Top. Quantum Electron.*, 12(6):1678–1687, 2006.

[47] M. Hochberg and T. Baehr-Jones. Towards fabless silicon photonics. *Nat. photonics*, 4(8):492, 2010.

[48] D. Thomson, A. Zilkie, J. E. Bowers, T. Komljenovic, G. T. Reed, L. Vivien, D. Marris-Morini, E. Cassan, L. Virot, J.-M. Fédéli, et al. Roadmap on silicon photonics. *J. Opt.*, 18(7):073003, 2016.

[49] T. Baehr-Jones, M. Hochberg, G. Wang, R. Lawson, Y. Liao, P. A. Sullivan, L. Dalton, A.-Y. Jen, and A. Scherer. Optical modulation and detection in slotted silicon waveguides. *Opt. Express*, 13(14):5216–5226, 2005.

[50] S. Sun, R. Zhang, J. Peng, V. K. Narayana, H. Dalir, T. El-Ghazawi, and V. J. Sorger. MO detector (MOD): a dual-function optical modulator-detector for on-chip communication. *Opt. Express*, 26(7):8252–8259, 2018.

[51] H. Jayatilleka, K. Murray, M. Á. Guillén-Torres, M. Caverley, R. Hu, N. A. Jaeger, L. Chrostowski, and S. Shekhar. Wavelength tuning and stabilization of microring-based filters using silicon in-resonator photoconductive heaters. *Opt. Express*, 23(19):25084–25097, 2015.

[52] D. Onural, H. Gevorgyan, B. Zhang, A. Khilo, and M. A. Popović. Ultra-high Q resonators and sub-GHz bandwidth second order filters in an SOI foundry platform. In *Optical Fiber Communication Conference*, pages W1A–4. Optical Society of America, 2020.

[53] C. Wang, M. Zhang, X. Chen, M. Bertrand, A. Shams-Ansari, S. Chandrasekhar, P. Winzer, and M. Lončar. Integrated lithium niobate electro-optic modulators operating at CMOS-compatible voltages. *Nature*, 562(7725):101, 2018.

[54] M. A. Foster, A. C. Turner, J. E. Sharping, B. S. Schmidt, M. Lipson, and A. L. Gaeta. Broad-band optical parametric gain on a silicon photonic chip. *Nature*, 441(7096):960, 2006.

[55] O. Boyraz and B. Jalali. Demonstration of a silicon Raman laser. *Opt. Express*, 12(21):5269–5273, 2004.

[56] N. T. Otterstrom, R. O. Behunin, E. A. Kittlaus, Z. Wang, and P. T. Rakich. A silicon Brillouin laser. *Science*, 360(6393):1113–1116, 2018.

[57] N. Izhaky, M. T. Morse, S. Koehl, O. Cohen, D. Rubin, A. Barkai, G. Sarid, R. Cohen, and M. J. Paniccia. Development of CMOS-compatible integrated silicon photonics devices. *IEEE J. Sel. Top. Quantum Electron.*, 12(6):1688–1698, 2006.

[58] C. Doerr, L. Chen, D. Vermeulen, T. Nielsen, S. Azemati, S. Stulz, G. McBrien, X.-M. Xu, B. Mikkelsen, M. Givehchi, et al. Single-chip silicon photonics 100-Gb/s

coherent transceiver. In *Optical Fiber Communication Conference*, pages Th5C–1. Optical Society of America, 2014.

[59] X. Chen, M. M. Milosevic, S. Stanković, S. Reynolds, T. D. Bucio, K. Li, D. J. Thomson, F. Gardes, and G. T. Reed. The emergence of silicon photonics as a flexible technology platform. *Proc. IEEE*, 106(12):2101–2116, 2018.

[60] H. Fukuda, K. Yamada, T. Shoji, M. Takahashi, T. Tsuchizawa, T. Watanabe, J.-i. Takahashi, and S.-i. Itabashi. Four-wave mixing in silicon wire waveguides. *Opt. Express*, 13(12):4629–4637, 2005.

[61] R. Claps, D. Dimitropoulos, Y. Han, and B. Jalali. Observation of Raman emission in silicon waveguides at 1.54 μm. *Opt. Express*, 10(22):1305–1313, 2002.

[62] J. Leuthold, C. Koos, and W. Freude. Nonlinear silicon photonics. *Nat. Photonics*, 4(8):535–544, 2010.

[63] R. Van Laer, B. Kuyken, D. Van Thourhout, and R. Baets. Interaction between light and highly confined hypersound in a silicon photonic nanowire. *Nat. Photonics*, 9(3):199, 2015.

[64] E. A. Kittlaus, H. Shin, and P. T. Rakich. Large Brillouin amplification in silicon. *Nat. Photonics*, 10(7):463, 2016.

[65] E. A. Kittlaus, N. T. Otterstrom, and P. T. Rakich. On-chip inter-modal Brillouin scattering. *Nat. Commun.*, 8:15819, 2017.

[66] N. T. Otterstrom, E. A. Kittlaus, S. Gertler, R. O. Behunin, A. L. Lentine, and P. T. Rakich. Resonantly enhanced nonreciprocal silicon Brillouin amplifier. *Optica*, 6(9):1117–1123, 2019.

[67] A. Choudhary, Y. Liu, B. Morrison, K. Vu, D.-Y. Choi, P. Ma, S. Madden, D. Marpaung, and B. J. Eggleton. High-resolution, on-chip RF photonic signal processor using Brillouin gain shaping and RF interference. *Sci. Rep.*, 7(1):5932, 2017.

[68] Z. Zhu, D. J. Gauthier, and R. W. Boyd. Stored light in an optical fiber via stimulated Brillouin scattering. *Science*, 318(5857):1748–1750, 2007.

[69] A. Zadok, A. Eyal, and M. Tur. Gigahertz-wide optically reconfigurable filters using stimulated Brillouin scattering. *J. Light. Technol.*, 25(8):2168–2174, 2007.

[70] X. Bao and L. Chen. Recent progress in distributed fiber optic sensors. *Sensors*, 12(7):8601–8639, 2012.

[71] X. Huang and S. Fan. Complete all-optical silica fiber isolator via stimulated Brillouin scattering. *J. Lightwave Technol.*, 29(15):2267–2275, 2011.

[72] Z. Bai, H. Yuan, Z. Liu, P. Xu, Q. Gao, R. J. Williams, O. Kitzler, R. P. Mildren, Y. Wang, and Z. Lu. Stimulated Brillouin scattering materials, experimental design and applications: A review. *Opt. Mater.*, 75:626–645, 2018.

[73] W. Hasi, Z. Lu, S. J. Liu, Q. Li, G. Yin, and W. He. Generation of flat-top waveform in the time domain based on stimulated Brillouin scattering. *Appl. Phys. B*, 90(3):503–506, 2008.

[74] D. T. Hon. Pulse compression by stimulated Brillouin scattering. *Opt. Lett.*, 5(12):516–518, 1980.

[75] D. Neshev, I. Velchev, W. Majewski, W. Hogervorst, and W. Ubachs. SBS pulse compression to 200 ps in a compact single-cell setup. *Appl. Phys. B*, 68(4), 1999.

[76] Z. Bai, Y. Wang, Z. Lu, L. Jiang, H. Yuan, and Z. Liu. Demonstration of an ultraviolet stimulated Brillouin scattering pulse compressed hundred picosecond laser in LiB_3O_5 crystals. *J. Opt.*, 19(8):085502, 2017.

[77] Z. Lu, W. Hasi, H. Gong, Q. Li, and W. He. Generation of flat-top waveform by double optical limiting based on stimulated Brillouin scattering. *Opt. Express*, 14(12):5497–5501, 2006.

[78] B. C. Rodgers, T. H. Russell, and W. B. Roh. Laser beam combining and cleanup by stimulated Brillouin scattering in a multimode optical fiber. *Opt. Lett.*, 24(16):1124–1126, 1999.

[79] Y. Wang, Z. Lu, S. Wang, Z. Zheng, W. He, and D. Lin. Investigation on efficiency of non-collinear serial laser beam combination based on Brillouin amplification. *Laser Part. Beams*, 27(4):651, 2009.

[80] L. Lombard, A. Brignon, J.-P. Huignard, E. Lallier, and P. Georges. Beam cleanup in a self-aligned gradient-index Brillouin cavity for high-power multimode fiber amplifiers. *Opt. Lett.*, 31(2):158–160, 2006.

[81] B. Steinhausser, A. Brignon, E. Lallier, J.-P. Huignard, and P. Georges. High energy, single-mode, narrow-linewidth fiber laser source using stimulated Brillouin scattering beam cleanup. *Opt. Express*, 15(10):6464–6469, 2007.

[82] Q. Gao, Z. Lu, C. Zhu, and J. Zhang. Mechanism of beam cleanup by stimulated Brillouin scattering in multimode fibers. *Appl. Phys. Express*, 8(5):052501, 2015.

[83] A. Bergman, R. Duggan, K. Sharma, M. Tur, A. Zadok, and A. Alù. Observation of anti-parity-time-symmetry, phase transitions and exceptional points in an optical fibre. *Nat. Commun.*, 12(1):1–9, 2021.

[84] I. Carr and D. Hanna. Performance of a Nd: YAG oscillator/ampflifier with phase-conjugation via stimulated Brillouin scattering. *Appl. Phys. B*, 36(2):83–92, 1985.

[85] A. Brignon and J.-P. Huignard. *Phase conjugate laser optics*. Wiley Online Library, 2004.

[86] D. A. Rockwell. A review of phase-conjugate solid-state lasers. *IEEE J. Quantum Electron.*, 24(6):1124–1140, 1988.

[87] D. Culverhouse, F. Farahi, C. Pannell, and D. Jackson. Potential of stimulated Brillouin scattering as sensing mechanism for distributed temperature sensors. *Electron. Lett.*, 25(14):913–915, 1989.

[88] X. Bao, M. DeMerchant, A. Brown, and T. Bremner. Tensile and compressive strain measurement in the lab and field with the distributed Brillouin scattering sensor. *J. Lightwave Technol.*, 19(11):1698, 2001.

[89] A. Motil, A. Bergman, and M. Tur. State of the art of Brillouin fiber-optic distributed sensing. *Opt. Laser Technol.*, 78:81–103, 2016.

[90] M. N. Alahbabi, Y. T. Cho, and T. P. Newson. 150-km-range distributed temperature sensor based on coherent detection of spontaneous Brillouin backscatter and in-line Raman amplification. *JOSA B*, 22(6):1321–1324, 2005.

[91] A. Zadok, Y. Antman, N. Primerov, A. Denisov, J. Sancho, and L. Thevenaz. Random-access distributed fiber sensing. *Laser Photonics Rev.*, 6(5):L1–L5, 2012.

[92] R. Cohen, Y. London, Y. Antman, and A. Zadok. Brillouin optical correlation domain analysis with 4 millimeter resolution based on amplified spontaneous emission. *Opt. Express*, 22(10):12070–12078, 2014.

[93] D. Elooz, Y. Antman, N. Levanon, and A. Zadok. High-resolution long-reach distributed Brillouin sensing based on combined time-domain and correlation-domain analysis. *Opt. Express*, 22(6):6453–6463, 2014.

[94] Y. Antman, A. Clain, Y. London, and A. Zadok. Optomechanical sensing of liquids outside standard fibers using forward stimulated Brillouin scattering. *Optica*, 3(5):510–516, 2016.

[95] H. H. Diamandi, Y. London, G. Bashan, and A. Zadok. Distributed opto-mechanical analysis of liquids outside standard fibers coated with polyimide. *APL Photonics*, 4(1):016105, 2019.

[96] D. M. Chow, Z. Yang, M. A. Soto, and L. Thévenaz. Distributed forward Brillouin sensor based on local light phase recovery. *Nat. Commun.*, 9(1):2990, 2018.

[97] G. Bashan, Y. London, H. H. Diamandi, and A. Zadok. Distributed cladding mode fiber-optic sensor. *Optica*, 7(1):85–92, 2020.

[98] A. Scott and K. Ridley. A review of Brillouin-enhanced four-wave mixing. *IEEE J. Quantum Electron.*, 25(3):438–459, 1989.

[99] A. Bergman and M. Tur. Brillouin dynamic gratings—a practical form of Brillouin enhanced four wave mixing in waveguides: The first decade and beyond. *Sensors*, 18(9):2863, 2018.

[100] J. Sancho, N. Primerov, S. Chin, Y. Antman, A. Zadok, S. Sales, and L. Thévenaz. Tunable and reconfigurable multi-tap microwave photonic filter based on dynamic Brillouin gratings in fibers. *Opt. Express*, 20(6):6157–6162, 2012.

[101] J.-J. Guo, M. Li, Y. Deng, N. Huang, J. Liu, and N. Zhu. Multichannel optical filters with an ultranarrow bandwidth based on sampled Brillouin dynamic gratings. *Opt. Express*, 22(4):4290–4300, 2014.

[102] Y. Dong, T. Jiang, L. Teng, H. Zhang, L. Chen, X. Bao, and Z. Lu. Sub-MHz ultrahigh-resolution optical spectrometry based on Brillouin dynamic gratings. *Opt. Lett.*, 39(10):2967–2970, 2014.

[103] K. Y. Song, S. Chin, N. Primerov, and L. Thévenaz. Time-domain distributed fiber sensor with 1 cm spatial resolution based on Brillouin dynamic grating. *J. Lightwave Technol.*, 28(14):2062–2067, 2010.

[104] A. Bergman, L. Yaron, T. Langer, and M. Tur. Dynamic and distributed slope-assisted fiber strain sensing based on optical time-domain analysis of Brillouin dynamic gratings. *J. Lightwave Technol.*, 33(12):2611–2616, 2015.

[105] J. R. Ackerman and P. S. Lebow. Optimization of the field of view of a Brillouin-enhanced four-wave-mixing phase conjugator. *Opt. Lett.*, 19(23):2015–2017, 1994.

[106] M. W. Bowers, R. W. Boyd, and A. K. Hankla. Brillouin-enhanced four-wave-mixing vector phase-conjugate mirror with beam-combining capability. *Opt. Lett.*, 22(6):360–362, 1997.

[107] H. G. Winful. Chirped Brillouin dynamic gratings for storing and compressing light. *Opt. Express*, 21(8):10039–10047, 2013.

[108] M. Santagiustina, S. Chin, N. Primerov, L. Ursini, and L. Thévenaz. All-optical signal processing using dynamic Brillouin gratings. *Sci. Rep.*, 3(1):1–6, 2013.

[109] R. Pant, E. Li, C. G. Poulton, D.-Y. Choi, S. Madden, B. Luther-Davies, and B. J. Eggleton. Observation of Brillouin dynamic grating in a photonic chip. *Opt. Lett.*, 38(3):305–307, 2013.

[110] R. Fedosejevs, I. Tomov, D. McKen, and A. Offenberger. Experimental study of an SF_6 Brillouin amplifier pumped by KrF laser radiation. *Appl. Phys. Lett.*, 45(4):340–342, 1984.

[111] A. A. Offenberger, D. C. Thompson, R. Fedosejevs, B. Harwood, J. Santiago, and H. Manjunath. Experimental and modeling studies of a Brillouin amplifier. *IEEE J. Quantum Electron.*, 29(1):207–216, 1993.

[112] N. Olsson and J. Van der Ziel. Cancellation of fiber loss by semiconductor laser pumped Brillouin amplification at 1.5 μm. *Appl. Phys. Lett.*, 48(20):1329–1330, 1986.

[113] N. Olsson and J. Van Der Ziel. Fibre Brillouin amplifier with electronically controlled bandwidth. *Electron. Lett.*, 22(9):488–490, 1986.

[114] O. Terra, G. Grosche, and H. Schnatz. Brillouin amplification in phase coherent transfer of optical frequencies over 480 km fiber. *Opt. Express*, 18(15):16102–16111, 2010.

[115] Y. Souidi, F. Taleb, J. Zheng, M. W. Lee, F. Du Burck, and V. Roncin. Low-noise and high-gain Brillouin optical amplifier for narrowband active optical filtering based on a pump-to-signal optoelectronic tracking. *Appl. Opt.*, 55(2):248–253, 2016.

[116] S. Raupach, A. Koczwara, and G. Grosche. Optical frequency transfer via a 660 km underground fiber link using a remote Brillouin amplifier. *Opt. Express*, 22(22):26537–26547, 2014.

[117] S. Droste, F. Ozimek, T. Udem, K. Predehl, T. Hänsch, H. Schnatz, G. Grosche, and R. Holzwarth. Optical-frequency transfer over a single-span 1840 km fiber link. *Phys. Rev. Lett.*, 111(11):110801, 2013.

[118] K. Hill, B. Kawasaki, and D. Johnson. CW Brillouin laser. *Appl. Phys. Lett.*, 28(10):608–609, 1976.

[119] L. Stokes, M. Chodorow, and H. Shaw. All-fiber stimulated Brillouin ring laser with submilliwatt pump threshold. *Opt. Lett.*, 7(10):509–511, 1982.

[120] S. Smith, F. Zarinetchi, and S. Ezekiel. Narrow-linewidth stimulated Brillouin fiber laser and applications. *Opt. Lett.*, 16(6):393–395, 1991.

[121] Z. Wu, L. Zhan, Q. Shen, J. Liu, X. Hu, and P. Xiao. Ultrafine optical-frequency tunable Brillouin fiber laser based on fiber strain. *Opt. Lett.*, 36(19):3837–3839, 2011.

[122] J. Li, H. Lee, T. Chen, and K. J. Vahala. Characterization of a high coherence, Brillouin microcavity laser on silicon. *Opt. Express*, 20(18):20170–20180, 2012.

[123] D.-G. Kim, S. Han, J. Hwang, I. H. Do, D. Jeong, J.-H. Lim, Y.-H. Lee, M. Choi, Y.-H. Lee, D.-Y. Choi, et al. Universal light-guiding geometry for on-chip resonators having extremely high Q-factor. *Nat. Commun.*, 11(1):1–7, 2020.

[124] F. Zarinetchi, S. Smith, and S. Ezekiel. Stimulated Brillouin fiber-optic laser gyroscope. *Opt. Lett.*, 16(4):229–231, 1991.

[125] Y. Tanaka, S. Yamasaki, and K. Hotate. Brillouin fiber-optic gyro with directional sensitivity. *IEEE Photon. Technol. Lett.*, 8(10):1367–1369, 1996.

[126] J. Li, M.-G. Suh, and K. Vahala. Microresonator Brillouin gyroscope. *Optica*, 4(3):346–348, 2017.

[127] Y.-H. Lai, M.-G. Suh, Y.-K. Lu, B. Shen, Q.-F. Yang, H. Wang, J. Li, S. H. Lee, K. Y. Yang, and K. Vahala. Earth rotation measured by a chip-scale ring laser gyroscope. *Nat. Photonics*, 14(6):345–349, 2020.

[128] Y. Okawachi, M. S. Bigelow, J. E. Sharping, Z. Zhu, A. Schweinsberg, D. J. Gauthier, R. W. Boyd, and A. L. Gaeta. Tunable all-optical delays via Brillouin slow light in an optical fiber. *Phys. Rev. Lett.*, 94(15):153902, 2005.

[129] A. Zadok, A. Eyal, and M. Tur. Stimulated Brillouin scattering slow light in optical fibers. *Appl. Opt.*, 50(25):E38–E49, 2011.

[130] K. Y. Song, K. S. Abedin, K. Hotate, M. G. Herráez, and L. Thévenaz. Highly efficient Brillouin slow and fast light using As_2Se_3 chalcogenide fiber. *Opt. Express*, 14(13):5860–5865, 2006.

[131] C. J. Misas, P. Petropoulos, and D. J. Richardson. Slowing of pulses to c/10 with subwatt power levels and low latency using Brillouin amplification in a bismuth-oxide optical fiber. *J. Lightwave Technol.*, 25(1):216–221, 2007.

[132] J. Liu, T.-H. Cheng, Y.-K. Yeo, Y. Wang, L. Xue, W. Rong, L. Zhou, G. Xiao, D. Wang, and X. Yu. Stimulate Brillouin scattering based broadband tunable slow-light conversion in a highly nonlinear photonic crystal fiber. *J. Lightwave Technol.*, 27(10):1279–1285, 2009.

[133] R. Pant, A. Byrnes, C. G. Poulton, E. Li, D.-Y. Choi, S. Madden, B. Luther-Davies, and B. J. Eggleton. Photonic-chip-based tunable slow and fast light via stimulated Brillouin scattering. *Opt. Lett.*, 37(5):969–971, 2012.

[134] M. Merklein, B. Stiller, K. Vu, S. J. Madden, and B. J. Eggleton. A chip-integrated coherent photonic-phononic memory. *Nat. Commun.*, 8(1):1–7, 2017.

[135] M. Merklein, B. Stiller, and B. Eggleton. Brillouin-based light storage and delay techniques. *J. Opt.*, 20(8):083003, 2018.

[136] I. A. Williamson, M. Minkov, A. Dutt, J. Wang, A. Y. Song, and S. Fan. Integrated nonreciprocal photonic devices with dynamic modulation. *Proc. IEEE*, 108(10):1759–1784, 2020.

[137] M. S. Kang, A. Butsch, and P. S. J. Russell. Reconfigurable light-driven opto-acoustic isolators in photonic crystal fibre. *Nat. Photonics*, 5(9):549, 2011.

[138] C. G. Poulton, R. Pant, A. Byrnes, S. Fan, M. Steel, and B. J. Eggleton. Design for broadband on-chip isolator using stimulated Brillouin scattering in dispersion-engineered chalcogenide waveguides. *Opt. Express*, 20(19):21235–21246, 2012.

[139] E. A. Kittlaus, N. T. Otterstrom, P. Kharel, S. Gertler, and P. T. Rakich. Non-reciprocal interband Brillouin modulation. *Nat. Photonics*, 12(10):613–619, 2018.

[140] R. Aigner. SAW and BAW technologies for RF filter applications: A review of the relative strengths and weaknesses. In *IEEE Int. Ultrason.*, pages 582–589. IEEE, 2008.

[141] Y. Stern, K. Zhong, T. Schneider, R. Zhang, Y. Ben-Ezra, M. Tur, and A. Zadok. Tunable sharp and highly selective microwave-photonic band-pass filters based on stimulated Brillouin scattering. *Photonics Res.*, 2(4):B18–B25, 2014.

[142] B. Morrison, D. Marpaung, R. Pant, E. Li, D.-Y. Choi, S. Madden, B. Luther-Davies, and B. J. Eggleton. Tunable microwave photonic notch filter using on-chip stimulated Brillouin scattering. *Opt. Commun.*, 313:85–89, 2014.

[143] A. Mahendra, Y. Liu, E. Magi, A. Choudhary, D. Marpaung, and B. J. Eggleton. High link performance of Brillouin-loss based microwave bandpass photonic filters. *OSA Continuum*, 1(4):1287–1297, 2018.

[144] Y. Xie, A. Choudhary, Y. Liu, D. Marpaung, K. Vu, P. Ma, D.-Y. Choi, S. Madden, and B. Eggleton. System-level performance of chip-based Brillouin microwave photonic bandpass filters. *J. Lightwave Technol.*, 2019.

[145] D. Culverhouse, K. Kalli, and D. Jackson. Stimulated Brillouin scattering ring resonator laser for SBS gain studies and microwave generation. *Electron. Lett.*, 27(22):2033–2035, 1991.

[146] T. Schneider, M. Junker, and K.-U. Lauterbach. Theoretical and experimental investigation of Brillouin scattering for the generation of millimeter waves. *JOSA B*, 23(6):1012–1019, 2006.

[147] S. Preussler, N. Wenzel, R.-P. Braun, N. Owschimikow, C. Vogel, A. Deninger, A. Zadok, U. Woggon, and T. Schneider. Generation of ultra-narrow, stable and tunable millimeter-and terahertz-waves with very low phase noise. *Opt. Express*, 21(20):23950–23962, 2013.

[148] M. Merklein, B. Stiller, I. V. Kabakova, U. S. Mutugala, K. Vu, S. J. Madden, B. J. Eggleton, and R. Slavík. Widely tunable, low phase noise microwave source based on a photonic chip. *Opt. Lett.*, 41(20):4633–4636, 2016.

[149] R. O. Behunin, N. T. Otterstrom, P. T. Rakich, S. Gundavarapu, and D. J. Blumenthal. Fundamental noise dynamics in cascaded-order Brillouin lasers. *Phys. Rev. A*, 98(2):023832, 2018.

[150] L. Zhan, J. Ji, J. Xia, S. Luo, and Y. Xia. 160-line multiwavelength generation of linear-cavity self-seeded Brillouin-erbium fiber laser. *Opt. Express*, 14(22):10233–10238, 2006.

[151] D. Lim, H. Lee, K. Kim, S. Kang, J. Ahn, and M.-Y. Jeon. Generation of multiorder stokes and anti-stokes lines in a Brillouin erbium-fiber laser with a sagnac loop mirror. *Opt. Lett.*, 23(21):1671–1673, 1998.

[152] I. Aryanfar, D. Marpaung, A. Choudhary, Y. Liu, K. Vu, D.-Y. Choi, P. Ma, S. Madden, and B. J. Eggleton. Chip-based Brillouin radio frequency photonic phase shifter and wideband time delay. *Opt. Lett.*, 42(7):1313–1316, 2017.

[153] L. McKay, M. Merklein, A. Choudhary, Y. Liu, M. Jenkins, C. Middleton, A. Cramer, A. Chilton, J. Devenport, K. Vu, et al. Broadband Brillouin phase shifter utilizing RF interference: Experimental demonstration and theoretical analysis. *J. Lightwave Technol.*, 38(14):3624–3636, 2020.

[154] S. Gertler, P. Kharel, E. A. Kittlaus, N. T. Otterstrom, and P. T. Rakich. Shaping nonlinear optical response using nonlocal forward Brillouin interactions. *New J. Phys.*, 22(4):043017, 2020.

[155] S. Gertler, E. A. Kittlaus, N. T. Otterstrom, P. Kharel, and P. T. Rakich. Microwave filtering using forward Brillouin scattering in photonic-phononic emit-receive devices. *J. Lightwave Technol.*, 38(19):5248–5261, 2020.

[156] S. Gertler, E. A. Kittlaus, N. T. Otterstrom, and P. T. Rakich. Tunable microwave-photonic filtering with high out-of-band rejection in silicon. *APL Photonics*, 5(9):096103, 2020.

[157] R. W. Boyd. *Nonlinear optics*. Academic Press, 2003.

[158] A. Yariv. *Quantum electronics*. Wiley, 1989.

[159] C. Wolff, M. J. Steel, B. J. Eggleton, and C. G. Poulton. Stimulated Brillouin scattering in integrated photonic waveguides: Forces, scattering mechanisms, and coupled-mode analysis. *Phys. Rev. A*, 92(1):013836, 2015.

[160] D. Royer and E. Dieulesaint. *Elastic waves in solids II: generation, acousto-optic interaction, applications*. Springer Science & Business Media, 1999.

[161] P. T. Rakich, C. Reinke, R. Camacho, P. Davids, and Z. Wang. Giant enhancement of stimulated Brillouin scattering in the subwavelength limit. *Phys. Rev. X*, 2(1):011008, 2012.

[162] P. T. Rakich, P. Davids, and Z. Wang. Tailoring optical forces in waveguides through radiation pressure and electrostrictive forces. *Opt. Express*, 18(14):14439–14453, 2010.

[163] W. Qiu, P. T. Rakich, H. Shin, H. Dong, M. Soljačić, and Z. Wang. Stimulated Brillouin scattering in nanoscale silicon step-index waveguides: a general framework of selection rules and calculating SBS gain. *Opt. Express*, 21(25):31402–31419, 2013.

[164] P. Milonni. *An Introduction to Quantum Optics and Quantum Fluctuations*. Oxford Graduate Texts. OUP Oxford, 2019.

[165] J. P. Gordon. Radiation forces and momenta in dielectric media. *Phys. Rev. A*, 8(1):14, 1973.

[166] A. Feldman. Relations between electrostriction and the stress-optical effect. *Phys. Rev. B*, 11(12):5112, 1975.

[167] V. Laude and J.-C. Beugnot. Generation of phonons from electrostriction in small-core optical waveguides. *AIP Adv.*, 3(4):042109, 2013.

[168] W. Renninger, P. Kharel, R. Behunin, and P. Rakich. Bulk crystalline optomechanics. *Nat. Phys.*, 14(6):601, 2018.

[169] M. Merklein, I. V. Kabakova, T. F. Büttner, D.-Y. Choi, B. Luther-Davies, S. J. Madden, and B. J. Eggleton. Enhancing and inhibiting stimulated Brillouin scattering in photonic integrated circuits. *Nat. Commun.*, 6:6396, 2015.

[170] C. Wolff, B. Stiller, B. J. Eggleton, M. J. Steel, and C. G. Poulton. Cascaded forward Brillouin scattering to all stokes orders. *New J. Phys.*, 19(2):023021, 2017.

[171] J. Sipe and M. Steel. A Hamiltonian treatment of stimulated Brillouin scattering in nanoscale integrated waveguides. *New J. Phys.*, 18(4):045004, 2016.

[172] P. Kharel, R. Behunin, W. Renninger, and P. Rakich. Noise and dynamics in forward Brillouin interactions. *Phys. Rev. A*, 93(6):063806, 2016.

[173] G. S. Wiederhecker, P. Dainese, and T. P. Mayer Alegre. Brillouin optomechanics in nanophotonic structures. *APL Photonics*, 4(7):071101, 2019.

[174] H. Haus. *Electromagnetic Noise and Quantum Optical Measurements.* Advanced Texts in Physics. Springer Berlin Heidelberg, 2012.

[175] R. W. Boyd, K. Rzaewski, and P. Narum. Noise initiation of stimulated Brillouin scattering. *Phys. Rev. A*, 42(9):5514, 1990.

[176] Y. London, H. H. Diamandi, G. Bashan, and A. Zadok. Invited article: Distributed analysis of nonlinear wave mixing in fiber due to forward Brillouin scattering and Kerr effects. *APL Photonics*, 3(11):110804, 2018.

[177] F. Dabby and J. Whinnery. Thermal self-focusing of laser beams in lead glasses. *Appl. Phys. Lett.*, 13(8):284–286, 1968.

[178] M. Horowitz, R. Daisy, O. Werner, and B. Fischer. Large thermal nonlinearities and spatial self-phase modulation in $Sr_xBa_{1-x}Nb_2O_6$ and $BaTiO_3$ crystals. *Opt. Lett.*, 17(7):475–477, 1992.

[179] C. Rotschild, B. Alfassi, O. Cohen, and M. Segev. Long-range interactions between optical solitons. *Nat. Phys.*, 2(11):769, 2006.

[180] Y. V. Izdebskaya, V. G. Shvedov, P. S. Jung, and W. Krolikowski. Stable vortex soliton in nonlocal media with orientational nonlinearity. *Opt. Lett.*, 43(1):66–69, 2018.

[181] E. Shahmoon, P. Grišins, H. P. Stimming, I. Mazets, and G. Kurizki. Highly nonlocal optical nonlinearities in atoms trapped near a waveguide. *Optica*, 3(7):725–733, 2016.

[182] S. Sevinçli, N. Henkel, C. Ates, and T. Pohl. Nonlocal nonlinear optics in cold Rydberg gases. *Phys. Rev. Lett.*, 107(15):153001, 2011.

[183] R. Pollard, A. Murphy, W. Hendren, P. Evans, R. Atkinson, G. Wurtz, A. Zayats, and V. A. Podolskiy. Optical nonlocalities and additional waves in epsilon-near-zero metamaterials. *Phys. Rev. Lett.*, 102(12):127405, 2009.

[184] A. Krasavin, P. Ginzburg, G. Wurtz, and A. Zayats. Nonlocality-driven supercontinuum white light generation in plasmonic nanostructures. *Nat. Commun.*, 7:11497, 2016.

[185] P. Fakhri, M. R. Vaziri, B. Jaleh, and N. P. Shabestari. Nonlocal nonlinear optical response of graphene oxide-Au nanoparticles dispersed in different solvents. *J. Opt.*, 18(1):015502, 2015.

[186] H. Shin, J. A. Cox, R. Jarecki, A. Starbuck, Z. Wang, and P. T. Rakich. Control of coherent information via on-chip photonic–phononic emitter–receivers. *Nat. Commun.*, 6:6427, 2015.

[187] E. A. Kittlaus, P. Kharel, N. T. Otterstrom, Z. Wang, and P. T. Rakich. RF-photonic filters via on-chip photonic-phononic emit-receive operations. *J. Lightwave Technol.*, 36(13):2803–2809, 2018.

[188] H. H. Diamandi, Y. London, and A. Zadok. Opto-mechanical inter-core cross-talk in multi-core fibers. *Optica*, 4(3):289–297, 2017.

[189] H. H. Diamandi, Y. London, G. Bashan, A. Bergman, and A. Zadok. Highly-coherent stimulated phonon oscillations in a multi-core optical fiber. *Sci. Rep.*, 8(1):9514, 2018.

[190] A. Y. Petrov and M. Eich. Zero dispersion at small group velocities in photonic crystal waveguides. *Appl. Phys. Lett.*, 85(21):4866–4868, 2004.

[191] Y. Zhao, Y.-N. Zhang, D. Wu, and Q. Wang. Wideband slow light with large group index and low dispersion in slotted photonic crystal waveguide. *J. Light. Technol.*, 30(17):2812–2817, 2012.

[192] B. E. Little, S. T. Chu, H. A. Haus, J. Foresi, and J.-P. Laine. Microring resonator channel dropping filters. *J. Lightwave Technol.*, 15(6):998–1005, 1997.

[193] D. Marpaung, C. Roeloffzen, R. Heideman, A. Leinse, S. Sales, and J. Capmany. Integrated microwave photonics. *Laser Photonics Rev.*, 7(4):506–538, 2013.

[194] S. Noschese, L. Pasquini, and L. Reichel. Tridiagonal Toeplitz matrices: properties and novel applications. *Numer. Linear Algebra Appl.*, 20(2):302–326, 2013.

[195] M. Raymer and J. Mostowski. Stimulated Raman scattering: unified treatment of spontaneous initiation and spatial propagation. *Phys. Rev. A*, 24(4):1980, 1981.

[196] D. Marpaung, J. Yao, and J. Capmany. Integrated microwave photonics. *Nat. Photonics*, 13(2):80, 2019.

[197] J. Capmany, B. Ortega, and D. Pastor. A tutorial on microwave photonic filters. *J. Lightwave Technol.*, 24(1):201–229, 2006.

[198] V. J. Urick, K. J. Williams, and J. D. McKinney. *Fundamentals of microwave photonics*, volume 1. John Wiley & Sons, 2015.

[199] H. Nyquist. Thermal agitation of electric charge in conductors. *Phys. Rev.*, 32(1):110, 1928.

[200] P. Kharel, C. Reimer, K. Luke, L. He, and M. Zhang. Breaking voltage–bandwidth limits in integrated lithium niobate modulators using micro-structured electrodes. *Optica*, 8(3):357–363, 2021.

[201] A. Khilo, C. M. Sorace, and F. X. Kärtner. Broadband linearized silicon modulator. *Opt. Express*, 19(5):4485–4500, 2011.

[202] V. J. Urick, M. E. Godinez, P. S. Devgan, J. D. McKinney, and F. Bucholtz. Analysis of an analog fiber-optic link employing a low-biased Mach–Zehnder modulator followed by an erbium-doped fiber amplifier. *J. Lightwave Technol.*, 27(12):2013–2019, 2009.

[203] J. Coward, C. Chalfant, and P. Chang. A photonic integrated-optic RF phase shifter for phased array antenna beam-forming applications. *J. Lightwave Technol.*, 11(12):2201–2205, 1993.

[204] S.-S. Lee, A. H. Udupa, H. Erlig, H. Zhang, Y. Chang, C. Zhang, D. H. Chang, D. Bhattacharya, B. Tsap, W. H. Steier, et al. Demonstration of a photonically controlled RF phase shifter. *IEEE Microw. Wirel. Compon. Lett.*, 9(9):357–359, 1999.

[205] E. H. Chan, W. Zhang, and R. A. Minasian. Photonic RF phase shifter based on optical carrier and RF modulation sidebands amplitude and phase control. *J. Lightwave Technol.*, 30(23):3672–3678, 2012.

[206] G. C. Valley. Photonic analog-to-digital converters. *Opt. Express*, 15(5):1955–1982, 2007.

[207] S. Xu, X. Zou, B. Ma, J. Chen, L. Yu, and W. Zou. Deep-learning-powered photonic analog-to-digital conversion. *Light Sci. Appl.*, 8(1):1–11, 2019.

[208] S. A. Pappert, R. Helkey, R. Logan, and W. Chang. Photonic link techniques for microwave frequency conversion. In *RF Photonic Technology in Optical Fiber Links*, pages 293–333. Cambridge Univ. Press, 2002.

[209] Y. Liu, A. Choudhary, D. Marpaung, and B. J. Eggleton. Integrated microwave photonic filters. *Adv. Opt. Photonics*, 12(2):485–555, 2020.

[210] D. Dolfi, F. Michel-Gabriel, S. Bann, and J.-P. Huignard. Two-dimensional optical architecture for time-delay beam forming in a phased-array antenna. *Opt. Lett.*, 16(4):255–257, 1991.

[211] J. Mena, K. Bandura, J.-F. Cliche, M. Dobbs, A. Gilbert, and Q. Y. Tang. A Radio-Frequency-over-Fiber link for large-array radio astronomy applications. *J. Instrum.*, 8(10):T10003, 2013.

[212] P. Ghelfi, F. Laghezza, F. Scotti, G. Serafino, A. Capria, S. Pinna, D. Onori, C. Porzi, M. Scaffardi, A. Malacarne, et al. A fully photonics-based coherent radar system. *Nature*, 507(7492):341–345, 2014.

[213] X. Zhang, H. Zeng, J. Yang, Z. Yin, Q. Sun, and W. Li. Novel RF-source-free reconfigurable microwave photonic radar. *Opt. Express*, 28(9):13650–13661, 2020.

[214] J. Capmany and D. Novak. Microwave photonics combines two worlds. *Nat. photonics*, 1(6):319, 2007.

[215] C. K. Madsen and J. H. Zhao. *Optical filter design and analysis*. Wiley New York, 1999.

[216] J. Capmany, B. Ortega, D. Pastor, and S. Sales. Discrete-time optical processing of microwave signals. *J. Lightwave Technol.*, 23(2):702–723, 2005.

[217] R. A. Minasian. Photonic signal processing of microwave signals. *IEEE Trans. Microw. Theory Techn.*, 54(2):832–846, 2006.

[218] J. Mora, B. Ortega, J. Capmany, J. Cruz, M. Andres, D. Pastor, and S. Sales. Automatic tunable and reconfigurable fiber-optic microwave filters based on a broadband optical source sliced by uniform fiber Bragg gratings. *Opt. Express*, 10(22):1291–1298, 2002.

[219] G. Yu, W. Zhang, and J. Williams. High-performance microwave transversal filter using fiber Bragg grating arrays. *IEEE Photon. Technol. Lett.*, 12(9):1183–1185, 2000.

[220] C. Porzi, G. Serafino, P. Velha, P. Ghelfi, and A. Bogoni. Integrated SOI high-order phase-shifted Bragg grating for microwave photonics signal processing. *J. Lightwave Technol.*, 35(20):4479–4487, 2017.

[221] M. S. Rasras, K.-Y. Tu, D. M. Gill, Y.-K. Chen, A. E. White, S. S. Patel, A. Pomerene, D. Carothers, J. Beattie, M. Beals, et al. Demonstration of a tunable microwave-photonic notch filter using low-loss silicon ring resonators. *J. Lightwave Technol.*, 27(12):2105–2110, 2009.

[222] D. Marpaung, B. Morrison, R. Pant, C. Roeloffzen, A. Leinse, M. Hoekman, R. Heideman, and B. J. Eggleton. Si_3N_4 ring resonator-based microwave photonic notch filter with an ultrahigh peak rejection. *Opt. Express*, 21(20):23286–23294, 2013.

[223] A. Biberman, M. J. Shaw, E. Timurdogan, J. B. Wright, and M. R. Watts. Ultralow-loss silicon ring resonators. *Opt. Lett.*, 37(20):4236–4238, 2012.

[224] D. Pérez, I. Gasulla, L. Crudgington, D. J. Thomson, A. Z. Khokhar, K. Li, W. Cao, G. Z. Mashanovich, and J. Capmany. Multipurpose silicon photonics signal processor core. *Nat. Commun.*, 8(1):1–9, 2017.

[225] W. Bogaerts, D. Pérez, J. Capmany, D. A. Miller, J. Poon, D. Englund, F. Morichetti, and A. Melloni. Programmable photonic circuits. *Nature*, 586(7828):207–216, 2020.

[226] D. Pérez-López, A. López, P. DasMahapatra, and J. Capmany. Multipurpose self-configuration of programmable photonic circuits. *Nat. Commun.*, 11(1):1–11, 2020.

[227] L. Zhuang, C. G. Roeloffzen, M. Hoekman, K.-J. Boller, and A. J. Lowery. Programmable photonic signal processor chip for radiofrequency applications. *Optica*, 2(10):854–859, 2015.

[228] D. P. López, A. M. Gutierrez, and J. Capmany. Microwave photonics filters using a silicon nitride programmable processor with folded heaters. In *2020 International Topical Meeting on Microwave Photonics (MWP)*, pages 50–53. IEEE, 2020.

[229] C. C. Ruppel. Acoustic wave filter technology–a review. *IEEE Trans. Ultrason., Ferroelectr.,Freq. Control*, 64(9):1390–1400, 2017.

[230] R. Aigner, G. Fattinger, M. Schaefer, K. Karnati, R. Rothemund, and F. Dumont. BAW filters for 5G bands. In *2018 IEEE International Electron Devices Meeting (IEDM)*, pages 14–5. IEEE, 2018.

[231] O. Balysheva. SAW filters for mobile communications: Achievements and prospects. In *2019 Wave Electronics and its Application in Information and Telecommunication Systems (WECONF)*, pages 1–4. IEEE, 2019.

[232] M. de Lima Jr, F. Alsina, W. Seidel, and P. Santos. Focusing of surface-acoustic-wave fields on (100) GaAs surfaces. *J. Appl. Phys.*, 94(12):7848–7855, 2003.

[233] K. C. Balram, M. I. Davanço, J. D. Song, and K. Srinivasan. Coherent coupling between radiofrequency, optical and acoustic waves in piezo-optomechanical circuits. *Nat. Photonics*, 10(5):346, 2016.

[234] L. Shao, N. Sinclair, J. Leatham, Y. Hu, M. Yu, T. Turpin, D. Crowe, and M. Lončar. Integrated microwave acousto-optic frequency shifter on thin-film lithium niobate. *Opt. Express*, 28(16):23728–23738, 2020.

[235] C. J. Sarabalis, T. P. McKenna, R. N. Patel, R. Van Laer, and A. H. Safavi-Naeini. Acousto-optic modulation in lithium niobate on sapphire. *APL Photonics*, 5(8):086104, 2020.

[236] E. A. Kittlaus, W. M. Jones, P. T. Rakich, N. T. Otterstrom, R. E. Muller, and M. Rais-Zadeh. Electrically driven acousto-optics and broadband non-reciprocity in silicon photonics. *Nat. Photonics*, 15(1):43–52, 2021.

[237] D. Munk, M. Katzman, M. Hen, M. Priel, M. Feldberg, T. Sharabani, S. Levy, A. Bergman, and A. Zadok. Surface acoustic wave photonic devices in silicon on insulator. *Nat. Commun.*, 10(1):1–9, 2019.

[238] A. Klee, A. Cramer, E. Grafer, M. Jenkins, J. Devenport, C. Middleton, and R. DeSalvo. Applications of stimulated Brillouin scattering in microwave photonic links. In *2018 IEEE Research and Applications of Photonics In Defense Conference (RAPID)*, pages 1–4. IEEE, 2018.

[239] A. Zarifi, B. Stiller, M. Merklein, Y. Liu, B. Morrison, A. Casas-Bedoya, G. Ren, T. G. Nguyen, K. Vu, D.-Y. Choi, et al. On-chip correlation-based Brillouin sensing: design, experiment, and simulation. *J. Opt. Soc. Am. B*, 36(1):146–152, 2019.

[240] A. Casas-Bedoya, B. Morrison, M. Pagani, D. Marpaung, and B. J. Eggleton. Tunable narrowband microwave photonic filter created by stimulated Brillouin scattering from a silicon nanowire. *Opt. Lett.*, 40(17):4154–4157, 2015.

[241] Y. Liu, A. Choudhary, G. Ren, K. Vu, B. Morrison, A. Casas-Bedoya, T. G. Nguyen, D.-Y. Choi, P. Ma, A. Mitchell, et al. Integration of Brillouin and passive circuits for enhanced radio-frequency photonic filtering. *APL Photonics*, 4(10):106103, 2019.

[242] M. Shi, L. Yi, W. Wei, and W. Hu. Generation and phase noise analysis of a wide optoelectronic oscillator with ultra-high resolution based on stimulated Brillouin scattering. *Opt. Express*, 26(13):16113–16124, 2018.

[243] T. Schneider. Wavelength and line width measurement of optical sources with femtometre resolution. *Electron. Lett.*, 41(22):1234–1235, 2005.

[244] S. Preussler, A. Zadok, A. Wiatrek, M. Tur, and T. Schneider. Enhancement of spectral resolution and optical rejection ratio of Brillouin optical spectral analysis using polarization pulling. *Opt. Express*, 20(13):14734–14745, 2012.

[245] A. H. Atabaki, S. Moazeni, F. Pavanello, H. Gevorgyan, J. Notaros, L. Alloatti, M. T. Wade, C. Sun, S. A. Kruger, H. Meng, et al. Integrating photonics with silicon nanoelectronics for the next generation of systems on a chip. *Nature*, 556(7701):349, 2018.

[246] D. Marpaung, B. Morrison, M. Pagani, R. Pant, D.-Y. Choi, B. Luther-Davies, S. J. Madden, and B. J. Eggleton. Low-power, chip-based stimulated Brillouin scattering microwave photonic filter with ultrahigh selectivity. *Optica*, 2(2):76–83, 2015.

[247] A. Byrnes, R. Pant, E. Li, D.-Y. Choi, C. G. Poulton, S. Fan, S. Madden, B. Luther-Davies, and B. J. Eggleton. Photonic chip based tunable and reconfigurable narrowband microwave photonic filter using stimulated Brillouin scattering. *Opt. Express*, 20(17):18836–18845, 2012.

[248] B. Vidal, M. Piqueras, and J. Martí. Tunable and reconfigurable photonic microwave filter based on stimulated Brillouin scattering. *Opt. Lett.*, 32(1):23–25, 2007.

[249] A. Choudhary, Y. Liu, D. Marpaung, and B. J. Eggleton. On-chip Brillouin filtering of RF and optical signals. *IEEE J. Sel. Top. Quantum Electron.*, 24(6):1–11, 2018.

[250] R. Parihar, R. Dhawan, S. Goel, B. O. Subham, and A. Choudhary. Design of microwave photonic subsystems using Brillouin scattering. *J. Lightwave Technol.*, 2020.

[251] A. Choudhary, I. Aryanfar, S. Shahnia, B. Morrison, K. Vu, S. Madden, B. Luther-Davies, D. Marpaung, and B. J. Eggleton. Tailoring of the Brillouin gain for on-chip widely tunable and reconfigurable broadband microwave photonic filters. *Opt. Lett.*, 41(3):436–439, 2016.

[252] Y. Liu and H. Tsang. Nonlinear absorption and Raman gain in helium-ion-implanted silicon waveguides. *Opt. Lett.*, 31(11):1714–1716, 2006.

[253] P. Dong, N.-N. Feng, D. Feng, W. Qian, H. Liang, D. C. Lee, B. Luff, T. Banwell, A. Agarwal, P. Toliver, et al. GHz-bandwidth optical filters based on high-order silicon ring resonators. *Opt. Express*, 18(23):23784–23789, 2010.

[254] M.-C. Tien, J. F. Bauters, M. J. Heck, D. T. Spencer, D. J. Blumenthal, and J. E. Bowers. Ultra-high quality factor planar Si_3N_4 ring resonators on Si substrates. *Opt. Express*, 19(14):13551–13556, 2011.

[255] D. Dai, J. Bauters, and J. E. Bowers. Passive technologies for future large-scale photonic integrated circuits on silicon: polarization handling, light non-reciprocity and loss reduction. *Light Sci. Appl.*, 1(3):e1, 2012.

[256] Y. Liu, D. Marpaung, A. Choudhary, and B. J. Eggleton. Lossless and high-resolution RF photonic notch filter. *Opt. Lett.*, 41(22):5306–5309, 2016.

[257] Y. Liu, D. Marpaung, B. J. Eggleton, and A. Choudhary. High-performance chip-assisted microwave photonic functionalities. *IEEE Photon. Technol. Lett.*, 30(21):1822–1825, 2018.

[258] J. Van Campenhout, W. M. Green, S. Assefa, and Y. A. Vlasov. Low-power, 2×2 silicon electro-optic switch with 110-nm bandwidth for broadband reconfigurable optical networks. *Opt. Express*, 17(26):24020–24029, 2009.

[259] H. Rong, R. Jones, A. Liu, O. Cohen, D. Hak, A. Fang, and M. Paniccia. A continuous-wave Raman silicon laser. *Nature*, 433(7027):725, 2005.

[260] R. W. Ridgway, C. L. Dohrman, and J. A. Conway. Microwave photonics programs at DARPA. *J. Lightwave Technol.*, 32(20):3428–3439, 2014.

[261] J. Zhang, A. N. Hone, and T. E. Darcie. Phase-modulated microwave-photonic link with optical-phase-locked-loop enhanced interferometric phase detection. *J. Lightwave Technol.*, 26(15):2549–2556, 2008.

[262] D. Zibar, L. A. Johansson, H.-F. Chou, A. Ramaaswamy, M. Rodwell, and J. E. Bowers. Phase-locked coherent demodulator with feedback and sampling for optically phase-modulated microwave links. *J. Lightwave Technol.*, 26(15):2460–2475, 2008.

[263] B. Moslehi. Noise power spectra of optical two-beam interferometers induced by the laser phase noise. *J. Lightwave Technol.*, 4(11):1704–1710, 1986.

[264] R. Tkach and A. Chraplyvy. Phase noise and linewidth in an InGaAsP DFB laser. *J. Lightwave Technol.*, 4(11):1711–1716, 1986.

[265] F. Bucholtz, V. J. Urick, M. Godinez, and K. J. Williams. Graphical approach for evaluating performance limitations in externally modulated analog photonic links. *IEEE Trans. Microw. Theory Tech.*, 56(1):242–247, 2008.

[266] W. B. Bridges and J. H. Schaffner. Distortion in linearized electrooptic modulators. *IEEE Trans. Microw. Theory Tech.*, 43(9):2184–2197, 1995.

[267] K. S. Olsson, N. Klimovich, K. An, S. Sullivan, A. Weathers, L. Shi, and X. Li. Temperature dependence of Brillouin light scattering spectra of acoustic phonons in silicon. *Appl. Phys. Lett.*, 106(5):051906, 2015.

[268] P. Kharel, Y. Chu, M. Power, W. H. Renninger, R. J. Schoelkopf, and P. T. Rakich. Ultra-high-Q phononic resonators on-chip at cryogenic temperatures. *APL Photonics*, 3(6):066101, 2018.

[269] T. Purdy, R. Peterson, P. Yu, and C. Regal. Cavity optomechanics with Si_3N_4 membranes at cryogenic temperatures. *New J. Phys.*, 14(11):115021, 2012.

[270] T. P. McKenna, R. N. Patel, J. D. Witmer, R. Van Laer, J. A. Valery, and A. H. Safavi-Naeini. Cryogenic packaging of an optomechanical crystal. *Opt. Express*, 27(20):28782–28791, 2019.

[271] R. Umar and A. U. Sheikh. A comparative study of spectrum awareness techniques for cognitive radio oriented wireless networks. *Phys. Commun.*, 9:148–170, 2013.

[272] G. W. Anderson, D. C. Webb, A. E. Spezio, and J. N. Lee. Advanced channelization for RF, microwave, and millimeter-wave applications. *Proc. IEEE*, 79(3):355–388, 1991.

[273] F. Vollmer and S. Arnold. Whispering-gallery-mode biosensing: label-free detection down to single molecules. *Nat. Methods*, 5(7):591, 2008.

[274] T. Horiguchi, T. Kurashima, and M. Tateda. Tensile strain dependence of Brillouin frequency shift in silica optical fibers. *IEEE Photon. Technol. Lett.*, 1(5):107–108, 1989.

[275] Y.-J. Pan and R.-J. Yang. A glass microfluidic chip adhesive bonding method at room temperature. *J. Micromech. Microeng.*, 16(12):2666, 2006.

[276] Y. H. Tennico, M. T. Koesdjojo, S. Kondo, D. T. Mandrell, and V. T. Remcho. Surface modification-assisted bonding of polymer-based microfluidic devices. *Sens. Actuator B-Chem.*, 143(2):799–804, 2010.

[277] S. Y. Ryu, J. Xiao, W. I. Park, K. S. Son, Y. Y. Huang, U. Paik, and J. A. Rogers. Lateral buckling mechanics in silicon nanowires on elastomeric substrates. *Nano Lett.*, 9(9):3214–3219, 2009.

[278] T. Iida, T. Itoh, D. Noguchi, Y. Takanashi, Y. Takano, and Y. Kanda. Residual lattice strain in thin silicon-on-insulator bonded wafers: Effects on electrical properties and Raman shifts. *J. Appl. Phys.*, 89(4):2109–2114, 2001.

[279] J. Wang, Y. Zhu, R. Zhang, and D. J. Gauthier. FSBS resonances observed in a standard highly nonlinear fiber. *Opt. Express*, 19(6):5339–5349, 2011.

[280] D. M. Chow, M. A. Soto, and L. Thévenaz. Frequency-domain technique to measure the inertial response of forward stimulated Brillouin scattering for acoustic impedance sensing. In *2017 25th Optical Fiber Sensors Conference (OFS)*, pages 1–4. IEEE, 2017.

[281] C. Wolff, R. Van Laer, M. J. Steel, B. J. Eggleton, and C. G. Poulton. Brillouin resonance broadening due to structural variations in nanoscale waveguides. *New J. Phys.*, 18(2):025006, 2016.

[282] A. Zarifi, B. Stiller, M. Merklein, and B. J. Eggleton. High resolution Brillouin sensing of micro-scale structures. *Appl. Sci.*, 8(12):2572, 2018.

[283] O. Mouawad, C. Strutynski, J. Picot-Clémente, F. Désévédavy, G. Gadret, J. Jules, and F. Smektala. Optical aging behaviour naturally induced on As_2S_3 microstructured optical fibres. *Opt. Mater. Express*, 4(10):2190–2203, 2014.

[284] S. Geiger, Q. Du, B. Huang, M. Y. Shalaginov, J. Michon, H. Lin, T. Gu, A. Yadav, K. A. Richardson, X. Jia, et al. Understanding aging in chalcogenide glass thin films using precision resonant cavity refractometry. *Opt. Mater. Express*, 9(5):2252–2263, 2019.

[285] N. T. Otterstrom, S. Gertler, Y. Zhou, E. A. Kittlaus, R. O. Behunin, M. Gehl, A. L. Starbuck, C. M. Dallo, A. T. Pomerene, D. C. Trotter, et al. Backscatter-immune injection-locked Brillouin laser in silicon. *Phys. Rev. Appl.*, 14(4):044042, 2020.

[286] B. Little, S. Chu, P. Absil, J. Hryniewicz, F. Johnson, F. Seiferth, D. Gill, V. Van, O. King, and M. Trakalo. Very high-order microring resonator filters for wdm applications. *IEEE Photon. Technol. Lett.*, 16(10):2263–2265, 2004.

[287] H. Qiu, F. Zhou, J. Qie, Y. Yao, X. Hu, Y. Zhang, X. Xiao, Y. Yu, J. Dong, and X. Zhang. A continuously tunable sub-gigahertz microwave photonic bandpass filter based on an ultra-high-Q silicon microring resonator. *J. Lightwave Technol.*, 36(19):4312–4318, 2018.

[288] S. Mirabbasi and K. Martin. Classical and modern receiver architectures. *IEEE Commun. Mag.*, 38(11):132–139, 2000.

[289] K.-Y. Tu, M. S. Rasras, D. M. Gill, S. S. Patel, Y.-K. Chen, A. E. White, A. Pomerene, D. Carothers, J. Beattie, M. Beals, et al. Silicon RF-photonic filter and down-converter. *J. Lightwave Technol.*, 28(20):3019–3028, 2010.

[290] J. Palací, G. E. Villanueva, J. V. Galán, J. Martí, and B. Vidal. Single bandpass photonic microwave filter based on a notch ring resonator. *IEEE Photon. Technol. Lett.*, 22(17):1276–1278, 2010.

[291] P. Alipour, A. A. Eftekhar, A. H. Atabaki, Q. Li, S. Yegnanarayanan, C. K. Madsen, and A. Adibi. Fully reconfigurable compact RF photonic filters using high-Q silicon microdisk resonators. *Opt. Express*, 19(17):15899–15907, 2011.

[292] R. S. Guzzon, E. J. Norberg, J. S. Parker, L. A. Johansson, and L. A. Coldren. Integrated InP-InGaAsP tunable coupled ring optical bandpass filters with zero insertion loss. *Opt. Express*, 19(8):7816–7826, 2011.

[293] E. J. Norberg, R. S. Guzzon, J. S. Parker, L. A. Johansson, and L. A. Coldren. Programmable photonic microwave filters monolithically integrated in InP-InGaAsP. *J. Lightwave Technol.*, 29(11):1611–1619, 2011.

[294] M. Burla, D. Marpaung, L. Zhuang, C. Roeloffzen, M. R. Khan, A. Leinse, M. Hoekman, and R. Heideman. On-chip CMOS compatible reconfigurable optical delay line with separate carrier tuning for microwave photonic signal processing. *Opt. Express*, 19(22):21475–21484, 2011.

[295] B. Guan, S. S. Djordjevic, N. K. Fontaine, L. Zhou, S. Ibrahim, R. P. Scott, D. J. Geisler, Z. Ding, and S. B. Yoo. CMOS compatible reconfigurable silicon photonic lattice filters using cascaded unit cells for RF-photonic processing. *IEEE J. Sel. Top. Quantum Electron.*, 20(4):359–368, 2013.

[296] L. Zhuang. Flexible RF filter using a nonuniform SCISSOR. *Opt. Lett.*, 41(6):1118–1121, 2016.

[297] Q. Sun, L. Zhou, L. Lu, G. Zhou, and J. Chen. Reconfigurable high-resolution microwave photonic filter based on dual-ring-assisted MZIs on the Si_3N_4 platform. *IEEE Photonics J.*, 10(6):1–12, 2018.

[298] S. Song, S. X. Chew, X. Yi, L. Nguyen, and R. A. Minasian. Tunable single-passband microwave photonic filter based on integrated optical double notch filter. *J. Lightwave Technol.*, 36(19):4557–4564, 2018.

[299] X. Xu, J. Wu, M. Tan, T. G. Nguyen, S. T. Chu, B. E. Little, R. Morandotti, A. Mitchell, and D. J. Moss. Orthogonally polarized RF optical single sideband generation and dual-channel equalization based on an integrated microring resonator. *J. Lightwave Technol.*, 36(20):4808–4818, 2018.

[300] Z. Zhu, Y. Liu, M. Merklein, O. Daulay, D. Marpaung, and B. J. Eggleton. Positive link gain microwave photonic bandpass filter using Si_3N_4-ring-enabled sideband filtering and carrier suppression. *Opt. Express*, 27(22):31727–31740, 2019.

[301] B. Zhang, K. Al Qubaisi, M. Cherchi, M. Harjanne, Y. Ehrlichman, A. N. Khilo, and M. A. Popović. Compact multi-million Q resonators and 100 MHz passband filter bank in a thick-SOI photonics platform. *Opt. Lett.*, 45(11):3005–3008, 2020.

[302] X. Xue, Y. Xuan, H.-J. Kim, J. Wang, D. E. Leaird, M. Qi, and A. M. Weiner. Programmable single-bandpass photonic RF filter based on Kerr comb from a microring. *J. Lightwave Technol.*, 32(20):3557–3565, 2014.

[303] X. Xu, J. Wu, T. G. Nguyen, M. Shoeiby, S. T. Chu, B. E. Little, R. Morandotti, A. Mitchell, and D. J. Moss. Advanced RF and microwave functions based on an integrated optical frequency comb source. *Opt. Express*, 26(3):2569–2583, 2018.

[304] X. Xu, M. Tan, J. Wu, T. G. Nguyen, S. T. Chu, B. E. Little, R. Morandotti, A. Mitchell, and D. J. Moss. Advanced adaptive photonic RF filters with 80 taps based on an integrated optical micro-comb source. *J. Lightwave Technol.*, 37(4):1288–1295, 2019.

[305] X. Xu, M. Tan, J. Wu, T. G. Nguyen, S. T. Chu, B. E. Little, R. Morandotti, A. Mitchell, and D. J. Moss. High performance RF filters via bandwidth scaling with Kerr micro-combs. *APL Photonics*, 4(2):026102, 2019.

[306] J. Hu, J. He, J. Liu, A. S. Raja, M. Karpov, A. Lukashchuk, T. J. Kippenberg, and C.-S. Brès. Reconfigurable radiofrequency filters based on versatile soliton microcombs. *Nat. Commun.*, 11(1):1–9, 2020.

[307] T. X. Huang, X. Yi, and R. A. Minasian. Single passband microwave photonic filter using continuous-time impulse response. *Opt. Express*, 19(7):6231–6242, 2011.

[308] J. Sancho, J. Bourderionnet, J. Lloret, S. Combrié, I. Gasulla, S. Xavier, S. Sales, P. Colman, G. Lehoucq, D. Dolfi, et al. Integrable microwave filter based on a photonic crystal delay line. *Nat. Commun.*, 3(1):1–9, 2012.

[309] Y. Liu, J. Hotten, A. Choudhary, B. J. Eggleton, and D. Marpaung. All-optimized integrated RF photonic notch filter. *Opt. Lett.*, 42(22):4631–4634, 2017.

[310] J. S. Fandiño, P. Muñoz, D. Doménech, and J. Capmany. A monolithic integrated photonic microwave filter. *Nat. Photonics*, 11(2):124, 2017.

[311] A. J. Metcalf, H.-J. Kim, D. E. Leaird, J. A. Jaramillo-Villegas, K. A. McKinzie, V. Lal, A. Hosseini, G. E. Hoefler, F. Kish, and A. M. Weiner. Integrated line-by-line optical pulse shaper for high-fidelity and rapidly reconfigurable RF-filtering. *Opt. Express*, 24(21):23925–23940, 2016.

[312] S. Mohammadi, A. A. Eftekhar, A. Khelif, W. D. Hunt, and A. Adibi. Evidence of large high frequency complete phononic band gaps in silicon phononic crystal plates. *Appl. Phys. Lett.*, 92(22):221905, 2008.

[313] Z. Jia, Y. Chen, H. Yang, and L. Wang. Designing phononic crystals with wide and robust band gaps. *Phys. Rev. Appl.*, 9(4):044021, 2018.

[314] G. T. Reed, G. Mashanovich, F. Y. Gardes, and D. Thomson. Silicon optical modulators. *Nat. Photonics*, 4(8):518, 2010.

[315] J. Yao. Photonics to the rescue: A fresh look at microwave photonic filters. *IEEE Microw. Mag.*, 16(8):46–60, 2015.

[316] E. Xu and J. Yao. Frequency-and notch-depth-tunable single-notch microwave photonic filter. *IEEE Photon. Technol. Lett.*, 27(19):2063–2066, 2015.

[317] W. Zhang and R. A. Minasian. Ultrawide tunable microwave photonic notch filter based on stimulated Brillouin scattering. *IEEE Photon. Technol. Lett.*, 24(14):1182–1184, 2012.

[318] C. Feng, S. Preussler, and T. Schneider. Investigation of the dispersion effect on stimulated Brillouin scattering based microwave photonic notch filters. In *2018 International Topical Meeting on Microwave Photonics (MWP)*, pages 1–4. IEEE, 2018.

[319] P. Zheng, H. Hong, J. Li, G. Hu, B. Yun, and Y. Cui. Performances of microwave photonic notch filter based on microring resonator with dual-drive modulator. *IEEE Photonics J.*, 11(1):1–13, 2018.

[320] O. Daulay, G. Liu, and D. Marpaung. Microwave photonic notch filter with integrated phase-to-intensity modulation transformation and optical carrier suppression. *Opt. Lett.*, 46(3):488–491, 2021.

[321] Y. Liu, Y. Yu, S. Yuan, X. Xu, and X. Zhang. Tunable megahertz bandwidth microwave photonic notch filter based on a silica microsphere cavity. *Opt. Lett.*, 41(21):5078–5081, 2016.

[322] Z. Yuan, X. Lou, and Y. Dong. Microwave photonic notch filter with a tunable frequency and a bandwidth based on gas absorption. *Opt. Lett.*, 45(1):248–251, 2020.

[323] J. Dong, L. Liu, D. Gao, Y. Yu, A. Zheng, T. Yang, and X. Zhang. Compact notch microwave photonic filters using on-chip integrated microring resonators. *IEEE Photonics J.*, 5(2):5500307–5500307, 2013.

[324] Y. Long and J. Wang. Ultra-high peak rejection notch microwave photonic filter using a single silicon microring resonator. *Opt. Express*, 23(14):17739–17750, 2015.

[325] S. X. Chew, X. Yi, S. Song, L. Li, P. Bian, L. Nguyen, and R. A. Minasian. Silicon-on-insulator dual-ring notch filter for optical sideband suppression and spectral characterization. *J. Lightwave Technol.*, 34(20):4705–4714, 2016.

[326] X. Liu, Y. Yu, H. Tang, L. Xu, J. Dong, and X. Zhang. Silicon-on-insulator-based microwave photonic filter with narrowband and ultrahigh peak rejection. *Opt. Lett.*, 43(6):1359–1362, 2018.

[327] H. Jayatilleka, H. Shoman, L. Chrostowski, and S. Shekhar. Photoconductive heaters enable control of large-scale silicon photonic ring resonator circuits. *Optica*, 6(1):84–91, 2019.

[328] Z. Yu and S. Fan. Complete optical isolation created by indirect interband photonic transitions. *Nat. Photonics*, 3(2):91–94, 2009.

[329] D. B. Sohn, S. Kim, and G. Bahl. Time-reversal symmetry breaking with acoustic pumping of nanophotonic circuits. *Nat. Photonics*, 12(2):91, 2018.

[330] C. J. Sarabalis, R. Van Laer, R. N. Patel, Y. D. Dahmani, W. Jiang, F. M. Mayor, and A. H. Safavi-Naeini. Acousto-optic modulation of a wavelength-scale waveguide. *Optica*, 8(4):477–483, 2021.

[331] N. Dostart, Y. Ehrlichman, C. Gentry, and M. A. Popović. Integrated optical isolators using electrically driven acoustic waves. *Opt. Express*, 28(24):36055–36069, 2020.

[332] L. Ranzani and J. Aumentado. Graph-based analysis of nonreciprocity in coupled-mode systems. *New J. Phys.*, 17(2):023024, 2015.

[333] M. Tymchenko, D. Sounas, and A. Alù. Composite Floquet scattering matrix for the analysis of time-modulated systems. In *2017 IEEE International Symposium on Antennas and Propagation & USNC/URSI National Radio Science Meeting*, pages 65–66. IEEE, 2017.

[334] L. Yin, Q. Lin, and G. P. Agrawal. Dispersion tailoring and soliton propagation in silicon waveguides. *Opt. Lett.*, 31(9):1295–1297, May 2006.

[335] X. Liu, W. M. J. Green, X. Chen, I.-W. Hsieh, J. I. Dadap, Y. A. Vlasov, and J. Richard M. Osgood. Conformal dielectric overlayers for engineering dispersion and effective nonlinearity of silicon nanophotonic wires. *Opt. Lett.*, 33(24):2889–2891, December 2008.

[336] L. Zhang, Y. Yue, R. G. Beausoleil, and A. E. Willner. Flattened dispersion in silicon slot waveguides. *Opt. Express*, 18(19):20529–20534, September 2010.

[337] M. Zhu, H. Liu, X. Li, N. Huang, Q. Sun, J. Wen, and Z. Wang. Ultrabroadband flat dispersion tailoring of dual-slot silicon waveguides. *Opt. Express*, 20(14):15899–15907, July 2012.

[338] L. Zhang, Q. Lin, Y. Yue, Y. Yan, R. G. Beausoleil, and A. E. Willner. Silicon waveguide with four zero-dispersion wavelengths and its application in on-chip octave-spanning supercontinuum generation. *Opt. Express*, 20(2):1685–1690, January 2012.

[339] H. Ryu, J. Kim, Y. M. Jhon, S. Lee, and N. Park. Effect of index contrasts in the wide spectral-range control of slot waveguide dispersion. *Opt. Express*, 20(12):13189–13194, June 2012.

[340] H. Liang, Y. He, R. Luo, and Q. Lin. Ultra-broadband dispersion engineering of nanophotonic waveguides. *Opt. Express*, 24(26):29444–29451, December 2016.

[341] A. V. Oppenheim. *Discrete-time signal processing*. Pearson Education India, 1999.

[342] R. Kashyap. *Fiber Bragg gratings*. Academic press, 2009.

[343] S. Harris, S. Nieh, and R. Feigelson. $CaMoO_4$ electronically tunable optical filter. *Appl. Phys. Lett.*, 17(5):223–225, 1970.

[344] L. Kuhn, P. Heidrich, and E. Lean. Optical guided wave mode conversion by an acoustic surface wave. *Appl. Phys. Lett.*, 19(10):428–430, 1971.

[345] H. Sasaki, J. Kushibiki, and N. Chubachi. Efficient acousto-optic TE⇌TM mode conversion in ZnO films. *Appl. Phys. Lett.*, 25(9):476–477, 1974.

[346] Y. Ohmachi and J. Noda. $LiNbO_3$ TE–TM mode converter using collinear acoustooptic interaction. *IEEE J. Quantum Electron.*, 13(2):43–46, 1977.

[347] L. Binh, J. Livingstone, and D. Steven. Tunable acousto-optic TE–TM mode converter on a diffused optical waveguide. *Opt. Lett.*, 5(3):83–84, 1980.

[348] D. B. Sohn and G. Bahl. Direction reconfigurable nonreciprocal acousto-optic modulator on chip. *APL Photonics*, 4(12):126103, 2019.

[349] H. Haus and K. Šipilov. *Waves and Fields in Optoelectronics*. Prentice-Hall series in solid state physical electronics. Prentice-Hall, 1984.

[350] J. Joannopoulos, S. Johnson, J. Winn, and R. Meade. *Photonic Crystals: Molding the Flow of Light - Second Edition*. Princeton University Press, 2011.

[351] J. S. Domingo, J. Pelayo, F. Villuendas, C. Heras, and E. Pellejer. Very high resolution optical spectrometry by stimulated Brillouin scattering. *IEEE Photon. Technol. Lett.*, 17(4):855–857, 2005.

[352] Y. Stern, K. Zhong, T. Schneider, Y. Ben-Ezra, R. Zhang, M. Tur, and A. Zadok. Brillouin optical spectrum analyzer monitoring of subcarrier-multiplexed fiber-optic signals. *Appl. Opt.*, 52(25):6179–6184, 2013.

[353] S. Preussler, A. Wiatrek, K. Jamshidi, and T. Schneider. Brillouin scattering gain bandwidth reduction down to 3.4 MHz. *Opt. Express*, 19(9):8565–8570, 2011.

[354] S. Preussler, A. Wiatrek, K. Jamshidi, and T. Schneider. Ultrahigh-resolution spectroscopy based on the bandwidth reduction of stimulated Brillouin scattering. *IEEE Photon. Technol. Lett.*, 23(16):1118–1120, 2011.

[355] S. Preussler and T. Schneider. Attometer resolution spectral analysis based on polarization pulling assisted Brillouin scattering merged with heterodyne detection. *Opt. Express*, 23(20):26879–26887, 2015.

[356] C. Wolff, P. Gutsche, M. J. Steel, B. J. Eggleton, and C. G. Poulton. Impact of nonlinear loss on stimulated Brillouin scattering. *JOSA B*, 32(9):1968–1978, 2015.

[357] R. Van Laer, A. Bazin, B. Kuyken, R. Baets, and D. Van Thourhout. Net on-chip Brillouin gain based on suspended silicon nanowires. *New J. Phys.*, 17(11):115005, 2015.

[358] R. Dekker, N. Usechak, M. Först, and A. Driessen. Ultrafast nonlinear all-optical processes in silicon-on-insulator waveguides. *J. Phys. D: Appl. Phys*, 40(14):R249, 2007.

[359] R. Claps, V. Raghunathan, D. Dimitropoulos, and B. Jalali. Influence of nonlinear absorption on Raman amplification in silicon waveguides. *Opt. Express*, 12(12):2774–2780, 2004.

[360] S. Afshar and T. M. Monro. A full vectorial model for pulse propagation in emerging waveguides with subwavelength structures part I: Kerr nonlinearity. *Opt. Express*, 17(4):2298–2318, 2009.

[361] C. Wolff, P. Gutsche, M. J. Steel, B. J. Eggleton, and C. G. Poulton. Power limits and a figure of merit for stimulated Brillouin scattering in the presence of third and fifth order loss. *Opt. Express*, 23(20):26628–26638, 2015.

[362] M. Dinu, F. Quochi, and H. Garcia. Third-order nonlinearities in silicon at telecom wavelengths. *Appl. Phys. Lett.*, 82(18):2954–2956, 2003.

[363] G. Thurner and R. Abermann. Internal stress and structure of ultrahigh vacuum evaporated chromium and iron films and their dependence on substrate temperature and oxygen partial pressure during deposition. *Thin Solid Films*, 192(2):277–285, 1990.

[364] B. D. Chalifoux, Y. Yao, K. B. Woller, R. K. Heilmann, and M. L. Schattenburg. Compensating film stress in thin silicon substrates using ion implantation. *Opt. Express*, 27(8):11182–11195, 2019.

[365] H. Rong, A. Liu, R. Jones, O. Cohen, D. Hak, R. Nicolaescu, A. Fang, and M. Paniccia. An all-silicon Raman laser. *Nature*, 433(7023):292–294, 2005.

[366] B. Saleh and M. Teich. *Fundamentals of Photonics*. Wiley Series in Pure and Applied Optics. Wiley, 2007.

[367] N. S. Lagali. *The generalized Mach-Zehnder interferometer using multimode interference couplers for optical communications networks*. PhD thesis, University of Alberta, 2000.

[368] L. B. Soldano and E. C. Pennings. Optical multi-mode interference devices based on self-imaging: principles and applications. *J. Lightwave Technol.*, 13(4):615–627, 1995.

[369] M. Bachmann, P. A. Besse, and H. Melchior. General self-imaging properties in N×N multimode interference couplers including phase relations. *Appl. Opt.*, 33(18):3905–3911, 1994.

[370] M. Bachmann, P. Besse, and H. Melchior. Overlapping-image multimode interference couplers with a reduced number of self-images for uniform and nonuniform power splitting. *Appl. Opt.*, 34(30):6898–6910, 1995.

[371] J. Leuthold, J. Eckner, E. Gamper, P. A. Besse, and H. Melchior. Multimode interference couplers for the conversion and combining of zero-and first-order modes. *J. Lightwave Technol.*, 16(7):1228, 1998.

[372] T. Uematsu, Y. Ishizaka, Y. Kawaguchi, K. Saitoh, and M. Koshiba. Design of a compact two-mode multi/demultiplexer consisting of multimode interference waveguides

and a wavelength-insensitive phase shifter for mode-division multiplexing transmission. *J. Lightwave Technol.*, 30(15):2421–2426, 2012.

[373] K. S. Chiang. Effective-index analysis of optical waveguides. In *Physics and Simulation of Optoelectronic Devices III*, volume 2399, pages 2–13. International Society for Optics and Photonics, 1995.

[374] K. Okamoto. *Fundamentals of optical waveguides*. Academic press, 2006.